ANNUAL REPORT

OF THE

INSTITUTE OF PHYSICS

ACADEMIA SINICA

1972

Published by

The Institute of physics, Academia Sinica

Nankang, Taipei, Taiwan, Republic of China

August 1973

中央研究院物理研究所集刊

編輯委員會

本集刊每年在八月出版一次

非　賣　品

中央研究院

物理研究所集刊

第三卷

發行人：吳　大　猷

編輯者：中央研究院物理研究所集刊編輯委員會

出版者：中央研究院物理研究所　臺北市南港區

印刷者：崇　文　企　業　有　限　公　司

中華民國六十二年八月出版

中央研究院物理研究所集刊

第 三 卷

中央研究院物理研究所印行

CONTENTS 目 錄

Annual Report of the Institute of Physics, Academia Sinica, 1972

The Collisional Broadening of Hydrogen Lines in the Nebulae

Ta-You Wu (吳大猷)

Department of Physics and Astronomy

State University of New York at Buffalo

Abstract

The theory of Baranger and Griem of the collisional broadening of spectral lines as applied to the observed widths of hydrogen lines in the nebulae seems to lead to rather low values for the electron desnities of the emitting regions. In Griem's work, in calculating the collisional transition probabilities, the dipole approximation is made for the interaction between the hydrogen atom and the colliding electron. In the present work, an estimate has been made for a correction factor for this approximation. It is found that for states $n = 170$, $n = 240$ and electron temperatures $7000°K - 10^4°K$, the dipole approximation overestimates the transition probability rates by a factor $\sim \frac{1}{0.51}$. This correction will reduce the theoretical collisional width in Griem's theory by a factor 0.5.

In the present work, it has also been found that the effect of exchange on the transition probabilities for the above states n and electron energies is entirely negligible.

I. INTRODUCTION

In recent years, radioastronomy has been extended to the observation and the accurate measurement on the emission lines of hydrogen in the HII region in certain nebulae, corresponding to transitions from high levels n (n=253, Penfield, Palmer and Zuckerman, 1967; n=248, Parrish, Pankonin, Hailes, Rankin, Terzian, 1972). From the measured widths of the spectral lines, it is possible to deduce some information concerning the physical state of the emitting region, such as the "temperature" and the electron and ion densities. The theoretical analysis is based on the theory of such processes as Doppler effect and the collision effect. By the latter is meant the broadening of the energy levels due to the interaction between an incident electron or ion and the emitting atom. The theory of this collisional broadening has been developed by Baranger (Baranger, 1958, 1963), Griem (Griem, 1967) and others (Brockehurst and Leeman, 1971, and Peach, 1972). The observed widths however, for H248α by Parrish et al(Parrish et al, 1972) and for H225δ by Williams (Williams, 1967) seem to have been completely accounted for by Doppler broadening alone. If the theoretical values for $\Delta\omega_c$ are accepted, they will set an upper limit to the electron density in the emitting region.

Since the disagreement between the observed widths and the theoretical values is of

concern in relation to the question of the temperature and the electron density of the region of emission, it is of interest to reexamine the problem of "Stark" or "collisional" broadening of the energy levels of an atom, in view of certain approximations made in Griem's theory.

One of the approximations is the dipole approximation for the interaction between the hydrogen atom and the colliding electron in the evaluation of the transition probabilities, i.e., the replacement of

$$V = -e^2\left(\frac{1}{R} - \frac{1}{|\vec{R}-\vec{r}|}\right) \tag{1}$$

by

$$V' = -e^2\frac{(\vec{r}\cdot\vec{R})}{R^3} \tag{2}$$

where r is the atomic electron coordinate and R the incident electron coordinate.

Consider the transition probability $W_{n,n'}$ per second of the hydrogen atom in an inelastic collision with energy $\frac{1}{2m}\hbar^2k^2$. It is given by

$$W_{n,n'} = \frac{2\pi}{\hbar}\int |\langle n,\ k|V|n'\ ,k'\rangle|^2 \frac{mk'\hbar\Omega}{(2\pi\hbar)^3}\sin\theta d\theta d\phi \tag{3}$$

where $\langle n,k|V|n',k'\rangle$ is the matrix element between the initial and the final state of the system (atom + colliding electron), Ω the normalization volume of the colliding electron, and the integration is over the scattering angles θ,ϕ. In Born approximation,

$$|k\rangle = \frac{1}{\sqrt{\Omega}}e^{i\mathbf{k}\cdot\mathbf{R}}\ ,\quad |k'\rangle = \frac{1}{\sqrt{\Omega}}e^{i\mathbf{k}'\cdot\mathbf{R}}$$

and

$$\langle n,k|V|n'\ ,k'\rangle = -\frac{4\pi e^2}{\Omega Q^2}\langle n|1-e^{i\mathbf{Q}\cdot\mathbf{r}}|n'\rangle \tag{4}$$

$$\langle n,k|V'|n'\ ,k'\rangle = -\frac{4\pi e^2}{\Omega Q}\langle n|z|n'\rangle \tag{5}$$

where

$$E_n + \frac{\hbar^2k^2}{2m} = E_{n'} + \frac{\hbar^2k'^2}{2m} \tag{6}$$

$$Q^2 = k^2 + k'^2 - 2kk'\cos\theta \tag{7}$$

θ being the angle between k' and k, the scattering angle.

The evaluation of (5) is elementary, but the evaluation of (4) in spherical polar coordinates for $|n\rangle$ is extremely inconvenient for large values of n and ℓ. To estimate the effect of the dipole approximation (5), we may evaluate both (4) and (5) for $|n\rangle$, $|n'\rangle$ in parabolic coordinates. Consider the transition

$$|n,o,o,n-l\rangle|k\rangle \to |n+l,l,o,n-l\rangle|k'\rangle \tag{8}$$

where n (n,k_1,k_2,M) are the quantum numbers of a state in parabolic coordinates. With the formulas given in the Appendix, we obtain, for V in (1),

$$W_{n,n'} = \frac{\pi\mu a_0^2e^4}{\Omega k\hbar^3}\left[\frac{2n(2n+2)}{(2n+1)^2}\right]^{2n+1}n^2(n+1)\int_{x_{min}}^{x_{max}}\frac{dx}{x(1+x)^{3n+3}} \tag{9}$$

and for the dipole approximation (2),

$$W'_{n,n'} = \frac{\pi\mu a_0^2 e^4}{k\hbar^3}\left[\frac{2n(2n+2)}{(2n+1)^2}\right]^{2n+1} n^2(n+1)\int_{x_{min}}^{x_{max}} \frac{dx}{x} \tag{10}$$

where

$$x_{min} = \left[\frac{n(n+1)}{2n+1}\right] a_0|k-k'| \,, \tag{11}$$

$$x_{max} = \left[\frac{n(n+1)}{2n+1}\right] a_0|k+k'|$$

For large n, the integrand in (9) is much smaller than that in (10) for both small and large x, showing that the dipole approximation overestimates the contribution for both large and small distances.

The integral in (9) can be calculated

$$\int_{x_{min}}^{x_{max}} \frac{dx}{x(1+x)^{2n+3}} = \ell n \frac{x_{min}+1}{x_{min}} - \sum_{j=1}^{2n+2} \frac{1}{j} - \ell n \frac{x_{max}+1}{x_{max}}$$

For the relevant values of k, k' and n, x_{min} is $0(10^{-8})$ and x_{max} is $0(10^{8})$. Actual calculation gives for the ratio of the two integrals in (9) and (10), and hence

$$\frac{W_{n,n+1}}{W'_{n,n+1}} = 0.511 \text{ for } n = 170 \tag{12}$$

$$= 0.510 \text{ for } n = 240 \,.$$

The value of the ratio of the two expressions in (9) and (10) is not sensitive to the value of k within such a range of temperatures as 10^4 °K - 7×10^3 °K. For other transitions such as $|n,1,o,n-2\rangle \rightarrow |n+1,2,o,n-2\rangle$,..the integrals corresponding to (9) look more complicated, but the ratio (12) remains practically the same.

In Griem's theory, the dipole approximation has been used. Thus we suggest that a correction be applied by multiplying the $\Delta\omega_c$ on that theory by the above factor 0.51, even though in griem's work the incident electron is represented by a classical trajectory whereas the ratio (12) has been obtained on the Born approximation.//

Another effect in all electron-atom collisions is the exchange effect as the result of the Pauli principle. To estimate this effect, a somewhat lengthy calculation has been carried out and it is found that for such transitions $n \rightarrow n'$ as $n,n' \sim 240$ and $T_e \sim 10^4$°K (electron energies about^1 electron volt), the effect entirely negligible. This is just as expected since the electron energy is 10^4 times the binding energy of the electron in these states and is not "slow".

The writer is grateful to his colleague Dr. Y. C. Lee for helpful discussions and to Dr. V. Pankonin for useful comments.

// The classical approximation should be valid for slow electrons, although the introduction of maximum and minimum impact parameters in griem's work leads to the ratio

$$\frac{\rho max}{\rho min} = \sqrt{\frac{6}{5}}\,\frac{v_e^2 n\hbar^2}{e^4} \tag{6}$$

which becomes less than 1 for $n \leq 24$ —— a somewhat unsatisfactory feature even though we are not here concerned with such "low" states.

On the other hand, the Born approximation has neglected the "distortion" of the plane waves and the coupling of all scattering states. The ratio (12), however, may be expected to be valid even though the absolute values of the transition probabiliiies are not accurate.

APPENDIX

The matrix elements of V in (3)

$$\langle n,K|\frac{1}{R}-\frac{1}{|R-r|}|n',K'\rangle=\frac{4\pi}{Q^2}\langle n|1-e^{iQr}|n'\rangle$$

can be evaluated in parabolic coordinates. The hydrogenic wave function is

$$\psi n,k_1,k_2,M=N_{n,k_1,k_2,M}\,e^{-\frac{\mu}{2}(\xi+\eta)}(\xi\eta)^{\frac{M}{2}}L^M_{M+k_1}(\mu\xi)\,L^M_{M+k_2}(\mu\eta)\,e^{\pm iM\phi}$$

$$Nnk_1k_2M=\frac{1}{\sqrt{2\pi}}\left[\frac{2\,k_1!k_2!\mu^3}{n(M+k_1)!^3\,(M+k_2)!^3}\right]^{1/2}\mu^M\ ,\ M=0,1,\ldots n-1,$$

$$n=\frac{1}{na_0}\ ,\ d\vec{r}=\frac{1}{4}(\xi+\eta)\,d\xi\,d\eta\,d\phi\ . \tag{A1}$$

One meets integrals of the type

$$\int_0^\infty e^{-\lambda x}\,x^{c+d}\,L^c_m(ax)L^c_n(bx)\,dx\ ,\ d=0,1,2,\ldots \tag{A2}$$

$$Re\ \lambda>0\ .$$

Elwert (Elwert, 1955) has applied Kallmann and Päsler's (Kallmann and Päsler, 1950) method of Laplace transform to evaluate this integral. The result is expressed in the form of a series whose successive terms contain various orders of differentiation of a certain function, and is therefore not quite explicit. We have obtained, by the method of generating functions, the following result for $\alpha=0,1,2$.

The associated Laguerre polynomial $L^\beta_n(x)$ here is as defined in the physics literature (differently from many mathematical works)

$$L^c_n(x)=(-1)^c\,n!\sum_{k=0}^{n-c}\binom{n}{c+k}\frac{1}{k!}(-x)^k.$$

Let

$$\sigma=\frac{\lambda-a}{\lambda}\ ,\ \tau=\frac{\lambda-b}{\lambda}\ ,\ \rho=\frac{b+a-\lambda}{\lambda}\ ,\ \xi=\frac{\sigma\tau}{\rho}\ .$$

$$I_0\equiv\int_0^\infty e^{-\lambda x}\,x^c\,L^c_m(ax)\,L^c_n(bx)\,dx$$

$$=\frac{m!n!}{\lambda^{c+1}}\rho^{n-c}\,\sigma^{m-n}\sum_{s=0}^{n-c}\frac{(m+s)!}{(n-c-s)!(m-n+s)!s!}\,\xi^s \tag{A3}$$

$$I_1\equiv\int_0^\infty e^{-\lambda x}\,x^{c+l}\,L^c_m(ax)\,L^c_n(bx)\,dx$$

$$= \frac{m!n!}{\lambda^{c+2}} \rho^{n-c} \sigma^{m-n} \left[\sum_{s=0}^{n-c} \frac{(m+1+s)!}{(n-c-s)!(m-n+s)!s!} \xi^s \right.$$

$$+ \frac{1}{\rho} \sum_{s=0}^{n-c-1} \frac{(m+s)!}{(n-c-1-s)!(m-n+s)!s!} \xi^s - \frac{1}{\sigma} \sum_{s=0}^{n-c} \frac{(m+s)!}{(n-c-s)!(m-n-1+s)!s!} \xi^s$$

$$\left. - \frac{\sigma}{\rho} \sum_{s=0}^{n-c-1} \frac{(m+1+s)!}{(n-c-1-s)!(m-n+1+s)!s!} \xi^s \right] \qquad \text{(A4)}$$

$$I_2 = \int_0^\infty e^{-\lambda x} x^{c+2} L_m^c (ax) L_n^c (bx) dx$$

$$= \frac{m!n!}{\lambda^{c+3}} \rho^{n-c} \sigma^{m-n} \left\{ \sum_{s=0}^{n-c} \frac{(m+2+s)!}{(n-c-s)!(m-n+s)!s!} \xi^s \right.$$

$$+ \frac{4}{\rho} \sum_{s=0}^{n-c-1} \frac{(m+1+s)!}{(n-c-1-s)!(m-n+s)!s!} \xi^s + \frac{1}{\rho^2} \sum_{s=0}^{n-c-2} \frac{(m+s)!}{(n-c-2-s)!(m-n+s)!s!} \xi^s$$

$$- \frac{2}{\sigma} \sum_{s=0}^{n-c} \frac{(m+1+s)!}{(n-c-s)!(m-n-1+s)!s!} \xi^s - \frac{2\sigma}{\rho} \sum_{s=0}^{n-c-1} \frac{(m+2+s)!}{(n-c-1-s)!(m-n+1+s)!s!} \xi^s$$

$$- \frac{2}{\sigma\rho} \sum_{s=0}^{n-c-1} \frac{(m+s)!}{(n-c-1-s)!(m-n-1+s)!s!} \xi^s - \frac{2\sigma}{\rho^2} \sum_{s=0}^{n-c-2} \frac{(m+1+s)!}{(n-c-2-s)!(m-n+1+s)!s!} \xi^s$$

$$+ \frac{1}{\sigma^2} \sum_{s=0}^{n-c} \frac{(m+s)!}{(n-c-s)!(m-n-2+s)!s!} \xi^s + \frac{\sigma^2}{\rho^2} \sum_{s=0}^{n-c-2} \frac{(m+2+s)!}{(n-c-2-s)!(m-n+2+s)!s!} \xi^s \Big\} \qquad \text{(A5)}$$

(A3), (A4), (A5) are for $m \geq n$. For $m < n$, one interchanges the role of m and n (and a, b). In all cases, s must be such that there are no factorials of negative integers. From these formulas, one obtains for the case

$$\lambda = \frac{a+b}{2} \ , \ \xi = -\left(\frac{b-a}{b+a}\right)^2 \ ,$$

the results of Kallmann and Päsler (Kallmann and Päsler, 1950) in a different form. (A3), (A4) express the result of Elwert (Elwert, 1955) in a much more explicit form.

REFERENCES

Baranger, M. (1958), Phys. Rev. **171**, 481, 494; **112**, 855

Baranger, M, (1962), Article in Atomic and Molecular Processes, D. R. Bates, editor, Academic Press, N.Y.

Brockehurst, M. and Leeman, S. (1971), Nature Phys. Sci. **231**, 49

Elwert, G. (1955), Z.F. Naturforsch, **10A**, 361.

Griem, H.R. (1967), Ap. J. 148, 547.

Kallman, H. and Pasler, M. (1950), Z.f. Phys. **128**, 178.

Parrish. A., Pankonin, V., Hailes, E.E., Rankin, J. M. and Terzian, Y. (1972), Ap. J. 178, 673.

Peach, G. (1972) Ap. Letters **10**, 129.

Penfield, Palmer, and Zuckerman (1967), Ap. J. Letters 148, 125

Williams, (1967), Ap. Letters **1**, 59

Annual Report of the Institute of Physics, Academia Sinica, 1972

Gamma Rays from Thermal Neutron Capture in ^{128}Te

H. Y. YU (余祥雲), E. K. LIN (林爾康)
and W. N. WANG (王唯農)

Tsing Hua University and Academia Sinica, Taiwan

(Received 20 September 1972)

Thermal neutron capture gamma rays from ^{128}Te have been measured by means of a 43 cm^3 Ge(Li) detector and a NaI(Tl) scintillator. A great number of gamma rays has been identified belonging to the energy levels in ^{129}I populated in the beta decay of ^{129}Te from ^{128}Te (n, γ) reaction. The detailed decay scheme of ^{129}I was constructed. Possible transitions between levels of ^{129}I were given and discussed.

I. INTRODUCTION

THE measurement of gamma rays is one of the principal ways of establishing the decay schemes of radioactive nuclei and of observing the levels excited in nuclear reactions. An analysis of the transition energies as derived from gamma-ray measurements is a convenient starting point for the construction of an energy level scheme. The method of analysis is based on the Ritz combination principle first employed in optical spectroscopy. If one has three gamma rays which are thought to connect three levels and it is believed that two of the gamma rays are in cascade while the third is a cross over transition, then the sum of the first two energies must equal to the third within the errors of measurement. Measurements of coincidences between gamma rays or conversion lines are useful for determining the cascade relationships between transitions. Such data alone can establish cascades or they can confirm cascade-crossover sum relationships.

Gamma-ray energy, intensity, and coincidence measurements can do much toward establishing the positions of levels and the order of transitions. For example, the nuclear energy levels of ^{129}I have been investigated experimentally[1-7]

* Work performed at the Physics Research Center in Hsinchu and supported by the Academia Sinica and Tsing Hua University.

(1) W. E. Graves and A. C. G. Mitchell, Phys. Rev. **101**, 701 (1956).
(2) A. V. Ramayya, Y. Yoshizawa, and A. C. C. Mitchell, Nucl. Phys. **56**, 129 (1964).
(3) S. H. Devare and H. G. Devare, Phys. Rev. **134**, B705 (1964).
(4) J. P. Hurley and J. M. Mathiesen, Nucl. Phys. **73**, 328 (1965).
(5) D. D. Bornemeier, V. R. Potnis, L. D. Ellsworth and C. E. Mandeville, Phys. Rev. **138**, B525 (1965).
(6) G. Berzins, L. M. Beyer, W. H. Kelly, W. B. Walters and G. E. Gordon, Nucl. Phys. **A93**, 456 (1967).
(7) W. C. Dickinson, S. D. Bloom and L. G. Mann, Nucl. Phys. **A123**, 481 (1969).

*This paper has been publish in Chinese Jaurnal of Physcis vol 11, No. 1 (1973) 1 - 17

through the β^- decay of ^{129m}Te (33 days) and ^{129g}Te (70 m). Results of these experiments show that ^{129m}Te decays by de-excitation of the 105 keV isomeric state to the ^{129g}Te ground state and both ^{129m}Te and ^{129g}Te decay by β^- transition to the excited states in ^{129}I. However, the observed gamma rays and proposed decay schemes in these experiments showed somewhat disagreement with each other. In the present work we undertook a detailed study of the decay spectrum for the energy levels of ^{129}I, employing a 43 c. c. coaxial Ge(Li) detector of better energy resolution and efficiency than those of previous works. Also, the decay scheme was studied with slow gamma-gamma coincidence measurement.

II. SOURCE PREPARATION

The ^{129m}Te and ^{129g}Te sources were obtained by irradiating 100 mg samples of tellurium powder, enriched to 99.46% in ^{128}Te (see ref. 8), in a thermal neutron flux of about 5×10^{11} n-cm^{-2}-sec^{-1} for 30 hours in the reactor of National Tsing Hua University. After 10 days cooling period the ^{129}Te sample was chemically purified in a procedure similar to that described by Hahn[9]. The priminary thermal neutrons capture reaction on ^{128}Te produced the desired source material ^{129}Te. However, the presence of small amounts of ^{120}Te, ^{122}Te, ^{124}Te, ^{126}Te and ^{130}Te in the enriched ^{128}Te sample[8] produced the activities of ^{121}Te, ^{123m}Te, ^{125m}Te, ^{127}Te, ^{127m}Te, ^{131}Te, respectively, all with half-lives longer than that of 33 days ^{129m}Te. In addition to the tellurium impurities an easily detectably admixture of ^{109}Ag was found to be present in the prepared source. Since in the chemical purification, silver is added routinely as a carrier and then removed subsequently in the separation, approximately 0.1% of the silver remains after one separation procedure. Because of high thermal neutron capture cross section a small amount of silver contanmination will lead to considerable production of 250 days ^{110m}Ag in the irradiation process. We have identified a number of gamma rays belonging to the decay of ^{110m}Ag in present measurement.

III. APPARATUS

The electronic circuit used in the single spectrum measurement consists of 41.3 mm dia × 36.5 mm length (43 cc) Ge(Li) coaxial detector, pre-amplifier, linear amplifier, biased amplifier, pulse strectcher, and 1024-channel pulse height analyzer. The biased amplifier module is designed for pulse amplifiers. For high resolution spectroscopy with a multichannel analyzer, the biased amplifier provides a variable bias level and subsequent gain to expand a region of interest in a spectrum. When used with the linear amplifier, this combination offers high counting rate

(8) The sample and its impurities information were given by Oak-Ridge National Laboratory.
(9) R. L. Hahn, J. Chem. Phys. **39**, 3482 (1963).

capability, good overload recovery, and excellent resolution necessary for use with semiconductor, gaseous, or scintillation detectors. But when a biased amplifier is used in a linear system, there is a problem of pulse width variations below some minimum impractical width feeding into the multichannel analyzer. These can be eliminated by using a pulse stretcher to strech all input pulses to the analyzer to a suitable width. The pulse stretcher module accepts linear signals from a source such as a linear amplifier, linear gate, or a biased amplifier and reshapes the input signal to a waveform that is suitable to drive a multichannel analyzer. The pulse stretcher stretches the peak voltage of narrow, input signals to some selectable minimum width, without altering the linear nature of the input signal. The linear parameter of the input signal is its relative amplitude. The stretching reduces the band-width requirements of subsequent analog-to-digital circuits in multichannel pulse height analyzers and thereby accomplishes improved linearity. For this system the energy resolution (energy per channel $\times$FHW) for ^{60}Co 1.332 MeV peak is 1.96 keV, and for ^{57}Co 0.122 MeV peak is 1.23 keV.

A block diagram of electronic circuit used in the gamma-gamma coincidence experiments is shown in Fig. III-1 which consists of 7.6 cm $\times$ 7.6 cm NaI(Tl) detector, a 43 c.c. Ge(Li) detector, pre-amplifiers, linear amplifiers, biased amplifier, pulse strectcher, delay amplifiers, time-pickoff unit, time-pickoff control, timing single channel analyzers, time to pulse height converter, linear gate and 1,024-channel analyzer. The time-pickoff unit is a time derivation unit for systems

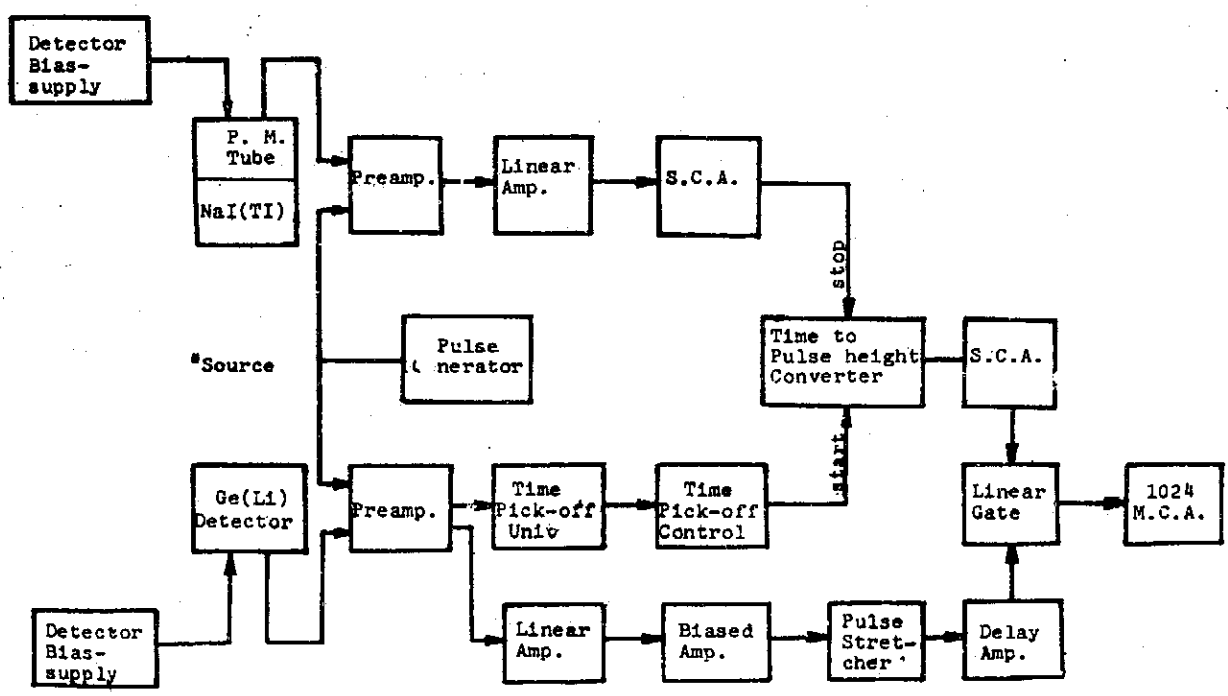

Fig. III-1. Electronics for coincidence measurement

capable of "state of the art" subnanosecond time measurements. It obtains a timing signal by sending the charge collection current from the detector to a charge-sensitive preamplifier. A unique pulse transformer method of leading edge time signal derivation applies to both semiconductor and scintillation detectors delivering fast rise time output pulses. The time pickoff control furnishes *dc* power and remote control bias for the fast time deriviation discriminators in time pickoff. The time resolution of this system for ^{60}Co measurement is 17.6 ns.

IV. CALIBRATIONS

(1) Energy calibration for the single spectrum

Several well known standard gamma-ray sources were used for the calibration of energies of observed gamma-rays. From the energies of the well known gamma rays and with using of the IBM 1,130 computer under going first and second-order least squares fit in the calibration, we can determine energies of the prominent ^{129}I gamma radiation. These prominent gamma-rays in turn served as calibration points for the weaker ^{129}I gamma-rays. The quadratic fit to the calibration points was found desirable to take into account the deviation from linearity of the electronics which was typically 0.2%. The position of the centroid of the peak was taken to be the peak energy. Uncertaines in the determined of gamma-ray energy were based primarily on rms deviation from mean value. In cases of weak gamma-rays, larger errors arise because of poor statistics.

(2) Photo-peak efficiency for 43 c. c. Ge(Li) detector

The measurement for the photo-peak efficiency was formed with several standard sources at a distance 10 cm along the detector axis. The energies of the stadard sources range from 87 keV to 1,332 keV. The efficiency was determined by the relation

$$\varepsilon_p = \frac{A}{DW},$$

where A: photo peak area per sec.
D: absolute disintegration of the sources.
W: solid angle extended from the source to the detector.

(3) Time resolution of electronic circuit for coincidence measurement

In the measurement the positive high voltage applied to the Ge(Li) and NaI(Tl) detectors are 3,000 keV and 1,200 keV respectivily. The fasting timing output from the Ge(Li) detector is accumulated by time pickoff unit and time pickoff control, and serves as a start signal for the time to pulse convertor. The energy output from the NaI(Tl) detector passing through the preamplifier, linear

amplifier and single channel analyzer serves as a stop signal for the time to pulse height converter. The range of the time to pulse height converter is 4,000 nsec and the full amplitude range is 10 V. By increase the delay time of the single channel analyzer step by step and record the peak locations then plot a delay vs channel curve, from this we can obtain the time resolution of this system which is given by relation: (the slope of this curve)

$$\text{Time resolution } (\tau) = \frac{\partial D}{\partial ch}\,(FWHM),$$

where ∂D and ∂ch are the shift of the delay time and shift of channel numbers of 1,024-channel analyzer respectively and *FWHM* is the full width half maximum of the spectrum. A ^{60}Co standard source was used for the measurement and the result is 17.6 ns and the *FWHM* is 4 channels.

V. SINGLE GAMMA-RAY SPECTRUM

Figs. V-1 to V-9 show the measured gamma-ray spectra of ^{129}I from beta decay of ^{129m,g}Te. The gamma-ray spectrum from Fig. V-1 to Fig. V-5 was measured in 3 hours runs, Fig. V-6 to Fig. V-9 was measured in a 10 hours run. Half-life measurement showed that among the 54 radiations detected, only 33 lines belong to the ^{129}I decay. The comparision with their corresponding results reported by some previous workers is listed in Table 1. In Figs. V-1 to V-4 the energy resolution is 1.23 keV for ^{57}Co 122 keV peak. The peak shown at 343 keV appears to be a doublet. In Figs. V-5 to V-9 the energy resolution is 1.96 keV for ^{60}Co 1.33 MeV peak. Several radiations which were reported by W. C. Dickinson[7] such as 551.5, 559.7, 716.8, 794, 825.8, 829.9, 925.8, 1,013.6, 1,204.2, 1,254.2, 1,282, 1,374 keV lines were obviously missing from the single spectrum in the present measurement.

We have carried out a measurement in 6 hours run with ^{128}Te taken right after the 2 hours ridiation in the reactor of National Tsing Hua University. All of the above mentioned gamma-rays were also not observed. In general our result agree fairly well with the measurement by G. Berzins (M. S. U.)[6], except they missed the 270.3, 705.6, 768.9 and 1,265 keV radiations.

VI. COINCIDENCE MEASUREMENTS AND DECAY SCHEMES

Pulses from the Ge(Li) detector in coincidence with the desired pulses from the NaI(Tl) detector were stored in the memory of the analyzer. The good resolution in the Ge(Li) detector makes this technique valueable in spite of the low efficiency of the Ge(Li) detector. From coincidence measurement and single spectrum it is possible to determine gamma-ray decay scheme of ^{129}I.

GAMMA RAYS FROM THERMAL NEUTRON CAPTURE IN ^{128}Te

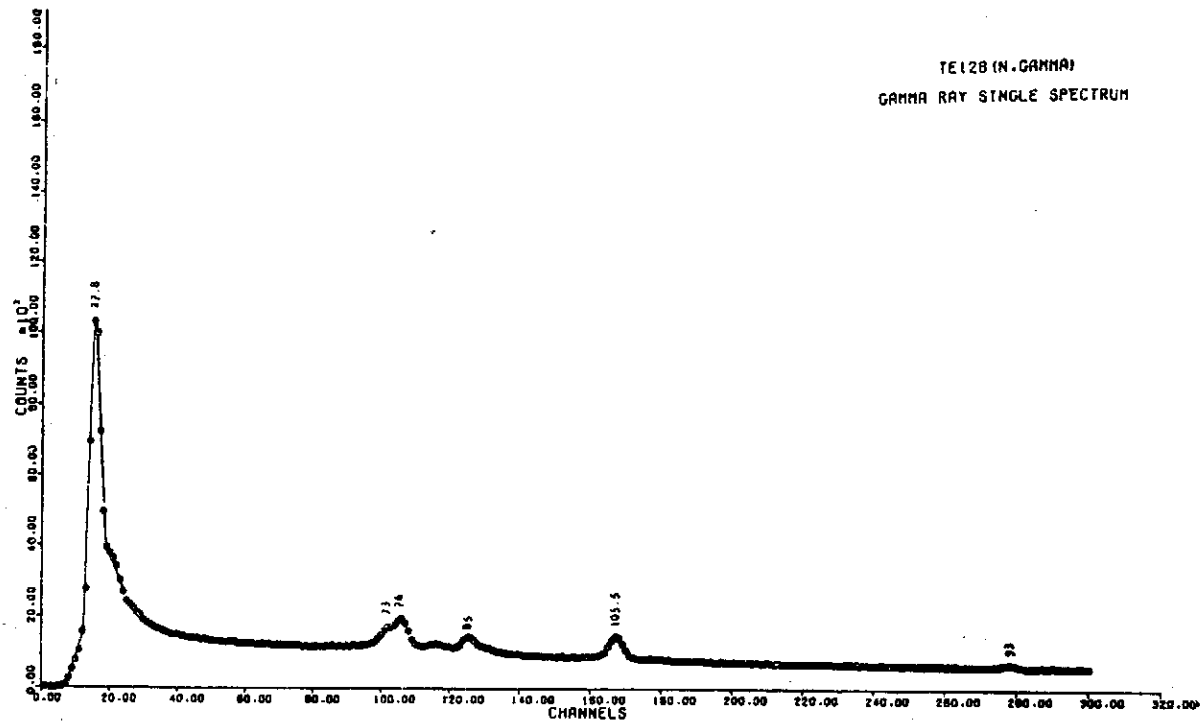

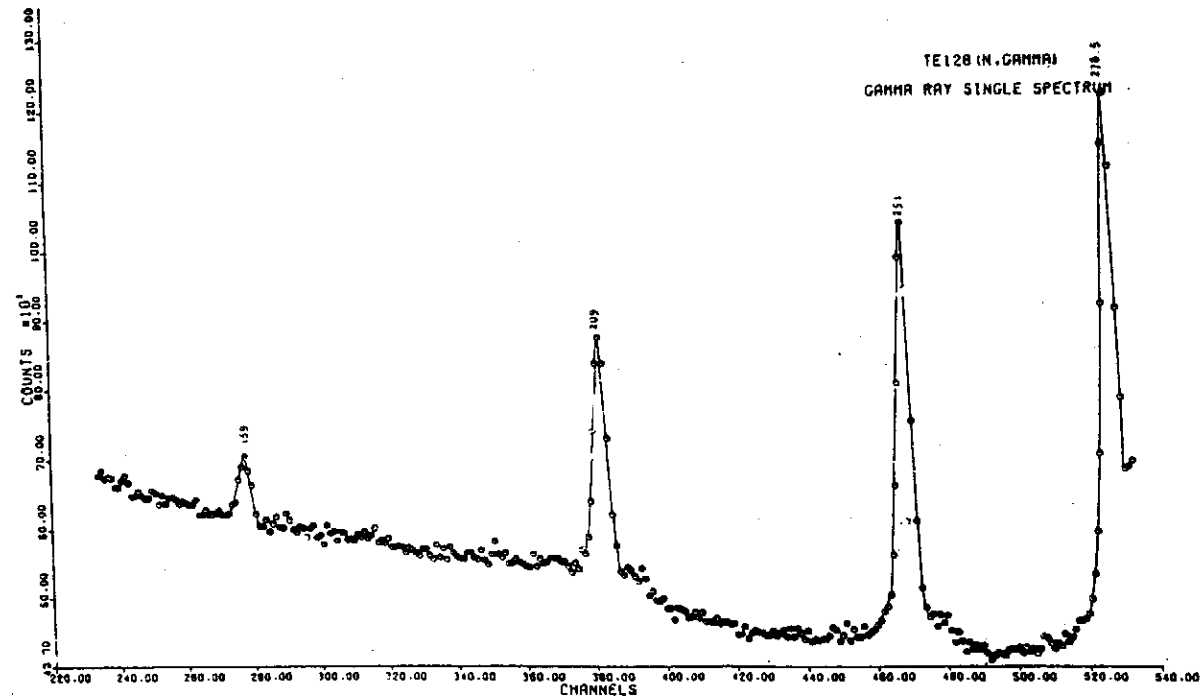

Fig. V-2.

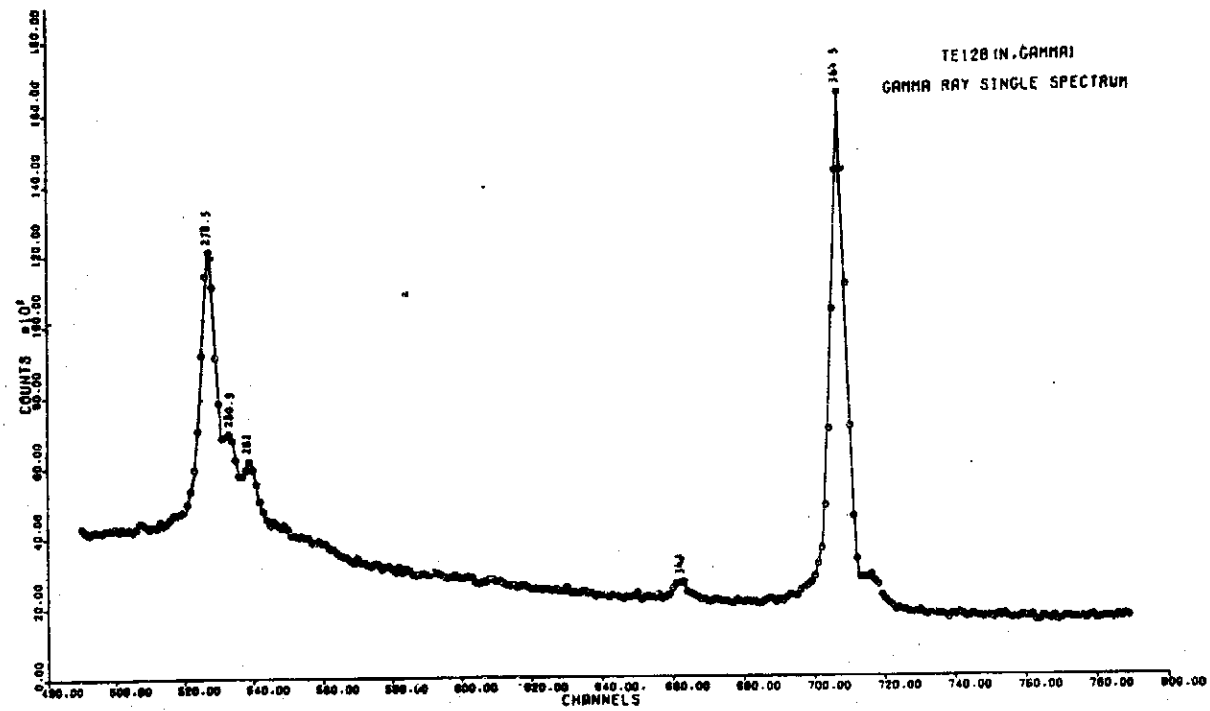
TE128(N,GAMMA)
GAMMA RAY SINGLE SPECTRUM
COUNTS
CHANNELS

Fig. V-3.

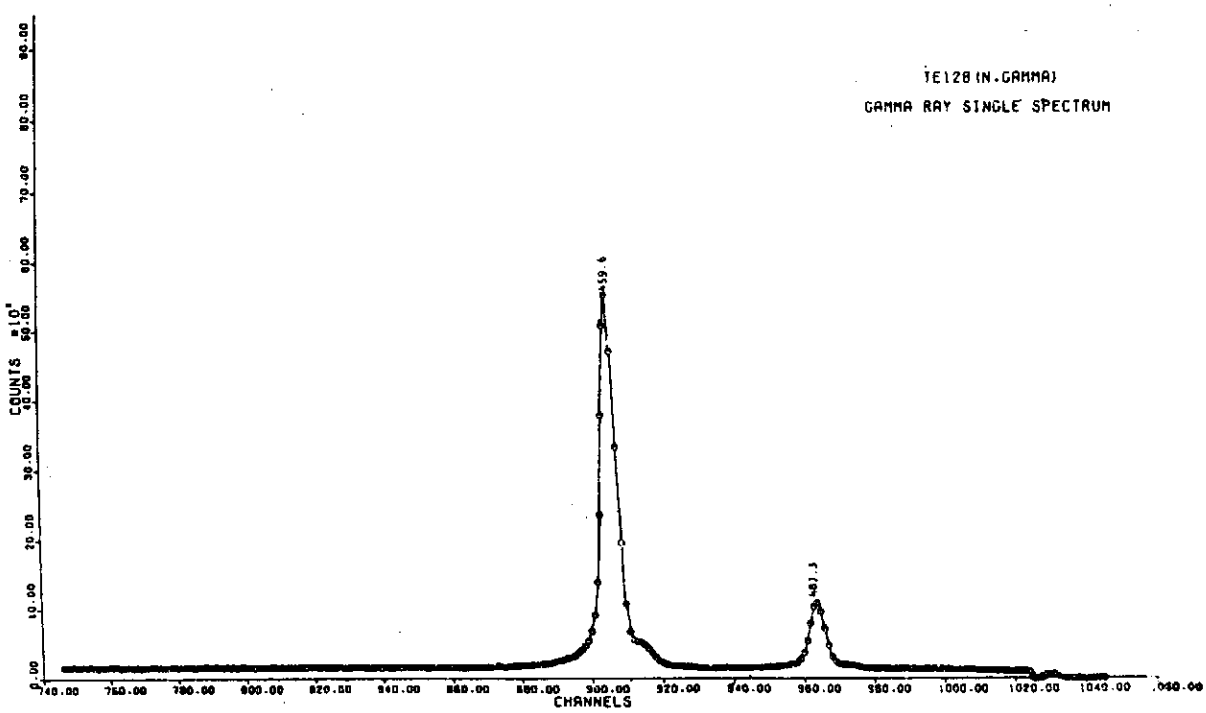
TE128(N,GAMMA)
GAMMA RAY SINGLE SPECTRUM
COUNTS
CHANNELS

Fig. V-4.

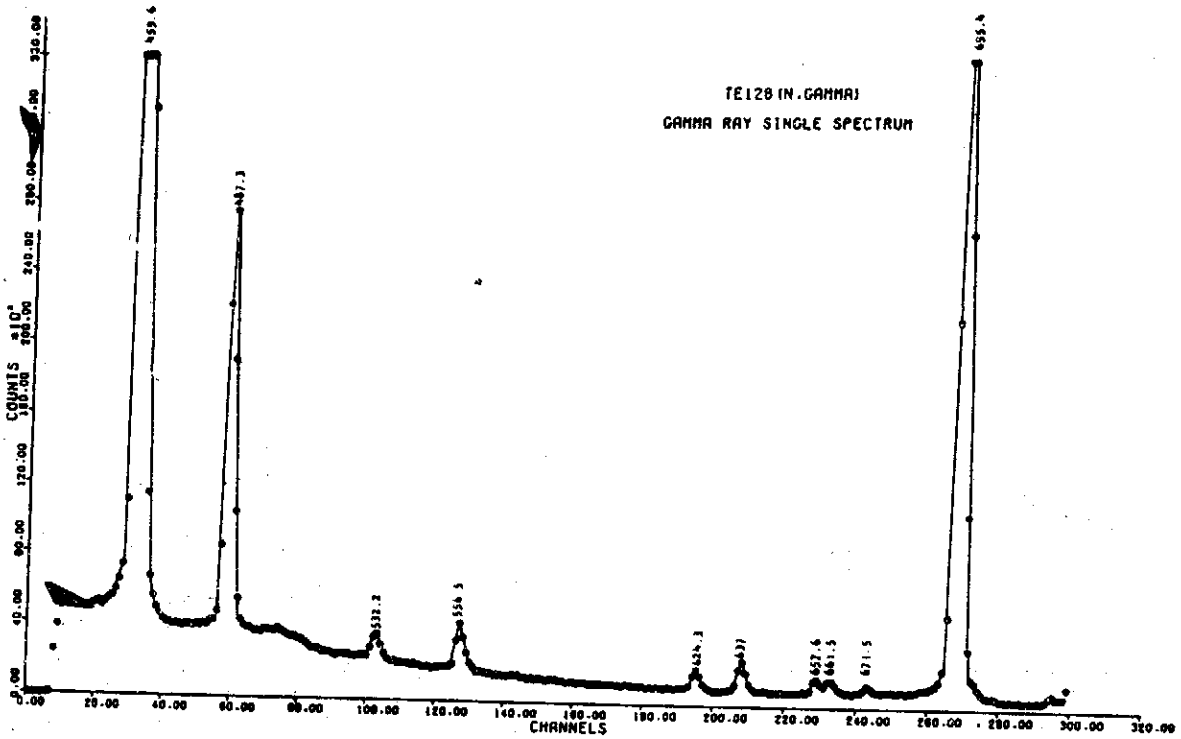
TE128(N,GAMMA)
GAMMA RAY SINGLE SPECTRUM
COUNTS
CHANNELS

Fig. V-5.

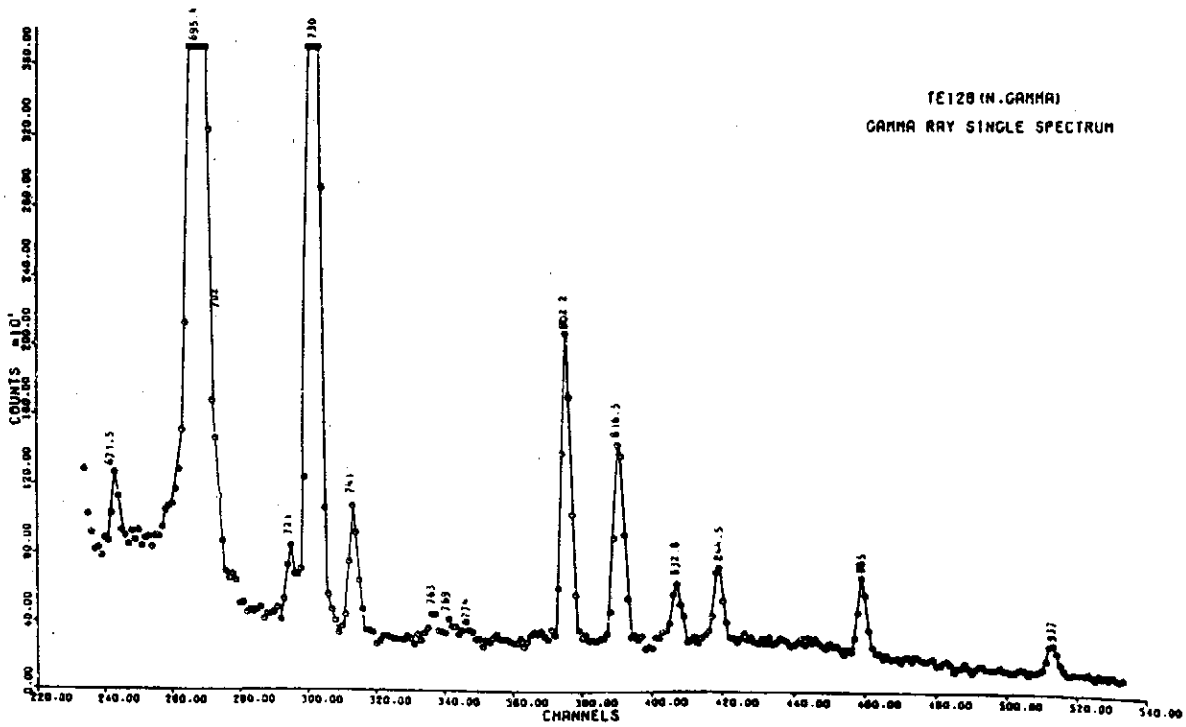
TE128(N,GAMMA)
GAMMA RAY SINGLE SPECTRUM
COUNTS
CHANNELS

Fig. V-6.

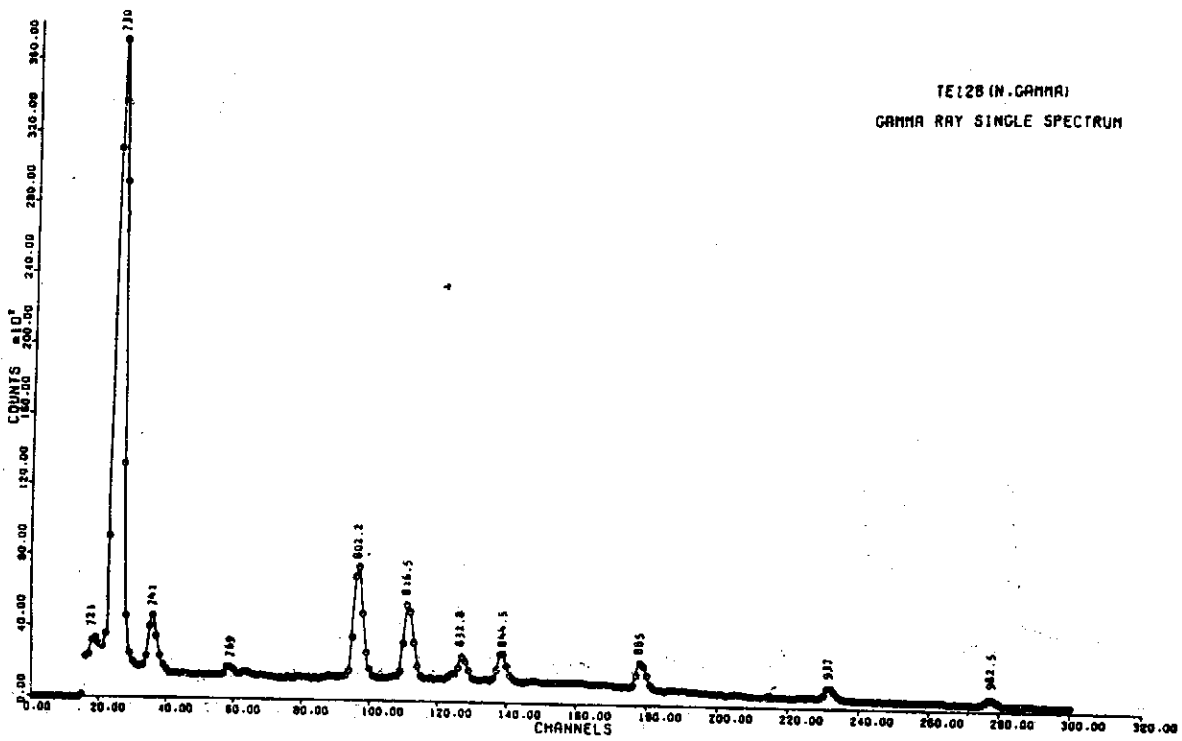
TE128(N,GAMMA)
GAMMA RAY SINGLE SPECTRUM
COUNTS
CHANNELS

Fig. V-7.

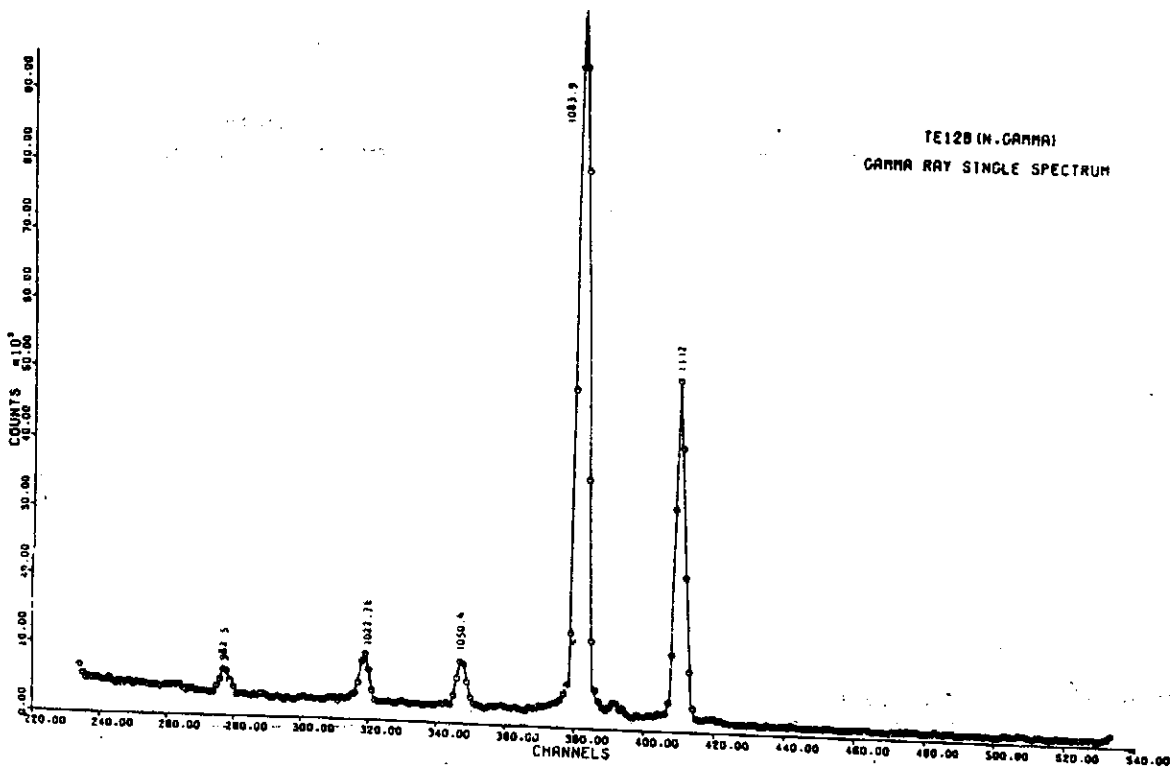
TE128(N,GAMMA)
GAMMA RAY SINGLE SPECTRUM
COUNTS
CHANNELS

Fig. V-8.

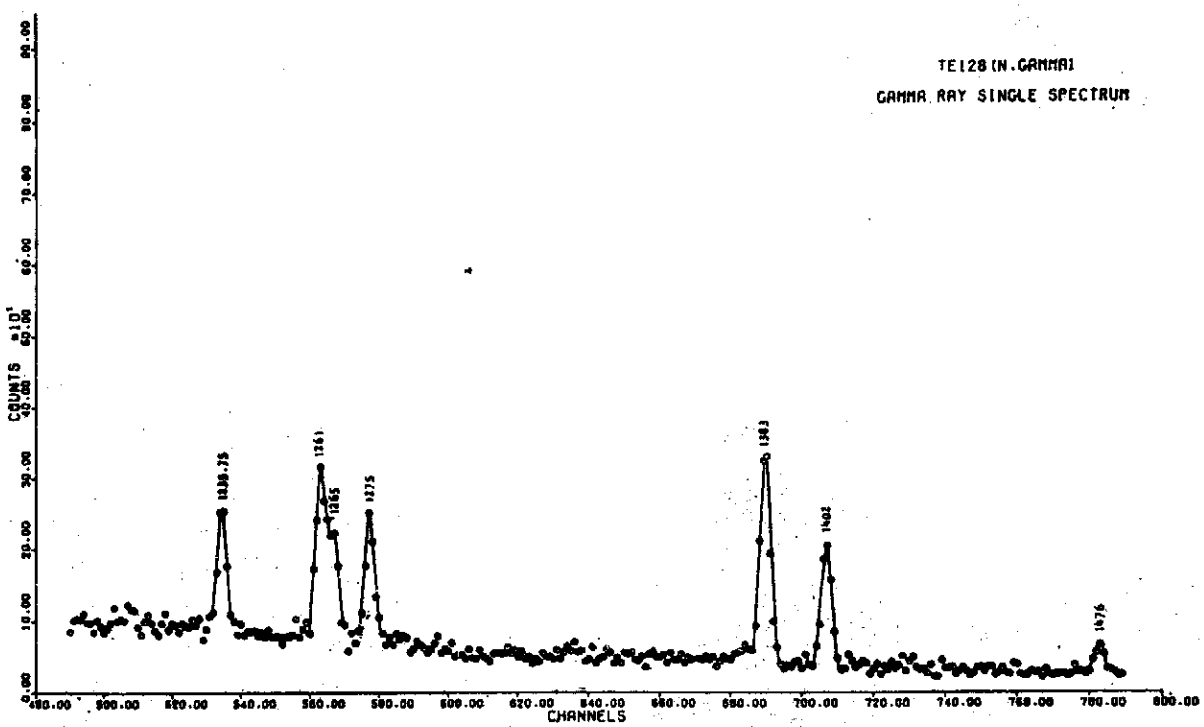

Fig. V-9.

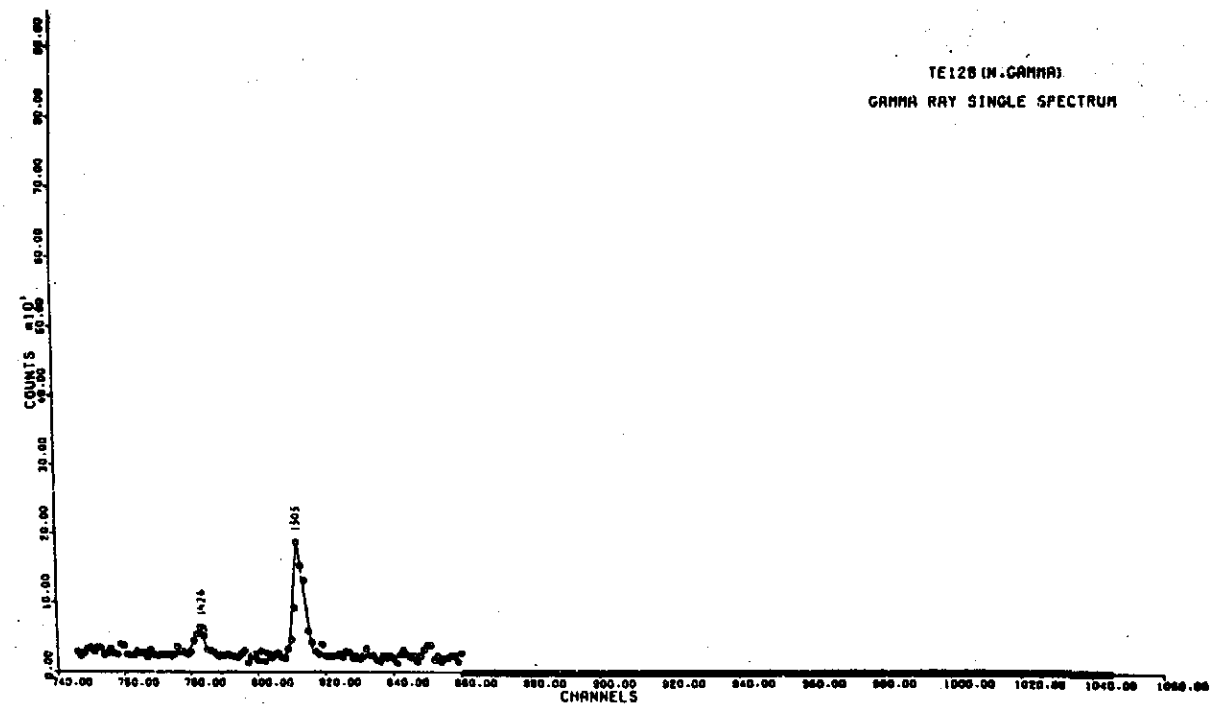

Fig. V-10.

Table 1. Comparison of observed gamma-rays from the decay of ^{129}I in the single measurement

This work (keV)	ref. 6		ref. 7
	MIT	MSU	
27.8		27.7	17.77
105.5		105.7	105.5
209	209.2	208.82	208.98
251	250.8	250.3	250.65
	271		270.3
278.5	278.7	278.5	278.43
280.9	281.7	281	281.16
343	343.5	343.2	342.6
			342.8
459.6	459.5	459.7	459.6
487.3	487.3	487.6	487.39
532.2	531.8	532.3	531.83
			551.5
556.5	556.2	556.9	556.65
	560		559.7
624.3	624.8	624.1	624.4
671.5	672.1	672.1	672.03
695.4	696.1	696.0	695.98
702	702.0		701.8
705.6			705.6
			716.8
730	730.0	729.6	729.62
741	741.1	741.0	741.1
769	769		768.9
			794.9
802.2	802.0	802.2	802.17
816.5	816.9	817.1	817.2
	829.8		829.9
832.9	833.5	833.1	833.4
844.5	844.7	844.6	844.9
			925.8
982.5	982.0	981.7	982.4
			1 003.6
			1,013.8
1,022.76	1,022.8	1,021.9	1,022.6
1,050.4	1,050.2	1,049.9	1,050.4
1,083.9	1,084.4	1,083.7	1,083.99
1,112	1,112.0	1,111.4	1,111.74
			1,204.2
1,233.75	1,232.1	1,231.9	1,233.0
			1,254.2
1,261	1,259.8	1,260.9	1,260.8
1,265	1,263.3		1,264.4
		1,374	1,373.8
1,402		1,402	1,401.6

From single spectrum, there are 8-pairs of gamma-radiations namely 250-278 keV, 460-487 keV, 702-730 keV, 741-769 keV, 817-845 keV, 1,022-1,050 keV, 1,084-1,112 keV, 1,233-1,261 keV, which all have the same energy difference of 28 keV. We can propose that there exist 28, 278, 487, 730, 769, 844, 1,050, 1,112 and 1,261 keV excited states of ^{129}I.

The results of the coincidence measurements are shown in Fig. VI-1 to Fig. VI-5 and are discussed as follows:

(1) Figs. VI-1a and 1b show the radiations in coincidence with the radiations in range 700-800 keV. Single spectra in Fig. V-5 and Fig. V-6 show five gamma-rays in 700-800 keV regions, 701, 705.6, 730, 741 and 769 keV. From the peak ratio of corresponding radiations in Fig. VI-1a and Fig. VI-1b, which are taken as a 1,500 min. run for purified sample and 400 min. run for unpurified sample respectively, we can sure that the true radiations that caused by ^{129}Te$(\beta^-)^{129}$I transition are 343, 532, 557, 672, 696 and 730 keV lines. The gate also included Compton scattered contribution from the 817 and 845 keV radiations. The 343 line is in coincidence with 741 and 769 keV radiations to the 28 keV and ground state respectively. The 532 keV line is in coincidence with 702 keV line which means that there exists a 560 keV level such that the 1,262 keV excited state decays by deexcitation of 702 keV gamma-ray to the 560 keV level and then decays to the 28 keV level by radiate 532 keV gamma-ray. The 672 keV line is in coincidence with 702 and 730 radiations which means that there exists a 1,402 keV level which decays to the 730 level by radiating 672 keV gamma-ray and then follow by 702 and 730 keV radiations transition to the first excited state and ground state respectively. The 1,402 keV state can decay directly to the ground state by radiating 1,402 keV gamma-ray which has been observed in the single spectrum. The 696 keV line is in coincidence with 705.5 keV line which means that there exists a 696 keV state such that the 1,402 keV level decays to this state by radiating 706 keV gamma-ray and then decays to the ground state. The summary of these results are shown in Fig. VI-1c. The line at 557 keV is attributed to the inclusion with the gate of the 817 and 845 keV Comptons. The others 658, 677, 687, 707, 742, 764, 817, 885, 937, 1,384, 1,478, 1,502 and 1,562 keV lines are caused by the impurities. We can sure this by the peak-height ratio of Fig. VI-1a and 1b which are taken a 1,500 min. run for purified sample and a 400 min. run for unpurified sample respectively, and the impurity has been identified as ^{113}Cd (ref. Fig. VII-2).

(2) In the measured coincidence spectrum gating with the region 450-482 keV, several lines at 343, 460, 556, 624, 658, 883 and 932 keV were observed. The 343 keV line is in coincidence with 460 keV radiation which means that there exists a 830 keV excited state which decays to the 487 keV by radiating 343 keV

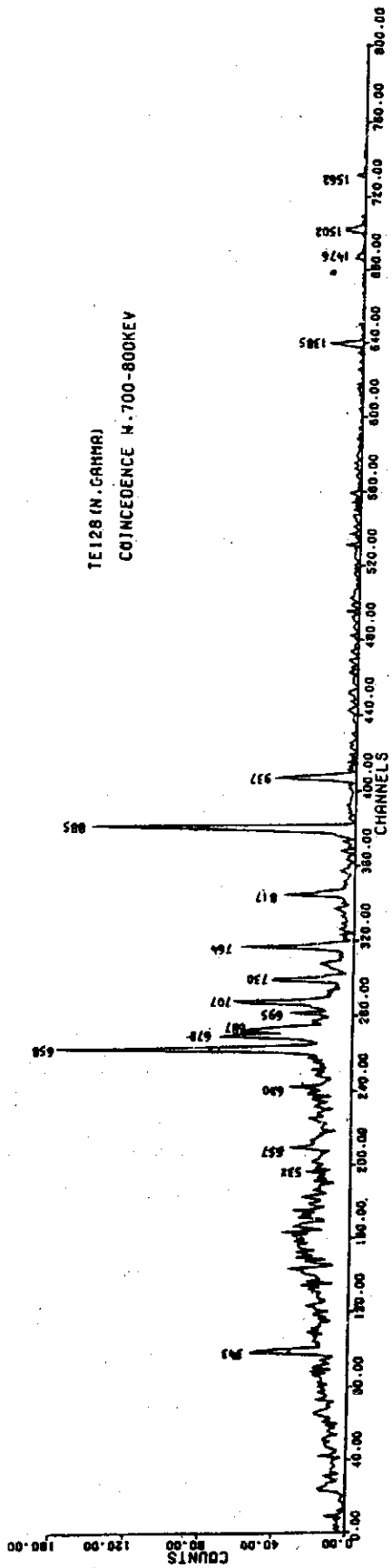

Fig. VI-1a.

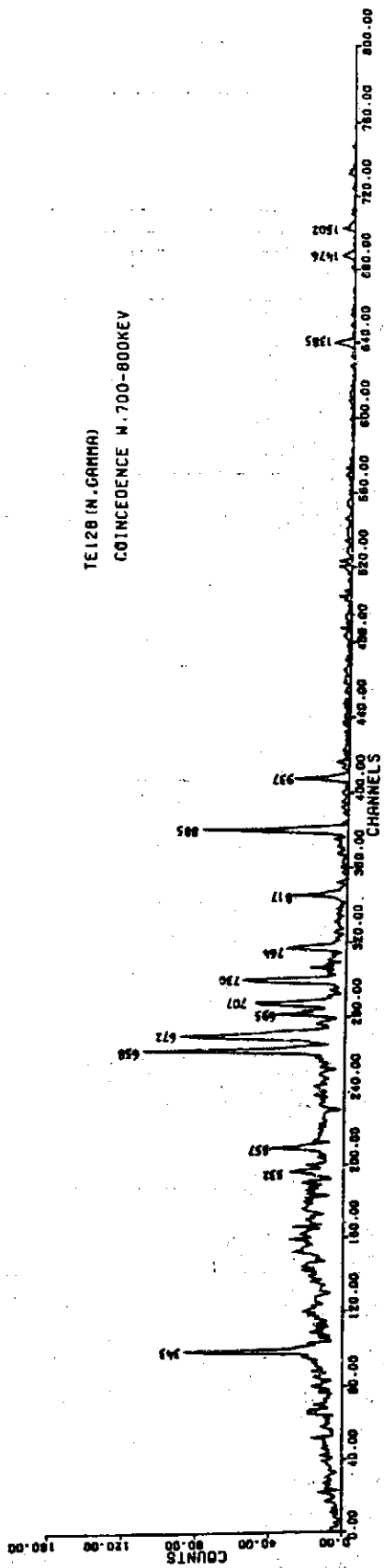

Fig. VI-1b.

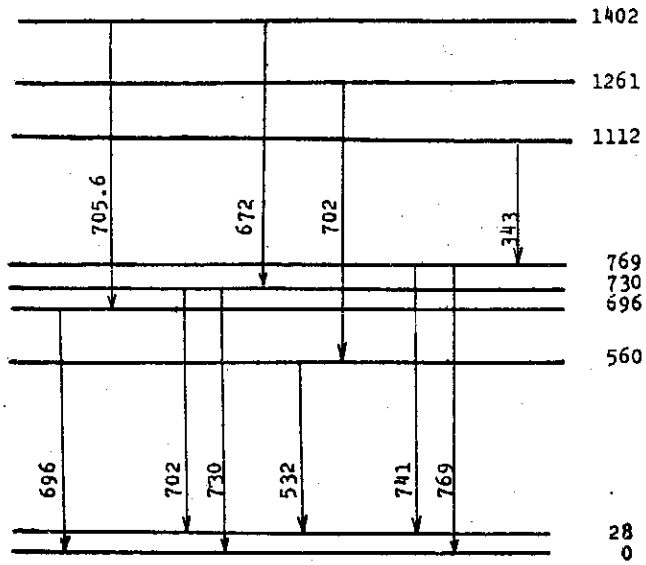

Fig. VI-1c. The decay scheme of coincidence with gate 700-800 keV

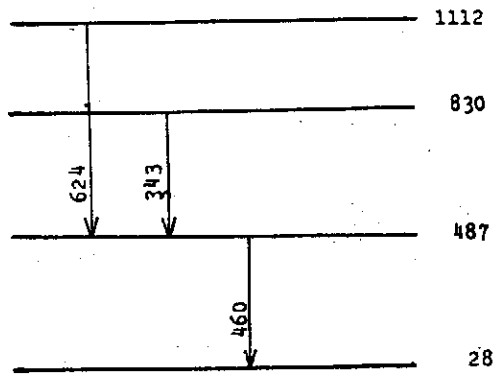

Fig. VI-2. The decay scheme of coincidence with 460 keV gamma-ray

gamma-ray and then decays directly to the 28 keV level. The 624 keV line is in coincidence with 460 keV gamma-ray which means that the 1,112 keV level also decay to the 487 keV level by radiating 624 keV gamma-ray. These results are given in Fig. VI-2. The 460 and 557 keV lines are from the contribution of the Comptons. The others are from coincidence with 447 keV radiation in ^{110}Cd (Fig. VII-2).

(3) In the coincidence spectrum gating with the region 798-857 keV which include radiations 802, 817, 834 and 845 keV, there appear four lines at 250, 278, 557 and 658 keV. The 557 keV line is in coincidence with 845 and 817 keV transitions. This agrees with 845 and 1,402 keV levels that the 1,402 keV level decays to the 845 keV level by radiating 557 keV gamma-ray and then decays to 28 keV and ground state by radiating 817 and 845 keV gamma-rays respectively. There is no indication for any other gamma-rays decay to 845 keV level. The 250 and 278 keV lines are in coincidence with 833 keV line that is, the 1,112 keV level decay to the 278 keV level by radiating 833 keV gamma-ray and then the 278 keV

level decays to 28 keV and ground state by radiating 278 and 250 keV gamma-rays respectively. The results are given in Fig. VI-3. The 658 keV line is in coincidence with 818 keV transition of ^{110}Cd (Fig. VII-2).

(4) The coincidence spectrum gating with 730 and 741 keV lines in the region between 725 and 750 keV shows that the 343 keV transition is in coincidence with 741 keV radiation, that is the 1,112 keV level decays to the 769 keV level and then decays to the 28 keV level by radiating 343 and 741 keV gamma-ray respectively. The 672 keV gamma-ray is in coincidence with 730 keV line which means the 1,402 keV level decays to the 730 keV level and then decays to the ground state. The result is in consistence with the discussions in (1). The 658 and 707 keV lines are in coincidence with 744 keV line in ^{110}Cd.

(5) In the coincidence spectrum gating with 557 keV line, we observed the 557, 658, 817 and 845 keV lines. The 817 and 845 keV lines are from true coincidence with 557 keV transition and agree with the statement in discussions (1). The 557 keV line is caused by chance and Compton effect, and the 658 keV line is caused by the impurity ^{110}Cd.

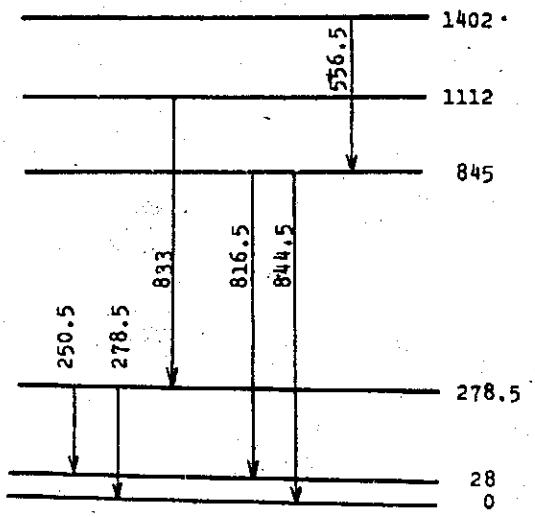

Fig. VI-3. The decay scheme of concidence with state 798-857

Table 2. Summary of results from coincidence measurements

Gate range (keV)	Type of coincidence			
	Photopeak (keV)	Compton (keV)	Chance (keV)	Impurity* (keV)
450-482	343, 624	460, 557	658	885, 940
540-265	817, 84	557	557, 658	
725-750	343, 672		658	707
700-800	343, 532, 672, 696, 730	557	658, 707, 817, 1,384, 1,502	677, 687, 742, 764, 885, 940, 1,478, 1,562
798-857	250.5, 278.5, 557		658	

* The impurity is from ^{110}Cd.

A decay scheme of the ^{129}I is proposed from the present work and is shown in Fig. VII-1. The diagram displays 15 energy levels and 33 gamma-rays.

A summary of the coincidence measurements is listed in Table 2.

VII. CONCLUSION

In this work we obtained a decay scheme of ^{129}I from measurements of single gamma-ray spectrum and gamma-gamma coincidence spectra as discussed in last section. We have observed thirty-three gamma-rays and their corresponding energies were accurately determined. As shown in Fig. VII-1, there are fifteen energy levels of ^{129}I obtained up to 1.402 MeV excitation. The results agree, in general, fairly well with previous measurement by G. Berzin *et al.*[6] and W. C. Dickinson *et al.*[7] Some important findings of present work are summarized as follows:

(1) We observed a new line at 702 keV corresponding to the transition from the 1,262 keV level to the 560 keV level. The spin and parities of both levels are known to be $3/2^+$.

(2) No indication for the existence of the levels at 1,282 and 1,204 keV as reported by W. C. Dickinson *et al.*[7] was found in the present measurement. Our result agrees with the measurement of G. Berzins *et al.*[6]

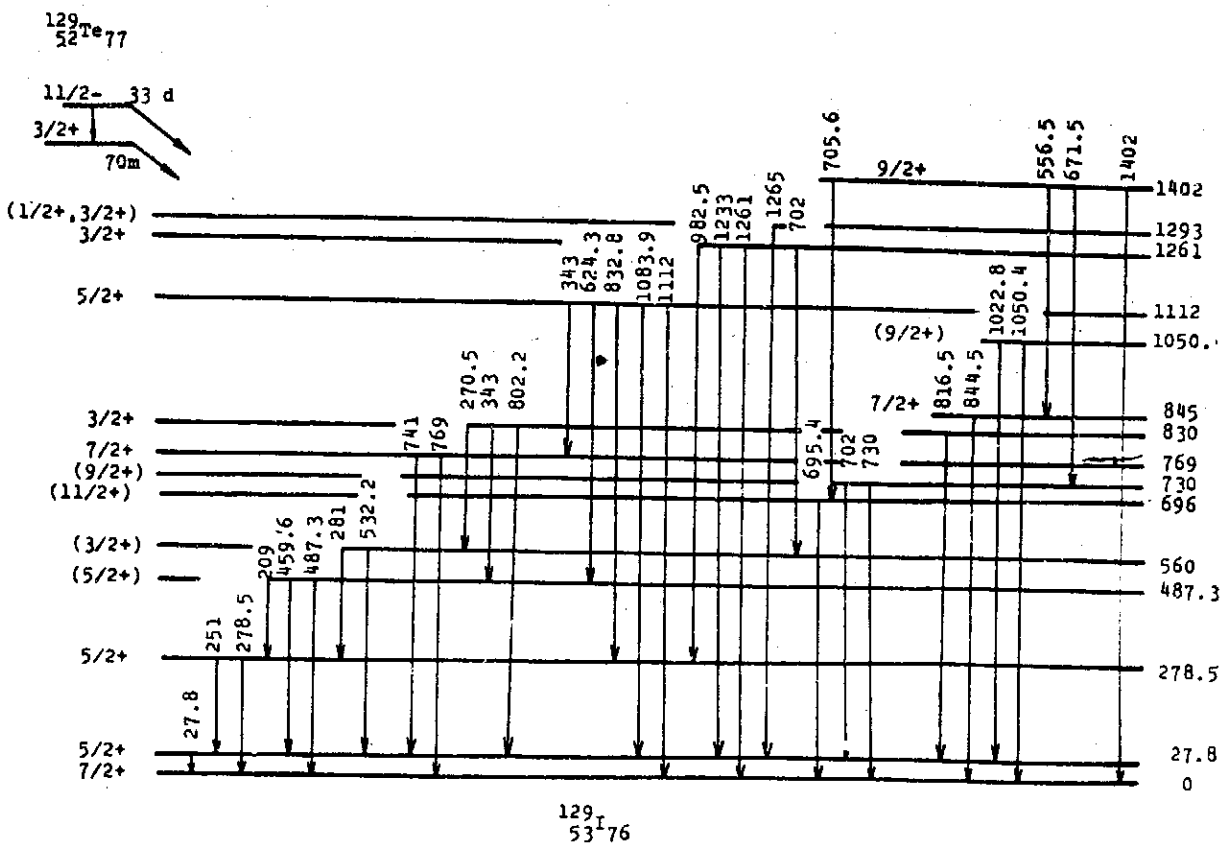

Fig. VII-1. The decay scheme of ^{129}I from bata decay of the isomers of ^{129}Te

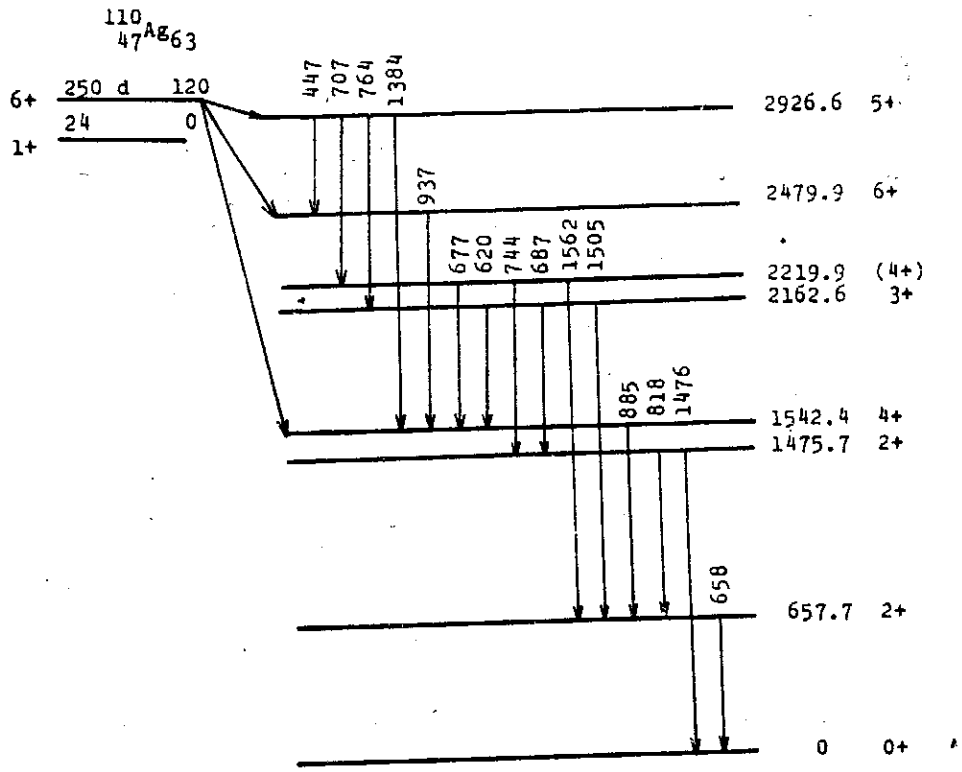

Fig. VII-2. The decay scheme of ^{110}Cd from beta decay of ^{110m}Ag

(3) The transitions from 830 and 560 keV levels to the ground state found in the privious work[6,7] were not observed in the present measurement.

(4) There is no evidence for existence of the 551.5 keV radiation as reported by W. C. Dickinson *et al.*[7] Our result agrees with the measurement of G. Berzins *et al.*[6]

(5) We observed the 705.6 keV radiation as reported by W. C. Dickinson *et al.*[7] This was not observed by G. Berzins *et al.*[6]

The ^{110}Cd level scheme was also obtained in the present work and is shown in Fig. VII-2. The result agrees fairly well with the report given by S. M. Brahmavar *et al.*[10]

(10) S. M. Brahmavar, J. H. Hamitton, A. V. Ramayya, E. F. Zganjar and C. E. Bemis, Jr. Nucl. Phys. **A125**, 217 (1969).

Target Chamber for Use with Radiative Transition Reactions Studies(*)

T.H. Hsu, E.K. Lin (林爾康) and Y.C. Liu

Tsing Hua University, Academia Sinica and Taiwan University

Abstract: A target chamber with a continuously moving target holder was designed for the investigation of radiative transition reactions on the medium-weight nuclei. This chamber has been successfully used to gather data from the $^{70}Ge(p,\gamma)^{71}As$, $^{72}Ge(p,\gamma)^{73}As$, $^{65}Cu(p,\gamma)^{66}Zu$, aud $^{27}Al(p,\gamma)^{28}Si$ reactions. Some of these results are presented and described.

1. Introduction

The radiative transition reactions induced by charged particles, such as (p,γ), $(p,\alpha\gamma)$ and (α,γ) reactions etc, have been successfully studied in various laboratories for several years[1-3]. The simplicity and the usefulness of this type of reaction in yielding nuclear structure informations have been hampered by the fact that the reaction cross section is rather small compared with other accessible reactions. This has resulted in the following technical obstacles:

1) target contamination due to long hours of heavy current bombardment,
2) deterioration of fragile target;
3) requirement of high efficiency and good resolution gamma ray detectors,
4) requirement of a high accuracy beam current integration system.

Accordingly the radiative transition reactions have rarely been explored beyond the $lf_{7/2}$ shell nuclei[4]. In order to overcome the above mentioned obstacles, considerable amount of effort has been paid in this laboratory on the improvement of design and construction of a target chamber suitable for investigation of the radiative transition reactions. In this paper, we report a target chamber constructed specially for measuremants of gamma-ray spectrum, its angular distribution, and excitation functions from the radiative transition reactions induced by charged particles. With this chamber we have successfully investigated the (p,γ) reaction on the medium-weight nuclei[5-6], namely ^{65}Cu and $^{70,72}Ge$, in the region beyond the $lf_{7/2}$ shell.

(*) Work performed at the Physics Research Center and supported by the National Science Council of Republic of China.

2. Chamber design and construction

The essential feature of the constructed chamber is as follows:

1) Target is surrounded by a wall of a cylindrical cold finger with a small circular window for the incident beam, and as located as close to the cold trap reservoir as possible. Thus, the target could be well free from the contamination due to incoming residual vapour in the system. Viton O-rings were used for all vacuum couplings. For a better vacuum in the chamber and also for more rapid oscillation of the target, it was suggested that nickel bellows can be used for the coupling of the brass shaft to the chamber. However, in present application, the Viton O-ring coupling was found to be satisfactory.

2) The target holder is made to move up and down uniformly and repeatedly so as to avoid deterioration due to the continuous bombardment of heavy current beam at the same spot on the fragile target. This capability makes it possible for accumulating gamma-ray spectrum over a long period (24 hours or longer) which is necessary in order to accumulate sufficient counts for an enough statistical accuracy.

3) The size and the shape of the target chamber are kept as small and compact as possible so that the gamma-ray detector can be brought very near to the target for a large geometrical efficiency. Thus, the requirement of high efficiency and good energy resolution of the detection can be fulfilled by the use of this target chamber together with a high-resolution Ge(Li) detector.

4) By a properly insulated coupling to the beam tube, the target chamber itself becomes a Faraday cup. The entrance for the incident beam to the target is designed to consist of a long tube (30 cm from the entrance slit to the target) and a small window at the cylindrical cold finger. This arrangement gives no way to the secondary electrons for escaping away from the Faraday cup. Therefore, an accurate current integration can be achieved through an integration system.

A schematic drawing of the target chamber is shown in fig. 1. The main body of the chamber is a T-shaped stainless steel tube 4 cm in diameter and an inner copper tube 2.5 cm in diameter which was used as cold finger. At the top of the chamber is a 2.5 liter liquid nitrogen cold trap reservoir. The copper tube finger is then attached to this reservoir. A 1.5 cm hole was bored through one side of this cold finger to make access for the beam to strike targets. The copper target holder is soldered directly onto a hollow brass shaft. The assembly of the target holder inside the target chamber can be made by slipping it into the cold finger at a proper position. Near by the target chamber a Ge(Li) detector can be placed at a small distance of ~2.5 cm from the target.

Shown in fig. 2 is the layout of the movable target holder driven by a motor. Fine threads were cut at the bottom end of the brass shaft. A gear disc made from nylon was attached to a nut which is made to fit these threads. By rotating the gear disc one may ascend or descend the target holder inside the chamber with respect to the beam.

The orientation of the target holder with respect to the beam direction was monitored

by an angular scale marked on a rotating disc which was fixed at the end of the shaft. Two small slots were cut to this disc at 0° and 180°. By sliding one of the slots along the micro-switch arm, which was fixed at outer body of the chamber, the target can then be raised or lowered without changing its angular orientation inside the chamber. Uniform and slow motion of the target holder was produced by an one rpm motor, driving the gear disc with a gear ratio of 1:10. Two micro-switchs were set on upper and lower sides of the micro-switch arm. They were activated by the contact of the moving disc, The target holder, therefore, traveled automatically and repeatedly between an adjustable distance set by the micro-switchs.

The chamber was maintained at high vacuum by a 100 ℓ/sec Vac-Ion pump which was installed just in front of the beam entrance slit. Typical vacuum at 3×10^{-7} torr can be readily obtained within a period of 30 min pumping.

As many as four targets can be mounted on the target holder, two targets on each side of the target holder, thus they can be interchanged inside the chamber as desired without breaking the vacuum. This is specially convenient for the calibration and background runs. Because of heavy current bombardment it is necessary to provide cooling of targets. This was done by cutting a cooling canal into the target holder as shown in fig. 2. Running tap water was used for the target indirect cooling.

3. Performance of the chamber

The constructed chamber has been used for a series of (p,γ) experiment[5-7]) in this laboratory. In the measurements, thin targets of about 2-10 $\mu g/cm^2$ were prepared by vacuum evaporation of uniform deposition of metallic elements onto a 1 cm x 3 cm gold sheet of 0.4 cm thickness. A few examples of measurements are presented in figs. 3 and 4. Fig. 3 shows part of the gamma ray spectrum from the $^{70}Ge(p,\gamma)^{71}As$ reaction[5]) at E_p=2434 keV measured by a 50 cc Ge(Li) detector. The measurement was performed with a 3 MeV Van de Graaff accelerator at Tsing Hua University. The ^{70}Ge target used is of ~5 $\mu g/cm^2$ in thickness. It was found that under the bombardment by a 2434 keV proton beam at 5 μA for a period of 24 hours, no noticeable deterioration of target and carbon build-up on the target were observed. Fig. 4 shows the yields of the gamma-rays from the $^{70}Ge(p,\gamma)^{71}As$ reaction[5]) measured in the proton-energy range 1293-2185 keV at a step of ΔE_p ~1 keV. It is seen that many resonances which correspond to the energy levels of ^{71}As at energy excitation ~6 MeV are sufficiently resolved.

In the similar way, we have successfully measured the gamma rays from the $^{73}Ge(p,\gamma)^{73}As$ reaction[5]). Further measurement was made for the $^{65}Cu(p,\gamma)^{66}Zn$ reaction[6]), and performance of the chamber was found to be quite satisfactory.

In order to show the stability and resolution of our system used for the measurement. An aluminium target of ~1.5 keV thickness was bombarded with proton beam in the region E_p=1.38-1.40 MeV[7]). The typical beam current was 5 μA. Well separated resonances at E_p=1381 and 1388 keV as shown in fig. 5 were obtained by repeated separate measurem-

ents. These data were taken at proton-energy step of 0.5 keV. The result shows the stability of our system to be within 0.5 keV.

The successful measurement with the constructed target chamber for the (p,γ) reaction on the medium-weight nuclei has encouraged us to take advantage of this chamber for more detailed investigation of the (p,γ) reaction. It is believed that the measurements with this chamber for the (α,γ) reaction can also be achieved.

The author acknowledges the help rendered by the members of accelerator laboratory at Tsing Hua University.

References

1) See for instance: A. Hossain, H.A. Rashid and M. Islam, Nuclear Structure (North-Holland Publishing Co., Amsterdam, 1967) P.58.
2) P.M. Endt and C. Van der Leun, Nucl. Phys. A105 (1967)1.
3) Nuclear Data A6, compiled by K. Way et al (Academic Press, New York and London, 1969).
4) See for instance: G.B. Vingiani, G. Chilosi and C. Rossi-Alvarez, The structure of $1f_{7/2}$ nuclei, edited by R.A. Ricci (Padova, 1971), P. 303.
5) Y.C. Liu, T.H. Hsu, E.K. Lin, C.C. Hsu, P.K. Tseng and C.W. Wang, to be published.
6) C.C. Hsu, E.K. Lin, Y.C. Lin, T.H. Hsu, C.W. Wang and P.K. Tseng, to be published.
7) T.H. Hsu, E.K. Lin, C.C. Hsu, Y.C. Liu, P.K. Tseng, C.W. Wang and W.S. Hsu, Chinese J. Phys. 10 (1972).

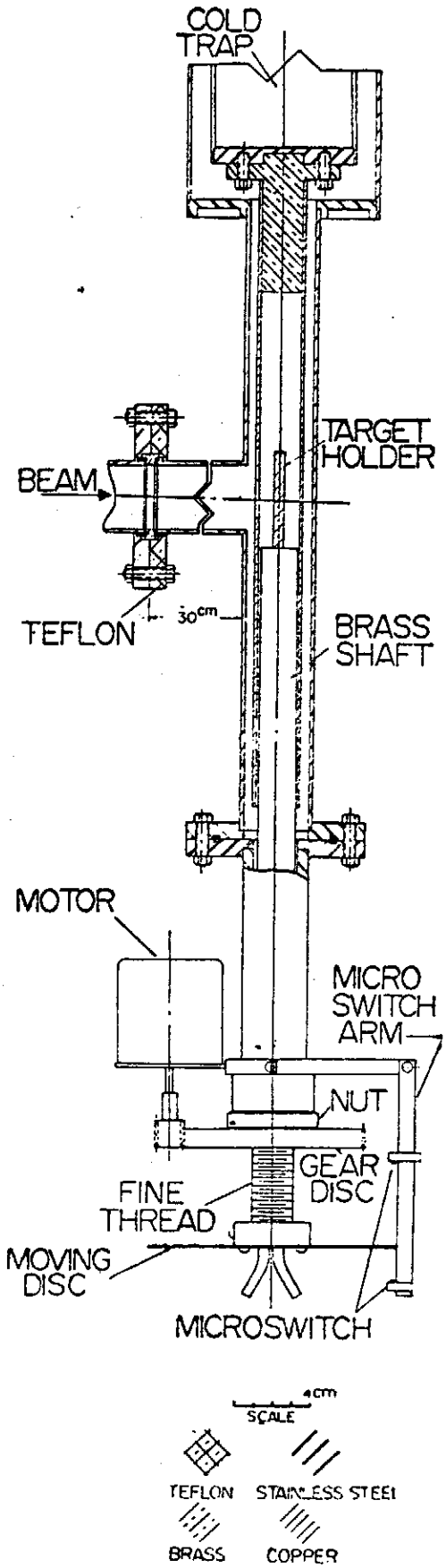

Fig 1 Schematic view of the target chamber.

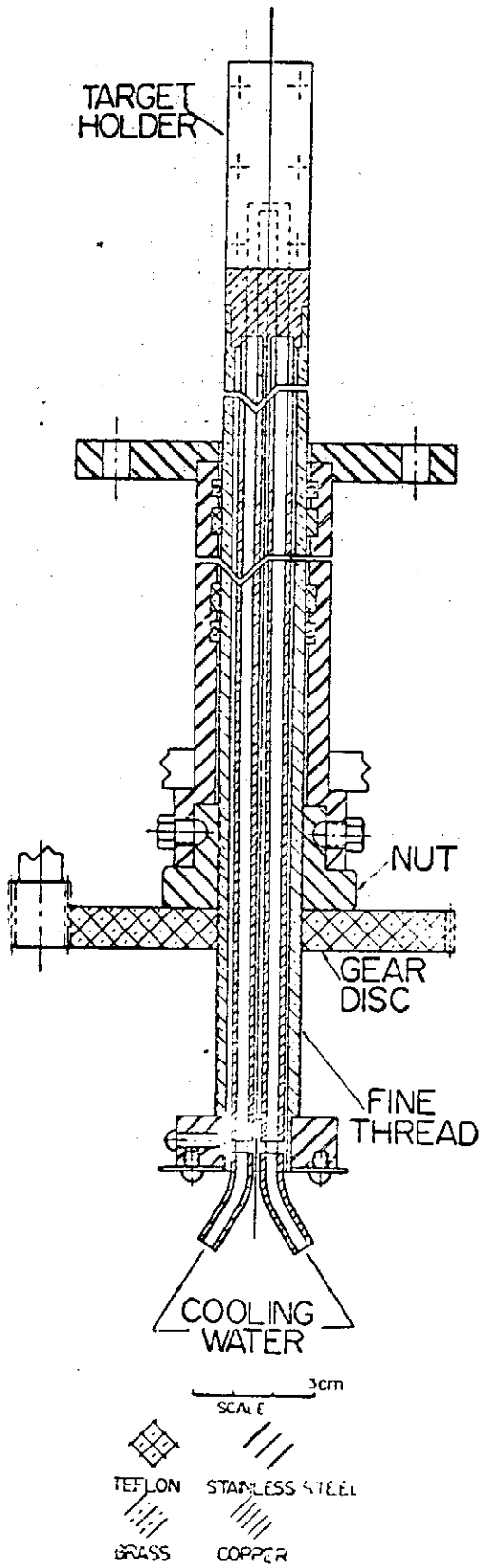

Fig 2 Layout of the movable target holder.

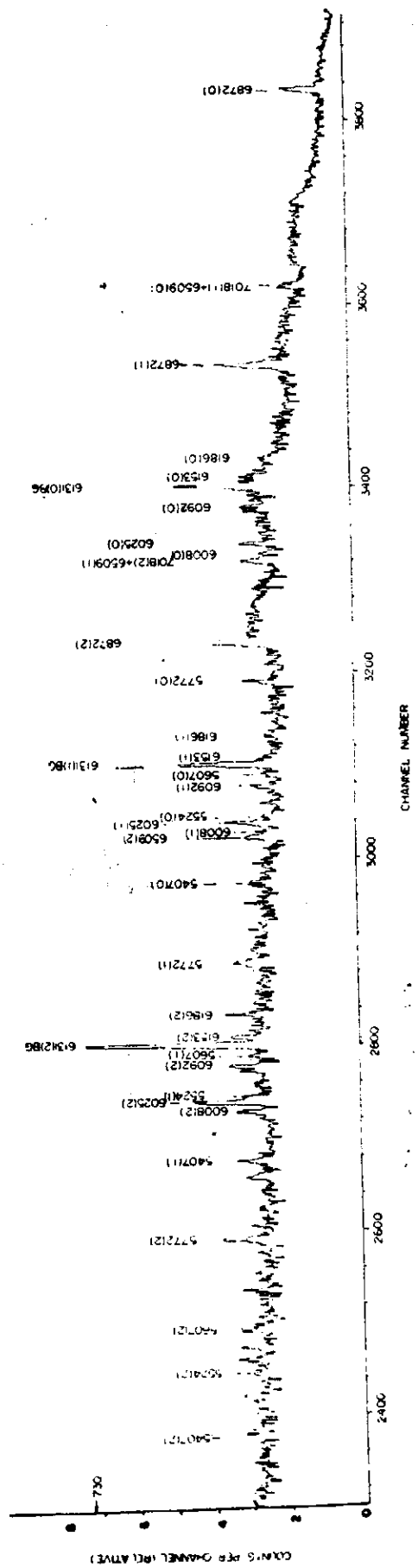

Fig. 3. A gamma-ray spectrum of the ^{70}Ge(p,γ)^{71}As reaction at E_b=2434 keV. Numbers over peaks refer to gamma-ray energy. BG, background; (0)(1) (2), full-energy, single-escape, and double-escape peaks, respectively.

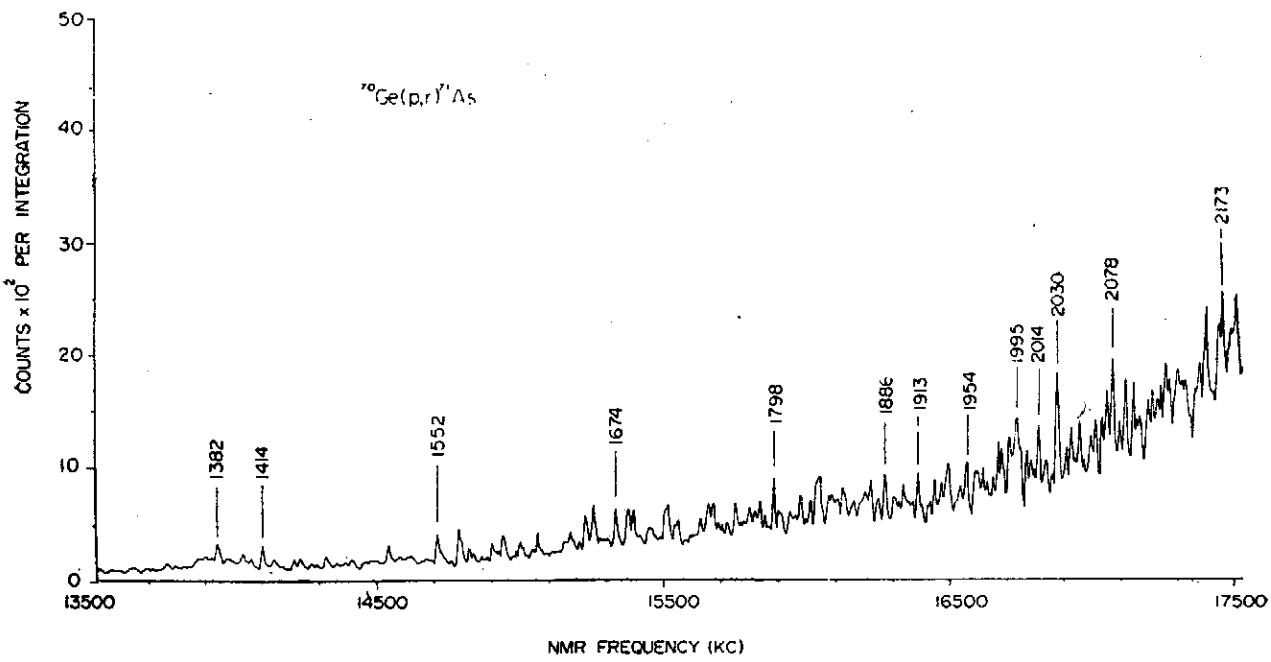

Fig. 4. Yield curve from the $^{70}Ge(p,\gamma)^{71}As$ reaction in the proton energy range 1293-2185 keV. Numbers over peaks refer to constant enegy.

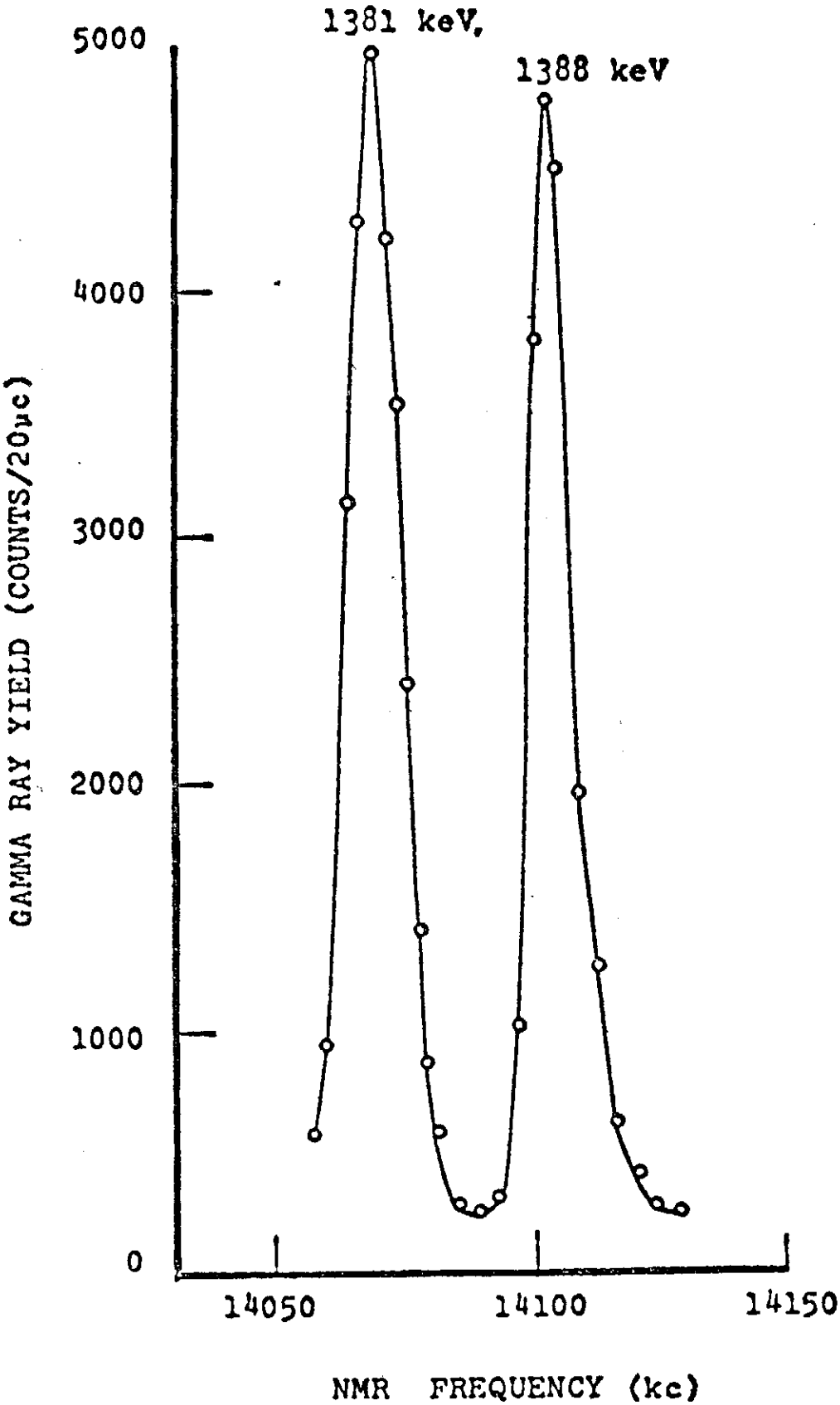

Fig. 5 Yield curve for the 1381 keV and 1388 keV resonances from the $^{27}Al(p,\gamma)^{28}Si$ reaction.

Calibration of a Time-of-Flight Neutron Detector

W. S. Hou and B. Chen

Institute of Physics, National Tsing Hua University

W. N. Wang*(王唯農) and L. P. Liang (梁靈平)

Institute of Physics, Academia Sinica

Abstract

A new calibration technique for obtaining the relation between absolute neutron detection efficiency vs energy is discussed. The coincidences between alpha particles and monitor neutrons, alpha particles and recoil protons in a "scientillation" target were measured. This measurment was used to obtain useful informations for determination of the absolute efficiency η (E). The corrections for neutron attenuation in the scientillation target are also considered. The measured η (E) and the calculated values were compared. The agreement is better than 5%.

1. Introduction

The accuracy of the experimental absolute cross sections on neutron scattering depends on the accuracy of η (E) of the detector used in its measurment. By comparing the results of many experimental data on the 14MeV neutron scattering serious discrepances can be observed (ref. [1,2,3,4,5]). In our opinion one of the most important sources of error is the incomplete knowledge of the energy dependence of the neutron detection efficiency η (E) (ref.[6]). The η (E) is determined both by the scientillation efficiency and the electronic efficiency. As discussed by C. C. Jonker et al (ref.[7]), an experimental determination of the η (E) must be preferred to its calculation, which does require detail knowledge about both contributions.

The efficiency η (E) up to 12.5 MeV has been determined by measuring the scattering of the 14.1 MeV neutrons from a "scientillation" target. The η (E) is then obtained from the known σ (θ) for the n-p scattering (ref.[8,9]). Apart from the measmements of the neutrons scattered from the scientillation target, the coincidence counts between the alpha particles and monitor neutrons and between alpha particles and recoil portons in this scientillation target were also measured. This measurment can be used to eliminate the inaccurate factors, the bias level of the scientillation target, which are required previously[2] for the calculation of the η (E). Besides, the background of chance coincidence is lower and the neutrons scattered from carbon in the target (ref.[1,2,6]) do not produce true coincidence.

To avoid extrapolation of the η (E) up to 14.1 MeV the η (14.1) was measured independently by counting alpha particles resulting from T(d,n) He^4 reaction directly.

Flux attenuation in the target was calculated by two different methods: one was based on the simple transmition equation and the other was based on the same method as discussed by Engelberecht (ref[10,11]). The experimental efficiency η (E) were then compared with the calculated value based only on simple n-p scattering as discussed by Zafirator (ref[12]).

2. Principle and Method.

2-1. Experimental determination of η (E) at 14.1 MeV.

The η (14.1) was determined by counting the alpha particles emitting from T(d,n)He^4 reaction. When the reaction occures, one alpha particles is produced simutanteneously with each neutron. By counting the alphas one can know the number of neutrons to within 1 to 2%. The angular relation between a neutron emitted at angle θ and an associated alpha particle at angle ϕ is given by

$$\sin \phi = (m_n E_n / m\alpha\ E\alpha)^{1/2} \sin \theta$$

Where m_n E_n and $m\alpha$ $E\alpha$ are the mass and energy of neutron and α particle respectively. Let $N\alpha$ is the number of alpha particles incident on the α-detector per second and N^{exp} the experimental counting rate of it,

then $N^{xp} = N\alpha\ \epsilon_\alpha$ where ϵ_α is the electronic efficiency of the α-detector, determining mainly by the bias levels. If the aperture of the α-detector is very small the incident neutrons can be considered approximately as parallel "beam". Then the neutron flux $\phi_n = N\alpha/A_D$, where A_D is the area of the nentron detector which received all the associated neutrons. In order to reduce background contributions, in stead of measuring neutron pulses directly, we measure the α-n coincidence outputs. The coincidence rate N_{coin} can be expressed as

$$N_{coin} = \phi_n\ A_D\ \epsilon_\alpha\ \epsilon_D\ \eta_o\ (E) = N\alpha'^{xp}\ \epsilon_D\ \eta_o\ (E)$$

where η_o (E) = the scientillation efficiency of the neutron detector.

ϵ_D = the electronic efficiency of the neutron detector. then η (E) $\equiv$ η_o (E) ϵ_D = $N_{ccin}/N\alpha^{exp}$, which is independent of ϵ_α.

2-2. The determination of η (E) up to 12.5 MeV by the "plastic scientillation" method.

The counting rate at angle θ due to hydrogen nuclei in the "scientillation" target is

$$N(\theta) = S_n\ (O^o)\eta_H\ V\ \sigma(\theta)\ \epsilon_\alpha\ \epsilon_s \frac{A_D}{R^2}\ \eta(E)\ F_1\ F_2(E) \qquad (1)$$

where V = the volume of the scientillation target.

R = the distance from the target to the detector.

ϵ_s = the electronic efficiency of the "scientillation" target.

S_n (O^o) = neutron flux at angle O^o and 1 cm apart from the source.

n_H = No. of hydrogen atoms per cm^3 of target.

σ (θ) = n-H differential section at neutron energy 14.1 MeV at angle θ

F_1 and F_2(E) are the flux attenuation factor of the incident and outgoing neutrons

respectely.

The coincidence rate between the monitor neutrons and the alpha particles is

$$N_M = S_n(O^\circ)\frac{A_M}{R^2_M}\epsilon_a\,\eta_M\,F \qquad (2)$$

where A_M = the area of the monitor normal to the incident neutrons.

η_M = the absolute detecting efficiency of the monitor at neutron energy 14.1 MeV.

F = the fraction of neutrons remaining in the beam after passage through the "scientillation" target.

R = distance from the target to the monitor.

The coincidence rate between the alpha particles and the recoiled protons in the scientillation target is

$$N_s = S_n(O^\circ)\frac{1}{R^2_H}\eta_H\,V\,\sigma_t\,\epsilon_a\,\epsilon_S\,F_1 \qquad (3)$$

where V is the volune of the scientillator.

R_H = distance from the target to the scientillator.

σ_t = *n-H total cross section at nentron energy 14. 1 Mev.*

N_S can be obtained experimentally by using a weak neutron beam.

From egu. (2) *and* (3), $\epsilon_S = \dfrac{N_s A_m\,\eta_M\,R^2_H\,F}{N_M\,R^2_M\,n_H\,V\,\sigma_t\,F_1}$.

From Egu. (1), (2) and the ϵ_S valve, η (E) can be expressed following

$$\eta(E) = \frac{N(\theta)\,R^2\,A_M\,\eta_M\,F}{N_M\,n_H\,V\,\sigma(\theta)\,A_D\,F_1\,F_2\,\epsilon_S\,R^2_M} \text{ or } \frac{N(\theta)\,\sigma_t\,R^2}{N_S\,A_D\,R^2_H\,\sigma(\theta)\,F_2}$$

with the known σ_t and $\sigma(\theta)$ for n-p scattering, the η(E) can be obtained.

3. Apparatus and Procedure.

3-1. The measurment of scattered neutrons by Time-of-Flight techniques.

The neutrons scattered from the "scientillation" target were measurment by Time-of-flight techniques. The arrangement was shown schematically in Fig. 1.

Neutrons from the $T(d,n)He^4$ reaction were produced by 130 KeV deuterons striking a thick Ti^3H target. The measured time was that between the detection of a recoiled alpha particle from the reaction and the corresponding scattered neutron in a NE213 scientillation counter 2m away. The 14.1 MeV neutron cone was at about 90° to the deuteron beam, and the associated alpda particles were at about 82° on the other side by the deuteron beam. The dimensions of the cone of the neutrons were determined by the geometry of the alpha counter. The alpha detector was a piece of NE102A plastic scientillator, 50 μm in thick, mounted on a pyrex glass light guide (2.5 cm in length), which was in contact with a 56 AVP photomultiplier, A Ta slit, 4 mm width and 8 mm high, at distance 6.7 cm from the center of Ti^3H target defined the aperture of the alpha counter, and thus the coincidence cone of incident neutrons. The neutron cone had an approximately Gaussian profile in both the vertical and the horizontal (scattering) planes. The experimental half angle (FWHM) of the cone was about 9.7° for the verticle profile

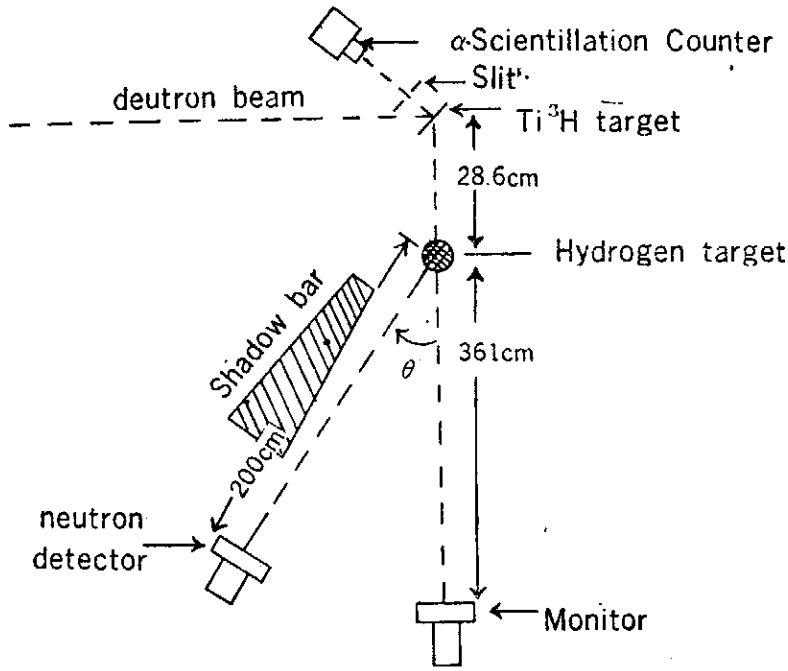

Fig. 1.

A schematic diagram of the experimental set-up used to measure differential Cross Section for n-p scatteirng.

and about 5.5° for the horizontal profile. The energy spread of the incident neutrons was about 150 KeV as seen from the spectrum of source neutrons. The main neutron detector was a NE213 liquid scientillator, 2 in. thick and 5 in. in diameter, mounted directly on a 58 AVP photomulipiler. A second neutron detector, also a NE213 liguid scientillator, 2 in. in diameter and 2 in. length, was used as monitor. The bias levels of the neutron detector and the monitor were determined by observating the spectrum of gamma sources, and checked carefully before and after each run by measuring the counting rates of these sources. A Am^{241} α-source, about 0.1 curie in strength seated on the Ta slit, was used to check the bias level of the alpha counter.

A copper and wolfram "shadow bar" 1 m long, was mounted between the neutron target and the neutron detector to reduce the flux of neutrons going directly from neutron source to detector.

The scattering target was supported on a light wood frame at distance 29 cm from the neutron source. The target was a NE 102A plastic scientillator, 1 in. in diameter and 2 in. long, mounted directely on a 56 AVP photomutiplier. The bias level of this "scattering" target was set at about 1.1 MeV proton energy to reject all recoiled carbon nucleus. A electronic block diagramme used to measure the flight time was shown in Fig. 2.

The constant fraction of pulse height trigger (ref. [13,14]), time pickoff method was used in the neutron side channel which provides good walk characteristics and optimum time resolution available from the NE213 liquid scientillator (ref [15,16,17]).

Overall time resolution better than 0.8 ns (FWHM) had been observed for gamma-

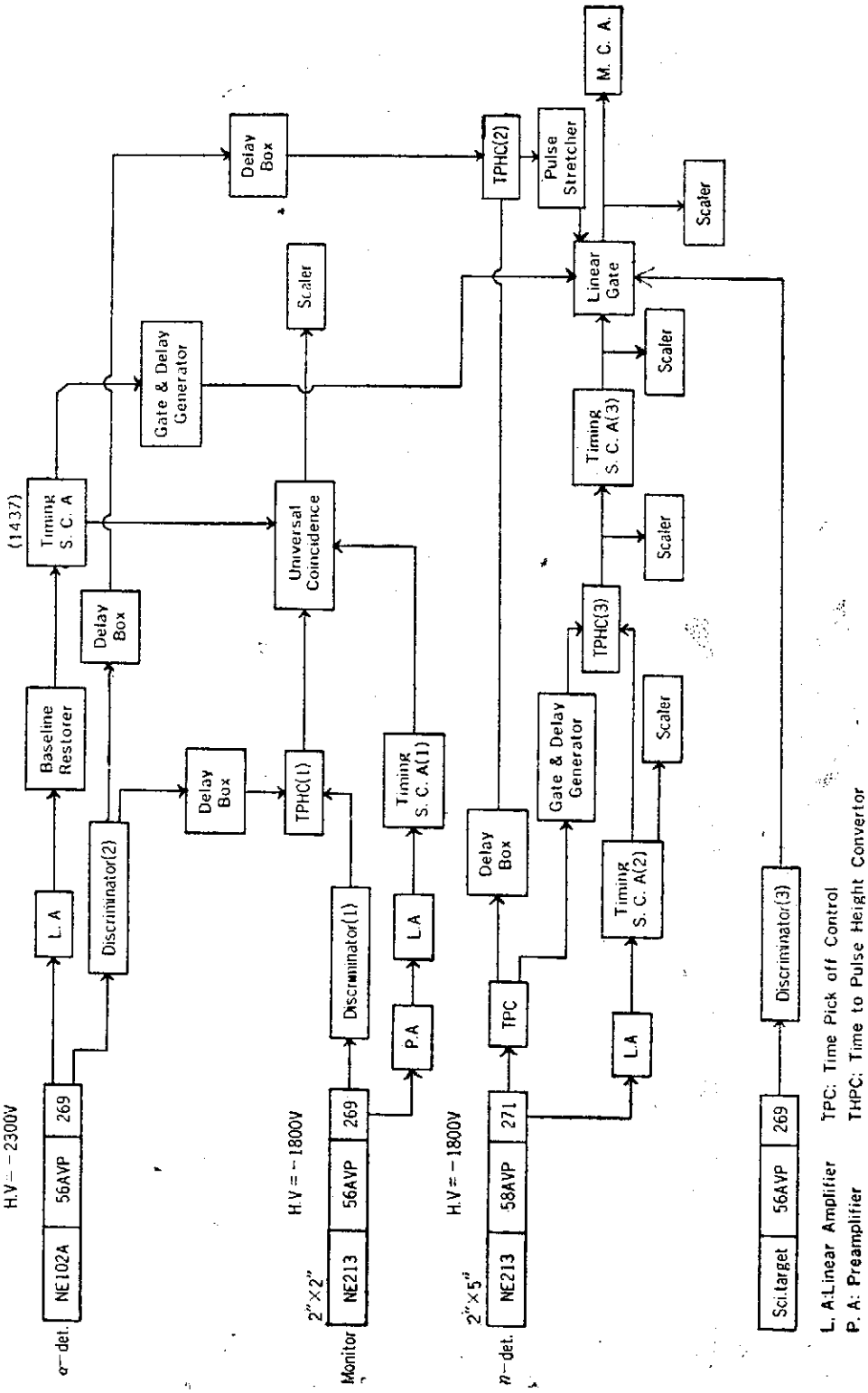

Fig.2. Blocke diagram of electronics of the Time-of-flight system for n-p scattering.

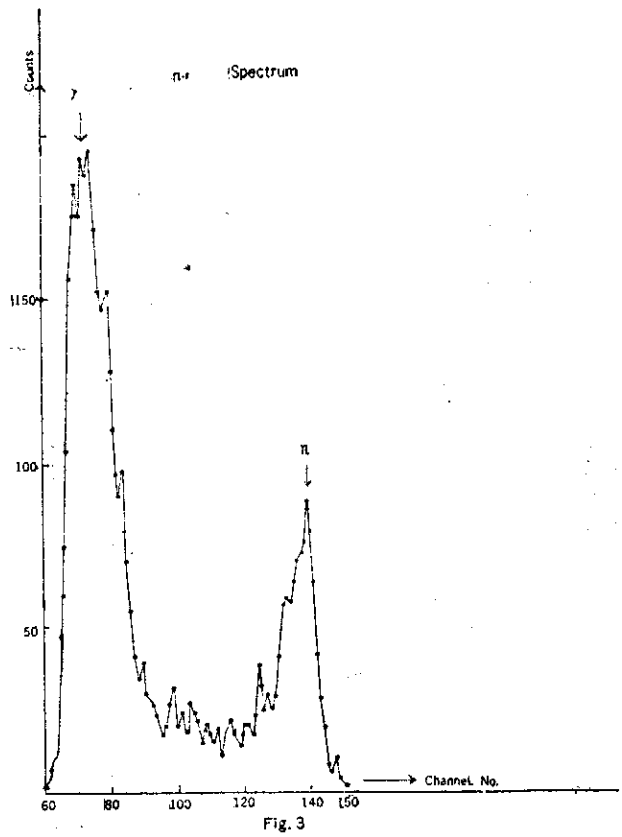

Fig. 3

Fig.3. The output of the gamma-n time to pulse height converter.

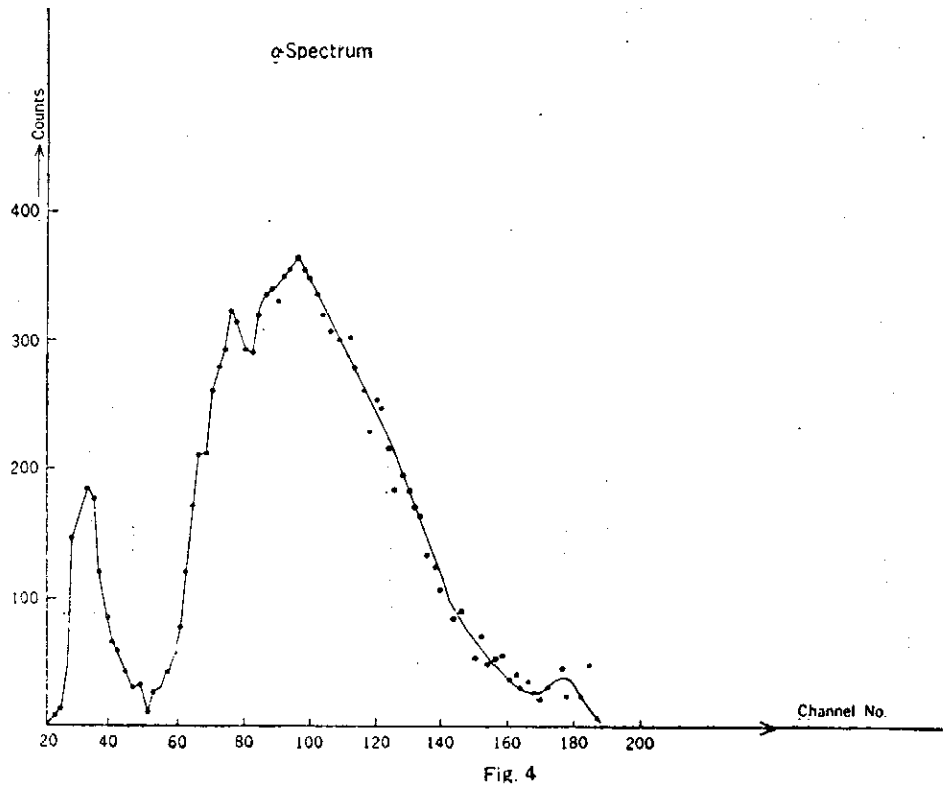

Fig. 4

Fig.4. The energy spectra of alpha particles

gamma coincidence measurment. Time resolution about 1.3 ns full width at half maximum and about 3 ns full width at 0.1 maximum were observed for 14.1 MeV neutron measur ment. Pulse shape discrimination method was used in this circuit to separate neutrons from gamma rays. The output of the r-n TPHC (time to pulse height converter) was shown in Fig. 3

After passing through Timing S.C.A. (3) the neutron pulses were selected to gate the 256-multichannel analyzer.

The α-particle spectrum was contaminated slightly on the high-channel side by neutron pulses and on the low-channel side by electronic noise as shown by Fig. 4. The low enerqy He^3 and H^3-particles were stop by a thin myler foil, about 0.9 mg/cm^3 covered on the surface of the alpha detector.

It was necessary to use a amplitude restriction in the α-particle spectrum to cut down the contamination. The Timing S.C.A. (1437) set a broad pulse height window around the α-particle peak and thus determined the electronic efficiency $\epsilon\alpha$. It's value was about 0.5, knowing from the ratio of counting rates of the α-counter from a α-source with and without the use of the amplitude restriction.

The background coincidence rate was low and approximately constant over the region of the pulse height spectrum displayed.

Measurment of scattered neutrons were taken from 20 degree to 60 degree at 5 degree intervals.

3-2 Detecting alpha particles.

The detecting efficiency of the monitor η_M (14.1) and the main neutron detector η (14.1) were obtained by counting rate of the alpha counter. A Ta slit, 2mm in diameter, at distance 6.7 cm from the center of the Ti^3H target defined a narrow "beam" of neutrons. The inner walls of the alpha counter were covered by thin sheets of Ta. A narrow pulse height window around the alpha particle peak was set, thus the contributions from background protons at high-channel side and the electronic noise at low-channel side could be neglected. The electonic arrangement was shown in Fig. 5

4. Results and Discussion

For 14.1 MeV neutrons, the measured absolute efficiency of the monitor η_M (14.1) was $(9.22\pm0.40)\%$. The η (14.1) of the main neutron detector was $(7.66\pm0.18)\%$.

The time-of-flight spectrum of neutrons scattered from the "scientillation" target were shown in Fig. 6-1,2, were N_M was the total neutron counts of the monitor. At scattering angles of 20°, 25° and 30°, "tails" were presented at the low channel side of the spectru m. We considered the "tail" neutrons also as true coincidence. The total counts $N(\theta)$ of the scattered neutrons can be found from the area of peak in the spectra and its uncertainty arises from background and statistics. The absolute efficiency η (E) at the neutron energy E were obtained using the formulas expressed in section 2-2.

The symbols in Table 1 had the following meanings:

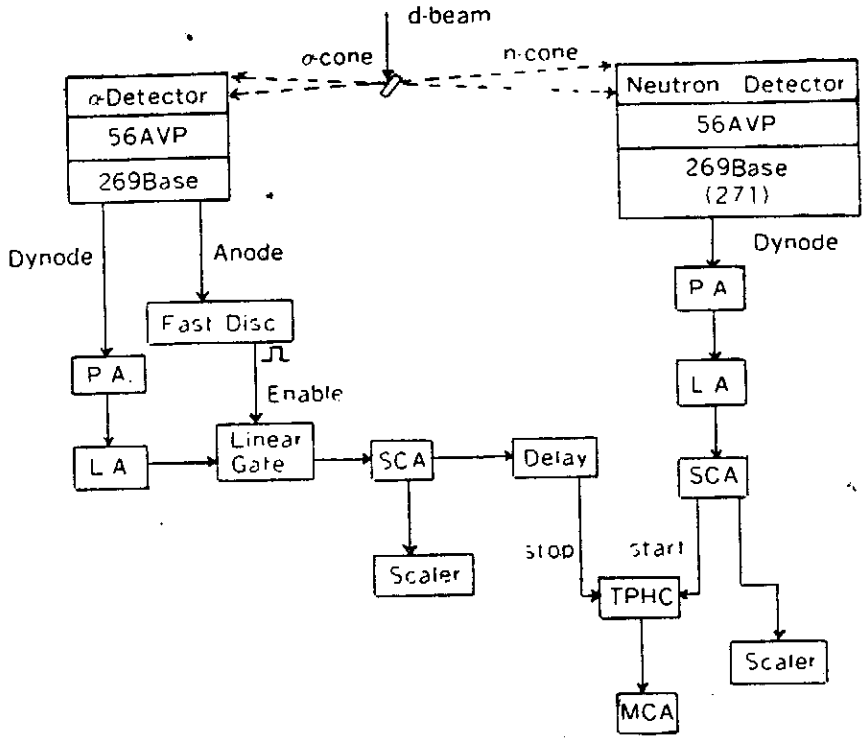

Fig.5. Block diagram of electronics used for the determination of n(14.1)

η(E) were the absolute efficiencies without the corrections of neutron flux attenuation in the scientillation target, i.e. setting $F_1 = F_2(E) = 1$.

η_1(E) were obtained by the assumption that the flux attenuation in the scattering target has the following simple form:

$$F_1 = e^{-\sum(14.1)R}$$

$$F_2(E) = e^{-\sum(E)R} \qquad \sum(E) = n_C\,\sigma_C(E) + n_H\,\sigma_H(E)$$

were R = the radius of the scattering target.

σ_C(E) = n-C cross section at neutron energy E.

n_C = No. of carbon atoms per cm^3 of the target.

η_2(E) were obtained with the neutron flux attenuaion as calculated by Engelberecht. (ref.[10,11]) where the detail shape of the target and the effects of proton recoil were considered.

η_{th} (E) = were the efficiencies calculated from the equation

$$\eta_{th}(E) = K(1-e^{-\sum(E)L})\left(1-\frac{E_B}{E}\right)$$

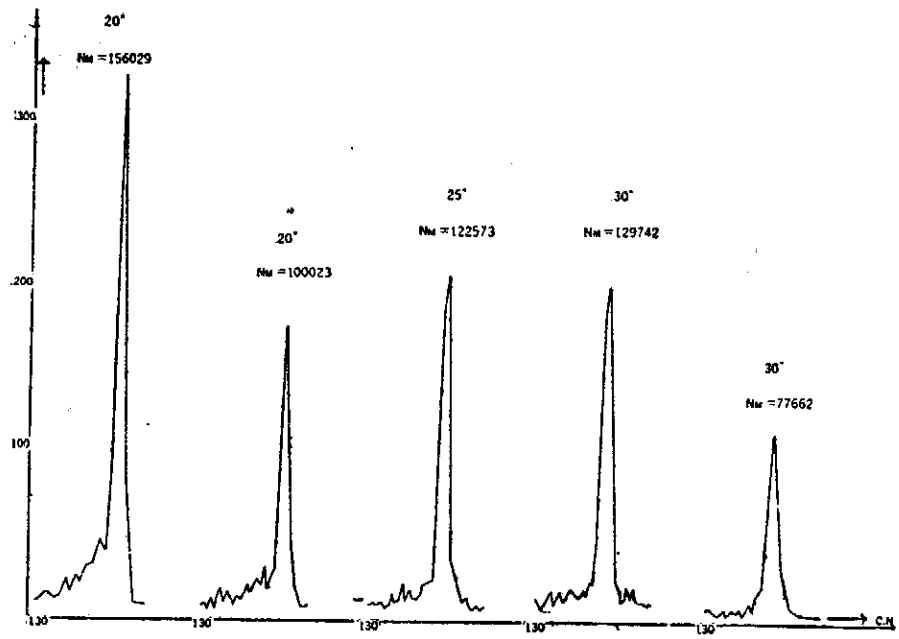

Fig.6-1 Time-of-flight spectra for neutrons seattered from hydrogen (plastic scientillator).

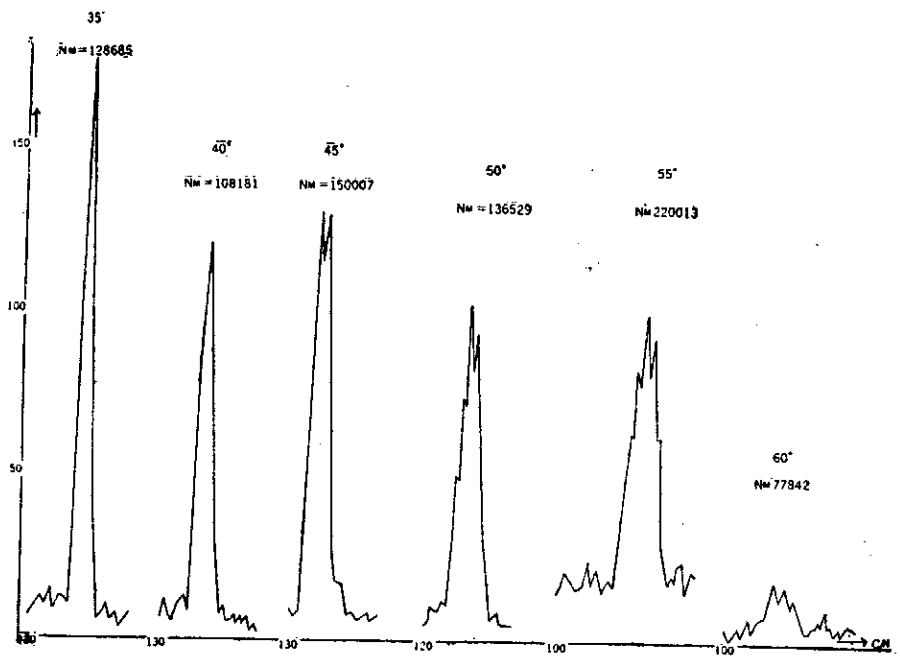

Fig.6-2 Time-of-flight spectra for neutrons seattered from hydrogen (plastic scientillator).

where L = the thickness of the neutron detector.

E_B = the bias level of the neutron detector.

The value of E_B, determined by the 3.3 MeV point, was found of be 2.7 MeV proton energy.

K = the electronic efficiency of the neutron counter, excluding the bias level E_B. Its value was determined from the experiment.

$$\sum(E) = n_H \sigma_R(E)$$

As shown in Fig. 7 and table 1, good agreement between the calculated and experimental neutron detection efficiencies were obtained at most neutron energies. At 12.5 MeV and 14.1 MeV the agreements were not good. This is similar to that observed by others (ref.[18],[19]). The disagreement might be due to the presence of the "tail" of the time-of-flight spectra. The detail shape of the efficiency curve was not reproduced by the more sophisticated calculation of Kurze, (ref.[20]) who had considered the effects of multipole scattering.

As also shown in Table 1, the values of the corrected efficiencies η_2 (E) were about 2% greater than n_1 (E) at most neutron energies. However, at 3.5 MeV, the difference was greater than 5% ($\frac{\Delta\eta}{\eta}$). The effects of proton recoil might become importance for neutrons with energy near the bias level of the neutron detector.

We are very grateful to Mr. M.S. Chen for maintenance and operation of the neutron generator throughout the experiment.

The results were given in table 1 and shown in Fig.7.

Table 1. Absolute neutron efficiency of the NE213 Counters

Energy E_n (MeV)	η(E) (%)	η_1(E) (%)	η_2(E) (%)	ηt (E) (%)	Exp. method detector in direct beam
14.1	7.66±o.17			7.02	(n,p)seattering at
12.5	7.45±0.21	8.22±0.23	8.40±0.24	7.61	20°
11.6	6.77±0.28	7.48±0.31	7.67±0.32	7.89	25°
10.6	7.25±0.21	8.02±0.23	8.21±0.24	8.21	30°
9.5	7.00±0.29	7.77±0.32	7.97±0.33	8.55	35°
8.3	7.12±0.25	8.05±0.28	8.27±0.28	8.55	40°
7.1	7.57±0.29	8.36±0.32	8.62±0.33	9.01	45°
5.8	7.19±0.30	8.11±0.34	8.35±0.35	8.82	50°
4.6	6.78±0.29	7.89±0.34	8.20±0.35	7.84	55°
3.5	3.60±0.34	4.41±0.42	4.66±0.43	5.09	60°

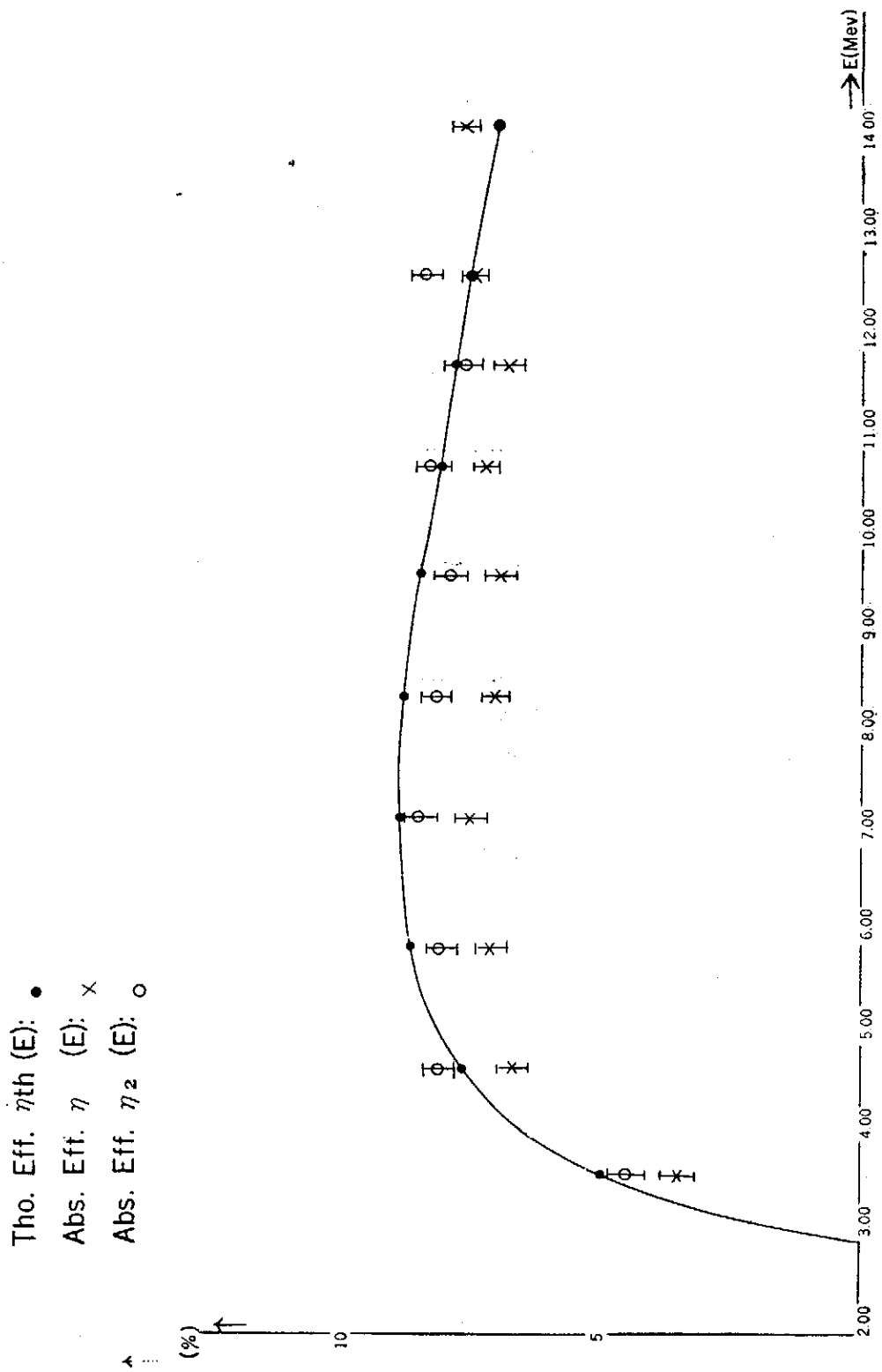

Fig. 7. Absolute neutron detection efficiency of the NE213 Counters.

References

1. R. L. Cassola et al., Phys. Rev. 144 (1966) 854
2. R. L. Clarke et al., Nucl. Phys. 53 (1964) 177; A 95 (1967) 320
3. P. H. Stelson et al., Nucl.Phys. 68 (1965) 97
4. W. J. McDonald et al., Nucl. Phys. 59 (1964) 321
5. J. Tesch, Nucl. Phys. 37 (1962) 412
6. C. C. Jonker et al., Nucl. Phys. A181 (1972) 545
7. C. C. Jonker et al., Nucl. Inst. and Meth. 42 (1966) 56
8. J. L. Cammel. in Fast Neutron Phys., Part II.
9. A. Horsley, Nucl. Data. A 2 (1966) 243
10. C. A. Engelberecht, Nucl. Inst. and Meth. 80 (1970) 187
11. C. A. Engelberecht, Nucl. Inst. and Meth. 93 (1971) 103
12. C. D. Zafirator, Nucl. Inst. and Meth. 32 (1964) 226
13. W. J. Dc Donlad et al., Nucl. Instr. and Meth. 55:377 (1967)
14. W. J. DcDonald et al., Nucl. Instr. and Meth. 58:253 (1968)
15. D. L. Wieber etc. IEEE Trans. Nucl. Sci. NS-B(1), 406 (1966)
16. P. R. Orman, N.I.M. 21(1) 121 (1963)
17. W. J. McDonald etc. N.I.M. 55(2), 377 (1967)
18. P. Perrin et al., Nucl. Phys. 43 (1963) 628
19. J. B. Hunt et al., Nucl. Inst. and Meth. 85 (1970) 269
20. R. J. Kurz, NURL report 11339 (1964)

Study of Excited States of ^{75}As with the ^{74}Ge (p, γ) ^{75}As Reaction*

C. W. Wang (王建萬), Y. C. Liu, E. K. Lin (林爾康), C. C. Hsu and G. C. Kiang (江紀成)

Tsing Hua University and Academia Sinica

Abstract

The gamma-radiation following the proton capture reactions, ^{74}Ge(p,γ)^{75}As, has been studied with a Ge(Li) detector. From the analysis of the measured gamma-ray spectra, a detailed decay scheme of ^{75}As was constructed in which the energy levels of ^{75}As up to 2938 keV excitation were determined. Among these three are new levels. Spin and parities for some levels are suggested. The deduced level-schemes are in good agreement with results of Wilenzick et al and Moreh and Shahal.

I. Introduction

Early information on low-lying levels in the ^{75}As nucleus has been obtained from the radioactive decay[1,3] of ^{75}Se and ^{75}Ge, Coulomb excitation[3] and neutron inelastic scattering[4]. Energy levels below 822 keV together with their spins and parities have been well-established. Only a few information on levels above 822 keV is available. In recent years investigations of the energy levels of ^{75}As above 1 MeV have been reported[5,6] from high resolution measurements with the use of the Ge(Li) detector. Wilenzick et al[5] has observed γ-ray transitions in ^{75}As in their (n,n'γ) reaction experiment and obtained the energy levels of ^{75}As up to 1606 keV. Moreh and Shahal[6] has measured the energy levels of ^{75}As up to 2687 keV excitation in a resonance scattering experiment, and proposed a decay scheme of ^{75}As from the resonance at 7646 keV. Among the energy levels reported in these two works, many are new. The energy levels of ^{75}As measured through (n,n'γ) reaction experiment are apparently not all populated in the resonance scattering, additional information is necessary to verify the new levels reported.

By using the ^{74}Ge(p,γ)^{75}As reaction it is possible to measure levels of ^{75}As up to rather high excitation. A brief study on the ^{74}Ge(p,γ)^{75}As reaction has been made in 1957 by Chick and Hunt[7], who obtained many resonances in ^{75}As at excitation energies between about 8.0 and 10.0 MeV. Among these three prominent resonances at E_p=2342 keV, 2528

(*) Work performed at the Physics Research Center in Hsinchu and supported by the National Science Council.

keV and 2664 keV were observed. In the present work we used the $^{74}Ge(p,\gamma)^{75}As$ reaction to determine the excitation energies of ^{75}As up to 2938 keV and suggested the corresponding spin values. The aim of this work was on one hand to supplement the information on the energy levels of ^{75}As higher than 822 keV and also to verify new levels reported recently, and on the other hand to confirm the 2531 keV resonance from the $^{74}Ge(p,\gamma)^{75}As$ reaction and to determine the branching ratios for γ-ray transitions and decay scheme of ^{75}As levels observed.

The experiment consists of yield measurements of γ-ray de-excited from the 9399 keV eresonance at proton energy E_p=2531 keV. The measurements were carried out by using a large volume, high resolution Ge(Li) detector. Level energies were determined to within 1.5 keV.

This paper is one of a series describing experimental investigations on the decay schemes of the arsenic isotopes by using proton capture reaction. Some data of (p,γ) reactions have been recently published[8,9].

II. Experimental Procedure

The proton beam was provided by the Van de Graaff accelerator at Tsing Hua University. The beam intensity was a few microamperes. The beam energy was determined by usual nuclear magnetic resonance method Several resonances in the $^{27}Al(p,\gamma)^{28}Si$ reaction were used as proton energy calibration standard.

The target was isotopically enriched ^{74}Ge deposited on a 0.4 mm gold backing, mounted in a specially designed target chamber[9]. The thickness of the prepared targets was between 10-30 $\mu g/cm^2$. In the course of the experiment, the target was water cooled.

The gamma rays from the $^{74}Ge(p,\gamma)^{75}As$ reaction were recorded by a 50 c.c. Ge(Li) detector and a 3″ x 3″ NaI(Tl) crystals enclosed in lead shields. These two detectors were mounted oppositively at 90° to the beam direction. The Ge(Li) detector was used for γ-ray spectra measurement, while the NaI(Tl) crystal for the γ-ray yields measurement. The data taking procedure was as follows:

1. The yield measurement was made in the proton energy range from 2450 keV to 2550 keV in steps of about 1 keV to confirm the 2528 keV resonance previously observed by Chick and Hunt[7]. The resonance energy was accuratly determined to be 2531±2 keV.
2. The proton beam energy was then kept at 2531 keV for γ-ray spectra measurement. Data were collected in a period of 24 hour run. The obtained γ-ray spectra were stored in a TMC 4096 channel analyzer with a conversion gain of 3 keV per channel.

A detailed description of the experimental method and data analysis has been described in a proceding paper[8].

III. Results

1. Level scheme of ^{75}As

The results of the γ-ray spectra measurements at E_p=2531 keV are summarized in Table I. Fig. 1 shows the high energy part of the measured γ-ray spectrum at E_p=2531 keV. The γ-ray energies obtained were used to construct a level scheme for the ^{75}As nucleus as shown in fig. 2. The first column of Table I shows the observed γ-ray energies. The third column lists the energy levels of ^{75}As as deduced in the present work, which are seen in good agreement with those reported by Wilenzick et al[5] and Moreh and Shahal[6], as given in the fourth and fifth columns.

In the excitation energy range of $E_x \leq 1605$ keV we obtained twenty-three levels, and confirmed all levels observed in the (n,n'γ) work by Wilenzick et al[5], except the 1595 keV level which, because of large background, is somewhat uncertain according to the present data. It was not observed in the resonance scattering experiment[6]. In the excitation energy range of 1605 keV $< E_{ex} \leq$ 2938 keV we observed ten energy levels, among these three are not previously reported. These are levels at 1808 keV, 2663 keV and 2938 keV.

2. Decayscheme of ^{75}As

The observed γ-rays (a total of 113 lines), except few, were all identified. The information from identified γ-lines was used to construct a decay scheme as shown in fig.3. For the low-energy γ-lines, this is similar in general detail to the scheme published in ref. 5, however, we have not observed the γ-ray lines corresponding to the 619-265 keV, 822-279 keV and 1422-400 keV transitions. It is seen that the decay scheme of ^{75}As is extremely complex as a result of the high level density of ^{75}As. It is remarkable that the 9399 keV resonance decays directly to all lower states except the 822 keV (7/2$^-$) state. The sum of the branching ratios for the transitions fitted to the total decay.

The broken lines in fig.3 indicate uncertain transitions and hence uncertain levels (the 1262 keV, 1595 keV and 2470 keV). The numbers in fig.3 are the percentage of the branching ratio for the γ-ray transitions. These were determined from the analysis of the observed γ-ray spectra, with correction for attenuation and detector efficiency. The errors in the branching ratios are probably low. Most are due to the errors in the peak area measurements. The relative accuracy is in the range 5 to 10% except for very small values where the error is larger.

3. Q value

The Q value of the ^{74}Ge(p,γ)^{75}As reaction was re-determined from the $\gamma \rightarrow$ground and lower excited states transitions in the E_p=2531$\pm$2 keV resonance. The excitation energy of the resonance was accurately calculated to be E_{ex}=9398.6$\pm$5 keV, and the Q value obtained is 6901.6$\pm$5 keV, which is in reasonable agreement with the one reported in the Nuclear Data[1].

IV. Discussion

In the present experiment we obtained more information on the energy levels of ^{75}As than those being reported previously[1-6]. A total of thirty-three energy levels up to 2938 keV were determined. Due to the use of an absorber in front of the detector, the γ-lines

with $E\gamma < 270$ keV could not been observed. In general, the level scheme of ^{75}As and decay scheme obtained in this work are in excellent agreement with recently available data of Wilenzick et al[5] and Moreh and Shahal[6]. Our data give additional evidence for the existence of the 865 keV level, and confirm the existence of the level at 1044 keV, 1064 keV and 1422 keV as reported in ref. 5, and also of the levels at 1872 keV, 2064 keV, 2097 keV, 2176 keV, 2572 keV and 2687 keV as reported in ref. 6.

Levels at 1134 keV, 1262 keV, 1355 keV, 2233 keV and 2596 keV found recently in the resonance scattering experiment[6] have not been observed in the present experiment. However, we obtained twelve energy levels between 279 keV ($5/2^-$) and 2683 keV which have not been found in the resonance scattering experiment[6]. These levels are most with spins of $\geq 5/2$, since the resonance scattering experiment selectively populates only those levels which have large dipole matrix elements and hence one observed only levels in ^{75}As with spins of 1/2 or 3/2.

In the present $^{74}Ge(p,\gamma)^{75}As$ experiment at low energy of $E_p=2531$ keV, the angular momentum of protons carrying into the resonance state is mainly of value $\ell=0$, it is expected that the levels with spins of 1/2 or 3/2 have appreciable branching ratios. It is seen from Table I that for the levels which were known or previously assigned to be (1/2,3/2), the measured branching ratios for the transitios r→these levels up to 2098 keV are falling into values of $\geq 4.0\%$. Only one level at 573 keV is exceptional, the measured branching ratio is 4.2%, but it is known to be $5/2^-$ as reported in ref. 1. The above consideration suggests that three new levels at 1808 keV, 2663 keV and 2938 keV and also the 2683 keV level may have spins of 1/2 or 3/2. In the subsequent decay from the 1044 keV level 10 per cent of the total decay was found to feed the 279 keV level and 45 per cent to feed the 304 keV and 400 keV levels, respectively. The 279 keV, 304 keV and 400 keV levels are known[1] to be $5/2^-$, $9/2^+$ and $5/2^+$, respectively. From consideration on the M1 and E1 transition probabilities, it is favorable to suggest the 1044 keV level to be $7/2^-$. A summary of suggested spins for the levels obtained in the present investigation and those assigned previously are listed in the last column of Table I. It is believed that the present data would give an useful information on the level structure of the ^{75}As.

Acknowledgement

It is a pleasure to thank all members of the Van de Graaff accelerator group for their generous assistance.

References

1. Nuclear Data Sheets, compiled by K. Way et al. (Printing and Publishing Office, National Academy of Science, National Research Counccil, Washington, D. C.)
2. S. C. Pancholi and H. Ikegami, Nucl. Data B6, 79 (1966)
3. R. L. Robinson, F. K. McGowan, P. H. Stelson, and W. T. Wilner, Nucl. Phys.

A104, 401 (1967)
4. D. L. Smith, Bull. Am. Phys. Soc. 15, 86 (1970)
5. R. M. Wilenzick, V. R. Dave, and J. A. Nelson, Phys. Rev. C4, 2126 (1971).
6. R. Moreh and O. Shahal, Phys. Rev. 188, 1765 (1969)
7. D. R. Chick and S. E. Hunt, Nature 180, 88 (1957)
8. T. H. Hsu, E. K. Lin, C. C. Hsu, Y. C. Liu, P. K. Tseng, C. W. Wang, and W. S. Hsu, Chin. J. Phys. 10, 56 (1972)
9. T. H. Hsu, P. K. Tseng, E. K. Lin and Y. C. Liu, Nucl. Inst. and Methods 106, 513 (1973)
10. F. C. Young, A. S. Figuera and G. Pfenfer (University of Maryland), unpublished (1970).

Table I

Gamma energies, branching ratios and level energies in ^{75}As from ^{74}Ge(p,γ)^{75}As reaction

High Eγ (keV)	Branching Ratio	Present work	Energy Level (keV) (γ,γ')	(n,n'γ)	Spin and Parity
9398	4.7	0	0	0	$3/2^-$
9200	6.2	199.3±1.5	199	198.6	$1/2^-$
9133	5.2	264.9±1.5	265	264.7	$3/2^-$
9120	2.6	278.7±1.5	—	279.0	$5/2^-$
9093	1.6	304.1±1.5	—	303.2	$9/2^+$
8997	2.4	400.4±1.5	(404)	400.3	$5/2^+$
8930	4.5	468.6±1.5	468	468.8	$(1/2^-)$
8828	4.2	572.6±1.5	(568)	572.8	$5/2^-$
8779	4.7	619.1±1.5	618	617.9	$(1/2^-,3/2^-)$
—	—	822	—	821.8	$7/2^-$
8536	3.9	864.8±1.5	—	864.5	—
8353	<1.0	1044.0±1.5	—	1043.6	$(7/2)^b$

8343	<1.0	1065.4±1.5	—	1063.8	$(1/2^-,3/2^-)^a$
8331	<1.0	1077.0±1.5	1076	1076.4	—
8268	2.1	1128.6±1.5	—	1129.3	$(1/2^-,3/2^-)^a$
—	—	—	1134	—	$(1/2^-,3/2^-)^a$
8193	5.5	1204.5±1.5	1203	1204.4	$(1/2^-,3/2^-)^a$
—	—	(1262)	1262	—	
8046	3.7	1351.3±1.5	—	1349.7	
—	—	—	1355	—	
7976	1.9	1422.0±1.5	—	1422.1	
7966	2.1	1431.7±1.5	1432	1431.9	$(1/2^-,3/2^-)^a$
7891	3.7	1504. ±1.5	1505	1503.2	$(1/2,3/2)^a$
—	—	(1595)	—	1595.4	
7793	4.2	1605. ±1.5	1607	1606.4	$(1/2,3/2)^a$
7591	4.1	1808 ±2	—		$(1/2,3/2)^b$
—	—	—	(1843)		
7524	6.0	1874 ±2	1872		$(1/2,3/2)^a$
7335	<1.0	2061 ±3	2064		
7299	6.2	2098 ±3	2097		$(1/2,3/2)^a$
7221	2.4	2180 ±3	2176		$(1/2,3/2)^a$
—	—	—	2233		$(1/2,3/2)^a$
—	—	(2470)	(2470)		
6824	<1.0	2572 ±3	(2572)		
—	—	—	2596		
6733	4.8	2663 ±4	--		$(1/2,3/2)^b$
6713	5.2	2683 ±4	(2687)		$(1/2,3/2)^b$
6461	6.7	2938 ±4	—		$(1/2,3/2)^b$

a) ref. 6

b) suggested from present work.

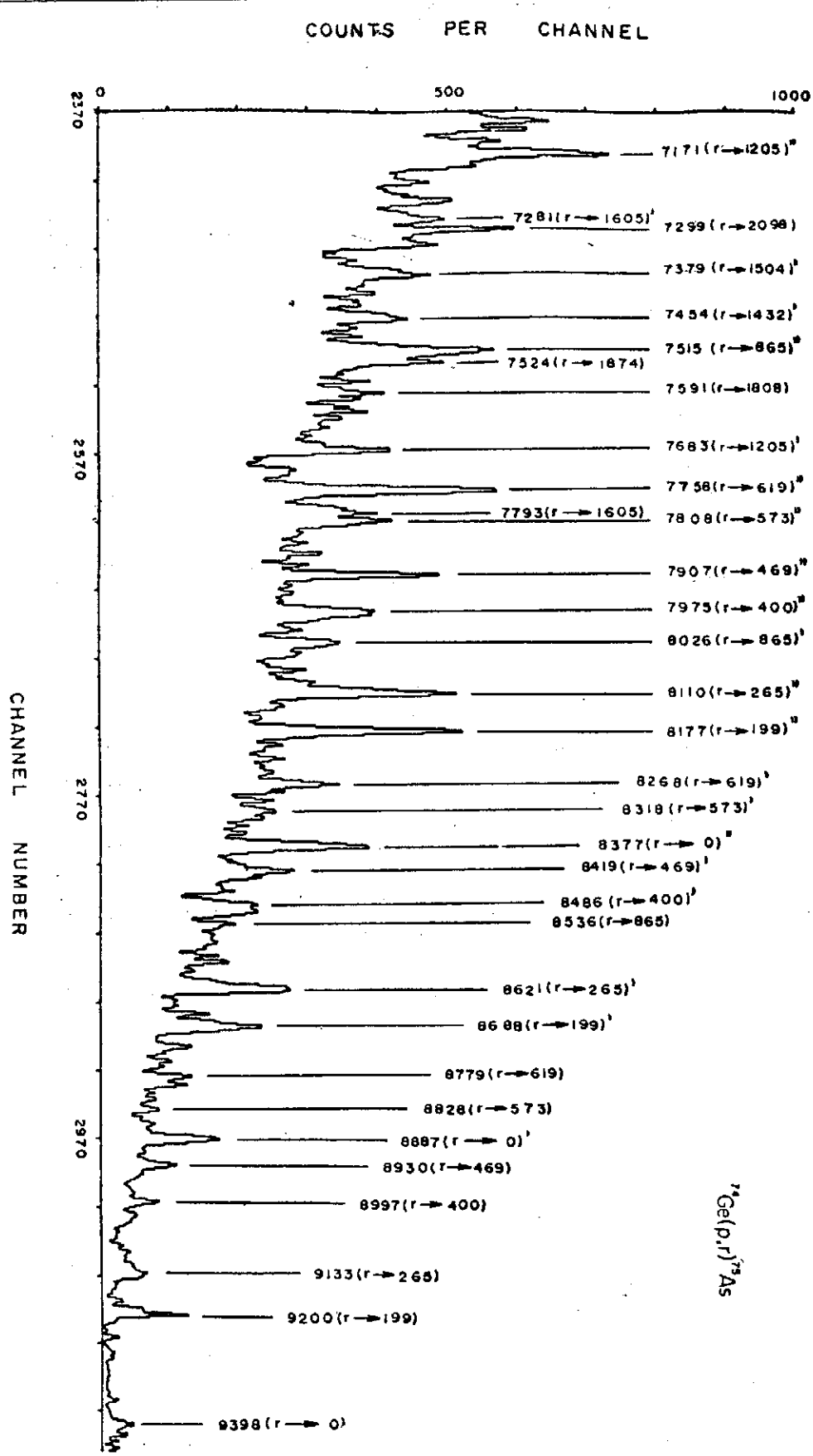

Fig. 1 Part of gamma-ray spectrum of the ^{74}Ge(p,γ)^{75}As reaction at E_p=2531 keV. Numbers over peaks refer to gamma-ray energy. ( ) ( )'( )" refer to the full-energy, single-escape, and double-escape peaks, respectively.

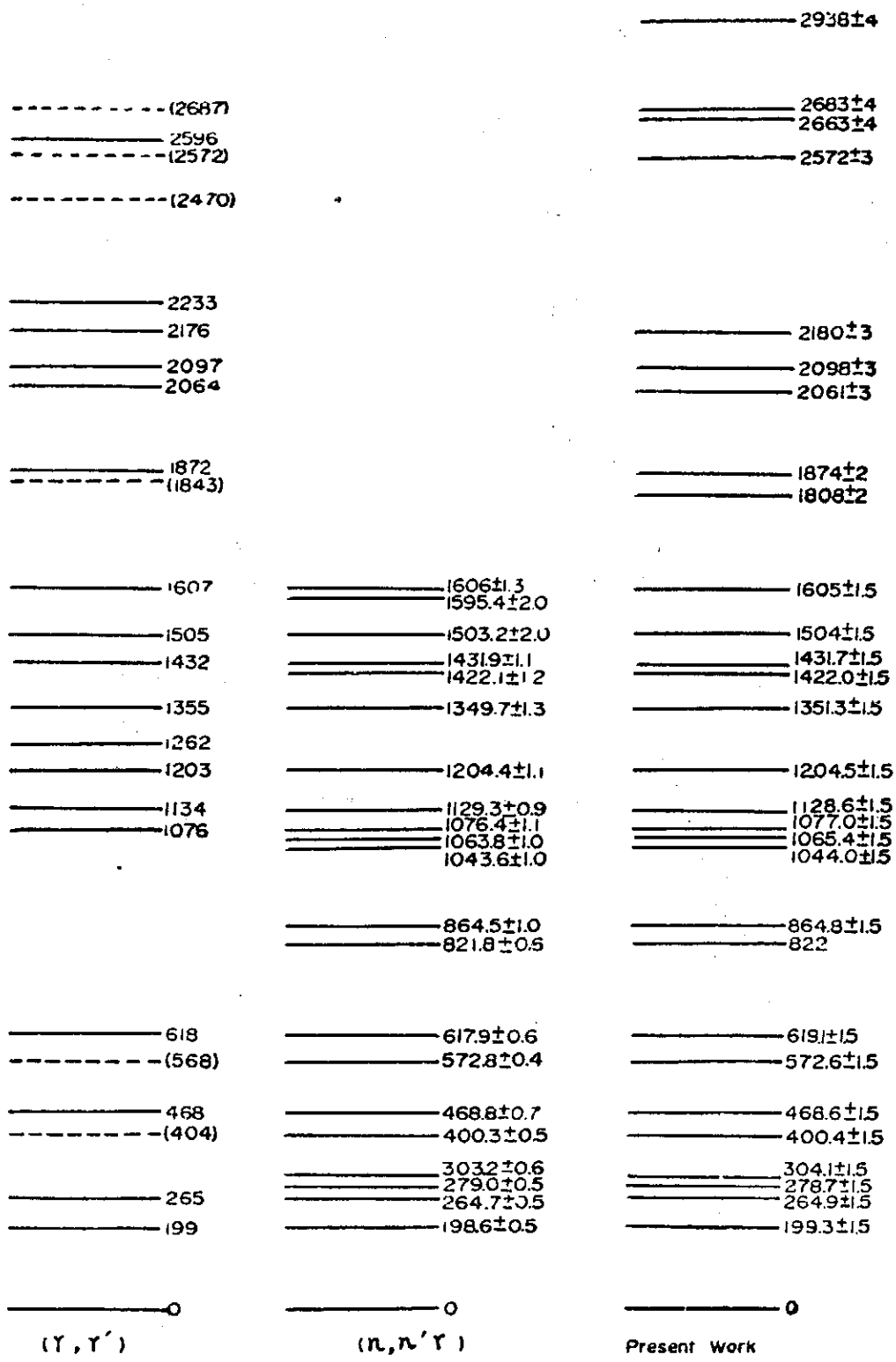

Fig. 2 A comparison of the energy levels of ^{75}As as obtained in the present work with the results of Moreh and Shahal (ref. 6) and of Wilenzick et al (ref. 5).

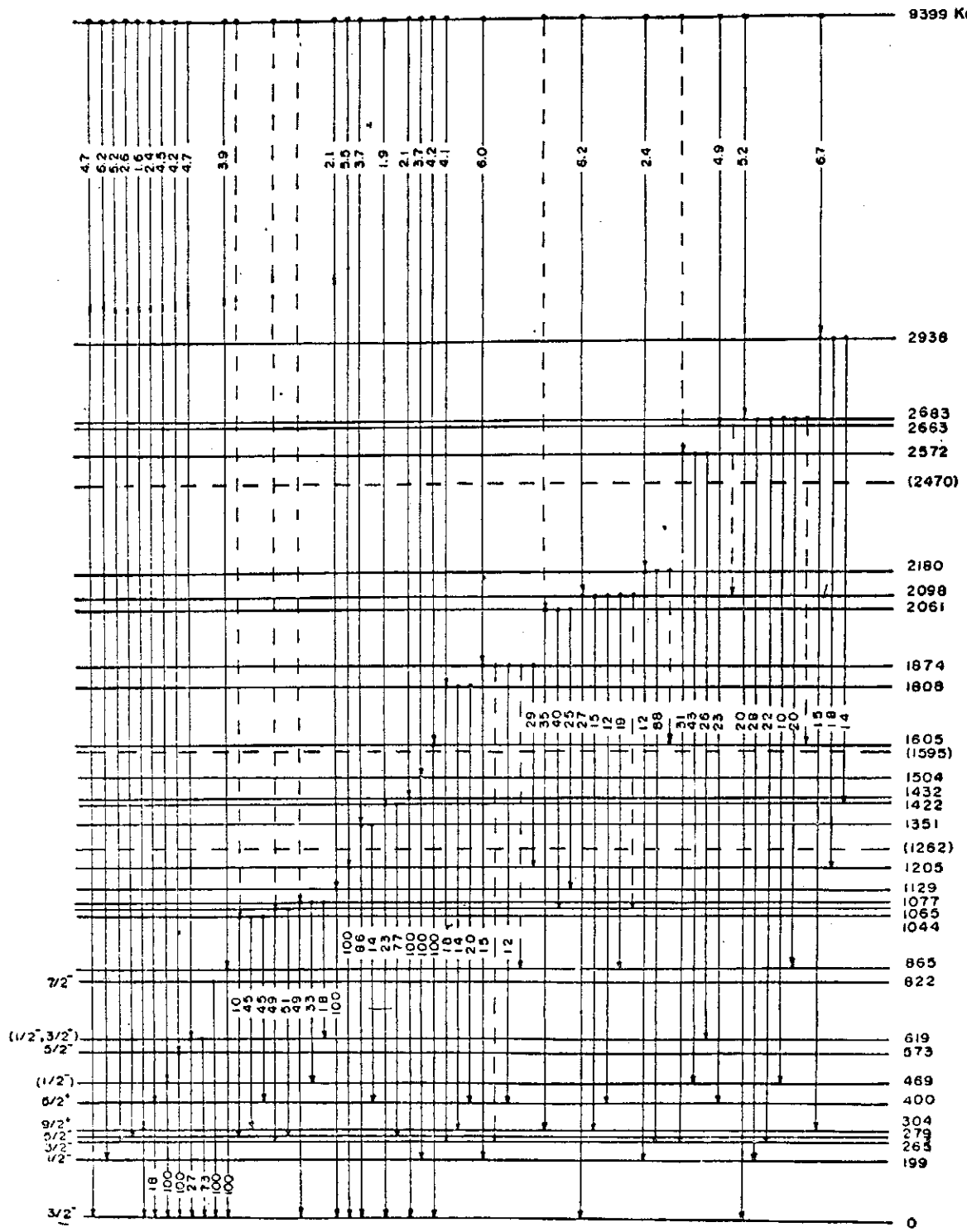

Fig. 3 The decay scheme of 9399 keV resonance in ^{75}As observed in the present work.

毛髮活性化分析研究

王定　董岐龍　王唯農

中央研究院物理研究所

摘要：

本實驗是利用 Ge(Li) 偵檢器用活性化分析來測試研究新竹地區人之頭髮內所含之元素及其成分，從所採取八組不同之頭髮樣品中共可找到14種不同之同位素，其中Hg,Br,Na Zn 等四種元素，在每組樣品中均可發現，其餘元素則因取樣不同而有所差異。

自一個人之頭上，分成五個部位（前中後右左）取樣分析其中 Zn,Na 兩元素隨部位之不同含量間之差距，Zn 元素之變化幅度約爲±20%，Na 元素之變化幅度約爲±50%，如將八組不同人之頭髮樣品，分別取樣分析Zn,Na兩元素，其含量間之差距較之因部位不同所產生之差距要顯著得多。

利用活性化分析對毛髮鑑定犯罪之可能性並加討論。

Ⅰ. 簡介：

近幾年來由於高分解力（high resolution） Ge(Li) 偵檢器（Detector）之發明及改良對於活性化分析之研究工作有顯著的進展，只須取極少量之毛髮樣品就可尋出其內所含之元素及成分，在美國、加拿大、日本、英國等地，許多學者對頭髮之活性化分析已從事了多項研究（參閱 1－7）被發現所含之同位素，因地區之不同而略有差異，頭髮中所發現之同位素，自13種到24種不等，其中除如 Hg,Na,Zn,Br,Mn 等同位素含量較多，在各地人的毛髮中均有發現外，其餘近約20種同位素因地區之不同，含量各異，此20餘種元素所放射之主要伽瑪射線能量及其半衰期均已知道，在檢測中兩者相輔爲用，減少許多檢定之困難。

本實驗爲在新竹地區取 8 組不同人之頭髮樣品，利用清華大學之原子爐及中央研究院物理研究所之 43C.C Ge(Li) 高分解能力偵檢器，從處理頭髮樣品，研究其定性，定量問題着手（參閱 8.9 ），進而對此 8 個人之樣品在頭上各不同部位之頭髮中，其所含元素之種類及含量間之關係，做一系統之分析研究。

Ⅱ. 樣品製備：

取一束頭髮約0.05g 放入濃度一定之非肥皂水溶液中，浸約半小時，取出，再用蒸餾水、丙酮、將頭髮洗淨、烘乾、用鋁箔包裝，製成樣品，然後送入原子爐中照射，照射之中子強度約爲10^{13} neutrous/cm^2sec.

Ⅲ. 運用儀器：

本實驗所用之偵檢器（Detector）爲 43C.C Ge（Li）偵檢器，其分解力（Energy Resolution ）對 Co^{60} 1.332 MeV 爲 3.8 KeV. 利用 1024 多頻導分析儀（Channel Analyzer）紀錄其結果。

Ⅳ. 能量測定：

由下列標準放射源（ Standard Source ）測試衰變能譜，各放射源所發射伽瑪射線之能量如下表。

標準發射源 (Standard Source)	能　量 (MeV)
Ba^{133}	0.081,0.274,0.302,0.356,0.384
Co^{57}	0.122
Na^{22}	0.511
Cs^{137}	0.662
Mn^{54}	0.835
Co^{60}	1.173,1.332

將上列所得之能量及其對應之頻導數 (Channel Number) 輸入 8 K 計算機 (On Line Computer) 則可得各頻導對應之能量。

圖 I 爲本實驗儀器依照上列標準發射源所繪之能量頻導關係圖，在實用範圍內，從0.1MeV至 2.0MeV 近乎一直線。

V. 資料測取及分析：

檢測頭髮樣品內各元素之靈敏度得視各該元素對中子之反應橫截面之大小及其所形成之放射原子核之半衰期長短而定，該樣品應照射之時間長短及取分析資料之時間長短均得因預測之元素性質及含量多少而變動，再者由於不破壞樣品之原則下，故不再利用化學分離，許多種元素的同時存在，在取資料的技術上需考慮之因素更爲增加。

(1)頭髮內主要元素之測定：

取用一人，同一部位，重約 0.1g 之頭髮一束，分成兩組，每組約重 0.05g ，一組照射 30min, 製成樣品A，一組照射 12hr 製成樣品B，將樣品A每隔一天測定其放射性計數 (Count) 1 次，共測 3 天，將此 3 次計數之單能譜 (Single Spectrum) 依對數比例大小繪如圖 II，由圖 II 中，每次可見到之同位素如表 1：

表 1

衰變時間 (Decay Time)	可見之同位素
1 天	Zn^{69m},Cu^{64},Br^{82},Mn^{56},Na^{24},K^{42}
2 天	Zn^{69m},Cu^{64},Br^{82},As^{76},Na^{24},K^{42}
3 天	Zn^{69m},Cu^{64},Br^{82},Na^{24},K^{42}

觀察圖 II 及表 1 知，衰變 2 天後短半衰期之 Mn^{56} 消失。自 Br^{82} 放射能量爲 0.554之射線及能量爲 0.559 MeV 之 As^{76} 放射線能量非常接近，但自圖上三天的測量分出此兩放射線。

將樣品B分 3 次測量，計數分別爲衰變 2 天，7 天及21天後各計數一次，將此 3 次計數之單能譜依對數比例大小繪如圖 III，由圖 III 中，每次衰變可見到之同位素列於表 2 。

表2

衰變時間（Decay Time）	可見之同位素
2天	Zn^{69m},Cu^{64},Br^{82},Zn^{65},Na^{24},K^{42}
7天	Hg^{203},Br^{82},As^{76},Zn^{65},Na^{24}
21天	Hg^{203},Zn^{65}

觀察圖Ⅲ，表2知衰變7天後，Zn^{69m}, Cu^{64},K^{42} 衰變消失，Hg^{203},As^{76}顯現，衰變21天後，僅剩 Hg^{203}, Zn^{65} 兩同位素，其他同位素均衰變消失。從表1、表2中可看出，因照射（30min,12hr）及衰變時間之不同，同一人，同一部位內所含之同位素能够被發現之可能性也隨之不同， Hg^{203},Zn^{65} 因需照射較長（12hr）之時間始易顯現，而 Mn^{56} 僅需照射較短時間（30 min），此乃由於其對中子之反應橫截面及其半衰期長短關係之故。

從表1、表2中可知此一人，同一部位頭髮內含有 Hg^{203},Zn^{69m},Cu^{64},Br^{82},As^{76},Mn^{56},Zn^{65}, Na^{24},K^{42} 等9種不同之同位素。

依上列同類之方法，分析本實驗所取八組不同人之頭髮，共可找到14種不同之同位素，將此14種同位素之半衰期（Half Life）及其主要用以定性之 r 射線列於表3。

表3

同位素	半衰期	用以定性之 r 射線能量（KeV）
Hg^{203}	46.9da	279.1;
Cr^{51}	27.8da	320.0;
Au^{198}	2.70da	411.8;
Zn^{69m}	13.8hr	438.7;
Cu^{64}	12.8hr	B^+(511.0);
Br^{82}	35.9hr	554.3; 619.0; 780; 1043.9;
As^{76}	26.3hr	657.0; 1228.8;
Cs^{134}	2.1yr	570; 604.7;
Sb^{124}	60da	602.6; 1690.7;
Sb^{122}	2.75da	1.13; 1.24;
Mn^{56}	2.58hr	846.9; 1810.7;
Zn^{65}	245.0da	1115.4;
Na^{24}	15.0hr	1368.4; 1732;
K^{42}	12.5hr	1524.7;

圖Ⅳ、圖Ⅴ是兩組不同人之頭髮樣品，重各約 0.05g在同一實驗情況下，各衰變7天後，計數 10hr 所繪之單能譜。

此兩能譜除對各元素含量略有參差外，圖Ⅳ中可很明顯看到含有 Cs^{134} 同位素，而圖Ⅴ中則不易察覺，但圖Ⅴ中可很明顯的看到圖Ⅳ中看不到的 Cr^{51}, Au^{198}, Sb^{124} 等同位素，其他類似情形，亦見於其他樣品中。人的頭髮其所含元素之成分因人而略有差異。

(2)對於頭髮內三種最主要同位素之含量比較之測定：

a)取同一人，同一部位頭髮一束，分成5組（a.b.c.d.e）定 Zn, Na, Br 三元素之量，如表4。

表4

元素＼組別 含量（P.P.M）	a	b	c	d	e
Zn	213	203	197	215	200
Na	330	370	310	320	380
Br	2.2	1.9	1.7	2.0	2.3

各元素測量之平均值爲

Zn:205±8P.PM　　Na:345±28P.P.M　　Br:2±0.2P.P.M

b)同一人不同部位之頭髮之研究：

將一個人之頭髮分成前、中、後、右、左五個部位，各取兩根頭髮樣品，先測定其質量，同時在同一情況下送入原子爐內照射，照射後，分別在同一情況下測量其放射能譜，每個部位衰變與計數的時間如表5。

表5

部　位	衰變時間（Decay Time）	計數時間（Counting Time）
前	148hr	5hr
中	153.5hr	5hr
後	159hr	5hr
右	164.5hr	5hr
左	170hr	5hr

其各部位之單能譜繪如圖Ⅵ，從圖Ⅵ中可看出同一人各部位頭髮均含有相同之元素或同位素。

爲作進一步之研究，對同一人各部位頭髮中主要元素含量之多少作定量之比較，表6爲本實驗所取八組不同人之頭髮，將同一人 Zn,Na 兩元素在前面部位之含量均修正爲1時，分析 Zn,Na 兩元素因部位之不同，其含量間之差異。

由此表中可看出，各部位頭髮中 Zn ，或 Na 之含量均不相同， Zn 元素各部位含量間之差距，最多不超過 40 %， Na 元素各部位含量間之差距最多不超過 110%。

表6

元素： Zn

組別 \ 部位 含量	前	中	後	右	左
A	1.00	1.02	0.77	0.81	0.85
B	1.00	0.98	0.79	1.08	1.18
C	1.00	0.89	0.73		
D	1.00	1.16	1.04		
E	1.00	0.93	1.09		
F	1.00	0.94	1.19		
G	1.00	0.94	0.74		
H	1.00	0.98	1.02		

元素： Na

組別 \ 部位 含量	前	中	後	右	左
A	1.00	0.84	1.10	0.81	0.69
B	1.00	0.64	1.20	0.60	0.68
C	1.00	0.72	1.40		
D	1.00	0.66	0.55		
E	1.00	1.00	2.00		
F	1.00	0.80	0.99		
G	1.00	1.40	1.10		
H	1.00	1.00	2.00		

c)不同人同一部位 Zn,Na 含量之比較

表7爲將本實驗所取八組不同人之頭髮，將H組中前、中、後三部位 Zn,Na 之含量修正成1時，分析 Zn, Na兩元素因組別之不同，其含量間之差異，由此表中可看出，各組頭髮中，Zn 或 Na 之含量間亦不相同，且各組 Zn 或 Na 含量間之差距較之同一人各部位 Zn 或 Na 含量間之差距尤甚，Zn 元素各組含量間之差距最多爲90%， Na 元素各組含量間之差距最多爲 470 %

表7

元素： Zn

部位＼組別	A	B	C	D	E	F	G	H
前	1.33	1.72	1.67	1.58	1.43	1.32	1.55	1.00
中	1.39	1.73	1.51	1.86	1.35	1.26	1.49	1.00
後	1.00	1.32	1.20	1.62	1.53	1.54	1.13	1.00

元素： Na

部位＼組別	A	B	C	D	E	F	G	H
前	4.60	3.10	2.30	4.50	1.70	3.50	1.10	1.00
中	3.80	2.00	1.60	2.90	1.90	2.70	1.60	1.00
後	2.50	2.60	1.60	1.20	1.70	1.70	0.65	1.00

d)分析本實驗所取八組樣品知每組樣品中均含有 Zn,Na,Br 三元素，列舉四組樣品，在同一組 ， 將 Zn 之含量修正成1時，分析 Zn,Na,Br 含量間之關係，列於表8：

表8

樣品A：

部位＼元素含量	Zn	Na	Br
前	1.00	2.50	1.8×10^{-3}
中	1.00	2.10	6×10^{-3}
後	1.00	3.80	4.1×10^{-3}

樣品B：

部位＼元素含量	Zn	Na	Br
前	1.00	1.30	1.1×10^{-3}
中	1.00	0.89	2.2×10^{-3}
後	1.00	2.10	1.1×10^{-3}

樣品C：

部位＼元素含量	Zn	Na	Br
前	1.00	1.00	7×10^{-3}
中	1.00	0.85	6.6×10^{-3}
後	1.00	2.00	8.9×10^{-3}

樣品D：

部位＼元素含量	Zn	Na	Br
前	1.00	2.10	1.1×10^{-3}
中	1.00	1.20	1.5×10^{-3}
後	1.00	1.10	1.1×10^{-3}

各組樣品，各元素求其平均值，將 Br 之含量修正成1，列如表9。

表 9

元素 / 含量 / 樣品	Zn	Na	Br
A	107	300	1.00
B	68.0	120	1.00
C	132	170	1.00
D	81.3	120	1.00

VI. 討論及結論：

本實驗自八個取自新竹清華大學學生的樣品中，發現其中含有對中子活化反應靈敏者有14種元素，此14種元素並非每一樣品中均可發現，如圖IV及圖V所示，兩不同人的樣品除主要幾種如 Na,Zn,Br,Hg 等均存在外，各含有不同之元素，對每一個人的頭髮而言，其因生活環境，飲食習慣，生理狀況，以及年齡的因素等，均會對頭髮內所含元素之數量及成分有所影響，而對同一人之毛髮而言，其所含之主要元素均爲相同，而每種成份之相對比例則隨部份之不同而略有出入，如圖VI及表 6 所示：

從八組取樣分析可知，同一人之頭髮內，因部位之不同各元素間之差異較小， Zn 之差異最多爲50%，而Na 之差異可達一倍，而對不同人之頭髮而言，在取樣之 8 組中，各元素之含量差異則較顯著，對 Zn 而言，差異幾近一倍，對 Na 而言可達四倍以上。對不同人而言，尤其是有些微少含量之元素，常因人而有所差別，用毛髮鑑定犯罪，利用活化分析可供相當可靠性之參巧依據。

在美、加、歐其他地區自頭髮分析中所發現的其他近十種同位素，本實驗中未能出現，主要原因應係由於本實驗取樣地區過小，樣品數目僅 8 組及歐、美其他地區因客觀環境及生活習慣等影響，毛髮中含元素種類也未必與臺灣者相同。本實驗對短半衰期及含量甚微（1ppm 以下者）之元素亦並未作特殊之努力，亦爲另一原因。

本實驗曾對某一取樣人頭上之白髮作初步的分析，其對元素間的含量變化很大， Zn 的含量有顯著的減少，對毛髮作較有系統之分析如生理習慣及地區分佈對它成分的影響等須作進一步之研究

其他如毛髮鑑定犯罪之可靠性及毛髮成份與健康之關係等亦是下一步有趣的工作。

作者特別對調查局田汝常先生之建議及有意義之討論表示感謝。

Reference:

1. N.E.Erickson, Arsenic in hair, paper for the First International Conference on Forensic Activation, San Diego, Calif., September, San Diego, Calif., 1966
2. "Activation Analysis of human head hair, 5 analysis of human head hair in a simulated case by Neutron Activation." Kozuka, Hiroshi (National Research Inst. of police Science, Tokyo). Eisei Kagaku; 17 No.5, 327-9 (Oct 1971). (In Japanese)
3. 狐塚 寬：科學警察研究所，藥局 Vol. XVII, No.8 (1966)
4. Application of NAA in Scientific Crime Investigation, Final Report, 2, Sep. 1971, Contract AT (04-3)-167, 109P. Dep. NTIS.

5. Neutron Activation Analysis to trace elements in hair. Huckabce, Jokn W. Laramic, Wyo: Univ. of Wyoming (1971). 75P. University Microfilms order No. 72-13. 028
6. Auseklies K. Perkons, Robert E. Jeruis, Recent Forensic Application of Instrument Activation Analysis, Forensic and Archaeological Applications 256-263, 1969
7. Activation Analysis of human head hair, 3. Activation Analysis of hair by short-time irradiation. Kozu Ka, Hiroshi (National Research Inst. of police Science, Tokyo); Tsunoda; Isono, Hideo; Niwase, Takeshi. Eisei Kagaku; 17: NO.4, 27-3 (Aug 1971)
8. Richard Dams John A. Robbins and John W. Winchester projector Director, Technical Report, Nondestructive Activation Analysis of Environmental Sample, The university of Michigan, May 1970.

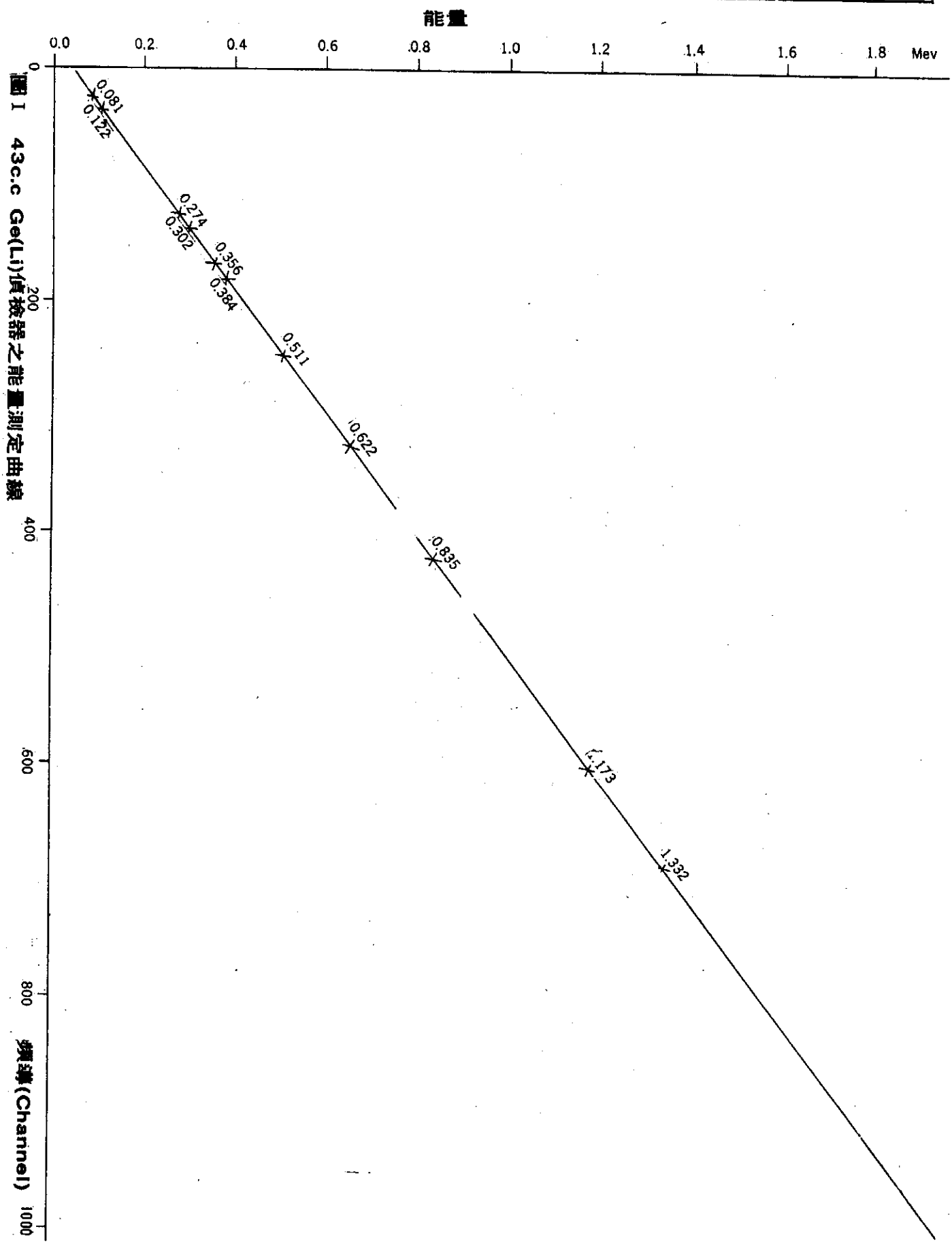

圖 I 43c.c Ge(Li)偵檢器之能量測定曲線

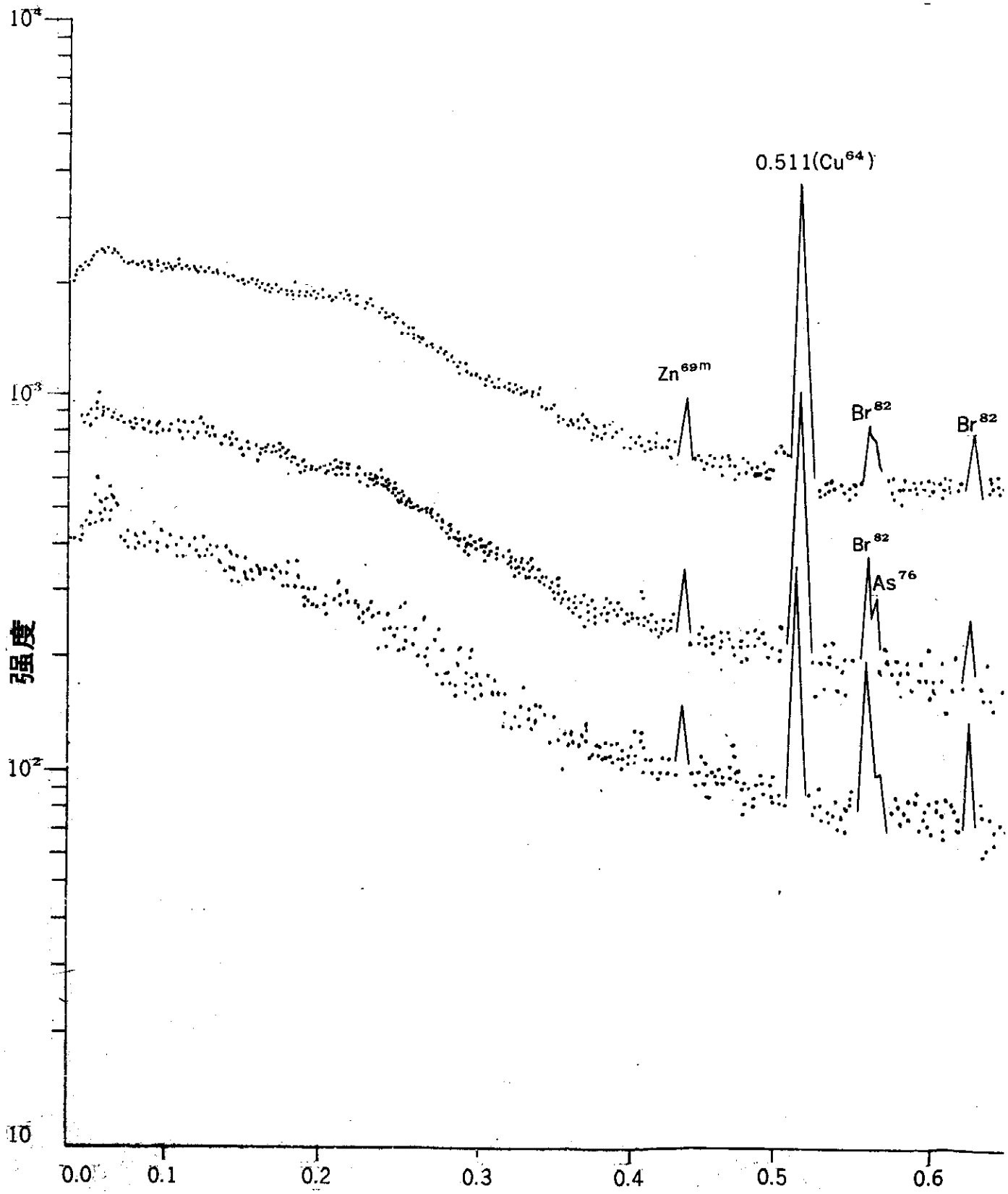

圖II 衰變 3 天之頭髮γ射線能量衰變圖

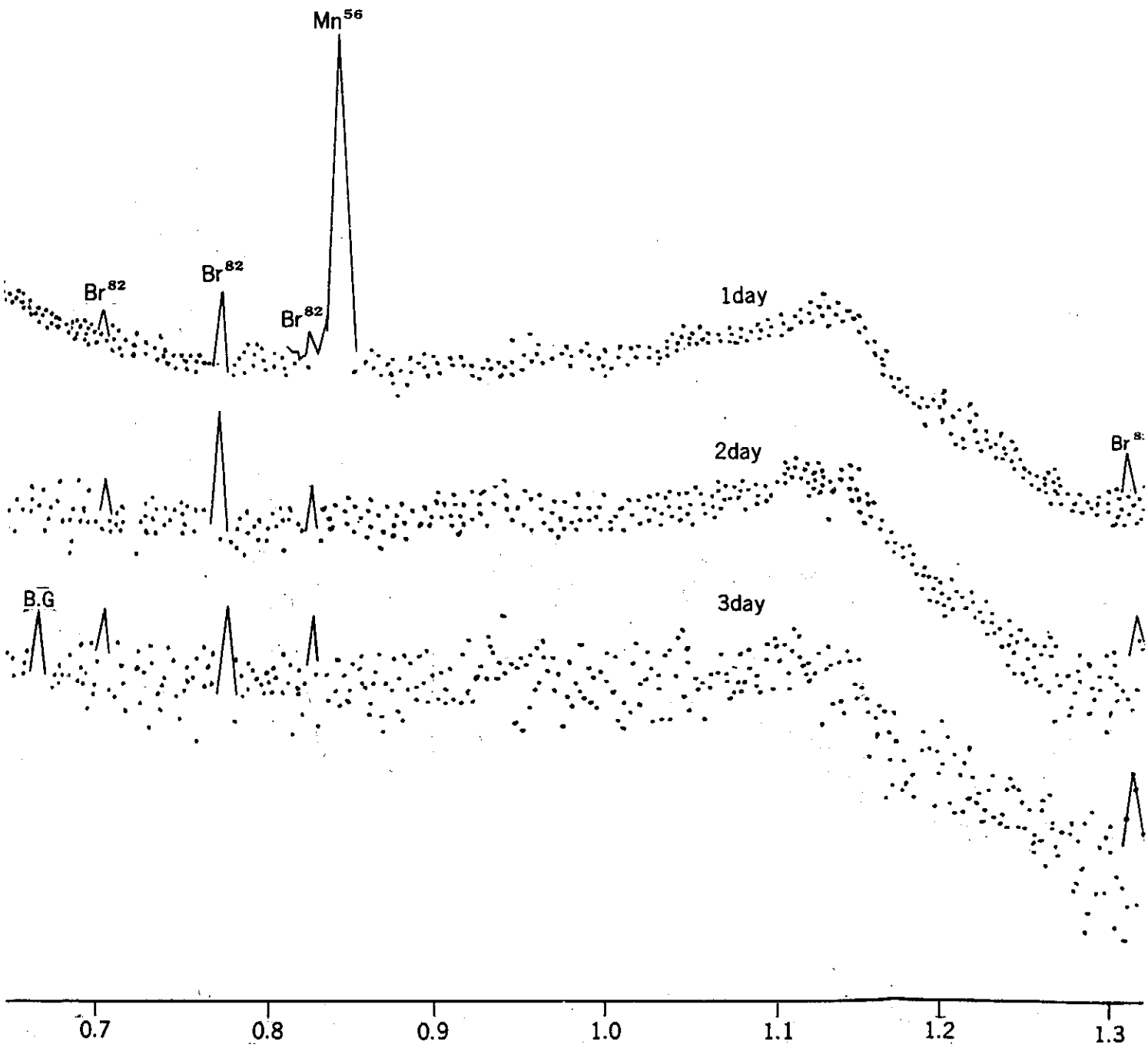
Mn56
Br82
Br82
Br82
1day
2day
3day
B.G
0.7
0.8
0.9
1.0
1.1
1.2
1.3

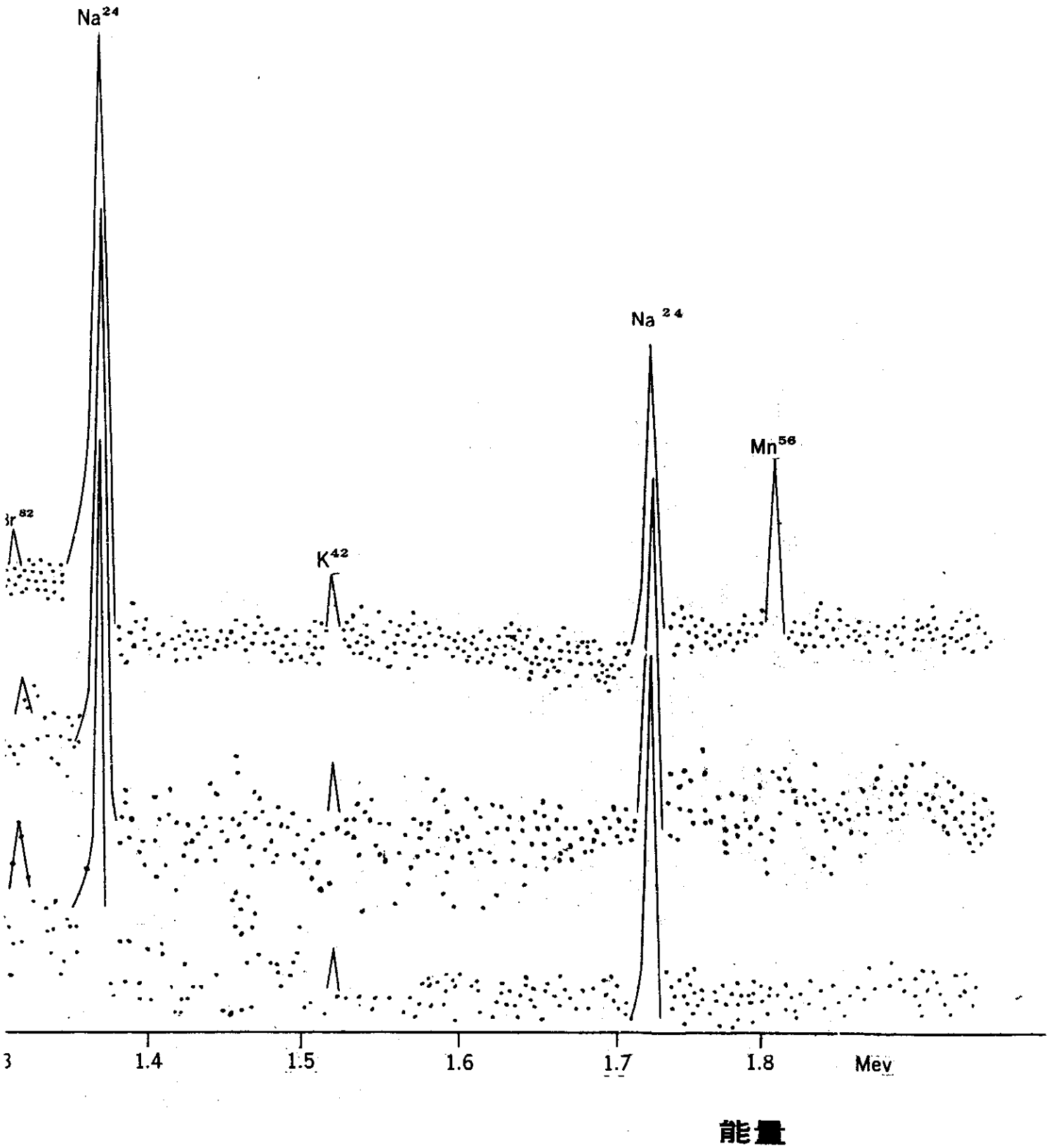
Na24
Na 24
Mn56
K42
Br82
1.4
1.5
1.6
1.7
1.8
Mev
能量

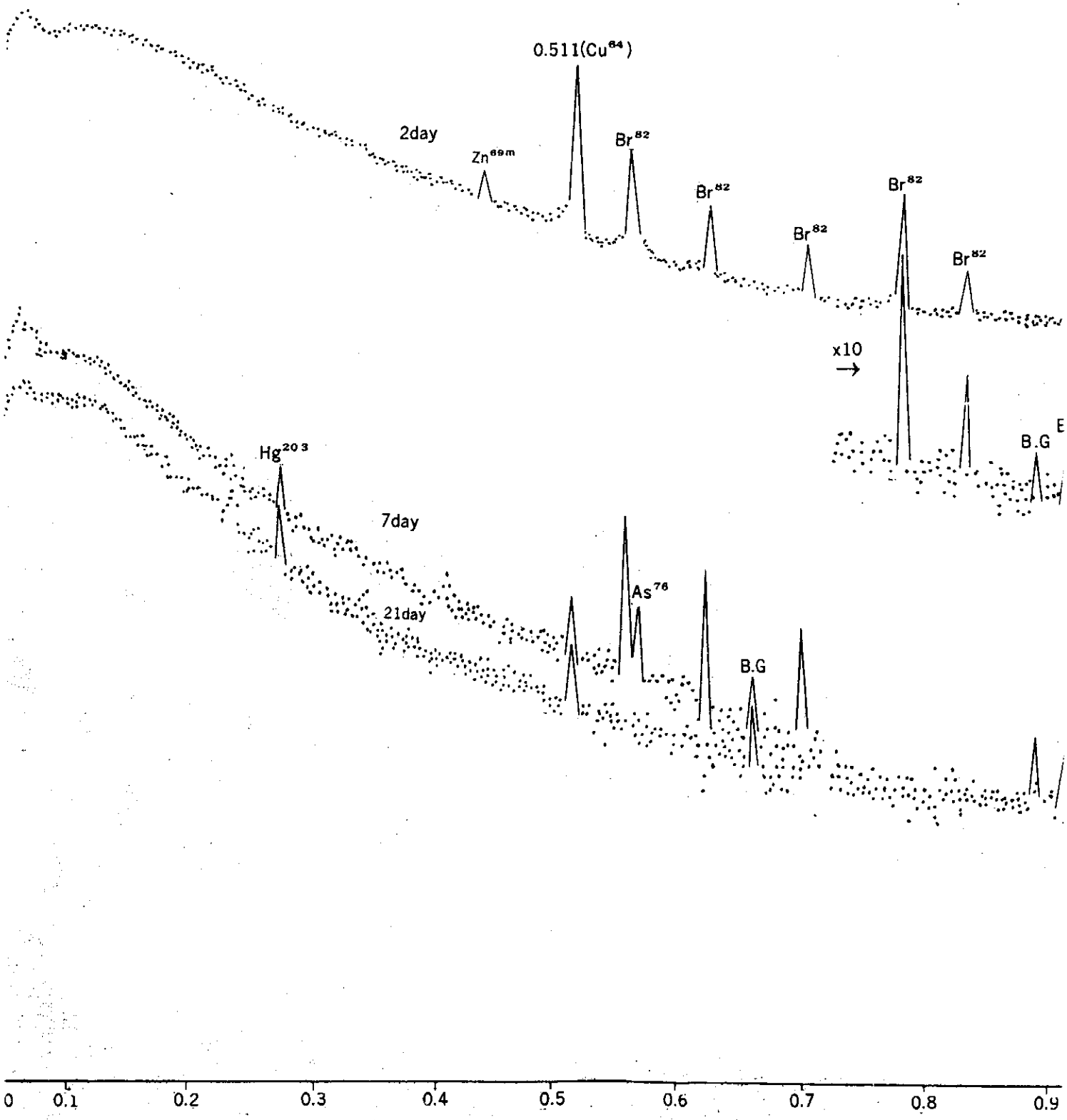

圖III　衰變21天之頭髮γ 射線能量衰變圖

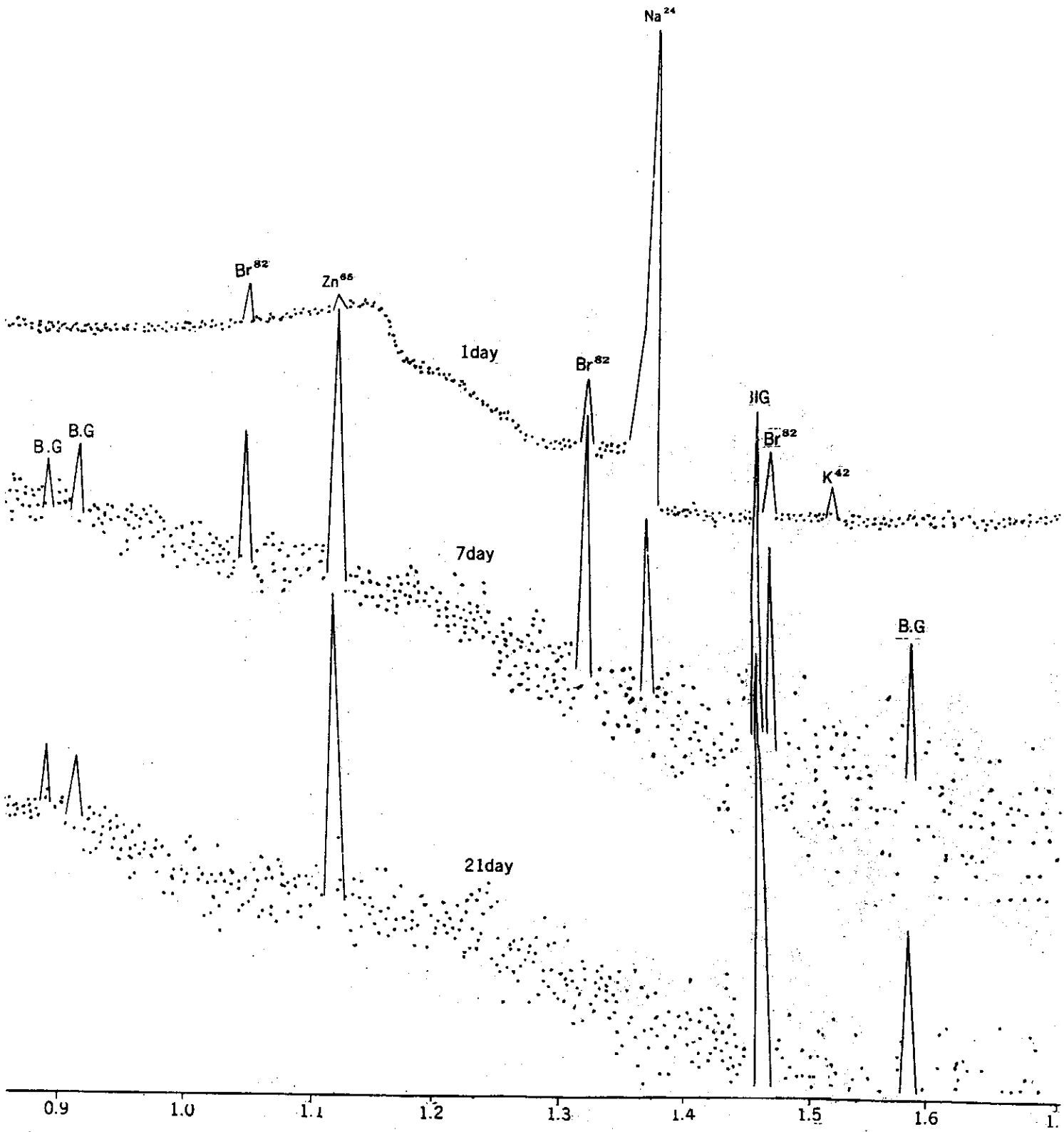
Na24
Br82
Zn65
1day
Br82
B.G
B.G
B.G
Br82
K42
7day
B.G
21day
0.9
1.0
1.2
1.3
1.4
1.5
1.6

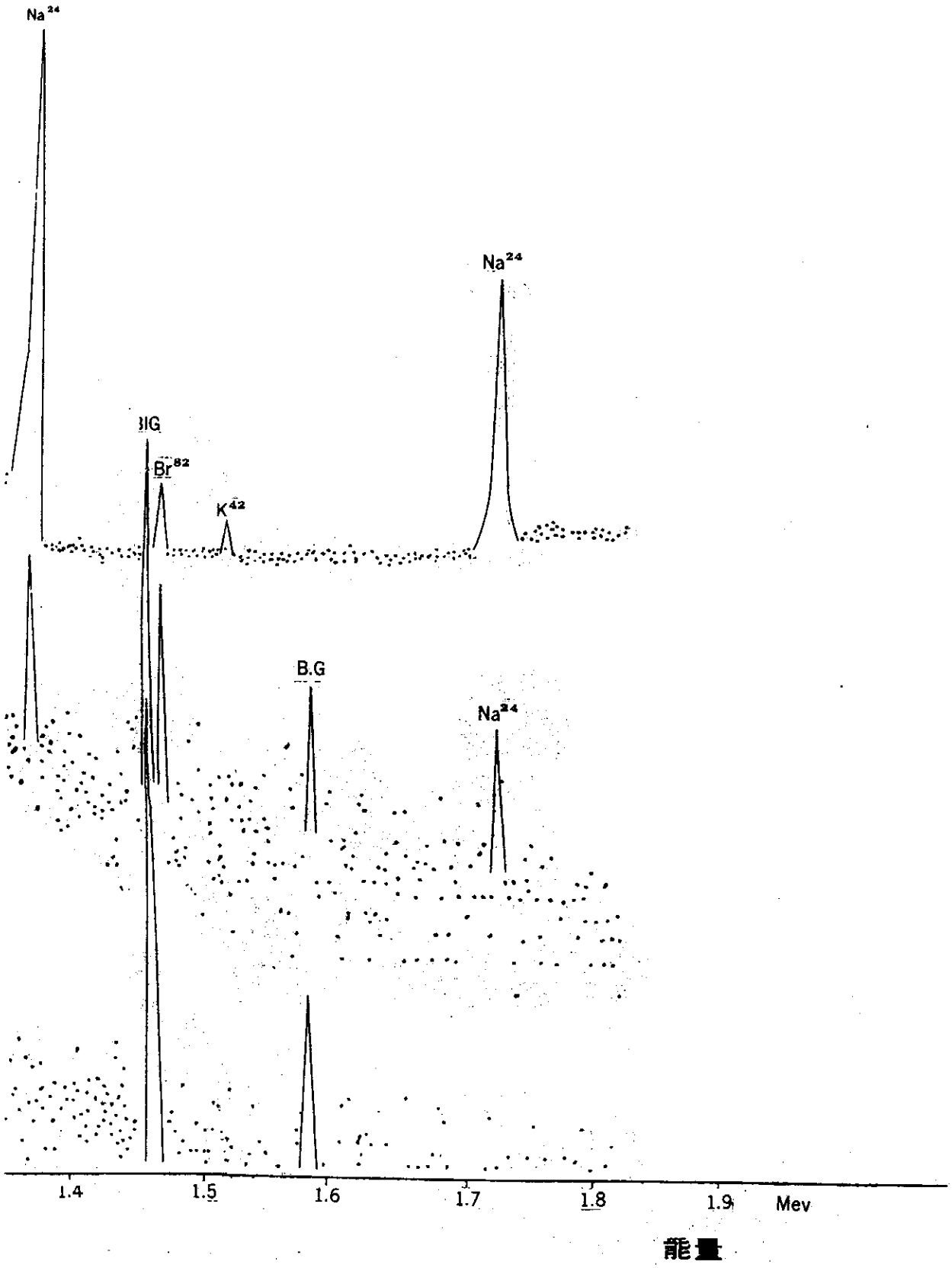
Na24
Na24
BIG
Br82
K42
B.G
Na24
1.4
1.5
1.6
1.7
1.8
1.9
Mev
能量

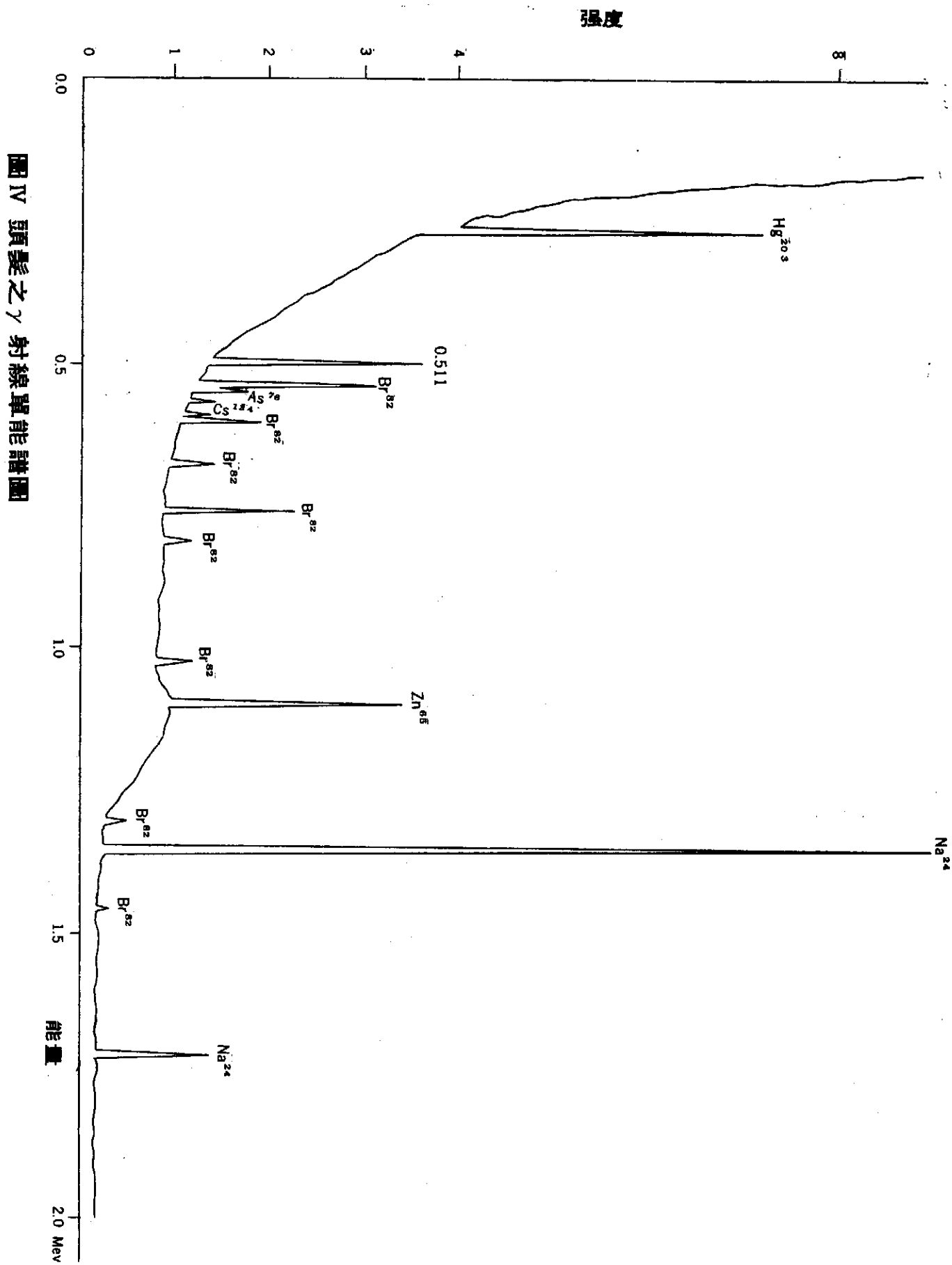

圖 IV 頭髮之 γ 射線單能譜圖

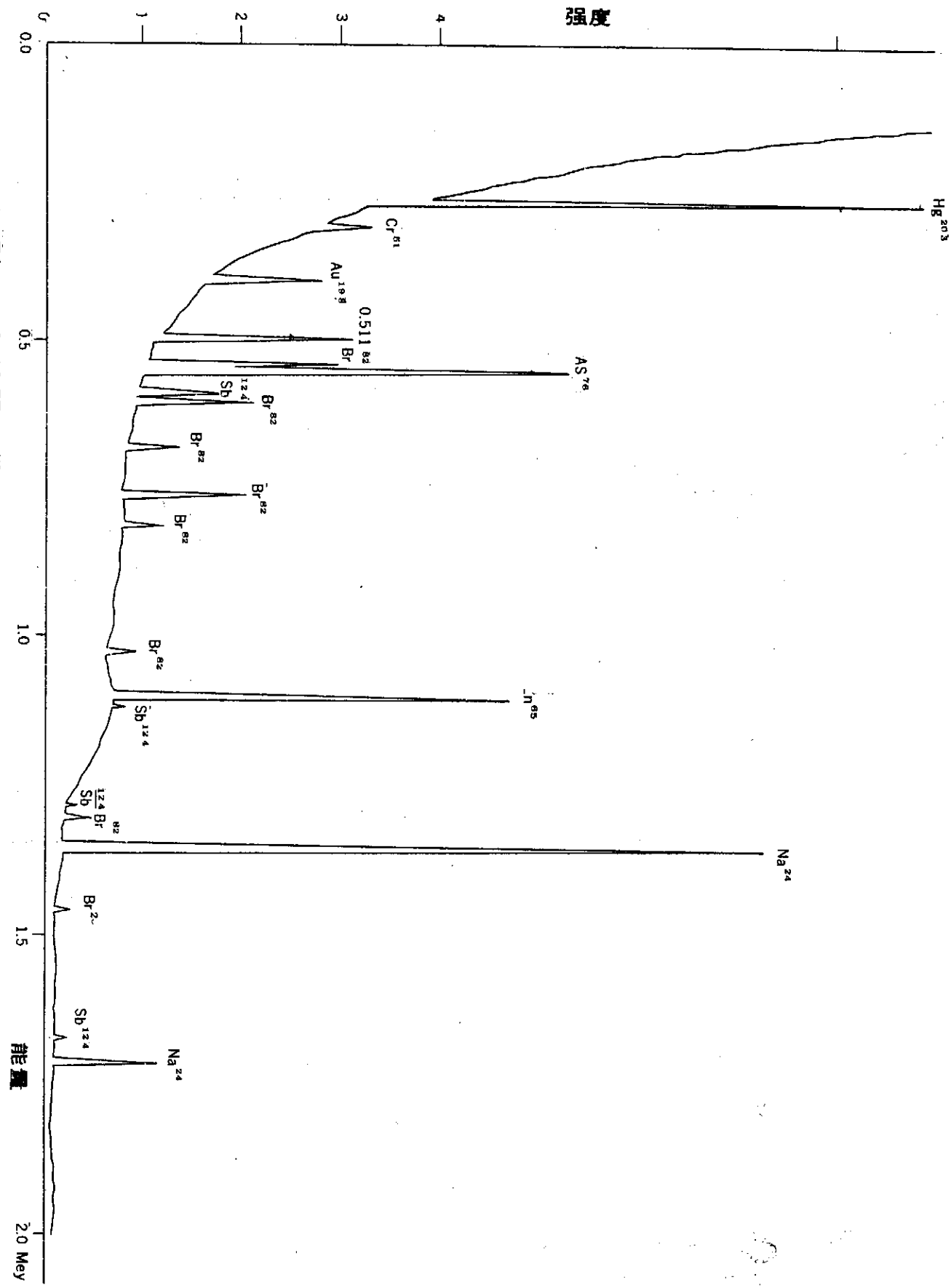

Fig. V 頭髮之 γ 射線單能譜圖

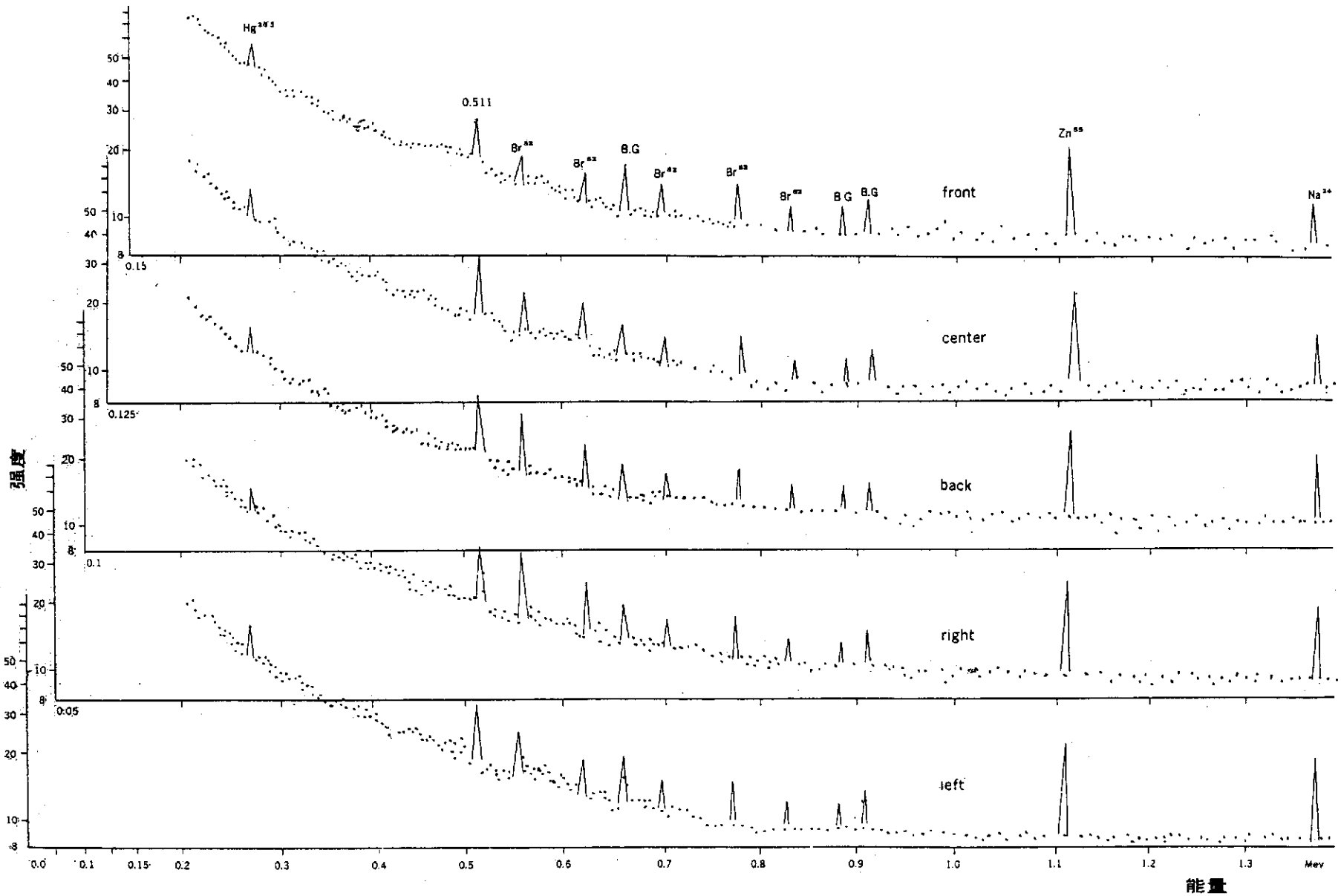

圖 VI　同一個人五個不同部位之頭髮能譜比較圖

Size Effect of Indium Antimonide at Room Temperature(*).

YU-TUNG YANG, HONG-TZER HO, CHENG-CHIH PEI,
SHUNG-CHEN YANG and BIAO-SHIAN YU

Physics Department, National Tsing-Hua University, Hsin-Chu; Taiwan

(ricevuto il 22 Novembre 1972; manoscritto revisionato ricevuto il 19 Gennaio 1973)

Summary.—Skin depth and related parameters of InSb have been measured by using the damped-radiowave technique at room temperature. The results show that there is difference between the data obtained with a marginal oscillator-detector system and with a fixed-frequency signal detector system. We found that the latter is more reliable. The former can only give qualitative results. Moreover, the mobility μ and the carrier concentration n found with the traditional galvanomagnetic (Hall and conductivity) methods are substantially different from those by the fixed-frequency method. We show the comparison of the two.

(*) This paper has been published in Nuovo Cimento 16B (1973) 188-202, also in Annual Report of the Institnte of Physics, Academia Sinica 1971 (1972)113-125

Annual Report of the Institute of Physics, Academia Sinica, 1972

The Equation of State of Solid Molecular Hydrogen

Wu-Shyong Wu and Shou-yih Wang (王守益)

Institute of Physics, National Tsing Hua University

ABSTRACT

Our work here is to employ the quasi-crystal approximation of Woo and Massey[5] to compute the ground state energy of solid molecular hydrogen at O°K for a wide range of densities, extending from $\rho=2.67\times10^{-3}$Å^{-3} to 5.574×10^{-3}Å^{-3}. Based on these an equation of state of cold solid molecular hydrogen is obtained. The result is compared with the KW's calculations and the experimental data of Stewart[7]. It appears to us as the best existing calculations for the high density region.

I. Introduction

It is generally believed that under exceedingly high pressure hydrogen will take on the metallic phase. Recently there are also speculations that the interier of Jupiter and/or Saturn is made up of metallic hydrogen. The question is how high the transition pressure is. To answer this, we need the equation of state or the energy vs. density relation for both metallic and molecular hydrogen. Ashcroft has made estimates of the former. Krumhansl and S.Y. Wu[1] have made some calculations on the latter. We wish to improve up the latter calculation.

II. Method of calculation

Like Krumhansl and Wu (hereafter refered to as KW), we begin with a correlated trial wavefunction:

$$\Psi(\vec{r}_1,\vec{r}_2,\cdots\vec{r}_N)=\prod_{1\le i<j\le N} exp\tfrac{1}{2}u(\vec{r}_{ij})\prod_{k=1}^{N}\phi_k(|\vec{r}_k-\vec{R}_k|) \tag{1}$$

The $e^{\frac{1}{2}u(r_{ij})}$ are functions which introduce short-range correlations between pairs of molecules, and ϕ's are taken to be a simple Gaussian form centered about their equilibrium lattice sites $\vec{R}_k$, namely,

$$\phi_k(|\vec{r}_k-\vec{R}_k|)=\left(\frac{\alpha}{\pi}\right)^{\frac{3}{4}}exp(-\tfrac{1}{2}\alpha^2|\vec{r}_k-\vec{R}_k|^2) \tag{2}$$

The Hamiltonian of a system of N H_2 molecules is taken to be

$$H=-\frac{\hbar^2}{2M}\sum_i\nabla_i^2+\sum_{j<k}V(r_{jk}) \tag{3}$$

The potential field $V(r_{jk})$ between two molecules is in general introduced as a superposition

of a repulsive and an attractive field. The two-body potential is assumed to be the Lennard-Jones type:

$$V(r)=4\varepsilon\left[\left(\frac{\sigma}{r}\right)^{12}-\left(\frac{\sigma}{r}\right)^{6}\right] \tag{4}$$

where ε gives the strength of the potential at its minimum and σ may be considered as the "diameter" of the hard core. For H_2, $\varepsilon=37°K$ and $\sigma=2.93$ A.[2] We have also used Buckingham exp-6 potential in our calculations. The exp-6 potential is defined as

$$V(r)=\frac{\varepsilon}{(1-6/\alpha)}\left\{6\frac{\alpha}{\alpha}exp\left[\alpha\left(1-\frac{r}{r_m}\right)\right]-\left(\frac{r_m}{r}\right)^{6}\right\} \quad for\ r\geq r_{max}$$

$$=\infty \qquad r<r_{max} \tag{5}$$

where ε is the depth of the potential minimum, r_m is the position of the minimum, α is a parameter which is a measure of the steepness of the repulsvie potential, and r_{max} gives the value or r for which V(r) has a maximum. The parameters for hydrogen as determined by Srivastava et al[3] are

$$\alpha=14.0$$
$$r_m=3.339\ \text{Å}$$
$$\varepsilon/k=38.02°K$$
$$r_{max}/r_m=0.20319.$$

The expectation value of the Hamiltonian is obtained via a cluster expansion technique, while KW employed a straight-forward ursell-Mayer type expansion first used by Nosanow[4]. In the case of solid helium, so-called quasi-crystal approximation has been employed by Woo and Massey[5]. The two procedures differ in that each term in the latter expansion results essentially from summing a large number of terms in the former expansion. Since it is in practice necessary in each case to truncate the cluster expansion at the 2-particle term, the Massey-Woo procedure will seem to be more reliable. Physically, the Nosanow procedure considers particles correlated in pairs, while the Massey-Woo procedure considers the same moving in a liquid-like medium.

Our work here consists of first parameterizing the pair distribution function G(r). The normalization of G(r) is given by

$$\rho\int[G(r)-1]d\vec{r}=-1$$

where ρ is the density of solid H_2. It is also assumed that $G(\infty)=1$. Our choice of G(r) is

$$G(r)=(C+1)exp\left[-\left(\frac{r_o}{r}\right)^{10}\right]-C\ exp\left[-(1+Z)\left(\frac{r_o}{r}\right)^{10}\right]$$

where

$$C=\left[\frac{1.155574}{2\pi\rho r_o^3}-1\right]/\left[1+(1+Z)^{0.3}\right]$$

We minimized the ground state energy with respect to the parameters, Z and r_o. Only those

G(r) which satisfy the following conditions are considered as trial pair-distribution functions:

(a) $G(r)\geq 0$ *for* $0\leq r\leq\infty$

(b) The structure function

$S(k)\geq 0$ *for* $0\leq k\leq\infty$

(c) $S(o)=0$

(d) $4\pi\rho^{\frac{2}{3}}\int_{o}^{\infty}[1-G(r)]r.\ dr\leq 2.8887$ (7)

Figure 1 shows the radial distribution function G(r) at density $\rho=3.34\times10^{-3}$Å^{-3}

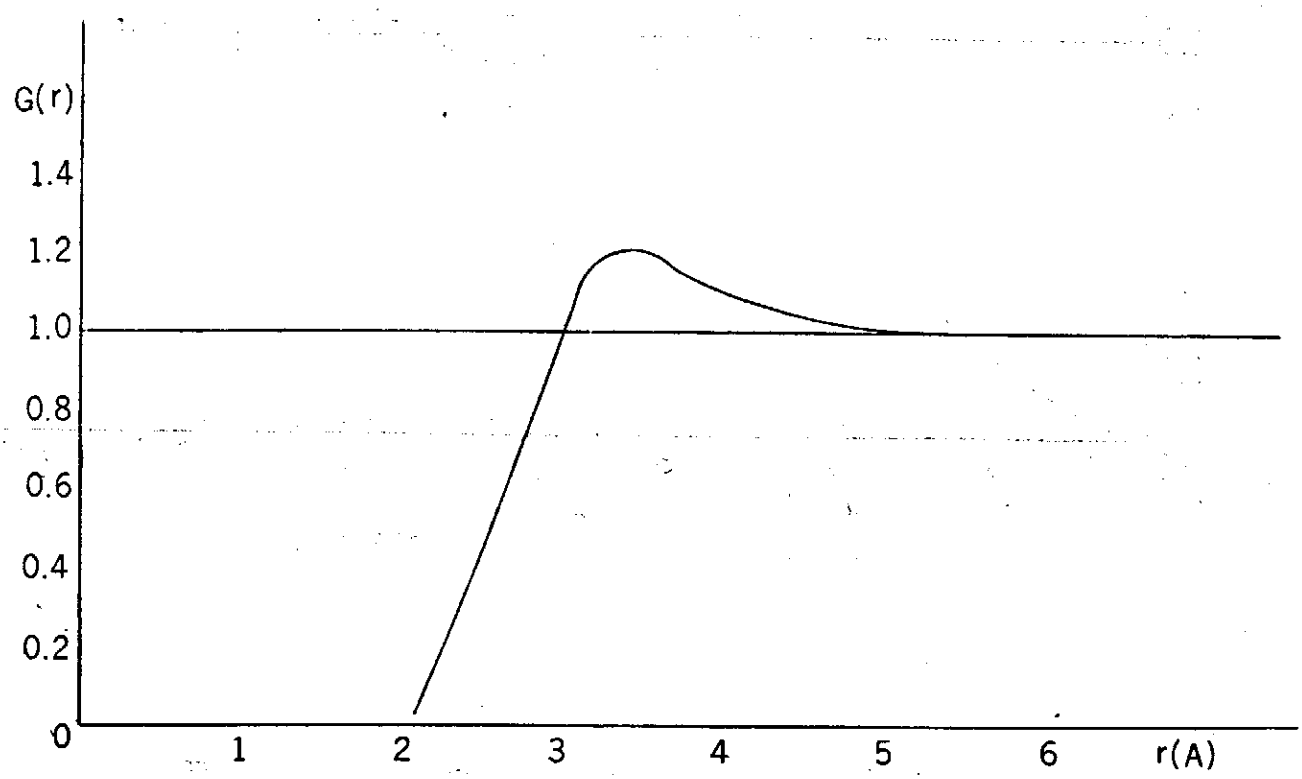

*Fig.*1 *G(r) VS.r for* $\rho=3.34\times10^{-3}$Å^{-3}

The structure function S(k) can be calculated from the pair distribution function G(r) through the equation

$$S(k)=1+\rho\int[G(r)-1]e^{i\vec{k}\cdot\vec{r}}\,\vec{dr} \qquad (8)$$

In Fig. 2 is shown the structure function for $\rho=3.34\times10^{-3}$Å^{-3}.

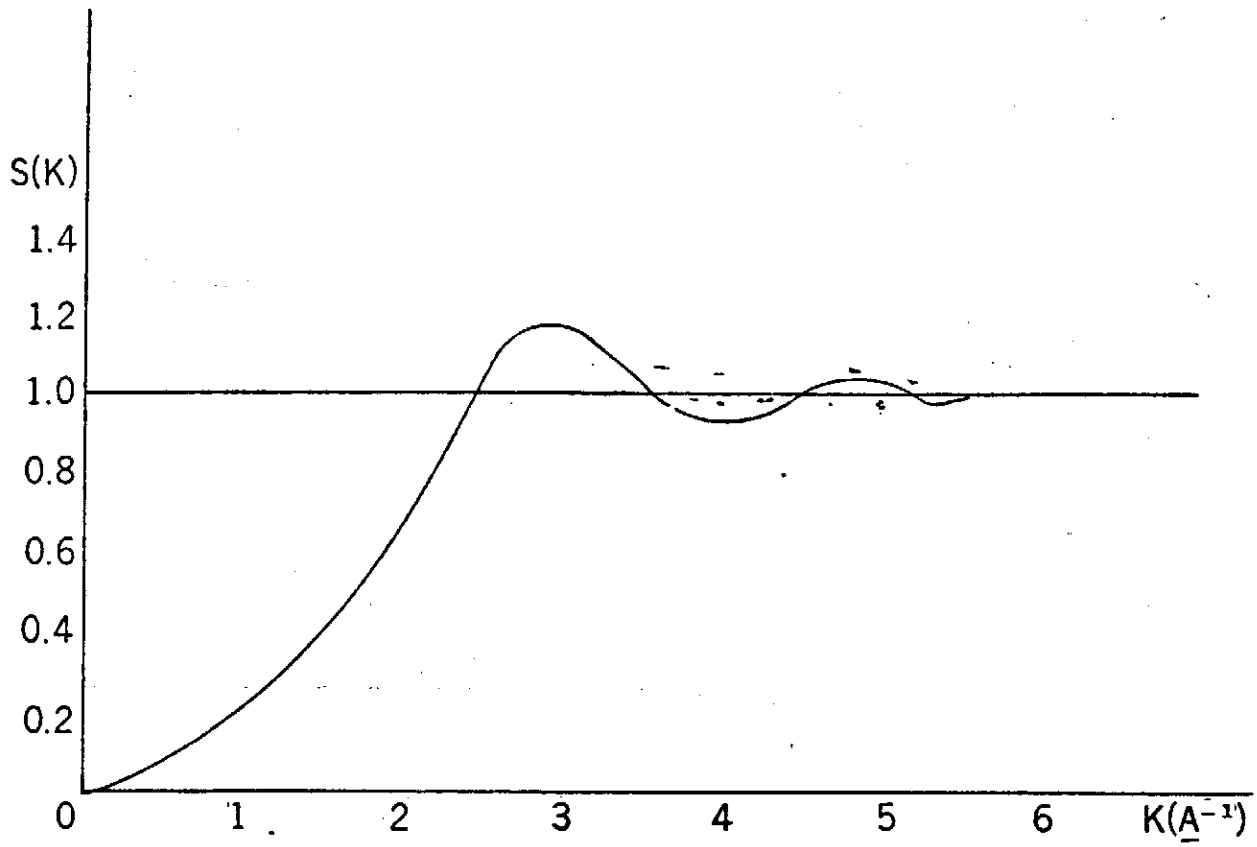

Fig.2 the structure function $S(k)$ *for* $\rho=3.34\times10^{-2}$Å^{-3}

Next, we use the Percus-Yevick equation to derive the correlation function u(r) from G(r) and S(k), i.e.

$$U(r)=\ln G(r)-\ln\left[1+\frac{1}{(2\pi)^3\rho}\int e^{i\vec{k}\cdot\vec{r}}\left(\frac{S(k)-1}{S(k)}\right)\vec{dk}\right] \tag{9}$$

The correlation function u(r) is shown in Fig. 3 for $\rho=3.34\times10^{-2}$Å^{-3}.

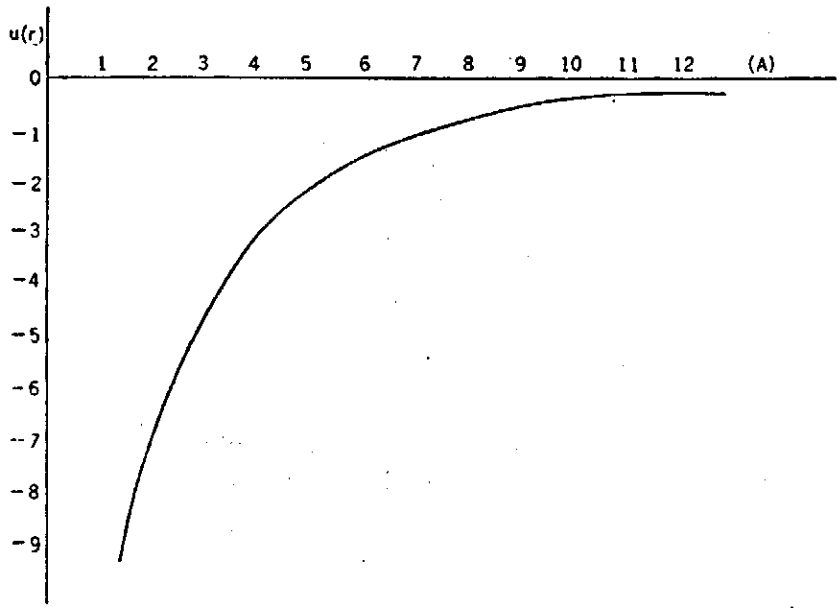

Fig.3 the correlation function U(r) for density $\rho=3.34\times10^{-2}$Å^{-3}

The expectation value of H with respect to Ψ, Eq. (1) and Eq. (3), is then

$$E=\frac{\langle\Psi|H|\Psi\rangle}{\langle\Psi|\Psi\rangle}\geq E_0 \qquad \text{for any } \Psi$$

where E_0 is the ground state energy of solid H_2. After some calculation, E may be expressed as E_T and E_v, i.e. if N is the number of H_2 molecules to be computed, and m is the mass of a H_2 molecule,

$$E=E_T+E_v$$

$$\frac{E_T}{N}=\frac{3\alpha^2-h^2}{4M} \tag{10}$$

$$E_v=E_v^{(2)}+E_v^{(3)}+\cdots$$

We now only truncate the cluster expansion at the 2-particles term, i.e. $E_v^{(2)}$ in our case,

$$\frac{E_v^{(2)}}{N}=\sum_d \tfrac{1}{2}N_d e^{(2)}(d;\alpha) \tag{11}$$

$$e^{(2)}(d;\alpha)=\frac{\int_0^\infty rV(r)\ G(r)\ Sinh\ (\alpha^2 rd)e^{-\frac{1}{2}\alpha^2(r^2+d^2)}dr}{\int_0^\infty r\ G(r)\ sinh\ (\alpha^2 rd)\ e^{-\frac{1}{2}\alpha^2(r^2+d^2)}dr} \tag{12}$$

where

$$V(r)=v(r)-\frac{\hbar^2}{2M}\nabla^2 \ln\left(e^{\frac{1}{2}u(r)}\right)$$

The summation over d is performed over 30 shells about a fixed lattice site. d and n_d denote the radius of the shell and the number of lattice sites in that shell.

Our calculation of the solid H_2 at 0°K is for a wide range of densities, extending from $\rho = 2.67\times10^{-2}$Å^{-3} to 5.574×10^{-2}Å^{-3}. From these data an equation of state of cold solid H_2 is obtained. The result will be compared with the empirical curve derived from the experimental P.V. data obtained by Stewart and KW's.

III. Results

Table I shows the ground state energy for closed packed solid H_2 at 0°K from 22.47 to 10.80 cm^3/mole. R(A) denotes the nearest neighbor distance.

Table I

(A) for Lennard-Jones 6-12 potential

R(Å)	V(cc/mole)	α^2	Z	r_o	E(10^{-14} erg)
3.75	22.47	5.3	1.2	2.2	−0.9348
3.607	20.00	6.2	1.15	2.15	−0.8655
3.483	18.00	8.4	1.1	2.1	−0.6668
3.356	16.10	10.4	1.1	2.05	−0.2173
3.285	15.10	11.8	1.05	2.03	0.2475
3.233	14.40	12.8	1.05	2.0	0.6900
3.149	13.30	14.8	1.0	1.95	1.7214
3.084	12.50	17.0	0.95	1.9	2.8818
2.982	11.30	22.0	0.95	1.85	5.5609
2.938	10.80	23.8	0.9	1.8	7.0763

(B) for Buckingham exp-6 potential

R(Å)	V(cc/mole)	α^2	Z	r_o	E(10^{-14} erg)
3.75	22.47	5.5	1.2	2.2	−1.0146
3.607	20.00	6.6	1.15	2.15	−0.9338
3.483	18.00	8.0	1.1	2.1	−0.7026
3.356	16.10	10.0	1.1	2.05	−0.1725
3.285	15.10	11.4	1.05	2.03	0.3394
3.233	14.40	12.4	1.05	2.0	0.8343
3.149	13.30	14.4	1.0	1.95	1.9695
3.084	12.50	16.2	0.95	1.9	3.2231

2.982	11.30	21.0	0.95	1.85	6.0902
2.938	10.80	21.8	0.9	1.8	7.6843

The relation between the ground state energy per molecule and volume relation is shown in Fig. 4. The pressure is determined from the expression $P=-\frac{\partial E}{\partial V}$. Table II shows the pressure-volume relations for both Lennard-Jones and exp-6 potential. The results, shown in Fig. 5, are compared with KW's[1] and with the experimental data of Stewart[7].

Table II Pressure vs. Volume

Volume (cc/mole)	Pressure (10^8 Kg/cm^2)		
	L-J-6-12	Exp-6 potential	KW
22.47	0.0985	0	0
20.00	0.4117	0.3108	0.405
18.00	1.0908	0.9624	1.03
16.10	2.2672	2.5137	2.44
15.10	3.1831	3.9201	3.93
14.40	4.0512	5.2013	5.27
13.30	6.6917	8.2515	8.22
12.50	9.6673	11.6787	11.6
11.80			15.4
11.30	15.8396	16.0141	

IV. Discussion

(1) The results, shown in fig. 5, are compared with KW's calculations and with the experimental data of Stewart[7]. Our results give better agreement than the KW's calculations at the higher densities but still do not compare very well with the experimental data.

(2) Our results indicate that the Woo and Massey method indeed give improved results over the KW's calculations.

(3) The Lennard-Jones type potential seems an improvent over the exp-6 model. The P-V result appears to be the best of the existing calculations since it agrees more satisfactorily with experiment at high densities. It suggests that the repulsive part of the model potentials used in the calculation is still too hard, as is clearly seen for the Buckingham's exp-6 potential.

(4) The difficulty in getting an accurate two body potential between hydrogen molecules arises mainly from the fact that there is a small moment of inertia of hydrogen molecule, resulting in a non-spherical potential.

(5) A 6-10 type potential would be more suitable than the usual 6-12 Lennard-Jones form. This is revealed when we compare the experimental data and the calculated P-V results in the high density region. It may be due to the softness in the diatomic structure of molecular hydrogen.

References

(1) J.A. Krumansl and S.Y. Wu, Phys. Letters **28A**, 263 (1968)
(2) N. Bernades, Phys. Rev. **120**, 807 (1960)
(3) I. B. Srivastava and A. K. Barua, Indian J. of Phys. **35**, 320 (1961)
(4) L. H. Nosanow, Phys. Rev. Letters **13**, 270 (1964)
(5) W. E. Massey and C. W. Woo, Phys. Rev. **169**, 241 (1968)
(6) E. Feenberg, J. Math. Phys. **6**, 658 (1965)
(7) J. W. Stewart, J. Phys. Chem. Solids **1**, 146 (1956)
(8) R. L. Mills and A. F. Schuch, Phys. Rev. Letters, **15**, 722 (1965).

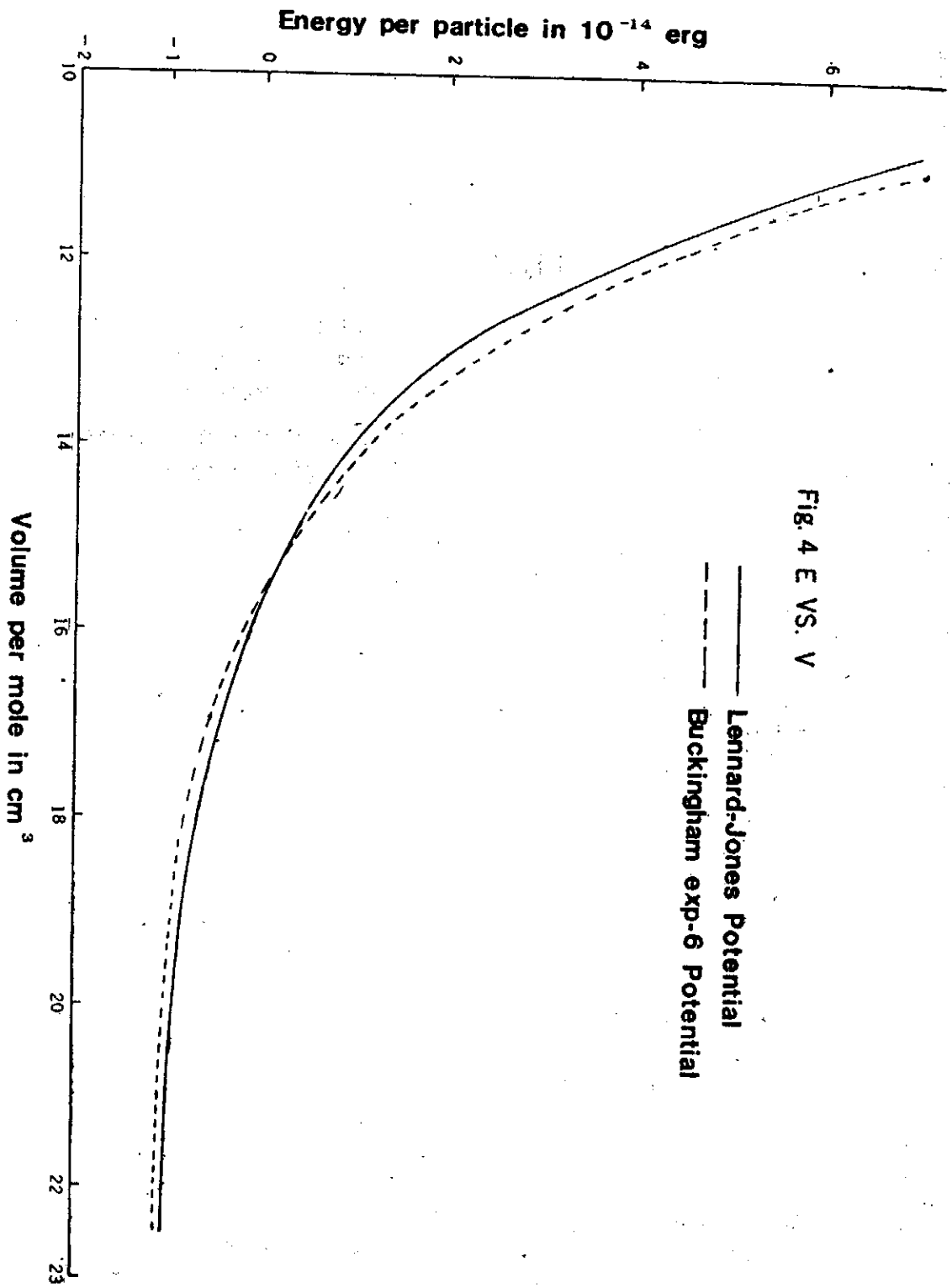
Energy per particle in 10^{-14} erg
$-2\ 10$
-1
0
2
4
6
12
14
16
18
20
22
23
Volume per mole in cm^3
Lennard-Jones Potential
Buckingham exp-6 Potential

Fig. 4 E VS. V

Fig. 5 P VS. V

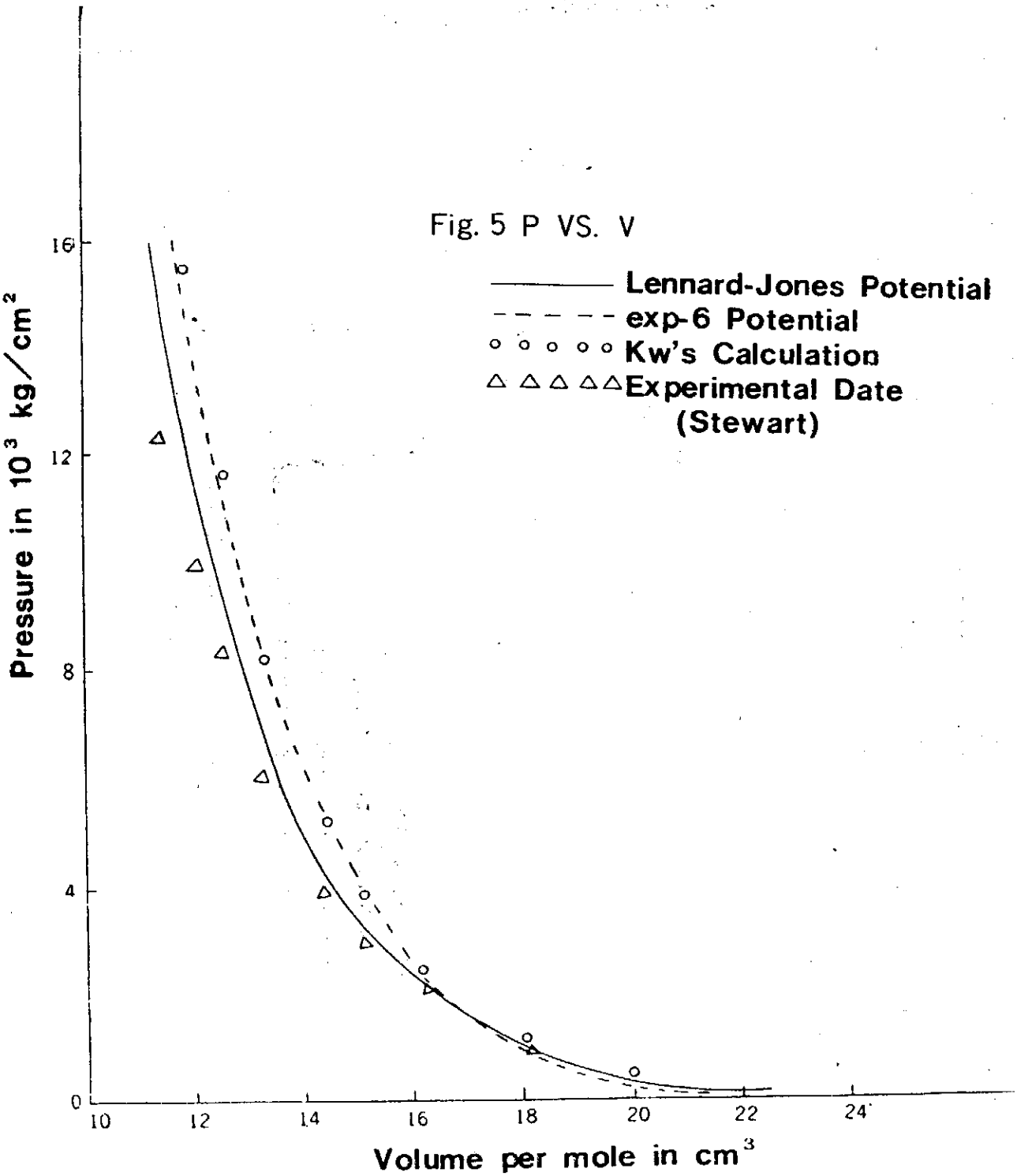
Lennard-Jones Potential
exp-6 Potential
Kw's Calculation
Experimental Date
(Stewart)
Pressure in 10^3 kg/cm^2
Volume per mole in cm^3
0
4
8
12
16
10
12
14
16
18
20
22
24

D.C. and R.F. Electrons in Indium Antimonide at Room Temperature*

Yu-Tung Yang **
(楊 毓 東)

Physics Department, National Tsing-Hua University
Hsin-Chu, Taiwan, Republic of China 300

Abstract

The rf electrons are found from the size effect measurements, and the dc electrons from the galvanomagnetic effects. The two types of electrons may independently exist at the same time in the same sample of indium antimonide. The size effect shows that the rf electrons are only slightly influenced by the presence of the dc power applied, and the galvanomagnetic effects show that the dc electrons are hardly influenced by the presence of the rf field applied. The two types of electrons are both conduction electrons according to the free electron model.

I. Introduction

The size effect theory deduced by Fischer and Kao has been satisfactorily applied to the study of the indium antimonide crystals[1],[2]. However, we have found [2] the rf size effect data is quite different from the galvanomagnetic effect data.

At first, we thought the difference might be reconciled if we let the indium antimonide sample be immersed in both the rf field and the dc field simultaneously, and we thought we could see some mean mobility μ and carrier concentration n which would be neither the pure $(\mu,n)_{rf}$ nor the pure $(\mu,n)_{dc}$. However, contrary to common belief, it is found that the $(\mu,n)_{rf}$ is only slightly affected by the externally applied dc field E_{dc}, and at the same time in the same sample the $(\mu,n)_{dc}$ is found hardly affected by the externally applied rf field around the sample. (The rf and the dc have the same cnmmon ground).

The $(\mu,n)_{rf}$ is only changed by a few percent when a fairly strong dc is applied, and the temperature of the sample is kept at 300°K. The rf conductivity σ_{rf} is found not changed by the presence of the dc power, neither does the σ_{dc} by the rf power. They seem to possess firm rigidity. The μ_{rf} and n_{rf} are found influenced by the dc power but they

* Project supported by the National Science Council, Republic of China, 1972-1973.
** Also at the Physics Institute, Academia Sinica, Republic of China.

change in such a way that the product remains the same.

It is found that the ratio between the rf conductivity σ_{rf} and the dc conductivity σ_{dc} is about 9, μ_{rf}/μ_{dc} is about 2.7, and n_{rf}/n_{dc} is about 3.2. The simultaneous presence of the rf field and the dc field in the same sample at the same time can not change the above ratios significantly.

There are two aims of the present report, namely: (i) to report the independence of the σ_{rf} and the σ_{dc}, and (ii) to present some preliminary semi-classical explanations of the influences of the dc power on the rf electrons.

II. Theory

We wish to accomplish the aim (ii) first, and (i) is shown in Table I at the end. In order to study the dc influence on the rf size effect, we shall modify the theory of size effect by Fischer and Kao. The modification is simple. We assume that there is an electric field E_{dc} produced by an externally applied V_{dc}. The E_{dc} felt by the dc electrons in the sample is not the same as that felt by the rf electrons, though they are both considered as coduction electrons.

There are two distinct effects following the introduction of V_{dc} to the sample, namely: (i) A constant amount of increment of the power dissipation in the sample if the V_{dc} is also a constant, and (ii) a constant amount of increment of the magnetic feld H accompanied by a constant amount of decrement of the electron mobility μ_{rf} and a constant amount of increment of n_{rf} as a consequence of the application of the same V_{dc}.

The shape of the rf size effect power dissipation curve is not changed, but the whole curve is shifted not only in the direction of the power dissipation $\mathcal{P}$ axis (the conventional Y-axis) but also along the H axis (the conventional X-axis).

For the above reasons, it seems to be adequate to add simply a dc energy density perturbation term to the size effect formula[1] as shown in eq. (1). The first term takes care of the phenomenon (ii) above, and the second term, the phenomenon (i).

$$\mathcal{P}(\phi)=\frac{2\omega d}{c}\left[\frac{1-2exp(-\phi)\ \ sin\phi-exp(-2\phi)}{1+2exp(-\phi)\ cos\phi+exp(-2\phi)}+\right]\frac{E^2_{dr}}{|A_o|^2}, \tag{1}$$

which is also

$$\mathcal{P}(\phi)=[\mathcal{P}(\phi)]_{size}+\Delta\mathcal{P}_{dr}. \tag{2}$$

The subscript dr means the influence of the dc field on the rf electrons. Equs. (1) and (2) may also be put in the form

$$\frac{\Delta\mathcal{P}_{dr}}{\mathcal{P}_{size}}=\frac{E^2_{dr}\ c\ (2+2exp(-\phi)\ cos\phi+exp(-2\phi))}{|A_o|^2\ 2\omega d\ (1-2exp(-\phi)\ sin\phi-exp(-2\phi))}, \tag{3}$$

where A_o is defined as the initial rf wave amplitude within the rf coil with the indium antimonide sample in place but without the size effect power dissipation taking place. All the other symbols remain the same as those defined in the references[1],[2].

If the influence of the dc field on the rf electrons is small, then,

$$\frac{\Delta f_{dr}}{f_{size}} \ll 1 \tag{4}$$

is expected.

Assuming $E_{dr} \propto V_{dc}$, then from eq.(1)

$$\Delta f_{dr} = \gamma V_{dc}^2, \tag{5}$$

where γ is a constant of proportionality to be determined by the experiments, provided we know the dc conduction follows the Ohm's law.

The E_{dr} around the rf electrons may disturb the equilibrium condition in such a way that the carrier concentration n_{rf} and the mean velocity v_{rf} are both changed, then, the increment of the mean rf velocity Δv_{rf} due to the dc electric field E_{dr} is

$$(ne\Delta v)_{rf} = \sigma_{rf} E_{dr} \tag{6}$$

if the Ohm's law is still followed. Since E_{dr} affects every electron therefore in eq. (6)

$$n_{rf} = (n_o + \Delta n)_{rf}, \tag{7}$$

and the total concentration n_{rf} can be found by the size effect experiment and calculation provided the shape of the rf power dissipation curves remains the same.

In the case of indium antimonide, the increment of magnetic field H caused by the introduction of the dc power implies an rf mobility μ_{rf} decrement from $\mu_{o,rf}$ to $(\mu_o - \Delta\mu)_{rf}$.

The Δn_{rf} and the $\Delta\mu_{rf}$ are both small in comparison with the $n_{o,rf}$ and the $\mu_{o,rf}$ respectively, if the E_{dr} is very small in comparison with A_o.

The galvanomagnetic effect data show that the dc conductivity σ_{dc} is not affected by the rf energy. If it does, the change must be less than 0.5% such that it is eclipsed by the present experimental error. According to the results of the experiment, the beharior of the dc electrons satisfies the Ohm's law, same as the rf electrons. The principle for the dc measurements is : if there is any change in the dc behavior of the material due to the influce of the rf power, it will be shown by the dc measurements alone of the μ_{dc} and n_{dc}.

III. Experiments

The sample is a slab. Its dimensions are 15 mm x 8 mm x 2.65 mm. It is a single crystal of 56S grade (Cominco Ltd., U.S.A. and Canada). It is spark cut, and the face of the slab is in the [211] direction. The Fermi surface is known to be spherical around k=0, and the conduction band is nonparabolic [8]. Nothing is known about the isolatation of the conduction electrons.

The general set-up for the experiment is shown in Fig.1. The transmitter receiver system is frequency stabilized and is instrumentwise distortion free. The frequency for the present experiment is fixed arbitrarily at 33,501,245 Hz ± 1 Hz.

The correct line shape of the power dissipation curve is known from a previous observation on the NMR line shape of pure H_2O. The dc perturbation is produced by connecting the sample placed in the rf coil with a stable but selective dc power supply. The dc power supply is stable to within ± 0.1 mV in the interval from 1 to 6 volts. The

direction of the E_{dc} is in parallel with the axis of the rf coil. (However, the magnitude of the dc influence on the rf power dissipation is found insensitive to the selection of the direction of E_{dc}, and the magnitude is about the same whether E_{dc} is in the X-, Y-, or Z-direction. If we can prove by expriment that $E_{dr} \propto E_{dc}$, then, we may say eq. (1) is a proper choice.

In order to obtain consistent results the sample in the flat rf coil is constantly cooled by a jet of air such that the temperature of the sample is kept at 300°K.

The instruments are stable enough such that the sweep rate of the magnetic field maybe kept low. The sweep rate is set at 20 to 30 G per second, such that the relaxation process within the sample will be complete.

The Hall and the dc conductivity measurements were also performed using the potentiometer five point method. The measurements were carried out with and without the rf field applied around the sample.

IV. Results

Fig.2 shows the size effect power dissipation vs the magnetic field H curve without dc influence. The curve fitting[2] shows that the theoretical characteristic value for this particular curve is $\Delta=14.0\pm0.1$.

Fig.3 shows that the power dissipation curve is shifted by the dc influence, and the higher the E_{dc} the larger the shifts. However, Fig.3 also shows that the shape of the curves are not changed by the dc applied at all. Thus, the Δ value remains the same ($=14.0$) regardless of the presence of the dc perturbation. The curve is shifted both along the the X- and the Y-direction.

Table I shows an example of the difference in μ_{rf} and n_{rf} with and without the dc applied.

Table II shows the difference between the results of the size effect measurements and those of the galvanomagnetic effect measurements. It shows that the dc influence on the rf properties of the material is small in comparison with the large differences between the $(\mu, n, \sigma)_{rf}$ and $(\mu, n, \sigma)_{dc}$. The rf and the dc experiments were performed simultaneously.

The E_{dr} is calculated from equs. (1) and (3), and

$$\frac{\Delta \mathcal{P}_{dr}}{\mathcal{P}_{size}} = \left(\frac{E^2_{dr}}{|A_0|^2}\right)\left(\frac{2\omega d}{c} f(\phi_0)\right)^{-1} = a\ measured\ constant. \tag{8}$$

In the-above equation, $\phi=\phi_0=2.2541$ at the peak of the power dissipation, and ϕ_0 is a universal constant. The $f(\phi_0)$ is the ϕ dependent function evaluated at $\phi=\phi_0$ (eq. (1)), thus, $f(\phi_0)$ is also a universal constant.

$$f(\phi_0)=0.7283. \tag{9}$$

The rf incident wave amplitude is known by observing the voltage indication displayed on the screen of the Tektronix 7704 oscilloscope. Thus, the p-p amplitude of the rf wave is found to be 0.35 volt, and since the length of the copper wire forming the rf coil is 36

cm, therefore, we obtain

$$A_0=\frac{V_{rf,coil}}{L}=\frac{0.35}{2\times 36}=0.0047\ volt\ cm^{-1}. \tag{10}$$

The rf wave has an angular velocity of $\omega=2\pi\times 33,501,245\ sec^{-1}$, and since the thickness of the sample d=0.265 cm (the direction of d is in parallel with the static magnetic field $\vec{H}$), therefore, the general expression of the E_{dr} in terms of $\Delta f_{dr}/f_{size}$ from eq. (8) is

$$E^2_{dr}=(2.657\times 10^{-3})(0.0047)^2\left(\frac{\Delta f_{dr}}{f_{size}}\right). \tag{11}$$

The value of $\Delta f_{dr}/f_{size}$ is directly obtained from the type of experimental results shown in Figs.3 and 4.

Since the dc influence is only a few percent on the rf electrons even a large dc (about an ampere) is applied, therefore, it is quite difficult to make very accurate $\Delta f_{dr}/f_{size}$ measurements. However, if numerous data are collected, a most probable conclusion may be drawn from the experimental results (Fig.5). We consider the existence of the expression

$$\frac{\Delta\rho_{dr}}{\rho_{size}}=\gamma V^2_{dc}, \tag{12}$$

and the constant

$$\gamma=16.5\ volt^{-2} \tag{13}$$

which is found from the least square fit of the data shown in Fig.5 The root mean square error of $\Delta f_{dr}/f_{size}$ is found to be $\pm$ 8%.

If we combine equs. (11) and (12), we have for the present crystal

$$E^2_{dr}=96.84\times 10^{-8}V^2_{dc}, \tag{14}$$

or

$$E_{dr}=9.84\times 10^{-4}V_{dc}. \tag{15}$$

Since r=1.5 cm for the particular sample, therefore,

$$E_{dc}=\frac{V_{dc}}{r}=\frac{V_{dc}}{1.5}, \tag{16}$$

and by combining equs. (16) and (15),

$$E_{dr}=9.84\times 10^{-4}\gamma\ E_{dc}, \tag{17}$$

and

$$E_{dr}=1.48\times 10^{-2}\ E_{dc}. \tag{18}$$

Thus we see the dc electric field E_{dc} is much larger than the efftective electric field (due to V_{dc} too) imposed on the rf electron.

Since the σ_{rf} is experimentally found nct affected by the presence of the V_{dc}, then, if the Ohm's law is followed, we have from equs. (6) and (7),

$$\Delta v_{rf}=\frac{\sigma_{rf}\ E_{dr}}{e(n_0+\Delta n)_{rf}}, \tag{19}$$

or

$$\Delta v_{rf}=1.176\times10^{22}\left(-\frac{E_{dr}}{(n_o+\Delta n)_{rf}}\right), \tag{20}$$

where E_{dr} is in volt per cm, and n in cm^{-3}. The Δv_{rf} thus found is of the order of a few cm/sec because E_{dr} is already small. On the other hand, the mean velocity of the rf electron, $v_{o,rf}$ which is not affected by the dc perturbation (i.e., the $E_{dr}=O$ case), is about 10^3 cm/sec when $n_{o,rf}\cong10^{16}$ cm^{-3}, $E_{rf}\cong A_o\cong 5\times10^{-3}$ volt/cm. Fig.6 shows the relation between E_{dr}, Δn_{rf}, andΔV_{rf}. E_{dr} is found from eq. (15), $n_{o,rf}$ and n_{rf} are found from the results of the size effect experiments. (i.e., from eq. (2) in the reference (2)), and Δv_{rf} from eq. (20).

The Δn_{rf} vs E_{dr} curve shown in Fig.6 is obviously not linear,

the Δv_{rf} vs E_{dr} relation seems quite linear by appearance, but in fact, the line bends slightly toward the E_{dr} axis.

Table III shows the results of the dc conductivity measurements. The average dc conductivity is

$$\sigma_{dc}=225\pm1\ (ohm\text{-}cm)^{-1}. \tag{21}$$

This σ_{dc} is slightly different from the one shown in Table II, and the difference is due to the non-uniformity of the crystal, and it is commonplace in semiconductor wafers. We have cut the samples from different part of the same InSb wafer.

Fig.7 is an experimental result of the XY plot of the magnetoresistance vs the magnetic field H. It shows the dc conductivity σ_{dc} is, except the magnetoresistance, effect, not influenced by the presence of thd rf field at all. The plot shows the magnetoresistance effect is about 4% off from the ideal case in the magnetic field range from 0 to 12,000 G. The $\Delta\mathcal{P}_{dr}/\mathcal{P}_{size}$ is not found affected by the deviation as such because only the power ratio is measured. The rf power dissipation $\mathcal{P}_{size}$ does not seem to be affected by such deviation either which can be seen from Fig.2.

V. Conclusions

(i) The rf size effect power dissipation is influenced by the dc perturbation only slightly. The main effect is still the rf size effect itself.

(ii) The dc conductivity σ_{dc} is not changed by the presence of the rf field around the sample at all.

(iii) The big difference between the $(\mu,n,\sigma)_{rf}$ and the $(\mu,n,\sigma)_{dc}$ can not be reconciled even in the simultaneous presence of the rf field and the dc field in the same sample.

(iv) The independence of the $(\mu,n,\sigma)_{rf}$ and the $(\mu,n,\sigma)_{dc}$ makes us believe that the conduction electrons may be divided into groups; e.g., the rf group and the dc group, and they are independent and isolated.

(v) The two groups of electrons can co-exist at the same time in the same space, and each of them possesses its own n, τ/m^*, and σ.

(vi) Evidences show that the conduction band structure of InSb is not so simple as it was

thought to be.

(vii) Formula (15) is more fundamental than (17).

(viii) Fig.8 is a general idea of the present report.

(ix) Contribution of holes to the room temperature dc conductivity is very small and may be neglected because the mobility of holes in InSb is only 0.97% of the electron mobility, and at room temperature, the material is found intrinsic[3],[4].

References

(1) Fischer,H. abd Kao,Y.H., Solid State Comm., **67**, 275,1969

(2) Yang,Y.T., et.al., Il Nuovo Cimento, XVIB, 188,1973

(3) Hilsum,C. and Rose-Innes,A.C., Semiconducting III-V Compounds, Pergamon, London, 1961

(4) Long,D., Energy Bands in Semiconductors, Ch.6, The III-V Compounds, Interscience Publishers, John Wiley and Sons, London,1968, and thereferences therein.

Acknowledgement

The author is grateful to Prof.S.Y.Wang, Prof.Y.C.Lee and Prof.T.T. Chen for their valuable suggestions, and Mr. H.C.Liu, and Miss T.P.Pai for their help with the computer programming.

Table I

T=300°K, f=33,501,245 Hz ± 1 Hz, Δ=14.0 ± 0.1

Sample: InSb, n-type, [211] direction, size: 15mm×8mm×2.65mm. d=2.65mm along the H direction.

rf conductivity: 1,887 $(\text{ohm-cm})^{-1}$.

dc (applied)	μ_{rf} $(\text{cm}^2\text{volt}^{-1}\text{sec}^{-1})$	n_{rf} (cm^{-3})	H_o (G)	σ_{rf}^{-1} (ohm-cm)
0V, 0A	1.78×10^5	6.56×10^{16}	3,630	0.00053
0.031 V, 1A	1.74×10^5	6.70×10^{16}	3,720	0.00053
amount of shift	(−) 4×10^3 (−) 2.2%	(+) 1.4×10^{15} (+) 2.2%	(+) 90 (+) 2.2%	0

Table II

Size effect: f= 33,501,245 Hz ± 1 Hz, Δ= 14.0 ± 0.1, d= 2.65 mm InSb, n-type, [211] ∥ H direction, single crystal, 300°K.

Hall effect: 5 point method, potentiometer measurement, 300°K, dc.

Conductivity: 4 point method, potentiometer measurement, 300°K, dc.

Measurement	μ (cm^2 $volt^{-1}$ sec^{-1})	n (cm^{-3})	σ^{-1} (ohm-cm)
Size effect (A)	1.78×10^5	6.56×10^{16}	0.00053
Galvanomagnetic effect (B)	$(6.57\pm0.60)\times10^4$	$(2.07\pm0.13)\times10^{16}$	0.0046
(A)/(B)	2.70	3.17	$(8.6)^{-1}$

Table III

The dc conductivity measurements

Method: 4 point, potentiometer measurement

Sample: n-type InSb, length= 1.5 cm, cross-section=0.21 cm^2. Temperature: 300°K

V volt	0.00135	0.00287	0.00645	0.01172	0.01425	0.02020	0.02438	0.02875
A ampere	0.0424	0.0906	0.204	0.372	0.454	0.648	0.763	0.896
σ $(ohm\text{-}cm)^{-1}$	224	225	225	226	226	227	225	224
$\sigma dc,av.$ $(ohm\text{-}cm)^{-1}$	225 ± 1.3							

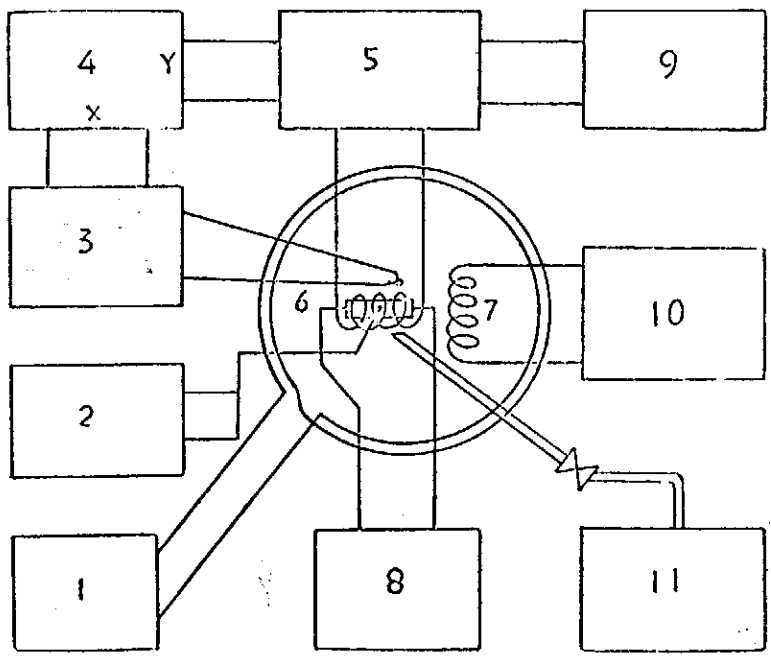

Fig.1 Experiment set-up. 1. Stable dc power supply for the electromagnet (feed-back stabilized). 2. Digital thermometer with thermocouple probe. 3. Gaussmeter (Hall effect, digital) with output terminal connected with the X-axis terminal of the HP 7001A XY recorder. 4. HP 7001A XY recorder. 5. Simple and distortion-free rf receiver with audio output connected with the Y-axis terminal of the XY recorder. 6. Cross coil head for the physical signal pick-up. The sample is put inside the receiver coil. The receiver coil is flat with inner space large enough to contain the flat sample. The filling factor is more than 0.9. 7. Transmitter coil. 8. Stable but selective dc power supply connected with the InSb sample. The dc can flow through the sample when the size effect experiment is performed. 9. HP 5245L frequency counter (a secondary standard) for ckecking the stability of the radio frequency at the receiver end. 10. Radio frequency transmitter. The frequency is determined by the quartz crystal selection. It is temporarily fixed at 33,501,245 Hz ± 1 Hz. It may be changed by another quartz crystal selection. 11. Air blower with nozzle and flow control.

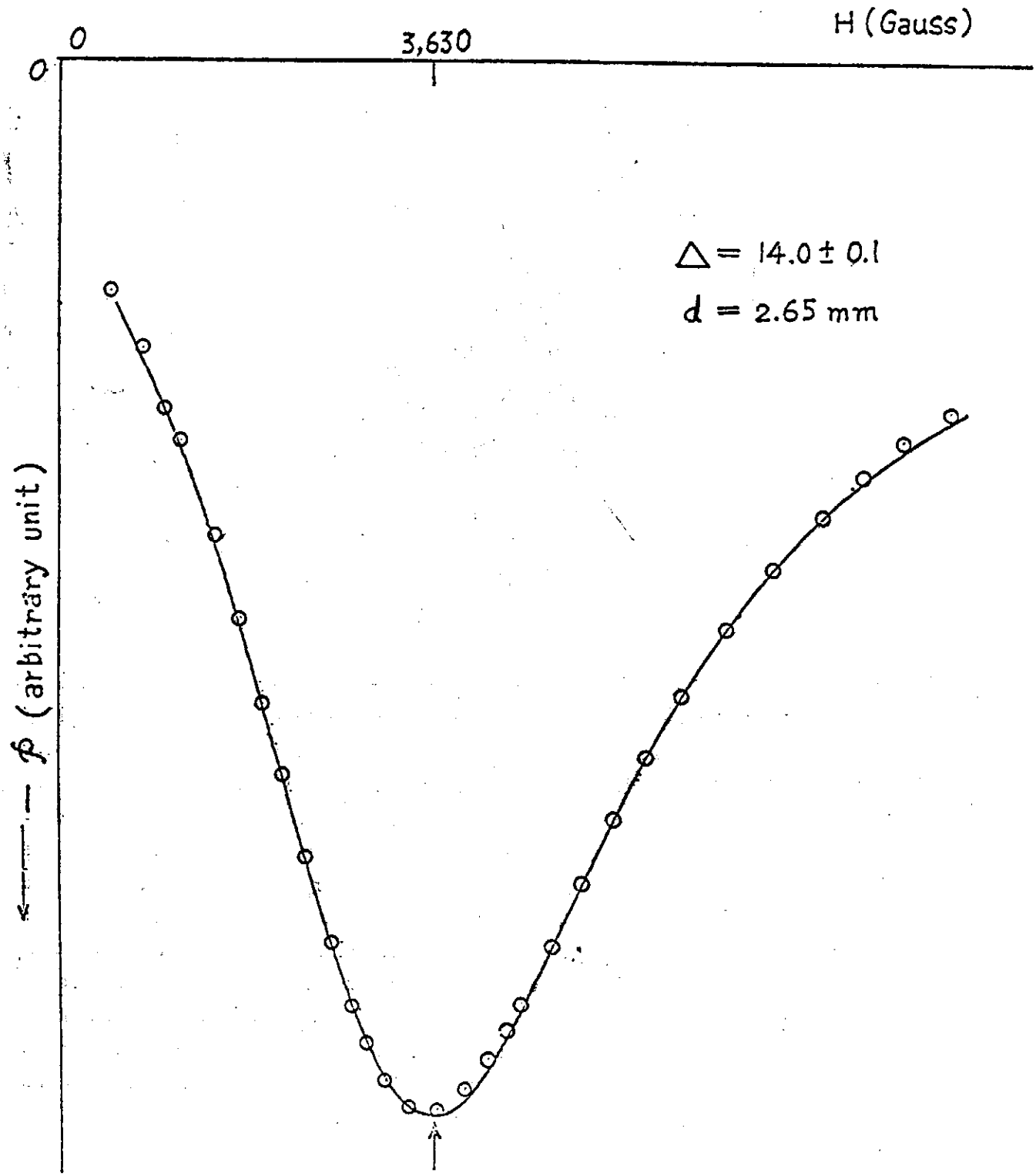

Fig.2 The experimental and the theoretical curve fitting. The Δ value which determines mainly the shape of the power dissipation curve is found to be 14.0 ± 0.1, while the thickness of the sample (parallel to the direction of H) is d=0.265cm

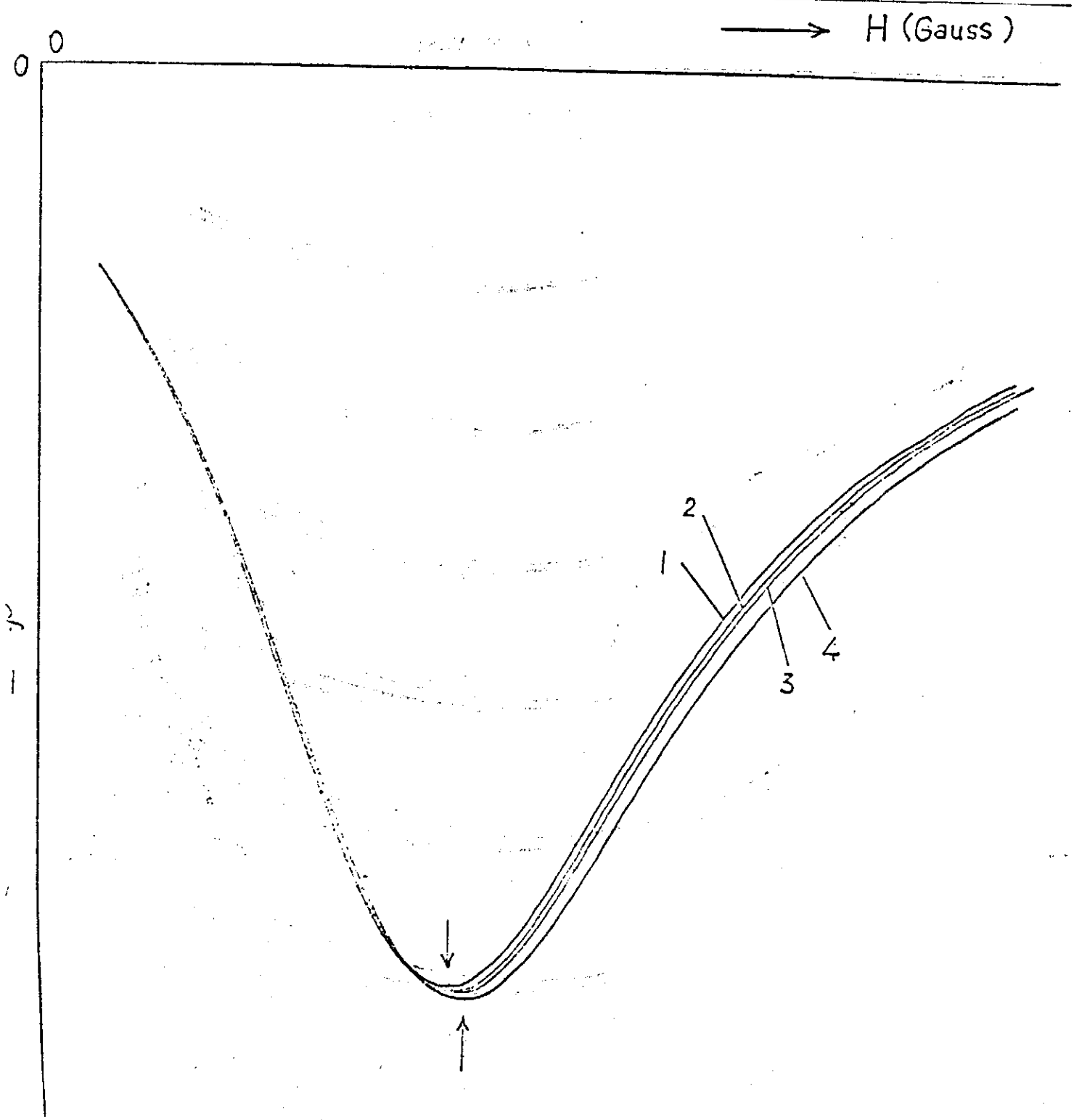

Fig.3 The shift of the rf power dissipation curves under the influence of the dc passing through the slab sample of InSb. Curve 1 is an rf power dissipation without the dc influence. Curve 2 is the shift of the rf power dissipation when the dc applied is 0.500 ampere and a V_{dc}= 0.0156 volt. Curve 3 is that at a dc of 0.600 ampere and a V_{dc}= 0.0188 volt. Curve 4 is that at a dc of 0.950 ampere and a V_{dc}= 0.0303 volt.
The shift changes the power dissipation from $|-\mathcal{P}|$ to $|-\mathcal{P}-\Delta\mathcal{P}|$ and the magnetic field from H to H+ΔH. The curves are shifted by the influence of the dc but the shape of the curves are found not changed at all. Therefore, the value of Δ is the same for all the curves. For such a reason, we are able to calculate the electron mobility shift and the carrier concentration shift due to the influence of the dc applied.

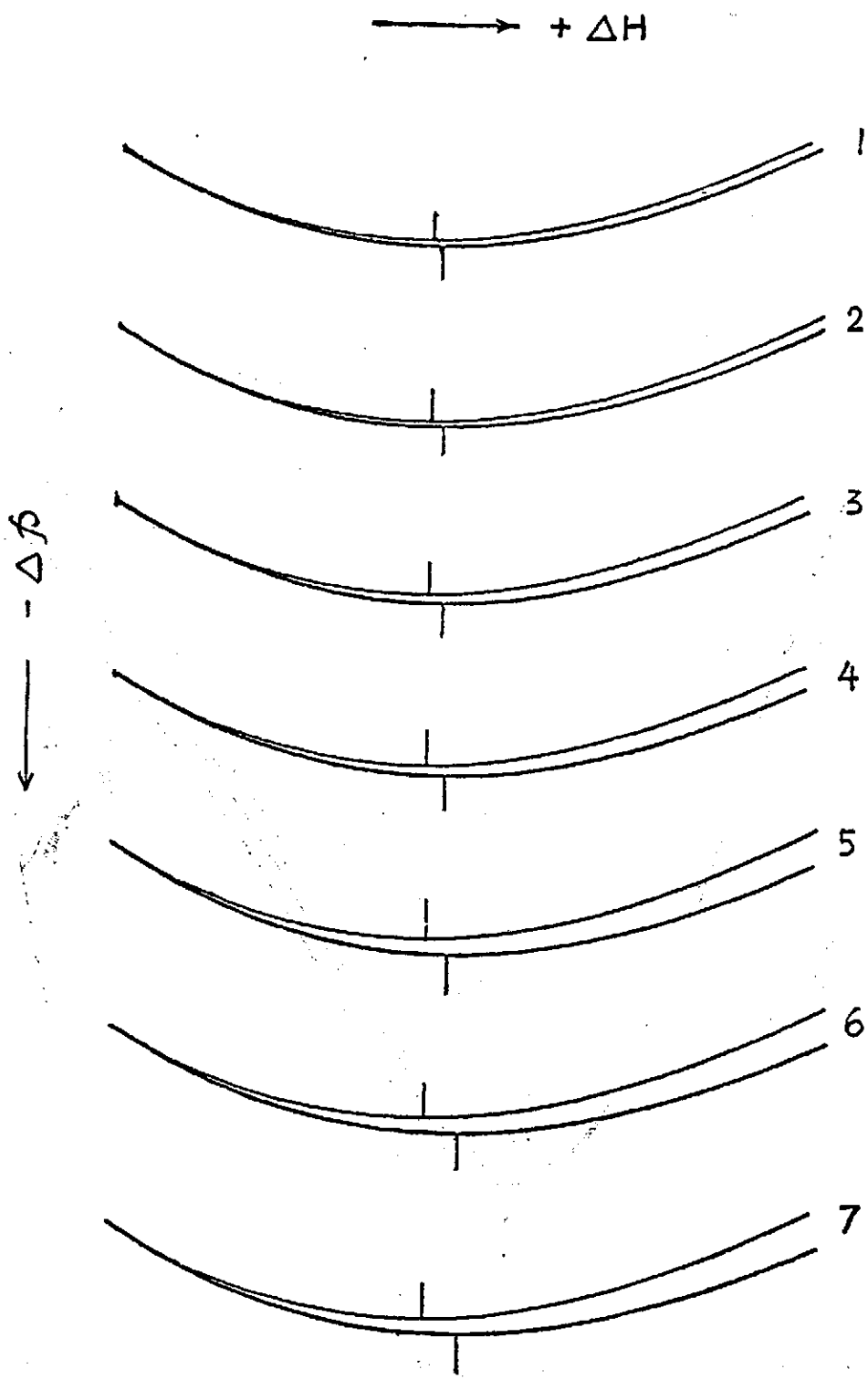

Fig.4 The enlarged view (by the voltage off-set) of the $-\Delta f$ and the $+\Delta H$ shifts near the tip of the power dissipation curves as shown in Fig.3. Whenthe dc applied is small the $-\Delta f$ and $+\Delta H$ are also small. The upper curves are those without the dc influence. More than 20 such curves have been recorded, and the $\Delta f_{dr}/f_{size}$ vs the V^2_{dc} relation is shown in Fig.5

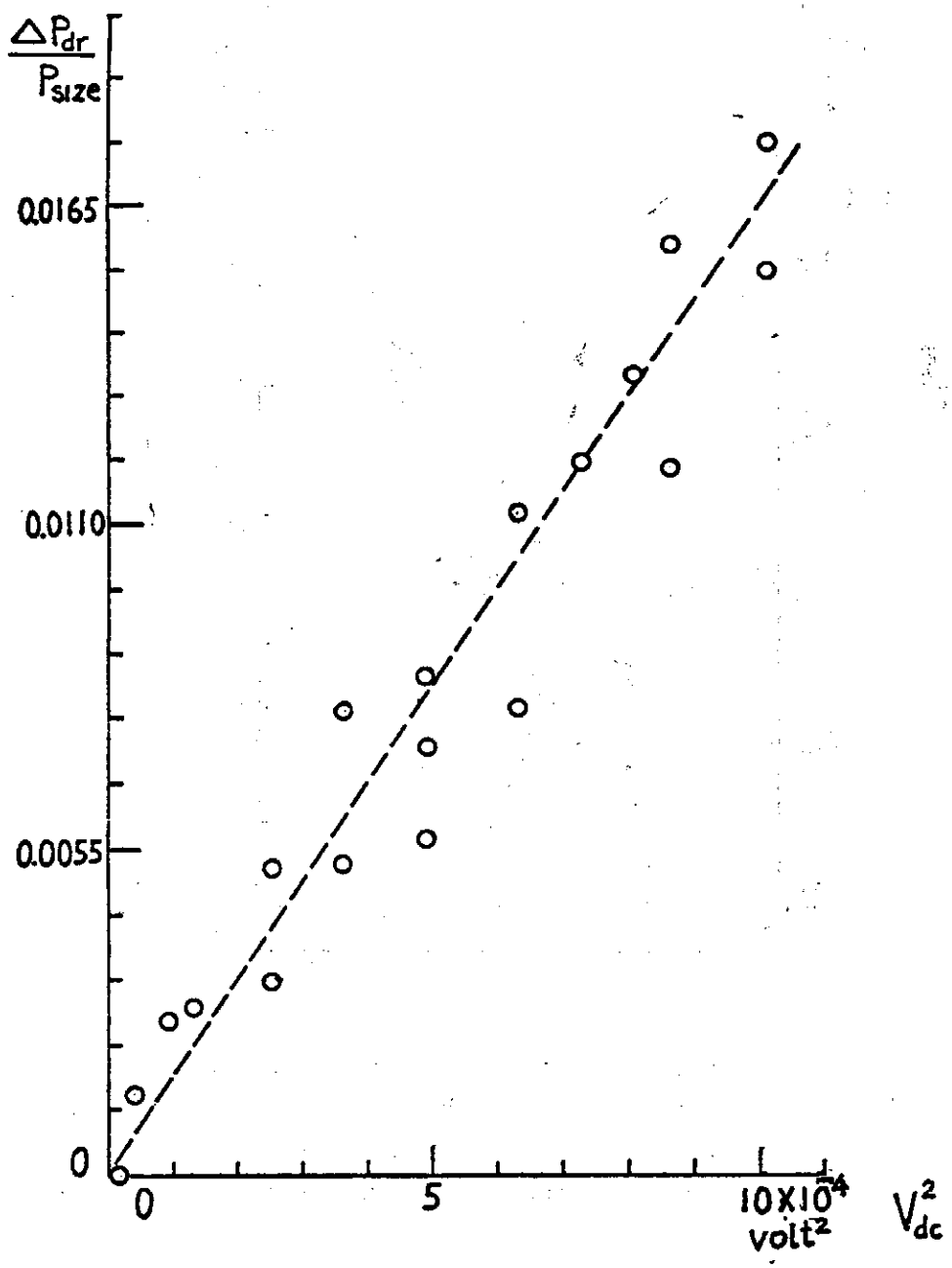

Fig.5 The $\Delta f_{dr}/f_{size}$ vs the V^2_{dc} plot according to the experimental results shown in the Fig.4. The least square fit shows $\Delta f_{dr}/f_{size} = 16.5\ V^2_{dc}$ according to the expression shown in eq. (12). The probable error of the $\Delta f_{dr}/f_{size}$ measurements is ± 8%.

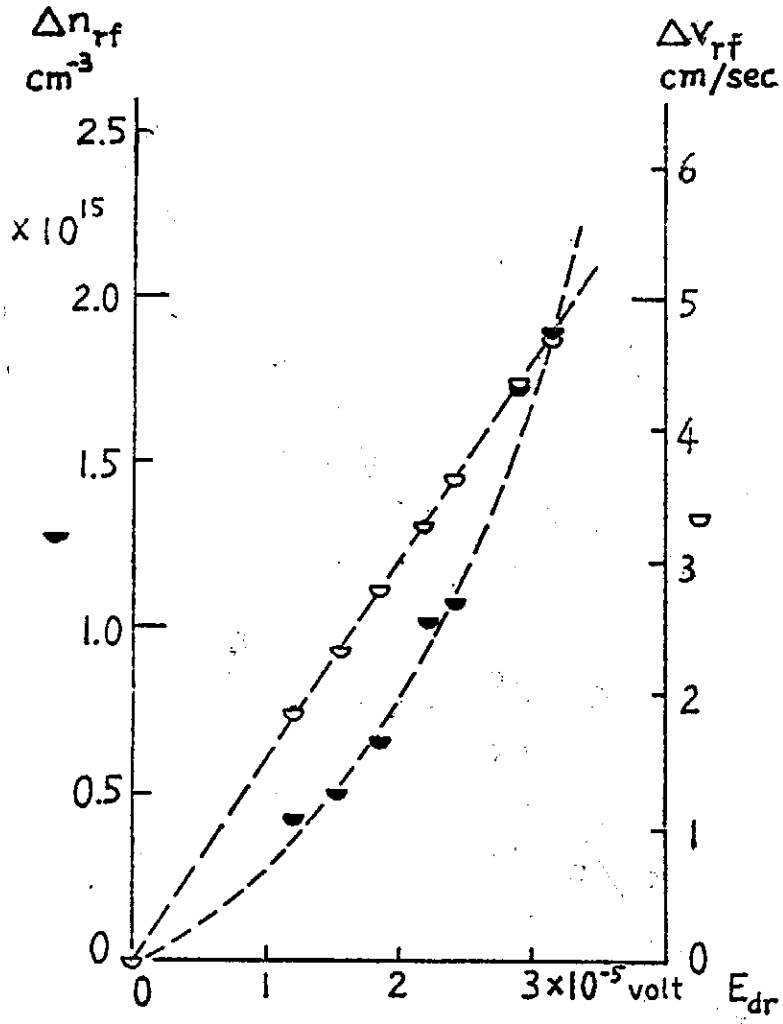

Fig.6 The increment of the carrier concentration $(\Delta n)_{rf}$ and the increment of the mean velocity of the rf electrons $(\Delta v)_{rf}$ due to the influence of the dc power applied vs E_{dr}. The $(\Delta n)_{rf}$ vs E_{dr} relation is obviously not linear. The $(\Delta n)_{rf}$ is obtained from the size effect measurements and eq. (2) in the reference (2). $n_{rf} = n_{o,rf} + \Delta n_{rf}$. The $(\Delta v)_{rf}$ is from eq. (6) and eq. (7) in this report. The E_{dr} is obtained from the results of the size effect experiments and from eq. (15) in the present report. The $(\Delta v)_{rf}$ vs E_{dr} relation seems quite linear by appearance, but in fact, the curve bends slightly toward the E_{dr} axis. The linear Ohm's law is assumed (eq. (6)), and the σ_{rf} is experimentally known to be a constant.

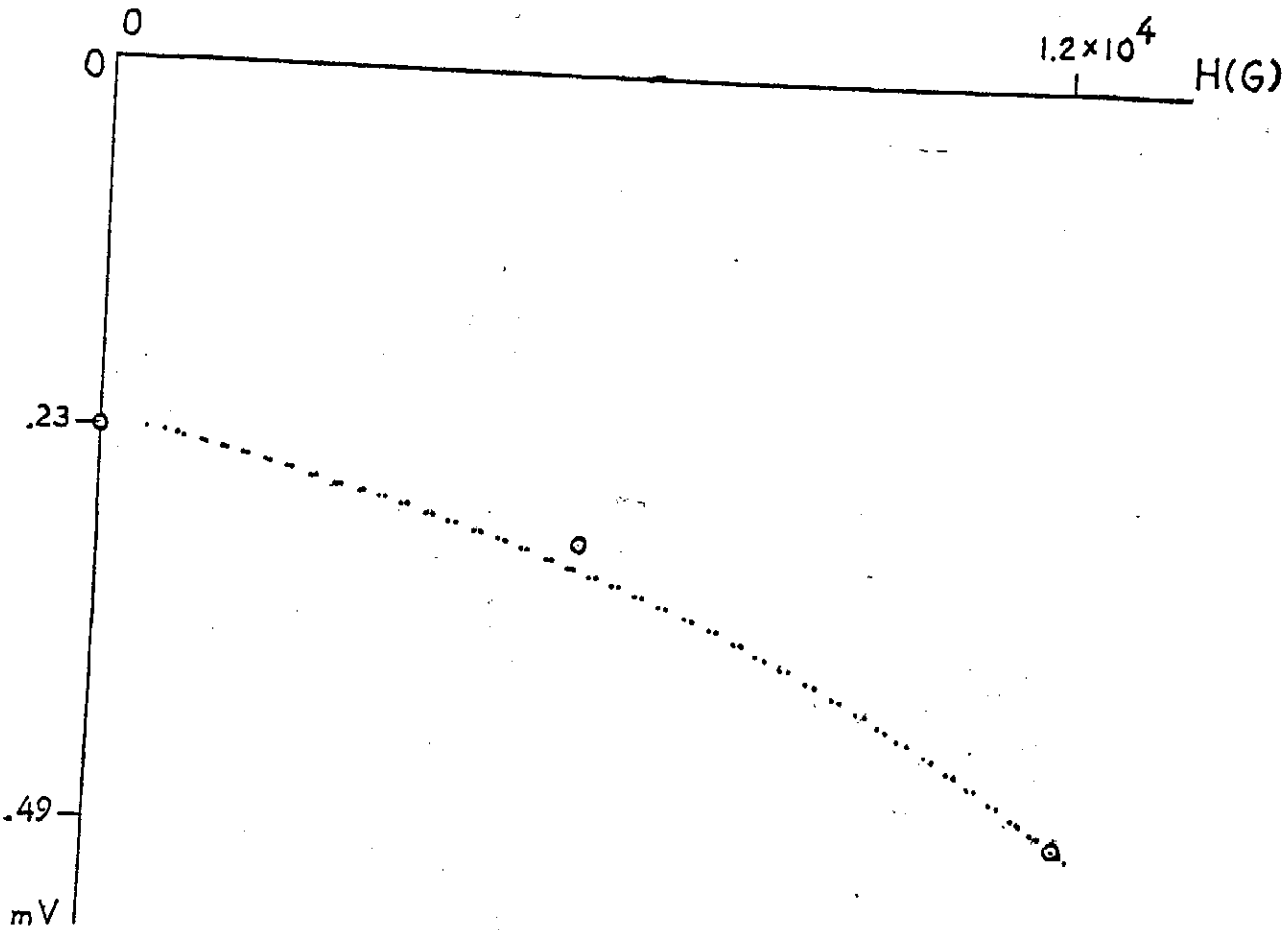

Fig.7 The dc magnetoresistance effect in the 56S grade InSb. The curve is obtained by using the XY recorder. The curve consists of a number of double points. The points on the left are those obtained when the rf power is applied around the sample, and those on the right are obtained without the rf power applied. There seems to be no difference between the two curves. The circles are the control points to show the ideal parabolic relation between the magnetoresistance and the magnetic field H. The deviation of the experimental result is 4% from the ideal condition. However, it is only a pure dc effect which has nothing to do with the rf phenomena (Fig.2 to Fig.4) and the power ratios $\Delta P_{dr}/P_{size}$.

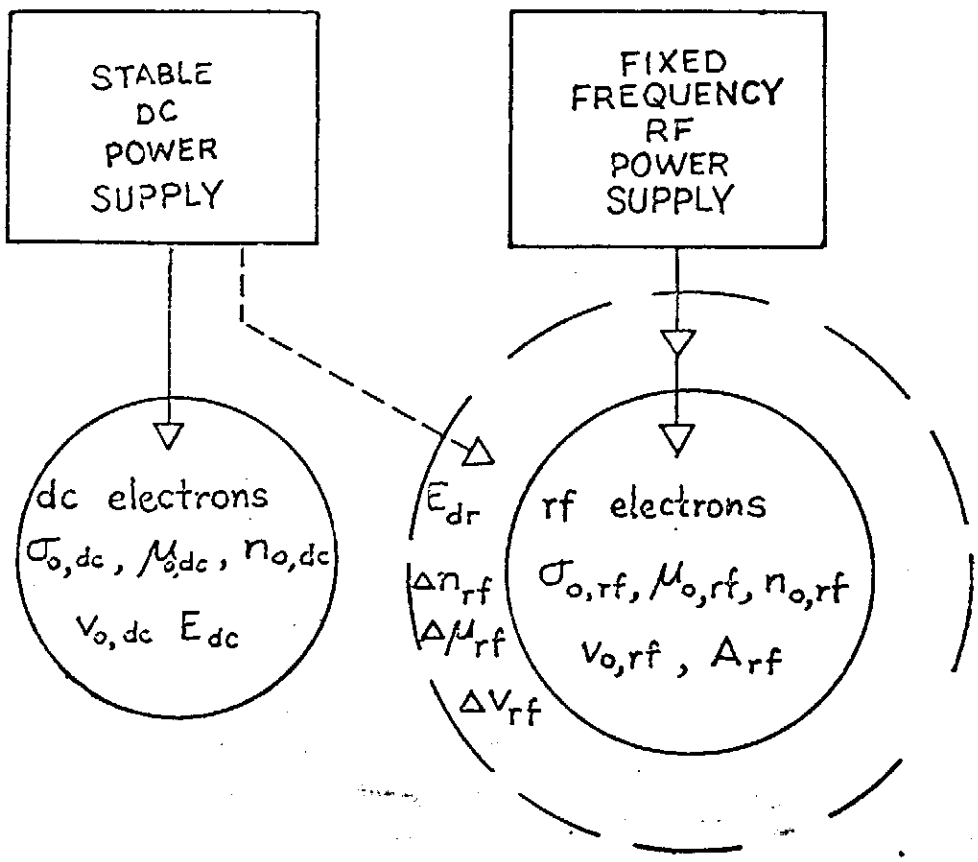
STABLE
DC
POWER
SUPPLY
FIXED
FREQUENCY
RF
POWER
SUPPLY
dc electrons
$\sigma_{o,dc}$, $\mu_{o,dc}$, $n_{o,dc}$
$v_{o,dc}$ E_{dc}
E_{dr}
Δn_{rf}
$\Delta \mu_{rf}$
Δv_{rf}
rf electrons
$\sigma_{o,rf}$, $\mu_{o,rf}$, $n_{o,rf}$
$v_{o,rf}$, A_{rf}

Fig. 8

PHYSICAL REVIEW B VOLUME 5, NUMBER 2 15 JANUARY 1972

Excitation Spectra and Piezospectroscopic Effects of Magnesium Donors in Silicon*

L. T. Ho and A. K. Ramdas
Department of Physics, Purdue University, Lafayette, Indiana 47907
(Received 23 August 1971)

Excitation spectra of magnesium impurities diffused into undoped silicon as well as into silicon doped with group-III acceptors have been measured. In the former, magnesium is a heliumlike neutral donor (Mg^0) with excited states similar to those of group-V donors and close to the effective-mass positions; its ionization energy at liquid-helium temperature is 107.50 ± 0.04 meV. In specimens containing group-III impurities, with the magnesium partially compensated, excitation spectra are observed similar to those of group-V donors and that of Mg^0 except that the spacings between corresponding lines are approximately four times larger and the $1s(A_1) \rightarrow 2p_\pm$ transition is a closely spaced doublet, 0.2 meV apart. These features are consistent with a singly ionized heliumlike magnesium donor (Mg^+) and a small chemical splitting of the $2p_\pm$ state; the ionization energy is 256.47 ± 0.07 meV at liquid-helium temperature. The excitation spectrum of Mg^+ was also observed in specimens containing Mg^0 subjected to high-energy electron irradiation. Study of the piezospectroscopic effects shows that both Mg^0 and Mg^+ occupy a T_d-symmetry site with $1s(A_1)$ as the ground state. A value of 8.7 ± 0.2 eV has been deduced for the shear-deformation-potential constant Ξ_u of the (100) conduction-band minima of silicon.

I. INTRODUCTION

The behavior of group-V impurities as donors and of group-III impurities as acceptors in silicon and germanium represents one of the most extensively studied and best understood aspects of semiconductor physics. The substitutional nature of these impurities, the large dielectric constant of the host, and the effective mass of the bound carrier are the significant features of the model used to explain a variety of phenomena[1-3] associated with these donors and acceptors which are solid-state analogs of the hydrogen atom. It is also now well established that the group-II elements, zinc,[4,5] mercury,[6] and beryllium[7] in germanium and beryllium in silicon,[7] are solid-state analogs of the helium atom in that they are double acceptors; by compensation with group-V donors one can study these double acceptors in their singly ionized state which then are the analogs of singly ionized helium. The group-VI element sulfur when introduced into silicon[8-10] behaves like a heliumlike double donor; several sulfur donor centers have been discovered though the exact structures of these have not yet been established. For example, the electron paramagnetic resonance (EPR) measurements by Ludwig[9] showed that the sulfur centers designated as D centers by Krag *et al.*[8] are isolated S^+ at T_d sites, but he could not determine if they occupied the substitutional or the interstitial sites with that symmetry. The group-I impurity copper in germanium,[11] is another element which has been studied to some extent. The acceptor states associated with this impurity are consistent with its being substitutional.

Of the impurities which are interstitial rather than substitutional, the best-known example is that of lithium in silicon and germanium.[12,13] Transition-metal ions in silicon and germanium, both as interstitial and substitutional impurities, have been studied by Woodbury and Ludwig[14] who investigated their EPR spectra. Interstitial aluminum has been reported in electron-irradiated aluminum-doped silicon where interstitial silicon and substitutional aluminum are believed to exchange their roles[15]; it has been shown that these interstitial aluminum impurities are then donors. Recently,[16,17] the group-II element magnesium, when diffused into silicon, has been shown to behave like a double donor rather than a double acceptor. This behavior can be understood only if magnesium is interstitial rather than substitutional. Singly ionized magnesium donors can be produced by diffusing magnesium into

*This paper has been published in Physical Review, 5B (1972) 5 462-474

silicon containing acceptors[17] like boron or aluminum or by electron irradiation as well as by thermally ionizing neutral magnesium.[18] The purpose of the present paper is to report and discuss the results of a detailed study of the Lyman spectra associated with both neutral and singly ionized magnesium donors in silicon including their piezospectroscopic effects.

II. EXPERIMENTAL PROCEDURE

Magnesium was diffused into silicon in the following manner. Pure magnesium[18] was deposited by evaporation on the surfaces of the optical sample. The optical sample was sandwiched between two other specimens, all three having magnesium on the surfaces in contact, and heated at ~1200 °C for ~1 h in a helium atomosphere; the sample and the "covers" weld together and thus the magnesium does not escape into the ambient. After the heat treatment, the sample, together with the covers, was quenched in liquid nitrogen. The covers were then ground off. By following this procedure an undoped floating-zone silicon, initially p type and of resistivity ~1700 Ω cm, was converted to a low-resistivity n-type specimen with a room-temperature carrier concentration $\sim 2\times 10^{15}$ cm^{-3}. These specimens were adequate for observing the excitation spectra of neutral magnesium (Mg^0) at low temperatures. In order to study singly ionized magnesium (Mg^+) donors, low-resistivity ~10-Ω-cm boron-doped or aluminum-doped floating-zone silicon was used instead of pure silicon. From experience it was found that diffusion times of ~10 h were required to produce sufficient concentration of Mg^+ for the present studies. The samples were too inhomogeneous to give reliable Hall measurements. The boron concentration in most of the specimens used was $\sim 1.5\times 10^{15}$ cm^{-3} and such specimens showed only Mg^+ spectrum and no trace of Mg^0 spectrum; an upper limit of 10^{15} cm^{-3} of Mg^+ is thus estimated. It was also found that Mg^+ could be produced in specimens containing initially Mg^0 only, by subjecting them to an irradiation with high-energy electrons. In this case magnesium-doped silicon was irradiated with 1-MeV electrons from a Van de Graaff accelerator. Specimens subjected to the same heat treatment and quench failed to show the spectra if no magnesium was deposited on them initially; this check was made to satisfy ourselves that we are indeed dealing with magnesium centers, Mg^0 or Mg^+ as the case may be.

The samples used in these experiments were oriented for appropriate crystallographic orientations either by x rays or by the optical method of Hancock and Edelman.[19] An optical cryostat[20] was used for low-temperature measurements, sample temperatures ~12°K are estimated in our liquid-helium measurements. Uniaxial compression was applied to the specimens for piezospectroscopic measurements using the differential-thermal-compression technique.[21] In order to determine the shear-deformation-potential constant Ξ_u, a calibrated stress was employed in some of the piezospectroscopic measurements; this was accomplished using a quantitative-stress optical cryostat[22] which is an adaptation of the glass cryostat described in Ref. 20.

A double-pass Perkin-Elmer spectrometer, model 112G, equipped with Bausch-and-Lomb plane-reflection gratings and appropriate filtering systems, was used for the measurements. Typical resolution in our measurements is ~0.5 cm^{-1}. The radiation was polarized for piezospectroscopic measurements by passing it through a Perkin-Elmer wire-grid polarizer with silver-bromide substrate. A Reeder[23] thermocouple with a cesium-iodide window was used as the detector.

III. EXPERIMENTAL RESULTS AND DISCUSSION: Mg^0

A. Zero Stress

The excitation spectrum for neutral magnesium donors in silicon measured with liquid helium as coolant is shown in Fig. 1. The energies of the excitation lines are given in Table I. The excitation spectrum for phosphorus[24] donors in silicon drawn on the same energy scale as that of Fig. 1 is shown in Fig. 2 for comparison. It is evident that the lines of the two spectra are strikingly similar in spacing and relative intensities. This can also be seen from Table II where the spacings for the two spectra are compared. The labeling of the excitation lines for magnesium donor is based on this similarity. The half-width for the excitation lines of Mg^0 is approximately twice as large as that of the phosphorus lines. The factors contributing to this feature have yet to be established. The broadening of the lines could also be the rea-

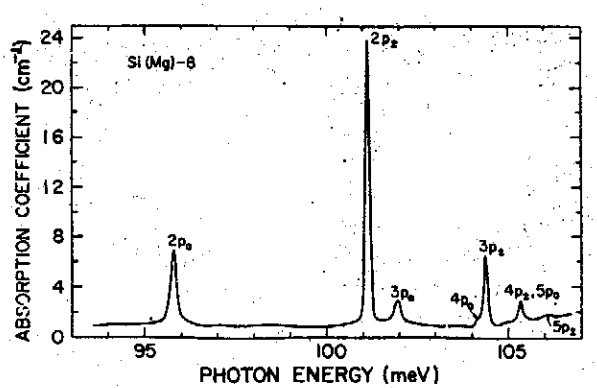

FIG. 1. Excitation spectrum of Mg^0 donors in silicon. Liquid helium was used as coolant. Carrier concentration, n(300 °K), estimated $\sim 1.2\times 10^{15}$ cm^{-3}.

TABLE I. Energies of excitation lines of Mg^0 donors in silicon (in meV).

Label	Assignment	Energy[a]
$2p_0$	$1s(A_1) - 2p_0$	95.80
$2p_\pm$	$1s(A_1) - 2p_\pm$	101.12
$3p_0$	$1s(A_1) - 3p_0$	101.95
$4p_0$	$1s(A_1) - 4p_0$	104.17
$3p_\pm$	$1s(A_1) - 3p_\pm$	104.38
$4p_\pm, 5p_0$	$1s(A_1) - 4p_\pm, 5p_0$	105.33
$5p_\pm$	$1s(A_1) - 5p_\pm$	106.05
E_I[b]		107.50 ± 0.04

[a]The experimental error is ± 0.015 meV. These values are in good agreement with those reported by Franks and Robertson (see Ref. 16).

[b]The ionization energy E_I was deduced by adding Faulkner's theoretically determined binding energy of the $3p_\pm$ state (Ref. 26) to the experimental energy of the transition labeled $3p_\pm$.

son why the a and b lines in the phosphorus spectrum are not seen in the Mg^0 spectrum.

As an interstitial impurity the donor electrons of magnesium are expected to be the two $3s$ valence electrons thus constituting neutral heliumlike centers. When one of these electrons is excited, the screening of the nuclear charge by the remaining electron and the other core electrons should result in hydrogenic excited states. The higher the excited state the more accurate will be this description. Comparison of energy levels of atomic hydrogen and helium shows this to be the case.[25] We expect the screening to be particularly effective for the p-like final states in the $1s \rightarrow np$ transitions. The remarkable similarity of the spacings between the excited states of Mg^0 and those of the group-V donors is thus explained. In the same manner it is also clear why the spacings observed in the excitation spectrum of Mg^0 are strikingly close to those calculated[26] for group-V donors in the effective-mass theory.

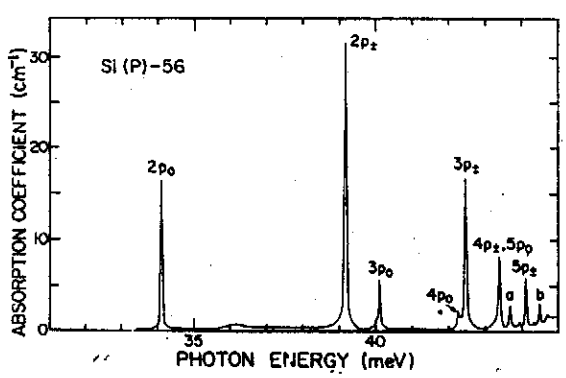

FIG. 2. Excitation spectrum of phosphorus donors in silicon. Liquid helium was used as coolant. $n(300\,°K) = 7.5 \times 10^{14}$ cm^{-3} (see Ref. 24).

As in the case of group-V donors, the positions of the excitation lines of Mg^0 will be determined by the location of the ground state which may lie below the effective-mass position due to the breakdown of the effective-mass theory in the vicinity of the impurity, giving the chemical splitting. The ground state is expected to be affected most seriously by this breakdown because of the large concentration of its wave function near the impurity core.[1] It is thus of interest to deduce the effective-mass ionization energy, which can perhaps be estimated by increasing the effective-mass ionization energy of group-V donors calculated by Faulkner[26] in the ratio of the first-ionization energy of the helium atom to that of the ionization energy of the hydrogen atom; this turns out to be $(31.27)(24.46)/(13.6) = 56.24$ meV. Here we have used the experimental values for the ionization energies of atomic helium and hydrogen, which, of course, are well known to be close to the calculated values [see Eyring, Walter, and Kimball (Ref. 27)]. The experimental ionization energy obtained by adding the calculated value[26] of the binding energy of the $3p_\pm$ state to the experimental energy of the transition labeled $3p_\pm$ in the Mg^0 spectrum is 107.50 meV; the justification for this procedure lies in the excellent agreement between the calculated and the experimental spacings of the excitation lines on the one hand and that between the spacings of the corresponding lines of phosphorus and magnesium donors on the other. Thus, it is evident that the ground state has suffered considerable chemical splitting. Presumably the sixfold degeneracy of the $1s$ state due to the multivalley nature of the conduction-band minima along $\langle 100 \rangle$ is lifted in the same manner as for group-V donors, and the ground state[27] is the totally symmetric linear combination $1s(A_1)$ with equal contribution of all the six $\langle 100 \rangle$ Bloch wave functions. The experimental proof for the singlet nature of the ground state will be forthcoming from the piezospectroscopic effects discussed in Sec. III B.

Recently Faulkner[26] has calculated in the effective-mass approximation the binding energies of energy

TABLE II. Spacings of donor excited states in silicon (meV).

States	Theory[a]	P[b]	Mg[b]
$2p_\pm - 2p_0$	5.11	5.06	5.32
$3p_0 - 2p_\pm$	0.92	0.93	0.83
$4p_0 - 2p_\pm$	3.07	3.09	3.05
$3p_\pm - 2p_\pm$	3.28	3.28	3.26
$4p_\pm - 2p_\pm$	4.21	4.21	4.21
$5p_0 - 2p_\pm$	4.17	4.21	4.21
$5p_\pm - 2p_\pm$	4.97	4.94	4.93

[a]Faulkner, see Ref. 26.

[b]The experimental error is ± 0.03 meV.

levels which are not expected to be observed in the Lyman spectrum, *viz.*, of $2s$, $3s$, $3d_0$, $4s$, $4d_0$, $4f_0$, . . . , etc. Though transitions from the $1s$ state to these levels are not allowed in the effective-mass approximation, they may become weakly allowed due to departures from it. Kleiner and Krag[28] have ascribed several weak lines to just such transitions. We have unsuccessfully searched for the corresponding transitions in the spectrum of Mg^0 in silicon. We can not rule out that the concentration of magnesium donors in the samples used was insufficient.

As mentioned already, a significant feature of the donor levels in silicon is the chemical splitting of the sixfold degenerate $1s$ ground state into singlet $1s(A_1)$, doublet $1s(E)$, and triplet $1s(T_2)$ levels, with $1s(E)$ and $1s(T_2)$ close to the effective-mass position and $1s(A_1)$ depressed considerably below it. In contrast to the case of shallower group-V donors,[29] it is not feasible to thermally populate the $1s(E)$ and $1s(T_2)$ for Mg^0 and observe excitation lines which originate from them. Attempts were made to observe the $1s(A_1)$–$1s(T_2)$ transition which is again allowed only to the extent of the breakdown of the effective-mass theory. Such transitions have been reported for bismuth donors in silicon,[30] and selenium and tellurium donors in aluminum antimonide.[31] However, we have been unsuccessful in observing the corresponding transitions in the spectral range from 41 to 95 meV. In the course of the above measurements we found several weak excitation lines at 87.18, 87.99, and 104.90 meV which occurred in only a few of the samples examined. They appear to be due to as yet unidentified centers.

Attention should be drawn here to the decrease in the intensity of the excitation spectrum when the same specimen is remeasured after a considerable lapse of time. Figure 3 shows a typical example of such a spectrum remeasured after 19 months. This may be a consequence of precipitation of magnesium. Time-dependent effects on donor excitation spectra have been noticed by Gilmer *et al.*[32] in the spectra associated with lithium-oxygen complexes and by Ludwig[9] in EPR studies of sulfur-doped silicon.

B. Piezospectroscopic Effect

The study of excitation spectra of donors and acceptors in semiconductors under uniaxial stress[3] —the piezospectroscopic effect—is very valuable in giving symmetry assignments to the energy levels and offers a direct means of determining deformation-potential constants. The relevent details applicable to the case of donor states[3,29,33] of a multivalley semiconductor are given below. The conduction-band minima of a multivalley semiconductor are shifted with respect to one another under the application of a uniaxial stress. The deformation-potential theory as applied to this problem by Herring[34] gives the shift in energy of the jth minimum as

$$\Delta E^j = (\Xi_d\,\delta_{\alpha\beta} + \Xi_u K_\alpha^{(j)} K_\beta^{(j)}) u_{\alpha\beta}\ , \tag{1}$$

where $K_\alpha^{(j)}$ and $K_\beta^{(j)}$ are components of a unit vector pointing from the center of the Brillouin zone towards the position in $\vec{k}$ space of the jth minimum. The subindex α or β designates a component along one of the cubic axes of the crystal, $u_{\alpha\beta}$ are the components of the strain tensor, and $\delta_{\alpha\beta}$ is the Kronecker-δ symbol. The symbols Ξ_d and Ξ_u are the dilatational- and shear-deformation-potential constants, respectively. In Eq. (1) a summation over α and β is implied. If it is assumed that both the dielectric constant and the effective masses characterizing the conduction-band minima are unaltered by strains used in the experiments, then, for a given valley, the energy-level scheme of a donor given in the effective-mass approximation will be unaffected by the stress. However, the energy-level schemes bearing different valley labels will be shifted relative to one another by the amounts given by Eq. (1). This will be true for all states well described by the effective-mass theory, for example, the p states.

Under a compressive force $\vec{F}$, the valleys $j=1$, 2, 3, 4, 5, and 6 along [100], [$\bar{1}$00], [010], [0$\bar{1}$0], [001], and [00$\bar{1}$], respectively, have energy shifts ΔE^j given by

$$\vec{F} \parallel [100],\ \begin{cases} \Delta E^{1,2} = [\Xi_d(s_{11}+2s_{12}) + \Xi_u s_{11}]T\,, & \text{(2a)} \\ \Delta E^{3-6} = [\Xi_d(s_{11}+2s_{12}) + \Xi_u s_{12}]T; & \text{(2b)} \end{cases}$$

$$\vec{F} \parallel [110],\ \begin{cases} \Delta E^{1-4} = \tfrac{1}{2}[2\Xi_d(s_{11}+2s_{12}) + \Xi_u(s_{11}+s_{12})]T, & \text{(2c)} \\ \Delta E^{5,6} = [\Xi_d(s_{11}+2s_{12}) + \Xi_u s_{12}]T; & \text{(2d)} \end{cases}$$

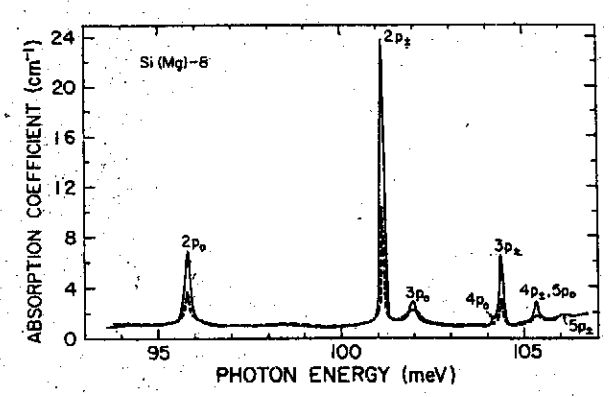

FIG. 3. Time-dependent effect on the excitation spectrum of Mg^0 donors in silicon. The dashed curve shows the decrease of intensity for the same sample remeasured after 19 months. Liquid helium was used as coolant in both measurements.

$\vec{F}\|[111]$, $\Delta E^{1-6} = \frac{1}{3}[3\Xi_d(s_{11}+2s_{12}) + \Xi_u(s_{11}+2s_{12})]T$, (2e)

where T is the applied force per unit area, and is defined to be positive for tension and negative for compression; the s_{ij}'s are the elastic compliance coefficients. It is thus clear that with $\vec{F}\|\langle 111\rangle$ there will be no splittings for the effective-mass donor states whereas for $\vec{F}\|\langle 100\rangle$ and $\vec{F}\|\langle 110\rangle$, a given donor level will split into two components whose shifts with respect to the center of gravity (c.g.) are given by

$$\vec{F}\|[100],\begin{cases}\Delta E^{1,2} - \Delta E_{\text{c.g.}} = \frac{2}{3}\Xi_u(s_{11}-s_{12})T\,, & \text{(3a)}\\ \Delta E^{3-6} - \Delta E_{\text{c.g.}} = -\frac{1}{3}\Xi_u(s_{11}-s_{12})T; & \text{(3b)}\end{cases}$$

$$\vec{F}\|[110],\begin{cases}\Delta E^{1-4} - \Delta E_{\text{c.g.}} = \frac{1}{6}\Xi_u(s_{11}-s_{12})T\,, & \text{(3c)}\\ \Delta E^{5,6} - \Delta E_{\text{c.g.}} = -\frac{1}{3}\Xi_u(s_{11}-s_{12})T. & \text{(3d)}\end{cases}$$

Wilson and Feher[35] have calculated the energies of the ground states $1s(A_1)$, $1s(E)$, and $1s(T_2)$ as a function of stress; the results are shown for $\vec{F}\|[100]$ in Fig. 4. The stress effect on a typical excited p state, the $2p_\pm$ state, is also shown in this figure for comparison. The labels on the stress-induced sublevels denote the irreducible representations of the new site symmetry to which they belong. As shown in the figure the shift of the singlet $1s(A_1)$ state shows a nonlinear dependence on stress. Both $1s(E)$ and $1s(T_2)$ states split into two components; one component of $1s(E)$ shifts linearly and the other nonlinearly with stress whereas both components of $1s(T_2)$ show a linear dependence on stress identical to that of the p states. It can be shown[12,29] that the transitions which have $1s(A_1)$ as their ground state should, under stress, exhibit two components, one on either side of the zero-stress position, while transitions from $1s(T_2)$ and $1s(E)$ exhibit one and three components, respectively.

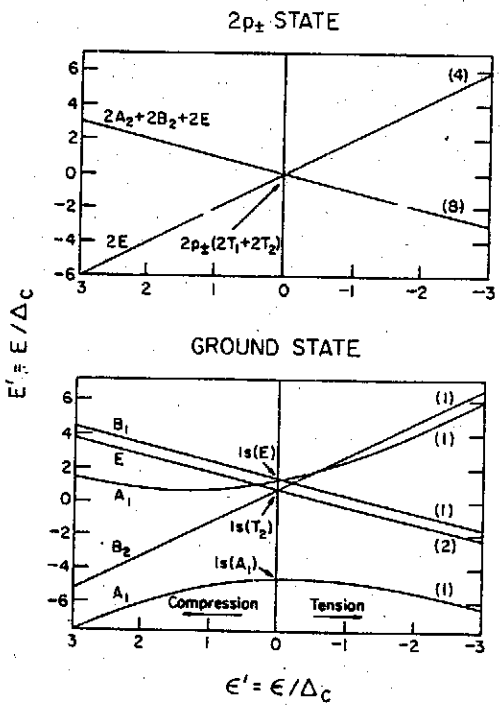

FIG. 4. Splitting of the $1s$ ground states and the $2p_\pm$ state of donors in silicon under strain for compressive force $\vec{F}$ along $\langle 100\rangle$. $E' = E/\Delta_c$ and $\epsilon' = \epsilon/\Delta_c$, where E is the energy of a given state. $\Delta_c = \frac{1}{6}$ [the spacing between $1s(A_1)$ and $1s(E)$], and 3ϵ is the energy difference between the $\langle 100\rangle$ conduction-band minima. The numbers in parentheses indicate the degeneracies of the various states while the letters denote the relevant irreducible representations of D_{2d}, the site symmetry of the donor for this direction of stress.

It should be noted that, though the $1s(A_1) - np$ excitation lines will not split under $\vec{F}\|\langle 111\rangle$, they may show shifts due to those of the $1s(A_1)$ ground state. The separation between the two components observed for $\vec{F}\|\langle 100\rangle$ or $\langle 110\rangle$ is the same for all the lines. If the $1s(A_1)$ level undergoes only very small shifts, then the energy difference between the low-energy component and the zero-stress position will be twice that between the high-energy component and the zero-stress position for $\vec{F}\|\langle 100\rangle$ and *vice versa* for $\vec{F}\|\langle 110\rangle$.

Another important feature of the uniaxial stress effect is the pronounced polarization exhibited by the stress-induced components of the excitation lines. The selection rules for electric-dipole transitions are shown in Figs. 5 and 6 for compression along [100] and [110], respectively, for the $1S(A_1) - np_0$, and $np_\pm$ transitions. These can be deduced[3,33] either by group theory or by an intensity calculation using linear combinations of wave functions appropriate for the new site symmetry of the impurity. The new site symmetry is deduced by enquiring which symmetry operations of the unperturbed crystal continue to be valid under stress. Thus, the T_d site symmetry is transformed into the tetragonal D_{2d} under $\vec{F}\|[100]$ and into the orthorhombic C_{2v} under $\vec{F}\|[110]$. From Fig. 5 for $\vec{F}\|[100]$, it can be seen that for $\vec{E}\|\vec{F}$, only transitions $1s(A_1) - np_0(-)$ and $np_\pm(+)$ are allowed, while for $\vec{E}\perp\vec{F}$, transitions $1s(A_1) - np_0(+)$, $np_\pm(-)$, and $np_\pm(+)$ are allowed. For $\vec{F}\|[110]$ in Fig. 6, the selection rules also depend on the direction of the light-propagation vector, $\vec{q}$. For $\vec{E}\|\vec{F}$, $1s(A_1) - np_0(-)$, $np_\pm(-)$, and $np_\pm(+)$ are allowed for all $\vec{q}$, and for $\vec{E}\perp\vec{F}$, $1s(A_1) - np_0(-)$, $np_0(+)$, and $np_\pm(-)$ are allowed for $\vec{q}\|[1\bar{1}0]$, while $1s(A_1) - np_0(-)$, $np_\pm(-)$, and $np_\pm(+)$ are allowed for $\vec{q}\|[001]$.

Let us now look at the experimental observations presented in Figs. 7–10 for uniaxial compression

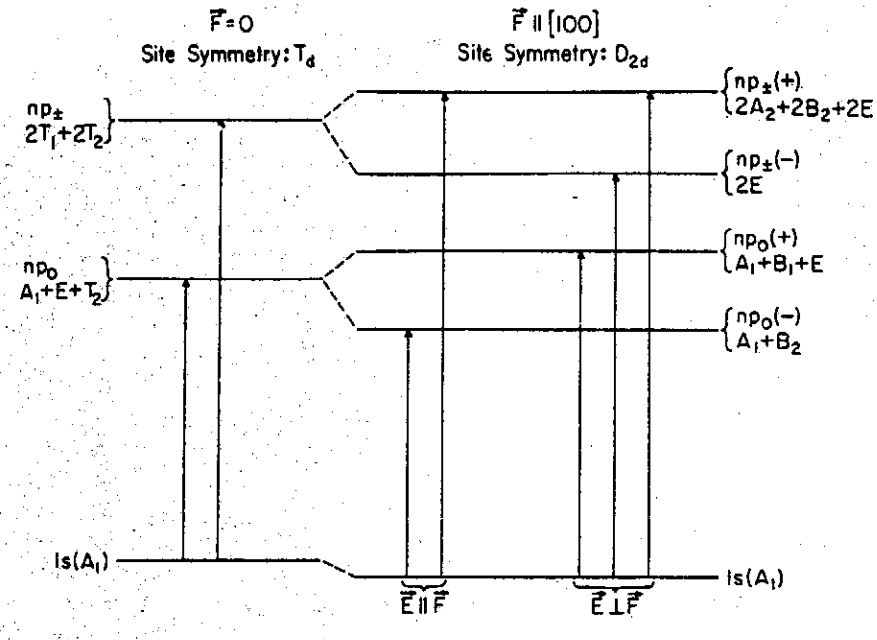

FIG. 5. Energy levels (not to scale) for $\vec{F}=0$ and $\vec{F} \parallel \langle 100 \rangle$. The arrows indicate the allowed transitions with $1s(A_1)$ as the ground state. The letters next to a level denote the irreducible representations of the appropriate site symmetry.

along [111], [100], [110], and [1$\bar{1}$0], respectively, and for electric vector $\vec{E}$ either parallel or perpendicular to $\vec{F}$. In these figures the positions of the excitation lines for zero stress are also indicated.

In Fig. 7, for $\vec{F} \parallel [111]$, no splittings are observed. This is consistent with Eq. (2e) together with either the tetrahedral T_d or the tetragonal D_{2d}-symmetry site for the neutral magnesium donors, since any departure from these symmetries would have resulted in splittings due to the lifting of an orientational degeneracy associated with a noncubic environment.[36] For example, splittings precisely due to the lifting of such an orientational degeneracy have been reported by Krag *et al.* for certain species of sulfur donors in silicon.[8]

In the case of $\vec{F} \parallel [100]$ shown in Fig. 8, all the excitation lines split into two components, one on either side of the zero-stress position. We therefore conclude that all the observed transitions originate from $1s(A_1)$ as their ground state and that the site symmetry is T_d, not D_{2d}. For small stresses, as predicted in Eqs. (3a) and (3b), the low-energy components have an energy shift from the zero-stress position twice as large as that of the high-energy components. Furthermore, the polariza-

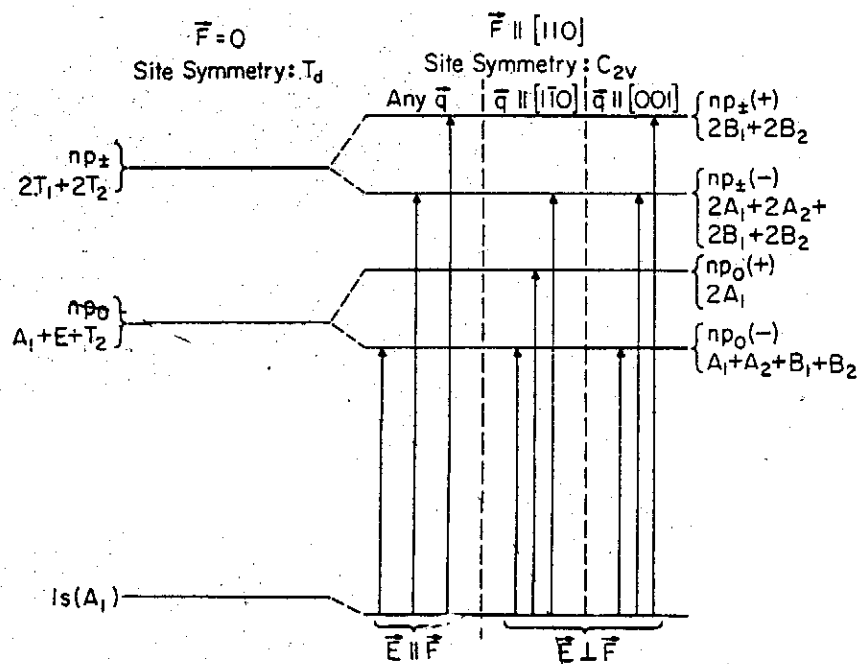

FIG. 6. Energy levels (not to scale) for $\vec{F}=0$ and $\vec{F} \parallel [110]$. The arrows indicate the allowed transitions with $1s(A_1)$ as the ground state and for the direction of light propagation $\vec{q}$ along [1$\bar{1}$0] and [001]. The letters next to a level denote the irreducible representations of the appropriate site symmetry. Note that a calculation (Ref. 33) of the intensity of the transition $1s(A_1) - np_0(-)$, using effective-mass wave functions, shows it to be forbidden for $\vec{E} \perp \vec{F}$ and $\vec{q} \parallel [1\bar{1}0]$.

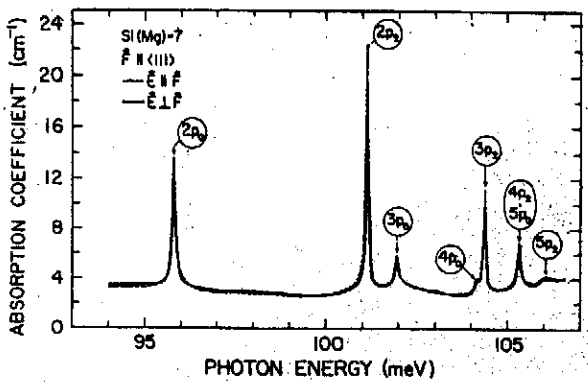

FIG. 7. Excitation spectrum of Mg^0 in silicon, with liquid helium as coolant and with $\vec{F} \parallel \langle 111 \rangle$. $n(300\,^\circ\mathrm{K}) = 2.7 \times 10^{15}$ cm^{-3}. The dashed curve is for $\vec{E} \parallel \vec{F}$ and the solid curve is for $\vec{E} \perp \vec{F}$. The arrows indicate the positions of the excitation lines for $\vec{F} = 0$.

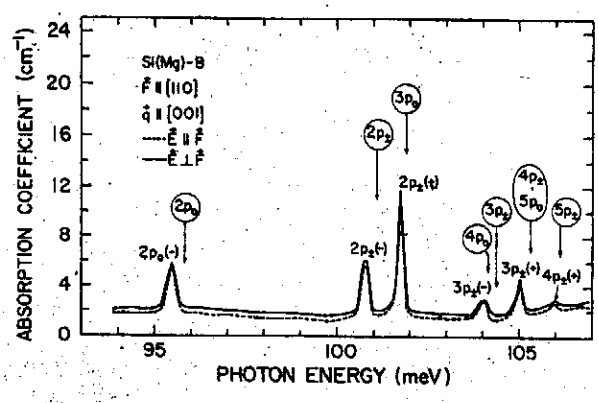

FIG. 9. Excitation spectrum of Mg^0 in silicon with liquid helium as coolant and with $\vec{F} \parallel [110]$ and $\vec{q} \parallel [001]$. $n(300\,^\circ\mathrm{K})$ was estimated to be $\sim 1.2 \times 10^{15}$ cm^{-3}. The dashed curve is for $\vec{E} \parallel \vec{F}$ and the solid curve is for $\vec{E} \perp \vec{F}$. The arrows indicate the positions of the excitation lines for $\vec{F} = 0$.

tion features completely agree with the predictions of Fig. 5, the high-energy component of the np_0 line appearing only for $\vec{E} \perp \vec{F}$ and the low-energy component only for $\vec{E} \parallel \vec{F}$, and both components of the $np_\pm$ line appearing for $\vec{E} \perp \vec{F}$ and only the high-energy components for $\vec{E} \parallel \vec{F}$.

In Figs. 9 and 10 are shown the results for $\vec{F} \parallel [110]$ with $\vec{q} \parallel [001]$ and $\vec{q} \parallel [1\bar{1}0]$, respectively. Both the splittings of the excitation lines and the polarization features agree with the selection rules given in Fig. 6 and Eqs. (3c) and (3d).

When a uniaxial stress is applied along an arbitrary direction, it can be shown from Eq. (1) that the six valleys will form three sets with each set having a different energy shift. As already mentioned, the excited p states will split into as many components as there are energetically different valleys. It is thus expected, for a stress along an arbitrary direction, each excitation line will split into three components.[37] In some of the measurements made, three components were indeed observed due to the misorientation of the $\langle 110 \rangle$ samples.

The shear-deformation-potential constant Ξ_u can be determined from the splittings of the excitation lines in a uniaxial stress measurement. A quantitative stress cell[22] was used for this purpose. Figure 11 shows a typical example of such measurements. For $\vec{F} \parallel [100]$, a given donor level, under stress T, splits into two components with their separation equal to $\Xi_u(s_{11} - s_{12})T$, as can be seen from Eq. (3). Figure 11 shows the energy spacing between the two components of $2p_\pm$ as a function of applied stress. From the slope we obtain for Ξ_u a value of 8.7 ± 0.2 eV.

The shift of the ground state $1s(A_1)$ under stress can also be determined from the above measurement. In Fig. 12, the positions of two experimentally observed components of the $1s(A_1) - 2p_\pm$ tran-

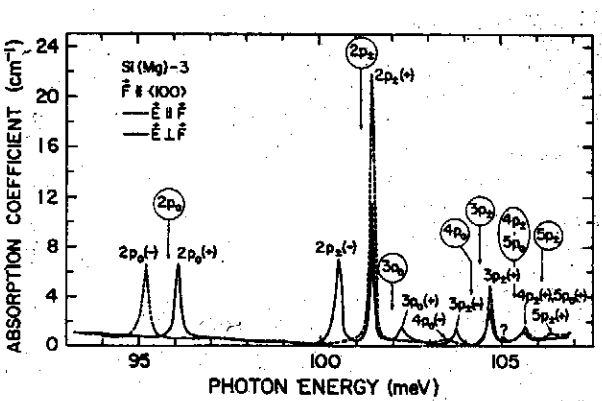

FIG. 8. Excitation spectrum of Mg^0 in silicon with liquid helium as coolant and with $\vec{F} \parallel \langle 100 \rangle$. $n(300\,^\circ\mathrm{K}) = 1.7 \times 10^{15}$ cm^{-3}. The dashed curve is for $\vec{E} \parallel \vec{F}$ and the solid curve is for $\vec{E} \perp \vec{F}$. The arrows indicate the positions of the excitation lines for $\vec{F} = 0$.

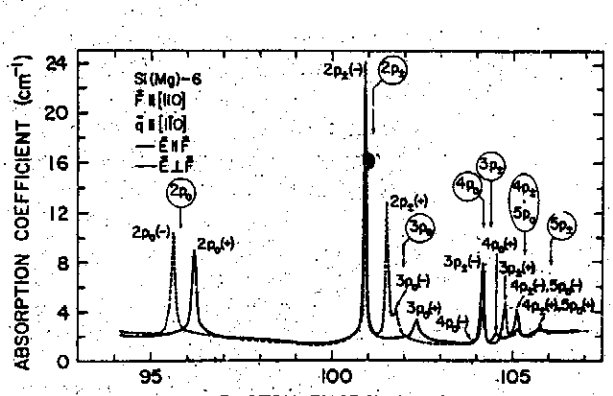

FIG. 10. Excitation spectrum of Mg^0 in silicon with liquid helium as coolant and with $\vec{F} \parallel [110]$ and $\vec{q} \parallel [1\bar{1}0]$. $n(300\,^\circ\mathrm{K}) = 2.1 \times 10^{15}$ cm^{-3}. The dashed curve is for $\vec{E} \parallel \vec{F}$ and the solid curve is for $\vec{E} \perp \vec{F}$. The arrows indicate the positions of the excitation lines for $\vec{F} = 0$.

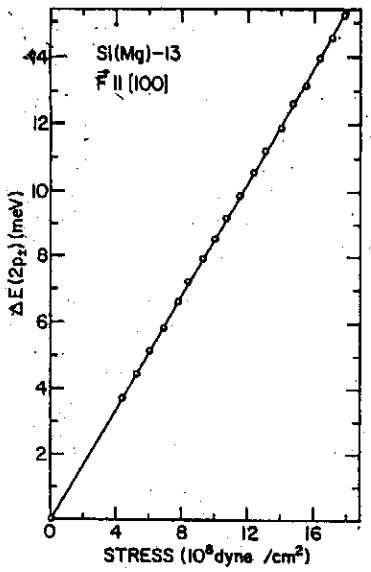

FIG. 11. The energy separation of the two stress induced components of the $2p_{\pm}$ line of Mg^0 in silicon as a function of stress. The compressive force $\vec{F}$ is along ⟨100⟩. The straight line represents a least squares fit; the experimental error is ±0.1 meV in ΔE and $\pm 0.2 \times 10^8$ dyn/cm² in stress.

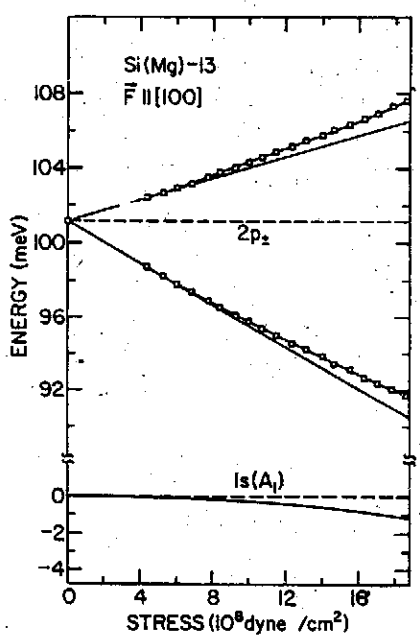

FIG. 12. Effect of uniaxial stress on the $2p_{\pm}$ and $1s(A_1)$ states of Mg^0 in silicon. The compressive force $\vec{F}$ is along ⟨100⟩. The positions indicated are those of the two observed components of the $1s(A_1) - 2p_{\pm}$ transition as a function of stress. The experimental error in the position of each line is estimated to be ±0.05 meV and that in stress to be $\pm 0.2 \times 10^8$ dyn/cm². Their energy shifts from the zero-stress position in the ratio of 2:1 are shown by the two solid straight lines. From the actual observed energy positions, the shifts of $1s(A_1)$ are determined; the solid curve shows its shift as a function of stress.

sition are shown as a function of stress. Also shown, with solid lines, are their energy shifts from the zero-stress position as calculated from their spacings divided in the ratio 2:1. From the actual observed energy positions, the ground state shifts are thus deduced; the resulting shift of the $1s(A_1)$ ground state is also shown in the figure. Compared with shallow group-V donors, the ground-state shift of Mg^0 is found to be smaller as indeed it should be, for the deeper the ground state, the less it is influenced by stress, as can be seen from the calculations of Wilson and Feher.[35] For stresses less than 5×10^8 dyne/cm², the shift of $1s(A_1)$ can almost be neglected. The stress-dependent energy shift ΔE, of the $1s(A_1)$ ground state is given by

$$\Delta E = \Delta_c \left[3 + \tfrac{1}{2}x - \tfrac{3}{2}\left(x^2 + \tfrac{4}{3}x + 4\right)^{1/2} \right], \qquad (4)$$

where Δ_c is $\frac{1}{6}$ of the spacing between $1s(A_1)$ and $1s(E)$, and $x = \Xi_u(s_{11} - s_{12})T/3\Delta_c$. Knowing the energy shift of $1s(A_1)$ under a stress T, it is possible to solve for the spacing between $1s(A_1)$ and $1s(E)$, i.e., $6\Delta_c$. Using the experimentally determined value of 8.7 eV for Ξ_u, we obtain for $6\Delta_c$ a value of 55 ± 3 meV. Subtracting this from the ionization energy 107.50 meV, an experimental value of 52.5 ± 3 meV is obtained for the binding energy of the excited $1s(E)$ state; presumably the $1s(T_2)$ lies close to this if the separation between it and $1s(E)$ is small compared to $6\Delta_c$ as in the case of group-V donors. This appears to suggest that our earlier estimate for the effective-mass first-ionization energy, *viz.*, 56.24 meV, is reasonable for heliumlike donors in silicon. It also suggests that the $1s(E)$ and $1s(T_2)$ states are close to the effective-mass position while $1s(A_1)$ is depressed considerably below it due to chemical splitting.

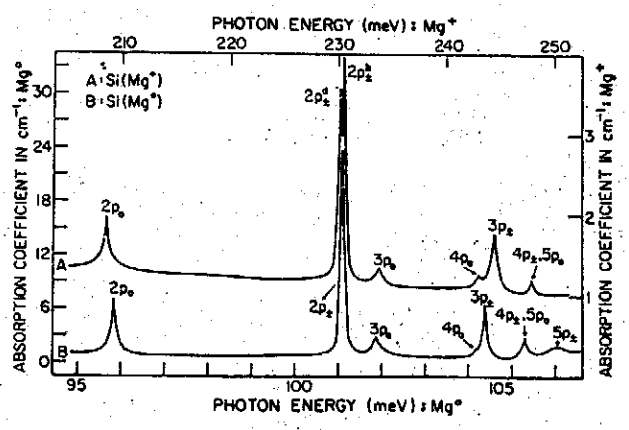

FIG. 13. Excitation spectra of Mg^0 and Mg^+ donors in silicon. Liquid helium was used as coolant. Mg^+ was produced by compensating Mg^0 with boron acceptors. Note that the energy scale for Mg^0 is four times larger than that for Mg^+.

TABLE III. Energies of excitation lines of Mg^+ donors in silicon (in meV).

Label	Assignment	Energy[a]
$2p_0$	$1s(A_1) \rightarrow 2p_0$	208.63 ± 0.015
$2p_\pm^a$	$1s(A_1) \rightarrow 2p_\pm^a$	230.22 ± 0.015
$2p_\pm^b$	$1s(A_1) \rightarrow 2p_\pm^b$	230.42 ± 0.015
$3p_0$	$1s(A_1) \rightarrow 3p_0$	233.87 ± 0.015
$4p_0$	$1s(A_1) \rightarrow 4p_0$	243.00 ± 0.045
$3p_\pm$	$1s(A_1) \rightarrow 3p_\pm$	243.99 ± 0.015
$4p_\pm, 5p_0$	$1s(A_1) \rightarrow 4p_\pm, 5p_0$	247.92 ± 0.015
E_I[b]		256.47 ± 0.07

[a]These values are larger by about 1 meV than those reported by Franks and Robertson (see Ref. 16). It should be noted, however, that the latter were obtained from a measurement at 135 °K. We have observed a shift to lower energies by ~ 0.3 meV in going from liquid-helium to liquid-nitrogen temperature. Such shifts taken together with larger uncertainties in positions at the higher temperature due to line broadening can account for the difference.

[b]The ionization energy E_I was deduced by adding four-times Faulkner's theoretically determined binding energy of the $3p_\pm$ state (Ref. 26) to the experimental energy of the transition labeled $3p_\pm$.

IV. EXPERIMENTAL RESULTS AND DISCUSSION: Mg^+

A. Zero Stress

The excitation spectrum for Mg^+ donors in silicon measured with liquid helium as coolant is shown in Fig. 13. The energies of the excitation lines are given in Table III. The excitation spectrum for Mg^0 donors in silicon is also shown in the same figure for comparison; note the energy scale for Mg^0 is four times larger than that for Mg^+ and the strongest line of Mg^0 spectrum, corresponding to $1s(A_1) - 2p_\pm$, is brought into coincidence with the strongest line of Mg^+ spectrum. It is to be noted that the half-width for the excitation lines of Mg^+ is approximately four times as large as that of the Mg^0 lines. This might explain why the lines corresponding to the $5p_\pm$, a and b lines in the phosphorus spectrum in Fig. 2 are not observable in the Mg^+ spectrum.

While the interstitial Mg^0 is a solid-state analog of the helium atom as already mentioned, Mg^+ can be considered as the analog of singly ionized helium when one of its two 3s valence electrons is ionized. In this manner, then, the Lyman spectrum associated with Mg^+ donors is expected to be like those of group-V and Mg^0 donors in silicon except that the binding energy for each energy state is increased by a factor of 4 since now the effective nuclear charge is 2 instead of 1. This explains why in Fig. 13 the two spectra are strikingly similar in relative intensities and why the energy separations between the corresponding lines of Mg^+ are ~4 times the corresponding spacings of Mg^0. The labeling of the excitation lines for Mg^+ donors is based on this comparison.

Presented in Table IV is the comparison of energy spacings for excited states of Mg^+ and Mg^0 in silicon. The ratio of the corresponding spacings is approximately 4 as expected. It should be noted, however, that the ratio is not exactly 4 but slightly larger. This could be due to the penetration of the donor electron, the 3s valence electron, inside the inner electron shell.[36] Thus each energy state could be more tightly bound than the corresponding state neglecting this effect. Also, the lower energy state is expected to be affected more than the higher energy state. This should also apply to Mg^0; however, since there is another 3s electron which provides shielding, the donor electron may not penetrate the inner electron shell as much, thus resulting in a smaller effect. Besides this, the orbits of Mg^+ should be smaller than those for the other donors.

As in the case of Mg^0, it is of interest to estimate the effective-mass ionization energy for Mg^+. It is reasonable to assume this to be four times the effective-mass ionization energy of group-V donors calculated by Faulkner, i.e., 125.08 meV. The experimental ionization energy obtained by adding four times the theoretical value of the binding energy of the $3p_\pm$ state to the experimental energy of the transition labeled $3p_\pm$ is 256.47 meV. It is thus quite clear that the ground state has suffered a very large chemical splitting. As in the case for Mg^0, it turns out that for Mg^+ the singlet $1s(A_1)$ state is the ground state, the experimental proof for which is presented in Sec. IV B. As in the case of Mg^0, quantitative stress measurements can provide a determination of the chemical splitting; such measurements have not yet been made.

A noteworthy feature in the Mg^+ spectrum shown in Fig. 13 is the doublet nature of the $2p_\pm$ line, $2p_\pm^a$ and $2p_\pm^b$. At liquid-nitrogen temperature this feature is obscured due to broadening. At liquid-helium temperature this splitting was observed in the samples irrespective of the method used for compensation. It is tempting to ascribe this to the chemical splitting of the excited states. The irre-

TABLE IV. Comparison of energy spacings for excited states of Mg^0 and Mg^+ donors in silicon (in meV).

States	Mg^+	Mg^0	Ratio
$3p_\pm - 2p_0$	35.36 ± 0.03	8.58 ± 0.03	4.12 ± 0.02
$3p_\pm - 2p_\pm$ (a)	13.77 ± 0.03	3.26 ± 0.03	4.22 ± 0.05
$3p_\pm - 2p_\pm$ (b)	13.57 ± 0.03		4.16 ± 0.05
$3p_\pm - 3p_0$	10.12 ± 0.03	2.43 ± 0.03	4.17 ± 0.06
$3p_\pm - 4p_0$	0.99 ± 0.06	0.21 ± 0.03	4.78 ± 0.97
$4p_\pm, 5p_0 - 3p_\pm$	3.93 ± 0.03	0.95 ± 0.03	4.14 ± 0.16

ducible representation for the $2p_\pm$ state is $2T_1 + 2T_2$ for a T_d-donor site symmetry. It could be that this state, due to chemical splitting, splits into two $T_1 + T_2$ states, or even four states with two belonging to T_1 and the other two belonging to T_2. Since the transition from the $1s(A_1)$ ground state is allowed to an excited state belonging to T_2 and not to T_1, a doublet feature is thus expected in either case. Though the $2p_\pm$ state of Mg^+ donors is still expected to be effective-mass-like, compared with the corresponding state of group-V and Mg^0 donors, its binding energy is four times larger with a smaller Bohr radius and hence a larger chemical splitting. This perhaps explains why the doublet feature of the $2p_\pm$ state is not observed in the group-V and Mg^0 spectra. The $2p_0$ state lies even deeper than the $2p_\pm$ state; it should have thus suffered a larger chemical splitting. It should be noted, however, that the symmetry of the $2p_0$ state is given by the combination of irreducible representations $A_1 + E + T_2$, and the transition from the $1s(A_1)$ ground state is allowed only to an excited state belonging to T_2. Thus no splitting would be observed for the $2p_0$ line, even if the final T_2 state had a chemical shift. As for the $3p_\pm$ and higher states, chemical splitting is presumably too small to be observed.

Attempts were again made to observe the $1s(A_1) - 1s(T_2)$ transition for Mg^+, which is expected to be $\sim 256.47 - 125.08 = 131.39$ meV, if the excited $1s$ states are still close to the effective-mass position. No excitation lines, however, were observed in the spectral range from 107 to 135 meV. Similar attempts were also made to observe the even-parity levels like $2s$, $3s$, $3d_0$, ... etc., for Mg^+. An excitation line at 248.80 meV occurred only in some of the samples examined. It lies to the higher energy side of the $4p_\pm$, $5p_0$ line. Its intensity is somewhat larger than that of the $4p_\pm$, $5p_0$ line. Its position, however, does not agree with any of the calculated donor levels.[26] This line thus appears to be due to some as yet unidentified center. In one of the samples examined, three extra excitation lines were observed at 238.66, 239.60, and 241.26 meV, respectively. They fall near the region of $3s$ and $3d_0$. Again, since these lines are not reproducible in other samples, their origin is not certain.

As mentioned earlier, irradiation of magnesium-doped silicon with high-energy electrons was one of the methods of compensation used for producing Mg^+ donors. Extensive studies[15] have shown that a variety of donor as well as acceptor states associated with vacancies, interstitials, and their complexes are produced in silicon as a result of irradiation with high-energy electrons; with sufficient irradiation the Fermi level moves towards the middle of the energy gap. It is thus to be expected that compensation of Mg^0 could occur yielding Mg^+ donors. It is also possible[39,40] that the compensation occurs in the following manner: A vacancy moves close to the interstitial magnesium donor, or *vice versa* and is annihilated yielding substitutional magnesium. The latter should be a double acceptor which in turn can compensate the magnesium donors. This is an intriguing possibility which needs further study. In this context it should be particularly interesting to discover in irradiated specimens excitation spectra characteristic of acceptors in silicon.

The magnesium-doped silicon samples studied in the present work were irradiated with 1-MeV electrons at 10 °C. Magnesium donors were only partially compensated after irradiation; thus both Mg^0 and Mg^+ spectra can be observed in the same specimen. In most of the samples compensated with group-III acceptors, the control was not sufficient to produce partial compensation and hence Mg^0 and Mg^+ excitation spectra were not observed in the same specimen. A typical example is presented in Fig. 14 which shows the appearance of the Mg^+ spectrum and a decrease in that of Mg^0 as a result of electron irradiation. It is clear that the concentration of the Mg^0 donors is decreased while the excitation spectrum for Mg^+ appears only after the sample is bombarded.

B. Piezospectroscopic Effect

In Figs. 15–19 are presented the excitation spectra of Mg^+ donors in silicon for uniaxial compression along ⟨111⟩, ⟨100⟩, and ⟨110⟩, and for electric vector $\vec{E}$ either parallel or perpendicular to $\vec{F}$. In these figures the positions of the excitation lines for zero stress are also indicated.

The absence of splittings observed for the excitation lines in Fig. 15 with $\vec{F} \parallel \langle 111 \rangle$ is consistent with Eq. (2e) together with a site symmetry T_d or

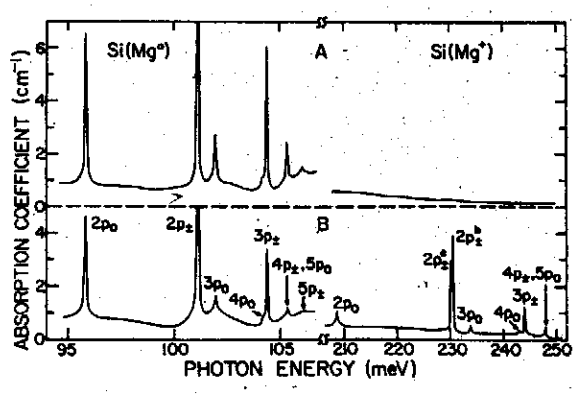

FIG. 14. Effect of 1-MeV electron irradiation on a magnesium-doped silicon sample. Excitation spectra of both Mg^0 and Mg^+ were measured using liquid helium as the coolant. *A* and *B* show the spectrum before and after the irradiation, respectively. The energy scale for Mg^0 is four times larger than that for Mg^+.

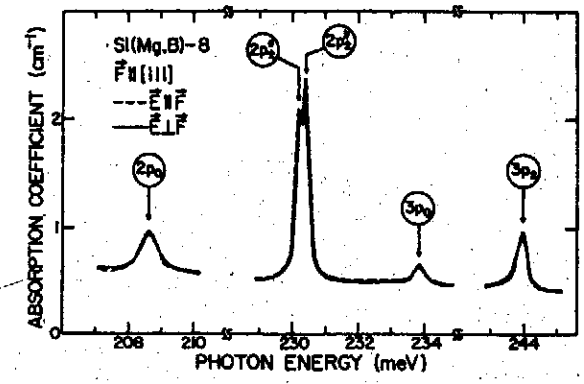

FIG. 15. Excitation spectrum of Mg^+ in silicon with liquid helium as coolant and with $\vec{F} \parallel \langle 111 \rangle$. Mg^+ was produced by compensating Mg^0 with boron acceptors. The dashed curve is for $\vec{E} \parallel \vec{F}$ and the solid curve is for $\vec{E} \perp \vec{F}$. The arrows indicate the positions of the excitation lines for $\vec{F} = 0$.

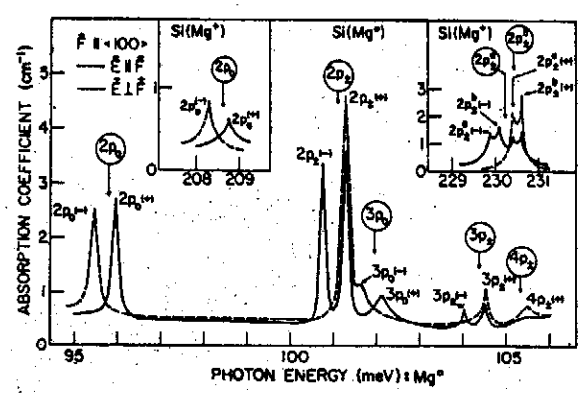

FIG. 17. Effect of a compressive force $\vec{F}$ along $\langle 100 \rangle$ on the excitation spectrum of Mg^0 in silicon. Liquid helium was used as coolant. The insets are for the $2p_0$, $2p_\pm^a$, and $2p_\pm^b$ lines of Mg^+ in the same specimen, partial compensation in it being achieved by electron irradiation. The dashed curve is for $\vec{E} \parallel \vec{F}$ and the solid curve is for $\vec{E} \perp \vec{F}$. The arrows indicate the positions of the excitation lines for $\vec{F} = 0$.

D_{2d}. In Fig. 16, for $\vec{F} \parallel \langle 100 \rangle$, all the excitation lines are observed to split into two components with one on either side of the zero-stress position. This strongly suggests that the interstitial singly ionized magnesium also occupies the T_d site with $1s(A_1)$ as the ground state. The polarization features also completely agree with Fig. 5, the high-energy component of the np_0 line appearing only for $\vec{E} \perp \vec{F}$, while the low-energy component, only for $\vec{E} \parallel \vec{F}$, and both the components of the $np_\pm$ line appearing for $\vec{E} \perp \vec{F}$ while only the high-energy component for $\vec{E} \parallel \vec{F}$. It should be noted here that shifts of the stress-induced components of the doublet $2p_\pm^a$ and $2p_\pm^b$ should be expected to include the effect of the chemical splittings; however, this difference appears to be too small to be observed in the present measurements. Also, the resolution in the measurement did not allow a clear separation of $2p_\pm^a(+)$ and $2p_\pm^a(-)$ from $2p_\pm^b(+)$ and $2p_\pm^b(-)$, respectively, for $\vec{E} \perp \vec{F}$. The spacing between the corresponding high- and low-energy components is, within experimental error, the same for all the lines.

In Fig. 17, results for a uniaxial compressive force $\vec{F}$ along $\langle 100 \rangle$ are presented for a specimen containing both Mg^0 and Mg^+ donors as a result of a partial compensation achieved by electron irradiation. The piezospectroscopic effect of the excitation spectrum of Mg^0 donors is identical to that given in Fig. 8. The insets in the figure show the splittings for the $2p_0$, $2p_\pm^a$, and $2p_\pm^b$ lines of Mg^+ donors during the same measurement. The results demonstrate that the corresponding lines of Mg^0 and Mg^+ show identical splittings and polarization

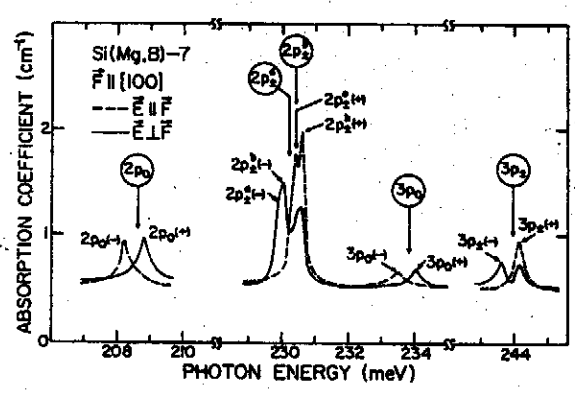

FIG. 16. Excitation spectrum of Mg^+ in silicon with liquid helium as coolant and with $\vec{F} \parallel \langle 100 \rangle$. Mg^+ was produced by compensating Mg^0 with boron acceptors. The dashed curve is for $\vec{E} \parallel \vec{F}$ and the solid curve is for $\vec{E} \perp \vec{F}$. The arrows indicate the positions of the excitation lines for $\vec{F} = 0$.

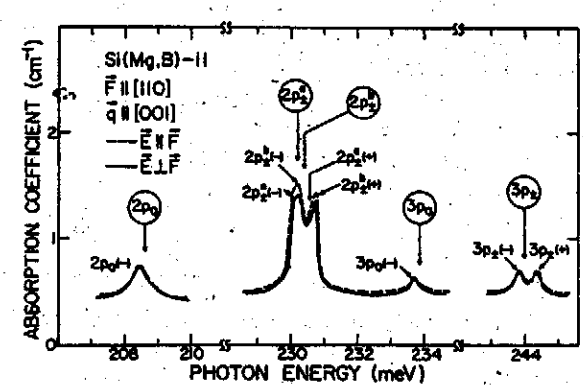

FIG. 18. Excitation spectrum of Mg^+ in silicon with liquid helium as coolant and with $\vec{F} \parallel [110]$ and $\vec{q} \parallel [001]$. Mg^+ was produced by compensating Mg^0 with boron acceptors. The dashed curve is for $\vec{E} \parallel \vec{F}$ and the solid curve is for $\vec{E} \perp \vec{F}$. The arrows indicate the positions of the excitation lines for $\vec{F} = 0$.

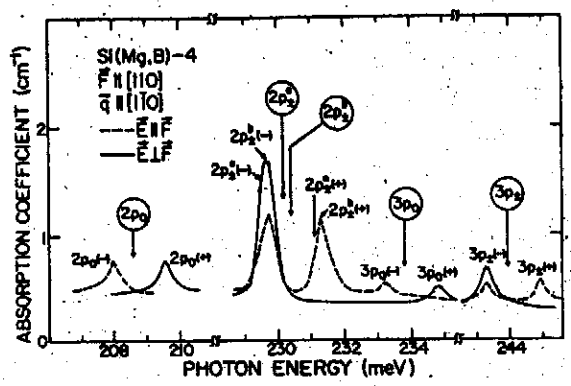

FIG. 19. Excitation spectrum of Mg^+ in silicon with liquid helium as coolant and with $\vec{F} \parallel [110]$ and $\vec{q} \parallel [1\bar{1}0]$. Mg^+ was produced by compensating Mg^0 with boron acceptors. The dashed curve is for $\vec{E} \parallel \vec{F}$ and the solid curve is for $\vec{E} \perp \vec{F}$. The arrows indicate the positions of the excitation lines for $\vec{F}=0$.

patterns. They also imply that the same value of Ξ_u holds for the two cases.

Figs. 18 and 19 show the results for $\vec{F} \parallel [110]$ with $\vec{q} \parallel [001]$ and $\vec{q} \parallel [1\bar{1}0]$, respectively. Both the splittings of the excitation lines and the polarization features agree with the selection rules given in Fig. 6 and Eqs. (3c) and (3d). This is consistent with all the observed transitions originating from a $1s(A_1)$ ground state and with a T_d-symmetry site for Mg^+. The resolution in the measurements was insufficient to separate $2p_x^a(+)$ from $2p_x^b(+)$ and $2p_x^a(-)$ from $2p_x^b(-)$.

V. CONCLUDING DISCUSSION

In the present investigation evidence has been accumulated to support the conclusion that magnesium enters the silicon lattice interstitially and as a consequence behaves as a heliumlike double donor. Baxter and Ascarelli[41] have recently carried out an EPR study of magnesium-doped silicon. As is to be expected they have observed EPR only in samples containing Mg^+ donors; using the isotope Mg^{25} they have recorded the hyperfine structure characteristic of it. The excitation spectra and their piezospectroscopic effects as well as EPR studies indicate a T_d site symmetry for the Mg^0 and Mg^+ donors. Thus, the present investigations on magnesium favor the tetrahedral rather than the hexagonal interstitial site. This is also the case for lithium donors in silicon,[12,13] the other interstitial impurity which has been extensively studied.

Another feature which emerges from these studies is how well the effective-mass theory predicts the p states even for donors with ionization energies very much larger than the calculated[26] value of 31.27 meV, e.g., 107.50 meV for Mg^0 and 187.2 meV for one of the neutral sulfur donors.[8] The positions of the $1s(E)$ and $1s(T_2)$ have yet to be experimentally established for both Mg^0 and Mg^+ donors. As discussed in Secs. III A, and IV A these should be close to the effective-mass position for the $1s$ state. Also they should be deeper for a heliumlike donor in comparison to a hydrogenic donor. In this connection the electronic Raman effect[42] should be of particular value. Attention should also be drawn to the fact that whereas for lithium donors in silicon, the $1s(A_1)$ state lies *above* the $1s(E)$ and $1s(T_2)$ states, the opposite is the case for magnesium donors, though both are interstitial impurities.

The value of Ξ_u determined from the piezospectroscopic effect of Mg^0 donors, 8.7 ± 0.2 eV, is in good agreement with that determined for the conduction-band minimum of silicon by a number of different techniques.[43] Krag and his co-workers[8,30] quote a value of 7.9 ± 0.2 eV from the piezospectroscopic effect of sulfur donors and 7.9 eV for phosphorus donors in silicon. It is not clear at the present what the origin is of the difference between our value and those of Krag and co-workers. The values determined from EPR measurements on lithium donors[13] and group-V donors[35] are ~11 eV; the serious discrepancy between the EPR value and the other values has still to be resolved.

ACKNOWLEDGMENTS

The authors wish to thank Professor P. Fisher, Professor J. W. MacKay, Professor S. Rodriguez, Professor G. Ascarelli, and J. E. Baxter for many stimulating discussions. Thanks are due Professor H. J. Yearian and Miss Louise Roth for orienting crystals, to Professor A. N. Gerritsen for supplying the pure magnesium, and to V. J. Tekippe and H. R. Chandrasekhar for help in the quantitative stress measurements.

*Work supported by the NSF and the Advanced Research Projects Agency.

[1]W. Kohn, in *Solid State Physics*, Vol. 5, edited by F. Seitz and D. Turnbull (Academic, New York, 1957), p. 257.

[2]G. W. Ludwig and H. H. Woodbury, in Ref. 1, Vol. 13, p. 223.

[3]P. Fisher and A. K. Ramdas, in *Physics of the Solid State*, edited by S. Balakrishna, M. Krishnamurthi, and B. Ramachandra Rao (Academic, New York, 1969), p. 149.

[4]P. Fisher, R. L. Jones, A. Onton, and A. K. Ramdas, J. Phys. Soc. Japan Suppl. 21, 224 (1966); W. J. Moore, Solid State Commun. 3, 385 (1965).

[5]F. Barra and P. Fisher, Phys. Letters 27A, 711 (1968).

[6]R. A. Chapman and W. G. Hutchinson, Phys. Rev. 157, 615 (1967).

[7]Beryllium in germanium is discussed in the following: H. Shenker, E. M. Swiggard, and W. J. Moore, Trans. AIME 239, 347 (1967); W. J. Moore and R. Kaplan, Bull.

Am. Phys. Soc. 11, 206 (1966); N. D. Tyapkina, M. M. Krivopolenova, and V. S. Vavilov, Fiz. Tverd. Tela 6, 2192 (1964) [Sov. Phys. Solid State 6, 1732 (1965)]. See J. B. Robertson and R. K. Franks, Solid State Commun. 6, 825 (1968) for beryllium in Si.

[8]W. E. Krag, W. H. Kleiner, H. J. Zeiger, and S. Fischler, J. Phys. Soc. Japan Suppl. 21, 230 (1966).

[9]G. W. Ludwig, Phys. Rev. 137, A1520 (1965).

[10]D. L. Camphausen, H. M. James, and R. J. Sladek, Phys. Rev. B 2, 1899 (1970).

[11]P. Fisher and H. Y. Fan, Phys. Rev. Letters 5, 195 (1960); R. L. Jones, P. Fisher, and S. Balasubramanian (unpublished).

[12]R. L. Aggarwal, P. Fisher, V. Mourzine, and A. K. Ramdas, Phys. Rev. 138, A882 (1965).

[13]G. D. Watkins and F. S. Ham, Phys. Rev. B 1, 4071 (1970).

[14]H. H. Woodbury and G. W. Ludwig, Phys. Rev. 117, 102 (1960); G. W. Ludwig and H. H. Woodbury, Phys. Rev. Letters 5, 98 (1960).

[15]G. D. Watkins, *Radiation Damage in Semiconductors, Paris-Royaumont*, 1964 (Dunod, Paris, 1965), p. 97.

[16]R. K. Franks and J. B. Robertson, Solid State Commun. 5, 479 (1967).

[17]L. T. Ho and A. K. Ramdas, Phys. Letters 32A, 23 (1970). This paper contains a preliminary account of the results presented here.

[18]Magnesium of 99.9948% purity, Dow Chemical Company, Midland, Michigan.

[19]R. D. Hancock and S. Edelman, Rev. Sci. Instr. 27, 1082 (1956).

[20]P. Fisher, W. H. Haak, E. J. Johnson, and A. K. Ramdas, in *Proceedings of the Eighth Symposium on the Art of Glassblowing* (The American Scientific Glassblowers Society, Wilmington, Delaware, 1963), p. 136.

[21]A. C. Rose-Innes, Proc. Phys. Soc. (London) 72, 514 (1958). Details of the jigs used in the differential compression technique are given in R. L. Jones, Ph.D. thesis (Purdue University, 1968) (unpublished).

[22]V. J. Tekippe, P. Fisher and A. K. Ramdas (unpublished).

[23]Charles M. Reeder & Co., Inc., Detroit, Michigan.

[24]R. L. Aggarwal and A. K. Ramdas (unpublished).

[25]C. E. Moore, *Atomic Energy Levels*, Natl. Bur. Std. (U.S.) Circ. No. 467 (U.S. GPO, Washington, D. C., 1949), p. 5; see also H. G. Kuhn, *Atomic Spectra* (Academic, New York, 1963), p. 132; and H. A. Bethe and E. E. Salpeter, *Quantum Mechanics of One- and Two-Electron Atoms* (Springer-Verlag, Berlin, 1957), p. 127.

[26]R. A. Faulkner, Phys. Rev. 184, 713 (1969).

[27]The donor states are labeled according to the envelope wave function (1*s*, 2*s*, ..., etc.) and the irreducible representations of the site symmetry of the donor. Evidence presented in this paper suggests that the latter is T_d for both Mg^0 and Mg^+. Note that the notation for the irreducible representations follows Ref. 1, however, with labels T_1 and T_2 interchanged to conform to the usage current in the literature. See, for example, H. Eyring, J. Walter, and G. E. Kimball, *Quantum Chemistry* (Wiley, New York, 1944), p. 388, Table 37; E. B. Wilson, Jr., J. C. Decius, and P. C. Cross, *Molecular Vibrations* (McGraw-Hill, New York, 1955), p. 330, Table X-10, where $T_1 \equiv F_1$ and $T_2 \equiv F_2$. Readers should note that much of the earlier literature on donors use T_1 and T_2 as in Ref. 1.

[28]W. H. Kleiner and W. E. Krag, Phys. Rev. Letters 25, 1490 (1970).

[29]R. L. Aggarwal and A. K. Ramdas, Phys. Rev. 140, A1246 (1965).

[30]W. E. Krag, W. H. Kleiner, and H. J. Zeiger, *Proceedings of the Tenth International Conference on the Physics of Semiconductors, Cambridge, Mass.*, 1970, edited by S. P. Keller, J. C. Hensel, and F. Stern (U. S. AEC Division of Technical Information, Washington, D. C., 1970), p. 271.

[31]B. T. Ahlburn and A. K. Ramdas, Phys. Rev. 167, 717 (1968).

[32]T. E. Gilmer, Jr., R. K. Franks and R. J. Bell, J. Phys. Chem. Solids 26, 1195 (1965).

[33]R. L. Aggarwal and A. K. Ramdas, Phys. Rev. 137, A602 (1965).

[34]C. Herring, Bell System Tech. J. 34, 237 (1955); see also C. Herring and E. Vogt, Phys. Rev. 101, 944 (1956).

[35]D. K. Wilson and G. Feher, Phys. Rev. 124, 1068 (1961).

[36]A. A. Kaplyanskii, Opt. i Spektroskopiya 16, 602 (1964); 10, 165 (1961) [Opt. Spectry. (USSR) 16, 329 (1964); 10, 83 (1961)].

[37]This feature was experimentally observed in the course of a recent study of the excitation spectra of P and As donors in silicon by V. J. Tekippe, H. R. Chandrasekhar, P. Fisher, and A. K. Ramdas (unpublished). The details of the data processing used in Figs. 11 and 12 will be given in this paper.

[38]This was pointed out to us by Professor P. Fisher. Our thanks are due him and Professor S. Rodriguez for several discussions on this aspect.

[39]Our thanks are due to Professor J. W. MacKay for this suggestion.

[40]See H. H. Woodbury and G. W. Ludwig, Phys. Rev. Letters 5, 96 (1960), where a conversion of an interstitial impurity into a substitutional one by trapping a vacancy has been considered. Ludwig has also discussed it in Ref. 9 in the context of the substitutional vs interstitial nature of S^+ donors in silicon.

[41]J. E. Baxter and G. Ascarelli (unpublished).

[42]G. B. Wright and A. Mooradian, Phys. Rev. Letters 18, 608 (1967).

[43]L. D. Laude, F. H. Pollak, and M. Cardona, Phys. Rev. B 3, 2623 (1971); I. Balslev, Phys. Rev. 143, 636 (1966); see also the concluding sections in Refs. 13 and 29.

Annual Report of the Institute of Physics, Academia Sinica, 1972

Time-Dependent Effect on the Excitation Spectrum of Magnesium Donors in Silicon

L. T. Ho (何侗民)

Institute of Physics, Academia Sinica

Abstract

The excitation spectrum for magnesium donors in silicon is studied. The intensity of the excitation lines is found to decrease with time.

I. Introduction

The behavior of donor and acceptor impurities in silicon and germanium have been extensively studied by infrared absorption experiments. In these studies, the excitation spectra of only a few impurities have been observed to be time-dependent. One of the examples is reported by Gilmer et al.[1] They observe a decrease in the resonance absorption widths with time in the excitation spectra associated with lithium-oxygen complexes in silicon. Another case is the EPR studies of sulfur-doped silicon by Ludwig.[2] As for other impurities in silicon and germanium, such time-dependent effect on the excitation spectrum has not yet been reported. Recently, we have observed a similar effect on the spectra of magnesium donors in silicon. The purpose of this paper is to report and discuss our observations.

II. Experimental Procedure

Magnesium-doped silicon samples were prepared by the diffusion technique. Magnesium was diffused into silicon in the following manner. Magnesium of 99.9948% purity, after being etched in hydrochloric acid to remove the oxidized surface, was deposited on the surfaces of the optical sample using a vacuum evaporator. Evaporation of magnesium was achieved by passing current through a tantalum boat on which pure magnesium was held. The sample was then heated in a furnace at 1200°C for one hour in a helium atmosphere. During diffusion, the sample was kept in a quartz tube; a piece of tantalum sheet separated it from direct contact with the tube in order to avoid diffusion of oxygen from the quartz tube into the sample. It was found that when the optical sample was sandwiched between two other specimens, all three having magnesium on the surfaces in contact, the sample and its two covers weld together and thus the magnesium does not escape into the ambient. This is necessary to prevent magnesium from escaping since its boiling point, 1107°C, is

lower than the diffusion temperature. After the heat treatment, the sample, together with the covers, was quenched in liquid nitrogen. The covers were then ground off. By following this procedure, an undoped floating zone silicon, initially p-type and of resistivity~1700 ohm-cm, was converted to a low resistivity n-type specimen with a room temperature carrier concentration~2×10^{15} cm^{-3}. These specimens were adequate for observing the excitation spectra of neutral magnesium at low temperatures.

A double-pass Perkin-Elmer spectrometer, Model 112G, equipped with a Bausch-Lomb 12-micron plane reflection grating and appropriate filters, was used for the measurements. The source of the radiation was a heated globar whose power was furnished by a regulated power supply. A Reeder vacuum thermocouple with a cesium-iodide window was used as the detector. An optical cryostat with cesium-iodide windows was used for low temperature measurements. Samples were fastened directly to the tailpiece; sample temperature was estimated to be~12°K using liquid helium as coolant.

The data output of the spectrometer was obtained on a strip chart recorder. The intensities observed with the sample in the beam, I_s, and with the sample out of the beam, I_o, were taken to calculate percent transmission, T, and absorption coefficient, α, as a function of incident photon energy and wavelength using the following equation:[3]

$$T=I_s/I_o=(1-R)^2exp(-\alpha x)/\left[1-R^2exp(-2\alpha x)\right]$$

where x is the sample thickness and R the reflectivity, which is found to be constant, 0.315 for silicon, in the range of present interest.

III. Experimental Results and Discussion

Magnesium, a group-II element, has been shown to behave like a double donor when diffused into silicon.[4] It is a donor instead of an acceptor presumably due to its being interstitial rather than substitutional. The excitation spectrum for neutral magnesium donors in silicon measured with liquid helium as coolant is shown in Fig. 1-A. The excitation lines corresponding to the transitions $1s(A_1) \rightarrow np_o, np\pm$ have the following positions in milli-electron volts: 95.80($2p_o$), 101.12($2p\pm$), 101.95 ($3p_o$), 104.17 ($4p_o$), 104.38($3p\pm$), 105,33($4p\pm$,$5p_o$) and 106.05($5p\pm$). The energy separations between these lines are in excellent agreement with those of the corresponding lines of group-V impurities[5] clearly demonstrating that the excited states are effective-mass-like.[6] The labeling of the excitation lines is based on this similarity.

The decrease in the intensity of the magnesium excitation spectrum is observed when the same specimen is remeasured after a considerable lapse of time. Fig. 1 presents a typical example of such a spectrum. Shown in Fig. 1-A is the spectrum of a magnesium diffused silicon sample measured within a few days after the sample was made. The carrier concentration is estimated to be~1.2×10^{15} cm^{-3} at room temperature. Fig. 1-B shows the decrease of intensity for the same sample remeasured after 19 months. The excitation lines are clearly much weaker than before. After 30 more months the same sample was

again remeasured. The result is shown in Fig. 1-C. Except a few barely observable excitation lines such as $2p_o$, $2p\pm$ and $3p\pm$, other lines are too weak to be observed.

It is very clear that there is a time dependence of the intensity for the magnesium excitation spectrum in silicon. The positions of the excitation lines, however, remain to be the same. We can conclude, therefore, that the time has no effect on the $1s(A_1)$ ground level as well as the ionization energy of neutral magnesium donors in silicon.

The decrease in the excitation line intensities with time may be a consequence of precipitation of magnesium. Since magnesium impurity is introduced into silicon by diffusion, it is almost certain that the distribution of magnesium in silicon is hardly uniform and the sample is thus not homogeneous. Lithium diffused into oxygen containing silicon has also been observed to have similar time-dependent effect for the resonance absorption widths.[1] One more striking similarity to be noticed is that magnesium and lithium are both presumably interstitial in silicon. It should be much easier for interstitial impurities to move to the sample surface than those occupying substitutional sites. This can perhaps explain why no time-dependent effect has been observed for excitation spectra of group-V impurities, all of which are substitutional donors in silicon. The sample used to determine the spectra of Fig. 1 was maintained at room temperature. To keep it at lower temperatures can perhaps lessen the time-dependent effect on the excitation spectrum of magnesium donors in silicon.

References

(1) T. E. Gilmer, Jr., R. K. Franks and R. J. Bell, J. Phys. Chem. Solids 26, 1195 (1965).
(2) G. W. Ludwig, Phys. Rev. 137, A1520 (1965).
(3) D. L. Greenaway and G. Harbeke, Optical Properties and Band Structure of Semiconductors (Pergamon Press, Inc., New York, 1968), P. 9.
(4) L. T. Ho and A. K. Ramdas, Phys. Rev. B5, 462 (1972).
(5) P. Fisher and A. K. Ramdas, in Physics of the Solid State, edited by S. Balakrishna, M. Krishnamurthi, and B. Ramachandra Rao (Academic, New York, 1969), P. 149.
(6) R. A. Faulkner, Phys. Rev. 184, 713 (1969).

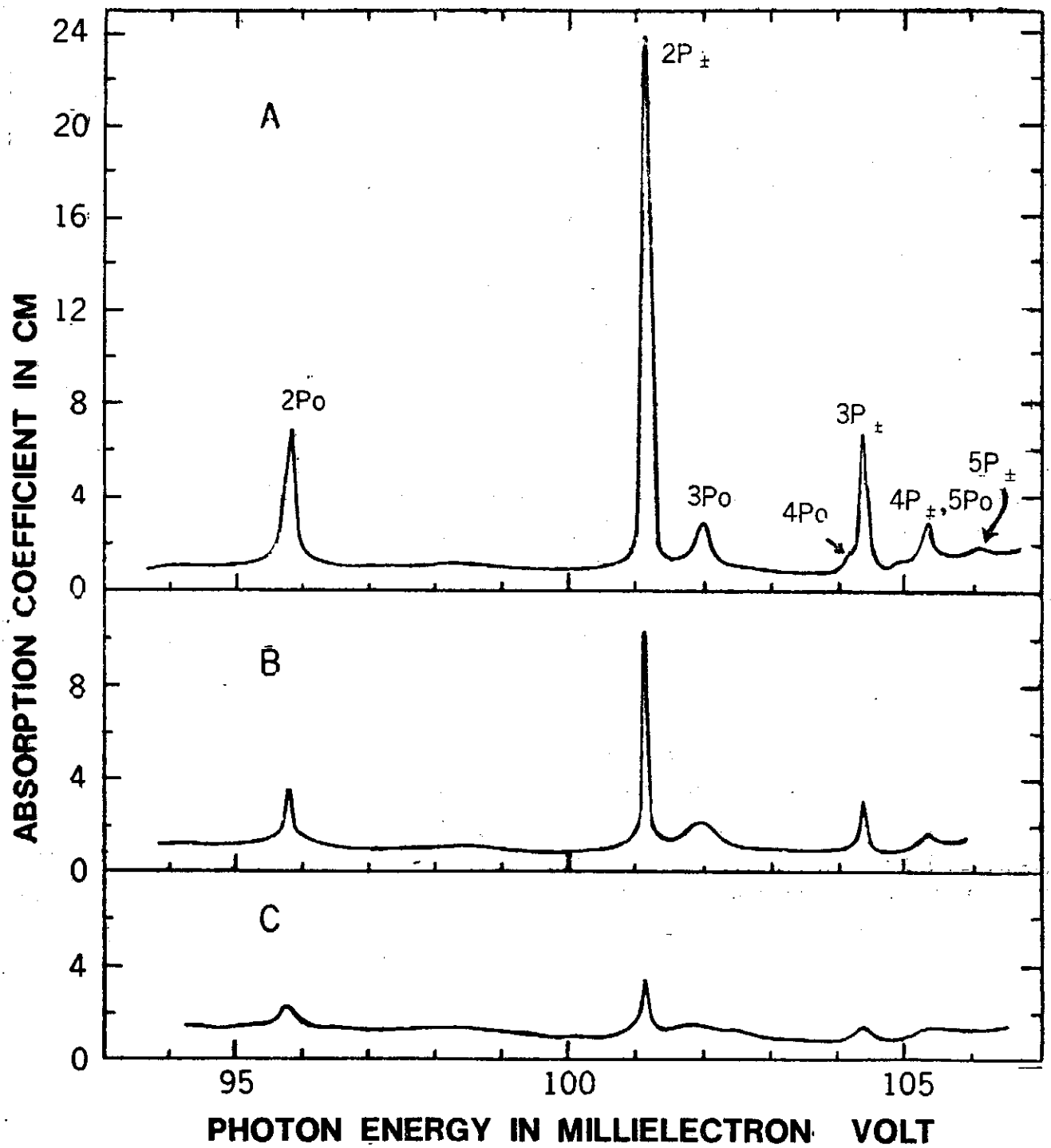

Fig. 1. Time-dependent effect on the excitation spectrum of magnesium donors in silicon. B and C show the decrease of intensity for the same sample remeasured after 19 and 49 months, respectively. Liquid helium was used as coolant in each measurement.

Annual Report of Institute of Physics, Academia Sinica, 1972

MOIRE TOPOGRAPHY

CHUN CHIANG (蔣炯)

Institute of Physics
Academia Sinica
NanKang, Taipei, Taiwan,
The Republic of China

ABSTRACT

Using geometrical optics, oblique-shadow method is shown to generate moire patterns, which under specific conditions can be interpreted as contour lines of the surface. The oblique-shadow method is to illuminate a viewing grid with equal spaced parallel lines. The light can be either a point source or parallel light, the observation point can either at finite distance or at infinity.

1. INTRODUCTION

Recently, several paper [1,2,3] have appeared in this journal discussing the measurment of surface topography with moire technique. The communication theory has been used to show that a periodic grating together with its shadow on a surface can form moire patterns; these patterns may be interpreted as contour lines of the surface. Earlier, oblique-shadow method [4,5,6] has been shown to form the moire patterns using geometrical optics consideration, the conditions under which the moire patterns may represent the contour lines of the surface has been given. Furthermore, if the surface is shining and can be served as a mirror, then the grating together with its mirror image can also form moire patterns[6]. Under certain conditions, these moire patterns also represent the contour line of the surface. The mirror image method and the conditions required for having the contour lines seem not have been borne out in those recent papers. Due to the simplicity of the calculation using the geometrical optics, we use again this method to calculate the moire patterns produced under various experimental condition and point out the conditions required for representing the moire patterns as contour lines in thse experimental arrangement.

II. GENERAL EQUATION FOR MOIRE PATTERNS

Suppose the x-coordinate spacing of the parallel lines on the viewing grid and on the surface is a and b respectively, thus the lines can be represented as

$$x = mb + c_1 \tag{1}$$

$$x=nb+c_2 \tag{2}$$

where m and n are integers, 0, ±1, ±2……c_1 and c_2 are the phase constant. Using the similar method as Chiang [6,7] and Meadows et el[3], the projection of the lines from the surface to the viewing grid with the viewing point at
$O(x_o, O, z_o)$ *is*

$$x=x_o \frac{d(x_1, y_1)}{z_o + d(x_1, y_1)} + (nb+c_2) \frac{z_o}{z_o + d(x_1, y_1)} \tag{3}$$

where d is the distance between the surface and the viewing grid, with the coordinate represented by x_1 and y_1. With the index equation

$$m-n=k \tag{4}$$

the moire patterns can be obtained by combining Eqs. (1), (3) and (4) to be

$$x= \frac{d(x_1, y_1)\, x_o}{z_o + d(x_1, y_1)} + [(x-c_1)b/a-kb+c_2] \frac{z_o}{z_o+d(x_1, y_1)} \tag{5}$$

where k is also an integer. Eq. (5) can simplify to be

$$d(x_1, y_1) = \frac{(a-b)x-ac_2+bc_1+abk}{a(x_o-x)}\, z_o \tag{6}$$

Since the point $(x_1, y_1, -d)$ on the surface, the point (x, y, o) of the moire patterns on the viewing grid and the observation point $O(x_o, o, z_o)$ have to be on the same line, thus

$$\frac{x_o-x_1}{x_o-x} = \frac{y_1}{y} = \frac{z_o+d(x_1, z_1)}{z_o} \tag{7}$$

Introducing Eq.(6) into Eq.(7), we have

$$x_1=(bx+ac_2-bc_1-abk)/a \tag{8}$$

$$y_1=y(ax_o-bx-ac_2+bc_1-abk)/a(x_o-x) \tag{9}$$

Introducing Eqs. (8) and (9) into Eq.(6), we have

$$d\left(\frac{bx+ac_2-bc_1-abk}{a}, \frac{(ax_o-bx-ac_2+bc_1+abk)y}{a(x_o-x)} \right) = \frac{(a-b)x-ac_2+bc_1+abk}{a(x_o-x)} z_o \tag{10}$$

This is the general equation of the moire patterns produced by viewing grid and any surface, for which both are ruled with parallel lines.

III. POINT ILLUMINATION AND POINT OBSERVATION AT FINITE DISTANCE

If the lines on the viewing grid are

$$x=na+c_1 \tag{11}$$

with the illumination of a point source at $S(x_2, y_2, z_2)$, the projection of the shadow of the lines from the viewing grid to the surface is

$$x=(na+c_1) \frac{z_2+d(x_1, y_1)}{z_2} \tag{12}$$

Comparing with Eq.(2), we have

$$b=\frac{z_2+d(x_1,\ y_1)}{z_2}\ a \tag{13}$$

$$c_2=\frac{z_2+d(x_1,\ y_1)}{z_2}\ c_1 \tag{14}$$

From Eqs.(10), (13) and (14), we have

$$d\left(\ (1+d/z_2)(x-ak),\ (1+\frac{ak(1+d/z_2)-dx/z_2}{x_0-x})y\ \right)=\frac{akz_0z_2}{x_0z_2-akz_0+x(z_0-z_2)} \tag{15}$$

Note that this equation has no phase constants c_1 or c_2, thus the moire patterns will be stationary against parallel movement of the grating. This has been previously pointed out by Takasaki[1].

(a) If $z_0 = z_2$ we have

$$\left(\ (1+d/z_2)\ (x-ak),\ (1+\frac{ak(1+d/z_2)-xd/z_2}{x_0-x})\ y\ \right)=akz_2/(x_0-ak) \tag{16}$$

(b) If $z_1 = z_2$ and $x_0 \gg ak$, then

$$d\left(\ (1+d/z_2)\ (x-ak),\ (1+\frac{ak(1+d/z_2)-xd/z_2}{x_0-x})\ y\ \right)=akz_2/x_0 \tag{17}$$

This equation indicates that the moire patterns are contour lines of the surface under the condition that the viewing grid is illuminated at point S and observed at point O; furthermore, the conditions that $z_0=z_2$ and $x_0 \gg ak$ have to be fullfilled. Eq.(17) is similar to Eq.(14) in the paper of Meadows et el[3], however, they derive this equation with the conditions that z_1 and z_2 are equal and very large. While this derivation may be valid, nevertheless, it may be misleading. As we can see from Eq.(16), if $x_0 \gg ak$, then Eq.(17) is valid, $x_0 \gg ak$ can be fullfilled if either x_0 is very large or ak is very small. Meadows et el's condition that z_0 is very large requires that ak is very small as can be seen from Eq.(16). Since ak is very samll, then k is small, thus there are only a few contour lines appeared. This is inconvenient for interpreting the contour surface. Furthermore, if x_0 is also very small, then even if ak is very small, the condition that $x_0 \gg ak$ is not fullfilled, thus the moire patterns appeared are not the contour lines as can be demonstrated in the diagram in Chiang's paper[6]. Thus the conditions that z_0 and z_2 are equal and large may be valid for Eq.(17) to be true, but are not necessary the sufficient nor the necessary conditions. However, the conditions that $z_0=z_2$ and $x_0 \gg ak$ are the necessary and sufficient conditions for Eq.(17) to be true.

Futhermore, Eq.(17) indicates that the moire contour lines are not the true contour lines and have to be corrected with the amount as follows:

$$x_1=(1+d/z_2)\ (x-ak) \tag{18}$$

$$y_1=(1+\frac{ak(1+d/z_2)-dx/z_2}{x_0-x})\ y \tag{19}$$

Formula has been proposed by Takasaki[2] to account for this kind of errors, the procedures

presented here seem to be the most exact and direct derivation.

(c) If $z_2 \gg z_0$, $z_2 \gg d$ and $x_0 \gg x$, then Eq.(15) becomes

$$d\left(x-ak,\ (1+\frac{ak-dx/z_2}{x_0-x})\ y \right)=d\ (x-ak,\ y)=akz_0/x_0 \tag{20}$$

This equation indicats that the moire patterns are the contour lines of the surface with only a small amount of correction ak for x-corrdinate.

IV. ILLUMINATION BY POINT SOURCE AND OBSERVATION AT INFINITY

(a) If we focus the surface at infinity with an angle β , then

$$(x_0-x)/z_0=tan\ \beta. \tag{21}$$

This corresponds to the observation at infinity. Introducing Eq.(21) to Eq.(15), we obtain

$$d\left((1+d/z_2)\ (x-ak),\ (1+\frac{ak(1+d/z_2)-dx/z_2}{x_0-x})\ y \right)=\frac{akz_2}{z_2 tan\beta\ +x-ak} \tag{22}$$

(b)If $z_2 \gg d$, $x_0 \gg x$ and $\tan\beta \gg (x-ak)/z_2$, then Eq.(22) becomes

$$d\ (x-ak,\ y)\ =\frac{ak}{tan\beta} \tag{23}$$

Thus, the moire patterns under these conditions are the contour lines of the surface.

V. PARALLEL ILLUMINATION AND POINT OBSERVATION

(a) If the viewing grid is illuminated with parallel light at an angle α, then

$b=a$ *and* $c_2=c_1+dtan\ \alpha$. *Thus Eq.* (10) *becomes*

$$d\left(x-ak+dtan\alpha, \frac{x_0-x+ak-dtan\alpha}{x_0-x}y \right)=akz_0/(z_0\ tan\alpha+x_0-x) \tag{24}$$

(b) If $x_0 \gg x$, *and since* x, ak *and* $dtan\alpha$ *are in the same order, thus* Eq.(24) becomes

$$d\ (x,y)\ =\frac{az_0k}{z_0\ tan\alpha+x_0} \tag{26}$$

(c)If $\tan\alpha \gg x_0$, then

$$d\left(x-ak+dtan\alpha,\ \frac{x_0-x+ak-dtan\alpha}{x_0-x}y \right)=ak/tan\alpha \tag{27}$$

Thus, the moire patterns under these two conditions are also the contour lines of the surface.

VI. PARALLEL ILLUMINATION AND OBSERVATION AT INFINITY

(a) Under this condition, Eq.(21) can be applied. Substituting Eq. (21) into Eq. (24), we obtain

$$d\left(x-ak+dtan\alpha,\ \frac{x_0-x+ak-dtan\alpha}{x_0-x}y \right)=ak/(tan\alpha+tan\beta) \tag{28}$$

(b) If $x_0 \gg x$ and $x \gg ak$, then Eq.(28) becomes

$$d(x, y) = ak/(\tan\alpha+\tan\beta) \tag{29}$$

Both Eqs. (27) and (28) indicate that the moire patterns are the contour lines of the surface.

VII. CONCLUSIONS

The moire patterns can be produced when a viewing grid with parallel lines is illuminated with light. The illumination can be either parallel light or point source. The observation point can either at finite distance or at infinity. Under these experimental situations, the moire patterns produced are the contour lines of the surface if proper conditions are met. Furthermore, correction has to be made if exact location of the contour lines are required.

(Snbmitted to Applied Optics)

REFERENCES

1. H. Takasaki, Appl. Opt. 9, 1467 (1970).
2. H. Takasaki, Appl. Opt. 12, 845 (1973).
3. D. M. Meadows, W. O. Johnson and J. B. Allen, Appl. Opt. 9, 942 (1970).
4. P. S. Theocaris, J. Sci. Instrum., 41, 133 (1964).
5. P. S. Theocarus, Exp. Mech· 5, 153 (1964).
6. C. Chiang, Brit. J. App. Phys. (J. Phys. D), ser 2, vol. 2, 287 (1969).
7. C. Chiang, J. Opt. Soc. Am. 57, 1088 (1967).

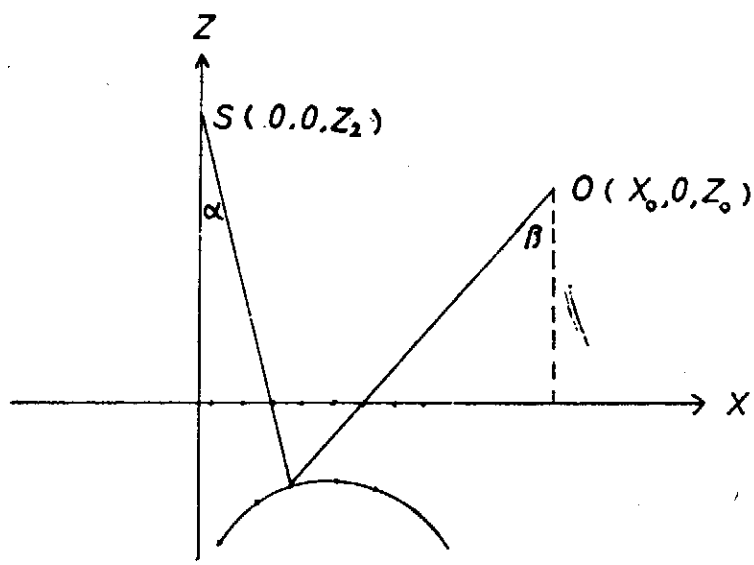

Fig. 1 A diagram showing the parallel lines on the viewing grid and their shadow on the surface interfere to form the moire patterns.

Annual Report of the Institute of Phyiscs, Academia Sinica, 1972

ILLUSION AND PERCEPTUAL PROCESS

CHUN CHIANG (蔣炯)

Biophysics Laboratory
Institute of Physics
Academia Sinica
NanKang, Taipei, Taiwan
The Republic of China

ABSTRACT

Illusion is shown in a block diagram to include the instrumental errors in the sensing device, the transmission distortion in the nerves and the perceptual misjudgment in the high center. The perceptual misjudgment originates from the variation of comparision standards and the method of comparision, and would correspond to the mis-programming of the computer. Ebbinghaus illusion is used to illustrate the point and an equation for predicting the illusion is suggested. It is emphasized that the group data may obscure the important information concerning the individual perceptual process. It is suggested that in order to design a computer with higher capacity and intelligence, illusion (error) in certain situation has to be allowed.

ILLUSION

Men obtain information from the outside world through a series of steps. Firstly, the signals from the outside world are detected by some kind of sensing devices (sensation). If the signals come by way of electromagnetic waves such as light, then the eyes may detect them. If the signals come by way of mechanical waves such as sound, then the ears may detect them. The signals detected by the sensing devices will then be transmitted through neurons (transmission) and perceived by the brain (perception). The brain will then express the perceived information by talking or writing as a output. These steps are illustrated in the block diagram in Fig. 1.

The signal transmission process in the nerve is a very important step. It is clear from the diagram that if the nerve does not transmit the signal, one can have the "sensation" yet have no "perception", because the signal in the "sensation" cannot reach to the high center in the brain. For example, it is possible that one can have his eyes wide open and "see" words on a page (the image of the words is apparently on the retina); yet he "perceives" nothing about those words therefore "knows" nothing about what are those words on the page. It is also possible that one can "perceive" something, yet that "something" does not

exist in the physical space. For example, imagination and hullucination belong to this class.

At this point, we should define specifically the meanings of the words "sensation" and "perception", which we have used without defining. These two words have been used interchangeably in the past and considerable confusion has arisen. Within the present paper, it is specifically defined that "sensation" means the impulses arisen from the stimulation of signals from the outside world at the sensing devices such as eyes or ears; on the otherhand, "perception" means the impulses in the brain arisen from the processings of the coming signals transmitted through the nerves.

In the processing of information from the outside world through the steps of sensing, transmission and perception, there are three main types of errors; namely, the unfaithful detection of signals in the sensing device (instrumental errors), the unfaithful transmission of signals in the nerves (transmission distortion) and the misjudgement or misprocessings in the perception processes (illusory perception). Let us discuss three types of errors in more detail.

a. Instrumental errors: It is safe to say that no device can record and reconstruct the original signals exactly as they were. The fine instruments are those which can map the original signals closely such that the errors are negligible. However, no instrument is able to eliminate the errors completely. In the case of visual illusions of crossing line class, the diffraction and aberrations have been attributed as the cause of illusions (1), (2). Similar type of instrumental errors should also exist in hearing, touching and other sensing devices. However, this type of error alone is not sufficient to explain the illusion to the full satisfaction. This has been pointed out by many authors (For example, Cumming, (3); Pressey & den Heyer, (4); Restle, (5)).

b. Transmission destortion: The transmission process through the nerves can also introduce errors. This is because the transmission is through a series of physiological processes in the body. Any imbalance in the body will exert some kind of influence on transmission process, therefore causing errors in transmission. However, under ordinary conditions, this type of error may be negligible.

c. Perceptual illusion: The signals transmitted through the nerves have to be stored, classified and compared in order to make a conclusion. These processes depend on the past experience, the present environment and the particular method adopted for processing the information. These vary from time to time and from person to person. Therefore, the perception process is also subject to error. The situation is similar to the computer programming; by specific programming, the computer is set to perform the operation in a specific way, or to utilize certain memorized information. Thus the output perception would consequently be different depending on the individual.

The instrumental type of illusion has been discussed in detail (1); the transmission type of illusion is probably not important in the ordinary condition; the perceptual illusion will now be discussed in more detail. However, before we can understand how the illusory perception arises, we have to understand the perceptual process.

PERCEPTUAL PROCESS AND PERCEPTUAL ILLUSION

The perceptual process can be put in a word as a comparision process or a judgemental process. When we see a building and perceive that the building is tall, we actually mean that the building is taller then "those" we "usually" see. (The comparision process is however not readily realized in the consciousness). When we see a ship and perceive that the ship is very big, we actually mean that the ship is bigger than "those" we "usually" see. "Those" bits of information obtained by observation around the world since we were born are stored in the brain and used as the standards for comparision in every perception process. A block diagram is shown in Fig. 2, where t_{-1}, t_{-2} $\cdots t_{-n}$ represent the time in the past, t_0 represents the time at the present and t_1, t_2 $\cdots\cdots$ t_n represent the time in the future. Those bits of information obtained in the past were stored in the memory and are ready to be activated and retrieved for comparision with the information obtained at the present and future time. When an input information at the present time t_0 is coming into the brain, it is first stored in the short-term-memory and then a relevant information stored in the past is retrieved at time t_1 and a comparision is made. The result of the comparision is given out at t_2 as the perception (For the evidence of short-term memory in vision, see Averbach and Coriell (6), Averbach and Sperling (7)).

It is clear from this argument that the information stored in the brain determines strongly the outcome of the perception. Any thing influences the content of the information stored may affect the outcome of the perception. For example, if a person is born and living in a place with all the building no less than ten-story heigh; the height of the ten-story-building is stored in his memory and used as the standard. When he comes across a five-story-building, he will preceive that the five-story-building is very low (actually, he means that it is lower than the ten-story-building he used to see). On the other hand, if a person is born and living in a place with all the buildings not higher than, say, two story; the height of the building is stored in his memory and used as a standard. When he come across a five-story-building, he will perceive that the five-story-building is very high (higher than the two-story-building he used to see). Thus, for the same five-story-building, the outcome of the perception is different for different persons with different stored information.

The above discussion concerns with relatively a simple perception process, namely, the input information is relatively simple, for example, the perceiving of tallness, bigness, etc. For this kind of simple signals, one comparision process is sufficient to give the perception. For a complicated input information, one comparision process may not be sufficient to complete the task and several combined processes of comparision may be required to perform the task. A general scheme of comparision processes is shown in the block diagram in Fig. 3.

For a complicated input information, the brain cannot perceive all the features in the information at the same time. Only one feature may be perceived at a time and the other

features may only be perceived later. The selection of features may be complished either by eye movement (8) (9) and / or by the fluctuation of the attention field (10). Thus, one feature from the input information fed in at time t_0 is memorized in Memory I and compared with the retrieved relevant information at t_1 to form a perception. The result of the comparision is coded in Memory II. The other feature from the input information perceived at time t_2 is also memoized and compared with the retrieved relevant information at t_3 to form a perception. The result of this comparision is coded in Memory IV. Same procedure is used for the feature fed in at t_4 ··· and the results of comparision are coded in Memory VI···. The results of comparision coded in Memory II, IV, VI ····· may then be evaluated and compared again to from a final perception. It should be noted that those bits of information freshly stored in the Memory I, III, V ····· exert more influences in comparision than those stored in the past. Furthermore, there are many possible ways for evaluation and comparision. The selection of any particular method for evaluation and comparision, thus forming a certain particular output perception, depends on the individual's past experience, the instruction given by the experimenter and the bits of information perceived during the perception.

Thus, the individual's past experience and the instruction given during the experiment can influence the outcome of the perception (perceptual illusion) at two levels. Firstly, they can change the standards in the memory which are used for comparision. Secondly, they can change the particular method ultilized for comparision. The finding that age has significant effect on the magnitude of illusion (11) can be interpreted as the result of the influence due to past experience, among other possible reasons such as physiological change of the eyes. Ames (12) and Ittelson (13) show that the subject's past work may determine his perception. The finding of the effect of inspection points on the magnitude of illusion (14) (15) shows the importance of instructions upon perception. Gilinsky (16) found that the instruction have a very great effect on the perception of size and Graham (17) interpreted this as indicating that the subject probably does one thing under one instruction and another thing under other instruction.

It should be noted that the illusory perception as discussed above is purely due to the cognitive process and no neural structure changes are involved. This illusory perception corresponds to the different output of computer due to different computer programming and computer memory. With different computer memory and program and thus performing different calculation, the output would necessary be different. This kind of process does not involve any structure changes. On the other hand there has been a long debate concerning the effect of early visual influence on man's ability to perceive the visual world in later life (for example. see Ref. (18), (19)) due to the neural structure changes: only recently, strong evidence has gained that the visual experience in the first few months of life permanently influences the properties of visual cortical neurons (20), (21), (22). This kind of neural changes during early devolopment correspond to the structure change of the integral circuit or semiconductor due to the stress during the manufacturing stages. To push further

the analog between the computer technology and human perception, the realibility problem of adult human performance corresponds to the realibility problem of the out-of-factory instruments, and the human ageing processes could correspond to the deteriorating processes in the instruments in uses. While all these may introduce distortion of signals in the instrument, and cause illusion in human being, this paper emphasizes only the cognitive aspects, namely, the illusion arisen from difference of the memory and the comparision processes. The variations of the standards and the comparision methods form the basis of this illusory perception.

Many authors have used the judgement and relational concept to explain the illusion. For example, Helson's adaptation-level theory (23), Parducci's range frequency model (24), Anderson's integration model (25), and those works by Girgus et al (26), Massaro & Anderson (27), Restle & Merryman (28) and Hake et el (29). However, the exact formulation seems to be different from this one.

To formulate the idea more precisely, we can write mathematically as follows:

$$P(x)=T(x) \tag{1}$$

where P(x) represents the perceived stimulus of x, T represents the transformation and X represents the physical stimuli x_1, x_2 ……. T may depend on time, the stored memory, the instruction etc. We may under many ordinary conditions write Eq.(1) in a matrix form as

$$P\begin{pmatrix} x_1 \\ x_2 \\ \cdot \\ \cdot \\ x_n \end{pmatrix} = \begin{pmatrix} a_{11} & a_{12} & \cdots \\ a_{21} & a_{22} & \cdots \\ \cdot & \cdots & \cdots \\ \vdots & \cdots & \cdots \end{pmatrix} \begin{pmatrix} x_1 \\ x_2 \\ \cdot \\ \cdot \\ x_n \end{pmatrix} \tag{2}$$

where x_1, x_2 …… may represent size, length, distance or color …… of various objects in the visual field; a_{11}, a_{12} …… are the elements of the transformation matrix.

Eq.(2) means that the perceived stimulus x_1 is a linear combination of the stimuli in the visual field and is different from the absolute value of x_1. Eq.(1) or Eq.(2) is very basic to perception and we may call this equation the basic law of perception.

Similar mathematical expression has been proposed by Anderson(32), however, the exact meaning of the terms seem to be different. Furthermore, there is some debate (33) concerning the requirments of the coefficients, however, this shall not concerns us here. As an example of the application of Eq.(2), we use the Ebbinghaus illusion for illustration. Ebbinghaus illusion as shown in Fig. 4 is that, the inner circle with radius R surrounded by larger circles with radius r appears smaller; and R appears larger when surrounded by smaller circles with radius r′. Using Eq. (2), and if we choose R and R-r as the vector space coordinate, we may write following equation to describe the phenomenon.

$$P(R)=a_{11}R+a_{12}(R-r)$$
$$P(r)=a_{21}r+a_{22}(r-R) \quad (3)$$

The block diagram for this illusory perception mechanism is shown in Fig. 5. Since the memory plays litter part in this illusion, it is omitted in the block diagram. The radius of the inner circle R is compared with the radius of the outer circles r, and the perceived difference D is

$$D=k\ e^{-d/\lambda_1}(1-e^{-n/\lambda_2})\ (R-r) \quad (4)$$

Where k, λ_1 and λ_2 are constant, d is the distance between the inner and outer circles, and n is the number of the outer circles. $e\times p(-d/\lambda_1)$ and $e\times p(e-n/\lambda_2)$ show the influences of the distance and the number of the outer circles on the comparision difference D. The more the number of the outer circles and the shorter the distance between the inner and the outer circles, the more is the difference D. This difference D is further integrated with the radius R of the inner circle, and the perceived radius of the inner circle is

$$P(R)=R+k\ e^{-d/\lambda_1}(1-e^{-n/\lambda_2})\ (R-r) \quad (5)$$

Comparing with Eq.(3), we see that a_{11} is 1 and a_{12} is $k\ e^{-d/\lambda_1}(1-e^{-n/\lambda_2})$. With proper value of k, λ_1 and λ_2, Eq.(4) can fit the data of Massaro and Anderson(27) nicely. Eq.(3) shows that the perceived radius of outer cirles should also be changed, however, no data seem yet to be available.

Massaro and Anderson (27) have used their judgemental model (25) (30) to treat the data, the equation they used was

$$J=WS+(1-W)\ S^* \quad (6)$$

where J is the judgment of the center circle, S is the absolute size of the center circle, S* is the relative size of the center circle and W is a constant. The shortcomings of this equation seems to be: (a) The absolute size of the outer circles, a very important parameter in the illusion, has not been included in the equation. (b) Both J and S* are the relative size of the center circle and can only be determined from the experimental data, thus the meaning of S* seems to be obscured and the equation has little value in predicting the amount of illusion. However, Eq. (4) in this paper gives a correlation between the perceived size of the center circle, the absolute size of the inner cirle and outer circles, the distance between the inner and outer circles, and the number of the outer circles: furthermore, this equation may predict the amount of illusion.

SIGNIFICANCE OF THE GROUP DATA

From the above discussion, the individual's past training, his ethnical background, the instruction and hint, as well as the information perceived at the time of the experiment are important factors in perecption. A variation of these could to different output-perception, therefore a different amount of illusion. Helson (23) and Merryman & Restle (31) have also

emphasized these factors. Unfortunately, these seem not have been properly recoginzed and controlled in performing experiment. Improper control of these factors may quite often lead to the discrepency in experimental data. A usually accepted procedure in obtaining data on illusion is that a large number of persons are selected and the data obtained on the individual person are averaged over the entire number of persons. This procedure may be practically desirable, however theoretically questionable in certain cases. This is so because the extent of the illusions may not occur randomly but is dependent on the individual' spast stored information, including the instruction given before the experiment. Consequently, the data obtained on a particular person may only represent the result of the perception of this particular person or persons with similar past experience. Thus, a statistical procedure which assumes that errors occur randomly may not be applied. An important objective in psychology may be to find out how the perception may be different for different person. An averaging procedure may obscure this important information. However, this does not mean that we should reject group data entirely. In certain cases, the group data is desirable. The point is that while group data is desired in certain cases, the averaging procedure may obscure the important information regarding how the individual variation on illusion may arise. Looking into the literature, one can see the striking difference between the papers in physical science and those in life science. While papers in physical science usually investigate one single sample throughly, the papers in life science usually deals with a group of samples, and it seems that little attention is paid to the cause of variation of individual sample. It is called to the attention that there is much to be learned from the individual's variation on illusion and caution should be exerted in interpreting the group data. It is suggested that in order to obtain consistent and homogenous data, it is necesssary to control the experimental conditions such as fixation point of eyes, visual angle of the stimulus, and particularly the instruction regarding what kind of information to be retrieved and what kind of mental operation needed to perform the task.

ILLUSION AND ARTIFICIAL INTELLIGENCE

Illusion as it implies usually means an undesirable effect, because it gives one the perception which does not correspond to the reality. However this may be an advantage rather than an disadvantage under certain situation. For example one can always recognize an old friend no matter whether he is far away or very close, whether we can have a front view or only a side view of his face: furthermore, the size of this old friend will perceive to be approximately constant regardless of the distance. The fact that the object at various orientation and distance under various mask can be perceived to be the same object is an illusion, however, this illusion gives us a tremendous advantage, and is the major difference between the human brain and the computer. The brain can extract information from various input source and make an identification of seemingly different object, the existent computer however can not have this capability and intelligence. This suggests that in order for the computer to have a better capability and intelligence, we have to design the computer which

can give the illusion. Namely, we can only achieve the greater information processing capability and artificial intelligence at the expense of the illusion.

(Submitted to IEEE Man, System, Cybernetics)

REFERENCES

1. C. Chiang, A new theory to explain geometrical illusions produced by crossing lines. Percept. & Psychophys., Vol. 3, 174-176, (1968).
2. S. Coren, The influence of optical aberrations on the magnitude of the Poggendorff illusion. Percept. & Psychophys., Vol. 6(3), 185-186, (1969).
3. G. D. Cumming, A criticism of the diffraction theory of some geometrical illusion. Percept. & Psychophys., Vol. 4, 375-376, (1968).
4. A. W. Pressey, & K. den Heyer, Observation of Chiang's new theory of geometrical illusion. Peecept. & Psychophys., Vol. 4, 313-314, (1968).
5. F. Restle, Illusion of bent line. Percept. & Psychophys., Vol. 5, 273-274, (1969).
6. E. Averbach, & A. S. Coriell, Short-term memory in vision. Bell syst. Tech. J., Vol. 40, 309-328, (1961).
7. E. Averbach, & G. Sperling, Short-term storage of information in vision. In C. Cherry (Ed.) Proceeding of the fourth London Symposium on information theory. London: Butterworth, p. 196-211, (1961).
8. D. Noton & L. Stark, Scanpaths in eye movements during pattern perception. Science, Vol. 171, 308-311, (1971).
9. D. Noton, A theory of visual pattern perception, IEEE transactions on Systems Science and Cybernetics, Vol. SSC-6, 349-357, (1970).
10. C. Chiang, A theory of the Muller-Lyer illusion, Vision, Vision Res. Vol. 13, 347-353, (1973).
11. H. W. Leibowitz & J. Cwozdecki, The magnitude of the Poggendorff illusion as a function of age. Child Develpment, Vol. 38, 573-580, (1967).
12. A. Ames, Binocular vision as affected by relations between uniocular stimulus-patterns in common-place enviroments. Amer. J. Psychol., Vol. 59, 333-357, (1946).
13. W. H. Ittelson, The Ames demonstrations in perception. Princeton: Princeton University Press, (1952).
14. S. Novak, Effects of free inspection and fixation on the magnitude of the Poggendorff illusion. Percept. Mot. Skills, Vol. 23, 663-670, (1966).
15. R. H. Pollack, The effects of fixation upon the apparent magnitude of bounded horizontal extent. Amer. J. Psychol, Vol. 77, 177-192, (1964).
16. A. S. Gilinsky, The effect of attitude upon the perception of size. Amer. J. Psychol., Vol. 68, 173, (1955). 18.
17. C. H. Graham, Vision and Visual perception. Wiley: New York (1965), Chapter
18. G. L. Walls, The probelm of visual direction, Part. I. The history to 1900. Am. J. Optom. and Arch. Am. Acad. Optom., Vol. 28, 55-83, (1951).

19. R. L. Gregory, Eye and Brain: The psychology of seeing world, University Library (McG¬aw-Hill), New York, (1966).
20. T. N. Wiesel, & D. H. Hubel, & D. H. Hubel, Effects of visual deprivation on morphology and Physiology of cells in the cat's lateral geniculate body. J. Neurophysiol. Vol.26, 978-993, (1963).
21. C. Blakemore, G. F. Cooper, Devolopment of the brain depends on the visual environment, Nature, Vol. 228, 447-478, (1970).
22. D. Mitchell, R. Ereeman, M. Millodot & G. Haegerstrom, Meridional Amblyopia: Evidence for modification of the human visual system by early visual experience. Vision Res., Vol. 13, 535-557, (1973).
23. H. Helson, Adaptation-level theory, New-York: Harper & Row, (1964).
24. A. Parducci, Category judgment: A range-frequency model. Psychol. Rev., Vol. 72, 407-418, (1965).
25. N. H. Anderson, A simple model for information integration. In R. P. Abelson et al. (Eds.), Theories of cognitive consistency: A sourcebook. Chicago: Rand McNally, (1968).
26. J. S. Girgus, S, Coren, & M. Agdern, The interrelationship between the Ebbinghaus and Delboeuf illusion. J. Exp. Psychol., Vol. 95, 453-455, (1972).
27. D. W. Massaro, & N. H. Anderson, Judgemental model of the Erbinghaus illusion. J. Exp. Psychol., Vol. 89, 147-151, (1971).
28. F. Restle, & C. T. Merrman, Adaptation-level theory account of a relative size illusion. Psychonomic Science, Vol. 12, 229-230, (1968).
29. H. W. Hake, W. G. Faust, J. S. McIntyer, & H. C. Mueray, Relational perception and modes of perceiver operation. Percept. & Psycholphys., Vol. 2, 469-478, (1967).
30. N. H. Anderson, Functional measurement and psychophysical judgement. Psychol. Rev., Vol. 77, 153-170, (1970).
31. C. T. Merryman, & F. Restle, Perceptual displacement of a test mark toward the larger of two visual objects. J. Exp. Psychol., Vol. 84, 311-318, (1970).
32. N. H. Anderson, Averaging vesus adding as a stimulus-combination rule in impression formation. J. Exp. Psychol., Vol. 70, 394-400, (1965).
33. B. H. Hoges, Adding and Averaging models for information integration, Psychol. Rev., Vol. 80, 80-84, (1973).

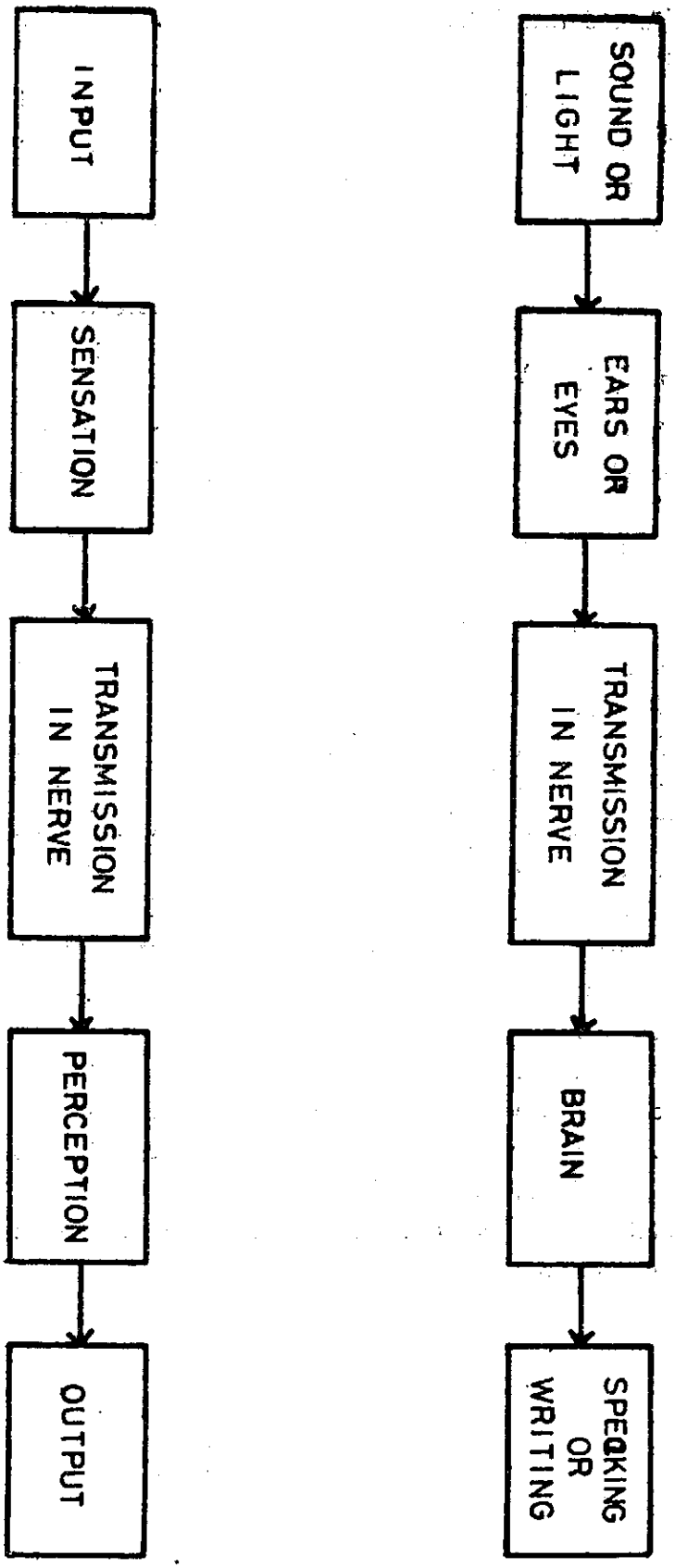

Fig. 1. A block diagram showing the processing of information.

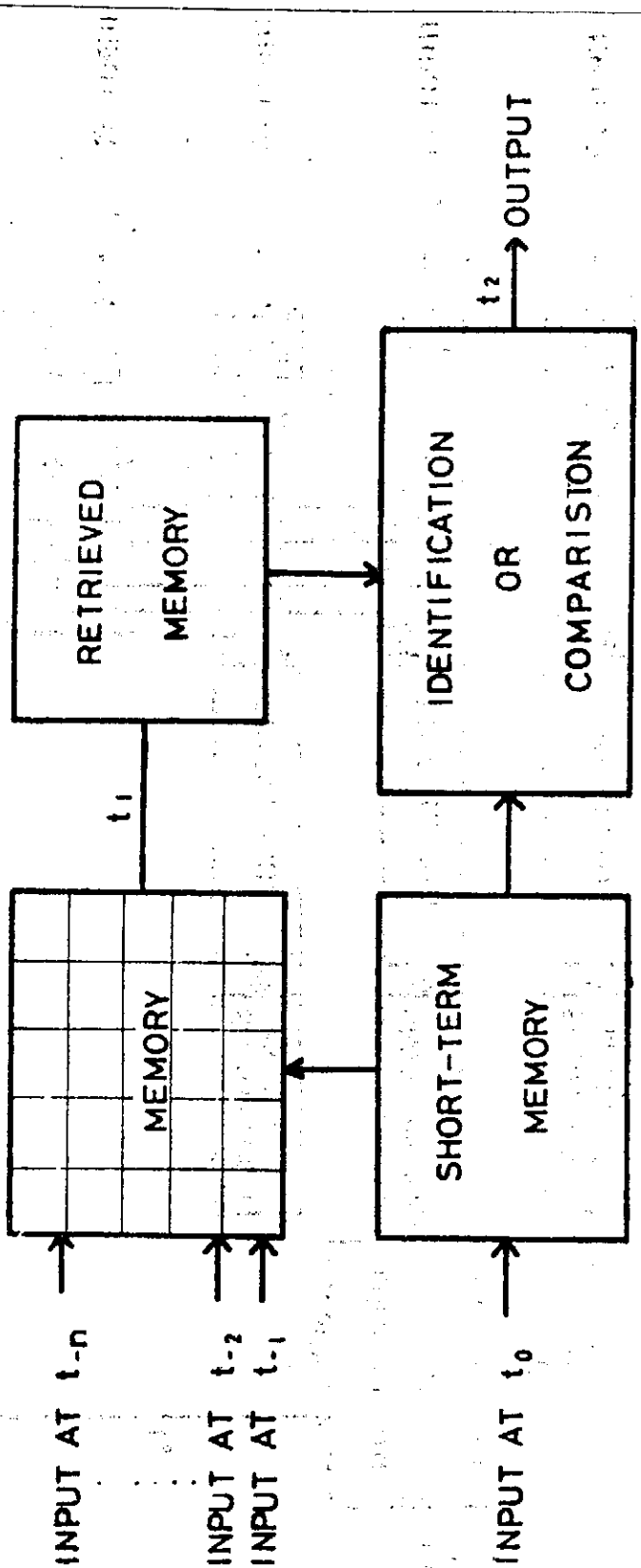

Fig. 2. A block diagram showing a simple perception process.

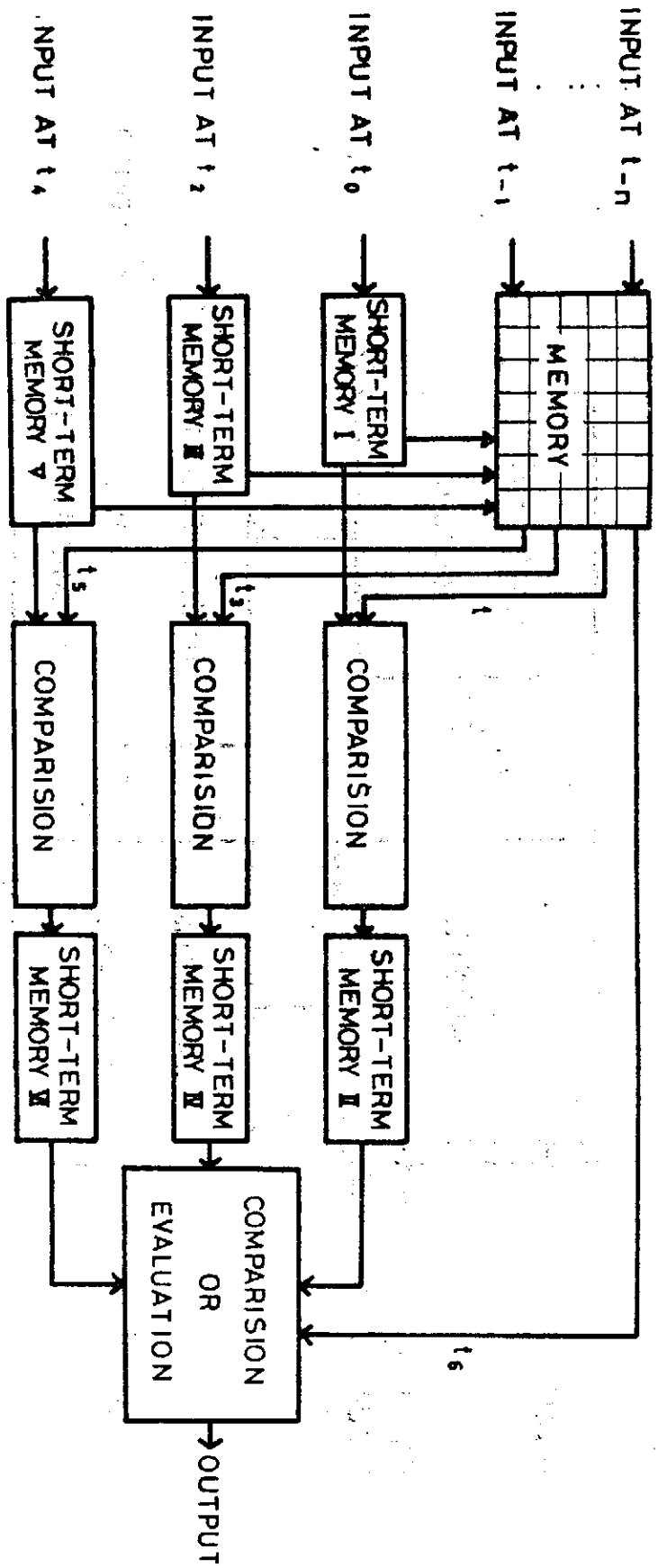

Fig. 3. A block diagram showing the perception processes for a complicated input information.

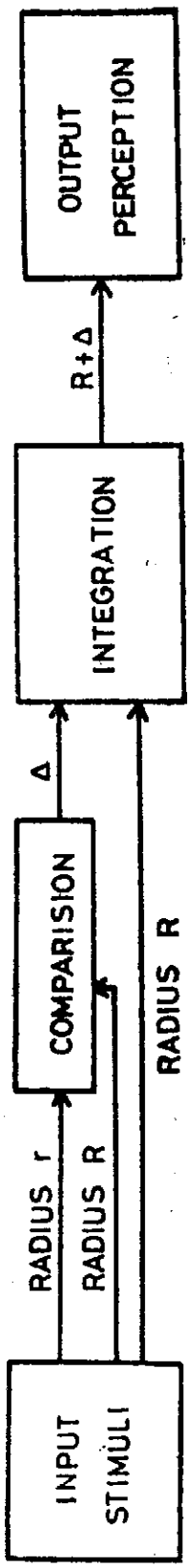

Fig. 4. Ebbinghaus figure, The sizes of the two inner circles are the same, but they appear differently.

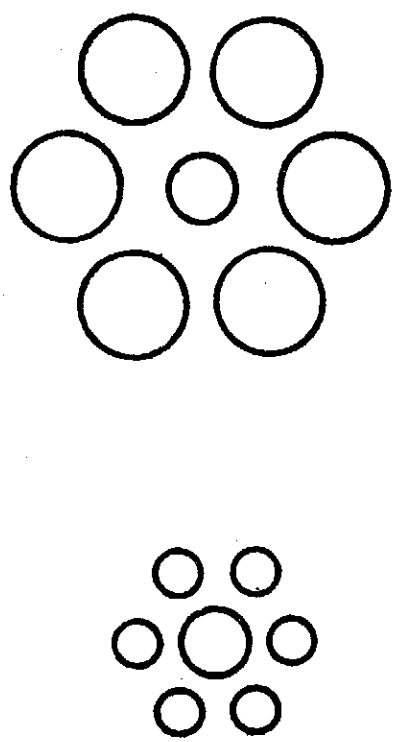

Fig. 5. A block diagram showing the illusory perception process for Ebbinghaus figure.

Annual Report of Institute of Physics, Academia Sinica, 1972

A THEORY OF POGGENDORFF ILLUSION

CHUN CHIANG (蔣炯)

Institute of Physics

Academia Sinica

NanKang, Taipei, Taiwan,

The Republic of China

ABSTRACT

Poggendorff illusion is attributed to be the consequence of the optical image blurring, the perceptual image distribution and the variation of reference standards. Rotation effect on illusion is explained on the basis that the physical horizontal and vertical are adopted in the physiological system for reference, thus it is more difficult to induce the illusion when the orientation is in either horizontal or vertical. The equation to incorporate above effects is

$$I=w(B+Sin2\phi)\ (k'_1+k'_2+k'_3)\ d\ cot\theta-(1-w)\ Sin4\phi,$$

where w and B are constants; k'_1, k'_2 and k'_3 represent the effect of the optical image blurring, the perceptual image distribution and the variation of reference standards respectively; d is the width of the two parallel lines; θ is the angle between the inclined line and the parallel lines; ϕ is the angle between the inclined line and the horizontal; $(B+Sin2\phi)$ represents the easiness to induce the illusion and $Sin4\phi$ represents the illusion when there is no inducing parallel lines.

1. INTRODUCTION

In a previous paper (Chiang, 1968), Poggendorff illusion has been explained on the basis of the optical image blurring in the retina and other illusion of the crossing lines type in turn have been explained by the Poggendorff effect.

The effect of optical blurring is that when two objects are presented to the eyes, the optical image of the objects on the retina do not quite correspond to the physical shape of the objects, and line AC and line BC (see Fig.1) converge before they really reach the intersection points. Thus line BC and line EH seems to be misaligned. The contribution of the optical blurring to the illusion has been experimentally verified by Coren (1969), however, many authors (For example Cumming, 1968; Pressey & den Heyer, 1968; Restle, 1969; Farne, 1970) have pointed out that optical blurring effect along is insufficient to explain all feature of the illusion. The purpose of this paper is to explore the Poggendorff illusion in more detail.

2. PERCEPTUAL IMAGE DISTRIBUTION

When physical objects are presented to the eyes, optical images are formed on the retina. These optical images are further projected onto the perception space via the nerve impulses, and these impulses in the perception space are interpreted as physical objects located in some points in the physical space. The positions of the objects in the physical space and the positions of the objects in the perception space maintain certain projection relationship, but the projection relationship may not be unique. Fig.2 shows the projection relationship between the physical space and the perception space. The horizontal axis represents the position and the vertical axis represents the probability of finding or perceiving the objects at the position. The projection function between the physical space and the perception space assumes to be a normal distribution. Thus there is a finite probability of perceiving the objects in some positions of the perception space for which there is no physical objects in the corresponding positions in the physical space; namely, the perceived position of the physical object is not unique, which fluctuates around the corresponging physical position. The autokinetic effect, a phenomenon of perceived random movement of a stationary light source in the dark, is a manifestation of this principle.

If two objects are well seperated as shown in Fig. 2a, the perceptual images of these two objects show no mutual interaction; however, if two objects are close enough as shown in Fig. 2b, then these two perceptual images are coupled to each other. With the superposition of two individual probability distribution, the position of each maximum probability of perceiving the object shifts to each other. Thus, the perceiving distance between the two objects decreases. Many illusions may be explained by this principle. In this paper, we confine our attention to the poggendorff illusion.

3. FACTORS INFLUENCING THE POGGENDORFF ILLUSION

1. Optical image blurring : This has been discussed in detail before (Chiang, 1968). The magnitude of illusion I_1 due to the enlargement of acute angle from optical blurring is (Gillam, 1971)

   $$I_1 \simeq k_1 \; d \; cot\theta \qquad (1)$$

   where θ is the angle between line AC and BC , d is the distance between two parallel lines and k is a constant.

2. Perceptual image distribution: From this principle, line AC and line BC will interact when they approach close enough (not necessary to intersect). The interaction is such that line AC and line BC will shift to each other near intersection point C. However, there is no interaction between point A and point B, because the distance between them is large. Thus the acute angle looks perceptually larger and this kind of illusion I_2 would also be (Gillam, 1971)

   $$I_2 \simeq k_2 \; d \; cot\theta, \qquad (2)$$

where k_2 is a constant. This effect is operative even if line AC and line BC do not intersect.

3. Variation of reference standards: One judges the orientation of the lines by some standards stored in memory. However, when the lines are blocked by some other strong signals such as the two long, parallel lines in Poggendorff figure, the original orientation standards are overshadowed and the two long, parallel lines are used as orientation standard. Since line BE intersects the two vertical lines at point C and point H, and point C is higher than point H; thus one erroneously perceives that line EH and line BC are misaligned with line BC being shifted upwards and line EH downwards. Thee magnitude of the illusion I_3 due to this effect is proportional to the vertical distanc h between point H and point C,

$$I_3=k_3 \cdot h=k_3 d\cot\theta, \qquad (3)$$

where k_3 is a constant. Gillam (1971) have used the depth processing theory to explain the illusion, however, it is difficult to see how a two-dimensional figure without a strong three-dimensional cue as such can give a depth perception. Thus, the contribution of the depth processing to the Poggendorff illusion without a three-dimensional cue would be in my opinion, not very much. The total magnitude of illusion due to above effects are

$$I=I_1+I_2+I_3=(k_1+k_2+k_3)d\ \cot\theta, \qquad (4)$$

If we reduce the optical blurring, k_1 would also be reduced; thus the illusion would decrease. The data of Coren (1969) have confirmed this point. Weintraub and Krantz (1971) have presented some data on the variation of Poggendorff illusion, they use equation (4) to fit the data with $k_1+k_2+k_3$ equal to 0.162. Velinsky's data (1925) can also be fitted by Eq. 4 with $k_1+k_2+k_3$ equal to o.33. Pressey (1971, 1972) has used the assimilation theory to explain Velinsky's data, he argues that in judging the objective continuation of the inclined BC line, a series of lines shorter than the objective continuation are formed, and O's choice of the line will assimilate to the mean of the series; this effect produces the illusion. However, it is not quite clear why only the shorter lines are extended, also, it is not quite clear how his argument could quantitatively lead to the predicted Velinsky's data.

4. Negative illusion: Bouma and Andriessen (1970) have presented some interesting data on the orientation of line segments influenced by other lines. His data show that when the angle between the inducing and the induced lines are small, the direction of the illusion is reversed. This is contradictory to other data (Velinsky, 1925; Weintraub & Krantz, 1971); however, a closer look reveals that Bouma and Andriessen used a very short line segment. Using the principle of perceptual image distribution, it is possible to explain it as follows: If BC line in Fig. 1 is very short such that the distance between point A and point B is close enough to have mutual influence as explained in last section, then point B will shift toward A and the angle ACB will look perceptually smaller instead of larger. This would result in the negative illusion as observed.

5. Effect of Rotation: Many researchers (For example, Obonai, 1931; Leibowitz & Toffey, 1966; Weintraub & Krantz, 1971; Bouma & Andriessen, 1970; Green & Hoyle, 1964) have found that the rotation of the Poggendorff figure has great influence on illusion; the magnitude of illusion is significantly less when the inclined line is near either horizontal or vertical. This effect is understandable, because the vertical and horizontal direction are two strong standards we can employ during our daily life. The physiological system in our inner ear maintains our sense of body orientation and we are constantly aware of the horizontal and vertical direction. These directions are two very strong references we can use and are thus less susceptible to be deviated by other inducing lines. This effect of rotation can be incorporated into equation (4) as follows:

$$I=(B+Sin2\phi)\ (k'_1+k'_2+k'_3)dcot\theta, \qquad (5)$$

where ϕ is the angle between line BC and X-axis, B is a constant and (B+Sin2ϕ) is a measure of easiness for deviating the lines from its physical orientation by the inducing parallel lines. k'_1, k'_2 and k'_3 are also constant which are different from k_1, k_2 and k_3 in Eq. (4) Due to the introduction of term (B +Sin2ϕ), Eq. (5) is consistent with the rotation data of Bouma and Andriessen (1970), Weintraub and Krantz (1971). In principle, Eq. (5) is more general than Eq. (4), since Eq. (5) incorporates the effects of rotation; however, both Eqs. (4) and (5) can fit the data in Fig.1 of Weintraub and Krantz's paper (1971), thus the data do not permit us a choice between them.

6. Farne (1970) has shown that a modified Poggendorff display (Fig.3) containing remote contours instead of the usual pair of parallel lines can also induce illusion. Furthermore, Goldstein and Weintraub (1972) have shown that the illusion magnitude in the Farne figure increases, contrary to the conventional Poggendorff figure, when the inclination angle θ increased from 45° to 51°; they conclude that Farne figure would require a separate explanation. However, it is possible to give this phenomenon an unified treatment and incorporate these data in a single equation.

In the conventional Poggendorff illusion, the two parallel lines are strong standards for references, thus the orientation of the BC line is judged in reference to the parallel lines. In the Farne figure, the parallel contour is not very visible thus can only serve as a weak standard. Without the inducing parallel lines, Bouma and Andriessen (1968) have shown that the inclined lines would perceive to be closer to the vertical or horizontal (whichever is nearer) than their geometrical orientation. The amount of illusion due to this effect has been shown to be k_4 Sin4ϕ, where k_4 is a constant and ϕ is the angle between the inclined line and the X-axis. Thus, the total illusion may be written as follows:

$$I=w(B+Sin2\phi)\ (k'_1+k'_2+k'_3)\ dcot\theta-(1-w)k_4\ Sin4\phi, \qquad (6)$$

where w is a weighing factor with a value between 0 and 1. The significance of this weighing factor is that w is a measure of the reference of the standard. If the two parallel lines or contours can serve as strong reference such as the case in the conventional Poggendorff figure, then w is close to 1 and the illusion is induced

entirely by the parallel lines; if there are no parallel lines to block the inclined BC line, then w is zero and the illusion is induced only by physiological vertical or horizontal; if the two parallel lines or contours are not very vivid and can only serve as weak reference such as the case in the Farne figure, then w is between 0 and 1, and the illusion is induced by both the parallel line and the physiological vertical or horizontal. Thus the illusion may increase instead of decrease according to Eq. (6) when the angle θ changes from 45° to 51°.

7. Variations of the Poggendorff illusion: Fig. 4 shows some variations of the Poggendorff illusion. For Fig.4A, there are no parallel lines to block the inclined line, thus k'_3 would be zero; for Fig.4B, there is no optical image blurring effect, thus k'_1 would be zero; for Fig. 4C, both k'_1 and k'_2 would be zero. Thus, the illusion in these figures would be significantly reduced than the conventional Poggendorff figure as shown by Restle (1969) and Pressey & den Heyer (1968). Furthermore, k'_1, k'_2, k'_3 and k_4 may depend on the probability perception function (Chiang, 1972). With different fixation point, k'_1, k'_2..... would assume different weighing value, thus the magnitude of illusion may change (Novak, 1966).

4. CONCLUSIONS

The Poggendorff illusion is attributed to be the result of optical image blurring, perceptual image distribution, variation of the reference standards and the induction of the physiological horizontal and vertical. The above effect can be represented by

$$I=w(B+Sin2\phi)(k'_1+k'_2+k'_3)cot\theta-(1-w)k_4\ Sin4\phi,$$

where k'_1, k'_2 and k'_3 represents the contribution from optical image blurring, perceptual image distribution and variation of the reference standard respectively, $(B+Sin2\phi)$ represents the easiness to deviate the test line by the inducing parallel lines and $k_4\ Sin4\phi$ represents the illusion due to the physiological horizontal and vertical alone. It is suggested that a systematic investigation of all those parameters in a single experiment is needed to determine the relative value of those parameters.

(Snbmitted to Vision Research)

REFERENCES

Bouma, H. and Andriessen, J.J. (1968). Perceived orientation of isolated line segments. *Vision Res.* 8, 493-507.

Bouma, H. and Andriessen, J.J. (1970). Induced changes in the perceived orientation of line segments. *Vision Res.* 10, 333-349.

Chiang, C. (1968). A new theory to explain geometrical illusions produced by crossing lines. *Percept. & Psychophys.* 3, 174-176.

Chiang, C. (1972). A theory of the Muller-Lyer illusion. *Vision Res.* in press.

Coren, S. (1969). The influence of optical aberrations on the magnitude of Poggendorff

illusion. *Percept. & Psychophys.* 6(3), 185-186.

Cumming, G. D. (1968). A criticism of the diffraction theory of some geometrical illusions. *Percept. & Psychophysl.* 4(6), 375-376.

Farne, M. (1970). On the Poggendorff illusion: A note to Cumming's criricism of Chun Chiang's theory. *Percept. & Psychophys.* 8, 112.

Gillam, M. (1971). A depth processing theory of the Poggendorff illusion. *Percept. & Psychophys.* 10 (4A), 211-216.

Goldstein, M. and Weintraub, D. (1972). The parallel-less Poggendorff: Virtual contours put the illusion down but not out. *Percept. & Psychophys.* 11(5), 353-355.

Green, R. T. and Hoyle, E. M. (1964). The influence of spatial orientation on the Poggendorff illusion. *Acta Psychologica*, 22, 348-366.

Leibowitz, H. and Toffey, S. (1966). The effect of rotation and tilt on the magnitude of the Poggendorff illusion. *Vision Res.* 6, 101-103.

Novak, S. (1966) Effects of free inspection and fixation on the magnitude of the Poggendorff illusion. *Perceptual & Motor Skills*, 23, 663-670.

Obonai, T. (1931). Experimentelle Untersuchungen über den Aufbau des Schraumes. *Archir für die gesamte Psychologie*, 82, 308-328.

Pressey, A. W. and den Heyer, K. (1968). Observations on Chiang's new theory of geometrical illusion. *Percept. & Psychophys.* 4(5), 313-314.

Pressey, A. W. (1971). An extension of assimilation theory to illusions of size, area and direction. *Percept. & Psychophys.* 9, 172-176.

Pressey, A. W. (1972). The assimilation theory of geometric illusion: an additional postulate. *Percept. & Psychophys.* 11, 28-30.

Restle, F. (1969). Illusions of bent line. *Percept. & Psychophys.* 5(5), 273-274.

Velinsky, S. (1925). Explication Physiologique de I'illusion de Poggendorff. *Annee Psychologique*, 26, 107-116.

Weintraub, D. J. and Krantz, D. H. (1971). The Poggendorff illusion: Amputations, rotations and other perturbations. *Percept. & Psychophys.* 10, 257-264.

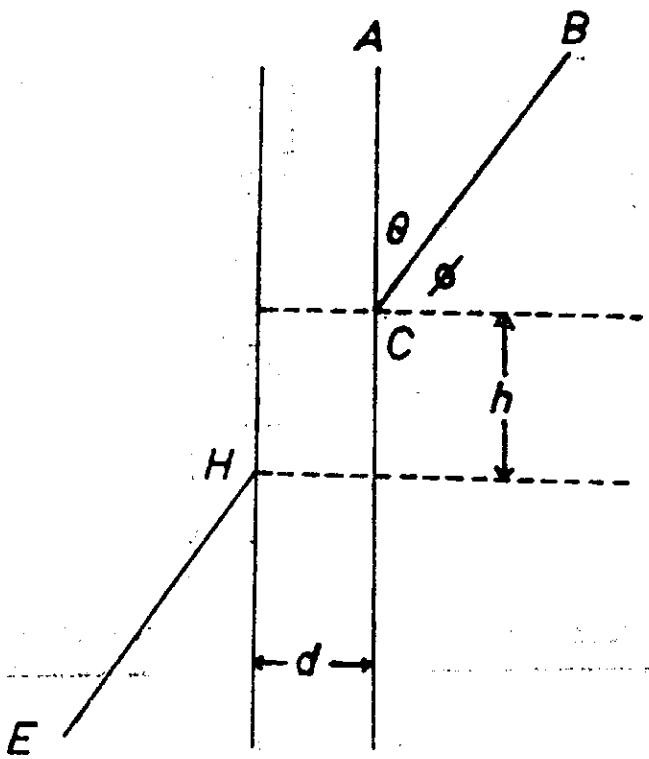

Fig. 1. A conventional Poggendorff illusion.

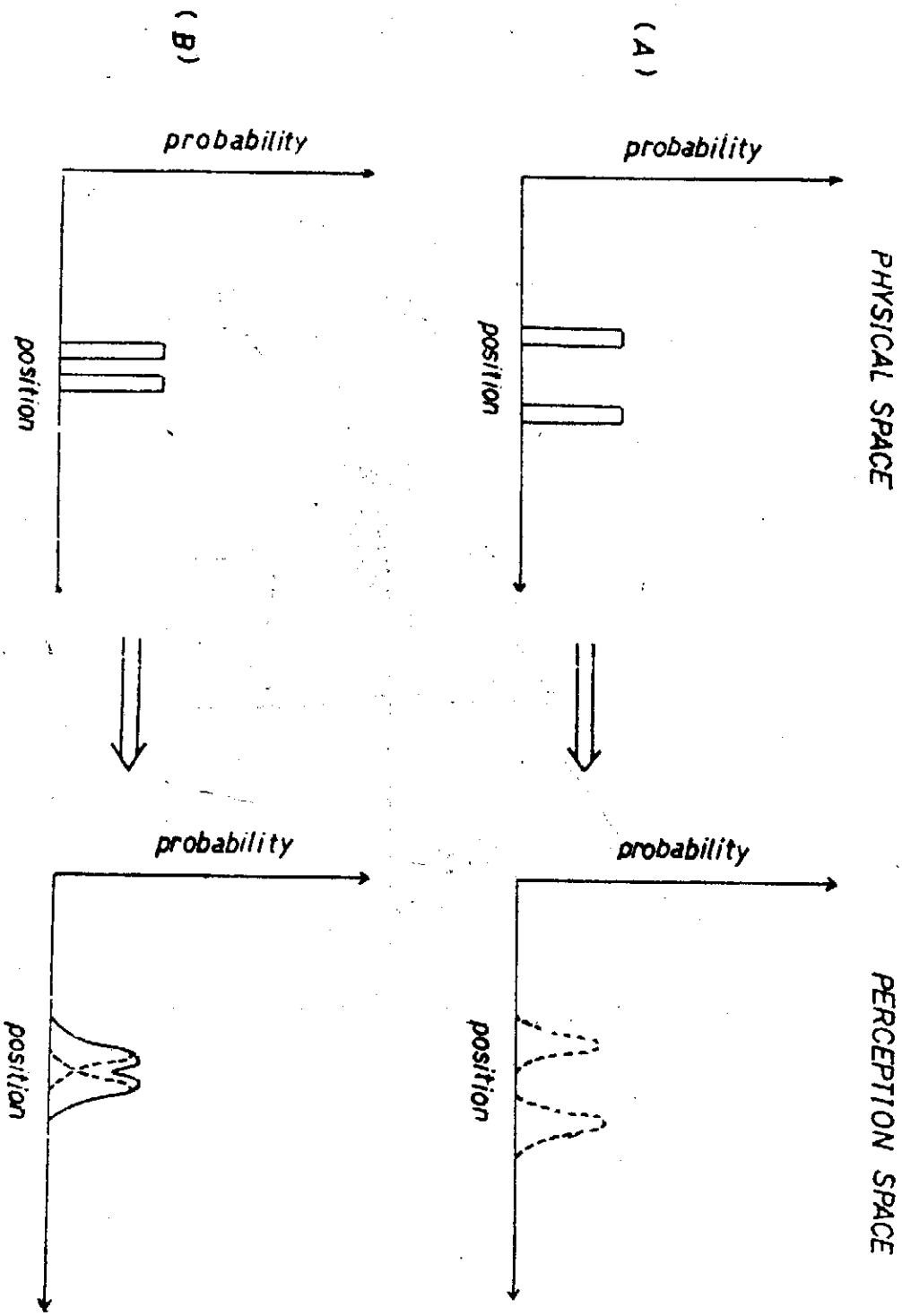

Fig. 2. The projection relationship between the physical space and the perception space. An object fixed in the physical space may be perceived to locate in different position in the perception space.
(a) when the separation between two objects is large, there is no interaction in the perception space.
(b) when the separation between two objects is samll, there is interaction in the perception space such that the maximum probability positions shift to each other.

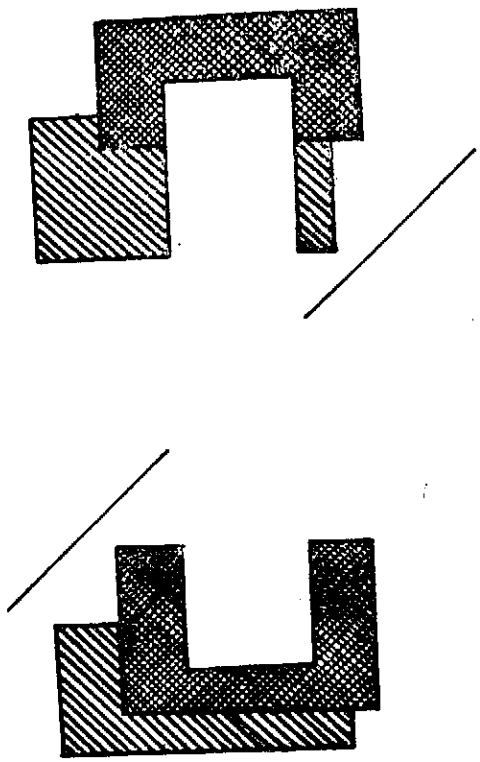

Fig. 3. A Poggendorff figure with the parallel lines replaced by contours.

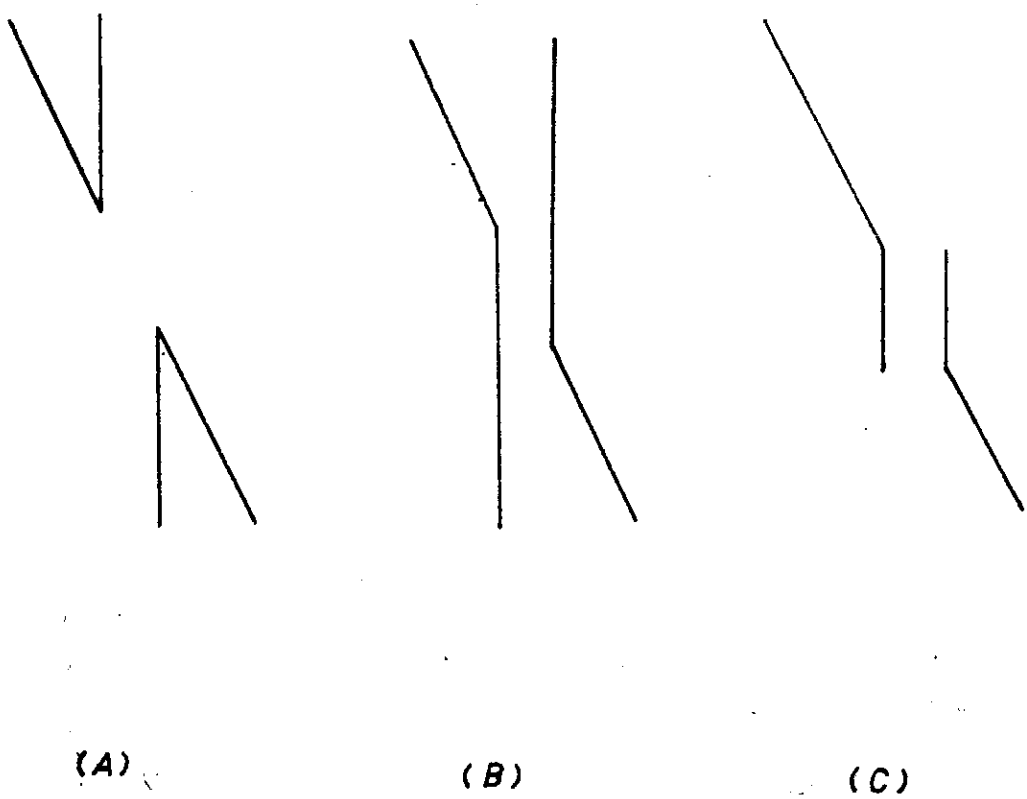

Fig. 4. Some variations of Poggendorff figure.

Annual Report of Institute of Physics, Academia Sinica, 1972

PHYSICAL BASIS OF ACUPUNCTURE AND CHING-LO SYSTEM

Chun Chiang (蔣炯)

Biophysics Laboratory
Institute of Physics
Academia Sinica
NanKang, Taipe, Taiwan
The Republic of China

The Ching-Lo has long been thought in the traditional Chinese medicine as a very essential system in the human body dated as far back as several thousands years ago (1). The traditional Chinese medicine theory, especially the acupuncture and moxibustion, has been devoloped to be quite sophisticated based on this Ching-Lo system. It was established (1) that the Ching-Lo system consists of 14 main routes running vertically and numerous horizontal routes connecting between them. These Ching-Lo are thought to be the vital transport system. However, except some subjective description, concrete experimental evidences and theoretical justifications for the existance of such a system are lacking. The existance of Ching-Lo system is particularly questioned by those with modern scientific background for the very reason that anatomically no such a system as a physically distinct entity can be found contrarily to the other system such as blood circulation in the blood vessels and impulses transmission in the nerves; for which both the blood vessels and nerves can be clearly observed anatomically. Thus, if there exists such a Ching-Lo system, how such a system may devolop under a seemingly homogeneous medium in the body becomes a major problem.

The purpose of this paper is to present some theoretical justification of such a Ching-Lo system, its implication and interaction with other system, and a summary of some experimental evidence for such a system.

In the human body, the air is pumped in and out from the lung by the contraction and expansion mechanism of the chest, and the blood circulates around the body by the heart pump. The oxygen and carbon dioxide may be exchanged between the lung and the blood, and the nutrients and waste products may also be exchanged between the blood and the tissues. Between the tissues, the exchanging processes are completed by the diffusion processes. These are all pretty well known facts. However, another flow system, the Ching-Lo system, has not been widely accepted as a foundamental system. In this paper, we define the Ching-Lo system as the route where the interstitial fluid (including both liquid form and gas form) may flow.

Anatomically, no confined route corresponding to Ching-Lo can be observed. However,

functionally we may feel its existance under certain circumstance. The situation is similar to the ocean current or atmospheric current. Even though the ocean all over is basically filled by the same chemical ingredient, namely, the water, yet the water may flow with more or less definite pattern depending on the geography, the temperature, the wind, etc. This flow is called the ocean current (2). In certain situation, the ocean currents may even flow side by side with opposite direction. Thus, even though these is no seperate physical entity such as the tube to confine the current flow, yet the current flows within certain specific route quite stably; we already understand certain causes of ocean current, however, the exact mechanisms of the current flow, especially the deep sea current are still out of our reach yet.

Other physical phenomena which are similar to the Ching-Lo system are the flow system of the underground gas, the underground petroleum and the underground water. Evidences have been gained (8) that the underground petroleum and gas can migrate from the location of its original formation to other places. That the underground water can flow the pores of the rocks and sands is established beyond question (9). This flow depends on the porosity of the underground material, the morphology and the potential.

For the human being, the chemical constituents of the tissues may be more or less the same all over the body, however, the interstitial fluid in different parts of the tissues may correlate and is co-operative, they may also flow with certain definite pattern. The route where the interstitial fluid flows is defined as the Ching-Lo. Similar to the ocean current or the underground water, the interstitial flow pattern depends on the physical structure of the human body and the morphology of the tissues, and usually flows between the bones and the tendons; the porosity of the bone and tissue is a major factor for the flow. We know that the tissue contains about 70-80% of water, and the turn-over rate of the material in the tissue is very high, it is difficult to see that such a high turn-over rate can be complished purely by diffusion processes alone. Thus a flow system similar to the underground water seems to be necessary to account for this high turn-over rate. As for the exact cause of this interstitial flow, no detailed mechanism can be proposed yet; however, it seems the breath may be the major factor. A hypothesis may be as follows: By the rhythmic contraction-expansion mechanism of the muscles from the breath, the diaphragm is pushed up and down. This movement can not only pump the air to the lung, but also set out a rhythmic pressure waves to the interstitial fluid in the abdominal area. This pressure provides the energy source and disturbs the interstitial fluid, thus the flow may migrate in a confined route according to the morphology and the structure of the body following this disturbance. If one stops breathing and all the living mechanisms (the metabolism) of the body, then the energy source is eliminated and the migration in the Ching-Lo also stops. The importance of the proper way of breathing for achieving good health has long been emphysized in the oriental excises such as Zen and Yoga.

It should be emphasized that the phrase "interstitial fluid" defined in this paper may not only mean the mass (liquid, gas, water, nutrients and hormones), but also the energy

(heat flow, electricity flow). This is also similar to the case of ocean current, which may not only include the mass movement (water, salt, bacteria, organic materials etc.), but also the energy flow (warm current, cold currnet). In the traditional Chinese medicine theory, the substance which flows in the Ching-Lo is calle Ch'i (literary means gas). However, the meaning of Ch'i is obscure; while Ch'i may mean some thing else, we define in this paper that the flow in the Ching-Lo contains mass and energy similar to the ocean current or underground water.

The above argument only shows theoretically the feasibility of an interstitial fluid flow system. The experimental evidence for this system can be summarized as follows:

1. Subjective feeling of generation and movement of interstitial fluid along the Ching-Lo during the acupuncture. It is observed that for certain people, a strong sensation of warmth may be felt along certain route of the body, radiating from the point of acupuncture. This phenomenon can hardly be explained by other means except the interstitial flow along the Ching-Lo system. The instrumental recording of some suprising physiological changes during meditation (7), which could not be understood by usual explanation, could also be understood as due to the influences through the Ching-Lo.
2. Correlation of the point of the acupuncture and the point of sickness. The path between these two points may not be the path where the nerves go through, thus the cure of desease by acupuncture may not be explained by the direct nerve influence; however, a theory based on Ching-Lo may do so. This is also similar to the traffic situation. We have both the railroad network (nerves) and highway network (Ching-Lo) around the country. The transport speed on railroad may be faster than that on the highway, however, there are certain places railroad may not reach. Similarly, the signal transmission speed by nerves may be faster, however, there are certain spots in the body where the nerves may not reach. These spots may be reached through the Ching-Lo system. With the stimulation of acupuncture, the disturbance propagates from the point of stimulation to remote places along the Ching-Lo, thus the desease in a remote spot may be cured.
3. From the electric resistance measurment of the tissue it can be shown that the tissue resistance on certain route is lower than that on other parts of the body. This electric resistance is influenced by the breathing, the detailed experimental results will be reported latter (3). We can deduce from this that there is a specific route which contains ionizable materials. This route is defined as the Ching-Lo. The fact that breath may influence the Ching-Lo electric resistance may also support the idea that breath is a major factor in the interstitial fluid movement in Ching-Lo. It is interesting to note that the electric resistance method is also used to explore the underground water. By placing the electrodes under the ground and measuring the current, one can deduce whether there is water under the ground. Similarly, by placing the electrodes in the tissue and measuring the current, we can deduce whether the Ching-Lo passes through these two points underneath the skin.

Besides the blood, nerve, and the respiration systems mentioned above, there are also

lymphatic system and endocrine system. While the lymphatic system can be observed anatomically, the endocrine system can not. Large portion of endocrine secretion may be transported through blood, many may also be transported in the Ching-Lo. The implication of a Ching-Lo system presented above is that the interstitial fluid flow may influence the blood circulation and heart rate by the coupling of diffusion process of the interstitial fluid between the Ching-Lo and the blood vessels. The situation is also similar to the fact that ocean warm current may bring nutrients and benefit the area by the diffusion process along the route of the ocean current; the transport speed and efficiency with such a Ching-Lo system is much higher than that due to the diffusion alone. The Ching-Lo may also affect the autonomic nervous system through coupling between the Ching-Lo and the nerves. Thus the part which can not be controled by the motor nerves directly may be controled indirectly by manipulation of Ching-Lo. This could give a theoretical foundation for the finding that conditioning procedures can alter autonomic functions (4-6). Some bio-feedback experiments reveal that the subjects can control their physiological functions such as heart beats, etc. even though they do not know how they did it. This and many physiological changes during meditation (7) could also be explained on this basis.

In summary, this paper gives a physical model and some theoretical justification of Ching-Lo system based on the analogy of the ocean current and underground water. A brief summary of experimental evidence is discussed, it suggests that many presently suprised medical data may be explained based on this Ching-Lo system.

REFERENCES

1. Nea-Ching and Nan-Ching. The authors and the exact date of the writing are not known.
2. G. Neumann, Ocean current, Elsevier, Amsterdam (1968); G. Dietrich, General Oceanography, Wiley & Sons, N. Y. (1967).
3. in preparation.
4. J. Hart, Psychophysiol. 4, 506(1968); J. Kamiya, Psychol. Today 1, 56 (1968).
5. N. E. Miller, Science 163, 434 (1969).
6. E. S. Katkin and E. N. Murray, Psychol. Bull. 70, 52 (1968).
7. For example, R. Wallace, Science 167, 1754 (1970).
8. A. I. Levorsen, Geology of Petroleum, W. H. Freman & Comapny, San Fransisco, California (1954).
9. C. F. Tolman, Ground water, McGraw-Hill, N. Y. (1937)

A THEORY OF ACUPUNCTURE ANESTHESIA

CHUN CHIANG (蔣炯)

Biophysics Laboratory
Institute of Physics
Academia Sinica
NanKang, Taipei, Taiwan
The Republic of China

Acupuncture has been used as a therapy to relieve various pain in the patient for several thousand years, however, the use of acupuncture as a means for anesthesia purpose is only a recent invention. However, despite the long time use of acupuncture for relieving the pain and the recent emphasis of its application in anesthesia, the mechanism of acupuncture for achieving these purposes is still not very clear.

Before we review the current theories of acupuncture anesthesia and propose a new theory, we would like to summerize some of those important facts about acupuncture anesthesia. Any proposed theory of acupuncture anesthesia should be able to incorporate these facts. They are:

(1) The anesthesia and analgesic action can be obtained by using needles made of gold, silver, stainless steel, bamboo or by appling pressure, heat or electricity at certain specific points in the body.

(2) An induction time is needed. In practice, usually 30 minutes has to be waited after the insertion of needles, before the operation can be started.

(3) Persistence effect: once achieving the anesthesia, the effect can persist for some time without further manipulating the needles.

(4) In order to achieve the anesthesia effect, the patients have to gain the feeling of soreness, swelling, heaviness and numbness.

(5) Depending on the psychological and physiological conditions of the patients, acupuncture anesthesia effect varies with individual.

(6) During acupuncture, the patient is in full conscious condition, and acupuncture anesthesia is only a local effect.

(7) During acupuncture, the nerve conduction velocity is changed.

(8) Pain on one side of the body can be relieved by stimulation of the needles on either side of the body.

(9) The feeling of the acupuncture does not necessary transmit along the nerves near the point of the stimulation. For example, the needling of Nei-Kuan in the hand initiates a feeling conducted to the sub-auxillary region and the area in front of the chest, not to the finger tips which the nerve under the Nei-Kuan would lead to.

For the explanation of these effects, it has been suggested that[1] the stimulation by needles during acupuncture would result in valleys of nerve impulses being sent along sensory fibers to the spinal cord and back to various organs and tissues along motor fibers of the ANS. Other people[2] maintain that the secret of anesthesia effect lies in the brain, the mechanism of pain relief is either due to the inhibition of the pain signals by the sensation of acupuncture in the brain cell, or, the needling at loci on the body raises the pain threshold in the cortex, thus diminishing the pain. They showed that the electroencephalogram pattern due to the pain in the high cortical region of the brain is disappeared and replaced by other signals during the acupuncture. However, this EEG pattern change alone is not sufficient to proof that the relief of pain is at brain cortex; furthermore, what is the inhibition mechanism and how the pain threshold is increased are not clear. Man[4], using the Melzack and Walls' gate-control theory[5], proposes that the overwhelming valley of impulses coming from the A-Beta fiber during acupuncture will close the gate in the substantia gelationosa and prevent the painful impulses from coming through the C fibers. Tien[3] however does not agree with the explanation of the gate control theory and presented the neurogenic interference model at the cortex. He pictured the cortical matrix as a TV screen and proposed that the recording of the pain signals on the screen can be erased by electrical signals from the acupuncture stimulation.

While these theories may all have their merits and cortex may be involved in the pain relief, it is clear that not all the facts presented above can be incorporated in their theories.

This paper suggests that the pain relief and the anesthesia effect locate at the sensory nerve. During the acupuncture, the pain signals along the sensory nerve are blocked, thus the pain signals can not transmit along the nerve, consequently the analgesic and the anesthesia effect are obtained. The blocking of the pain signals along the nerves is due to the local pressure, the electrostatic field of the ionic medium and the piezoelectricity effect.

(a) pressure effect: An important criteria for achieving the anesthesia is to gain the feeling of soreness, swelling, heaviness and numbness, and these feelings are obtained in a series. The feelings of swelling and heaviness are strong indications that the pressure has been exerted locally in the area. The insertion, pulling and twirling of the needles in the body set out a series of pressure waves, these pressure waves propagate and transport the interstitial fluid along the route which is best suitable for propagation. The existance of such kind of route for interstitial fluid movement has long been proposed and the physical basis for the posibility of such a system has recent been discussed[6]. This route is called Ching-Lo in traditional Chinese medicine and distributes all over the body, but not necessary follow the nerve distribution. If there is nerve passing near this propagation route, the nerve will be pressured locally, thus-the nerve conduction velocity may be changed and the pain signals may be modified or blocked; consequently the pain can not transmit from its origin to the pain perception center in the cortex. We all have the experience that when we sit in one posture for a long period, our feet may temporarily be swollen and immobilized; this may partially be due to the local pressure effect. Also, many authors[7,8]

[9,10] have reported that, for the nerves in vitro, the hydrostatic pressure can decrease the conduction velocity and the amplitude of the action current, can increase the spike duration and the refractory period. Schaffeniels[11] has shown that the hydrostatic pressure can modify the skin membrane potential and Chiang[13] has interpreted this as due to the pressure effect on the biochemical reactions involved in the active transport. All these evidences show indeed that the pressure can modify the membrane potential and thus interfere or block the normal pain signals from transmitting along the nerves. Application of heat, instead of needle, would expand the interstitial fluid and also sets out the heat and pressure waves slong the Ching-Lo to interfere with the nerve transmision.

(b) Electrostatic effect: The interstitial fluid may contain highly ionizable materials such as water, CO_2 and organic acids; when these materials are transported to the area near the nerve, they may diffuse across the nerve memberane. These highly ionizable material may short-circuit the membrane and the signals transmision along the nerve may be blocked, The situation is very similar to the interference of radio communication by the explosion of the black spots on the sun. The tremendous output of the radio wave from the sun black spot can interfere and block the normal comunication radio waves. Furthermore, the hormones and endocrine secretion may be distributed in the interstitial fluid in the Ching-Lo system; that the hormones and enzymes can modify the active transport and the membrane potential is well known[15,16], and this may strongly inhibit the signal transmission along the nerves.

(c) Piezoelectricity effect: Shamos and Lavine[18] have shown that soft tissues such as skin, callus and cartilage as well as the hard tissues such as bone and tendon can exhibit the piezoelectricity, a property for a group of well ordered molecules to exhibit electrical charges on their surfaces when mechanically stressed or, conversely, to form strains when their surfaces are electrically charged. The twirling and pulling of the needle during acupuncture may produce electrical signals due to the tissues' piezoelectricity, the produced electrical signals together with the pressure waves may popagate along the route which is most easily for the signals to pass through. The Ching-Lo system may have this required property. Fisch[14] has shown that one can pick up electrical signals from Ching-Lo system when a remote point on Ching-Lo system is stimulated; on the other hand, if the stimulation point is not on the Ching-Lo, no electrical signals can be picked up even if the stimulation point is very near to the pick-up points. This electrical signals together with its mechanical stress due to tissues' piezoelectricity can interfere with the nerves near by and the pain signals may be blocked.

It can be seen that all above three processes need time to develop. It takes time to propagate and transport the interstitial fluid from the stimulation point to the point where nerve can interact; furthermore, the ionizable material have to diffuse from outside of the nerve membrane to the inside of the nerve membrane. This explains that the induction time is required for anesthesia. Once the interstitial fluid is built up at the interaction point, it

takes time for the diffusion process to restore the tissues and nerve membranes to the normal conditions; this explains the persistence effect of anesthesia.

Depending on the physiological and psychological condition of the patient, the anesthesia effect varies with individual. This is because the amount of the interstitial fluid varies with the physiological condition of the individual, and the psychological state of the patient influences the physiological condition such as muscle tremble, irritation, etc. The muscle tremble and irritation may hider the movement of the intersitial fluid thus reduce the anesthesis effect.

In summary, we have proposed that the needle stimulation can mobilize the intersitial fluid. This fluid can exert pressure, electrostatic and piezoelectricity effect locally on the nerves. This kind of interactions prevent the pain signals from trasmitting along the nerves. It seems that this theory can nicely explain all those important facts about the acupuncture anesthesia.

1. Smith, A. E. and Kenyon, D. H., Am. J. Chinese Med., 1, 91 (1973).
2. Am. J. Chinese Med., 1, 159 (1973).
3. Tien, H. C., Am. J. Chinese Med., 1, 105 (1973).
4. Man, P. L., International Symp. on Acupuncture pp.48 (1973), Monarch Services. St. Petersburg, Florida, U. S. A.
5. Melsack, R. and Wall, P. D., Science, 150, 971 (1965).
6. Chiang, C., Physical Basis of Acupuncture and Ching-Lo system, submitted for consideration.
7. Spyropoulos, C. S., Am. J. Physiol. 189, 214 (1957).
8. Grundfest, H. and Cattell, M., Am. J. Physiol. 113, 56 (1935).
9. Grundfest H., Cold Spring Harbor Symp., Quant. Biol., 5, 179 (1936).
10. Ebbecke, V. and Schaefer, H.,Pfluger's Arch. ges. Physiol. 236, 678 (1935).
11. Schaffeniels, E., Cellular Aspects of membrane permability, pp.223 (1967), Pergamon Press, Oxford, England.
12. Chiang, C., Properties and responses of frog skin membranes, submitted for publication.
13. Shamos, M. H. and Lavine, L. S., Nature (London), 213, 267 (1967).
14. Fisch, G., International Symp. on Acupuncture, pp. 112 (1973) Monarch Services, St. Petersburg, Florida, U. S. A.
15. Johnston, K. H.,and Hoshiko, T., Am. J. P hysiol., 220, 792 (1971).
16. Katchalski, E., Silman, I. and Goldman, R., In Advances in Enzymology (Ed. F. F. Nord) 34, 445 (1971) Interscience, N. Y.

Annual Report of Institute of Physics, Academia Sinica, 1972

ON MEMORIZING SOME THERMODYNAMIC EQUATIONS

Chun Chiang (蔣炯)

Institute of Physics
Academia Sinica
NanKang, Taipei, Taiwan,
The Republic of China

Thermodynamics is a very important subject for a science student; however, the throughout understanding of this subject presents some problems to the students. One of the difficulties may be due to the numerous equations involved in the subject. Despite many existing methods (1-12) designed to help the students to understand and memorize the equations, it seems that the difficulties still exist.

Most methods mentioned in the reference 1-12 arrange the thermodynamics symbols orderly in a diagram, and the required equations are derived from this diagram following certain specific rules, The short coming of these methods is that: a diagram have to be drawn, and time is wasted in doing this. Furthermore, in deducing the required equations from this diagram, considerable effort and time is required and mistakes may happen.

The purpose of this note is to present a few simple rules such that one can easily write down many equations without referring to the diagram. These rules are easily remembered and may give the students some feeling of understanding. Eventhough memorization should not be emphasized in studing the subject, neverthless, proper method of memorization these equations does seem to help and facilitate the understanding of the whole subject. It saves the student a lot of time.

The equations covered in these rules are:

$$dE=TdS-PdV \tag{1}$$

$$dH=TdS+VdP \tag{2}$$

$$dA=-SdT-PdV \tag{3}$$

$$dG=-SdT+VdP \tag{4}$$

$$\left(\frac{\partial E}{\partial S}\right)_V=T, \qquad \left(\frac{\partial E}{\partial V}\right)_S=-P \tag{5}$$

$$\left(\frac{\partial H}{\partial S}\right)_V=T, \qquad \left(\frac{\partial H}{\partial P}\right)_S=V \tag{6}$$

$$\left(\frac{\partial A}{\partial T}\right)_V=-S, \qquad \left(\frac{\partial A}{\partial V}\right)_T=-P \tag{7}$$

$$\left(\frac{\partial F}{\partial T}\right)_P=-S, \qquad \left(\frac{\partial F}{\partial P}\right)_T=V \tag{8}$$

and the Maxwell equations

$$-\left(\frac{\partial P}{\partial S}\right)_V=\left(\frac{\partial T}{\partial V}\right)_S \quad (9) \qquad \left(\frac{\partial P}{\partial T}\right)_V=\left(\frac{\partial S}{\partial V}\right)_T \quad (10)$$

$$-\left(\frac{\partial P}{\partial S}\right)_T=\left(\frac{\partial T}{\partial V}\right)_P \quad (11) \qquad \left(\frac{\partial P}{\partial T}\right)_S=\left(\frac{\partial S}{\partial V}\right)_P \quad (12)$$

Eqs.(1)-(4) can be derived from the thermodynamics first law

$$dE=dQ-PdV \quad (13)$$

and from the following definitions

$$dQ=TdS \quad (14)$$

$$H=E+PV \quad (15)$$

$$A=E-TS \quad (16)$$

$$G=H-TS \quad (17)$$

Eqs.(5)-(8) can be deduced from eqs.(1)-(4), and Eqs.(9)-(12) can be derived from eqs.(5)-(8) by deferentiation.

The rules we would like to propose are:

1. P and V are always in a pair, T and S are always in a pair. This is easily remembered because the products of both P, V and T, S is the energy. Furthermore, if one element in the pair is the *numerator* of one side of the equation, then the other element in the pair must be the *denominator* of the other side of the equation and vice versa.
2. For Maxwell equations, if the *subscript* and the *denominator* belong to the same pair on one side of the equation, then the *subscript* and the *denominator* on the other side of the equation must also belong to the same pair. If the *subscript* aod *numerator* belong to the same pair on one side of the equation, then the *subscript* and the *numerator* on the other side of the equation must also belong to the same group.
3. For Eqs.(1)-(8), P and S are negative and other elements are positive. For eqs.(9)-(12), the negative sign is adopted when P and S are on the same side of the equation, otherwise, positive sign is adopted.
4. In Eqs.(1)-(4) the infinitesimal elements E, S, V form a group, H, S, P form a group, A, T, V form a group and G, T, P form a group. These infinitesimal elemets of the groups can be memorized by extracting the alphabats from the words *ELVES*, *HOPES*, *GET-UP* AND *ADVENTURE*. These infinitesimal elements in the group can also apply to the partial derivatives in Eqs.(5)-(8).

Once we understand the meaning of above rules, they can be easily remembered without much effort. With these rules, Eqs.(1)-(12) can be written down immediatly without any hesitation. This not only can help the students for the examination, but may also facilitate the understanding for the thermodynamics.

A few examples of the application of these rules are as follows:

1. In order to write down eq.(1), we extract E, V, S from the word "ELVES", thus:
   dE=?dV+?dS,
   From rule 1, P and V form a group, S and T form a group, thus
   dE=PdV+TdS,

From rule 3, P is negative and T is positive, thus we obtain

$dE=-PdV+TdS$.

Eqs.(2) (3) can be written down similarly.

2. In order to write down Eq.5, we also extract the alphabats E, V, S from the word "*ELVES*" to form the partial derivatives $(\frac{\partial E}{\partial V})_S$ or $(\frac{\partial E}{\partial S})_V$. By rule 1, P and V from a pair, S and T form a pair, thus

$(\frac{\partial E}{\partial V})_S=P$, and $(\frac{\partial E}{\partial S})_V=T$.

From rule 3, P is negative and T is posive, thus we obtain

$(\frac{\partial E}{\partial V})_S=-P$, and $(\frac{\partial E}{\partial S})_V=T$.

Eqs.(6)-(8) can be written down similarly.

3. To complete the following equations

$(\frac{\partial P}{\partial S})_V=?$ $(\frac{\partial P}{\partial S})_T=?$

Using rule 1, we have

$(\frac{\partial P}{\partial S})_V=(\frac{\partial T}{\partial V})$ and $(\frac{\partial P}{\partial S})_T=(\frac{\partial T}{\partial V})$

Using rule 2, we have

$(\frac{\partial P}{\partial S})_V=(\frac{\partial T}{\partial V})_S$ and $(\frac{\partial P}{\partial S})_T=(\frac{\partial T}{\partial V})_P$

Finally, using rule 3, we obtain

$-(\frac{\partial P}{\partial S})_V=(\frac{\partial T}{\partial V})_S$ and $-(\frac{\partial P}{\partial S})_T=(\frac{\partial T}{\partial V})_P$

REFERENCES

1. Chrstie, D. E., Am. J. Phys. 25, 486 (1957).
2. Focken, C. M., Am. J. Phys. 16, 450 (1948); 17, 225 (1949).
3. Haisley, W. E., Am. J. Phys. 17, 91 (1949).
4. Bugosh, J., Am. J. Phys. 17, 91 (1949).
5. Brinkman, H. C., Am. J. Phys. 17, 170 (1949).
6. Payne, R. E., Am. J. Phys. 17, 225 (1949).
7. Turner, L. A., Am. J. Phys. 17, 397 (1949).
8. Crawford, F. H., Am. J. Phys. 17, 450 (1949).
9. Satterly, J., Am. J. Phys. 18, 235 (1950).
10. Pietsch, L., Am. J. Phys. 18, 468 (1950).
11. Gilvarry, J. J., Am. J. Phys. 19, 131 (1951).
12. Cheng, C. C., Am. J. Phys. 38, 956 (1970).

Annual Report of the Institute of Physics, Academia Sinica, 1972

The Conduction Electron Spin Resonance of a Sodium Film

Juh Tzeng Lue

Department of Physics, National Tsing Hua University
Hsinchu, Taiwan, China

and

Nai Tsung Liang (梁乃崇)

Institute of Physics, Academia Sinica
Nankang, Taipei, Taiwan

I. Introduction

In this paper we use the usual homodyne reflection spectrometer to study the conduction electron spin resonance (CESR) of sodium and lithium films whose thicknesses range from 0.3 to 30 skin depths. The experimental results can be verified by Dyson's theory. The thickness dependence of the line shapes and the temperature dependence of the spin-lattice relaxation have been measured in this work. The whole theory and experimental technique can be referred from one of the authors' (Lue) Ph.D. thesis[1].

2. Experimental details

The alkali metals that purchassed commercially with purity of 99.9% were evaporated by vacuum on a mica plate to a thickness between o.3 to 30 skin depth. If We want to take this films out of vacuum system, we must protect them against the air, because the alkali metals are very activity which react with O_2 and H_2O in the air virously. We had used SiO film, Si oil and paraffin wax to protect the alkali metal films against the air, only paraffin wax succeeded, because it had lower melting point and no influence in ESR signal. The melting point of the paraffin wax had a range from 60°C to 90°C, the lower was be selected. When the alkali metal films were made in 4×10^{-6}torr. vacuum system, the paraffin wax was heated to liq. state and no more than 70°C, to dip the films in the liq. state paraffin wax, then we could take the film out of vacuum system because this films were protected by paraffin wax.

To measure the thickness of the alkali metal films were difficult, when the quartz crystal thickness monitor was used. The reason is that the alkali metals are active metals, they can damage the gold film on the quartz crystal. A SiO film was evaporated to odd on the gold film of the quartz crystal, to protect it. But the protected effect was very low. Finally, the thickness were measure by monitor the resistance of the film. On the substrate, two equal thickness films were made (see Fig. 1), one was used to measure the

thickness, the other was used for ESR. The resistivity of sodium is 4.3 $\times 10^{-6}\Omega$-cm, from equation $t=4.3\times10^{-6}\frac{\ell}{d\times R,}$ the thickness of film is got by it's resistance.

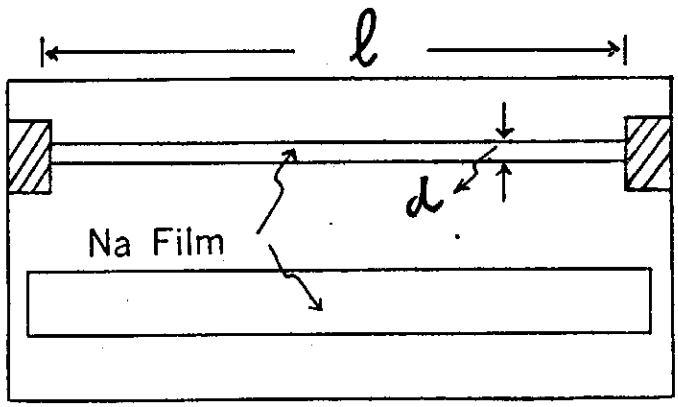

Fig. 1

At temperature between 100°K, the measurements were performed by using an Varian band homodyne reflection spectrometer. The film samples surrounded by a quartz dewar were mounted in a multipurpose rectangular cavity of mode TE_{102}. A 100kc/sec modulation field is used in order to improve the signal to noise ratio, To avoid the saturation effect, the microwave power is attenuated as high as possible. In our measurements the microwave power is attenuated 20 db down from a 400 MW klystron. In this work, we have measured the g-value at high temperatures, and also have measured the temperature dependence of spin-lattice relaxation times, of line shapes.

The magnetic field is stabilized to 1 part in 10^5 by the derivative field stabilization. By Lentz's law, if a coil is placed in the field of a magnet and the field varies, there develops within the coil an e.m.f. that is proportional to the rate of change of field. The e.m.f. is the error voltage which can be coupled to an D.C. amplifier and then, fed into the main amplifier of the magnet power supply to keep zero rate of change of the field.

Precise measurement of g-value requires careful determination of the magnetic field and the microwave frequency at which resonance occurs. The best accuracy in determination of the absolute magnitude of a magnetic field is obtained with an NMR fluxmeter. The fluxmeter made by one of us (Lue) has the stability of the frequency of the proton of one part in 10^8. The gyromagnetic ratio of the proton is known only to one part in 10^5, resulting in an absolute accuracy in measurement of the field of two parts in 10^6. To measure the microwave frequency, a Hewlett-Packard 5257A transfer oscillator accompanied with an 5245M electronic counter is used. The frequencies measured can have accuracies of 1 part in 10^5.

The temperature variation setup was similar to that of Walsh, Jeener and Bloember-

gen[3]. To avoid the shift of the base line of the spectrum due to the variation of the temperature of the cavity, the cavity is blown cold air or hot dry air depends on whether the temperature of the cavity is above or below room temperature.

3. Theory of the Line Shape and Surface Spin-Lattice Relaxation Time

The experimentally measured CESR line is the first derivative with respect to field of the r.f. power absorbed by the sample. Lampe and Platzman[3] have used Dyson's technique[4] to solve for the line shape in a plate where the thickness of the film is far greater than the skin depth subject to the boundary condition that the r.f. field is pointing perpendicularly inside the two faces of the film with equal magnitude but in opposite of sign. The power absorbed by the sample is

$$P=(\frac{c}{4\pi})^2 H_1^2 \; Re(Z),$$

where H_1 is the amplitude of the linearly polarized field at the surface of the film, and the surface impedance Z is given by

$$Z=\frac{\rho}{d}[F+(\pi\omega_0 T_2 X_0 d^2/\delta^2 e)G]$$

where

$$F=-4utanu$$
$$G=-i(u^2-\omega^2)^{-2}\{2u^2\omega^{-1}tan\omega-(3u^2-\omega^2)u^{-1}tan\,u$$
$$+4u^2tan^2u[(u^2-\omega^2)csc^2u+(3u^2-\omega^2)u^{-1}cot\,u$$
$$-2u^2\omega^{-1}cot\omega]\}$$

with d is the sample thickness and

$$u=(Hi)d/2\delta,\quad \omega=(\xi+i\eta)d/2\delta_e$$
$$\eta=[(1+x^2)^{1/2}+1]^{1/2},\quad \xi=(Sgnx)[(1+x^2)^{1/2}-1]^{1/2}$$

where $X=(\omega-\omega_0)T_2$, $\delta=(c^2\rho/2\pi\omega)^{1/2}$ is classical skin depth and $\delta_e=(2DT_2)^{1/2}$ is the spin depth-the distance perpendicular to the surface that a spin can diffuse in one relaxation time. D is the diffusion constant. The theoretical line shape is given in Fig. 4.3 of ref. 1.

Dyson finds the total spin relaxation time T_2 in film-thickness small in comparison to a skin depth is given by

$$1/T_2=1/T_1+1/T_s$$

where T_1 is the usual spin lattice relaxation time and Ts, the surface relaxation time is given by

$$T_s=-\frac{4V}{\epsilon vS}$$

where V is the volume and s the surface area of the sample, and ϵ=probability of a spin disorientation during a surface collision, and v=velocity of electrons at the top of the Fermi surface. The ϵ is found to be approximately equal to 10^{-4}.

4. Experimental results

For very thin films the line shape is totally absorptive, while for very thick ones it is dispersive. This has been proved experimentally. The best way to measure the line shape is to measure the A/B ratio, i.e. the ratio of the low field maximum and high field maximum. The A/B ratio is extremely sensitive to the condition of the surface of the sample. If the samples prepared have been stored several days there showed a large deviations in the A/B ratio, which may athibuted to surface oxidation. The data shown in Fig. 2 is satisfactorily agree with the theory.

For thick clean films where $\delta/\delta_e \ll 1$, the line should be a Lorentzian dispersion line with A/B=8.0 independent of d. For thin films with d comparable to δ, then $d/\delta_e \ll 1$, the line shape is a mixture of the derivatives of the absorptive and dispersive parts of a Lorentzian line. For very thin films the line shape is totally absorptive and the line width increase greatly as the thickness decrease. The relaxation between linewidth H and the thickness d/δ is shown in Fig. 3.

References

(1) J.T. Lue, The Temperature Dependence of Conduction Electrons in Pure and Impure Alkali Metals, Ph.D. Thesis, Duke University, 1973.
(2) W.M. Walsh, Jr., J. Jeener and N. Bloembergen, Phys. Rev. 139, A1338, 1965.
(3) M. Lampe and P.M. Platzman, Phys. Rev. 150, 340, 1966.
(4) F. Dyson, Phys. Rev. 98, 349, 1955.

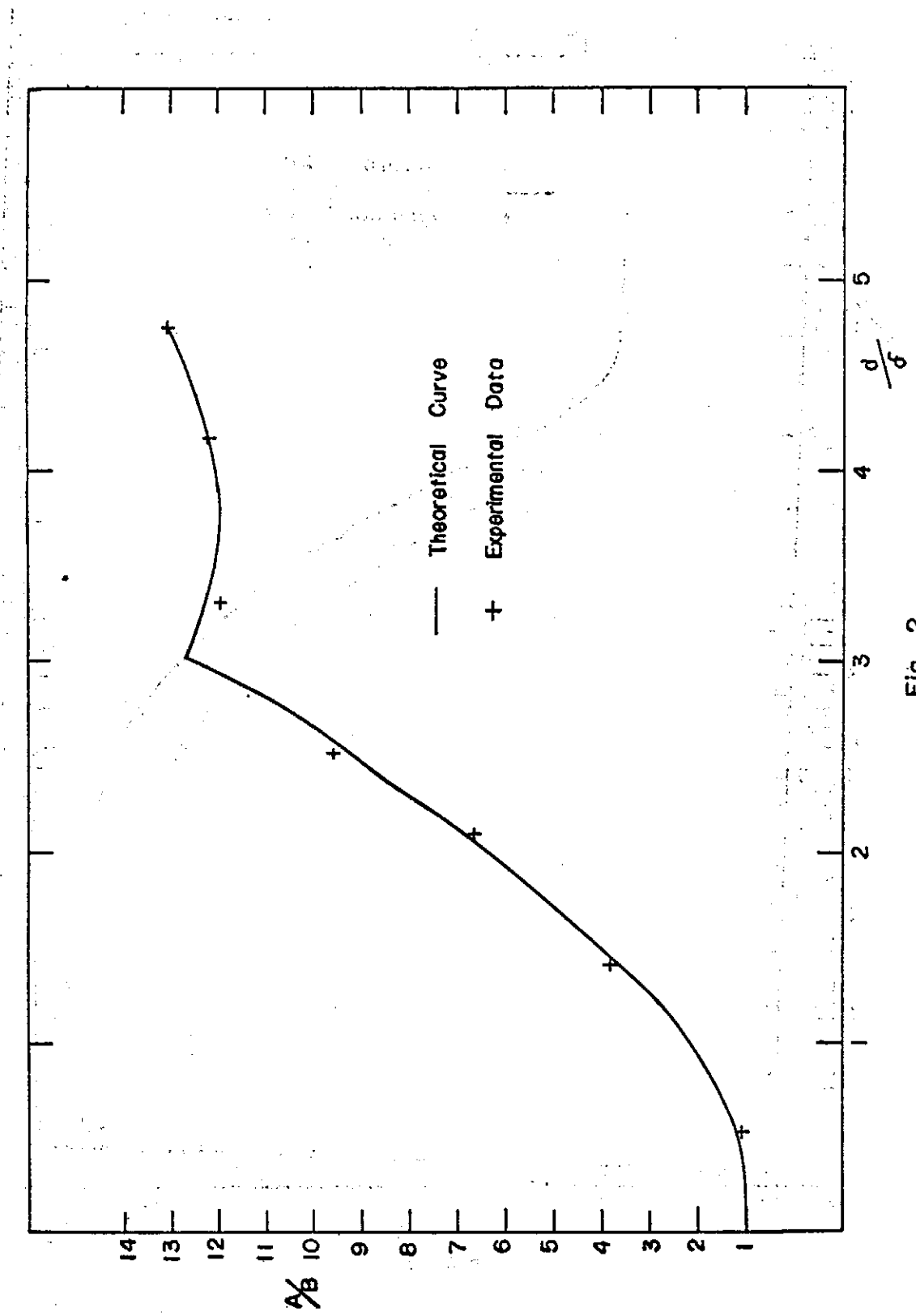
Theoretical Curve
Experimental Data
A/B
d/δ
1
2
3
4
5
6
7
8
9
10
11
12
13
14

Fig. 2

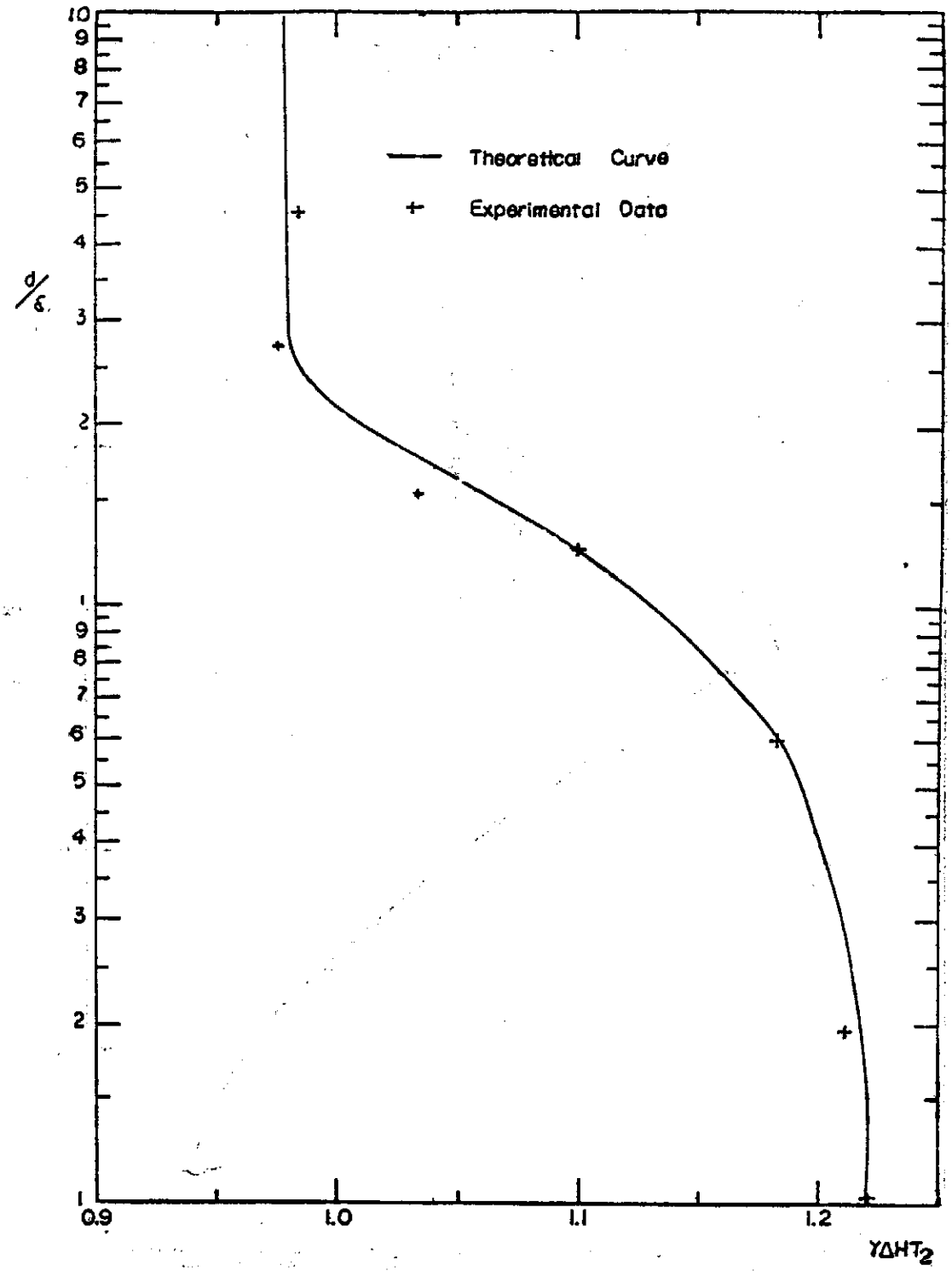
Theoretical Curve
Experimental Data
d/δ
10
9
8
7
6
5
4
3
2
1
0.9
1.0
1.1
1.2
γΔHT2

Fig. 3

Group-Theorectical Study of the Stark Effect of Acceptor in Germanium

S. S. Tai

Institute of Physics, Academia Sinica

ABSTRACT

This article uses group-theorectical techniques to deduce energy splitting and relative intensities of Stark components of electic-dipole transition lines of a single-hole acceptor in germanium. Results are obtain for different orientation of electric field: $\vec{E}\|[100]$, $\vec{E}\|[111]$, $\vec{E}\|[110]$, $\vec{E}$ in (001) and (110) plane. For some special directions, the last two cases would be reduced to first three cases. The relative intensities of a $\Gamma_8 \rightarrow \Gamma_8$ transition would be expressed in term of two real parameters, one of which can be determined from a measurment with electric field along [111] direction. In an uniform electric field only the four-fold degenerate states will split into two twofold degenerate states, and the twofold degenerate states would not split.

I. INTRODUCTION

Infared absorption spectrum of a neutral acceptor from groud state to various excited states are first observed by Burstein, [1,2] Since then the group III. impurties in group IV elements are studid extensively.[3-13] The effect of external pertubation such as magnetic field,[14,15] uniaxial stress,[16-19] electric field[20] provided a powerful means for determination of symmetry and lebelling the states of impurities. Theoretical works on this problem based on the effective mass approximation[21,22] have been developed and group-theorectical[23,24] study of the excitation spectrum of a single-hole acceptor were also been reported. In this work, we present a group theorectical study the relative intensities of Stark components of excitation lines. It is well know that the valence band of germanium exhibits spin-orbit splitting, the $p_{3/2}$ valence band lying above $p_{1/2}$ valence band about 0.29 ev.[25] thus we would neglect the effect of lower band. In this work, we established group-theoretical study of energy splitting in Sec. 11. and relative intensities of Stark components in Sec. III for five different directions $\vec{E}\|[001]$, $\vec{E}\|[111]$, $\vec{E}\|[110]$, $\vec{E}$ in (001) and (110) plane. Our procedure for calculating the relative intensities is based on the method developed by Rodrigues.[26,27] The relative intensities that are most determined at most by two parameters which related to dipole transition matrix elements.

II. Theory

A substitutional impurity of group-IV semiconductor is belonged to tetrahedral (T_d) symmetry. We now deal with a system containing a single hole with a particle of spin 1/2 bounded to an acceptor atom. The states of the system are characterized according to a

double-valued representation of $\overline{T}_d = D_{1/2} \times T_d$. The irreducible representations of group are given in Table 1, where X, Y, Z, behave as x, y, z which are the components of a polar vector with respect to cubic axis of crystal and ξ, η, ζ are behave as axis vector. The products of the basis functions of T_d with $|\downarrow\rangle$, $|\uparrow\rangle$ generate double-valued representation of $\overline{T}_d$. The characteristic table of $\overline{T}_d$ are given in Table II. From group theorem, there are two types of Γ_6 functions, two types of Γ_7 functions and three types of Γ_8 functions:

$$
\begin{aligned}
&\phi^{6}_{\frac{1}{2}} = f|\downarrow\rangle, \qquad \phi^{6}_{-\frac{1}{2}} = f|\downarrow\rangle;\\
&\Lambda^{6}_{\frac{1}{2}} = \frac{1}{\sqrt{3}}[(\xi+i\eta)|\uparrow\rangle + \zeta|\uparrow\rangle],\\
&\Lambda^{6}_{-\frac{1}{2}} = \frac{1}{\sqrt{3}}[(\xi-i\eta)|\uparrow\rangle - \zeta|\downarrow\rangle];\\
&\phi^{7}_{\frac{1}{2}} = -\frac{1}{\sqrt{3}}[(X+iY)|\downarrow\rangle + Z|\uparrow\rangle],\\
&\phi^{7}_{-\frac{1}{2}} = \frac{1}{\sqrt{3}}[(X-iY)]|\uparrow\rangle - Z|\downarrow\rangle];\\
&\Lambda^{7}_{\frac{1}{2}} = g|\uparrow\rangle, \qquad \Lambda^{7}_{-\frac{1}{2}} = g|\downarrow\rangle;\\
&\phi^{8}_{\frac{3}{2}} = -\frac{1}{\sqrt{2}}[(X+iY)|\uparrow\rangle],\\
&\phi^{8}_{\frac{1}{2}} = -\frac{i}{\sqrt{6}}[(X+iY)|\downarrow\rangle - 2Z|\uparrow\rangle],\\
&\phi^{8}_{-\frac{1}{2}} = -\frac{1}{\sqrt{6}}[(X-iY)|\uparrow\rangle + 2Z|\downarrow\rangle],\\
&\phi^{8}_{-\frac{3}{2}} = \frac{i}{\sqrt{2}}[(X-iY)|\downarrow\rangle];\\
&\Lambda^{8}_{\frac{3}{2}} = -\frac{1}{\sqrt{6}}[(\xi-i\eta)|\downarrow\rangle + 2\zeta|\downarrow\rangle],\\
&\Lambda^{8}_{+\frac{1}{2}} = \frac{i}{\sqrt{2}}(\xi-i\eta)|\downarrow\rangle,\\
&\Lambda^{8}_{-\frac{1}{2}} = -\frac{1}{\sqrt{2}}(\xi+i\eta)|\uparrow\rangle,\\
&\Lambda^{8}_{-\frac{3}{2}} = \frac{i}{\sqrt{6}}[(\xi+i\eta)|\downarrow\rangle - 2\zeta|\uparrow\rangle];\\
&\chi^{8}_{\frac{3}{2}} = \omega_1|\downarrow\rangle,\\
&\chi^{8}_{\frac{1}{2}} = +i\omega_2|\uparrow\rangle,\\
&\chi^{8}_{-\frac{1}{2}} = \omega_2|\downarrow\rangle,\\
&\chi^{8}_{-\frac{3}{2}} = i\omega_1|\uparrow\rangle.
\end{aligned}
\tag{1}
$$

The most general form of wave functions are a linear combination of these types

functions. The functions of the three sets $\{\phi_M\}$, $\{\Lambda_M\}$, $\{X_M\}$ are orthorgonal to one another and belong to the same row of Γ_1. The set of functions $\{\phi_M\}$ are eigenfunction of total angular momentum $\vec{J}$ and of J_z. In this representation, the corresponding angular momentum matrix for Γ_6 and Γ_7 are

$$J_x=\frac{1}{2}\begin{bmatrix}0&1\\1&0\end{bmatrix},\quad J_y=\frac{1}{2}\begin{bmatrix}0&-i\\i&0\end{bmatrix},\quad J_z=\frac{1}{2}\begin{bmatrix}1&0\\0&-1\end{bmatrix}. \tag{2}$$

and for Γ_8 states are

$$J_x=\frac{i}{2}\begin{pmatrix}0&\sqrt{3}&0&0\\-\sqrt{3}&0&2&0\\0&-2&0&\sqrt{3}\\0&0&-\sqrt{3}&0\end{pmatrix},\quad J_y=\frac{1}{2}\begin{pmatrix}0&\sqrt{3}&0&0\\\sqrt{3}&0&2&0\\0&2&0&\sqrt{3}\\0&0&\sqrt{3}&0\end{pmatrix},$$

$$J_z=\frac{1}{2}\begin{pmatrix}3&0&0&0\\0&1&0&0\\0&0&-1&0\\0&0&0&-3\end{pmatrix}. \tag{3}$$

TABLE 1. Characteristic table and basis functions for group T_d.

T_d	E	$8C_3$	$3C_2$	$6S_4$	$6\sigma_d$	Basis functions
Γ_1	1	1	1	1	1	$f:X^2+Y^2+Z^2$
Γ_2	1	1	1	1	−1	g
Γ_3	2	−1	2	2	0	$\omega_1:2Z^2-X^2-Y^2$, $\omega_2:\sqrt{3}(X^2-Y^2)$.
Γ_4	3	0	−1	1	−1	ξ,η,ζ.
Γ_5	3	0	−1	−1	1	X,Y,Z.

which are the angular momentum operators for manifolds of constant J.

In order to get the most general form of Hamiltonian, we make use the fact H_E must belong to Γ_1 representation. $\vec{E}$ transforms like polar vector and like the representation Γ_5 of the tetrahedral. Therefore one can classified E_i E_j according to their transformation properties under tetrahedral group,

$$\begin{aligned}&\Gamma_1: E_x^2+E_y^2+E_z^2,\\&\Gamma_3: 2E_z^2-E_x^2-E_y^2,\ \sqrt{3}(E_x^2-E_y^2),\\&\Gamma_4: E_iE_j,\ i\neq j,\\&\Gamma_5: E_x,\ E_y,\ E_z,\end{aligned} \tag{6}$$

where E_x, E_y, E_z are refere to cubic axes of the crystal.

$\vec{J}$ transforms like an axial vector and belongs to Γ_4 representation of T_d group. For $J=\frac{3}{2}$ states, one can get 16 linearly independent matrices, classifying according to their transformation properties,

$$\Gamma_1: J_x^2+J_y^2+J_z^2;$$
$$\Gamma_2: J_xJ_yJ_z+J_zJ_yJ_x;$$
$$\Gamma_3: 2J_z^2-J_x^2-J_y^2,\ \sqrt{3}(J_x^2-J_y^2);$$
$$\Gamma_4: J_x, J_y, J_z, J_x^3, J_y^3, J_z^3;$$
$$\Gamma_5: \{J_x,J_z\}=U_x, \{J_z,J_x\}\equiv U_y,\ \{J_x,J_y\}\equiv U_z,$$
$$\{J_x,(J_y^2-J_z^2)\}\equiv V_x,\ \{J_y,(J_z^2-J_x^2)\}\equiv V_y,$$
$$\{J_z,(J_x^2-J_y^2)\}\equiv V_z; \tag{7}$$

where $\{P,Q\}=\frac{1}{2}(PQ+QP)$.

Constructing out of the J's and E's which are invariant under tetrahedral group,

$$(E_x^2+E_y^2+E_z^2),$$
$$2(E_z^2-E_x^2-E_y^2)\ (2J_z^2-J_x^2-J_y^2)+3(E_x^2-E_y^2)\ (J_x^2-J_y^2),$$
$$E_xJ_x+E_yJ_y+E_zJ_z,\ E_xJ^3{}_x+E_yJ_y^3+E_zJ_z^3, \tag{8}$$

TABLE 11. Character table for the doubled-valued group $\overline{T}_d$

$\overline{T}_d$.	E	$\overline{E}$	$8C_3$	$8\overline{C}_3$	$3C_2, 3\overline{C}_2$	$6S_4$	$6\overline{S}_4$	$6\sigma_d, 6\overline{\sigma}_d$
Γ_6	2	−2	1	−1	0	$\sqrt{2}$	$-\sqrt{2}$	0
Γ_7	2	−2	1	−1	0	$-\sqrt{2}$	$\sqrt{2}$	0
Γ_8	2	−4	−1	1	0	0	0	0

11. Splitting of Impurity Levels in Static Electric Field

The symmetry group of Ge is tetrahedral symmetry. It is assumed that the foreign atom does not alter this symmetry, The Hamiltonian of a particle with charge q in a electric field is $-q\vec{E}\cdot\vec{r}$. In the first approximation, the corresponding matrix element vanish since the wave functions belong to symmetry T_d and the matrice of any odd operator on them are zero. Thus we must consider the second order approximation and the Hamiltonian is proportional to $(\vec{E}.\vec{r})^2$. In the presence of electric field, the Hamiltonian of the hole can be classified according to the symmetry properties of tetrahedral group:

$$H_E=\tfrac{1}{3}(E_x^2+E_y^2+E_z^2)(x^2+y^2+z^2)+\tfrac{1}{6}(2E_z^2-E_x^2-E_y^2)\ (2z^2-x^2-y^2)+\tfrac{1}{2}(E_x^2-E_y^2)$$
$$(x^2-y^2)+2E_xE_y\ xy+2E_yE_zyz+2E_zE_xzx. \tag{4}$$

It is important to note that

$E_x^2+E_y^2+E_z^2$ and $x^2+y^2+z^2$ belong to Γ_1 (5)

$2E_z^2-E_x^2-E_y^2$, $\sqrt{3}(E_x^2-E_y^2)$ and $2z^2-x^2-y^2$, $\sqrt{3}(x^2-y^2)$ belong to Γ_3

E_iE_j for $i\neq j$ and xy, yz, zx belong to Γ_4

E_x, E_y, E_z and x, y, z belong to Γ_5

The products of $\Gamma_1\times\Gamma_1$, $\Gamma_3\times\Gamma_3$, $\Gamma_5\times\Gamma_5$ contain Γ_1 and the Hamiltonian is invariant under the operation of group T_d.

In order to easy calculate the matrix element, one use the method can replace the potential function of similar operators, that is each x, y, z by J_x, J_y, J_z,

In the case, there are no magnetic field present, the Hamiltonian must be invariant under the operation of time-reversal. Since under the time reversal operation, J_i changes into $-J_i$, H_E contains an odd number of J_i is not allowed. Thus the most general form of Hamiltonian under application. of electric field is

$$H_E=\alpha E^2+\beta(\vec{E}.\vec{J})^2+\gamma(E_x^2J_x^2+E_y^2J_y^2+E_z^2J_z^2), \tag{9}$$

α,β,γ dependent on the unperturbed wave function of the levels. α gives the shift of valence band, it does not contribute to the energy splitting.

Case A. Applied Electric Field along [001]

In this case, the symmetry group of the system is $\overline{D}_{2d}$. The double-valued irreducible representation of $\overline{D}_{2d}$ are given in Table III.

The states of Γ_6 ($\overline{T}_d$) and Γ_7 ($\overline{T}_d$) do not split by the electric field and belong to Γ_6 ($\overline{D}_{2d}$) and Γ_7 ($\overline{D}_{2d}$) respectively. The Γ_8 ($\overline{T}_d$) levels decomposed into Γ_6 ($\overline{D}_{2d}$) and Γ_7 ($\overline{D}_{2d}$). In the electric field, Eq. (9) reduced to

$$H_E=\alpha E^2+\beta E^2J_z^2+\gamma E^2J_z^2. \tag{10}$$

The Γ_8 levels split into two sublevels with wave function $\phi_{\pm\frac{3}{2}}$ which belong to Γ_6 ($\overline{D}_{2d}$) coresponding to eigenvalue $\alpha E^2+-\frac{9}{4}(\beta+2)E^2$ and $\phi_{\pm\frac{1}{2}}$ which belong to $\Gamma_7(\overline{D}_{2d})$ corresponding to eigenvalue $\alpha E^2+\frac{1}{4}(\beta+\gamma)E^2$. The energy seperation between the two sublevels is

$$\Delta_{001}=2(\beta+\gamma)E^2. \tag{11}$$

TABLE III. Character table for double-valued group $\overline{D}_{2d}$.

$\overline{D}_{2d}$	E	$\overline{E}$	$C_2,\overline{C}_2$	$2S_4$	$2\overline{S}_4$	$2C'_2$, $2\overline{C}_2$	$2\sigma_d,2\overline{\sigma}_d$
Γ_6	2	−2	0	$\sqrt{2}$	$-\sqrt{2}$	0	0

Γ_7	2	−2	0	$-\sqrt{2}$	$\sqrt{2}$	0	0

Case B. Applied Electric Field along [111]

For electric field along [111] direction. The symmetry group of the system is $\bar{C}_{3v}$. The double-valued irreducible representation $\bar{C}_{3v}$ are give in Table IV.

The level Γ_6 ($\bar{T}_d$) and Γ_7 ($\bar{T}_d$) become $\Gamma_4(\bar{C}_{3v})$ and Γ_8 ($\bar{T}_d$) reduced to Γ_4 ($\bar{C}_{3v}$) $+\Gamma_5$ ($\bar{C}_{3v}$)$+\Gamma_6(\bar{C}_{3v})$. Since Hamiltonian is invariant under the operation of time reversal and the representation of Γ_5 ($\bar{C}_{3v}$) and Γ_6 ($\bar{C}_{3v}$) are complex conjugate of one another, the levels which are degenerate under time-reversal. The resultant level designed by Γ_{5+6} ($\bar{C}_{3v}$). Thus Γ_8 ($\bar{T}_d$) split into two two-fold degenerate states of Γ_{5+6} ($\bar{C}_{3v}$) and Γ_4 ($\bar{C}_{3v}$). Equation (9) reduced to

$$H_E=\alpha E^2+\beta(\vec{E}\cdot\vec{J})^2+\frac{E^2}{3}\gamma J^2. \tag{12}$$

H_E can be diagonalized by the orthornormal wave function

$$\begin{aligned}
\theta^8_{\frac{3}{2}}&=\frac{1}{\sqrt{6}}\phi^8_{\frac{3}{2}}+\frac{i}{\sqrt{2}}\phi^8_{-\frac{1}{2}}+\frac{1+i}{\sqrt{6}}\phi^8_{-\frac{1}{2}},\\
\theta^8_{\frac{1}{2}}&=\frac{-1+i}{\sqrt{2}}\phi^8_{\frac{3}{2}}-\frac{i}{\sqrt{2}}\phi^8_{\frac{1}{2}}+\frac{1}{\sqrt{6}}\phi^8_{-\frac{3}{2}},\\
\theta^8_{-\frac{1}{2}}&=\frac{1}{\sqrt{6}}\phi^8_{\frac{3}{2}}-\frac{i}{\sqrt{2}}\phi^8_{-\frac{1}{2}}+\frac{1+i}{\sqrt{6}}\phi^8_{-\frac{3}{2}},\\
\theta^8_{-\frac{3}{2}}&=\frac{-1+i}{\sqrt{6}}\phi^8_{\frac{3}{2}}+\frac{i}{\sqrt{2}}\phi^8_{\frac{1}{2}}+\frac{1}{\sqrt{6}}\phi^8_{-\frac{3}{2}}.
\end{aligned} \tag{13}$$

$\theta^8_{-\frac{3}{2}},\theta^8_{-\frac{1}{2}}$ belong to Γ_{5+6} ($\bar{C}_{3v}$) and corresponding to the eigenvalue $\alpha E^2+\frac{9}{4}\beta E^2+\frac{5}{4}\gamma E^2$, and $\theta^8_{\frac{3}{2}}$, $\theta^8_{\frac{1}{2}}$ belong to Γ_4 ($\bar{C}_{3v}$) and corresponding to the eigenvalue $\alpha E^2+\frac{1}{4}\beta E^2+\frac{5}{4}\gamma E^2$. The difference in energy of these sublevels is

$$\Delta_{111}=2\beta E^2. \tag{14}$$

Case C. Applied Electric Field along [110]

For E along [110], the symmetry group of the system is $\bar{C}_{2v}$, with only one double-valued representation Γ_5 ($\bar{C}_{2v}$). The level Γ_6 ($\bar{T}_d$) and Γ_7 ($\bar{T}_d$) become Γ_5 ($\bar{C}_{2v}$), and Γ_8 ($\bar{T}_d$) levels decomposed into $2\Gamma_5$ ($\bar{C}_{2v}$). Equation (9) yields

$$H_E=\alpha E^2+\frac{\beta}{2}(J_x^2+J_y^2)E^2+\frac{\gamma}{2}(J_x^2+J_y^2)E^2. \tag{15}$$

The orthogonal wave function that diagonalized H_E are

$$\begin{aligned}
\Psi^8_{\frac{3}{2}}&=(1+p^2)^{-\frac{1}{2}}(\phi^8_{\frac{3}{2}}-ip\phi^8_{-\frac{1}{2}})\\
\Psi^8_{\frac{1}{2}}&=(1+p^2)^{-\frac{1}{2}}(\phi^8_{\frac{1}{2}}+ip\phi^8_{-\frac{3}{2}})
\end{aligned}$$

$$\Psi^{8}_{-\frac{1}{2}}=(1+p^2)^{-\frac{1}{2}}(-ip\phi^{8}_{\frac{3}{2}}+\phi^{8}_{-\frac{1}{2}})$$

$$\Psi^{8}_{-\frac{3}{2}}=(1+p^2)^{-\frac{1}{2}}(ip\phi^{8}_{\frac{1}{2}}+\phi^{8}_{-\frac{3}{2}}) \tag{16}$$

where $p=[(\gamma+\beta)+\sqrt{(\gamma+\beta)^2+3\beta^2}]/\sqrt{3}\,\beta$ (17)

The eigenvalue $\alpha E^2+\frac{5}{2}(\gamma+\beta)E^2+\frac{1}{2}[(\gamma+\beta)^2+3\beta^2]^{\frac{1}{2}}E^2$ corresponds to eigenfunction $\Psi^{8}_{\pm\frac{3}{2}}$, and $\alpha E^2+\frac{5}{2}(\gamma+\beta)E^2-\frac{1}{2}[(\gamma+\beta)^2+3\beta^2]^{\frac{1}{2}}E^2$ is the eigenvalue of $\Psi^{8}_{\pm\frac{1}{2}}$. The seperation of two sublevels are found

$$\Delta_{110}=[(\gamma+\beta)^2+3\beta^2]^{\frac{1}{2}}=\tfrac{1}{2}\sqrt{\Delta^2_{100}+\Delta^2_{111}}. \tag{18}$$

TABLE IV. Character table of double-valued representation of $\overline{C}_{3v}$.

$\overline{C}_{3v}$	E	$\overline{E}$	$2C_3$	$2\overline{C}_3$	$3\sigma_v$	$3\overline{\sigma}_v$
Γ_4	2	−2	1	−1	0	0
Γ_5	1	−1	−1	1	i	$-i$
Γ_6	1	−1	−1	1	$-i$	i

Case D. Applied Electric Field in (001) Plane

In this case, the symmetry group of the system is $\overline{C}_s$. the double-valued representation of $\overline{C}_s$ are given in Table V. The representation Γ_3 $(\overline{C}_s)$ and Γ_4 $(\overline{C}_s)$ are complex conjugate to one another, these levels are degenerate under time reversal symmetry.

The level denited by Γ_6 $(\overline{T}_d)$ and Γ_7 $(\overline{T}_d)$ are belong to $\Gamma_3(\overline{C}_s)+\Gamma_4$ $(\overline{C}_s)$ which do not split by applied electric field and designed by Γ_{3+4} $(\overline{C}_s)$. The Γ_8 $(\overline{T}_d)$ reduced to $2(\Gamma_5$ $(\overline{C}_s)+\Gamma_4(\overline{C}_s))$. Thus Γ_8 $(\overline{T}_d)$ reduced to two two-fold degenerate states. Equation (9) becomes

$$H_E=\alpha E^2+(\gamma+\beta)\ (\cos^2\theta\, J_x^2+\sin^2\theta J_y^2)E^2+\beta\cos\theta\sin\theta(J_xJ_y+J_yJ_x)E^2, \tag{19}$$

where θ is the angle between electric field and x axis and we define

$$\begin{aligned}\epsilon_1&=\beta\cos\theta\sin\theta,\\ \epsilon_2&=(\beta+\gamma)\ (\sin^2\theta-\cos^2\theta),\\ \epsilon_3&=\gamma+\beta.\end{aligned} \tag{20}$$

The equation (19) can be diagonalized by the unitary transformation

$$D=\frac{1}{(1+dd^*)^{\frac{1}{2}}}\begin{pmatrix} d & 0 & 1 & 0\\ 0 & -d & 0 & 1\\ 1 & 0 & -d^* & 0\\ 0 & 1 & 0 & d^*\end{pmatrix}, \tag{21}$$

where $d=\dfrac{2\sqrt{3}\,i\epsilon_1+\sqrt{3}\,\epsilon_3}{\epsilon_3+\delta}$,

$$\delta=(\epsilon_3^2+3\epsilon_2^2+12\epsilon_1^2)^{\frac{1}{2}}. \tag{22}$$

The wave function are given by

$$\sum_M^8=\sum_{M'}D_{M'M}\phi_{M'}^8 \tag{23}$$

The eigenvalue $\alpha E^2+\frac{5}{4}\epsilon_3E^2+\frac{1}{2}\delta E^2$. corresponds to eigenfunction $\Psi_{\pm\frac{3}{2}}$ and $\alpha E^2+\frac{3}{2}\epsilon_3E^2-\frac{1}{2}\delta E^2$ is the eigenvalue of $\Psi_{\pm\frac{1}{2}}$.
The energy difference in energy of the two sublevels is

$$\Delta_{(100)}=\delta E^2=\tfrac{1}{2}(\Delta_{100}^2+3\Delta_{100}^2\cos^2 2\theta+3\Delta_{111}^2\sin^2 2\theta)^{\frac{1}{2}} \tag{24}$$

For $\theta=0°$, this can be reduced to case A and the energy seperation reduced to Δ_{100} For $\theta=45°$, this case can be reduced to case C and the energy seperation reduced to $\frac{1}{2}(\Delta_{100}^2+3\Delta_{111}^2)^{\frac{1}{2}}$. In this case the energy seperation between the two sublevels are function of 2θ.

TABLE V The double-valued representation of $\overline{C}_3$

$\overline{C}_3$	E	$\overline{E}$	σ	$\overline{\sigma}$
Γ_3'	1	−1	i	$-i$
Γ_4'	1	−1	$-i$	i

Case E. Applied Electric Field in (110) Plane

For electric field in (110) plane, the symmetry group of the system is $\overline{C}_2$, the irreducible representation of $\overline{C}_2$ are given in Table VI. Similar to group $\overline{C}_3$, the double-valued representation of $\overline{C}_2$ are complex conjugate of one another. In the presence of electric field the two states can not be split. Γ_8' ($\overline{T}_d$) and Γ_7 ($\overline{T}_d$) reduced to Γ_3' ($\overline{C}_2$) $+\Gamma_4'$ ($\overline{C}_2$) which are degenerate and designed by Γ_{3+4}' ($\overline{C}_2$). Γ_8' ($\overline{T}_d$) decomposed into $2(\Gamma_3'$ ($\overline{C}_2$) $+\Gamma_4'$ ($\overline{C}_2$)). Thus Γ_8 ($\overline{T}_d$) split into two two-fold degenerate states. Equation (9) becomes

$$H_E=\alpha E^2+\beta[\frac{1}{\sqrt{2}}\sin\theta(J_x+J_y)+J_z\cos\theta]^2E^2+\gamma^2[(J_x^2+J_y^2)\frac{\sin^2\theta}{2}+J_z^2\cos^2\theta]E^2 \tag{26}$$

$$=\alpha E^2+\epsilon J_z^2+(J_xJ_y+J_yJ_x)\epsilon'+[(J_x+J_y)J_z+J_z(J_x+J_y)]\epsilon''+\tfrac{1}{2}(\beta+\gamma)\sin^2\theta J^2E^2$$

where $\epsilon=(\gamma+\beta)(\cos^2\theta-\frac{1}{2}\sin^2\theta)E^2$,

$$\epsilon'=-\frac{\beta}{2}\sin^2\theta E^2,$$

$$\epsilon'' = \frac{\beta}{\sqrt{2}} \sin\theta\cos\theta E^2, \tag{27}$$

θ is the angle between electric field and z axis.

Using a matrix representation for J_x, J_y, $J_z$in (3), we get

$$H_E = \begin{pmatrix} -\frac{9}{4}\epsilon & (1+i)\sqrt{3}\,\epsilon'' & i\epsilon^1\sqrt{3} & 0 \\ (1-i)\epsilon''\sqrt{3} & -\frac{1}{4}\epsilon & 0 & i\epsilon'\sqrt{3} \\ -i\epsilon'\sqrt{3} & 0 & \frac{1}{4}\epsilon & -(1+i)\epsilon'' \\ 0 & -i\epsilon'\sqrt{3} & -(1-i)\epsilon''\sqrt{3} & \frac{9}{4}\epsilon \end{pmatrix}. \tag{28}$$

The matrix can be diagonalized by a unitary matrix

$$G = \frac{1}{M}\begin{pmatrix} \frac{\epsilon-\delta'}{\sqrt{3}\,\epsilon'}i, & -\frac{\epsilon''}{\epsilon'}(1-i) & 1 & 0 \\ -\frac{\epsilon''}{\epsilon'}(1+i) & -\frac{\epsilon-\delta'}{\sqrt{3}\,\epsilon'}i & 0 & 1 \\ 1 & 0 & \frac{\epsilon-\delta'}{\sqrt{3}\,\epsilon'}i & -(1-i)\frac{\epsilon''}{\epsilon'} \\ 0 & 1 & \frac{\epsilon''}{\epsilon'}(1+i) & -\frac{\epsilon-\delta'}{\sqrt{3}\,\epsilon'}i \end{pmatrix}, \tag{29}$$

where $\delta' = (\epsilon'+3\epsilon''+6\epsilon''')^{\frac{1}{2}}$,

$$M = \frac{\epsilon'-2\epsilon\delta'+\delta''+9\epsilon'''}{3\epsilon''}. \tag{30}$$

The eigenvalue are

$$E = \alpha E^2 + \frac{15}{8}\sin^2\theta\,(\beta+\gamma)E^2 + \frac{5}{4}\epsilon' \pm \delta', \tag{31}$$

and the eigenfunction are

$$\Delta_M^S = \sum_{M'} G_{M'M}\phi_{M'}^S. \tag{32}$$

The energy difference between the two sublevels is $2\delta'$. For $\theta=0°$, this case reduced to case A, The seperation between the two states can be reduced to $2(\gamma+\beta)E^2$, For $\theta=90°$, that is case C. the difference in energy of the states is $[(\beta+\gamma)^2+3\beta^2]^{\frac{1}{2}}$ same as Eq. (18).

TABLE VI The double-valued representation of $\overline{C_2}$.

$\overline{C_2}$	$\overline{E}$	$\overline{E}$	C_2	$\overline{C_2}$
Γ_3	1	−1	i	−i
Γ_4	1	−1	−i	i

III. Relative Intensities of Stark Components

The intensity of a system from states Ψ_M^i to the state Ψ_M^f induced by electric dipole are proportional to the square of the dipole transition matrix $<\Psi_M^i|\hat{Q}_j|\Psi_M^f,>$ where Ψ_M^i and $\Psi_M^f,$ are wave functions of the initial and final state belong to irreducible representation Γ_i and Γ_f of the symmetry group of the system, and $\hat{Q}_j$ is the component of the dipole moment along the direction of polarization of the light. Without application of electric field, the electric dipole are the irreducible representation of Γ_5 (T_d). From character table, we found that $\Gamma_5\times\Gamma_6=\Gamma_7+\Gamma_8$, $\Gamma_5\times\Gamma_7=\Gamma_6+\Gamma_8$, and $\Gamma_5\times\Gamma_8=\Gamma_6+\Gamma_7+2\Gamma_8$. Thus electric dipole transition between Γ_8 and $\Gamma_6,\Gamma_7,\Gamma_8$ are permitted. The ground state of an acceptor belongs to Γ_8 of tetrahedral group. Therefore, there are three types of excitation spectrum. When the electric field is introduced, the eigenstates of the system can be given by appreciate linear combination of the unperturbed wave function

$$\Psi_M^i=\sum_M S_{MM}\,\phi_M^i. \tag{33}$$

The transition matrix can be written

$$<\Psi_M^i|\hat{\vec{Q}}_j|\Psi_M^f,>=<\phi_M^i|S'^{i+}\hat{\vec{Q}}_jS^f|\phi_M^f,>. \tag{34}$$

For the transition from Γ_8 to Γ_6 or Γ_7 state only one complex matrix element is needed to express the dipole-moment operator. The most general form of wave function are linear combination of wave function in Eq. (1),

$$\Psi_M^i=a^i\phi_M^i+b^iA_M^i+c^iX_M^i. \tag{35}$$

For Γ_6 and Γ_7 state $c^6=c^7=0$.

For a $\Gamma_8\to\Gamma_6$ transition, the matrix element is $<a^6\phi_M'^6+b^6A_M^1|\hat{\vec{Q}}|a^8\phi_M^8+b^8A_M^8+c^8\times_M^8>$. From group theoem and orthgonal relation, the transition matrix become

$$\vec{Q}^{8\to6}=D_0\begin{pmatrix}\sqrt{3}(\hat{x}+i\hat{y}) & -2i\hat{z} & (\hat{x}-i\hat{y}) & 0\\ 0 & i(\hat{x}+i\hat{y}) & 2\hat{z} & i\sqrt{3}(\hat{x}-i\hat{y})\end{pmatrix}, \tag{36}$$

where D_0 is a complex parameter and can be obtained by unperturbed wave function,

$$D_0=\frac{a^{6*}a^8}{\sqrt{6}}\int fQ_xX\vec{dr}-\frac{ib^{6*}a^8}{\sqrt{18}}\int\zeta^1Q_xYd\vec{r}+i\frac{b^{6*}b^8}{\sqrt{6}}\int Y^1Q_xZd\vec{r}-\frac{i^{*6}c^8}{2}\int Q_x\xi\omega_zd\vec{r}. \tag{37}$$

For a $\Gamma_8\to\Gamma_7$ transition we need to evaluate the matrix

$$\vec{Q}^{8\to7}=<a^7\phi_M'^7+b^7A_M'^7|\hat{\vec{Q}}|a^8\phi_M^8+b^8A_M^8+c^8\Psi_M^8>, \tag{38}$$

in matrix form

$$\vec{Q}^{8\to7}=D'_0\begin{pmatrix}-(\hat{x}-i\hat{y}) & 0 & \sqrt{3}(\hat{x}+i\hat{y}) & 2i\hat{z}\\ -2\hat{z} & i\sqrt{3}(\hat{x}-i\hat{y}) & 0 & -i(\hat{x}+i\hat{y}).\end{pmatrix} \tag{39}$$

$$where\ D_0=-\frac{a'^{7*}a^8}{\sqrt{6}}\,i\int Y'Q_xZd\vec{r}+\frac{a'^{7*}b^8}{\sqrt{18}}\,i\int\zeta'Q_xYd\vec{r}-a'^{7*}c^8\int w'_1Q_xXdr$$
$$+\frac{b'^{7*}a^8}{\sqrt{6}}\int g'Q_x\xi d\vec{r}. \tag{39}$$

For a $\Gamma_8\to\Gamma_8$ transition. we note that Γ_8 appears twice in the product of $\Gamma_8\times\Gamma_8$, and the dipole moment matrix is a linear combination of two complex matrices. The most general form of $Q^{8\to8}$ can be get as a linear combination of 16 matrices list in (7). The matrices operator Q_x, Q_y, Q_z obey the transformation properties Γ_5 of the group T_d. There are only two sets of matrices (U_x,U_y,U_z) and (V_x,V_y,V_z) in (7) that belong to Γ_5. The transition matrix betwene two Γ_8 states, we can calculate the matrix

$$\vec{Q}^{8\to8}=<a'^8\phi'^8_{M'}+b'^8\Lambda'^8_{M'}+c'^8X'^8_{M'}\mid\vec{Q}\mid a^8\phi_M+b^8\Lambda_M+C^8X^8_M>. \tag{40}$$

From orthogonality theorem (40) can be written as follows:

$$\vec{Q}^{8\to8}=-\frac{-2}{\sqrt{3}}(D+D')\vec{U}-\frac{4i}{\sqrt{3}}D'\vec{V}, \tag{41}$$

The two complex parameters D and D′ can be determined by calculating with unperturbed wave function,

$$D=\frac{a'^{8*}a^8}{\sqrt{3}}\int Y'Q_xZd\vec{\tau}+\frac{b'^{8*}b^8}{\sqrt{3}}\int\eta'\,Q_x\xi d\vec{\tau}-\frac{a'^{8*}b^8}{3}\int Y'Q_x\xi d\vec{\tau}-2c'^{8*}a^8i\int$$
$$\omega'_1Q_xXd\vec{\tau},$$
$$D'=\frac{a'^{8*}b^8}{6}\int Y'Q_x\zeta d\vec{\tau}-\frac{b'^{8*}a^8}{6}\int\zeta'Q_xYd\vec{\tau}+b'^{*8}c^8\int\omega'_2Q_x\xi d\vec{\tau}. \tag{42}$$

In matrix form (41) is

$$\vec{Q}^{8\to8}=\begin{pmatrix}0 & -(D+2D')(\hat{x}+i\hat{y}) & -i(D-D')\hat{z} & \sqrt{3}D'(\hat{x}-i\hat{y})\\ D(-\hat{x}+i\hat{y}) & 0 & \sqrt{3}D'(\hat{x}+i\hat{y}) & i(D+2D')\hat{z}\\ i(D+3D')\hat{z} & \sqrt{3}D'(-\hat{x}+i\hat{y}) & 0 & D(\hat{x}+i\hat{y})\\ -\sqrt{3}D'(\hat{x}+i\hat{y}) & i(D-D')\hat{z} & (D+2D')(\hat{x}-i\hat{y}) & 0.\end{pmatrix} \tag{43}$$

I. Applied Electric Field along [001]

This is the simplest case, both S and S′ are unit matrices. The transition matrix components along x,y,z axes of the crystal will be denoted by Q_x [001], Q_y [001], Q_z [001], and we write them explicitly for each type:

case (a) $\Gamma_8\to\Gamma_6$:

$$Q_x[001]=D_0\begin{pmatrix}\sqrt{3} & 0 & 1 & 0\\ 0 & i & 0 & i\sqrt{3}\end{pmatrix},$$

$$Q_y[001]=D_0\begin{pmatrix} i\sqrt{3} & 0 & -i & 0 \\ 0 & -1 & 0 & \sqrt{3} \end{pmatrix},$$

$$Q_z[001]=D_0\begin{pmatrix} 0 & -2i & 0 & 0 \\ 0 & 0 & 2 & 0 \end{pmatrix};$$

case (b) $\Gamma_8\to\Gamma_7$:

$$Q_x[001]=D_0'\begin{pmatrix} -1 & 0 & \sqrt{3} & 0 \\ 0 & i\sqrt{3} & 0 & -i \end{pmatrix},$$

$$Q_y[001]=D_0'\begin{pmatrix} i & 0 & i\sqrt{3} & 0 \\ 0 & \sqrt{3} & 0 & 1 \end{pmatrix},$$

$$Q_z[001]=D_0'\begin{pmatrix} 0 & 0 & 0 & zi \\ -2 & 0 & 0 & 0 \end{pmatrix};$$

case(c) $\Gamma_8\to\Gamma_8$:

$$Q_x[001]=\begin{pmatrix} 0 & -(D+2D') & 0 & \sqrt{3}\,D' \\ -D & 0 & \sqrt{3}\,D' & 0 \\ 0 & -\sqrt{3}\,D' & 0 & D \\ -\sqrt{3}\,D' & 0 & (D+2D') & 0 \end{pmatrix},$$

$$Q_y[001]=\begin{pmatrix} 0 & -i(D+2D') & 0 & -i\sqrt{3} \\ iD & 0 & i\sqrt{3}\,D' & 0 \\ 0 & i\sqrt{3}\,D' & 0 & iD \\ i\sqrt{3}\,D' & 0 & -i(D+2D') & 0 \end{pmatrix},$$

$$Q_z[001]=\begin{pmatrix} 0 & 0 & -i[D-D'] & 0 \\ 0 & 0 & 0 & i(D-3D') \\ i(D+3D') & 0 & 0 & 0 \\ 0 & i(D-D') & 0 & 0 \end{pmatrix}.$$

For each polarization the intensity of a given Stark component is proportional to the absolute square of the corresponding element of the transition matrix. The matrix $Q_z[001]$ corresponds to linear polarization ($\epsilon\|$) parallel to $\vec{E}$ and $Q_x[001]$ or $Q_y[001]$ corresponds to linear polarization ($\epsilon\perp$) perpendicular to $\vec{E}$. The relative intensities are given in Table VII. In Faraday configuration, $\frac{1}{\sqrt{2}}(Q_x+Q_yi)$ and $\frac{1}{\sqrt{2}}(Q_x-Q_yi)$ corresponds to left-circular polarizaton] (ϵ_+) and right-circular polarization (ϵ_-) respectively. The relative intensities are given in Table VIII. For a $\Gamma_8\to\Gamma_8'$ transition, one can use two real parameter u and v to express the relative intensities. For each polarization, the sum of the relative intensities are given by

$$N=4|D+D'|^2+16|D'|^2. \tag{44}$$

The two real parameter u and v can be defined as below:

$$|D-D'|^2=\frac{N}{4}(1-v), \tag{45}$$

$$|D+D'|^2=\frac{N}{4}(1-u). \tag{46}$$

It is easy to find that

$$|D+3D'|^2=\frac{N}{4}(1+v), \tag{47}$$

$$|D'|^2=\frac{N}{16}u, \text{ and} \tag{48}$$

$$|D|^2=\frac{N}{4}\left(1-\frac{3u}{4}-\frac{v}{2}\right). \tag{49}$$

Therefor, u and v restrict to the range of inequalities:

$$O\leq u\leq 1,\ -1\leq v\leq 1 \text{ and } -\left(1-\frac{1}{4}\right)\leq\frac{v}{2}\leq\left(1-\frac{3u}{4}\right)$$

TABLE VII. Relative intensities of Stark components with $\vec{E}\parallel[001]$

Zero-field transition	Stark components	Transition probability $\epsilon\parallel$	Transition probability $\epsilon\perp$	Relative intensity $\epsilon\parallel$	Relative intensity $\epsilon\perp$
$\Gamma_8\longrightarrow\Gamma_6$	$\Gamma_6\longrightarrow\Gamma_8$	0	$6\|D_0\|^2$	0	$\frac{3}{4}$
	$\Gamma_7\longrightarrow\Gamma_7$	$8\|D_0\|^2$	$2\|D_0\|^2$	1	$\frac{1}{4}$
$\Gamma_8\longrightarrow\Gamma_7$	$\Gamma_6\longrightarrow\Gamma_7$	$8\|D_0'\|^2$	$2\|D_0'\|^2$	1	$\frac{1}{4}$
	$\Gamma_7\longrightarrow\Gamma_7$	0	$6\|D_0'\|^2$	0	$\frac{3}{4}$
$\Gamma_8\longrightarrow\Gamma_8$	$\Gamma_6\longrightarrow\Gamma_6$	0	$6\|D'\|^2$	0	$\frac{3}{8}u$
	$\Gamma_6\longrightarrow\Gamma_7$	$2\|D+3D'\|^2$	$2\|D\|^2$	$\frac{1}{2}(1+v)$	$\frac{1}{2}\left(1-\frac{3}{4}u-\frac{v}{2}\right)$
	$\Gamma_7\longrightarrow\Gamma_6$	$2\|D-D'\|^2$	$2\|D+2D'\|^2$	$\frac{1}{2}(1-v)$	$\frac{1}{2}\left(1-\frac{3}{4}u+\frac{v}{2}\right)$
	$\Gamma_7\longrightarrow\Gamma_7$	0	$6\|D'\|^2$	0	$\frac{3}{8}u$

TABLE VIII. Relative intensities of Stark components in Faraday configuration with $\vec{E}_{\parallel}[001]$ (Cicular polarizition)

Zero-field transition	Stark components	Transition probability ϵ_+	Transition probability ϵ_-	Relative intensity ϵ_+	Relative intensity ϵ_-
$\Gamma_8\longrightarrow\Gamma_6$	$\Gamma_6\longrightarrow\Gamma_6$	$6\|D_0\|^2$	$6\|D_0\|^2$	$\frac{3}{4}$	$\frac{3}{4}$

	$\Gamma_7 \longrightarrow \Gamma_7$	$2\lvert D_0\rvert^2$	$2\lvert D_0\rvert^2$	$\frac{1}{4}$	$\frac{1}{4}$
$\Gamma_8 \longrightarrow \Gamma_7$	$\Gamma_6 \longrightarrow \Gamma_7$	$6\lvert D_0'\rvert^2$	$6\lvert D_0'\rvert^2$	$\frac{1}{4}$	$\frac{1}{4}$
	$\Gamma_8 \longrightarrow \Gamma_7$	$2\lvert D_0'\rvert^2$	$2\lvert D_0'\rvert^2$	$\frac{3}{4}$	$\frac{3}{4}$
$\Gamma_8 \longrightarrow \Gamma_8$	$\Gamma_6 \longrightarrow \Gamma_6$	$6\lvert D'\rvert^2$	$6\lvert D'\rvert^2$	$\frac{3}{8}u$	$-\frac{3}{8}u$
	$\Gamma_6 \longrightarrow \Gamma_6$	$2\lvert D\rvert^2$	$2\lvert D\rvert^2$	$\frac{1}{2}(1-\frac{3}{4}u-\frac{v}{2})$	$\frac{1}{2}(1-\frac{3}{4}u-\frac{v}{2})$
	$\Gamma_7 \longrightarrow \Gamma_6$	$2\lvert D+2D'\rvert^2$	$2\lvert D+2D\rvert^2$	$\frac{1}{2}(1-\frac{3}{4}u+\frac{v}{2})$	$\frac{1}{2}(1-\frac{3}{4}u+\frac{v}{2})$
	$\Gamma_7 \longrightarrow \Gamma_7$	$6\lvert D'\rvert^2$	$6\lvert D'\rvert^2$	$\frac{3}{8}u$	$-\frac{3}{8}u$

II. Applied Electric Field along [111]

In this case, the transformation matrix S be found from Eq. (13),

$$S=\begin{pmatrix} \frac{1}{\sqrt{6}} & \frac{-1+i}{\sqrt{2}} & \frac{1}{\sqrt{6}} & \frac{-1+i}{\sqrt{6}} \\ 0 & \frac{-i}{\sqrt{2}} & 0 & \frac{i}{\sqrt{2}} \\ \frac{i}{\sqrt{2}} & 0 & \frac{-i}{\sqrt{2}} & 0 \\ \frac{1+i}{\sqrt{6}} & \frac{1}{\sqrt{6}} & \frac{1+i}{\sqrt{6}} & \frac{1}{\sqrt{6}} \end{pmatrix}.$$

For a Γ_8 to either Γ_6 or Γ_7 transition, S′ is 2×2 unit matrix. For a Γ_8 to Γ_8 transition S′=S. We chose $\hat{z}'$ parallel to [111] direction and $\hat{x}'$, $\hat{y}'$ are two orthogonal axes perpendicular to $\hat{z}'$ and the relationship with the crystal axes is

$\hat{x}=(\hat{x}+\hat{y}+2\hat{z})/\sqrt{6}$, $\hat{y}'=(\hat{x}-\hat{y})/\sqrt{2}$, and $\hat{z}'=(\hat{x}+\hat{y}+\hat{z})/\sqrt{3}$.

case (a) $\Gamma_8 \longrightarrow \Gamma_6$:

$$Q_x'[111]=\frac{D_0}{\sqrt{3}}\begin{pmatrix} 1+i & 1 & 0 & -3 \\ -i & 1+i & 3i & 0 \end{pmatrix},$$

$$Q_y'[111]=D_0\begin{pmatrix} 0 & i & -(1-i) & -i \\ -1 & 0 & 1 & 1-i \end{pmatrix},$$

$$Q_z'[111]=\frac{\sqrt{2}D_0}{\sqrt{3}}\begin{pmatrix} 1+i & -2 & 0 & 0 \\ 2i & 1+i & 0 & 0 \end{pmatrix};$$

case (b) $\Gamma_8 \longrightarrow \Gamma_7$:

$$Q_x'[111]=D_0'\begin{pmatrix} 0 & -i & 1-i & -i \\ 1 & 0 & 1 & -(1-i) \end{pmatrix},$$

$$Q_y'[111]=\frac{D_0'}{\sqrt{3}}\begin{pmatrix} -(1+i) & 1 & 2(1+i) & -1 \\ i & -(1+i) & i & 2(1+i) \end{pmatrix},$$

$$Q_z'[111]=\sqrt{2}\,D_0'\begin{pmatrix} -1+i & 0 & 0 & 0 \\ 0 & 1-i & 0 & 0 \end{pmatrix};$$

case (c) $\Gamma_8' \longrightarrow \Gamma_8'$:

$$Q_x'[111]=\frac{1}{\sqrt{2}}\begin{pmatrix} 0 & 2D'(1-i) & -2D' & -(1-i)(D'+D) \\ -2D'(1+i) & 0 & -(1+i)(D'+D) & -2D \\ -2D' & -(1-i)(D'+D) & 0 & 0 \\ (1+i)(D'+D) & 2D' & 0 & 0 \end{pmatrix},$$

$$Q_y'[111]=\frac{1}{\sqrt{6}}\begin{pmatrix} -4iD' & -2(1+i)D' & -2Di & -(1-i)(3D'+D) \\ 2(1-i)D' & 4iD' & -(1-i)(3D'+D) & -2Di \\ 2i(2D'+D) & (1+i)(D'-D) & 0 & 0 \\ -(1-i)(D'-D) & 2i(2D'+D) & 0 & 0 \end{pmatrix},$$

$$Q_z'[111]=\begin{pmatrix} D'+D & 0 & 0 & 0 \\ 0 & D'+D & 0 & 0 \\ 0 & 0 & -(D'+D) & 2D'(1-i) \\ 0 & 0 & -2D'(1+i) & -(D'+D) \end{pmatrix}.$$

The relative intensities for linear polarization are given in Table IX, and that for cicular polarization are given in Table X. We are interested to note that the relative intensities dependend only one parameter u. For all typy $(\Gamma_{5+6}' \longrightarrow \Gamma_4')\parallel$ are forbiddent. In a $\Gamma_8 \longrightarrow \Gamma_8'$ transition, if $D'=0$, $(\Gamma_4' \longrightarrow \Gamma_4)\perp$ would not allowed and all other allowed transition would be have equal intensities.

TABLE IX. Relative intensities of Stark components with $\vec{E}\parallel[111]$

Zero-field transition	Stark components	Transition probability $\epsilon\parallel$	Transition probability $\epsilon\perp$	Relative intensity $\epsilon\parallel$	Relative intensity $\epsilon\perp$
$\Gamma_8 \longrightarrow \Gamma_6$	$\Gamma_4 \longrightarrow \Gamma_4$	$8\lvert D_0\rvert^2$	$2\lvert D_0\rvert^2$	1	$\frac{1}{4}$
	$\Gamma_{5+6} \longrightarrow \Gamma_4$	0	$6\lvert D_0\rvert^2$	0	$\frac{3}{4}$
$\Gamma_8 \longrightarrow \Gamma_7$	$\Gamma_4 \longrightarrow \Gamma_4$	$8\lvert D_0'\rvert^2$	$2\lvert D_0'\rvert^2$	1	$\frac{1}{4}$
	$\Gamma_{5+6} \longrightarrow \Gamma_4$	0	$6\lvert D_0'\rvert$	0	$\frac{3}{4}$
$\Gamma_8 \longrightarrow \Gamma_8$	$\Gamma_4 \longrightarrow \Gamma_4$	$2\lvert D+D'\rvert^2$	$8\lvert D'\rvert^2$	$\frac{1}{2}(1-u)$	$\frac{u}{2}$
	$\Gamma_4 \longrightarrow \Gamma_{5+6}$	0	$2\lvert D+D'\rvert^2+4\lvert D'\rvert^2$	0	$\frac{1}{2}(1-\frac{u}{2})$

$\Gamma_{5+6}\longrightarrow\Gamma_4$	0	$\frac{1}{3}[4\|D\|^2+2\|3D'+D\|^2]$	0	$\frac{1}{2}(1-\frac{u}{2})$
$\Gamma_{5+6}\longrightarrow\Gamma_{5+6}$	$2\|D+D'\|^2+16\|D'\|^2$	0	$\frac{1}{2}(1+u)$	0

TABLE X. Relative intensities of Stark components in Faraday configuration with $\vec{E}\parallel[111]$ (Circular polarization)

Zero-field transition	Stark components	Transition probability ϵ_+	Transition probability ϵ_-	Relative intensity ϵ_+	Relative intensity ϵ_-
$\Gamma_8\longrightarrow\Gamma_6$	$\Gamma_4\longrightarrow\Gamma_4$	$2\|D_0\|^2$	$2\|D_0\|^2$	$\frac{1}{4}$	$\frac{1}{4}$
	$\Gamma_{5+6}\longrightarrow\Gamma_4$	$6\|D_0\|^2$	$6\|D_0\|^2$	$\frac{3}{4}$	$\frac{3}{4}$
$\Gamma_8\longrightarrow\Gamma_7$	$\Gamma_4\longrightarrow\Gamma_4$	$2\|D_0'\|^2$	$2\|D_0'\|^2$	$\frac{1}{4}$	$\frac{1}{4}$
	$\Gamma_{5+6}\longrightarrow\Gamma_4$	$6\|D_0'\|^2$	$6\|D_0'\|^2$	$\frac{3}{4}$	$\frac{3}{4}$
$\Gamma_8\longrightarrow\Gamma_8$	$\Gamma_4\longrightarrow\Gamma_4$	$8\|D'\|^2$	$8\|D'\|^2$	$\frac{u}{2}$	$\frac{u}{2}$
	$\Gamma_4\longrightarrow\Gamma_{5+6}$	$2\|D+D'\|^2+4\|D\|^2$	$2\|D+D'\|^2+4\|D'\|^2$	$\frac{1}{2}(1-\frac{u}{2})$	$\frac{1}{2}(1-\frac{u}{2})$
	$\Gamma_{5+6}\longrightarrow\Gamma_4$	$2\|D+D'\|^2+4\|D'\|^2$	$2\|D+D'\|^2+4\|D'\|^2$	$\frac{1}{2}(1-\frac{u}{2})$	$\frac{1}{2}(1-\frac{u}{2})$
	$\Gamma_{5+6}\longrightarrow\Gamma_{5+6}$	0	0	0	0

III. Applied Electric Field along [110]

In this case, the transformation matrix are found from (16),

$$S=\frac{1}{(1+p^2)^{\frac{1}{2}}}\begin{pmatrix}1 & 0 & -ip & 0\\ 0 & 1 & 0 & ip\\ -ip & 0 & 1 & 0\\ 0 & iP & 0 & 1\end{pmatrix}$$

For Γ_6 or Γ_7 state S′ is unit matrix and for Γ_8 state S′=S.

we chose $\hat{z}'=\frac{1}{\sqrt{2}}(\hat{x}+\hat{y})$ parallel to the direction of applied electric field and other two perpendicular directions are $\hat{y}'=\frac{1}{\sqrt{2}}(-\hat{x}+\hat{y})$ and $\hat{z}'=-\hat{z}$.

case (a) $\Gamma_8\longrightarrow\Gamma_6$:

$$Q_x'[110]=\frac{-2D_0}{(1+p^2)^{\frac{1}{2}}}\begin{pmatrix}0 & -i & 0 & -p\\ -pi & 0 & 1 & 0\end{pmatrix},$$

$$Q_y'[110]=\frac{-1}{[2(1+p^2)(1+q^2)]^{\frac{1}{2}}}\begin{pmatrix} 0 & -(1-i)[D(1+pq)+D'(2+\sqrt{3}\,p-\sqrt{3}\,q)] & 0 \\ -(1+i)[D(1+pq)+D'[(2pq+\sqrt{3}\,p-\sqrt{3}\,q)] & 0 & (+1-i)[D(q-p)+D'(2q+\sqrt{3}+\sqrt{3}\,pq)] \\ 0 & -(1+i)[D(q-p)+D'(2q+\sqrt{3}+\sqrt{3}\,pq)] & 0 \\ -(1-i)[D(p-q)+D'(\sqrt{3}\,pq-2p+\sqrt{3})] & 0 & -(1+i)[D(1+pq)+D'(2-\sqrt{3}\,q+\sqrt{3}\,p)] \end{pmatrix}$$

$$\begin{matrix} (1+i)[D(q-p)+D'(2+\sqrt{3}\,p-\sqrt{3}\,q)] \\ 0 \\ -(1-i)[D(1+p)+D'(2q+\sqrt{3}\,pq+\sqrt{3})] \\ 0 \end{matrix}\Bigg)$$

$$Q_z'[110]=\frac{1}{[2(1+p^2)(1+q^2)]^{\frac{1}{2}}}\begin{pmatrix} 0 & -(1+i)[D(1+pq)+D'(2+\sqrt{3}\,q-\sqrt{3}\,p)] & 0 \\ -(1-i)[D(1+pq)+D'(-\sqrt{3}\,p+\sqrt{3}\,q+2pq)] & 0 & (1+i)[D(p-q)+D'(\sqrt{3}+\sqrt{3}\,pq-2q)] \\ 0 & -(1-i)[D(p-q)+D'(\sqrt{3}+\sqrt{3}\,pq-2q)] & 0 \\ (1+i)[D(p-q)+D'(\sqrt{3}\,pq+\sqrt{3}+2p)] & 0 & (1-i)[D(pq+1)+D'(\sqrt{3}\,q-\sqrt{3}\,p+2)] \end{pmatrix}$$

$$\begin{matrix} (1-i)[D(p-q)+D'(2p+\sqrt{3}\,pq+\sqrt{3})] \\ 0 \\ (1+i)[D(1+pq)+D'(2pq-\sqrt{3}\,p+\sqrt{3}\,q)] \\ 0 \end{matrix}\Bigg)$$

$$Q_y'[110]=\frac{D_0}{\sqrt{2}\,(1+p^2)^{\frac{1}{2}}}\begin{pmatrix}-(\sqrt{3}+p)(1-i) & 0 & (\sqrt{3}p-1)(1+i) & 0\\ 0 & (\sqrt{3}p-1)(1+i) & 0 & (\sqrt{3}+p)(1-i)\end{pmatrix},$$

$$Q_z'[110]=\frac{D_0}{\sqrt{2}\,(1+p^2)^{\frac{1}{2}}}\begin{pmatrix}(\sqrt{3}-p)(1+i) & 0 & (\sqrt{3}p+1)(1-i) & 0\\ 0 & -(\sqrt{3}+p)(1-i) & 0 & (\sqrt{3}-p)(1-i)\end{pmatrix};$$

case(b) $\Gamma_8\longrightarrow\Gamma_7$:

$$Q_x'[110]=\frac{-2D_0'}{2\,(1+p^2)^{\frac{1}{2}}}\begin{pmatrix}0 & -p & 0 & i\\ 1 & 0 & p & 0\end{pmatrix},$$

$$Q_y'[110]=\frac{D_0'}{\sqrt{2}\,(1+p^2)^{\frac{1}{2}}}\begin{pmatrix}(1+\sqrt{3}p)(1+i) & 0 & (p-\sqrt{3})(1-i) & 0\\ 0 & (\sqrt{3}-p)(1+i) & 0 & (\sqrt{3}p+1)(1+i)\end{pmatrix},$$

$$Q_z'[110]=\frac{D_0'}{\sqrt{2}\,(1+p^2)^{\frac{1}{2}}}\begin{pmatrix}(\sqrt{3}p-1)(1-i) & 0 & (p+\sqrt{3})(1+i) & 0\\ 0 & (\sqrt{3}+p)(1+i) & 0 & (\sqrt{3}p-1)(1-i)\end{pmatrix};$$

case (c) $\Gamma_8\longrightarrow\Gamma_8$:

$$Q_x'[110]=\frac{-i}{[(1+p^2)(1+q^2)]^{\frac{1}{2}}}\begin{pmatrix}[D(p+q)+D'(3q-p)]i & 0 & [-D(1-pq)+D'(1+3pq)] & 0\\ 0 & [-D(p+q)+D'(b-3p)]i & 0 & -[D(1-pq)+D'(3+pq)]\\ D(1-pq)+D'(pq+3) & 0 & [-D(p+q)+D'(q-3p)]i & 0\\ 0 & [D(1-pq)-D'(3pq+1)] & 0 & [D(p+q)+D'(3q-p)]i\end{pmatrix}$$

In this case we should note that the direction of polarization depends on the direction of propagation $\vec{k}$. When $\vec{k}$ perpendicular to the electric field direction, there are two kinds of linear polarization, one parallel to electric field and the other perpendicular to $\vec{E}$ field. The relative intensities are given in Table XIA, and XIB. If light propagates along E field, thete are two kinds of circular polarization with equal intensities given in Table XII. Unlike to the case of $\vec{E}\parallel[001]$ and $\vec{E}\parallel[111]$, the $\Gamma_8 \longrightarrow \Gamma_6$ and $\Gamma_8 \longrightarrow \Gamma_7$ transition depends on the directly measurable splitting parameter p.

The variables that appear in $\Gamma_8 \longrightarrow \Gamma_8$ transition are defined by

$$\rho_+ \equiv p+q,$$
$$\rho_- \equiv p-q,$$
$$\rho_1 \equiv 3(p^2-1)(q^2-1)+16pq,$$
$$\rho_2 \equiv 1+pq,$$
$$\rho_3 \equiv 1-pq,$$
$$\rho_4 \equiv 3(p^2-1)(q^2-1).$$

TABLE XIA. Relative intensities of Stark components with $\vec{E} \parallel [110]$, for $\Gamma_8 \longrightarrow \Gamma_7, \Gamma_7$ transitions.

Zero-field Transition	Stark components	Transition probability $\epsilon \parallel$	$\vec{k} \parallel [1\bar{1}0]$	$\epsilon \perp$	$\vec{k} \parallel [00\bar{1}]$	Relative intensities $\epsilon \parallel$	$\vec{k} \parallel [110]$	$\epsilon \perp$	$k \parallel [001]$
$\Gamma_8 \longrightarrow \Gamma_6$	$\Gamma_5(\pm\frac{3}{2}) \longrightarrow \Gamma_5$	$(\sqrt{3}+p)^2\lvert D_0\rvert^2 f$	$4p^2\lvert D_0\rvert^2 f$	$(\sqrt{3}-p)^2\lvert D_0\rvert^2 f$	$\frac{f}{2}(\sqrt{3}+p)^2$	$p^2/2$		$f(\sqrt{3}-p)^2/8$	
	$\Gamma_5(\pm\frac{1}{2}) \longrightarrow \Gamma_5$	$(\sqrt{3}p-1)^2\lvert D_0\rvert^2 f$	$4\lvert D_0\rvert^2 f$	$(\sqrt{3}p+1)^2\lvert D_0\rvert^2 f$	$\frac{f}{2}(\sqrt{3}p-1$	$f/2$		$f(\sqrt{3}p+1)^2/8$	
$\Gamma_8 \longrightarrow \Gamma_7$	$\Gamma_5(\pm\frac{3}{2}) \longrightarrow \Gamma_5$	$(\sqrt{3}p-1)^2\lvert D_0'\rvert^2 f$	$4\lvert D_0'\rvert^2 f$	$(1+\sqrt{3}p)^2\lvert D_0'\rvert^2 f$	$\frac{f}{2}(\sqrt{3}p-1)^2$	$f/2$		$f(1+\sqrt{3}p)^2/8$	
	$\Gamma_6(\pm\frac{1}{2}) \longrightarrow \Gamma_5$	$(\sqrt{3}+p)^2\lvert D_0'\rvert f$	$4p^2\lvert D_0'\rvert^2 f$	$(\sqrt{3}-p)^2\lvert D_0'\rvert^2 f$	$\frac{f}{2}(\sqrt{3}+p)^2$	$fp^2/2$		$f(\sqrt{3}-p)^2/8$	

$f=2(1+p^2)^{-1}$

TABLE XIB. Relative intensities with $\vec{E} \parallel [110]$, for $\Gamma_8 \rightarrow \Gamma_8$ transition.

Stark Components	Transition probability $\epsilon \parallel$	$\epsilon \perp k \parallel [1\bar{1}0]$	$\epsilon \perp \vec{k} \parallel [00\bar{1}]$
$\Gamma_6(\pm\frac{3}{2}) \rightarrow \Gamma_6(\pm\frac{3}{2})$	$f_1\lvert D(p-q)+D'(\sqrt{3}pq+\sqrt{3}+2p)\rvert^2$	$f_1\lvert D(p+q)+D'(3q-p)\rvert^2$	$f_1\lvert D(q-p)+D'(\sqrt{3}+\sqrt{3}pq-2p)\rvert^2$
$\Gamma_6(\pm\frac{3}{2}) \rightarrow \Gamma_5(\pm\frac{1}{2})$	$f_1\lvert D(1+pq)+D'(2pq-\sqrt{3}p+\sqrt{3}q)\rvert^2$	$f_1\lvert D(1-pq)+D'(pq+3)\rvert^2$	$f_1\lvert D(1+pq)+D'(2pq+\sqrt{3}p-\sqrt{3}q)\rvert^2$
$\Gamma(\pm\frac{1}{2}) \rightarrow \Gamma_6(\pm\frac{3}{2})$	$f_1\lvert D(1+pq)+D'(2+\sqrt{3}q-\sqrt{3}p)\rvert^2$	$f_1\lvert D(1-pq)-D'(3pq+1)\rvert^2$	$f_1\lvert D(1+pq)+D'(2+\sqrt{3}p-\sqrt{3}q)\rvert^2$
$\Gamma_6(\pm\frac{1}{2}) \rightarrow \Gamma_6(\pm\frac{1}{2})$	$f_1\lvert D(p-q)+D'(\sqrt{3}+\sqrt{3}pq-2q)\rvert^2$	$f_1\lvert D(p+q)+D'(3p-q)\rvert^2$	$f_1\lvert D(q-p\rvert D+D'(2q+\sqrt{3}pq+\sqrt{3})\rvert^2$
	Relative intensity		
$\Gamma_6(\pm\frac{3}{2}) \rightarrow \Gamma_6(\pm\frac{3}{2})$	$f_1[\rho_-^2+\frac{u}{4}(\rho_1+2\sqrt{3}\rho_+\rho_2)+\frac{v}{2}(\sqrt{3}\rho_2+\rho_+)\rho_-]/4$	$f_1[\rho_+^2-4uPq-v(\rho_+\rho_-)]/4$	$f_1[\rho^{-2}\frac{u}{4}(\rho_1-2\sqrt{3}\rho+\rho_2)-\frac{v}{2}(\sqrt{3}\rho_2-\rho_+)\rho_-]/4$

$\Gamma_5(\pm\frac{3}{2})\to\Gamma_5(\pm\frac{1}{2})$	$f_1[\rho_2^2-\frac{u}{4}(\rho_1-2\sqrt{3}\rho_-\rho_3)-\frac{v}{2}(\rho_3+\sqrt{3})\rho_2]/4$	$f_1[\rho_3^2+4uf q+v(\rho_2\rho_3]/4$	$f_1[\rho_2^2-\frac{u}{4}(\rho_1+2\sqrt{3}\rho-\rho_3)-\frac{v}{2}(\rho_3-\sqrt{3}\rho-)\rho_2]/4$
$\Gamma_5(\pm\frac{1}{2})\to\Gamma_5(\pm\frac{3}{2})$	$f_1[\rho_2^2-\frac{u}{4}(\rho_1+2\sqrt{3}\rho-\rho_3)-\frac{v}{2}(\sqrt{3}\rho_--\rho_3)$	$f_1[\rho_3^2+4u_2 q-v(\rho_2\rho_3)]/4$	$f_1[\rho_2^2-\frac{u}{4}(\rho_1-2\sqrt{3}\rho_-\rho_3)+\frac{v}{2}(\sqrt{3}\rho_-+\rho_3)\rho_2]/4$
$\Gamma_5(\pm\frac{1}{2})\to\Gamma_5(\pm\frac{1}{2})$	$f_1[\rho_-^2+\frac{u}{4}(\rho_1-2\sqrt{3}\rho+\rho_3)+\frac{v}{2}(\sqrt{3}\rho_3-\rho_+)\rho_-]/4,$	$f_1[\rho_+^2-4uf q+v(\rho_+\rho_-]/4$	$f_1[\rho_-^2+\frac{u}{4}(\rho_1+2\sqrt{3}\rho_+\rho_3)-\frac{v}{2}(\sqrt{3}\rho_3+\rho_+)\rho_-]/4$

TABLEXII Relative intensities of Stark components in Faraday configuration with $\vec{E}\parallel[110]$

Zero-field transition	Stark components	Relative intensities ϵ_+	ϵ_-
$\Gamma_8\to\Gamma_6$	$\Gamma_5(\pm\frac{3}{2})\to\Gamma_5$	$\frac{f}{8}(5p^2+3-2\sqrt{3}p)$	$\frac{f}{8}(5p^2-2\sqrt{3}p+3)$
	$\Gamma_5(\pm\frac{1}{2})\to\Gamma_5$	$\frac{f}{8}(3p^2+2\sqrt{3}p+5)$	$\frac{f}{8}(3p^2+2\sqrt{3}p+5)$
$\Gamma_8\to\Gamma_7$	$\Gamma_5(\pm\frac{3}{2})\to\Gamma_5$	$\frac{f}{8}(3p^2+2\sqrt{3}p+5)$	$\frac{f}{8}(3p^2+2\sqrt{3}p+5)$
	$\Gamma_5(\pm\frac{1}{2})\to\Gamma_5$	$\frac{f}{8}(5p^2-2\sqrt{3}p+3)^2$	$\frac{f}{8}(5p^2-2\sqrt{3}p+3)$
$\Gamma_8\to\Gamma_8$	$\Gamma_5(\pm\frac{3}{2})\to\Gamma_5(\pm\frac{3}{2})$	$\frac{f}{4}[\rho_+^2\rho_-^2+\frac{u}{4}(\rho_4-2\sqrt{3}\rho_+\rho_3)-\frac{v}{2}(\sqrt{3}\rho_2+\rho_+)\rho_-]$	$\frac{f}{4}[\rho_+^2+\rho_-^2+\frac{u}{4}(\rho_4-2\sqrt{3}\rho_+\rho_2)-\frac{v}{2}(\sqrt{3}\rho_2+\rho_+)\rho_-]$
	$\Gamma_5(\pm\frac{3}{2})\to\Gamma_5(\pm\frac{1}{2})$	$\frac{f}{4}[\rho_2^2+\rho_3^2-\frac{u}{4}(\rho_4+2\sqrt{3}\rho-\rho_3)+\frac{v}{2}(\rho_3+\sqrt{3}\rho_-)\rho_2]$	$\frac{f}{4}[\rho_2+\rho_3^2-\frac{u}{4}(\rho_4+2\sqrt{3}\rho_-\rho_3)+\frac{v}{2}(\rho_3+\sqrt{3}\rho_-)\rho_2]$
	$\Gamma_5(\pm\frac{1}{2})\to\Gamma_5(\pm\frac{3}{2})$	$\frac{f}{4}[\rho_2^2+\rho_3^2-\frac{u}{4}(\rho_4-2\sqrt{3}\rho_-\rho_3)+\frac{v}{2}(\sqrt{3}\rho_--\rho_3)\rho_2]$	$\frac{f}{4}[\rho_2^2+\rho_3^2-\frac{u}{4}(\rho_4-2\sqrt{3}\rho_-\rho_3)+\frac{v}{2}(\sqrt{3}\rho_--\rho_3)\rho_2]$
	$\Gamma_5(\pm\frac{1}{2})\to\Gamma_5(\pm\frac{1}{2})$	$\frac{f}{4}[\rho_+^2+\rho_-^2+\frac{u}{4}(\rho_4+2\sqrt{3}\rho+\rho_2)-\frac{v}{2}(\sqrt{3}\rho_3-\rho_+)\rho_-]$	$\frac{f}{4}[\rho_+^2+\rho_-^2+\frac{u}{4}(\rho_4+2\sqrt{3}\rho+\rho_2)-\frac{v}{2}(\sqrt{3}\rho_3-\rho_+)\rho_-]$

IV. Applied Electric Field in (001) Plane

When electric field lies in (001) plane and the angle with $\hat{x}$ axis is θ, the trasformation matrix is given in (21). We chose $\hat{x}'=\hat{x}\cos\theta+\hat{y}\sin\theta$, $\hat{y}'=-\hat{x}\sin\theta+\hat{z}\cos\theta$ and $\hat{z}'=\hat{z}$, where $\hat{z}' \| \vec{E}$.

case (a) $\Gamma'_8 \longrightarrow \Gamma_6$:

$$Q_x'(001)=\frac{D_0}{N}\begin{pmatrix} \sqrt{3}\,d(c+is)+(c-is) & 0 & \sqrt{3}\,(b+is)-d^*(c-is) & 0 \\ 0 & -d(ic-s)+\sqrt{3}\,(ic+s) & 0 & (ic-s)+\sqrt{3}\,d^*(ic+s) \end{pmatrix},$$

$$Q_y'(001)=\frac{D_0}{N}\begin{pmatrix} \sqrt{3}\,d(-s+ic)-(s+ic) & 0 & \sqrt{3}\,(-s+ic)+d^*(s+ic) & 0 \\ 0 & d(is+c)+\sqrt{3}\,(-is+c) & 0 & -(si+c)+\sqrt{3}\,d^*(-is+c) \end{pmatrix},$$

$$Q_z'(001)=\frac{2D_0}{N}\begin{pmatrix} 0 & id & 0 & -i \\ 1 & 1 & -d^* & 0 \end{pmatrix};$$

case (b) $\Gamma_8 \longrightarrow \Gamma_7$:

$$Q_x'(001)=\frac{D_0'}{N}\begin{pmatrix} -d(c-is)+\sqrt{3}\,(c+is) & 0 & (is-c)-\sqrt{3}\,d^*(c+is) & 0 \\ 0 & -\sqrt{3}\,d(ic+s)+(-ic+s) & 0 & \sqrt{3}\,(s+ic)+d^*(-ic+s) \end{pmatrix},$$

$$Q_y'(001)=\frac{D_0'}{N}\begin{pmatrix} d(s+ic)+\sqrt{3}\,(-s+ic) & 0 & (is+c)+\sqrt{3}\,d^*(s-ic) & 0 \\ 0 & \sqrt{3}\,d(is-c)+(is+c) & 0 & \sqrt{3}\,(-is+c)+d^*(is+c) \end{pmatrix},$$

$$Q_z'(001)=\frac{D_0'}{N}\begin{pmatrix} 0 & i & 0 & id^* \\ -d & 0 & -1 & 0 \end{pmatrix};$$

where s and c are abbreviation of $\sin\theta$ and $\cos\theta$. The relative intensities for $\vec{E}$ in (100) plane are given in Table XI. The direction of polarizaion depend on the direction of propagation vector $\vec{k}$. When $\theta=0°$ and 45°, that could reduced to case 1 and 111. The $\Gamma_8 \longrightarrow \Gamma_8$ transition are tedious and we do not give here.

TABLE XIII. Relative intensities of Stark components with E in (001) plane.

Zero-field transition	Stark Component	Relative intensities $\epsilon\parallel$	$\vec{k}\parallel[001]$ $\epsilon\perp$	$\vec{k}\perp[001]$
$\Gamma_8\to\Gamma_6$	$\Gamma_{3+4}(\pm\frac{3}{2})\to\Gamma_{3+4}$	$N'[\lvert\sqrt{3}d+1\rvert^2c^2+\lvert\sqrt{3}d-1\rvert^2s^2+2\sqrt{3}isc(d-d^*)]$	$N'[\lvert\sqrt{3}d+1\rvert^2s^2+1\sqrt{3}d-1\rvert^2c^2+2\sqrt{3}sci(d^*-d)]$	$4N'$
	$\Gamma_{3+4}(\pm\frac{1}{2})\to\Gamma_{3+4}$	$N'[\lvert\sqrt{3}-d\rvert^2c^2+\lvert\sqrt{3}+d\rvert^2s^2+2\sqrt{3}is(d^*-d)]$	$N'[\lvert\sqrt{3}-d\rvert^2s^2+\lvert\sqrt{3}+d\rvert^2c^2+2\sqrt{3}sci(d-d^*)]$	$4N'\lvert d\rvert^2$
$\Gamma_6\to\Gamma_7$	$\Gamma_{3+4}(\pm\frac{3}{2})\to\Gamma_{3+4}$	$N'[\lvert\sqrt{3}-d\rvert^2c^2+\lvert\sqrt{3}+d\rvert^2s^2+2\sqrt{3}sci(d-d^*]$	$N'[\lvert d+\sqrt{3}\rvert^2c^2+1d-\sqrt{3}\rvert^2s^2+2\sqrt{3}sci(d^*-d)]$	$4N'\lvert d\rvert^2$
	$\Gamma_{3+4}(\pm\frac{1}{2})\to\Gamma_{3+4}$	$N'[\lvert\sqrt{3}d+1\rvert^2c^2+1d-\sqrt{3}d\rvert^2s^2+2\sqrt{3}sci(d^*-d)]$	$N'[\lvert1-\sqrt{3}d\rvert^2c^2+\lvert\sqrt{3}d+1\rvert^2s^2+2\sqrt{3}sci(d-d^*)]$	$4N'$

$N'=[4(1+dd^*)]^{-1}$

TABLE XIV. Relative Intensities of Stark components with E in (110) plane.

Zero-field transition	Stark component	Relative intensities $\epsilon\parallel$	$\vec{k}\parallel[110]$ $\epsilon\perp$	$\vec{k}\parallel[001]$
$\Gamma_6\to\Gamma_6$	$\Gamma_{3+4}(\pm\frac{3}{2})\to\Gamma_{3+4}$	$[(\sqrt{3}A-1)^2s^2+8B^2c^2+4c^2]/M'$	$[(\sqrt{3}A-1)^2c^2+8B^2s^2+2B^2c^2+4S^2]/M'$	$[(1+\sqrt{3}A)^2+2B^2]/M'$
	$\Gamma_{3+4}(\pm\frac{1}{2})\to\Gamma_{3+4}$	$[(A+\sqrt{3})^2s^2+(\sqrt{6}Bs+2Ac)^2]/M'$	$[(A+\sqrt{3})^2c^2+(\sqrt{6}Bc+2AS)^2]/M'$	$[(A-\sqrt{3})^2+3B^2]/M'$
$\Gamma_8\to\Gamma_8$	$\Gamma_{5+4}(\pm\frac{3}{2})\to\Gamma_{3+4}$	$[(\sqrt{3}-A)^2s^2+(\sqrt{6}Bs+2Ac)^2]/M'$	$[(\sqrt{3}-A)^2c^2+(\sqrt{6}Bc-2As)^2]/M'$	$[(A+\sqrt{3})^2+3B^2]/M'$
	$\Gamma_{3+4}(\pm\frac{1}{2})\to\Gamma_{3+4}$	$[(\sqrt{3}A+1)s+2\sqrt{2}BC]^2+(2c-\sqrt{2}Bs)^2/M'$	$[(\sqrt{3}A+1)c+2\sqrt{2}Bs]^2+(\sqrt{2}Bc-2S)^2]/M'$	$[(\sqrt{3}A-1)^2+2B^2]/M'$

$M'=4A^2+8B^2+4\sqrt{6}ABsc+4$

$M'=2A^2+5B^2+2$

V. Electric Field in (110) Plane

When electric field in (110) plane and θ is the angle between the x axis and the field direction. The transformation is given in (29). We chose $\hat{x}'=\frac{1}{\sqrt{2}}(\hat{x}+\hat{y})$, $\hat{y}'=\frac{1}{\sqrt{2}}(\hat{x}+\hat{y})\cos\theta+\hat{z}\sin\theta$ and $\hat{z}'=\frac{1}{\sqrt{2}}(\hat{x}+\hat{y})\sin\theta+\hat{z}\cos\theta$, $\hat{z}'\parallel\vec{E}$ For a short notation we replace $\frac{\epsilon_0-\delta}{\sqrt{3}\epsilon'}$ and $\frac{\epsilon''}{\epsilon'}$ by A and B respectively.

case (a) $\Gamma_8\longrightarrow\Gamma_6$:

$$Q_x=\frac{1}{\sqrt{2}}\frac{D_0}{M}\begin{pmatrix}(1+i)(1+\sqrt{3}A) & 2B\sqrt{3}i & (1-i)(\sqrt{3}-A) & 2Bi\\ 2B & (1-i)(A-\sqrt{3}) & -2B\sqrt{3} & (1+i)(1+\sqrt{3}A)\end{pmatrix},$$

$$Q_y=\frac{D_0}{M}\begin{pmatrix}(-1+i)(\frac{\sqrt{3}A-1}{\sqrt{2}}c+2Bs) & -\sqrt{6}Bc-2As & (\frac{1+i}{\sqrt{2}})(\sqrt{3}+A)c & \sqrt{2}Bc-2si\\ -\sqrt{2}Bci+2s & \frac{1+i}{\sqrt{2}}(A+\sqrt{3})c & (\sqrt{6}Bc+2As)i & (1-i)[\frac{\sqrt{3}A-1}{\sqrt{2}}c-2Bs\end{pmatrix},$$

$$Q_z=\frac{D_0}{M}\begin{pmatrix}(-1+i)[\frac{\sqrt{3}A-1}{\sqrt{2}}s+2Bc] & -\sqrt{6}Bs-2Ac & \frac{1+i}{\sqrt{2}}(\sqrt{3}+A)s & (\sqrt{2}Bs-2ci)\\ -\sqrt{2}Bsi+2c & \frac{1+i}{\sqrt{2}}(A+\sqrt{3})s & (\sqrt{6}Bs+2Ac)i & (1-i)[\frac{\sqrt{3}A-1}{\sqrt{2}}s-2Bc]\end{pmatrix};$$

casd (b) $\Gamma_8\longrightarrow\Gamma_7$:

$$Q_x=\frac{D_0'}{\sqrt{2}M}\begin{pmatrix}(1-i)(A+\sqrt{3}) & 2B & (1+i)(\sqrt{3}A-1) & 2B\sqrt{3}i\\ 2\sqrt{3}B & (1+i)(\sqrt{3}A-1) & -2Bi & -(1-i)(\sqrt{3}+A)\end{pmatrix},$$

$$Q_y=\frac{D_0'}{M}\begin{pmatrix}\frac{1}{\sqrt{2}}(1+i)(\sqrt{3}-A)c(-\sqrt{2}Bc+2s)i-(1-i)(\frac{\sqrt{3}A+1}{\sqrt{2}}c+2Bs)(+\sqrt{6}Bc+2As) & \\ -(\sqrt{6}Bc+2As)i & (1-i)(\frac{\sqrt{3}A+1}{\sqrt{2}}c+2Bs) \quad \sqrt{2}Bc-2s & (1+i)\frac{\sqrt{3}-A}{\sqrt{2}}c\end{pmatrix},$$

$$Q_z=\frac{D_0'}{M}\begin{pmatrix}\frac{1}{\sqrt{2}}(1+i)(\sqrt{3}-A)s(-\sqrt{2}Bs+2c)i-(1-i)(\frac{\sqrt{3}A+1}{\sqrt{2}}s+2Bc)(-\sqrt{6}Bs+2Ac) & \\ -(2\sqrt{6}Bs+2Ac)i & (1-i)(\frac{\sqrt{3}A+1}{\sqrt{2}}s+2Bc) \quad \sqrt{2}Bs-2c & \frac{(1+i)}{\sqrt{2}}(\sqrt{3}-A)s\end{pmatrix}.$$

The relative intensities are given in Table XIV.

In external uniform electric field that will cause the fourfold degenerate levels both shift and splitting into twofold degenerate states and the twofold degenerate levels shift only split. We have calculated the relative intensities of Stark components, rigorously, that not the relative value of transition probability, the relative intensities must be multiplied by fractional population of initial sublevels if the Stark splitting are sufficient small, and all initial sublevels may be assumed to be equally populated, then intensities would becom identical with what we calculated. In experiment,[19] only broaden and shift of absorption, which are quadratical with the applied field, are observed that would be supposed due to

unresolved partial splitting of spectrum lines. Bir[23] estimated the magnitute of Stark splitting about 5×10^{-9} E^2 mev for germanuim (E in V/cm), and who also estimated the splitting at maximum possible field above which low temperature "breakdown" happens about 2×10^{-5} mev that too small to observe.

ACKNOWLEDGEMENT

The author would like to express his hearty thank to Professor S. Y. Wang of National Tsing Hua University and L. T. Ho of Academia Sinica for their guidance and encouragement throughout this study.

REERENCES

1. E. Burstein, E. E. Bell, J. W. Davisson and M. Lax, J. Phys. Chem. 57, 849 (1953).
2. E. Burstein, G. S. Picus, B. Henvis and R. Wallis, J. Phys. Chem. Solids. 1, 65 (1956).
3. J. C. Slater, Phys. Rev. 76, 1592 (1949).
4. G. F. Koster and J. C. Slater, Phys. Rev. 95, 1167 (1954).
5. J. M. Luttinger and W. Kohn, Phys. Rev. 96, 802 (1954).
6. Kittel and A. H. Mitchell, Phys. Rev. 96, 1488 (1954).
7. J. M. Lutlinger and W. Kohn, Phys. Rev. 97, 869 (1955).
8. G. L. Pearson and J. Bardeen, Phys. Rev. 75, 865 (1949).
9. W. Kohn and J. M. Lutlinger, Phys. Rev. 97, 883 (1955).
10. W. Kohn and J. M. Lutlinger, Phys. Rev. 97, 1721 (1955).
11. W. Kohn, Phys. Rev. 98, 1856 (1955).
12. W. Kohn and J. M. Luttinger, Phys. Rev. 98, 916 (1955).
13. W. Kohn, Solid Staate Physics, edited by F. Seitz and D. Turnhull (Academic, New York, 1957), Vol. 5, p.257.
14. H. Y. Fan, and P. Fisher, J. Phys. Chem. Solids, 8, 270 (1959).
15. S. Ewerdling, K. J. Button and B. Lax, Phys. Rev. 118, 975 (1960).
16. A. Onton, P. Fisher and A. K. Ramdas, Phys. Rev. 163, 686 (1967).
17. R. L. Jones and P. Fisher, J. Phys. Chem. Solids, 26, 1125 (1965).
18. R. L. Jones and P. Fisher, Phys. Rev. B2, 2016 (1970).
19. D. H. Diskey and J. O. Dimmock, J. Phys. Chem. Solids, 28, 529 (1967).
20. J. J. White, Can. J. Phys. 45, 2695 (1967).
21. D. Schechter, J. Phys. Chem. Solids, 23, 237 (1962).
22. K. S. Mendelson and H. M. James, J. Phys. Chem. Solids, 25, 729 (1964).
23. A. A. Kaphyankii, Opt.:Spectroskopiya 16, 1031 (1964) [Opt. Spectry. (USSR) 16, 557 (1964)]
24. B. P. Eakharchenya and I. B. Rusanor, Opt.: Spectroskopiya 19, 365 (1965) [Opt. Spectry (USSR) 19, 207 (1965)].

25. E. O. Kane, J. Phys. Chem. Solids, 1, 82 (1956).
26. S. Rodriguez, P. Fisher and F. Barra, Phys. Rev. B5, 2219 (1972).
27. K. Anadi, Bhattacharjee and S. Rodriguez, Phys. Rev. B6, 3836 (1972).
28. G. L. Bir, E. I. Butikov and G. E. Pikus, J. Phys. Chem. Solids 24, 1475 (1963).

大氣及颱風運動模型*

Ⅱ. 運算範圍與網格大小

大氣物理組同仁

中央研究院物理研究所

一、簡　介

本研究計劃以侵襲臺灣颱風爲對象，藉控制區域性大氣運動變化的流力、熱力等方程式，探討大氣及颱風運動變化現象，以求率得較客觀的運動模型，供預報之用。

在大氣及颱風運動模型：I. 邊界條件 (1972) 文中，已探討不同邊界條件下可能引起的變化，本文將繼續探討運算範圍 (domain size) 及網格大小 (grid size) 變化之影響。

基本的運動方程式在 (x,y,p,t) 經化簡可得 (大氣物理組同仁，1972)

$$\frac{\partial}{\partial t}\nabla^2 Z = -J(Z,\zeta+f)+\frac{\bar{f}^2}{g}\frac{\partial\omega}{\partial p} = F^1(Z,\omega) \tag{1}$$

$$\frac{\partial}{\partial t}\frac{\partial Z}{\partial p}=-\frac{g}{\bar{f}}J\left(Z,\frac{\partial Z}{\partial t}\right)-\sigma\omega = F^2(Z,\omega) \tag{2}$$

$$\nabla^2\sigma\omega+\frac{\bar{f}^2}{g}\frac{\partial^2\omega}{\partial p^2}=\frac{g}{\bar{f}}\nabla^2\left[J\left(\frac{\partial Z}{\partial p},Z\right)\right]-\frac{\partial}{\partial p}\left[J\left(\frac{g}{\bar{f}}\nabla^2 Z+f,Z\right)\right] = F^3(Z) \tag{3}$$

式中 Z 爲高度，f 及 $\bar{f}$ 爲 Coriolis 參數及其空間平均值，g 爲重力加速度，

$$\zeta=\frac{g}{\bar{f}}\nabla^2 Z$$

$$\omega=\frac{dp}{dt} \tag{4}$$

$$\sigma=-\overline{\frac{1}{\rho g\theta}\frac{\partial\theta}{\partial p}}$$

ρ 爲大氣質量，θ 爲 potential temperature.

利用數值方法解 Eqs. 1及2，以求Z及 ω 變化時，整個運算範圍區分爲如 Fig.1 所示的網格。垂直方向共分爲四層，各層符號如圖中所示。在此網格系統下，numerical procedure 如 Fig.2 所示。Eq.3 化成 finite difference form 爲

$$\omega_{ijk}^{n+1}=\left[\omega_{i+1jk}+\omega_{i-1jk}+\omega_{ij+1k}+\omega_{ij-1k}+\frac{\bar{f}^2d^2}{\sigma gm^2\Delta p^2}(\omega_{ijk+1}-\omega_{ijk-1})\right.$$

$$\left.-\frac{F^3_{ijk}d^2}{m^2}\right]^n/\left[4+\frac{2\bar{f}^2d^2}{gm^2\Delta p^2}\right]^n \tag{5}$$

式中 k=2,3,4, i=2,…,NX−1, j=2,…,NY−1. m 爲 map-scale factor, d 爲 grid length, n 及

* 本文承行政院國家科學委員會支助完成。

n+1 爲 iteration process 中二連續步驟，在 fixed boundary condition (Z at lateral boundary 及其外在 time domain 內保持不變) Eq. 5 重複運用直至

$$Max. \mid \omega_{ijk}^{n+1\sigma} - \omega_{ijk}^{n} \mid \leq \epsilon \tag{6}$$

如此可據已知 Z-fields 解 400,600 及 800 mb 之 ω-fields.

Δt 爲 time increment, von Neumann necessary condition (Richtmyer & Morton, 1967) 要求

$$\Delta t \leq Min. \frac{d}{\frac{g}{f}\left(\left|\frac{\partial Z}{\partial x}\right|+\left|\frac{\partial Z}{\partial y}\right|\right)+\left|\omega\frac{\partial Z}{\partial p}\frac{d}{d_{\Delta p}}\right|} \tag{7}$$

式中 $d_{\Delta p}$ 爲 Δp 之厚度

Eq.1 可化爲

$$\frac{\partial Z}{\partial t}_{ijk}^{n+1} = 0.25\left[\frac{\partial Z}{\partial t}_{i+1jk}+\frac{\partial Z}{\partial t}_{i-1jk}+\frac{\partial Z}{\partial t}_{ij+1k}+\frac{\partial Z}{\partial t}_{ij-1k}-\frac{d^2}{m^2}F^1_{ijk}\right]^n \tag{8}$$

式中 k=2, i=2,…, NX-1, j=2,…, NY−1, 此式重複運用直至

$$Max. \left|\frac{\partial Z}{\partial t}_{ijk}^{n+1\sigma}-\frac{\partial Z}{\partial t}_{ijk}^{n}\right| \leq \epsilon$$

以解 500 *mb* $\frac{\partial Z}{\partial t}$ − *field.* (9)

Eq.2 可化爲

$$\partial Z_{ijk}^{t+\Delta t} = \partial Z_{ijk}^{t} + \Delta t\ \Delta p\ F_{ijk}^{2} \qquad \textit{at initial time step}$$

$$\partial Z_{ijk}^{t+\Delta t} = \partial Z_{ijk}^{t-\Delta t} + 2\Delta t\ \Delta p\ F_{ijk}^{2} \qquad \textit{at other time steps} \tag{10}$$

式中 k=2,3,4, i=2,…, NX−1, j=2,…, NY−1, 以解 400, 600 及 800 mb 之 ∂Z-field

二、天氣資料

據以探討大氣及颱風運動之原始天氣圖與「大氣與颱風運動模型：I. 邊界條件文」中所用者相同。該文中 Figs. 5及8在本文中重新以 Figs. 3及4繪出（大氣物理組同仁，1972）。Fig. 3 中實線部分爲原始天氣圖，Fig. 4 爲在 fixed boundary condition 下 12 及 24 小時左右後之天氣圖。

三、運算範圍

探討大氣運動最理想的是以全球爲探討對象（Arakawa, 1971 等），其次以半球爲對象（Shuman & Hovermale, 1968），但這都需要極好的高速計算機及充裕的預算。國內目前二者條件皆有限，所幸 Rosenthal (1971) 在探討 Hurricane 生成時，發現 domain size 祇需大於 2000 km, Baumhefner (1971) 在探討 southern boundary 時，發現即使南方邊界移至北緯15度，仍可做北半球短時間有效的天氣預測。本文暫不深入探討 domain size 對較長時間天氣變化的影響（將在下年度天氣資料分析後再研討），謹就 northern boundary 對天氣變化之影響做一檢討。

在 $NX=20$

$NY=20$

$d=3.322\times10^5$ *m* (*grid* 如 *Fig.*3 形示)

$g=9.8\ m/sec^2$
$\sigma=0.00355\ m/mb^2$
$\epsilon=10^{-6}$
$\bar{f}=0.659\times10^{-4}\ sec^{-1}$
$R/c_p=2/7$
$d_{\Delta p}=2.15\times10^5 m$ (11)

時，Fig.5 顯示在 fixed boundary condition 下12小時及24小時左右之 Z-field. 與 Fig. 4 比較可以看到12小時左右之 Z-fields二者極其相似，也就是說在短時間內 domain size 的大小尚不發生影響。進一步比較二者在24小時的 Z-fields，可以看出 300 及 500 mb 的 Z-fields 仍相類同，但 700 及 900 mb 的 Z-fields 則已漸有差異，尤其是 Fig.5 900 mb 的天氣圖上可明顯看出東北角低壓北移（實際天氣圖亦如此）。在 Fig.4 中由於該處 boundary value 固定不能變動，天氣圖顯示不同的變化。因之，在 computation domain邊界上有強烈天氣變化時，即使是24小時左右之天氣模擬也需要較大的computation domain。反過來說，如果 computation domain 邊界上無強烈天氣變化，即使更長時間的大氣變化模擬也可藉有限 domain 探討（Staff members, 1965）。一般來說，domain size 愈大，boundary 發生影響的問題愈小，但在運用計算機解問題時，花費的時間與經費亦增加。由於邊界上大氣變化對短時間颱風運動影響不大，因此本文以下仍將就 NX=20, NY=14 作爲模擬大氣與颱風運動變化的 domain. 不過由於原來繪製的天氣圖在東北角上梯度過大不甚合理，因之在繼續探討問題之前，先將該處天氣資料略施修正如 Fig.3 中虛線部分所示。修正後天氣圖12及24小時左右之變化在 Fig. 6 中顯示，與 Fig. 4 比較可知主要修正的是靠北邊邊界附近的天氣資料。

四、網格大小

在運用 finite difference scheme 解問題時，一般而言，grid size 愈小，solution 愈準確，但是由於計算機的 memory 及運用計算機的經費有限，選擇網格大小時，不能不有所選擇。探討大氣及颱風問題時，不同大小的網格選定時，小規模（micro-or meso-scale）大氣變化現象尚需配合運動方程式中有關變數表示出來。

探討颱風構造時，網格一般在 50 km 或更小（Rosenthal, 1971），探討 synoptic scale 運動時，網格一般在 150 km 或更大（Hawkins, 1972; Miller, 1969）。本研究計劃網格大小大多選在 300 多公里大小（Staff members, 1965），在檢討網格大小所生影響時，將 grid size 減半檢討。

在 $NX=39$
$NY=27$
$d=1.661\times10^5 m$
$g=9.8\ m/sec^2$
$\sigma=0.003252\ m/mb^2$
$\epsilon=10^{-6}$
$\bar{f}=0.648\times10^{-4}\ sec^{-1}$
$R/C_p=2/7$
$d_{\Delta p}=2.15\times10^5\ m$ (12)

時，Fig.7 顯示在 fixed boundary condition 下12及24小時左右之 Z-field. 與 Fig.6 比較可以看出 d=166 km 所得的天氣變化與 d=322 km 者大致相似，不過在 300 及 500 mb 處 fine grid size所得

的颱風中心變化向左下方偏斜，不甚合理，這可能由於

§. 西北有太平洋地區天氣資料缺乏，據之繪成的天氣圖誤差較大，當 grid size 小而 computational accuracy 未見提高時，high frequency components 容易顯出。

§. 原始 data 並未 balance，在 grid size 太小時，geostrophic wind assumption

$$\mathbf{V}=\mathbf{k}\times\frac{g}{f}\nabla Z \text{ 式中 } \nabla\cdot\mathbf{V}=0 \tag{13}$$

V 爲水平速度向量，所引起的 error 相對增大。此時，Eq. of Continuity. 可化爲

$$\frac{\partial\omega}{\partial p}=\epsilon' \tag{14}$$

ϵ' 本應爲零，但在 geostrophic assumption 下，不一定爲零，其數值愈大表示誤差愈大。同時顯示颱風中心附近 $\epsilon'\times10^6$ 之值

7	0.6 / 0.25	1 45 / 3.25	−3.05 / 4.5
6	−2.35 / −0.15	5.8 / 7.75	−16.3 / 1.8
5	−18.05 / −2.15	0.55 / 2.25	1.0 / −1.95
	8	9	10

i,j 係按 d=332 km 所繪就網格上相對位置，右上方 $\epsilon'\times10^6$ 值相對於 d=166 km，左下方 $\epsilon'\times10^6$ 值相對於 d=322 km。可以看出 d=166 km 之誤差要比 d=332 km 大不少。同時 Fig. 8 中顯示出在24小時左右 800 mb 處二種不同網格所得 ω-fields，可以看出 fine grid size 所得 ω-field 較爲紊亂，且在颱風中心北方有極強的下降氣流迫使颱風南移。

五、結論與建議

§. 本文主旨在探討運算範圍與網格大小發生變化時，可能造成運動模型答案之影響。Fig. 5 顯示在 fixed boundary condction 下，北方運算範圍加大的結果。雖然東北角低壓未影響到颱風運動，但東北部天氣變化在較大運算範圍時中較合理。Fig. 7 顯示在網格大小較 Fig. 6 中減半時，由於相對精度降低等綜故，d=166 km 所得答案反較 d=332 km 者爲差。

§. 本文探討時發現天氣圖的準確度影響結果甚大，雖經略施修正，但結果仍不甚佳。在下一篇探討熱變化影響時，仍需進一步校正。

§. Fig. 9 顯示使用 barotropic model，亦即解 (Sanders & Burpee, 1968)

$$\frac{\partial}{\partial t}\nabla^2 Z=-J(Z,\zeta+f) \tag{15}$$

所得結果，24 小時後颱風中心偏向北方移動（與 Fig. 6 比較）與實際天氣變化不符，顯然由於 Eq. 14 考慮情形比 Eqs. 1 & 2 之簡化許多的緣故。

六、後　記

參加本專題研究之大氣物理組同仁包括汪群從、彭立、簡來成、馬天驥、張文瀾、柯順德、梁文傑等人。計算機使用承物理中心支援，謹致謝意。

參 考 文 獻

Baumhefner, D.P., On the Effects of an Imposed Southern Boundary on Numerical Weather Prediction in the Northern Hemisphere, J. Atm. Sci., 28, 42, 1971.

Hawkins, H.F., Development of a Seven-Level, Balanced, Diagnostic Model and its Application to Three Disparate Tropical Disturbances, NOAA TM ERL NHRL-98, 1972.

Miller, B.I., Experiments in Forecasting Hurricane Development with Real Data, ESSA TM ERLTM-NHRL 85, 1969.

Richtmyer, R.D. & K.W.Morton, Difference Methods for Initial-Value Problems, Interscience Publishers, N.Y., 1967.

Rosenthal, S.L., The Response of a Tropical Cyclone Model to Variations in Boundary Layer Parameters, Initial Conditions, Lateral Boundary Conditions, and Domain Size, MWR, 99, 767, 1971.

Sanders, F. & R.W. Burpee, Experiments in Barotropic Hurricane Track Forecasting, J. Appl. Met., 7, 313, 1968.

Shuman, F.G. & J.B. Hovermale, An Operational 6-layer Primitive Equation Model, J. Appl. Meteoro., 7, 525, 1968.

Staff Members of Electronic Computation Center, 72-hr. Baroclinic Forecast by the Diabatic Quasi-Geostrophic Model, J. Meteoro. Soc. Japan, 43, 246, 1965.

大氣物理組同仁　大氣及颱風運動模型：I. 邊界條件，中研院物理所集刊 2, 177, 1972.

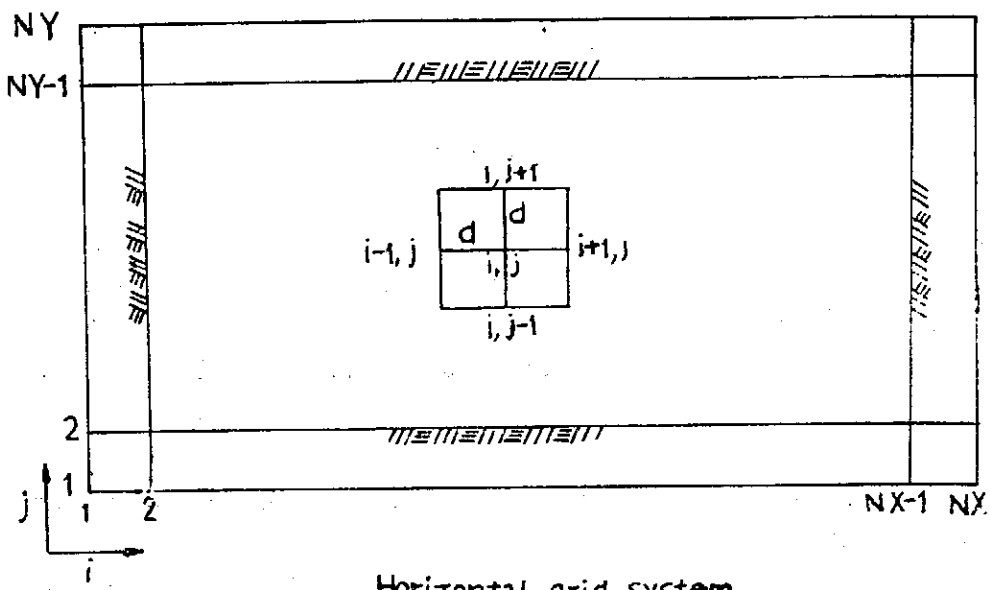

Horizontal grid system

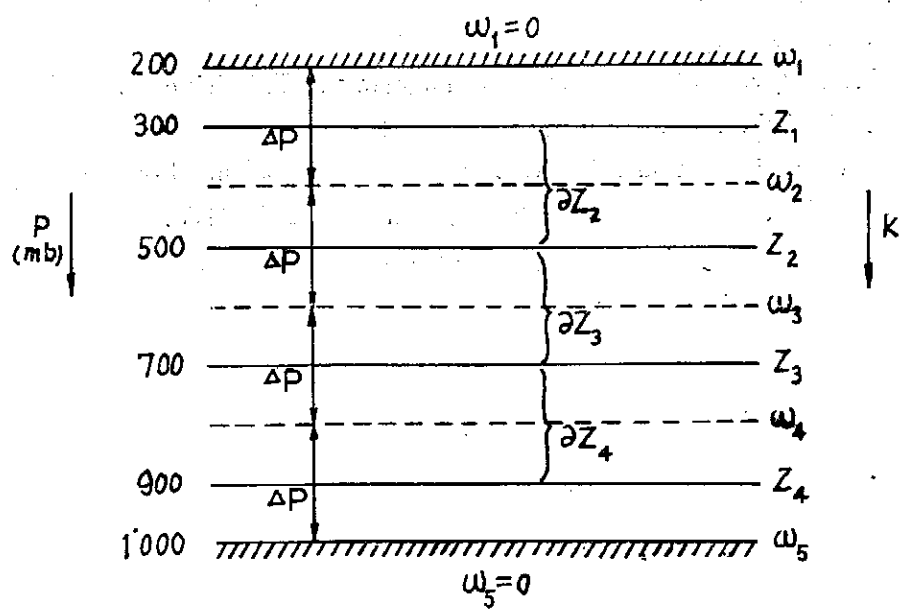

Vertical grid system

Fig.1. Grid systems

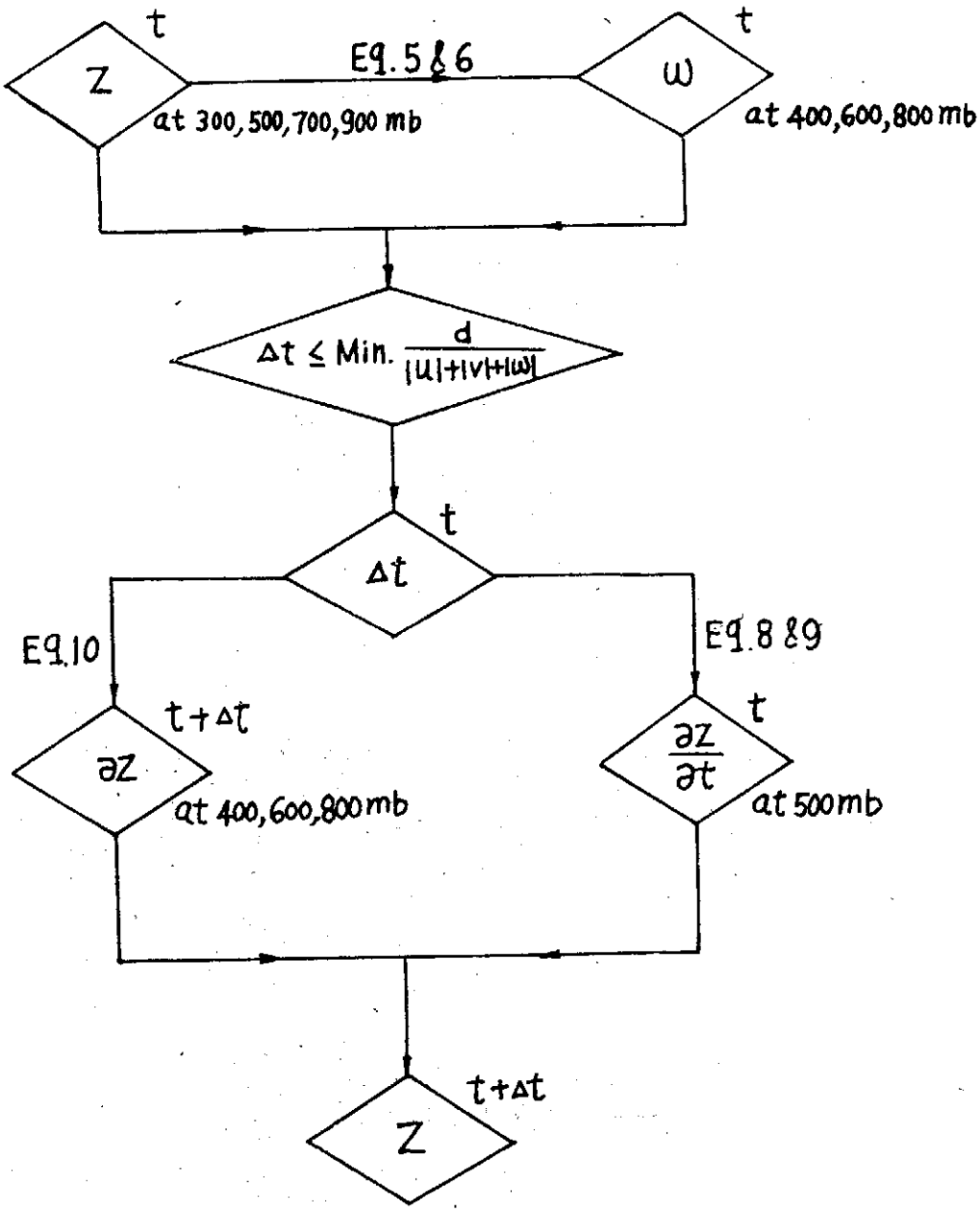

Fig. 2. Numerical procedures

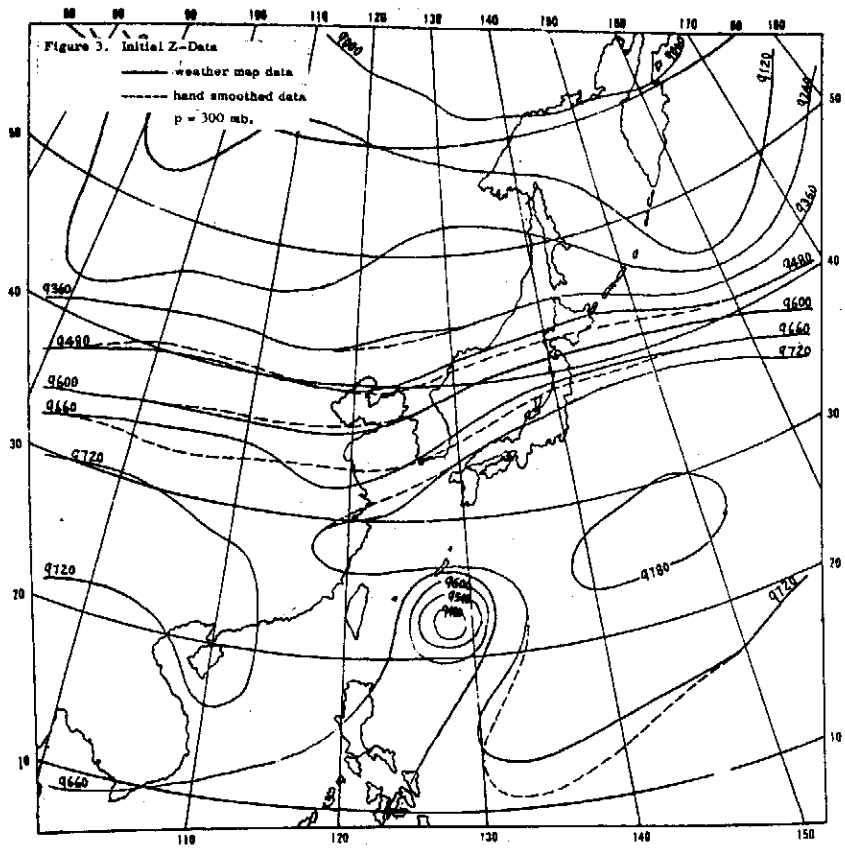
Figure 3. Initial Z-Data
weather map data
hand smoothed data
p = 300 mb.

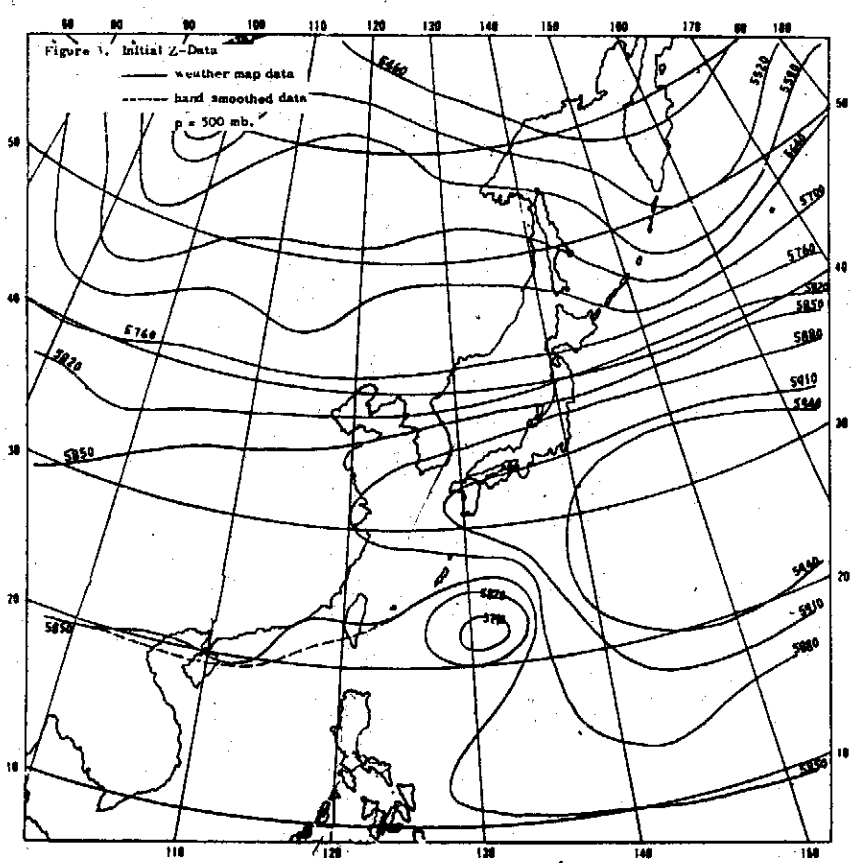
Figure 4. Initial Z-Data
weather map data
hand smoothed data
p = 500 mb.

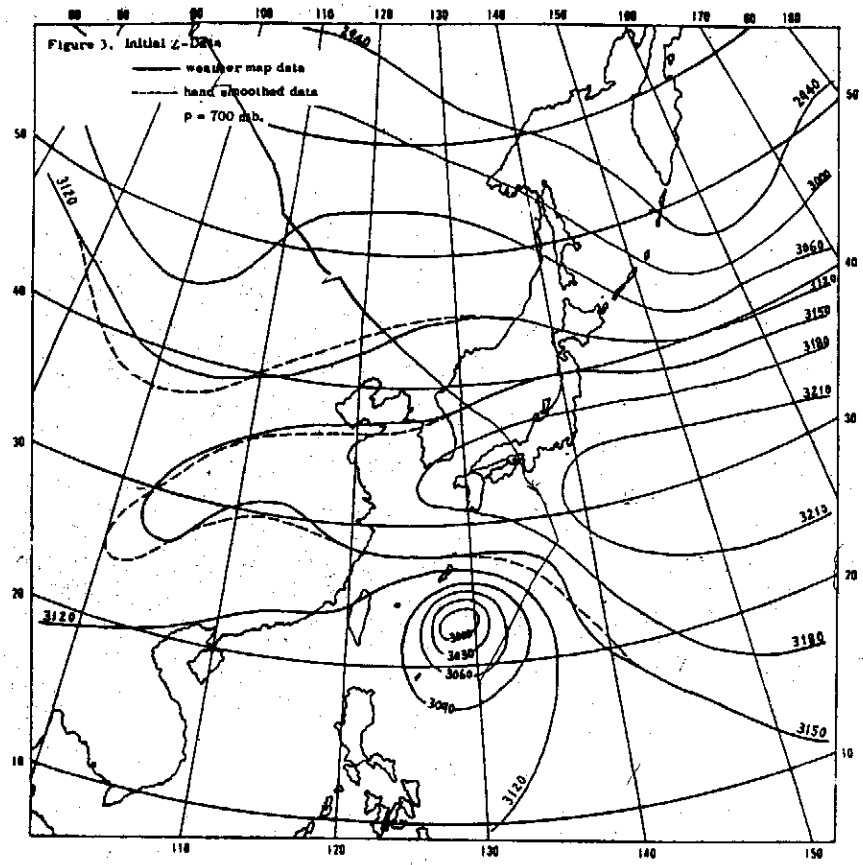
Figure 3. Initial Z-Data
weather map data
hand smoothed data
p = 700 mb.

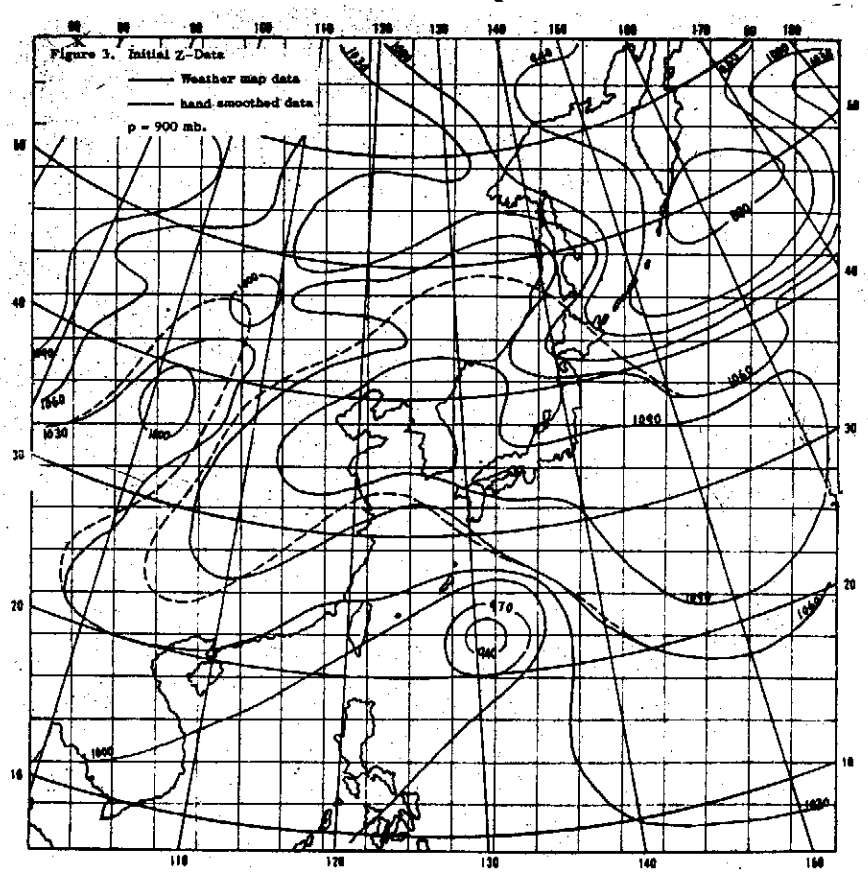
Figure 3. Initial Z-Data
Weather map data
hand smoothed data
p = 900 mb.

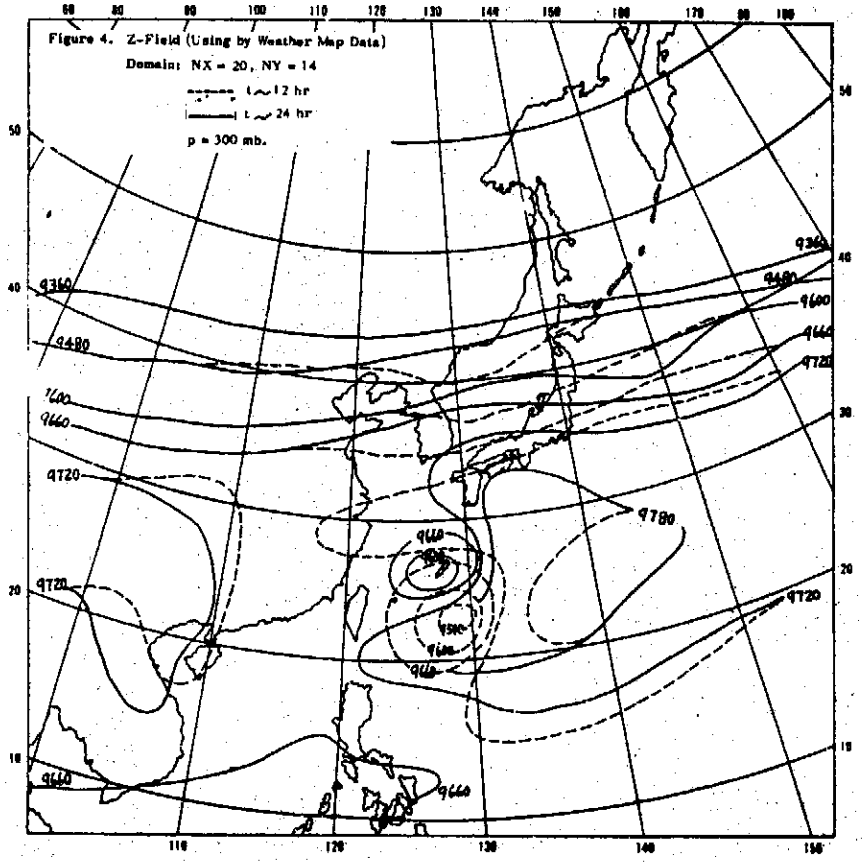
Figure 4. Z-Field (Using by Weather Map Data)
Domain: NX = 20, NY = 14
t ~ 12 hr
t ~ 24 hr
p = 300 mb.
9360
9480
9600
9660
9720
9780
9720
9660

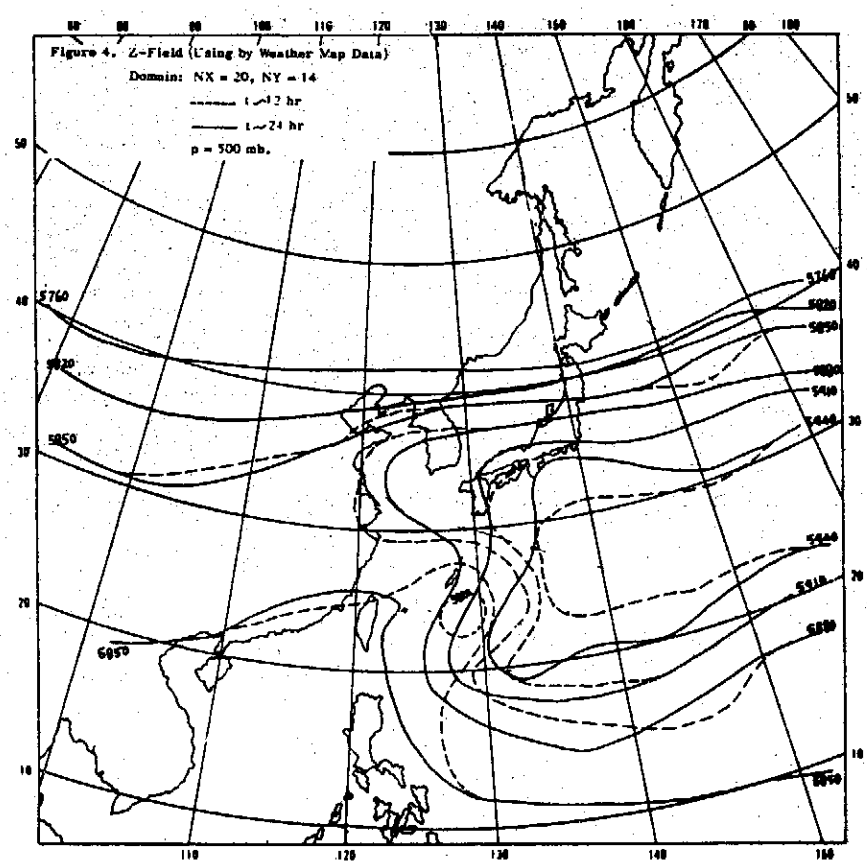
Figure 4. Z-Field (Using by Weather Map Data)
Domain: NX = 20, NY = 14
t ~ 12 hr
t ~ 24 hr
p = 500 mb.
5760
5850
5950

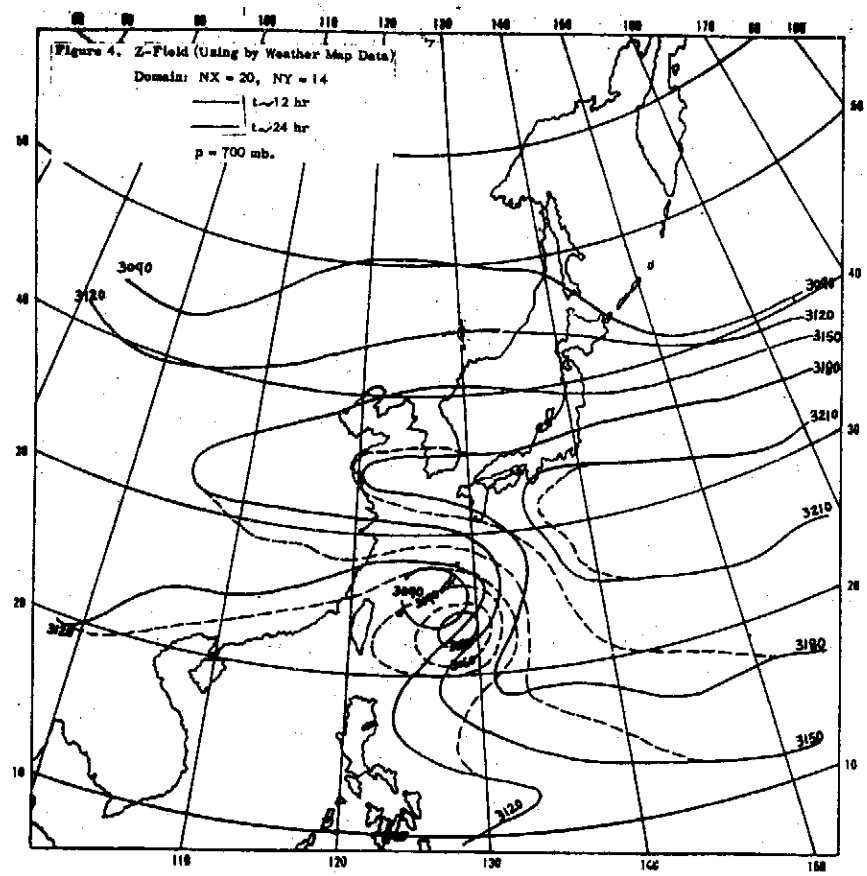
Figure 4. Z-Field (Using by Weather Map Data)
Domain: NX = 20, NY = 14
t=12 hr
t=24 hr
p = 700 mb.
3090
3120
3150
3180
3210
3240
3270

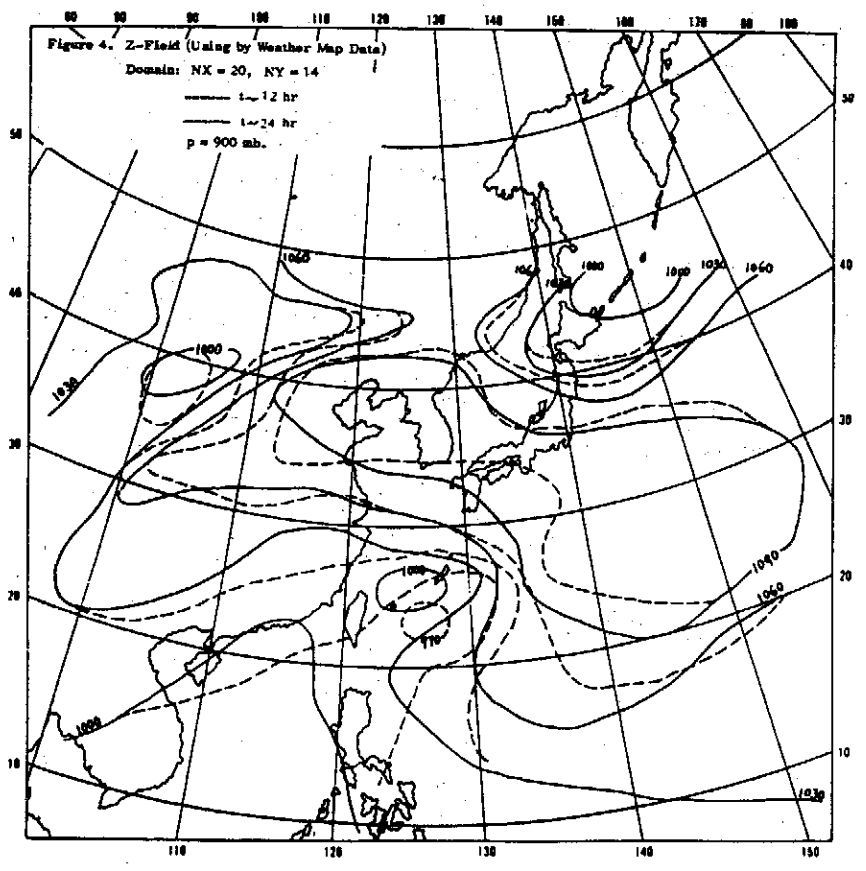
Figure 4. Z-Field (Using by Weather Map Data)
Domain: NX = 20, NY = 14
t=12 hr
t=24 hr
p = 900 mb.
1000
1020
1040
1060

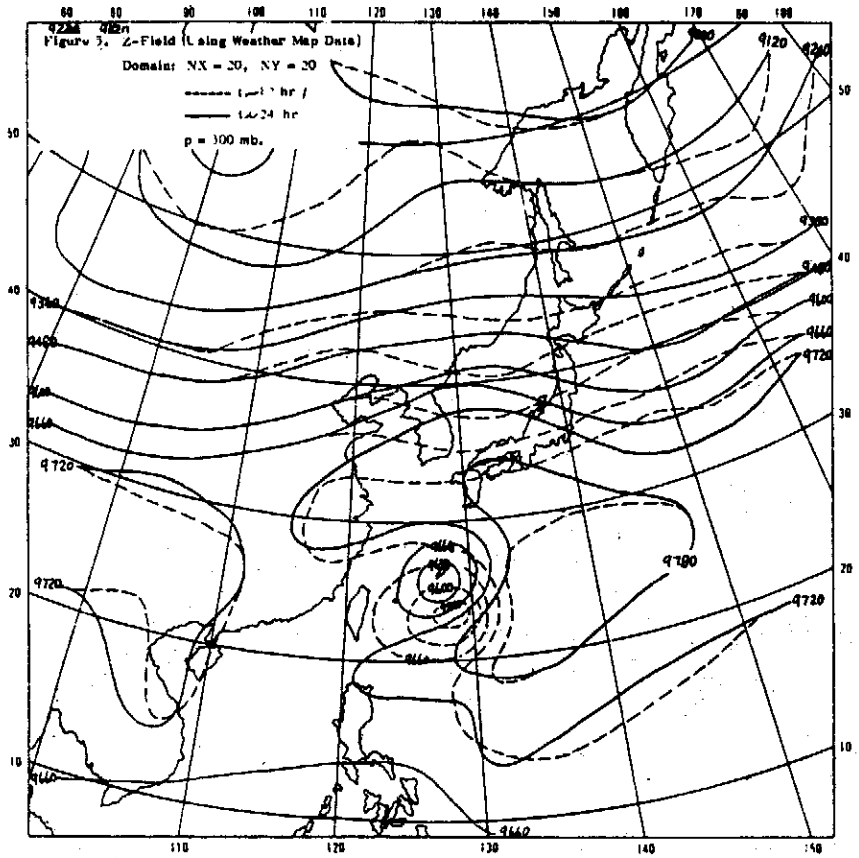
Domain: NX = 20, NY = 20
p = 300 mb.
9720
9780
9660

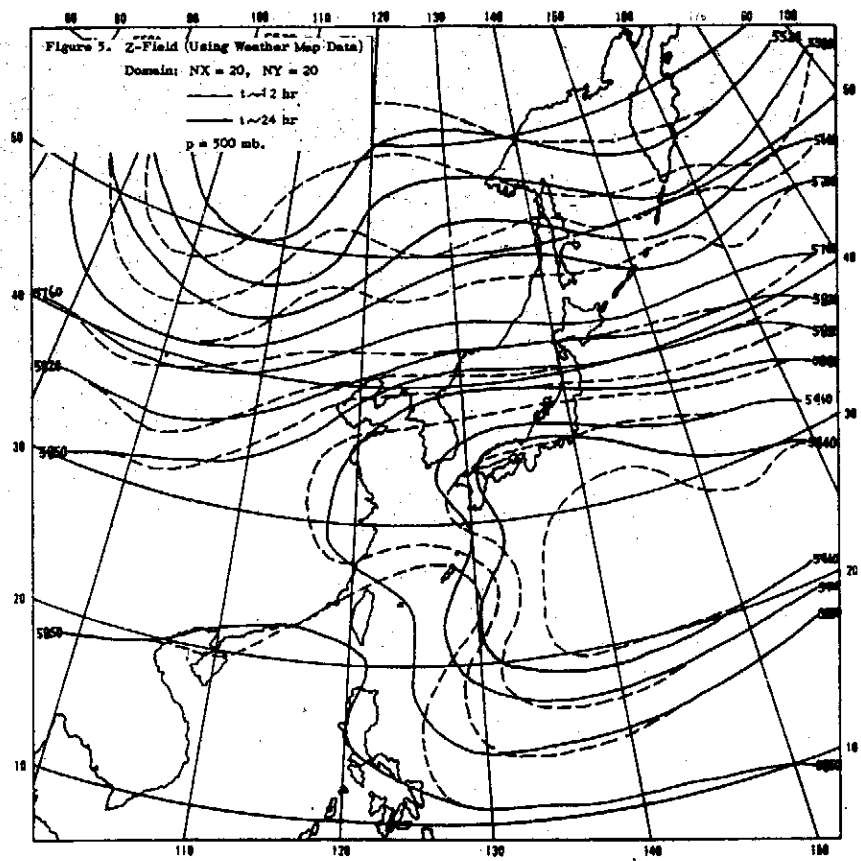
Domain: NX = 20, NY = 20
p = 500 mb.

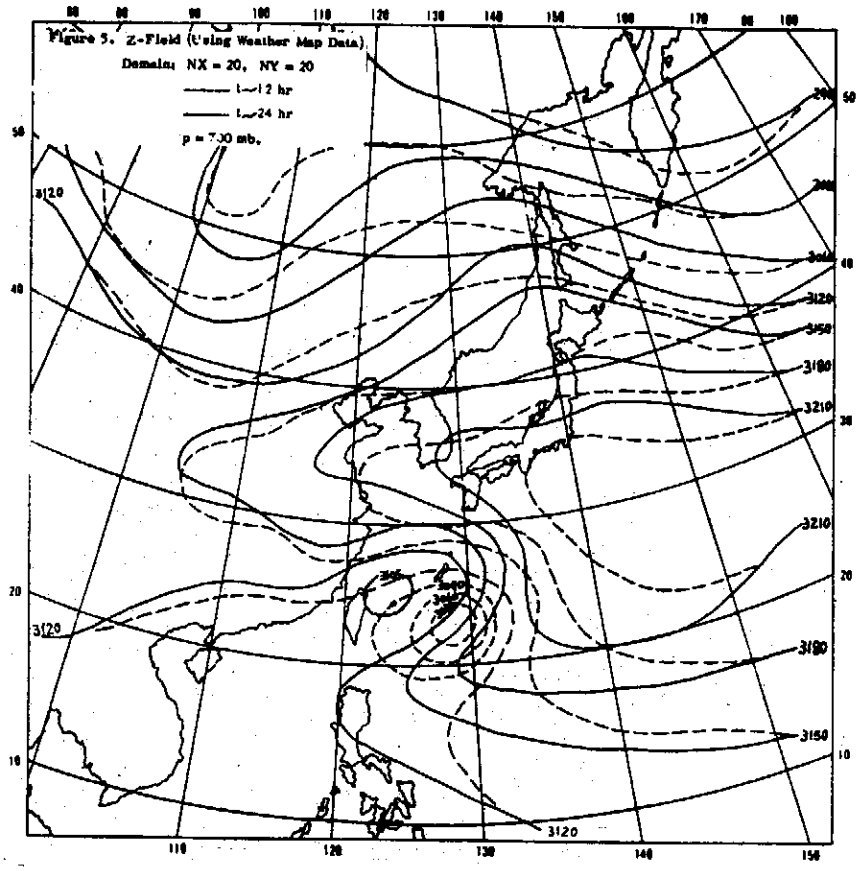
Figure 5. Z-Field (Using Weather Map Data)
Domain: NX = 20, NY = 20
p = 700 mb.
3120
3150
3180
3210
3240

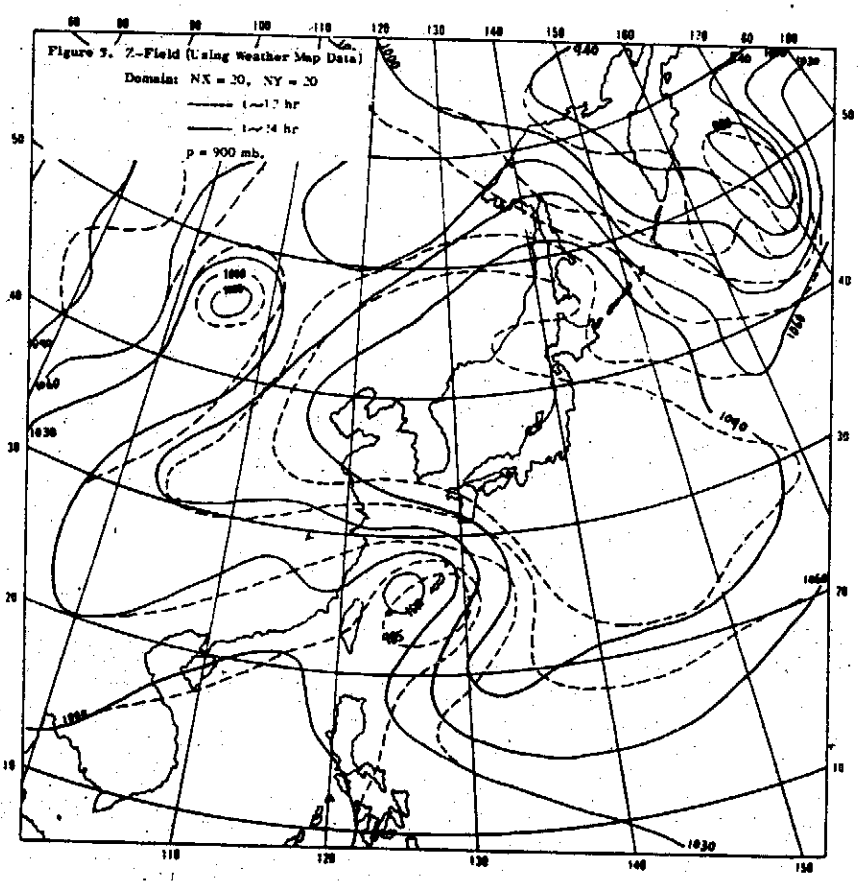
Figure 5. Z-Field (Using Weather Map Data)
Domain: NX = 20, NY = 20
p = 900 mb.
1000
1030
1060

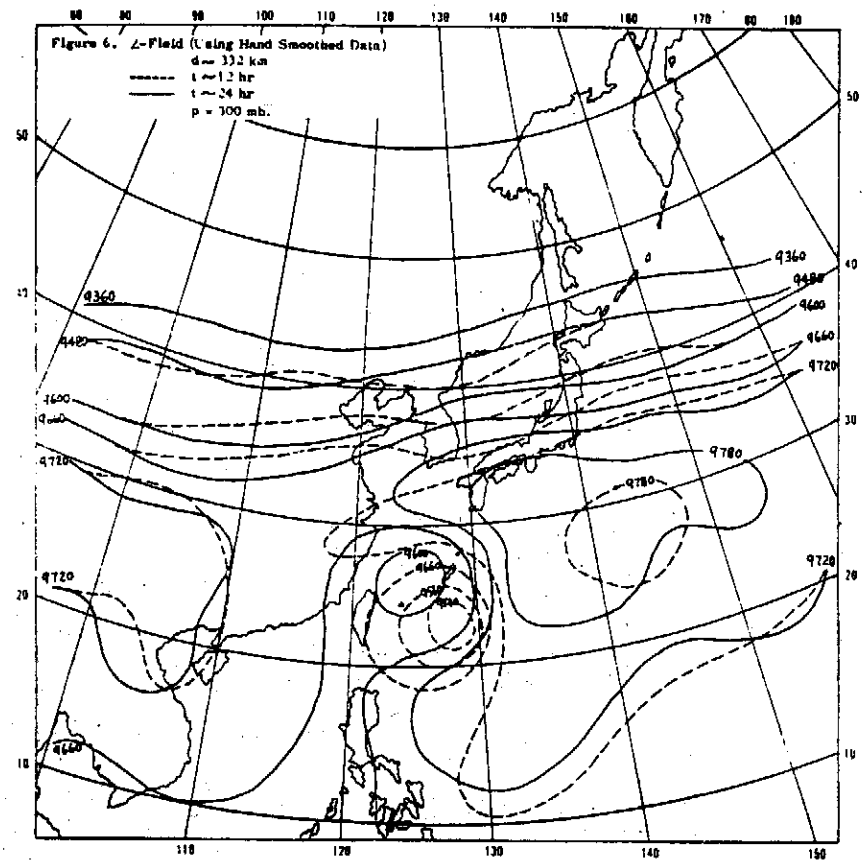
Figure 6. Z-Field (Using Hand Smoothed Data)
d ~ 332 km
t ~ 12 hr
t ~ 24 hr
p = 700 mb.
9360
9480
9600
9660
9720
9780
9720
9660

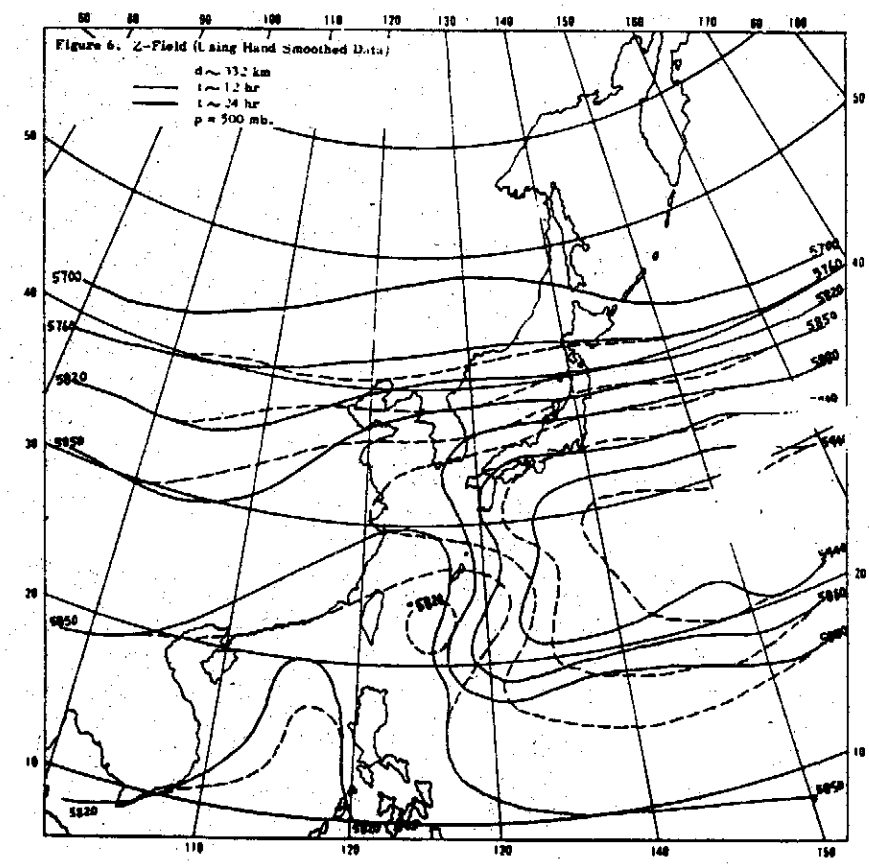
Figure 6. Z-Field (Using Hand Smoothed Data)
d ~ 332 km
t ~ 12 hr
t ~ 24 hr
p = 500 mb.
5700
5760
5820
5850
5880
5700
5760
5820
5850

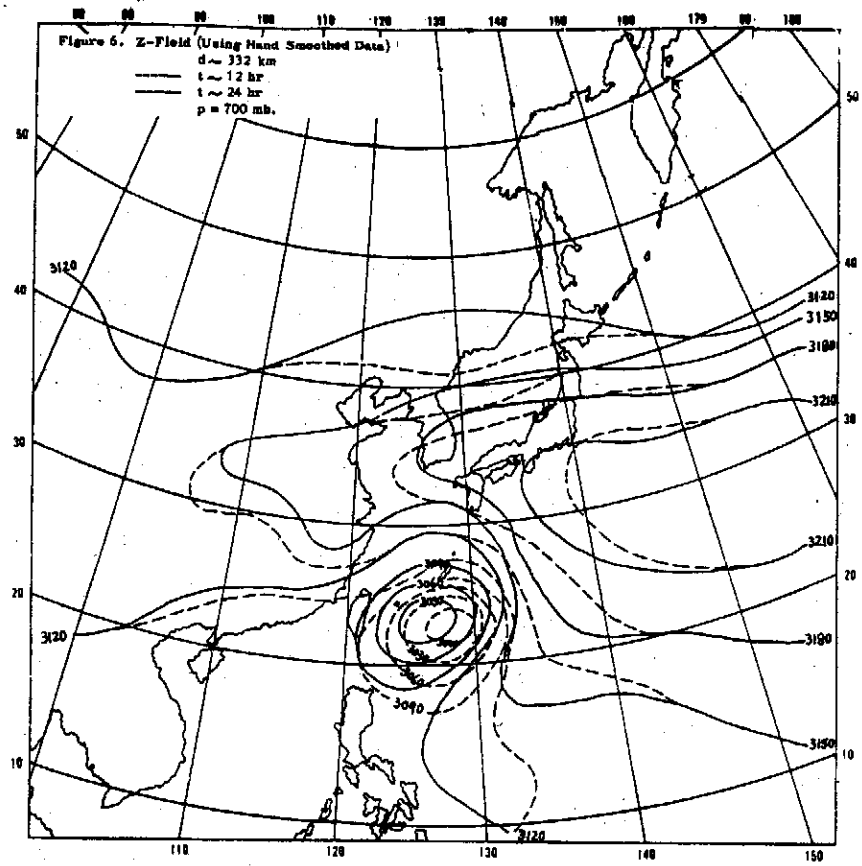
Figure 6. Z-Field (Using Hand Smoothed Data)
d ~ 332 km
t ~ 12 hr
t ~ 24 hr
p = 700 mb.

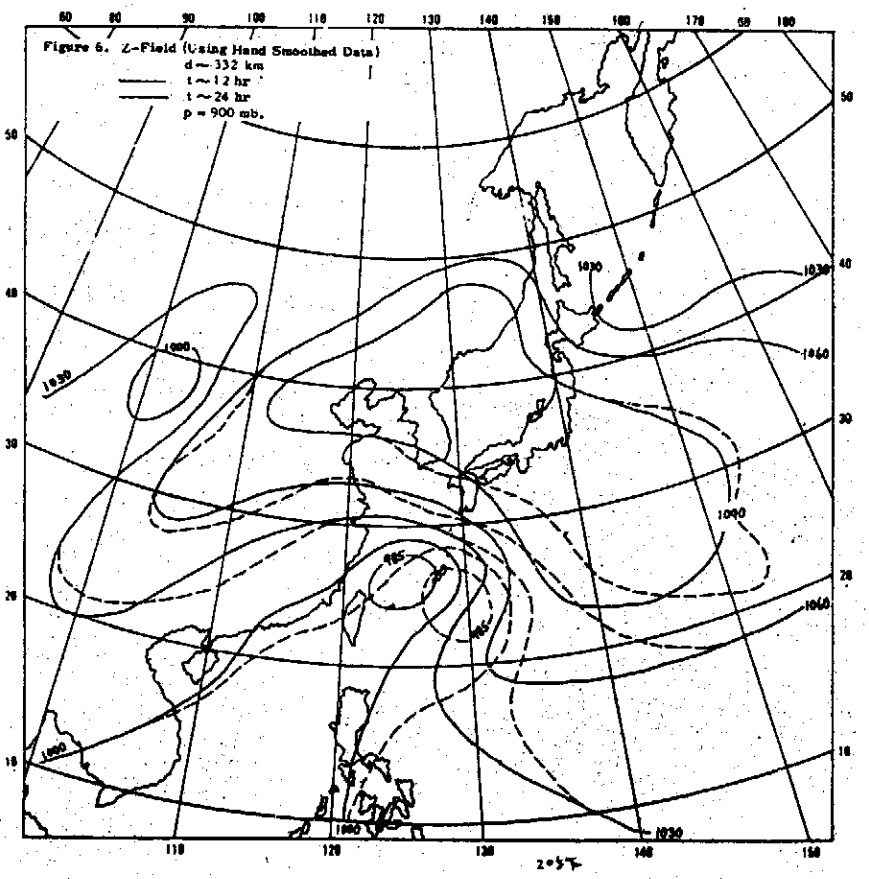
Figure 6. Z-Field (Using Hand Smoothed Data)
d ~ 332 km
t ~ 12 hr
t ~ 24 hr
p = 900 mb.

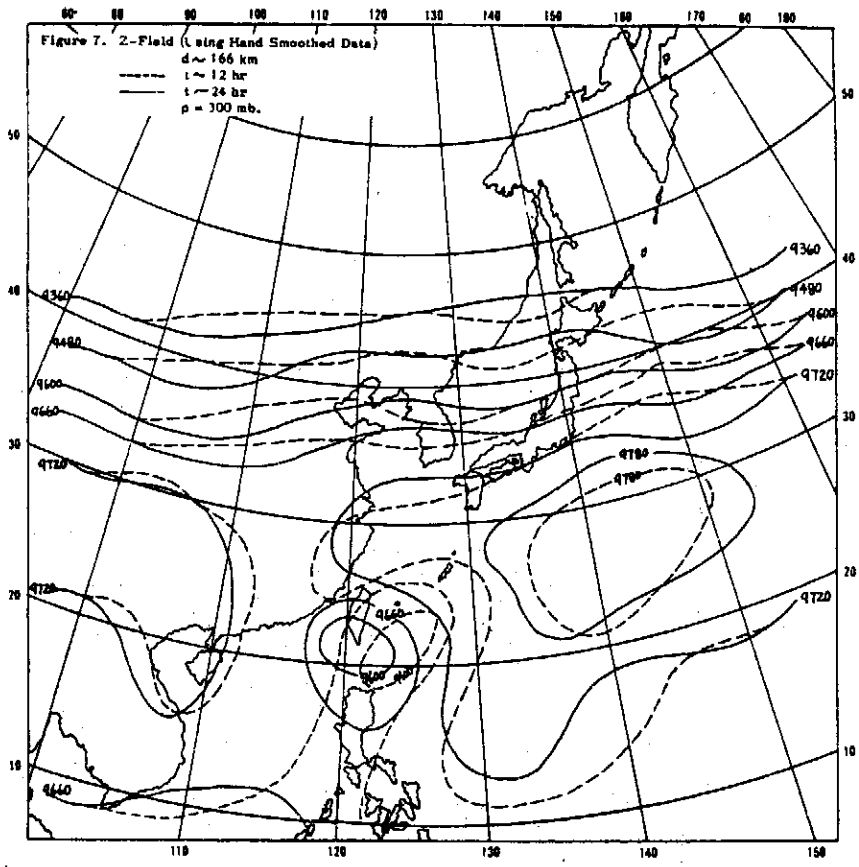
Figure 7. Z-Field (Using Hand Smoothed Data)
d ~ 166 km
t ~ 12 hr
t ~ 24 hr
p = 300 mb.

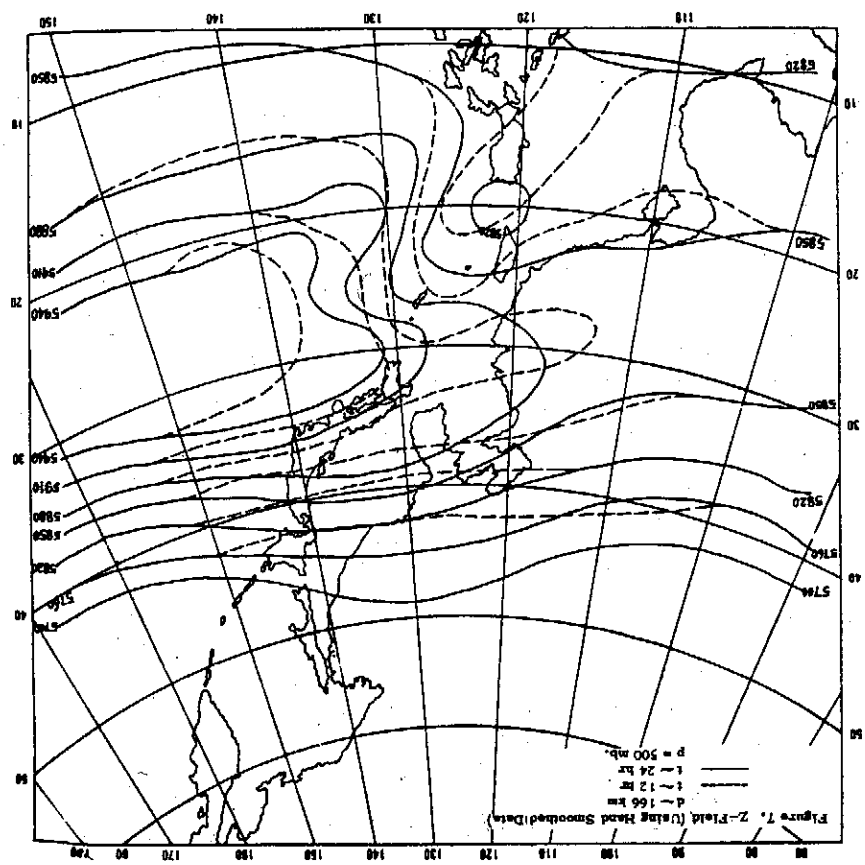
Figure 7. Z-Field (Using Hand Smoothed Data)
d ~ 166 km
t ~ 12 hr
t ~ 24 hr
p = 500 mb.

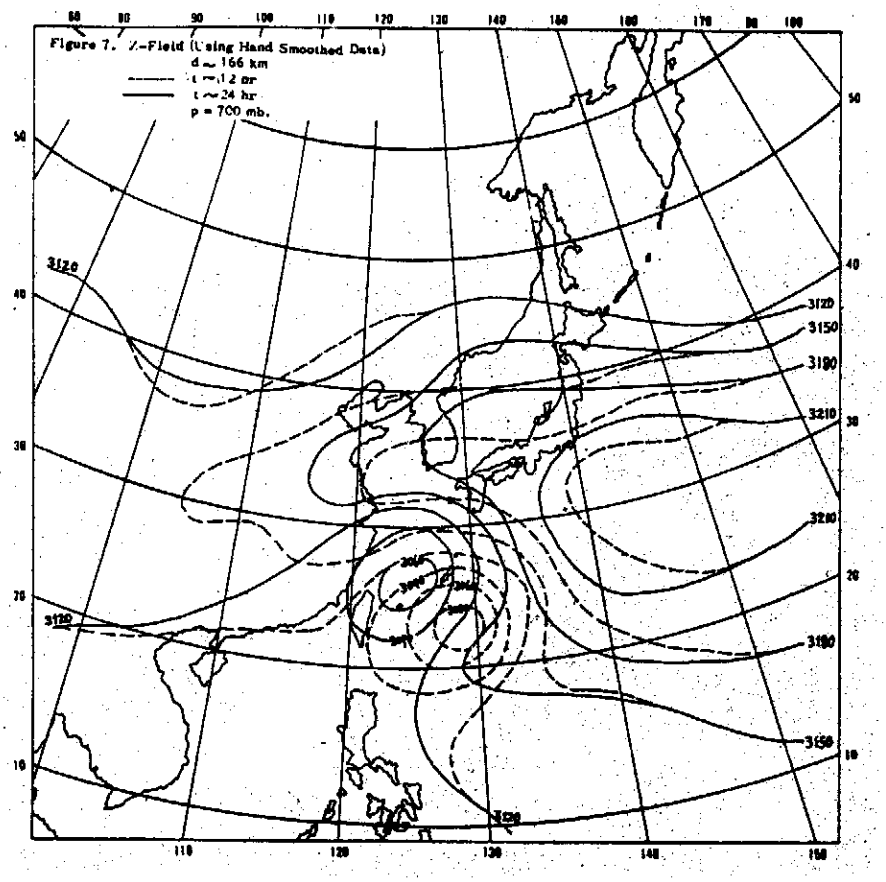
Figure 7. Z-Field (Using Hand Smoothed Data)
d ~ 166 km
t ~ 12 hr
t ~ 24 hr
p = 700 mb.
3120
3150
3180
3210
3240
3270

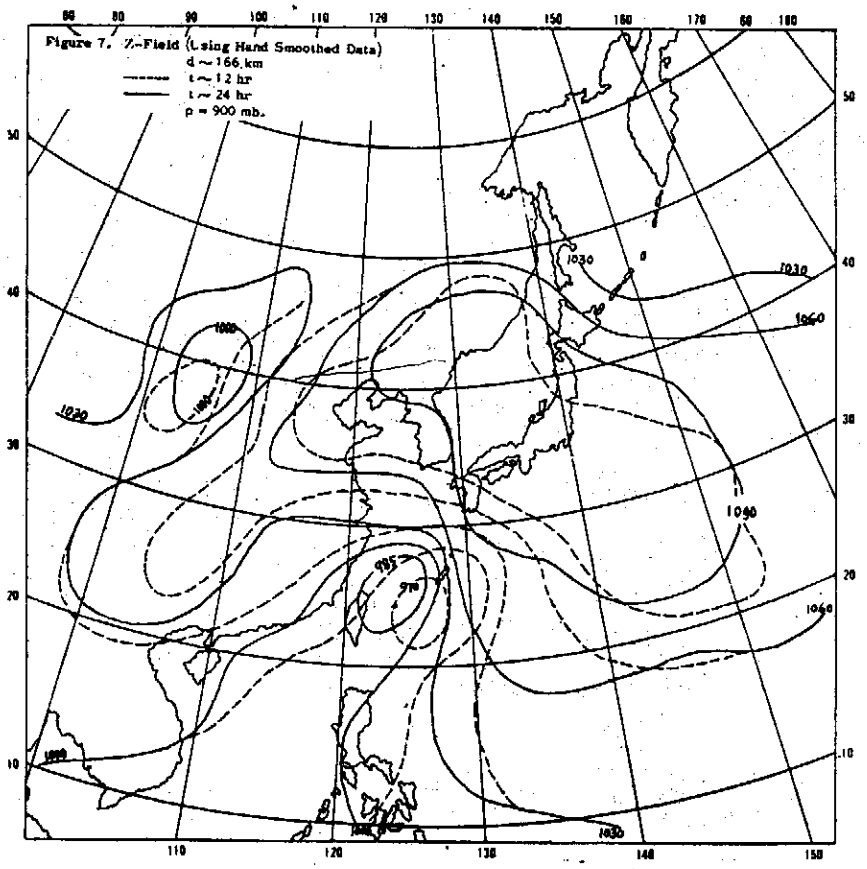
Figure 7. Z-Field (Using Hand Smoothed Data)
d ~ 166 km
t ~ 12 hr
t ~ 24 hr
p = 900 mb.
1030
1060
1090

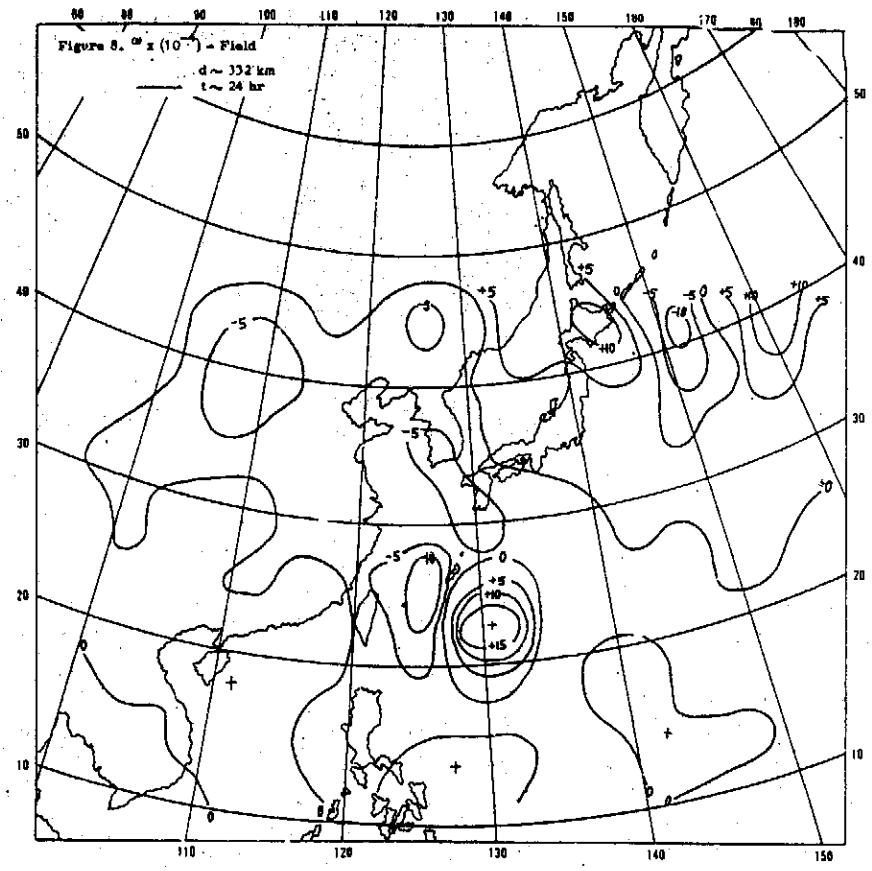
Figure 8. ω x (10⁻⁴) - Field
d ~ 332 km
t ~ 24 hr

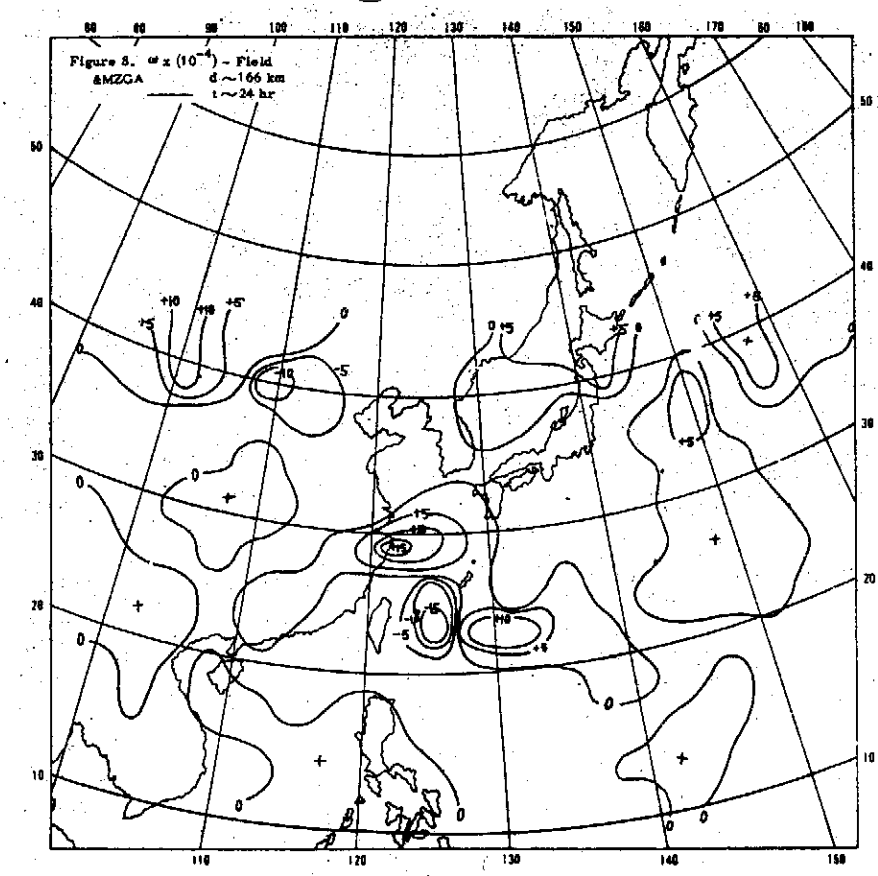
Figure 8. ω x (10⁻⁴) - Field
&MZGA
d ~166 km
t ~24 hr

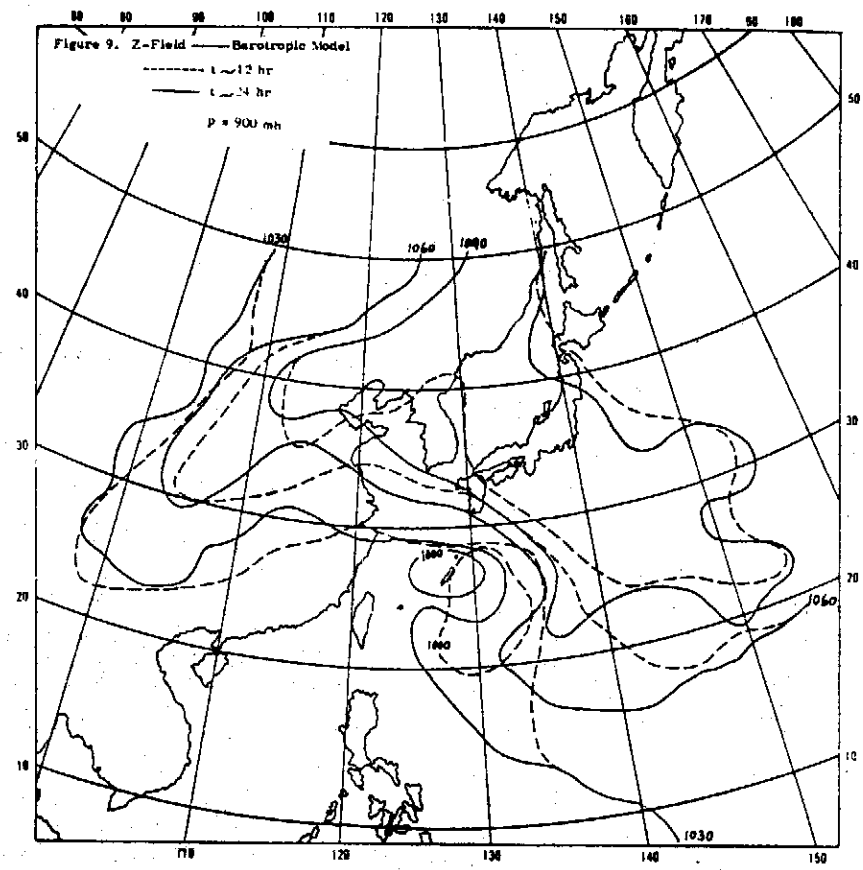
Figure 9. Z-Field —— Barotropic Model
P = 900 mb
1030
1060
1000
1030

Annual Report of the Institnte of Physics, Academia Sinica, 1972

大氣及颱風運動模型*

Ⅲ 熱及摩擦阻力

大氣物理組同仁

中央研究院物理研究所

物理數學模型

離地面不遠的大氣一般爲一連續流體，控制其運動之基本方程式爲（在 x.y.p.t coordinates 下）：

Equation of Motion

$$\frac{d\mathbf{V}}{dt}+\mathbf{k}\times f\mathbf{V}+g\nabla Z=-g\frac{\partial\tau}{\partial p} \tag{1}$$

式中V爲水平速度向量，k爲垂直單位向量，g爲重力加速度，Z爲高度，(isobaric height)，τ 爲阻力，t 爲時間，p 爲壓力，f 爲 Coriolis 參數。

Hydrostatic Equation

由於大氣層的厚度遠小於地球半徑，大氣流體運動在垂直方向可設爲

$$\frac{\partial Z}{\partial p}=-\frac{1}{\rho g} \tag{2}$$

式中 ρ 爲大氣質量。

Equation of Continuity

$$\nabla\cdot\mathbf{V}+\frac{\partial\omega}{\partial p}=0 \tag{3}$$

式中 $\omega\equiv\frac{dp}{dt}$

Equation of State

$$p=\rho RT \tag{4}$$

式中R爲空氣常數，T爲溫度。

First Law of Thermodynamics

$$\frac{d\theta}{dt}=\frac{\theta}{C_pT}\frac{dQ}{dt} \tag{5}$$

式中$\frac{dQ}{dt}$爲 heating rate, θ 爲 potential temperature

$$\theta\equiv T\left(\frac{p_{1000}}{p}\right)^{\frac{R}{C_p}} \tag{6}$$

P_{1000} 爲 1000 mb 處之壓力，C_p 爲等壓時大氣之 Specific heat 。以上六組方程式爲控制大氣運動的基本方程式（包含水文循環者參見 Shuman & Hovermale, 1968），原則上可解六個未知數 V,Z,ω,ρ,θ, T 。不過迄今在數學上仍不克解（exactly）此六組方程式，因之欲了解大氣運動，祇好藉數值方法利用高速計算機求其近似解。

Baroclinic Model

在 Rossby number 及 Froude number 不大的情形下， Eq. 2 代入 Eq. 1 化簡可得

* 本文承行政院國家科學委員會支助完成。

$$\frac{\partial \zeta}{\partial t}+\mathbf{V}\cdot\nabla(\zeta+f)-(\zeta+f)\frac{\partial \omega}{\partial p}+\omega\frac{\partial \zeta}{\partial p}+\mathbf{k}\cdot\nabla\omega\times\frac{\partial \mathbf{V}}{\partial p}=-g\mathbf{k}\cdot\nabla\times\frac{\partial \tau}{\partial p} \tag{7}$$

式中 $\zeta = \mathbf{k}\cdot\nabla\times\mathbf{V}$。在等壓面上，大氣層中的風常平行於等壓線吹動如果進一步假設

$$\mathbf{V}=\mathbf{k}\times\frac{g}{\bar{f}}\nabla Z \quad or \quad \zeta=\frac{g}{\bar{f}}\nabla^2 Z \tag{8}$$

代入 Eq.7 化簡可得 (Haltiner, 1971; Thompson, 1961)

$$\frac{\partial}{\partial t}\nabla^2 Z=-J(Z,\zeta+f)+\frac{\bar{f}^2}{g}\frac{\partial \omega}{\partial p}-\bar{f}\,\mathbf{k}\cdot\nabla\times\frac{\partial \tau}{\partial p}=F^1(Z,\omega) \tag{9}$$

式中—代表該值在 P-level, x 及 y 方向的平均值。此時原來運動方程式中的 high-frequency gravity-inertia waves 已被刪除，僅留下 low-freguency, quasi-geostrophic motion (Arakawa, 1971)，同時 f 值隨着緯度的變化亦不考慮。

將 Eqs. 2,3,4,6,8 代入 Eq. 5 中化簡可得

$$\frac{\partial}{\partial t}\frac{\partial Z}{\partial p}=-\frac{g}{\bar{f}}J(Z,\frac{\partial Z}{\partial p})-\sigma\omega-\frac{R}{C_p g p}\left[\frac{dQ}{dt}-\frac{d\bar{Q}}{dt}\right]=F^2(Z,\omega) \tag{10}$$

式中

$$\sigma \equiv -\frac{1}{\rho g\theta}\frac{\partial \theta}{\partial p} \tag{11}$$

$\frac{d\bar{Q}}{dt}$係爲保持熱能平衡，而加入之 spatially constant radiational cooling (Staff members, 1965). 。此時，由於 geostrophic wind assumption 之加入，原列六組方程式簡化爲由 Eqs. 9 及 10 解 Z 及 ω二個未知數。爲運算方便，

∇^2 (Eq. 10)$-\frac{\partial}{\partial p}$ (Eq. 9)可得

$$\nabla^2\sigma\omega+\frac{\bar{f}^2}{g}\frac{\partial^2\omega}{\partial p^2}=\frac{g}{\bar{f}}\nabla^2\left[J(\frac{\partial Z}{\partial p},Z)\right]-\frac{\partial}{\partial p}\left[J(\frac{g}{\bar{f}}\nabla^2 Z+f,Z)\right]$$
$$-\frac{R}{c_p g p}\nabla^2\frac{dQ}{dt}+\bar{f}\,\mathbf{k}\cdot\nabla\times\frac{\partial^2\tau}{\partial p^2} \tag{12}$$

此爲一般常見的 ω-equation,，由於式中無時間因素， ω可直接由 Z 求得。

摩擦阻力：

本文不考慮高聳山嶺之影響，並假設由 eddy viscosity 引起 lateral mixing 所造成的阻力不大，可予以忽略。則大氣與地球表面摩阻力可粗估爲 (Cressman, 1960)

$$\tau=\rho c_D \mid V_{1000} \mid V_{1000} \qquad at\ 1{,}000\ mb$$
$$=0 \qquad at\ higher\ altitude \tag{13}$$

式中 V_{1000} 爲 1000 mb 處之速度， C_D 爲阻力係數。

Benwell & Bushby (1970)假設

$$C_D=0.0068 \qquad over\ sea$$
$$=(1+0.0025H)\times10^{-3} \qquad over\ land \tag{14}$$

式中H爲地面高度 (in meter).

Arakawa (1971)假設

$$C_D=0.001(1+0.7|\mathbf{V}_{1000}|)\leq 0.025 \qquad over\ sea$$

$$=0.002+0.006H/5000. \qquad over\ land \tag{15}$$

本文假設 (Staff members, 1965; Miller, 1969)

$$C_D=[1.0+0.07|V_{1000}|]\times10^{-3} \qquad over\ sea$$
$$=0.003 \qquad over\ land \tag{16}$$

熱 變 化

基本的流力與熱力公式僅能控制大到能受地球自轉影響而又合乎 hydrostatic 情況之大氣系統。因之，在利用數值分析方法解大氣與颱風運動變化時就必需將小規模大氣變化現象以與控制方程式中有關變數表示出來。在深討熱帶氣象問題時，這種表示方法尚在不停地研討中，本文在熱變化中僅考慮

$$\frac{dQ}{dt}=\frac{dQ_s}{dt}+\frac{dQ_L}{dt} \tag{17}$$

式中右邊第一項考慮海面與大氣交界處 sensible heat 之傳遞，第二項考慮水氣凝聚時 latent heat 之釋出。在 sensible heat 之傳遞方面 Gambo (1963) 假設

$$\frac{dQ_s}{dt}=A|V_{1000}|(T_{sea}-T_4)\left(\frac{P}{P_{1000}}\right)^3$$
$$A=0.001 \qquad T_{sea}>T_4$$
$$=0.0001 \qquad T_{sea}<T_4 \tag{18}$$

式中 T_{sea} 爲海面溫度。

Haltiner (1971) 假設

$$\frac{dQ_s}{dt}=0.00323|V_{1000}|\ (T_{sea}-T_4) \quad at\ 900mb \tag{19}$$

本文引用 Miller (1969)，假設在 time domain 內

$$\frac{dQ_s}{dt}=g|V_{1000}|\ (\ T_{sea}-T_4)\rho_{1000}\ C_D\ C_p\ \eta/300 \qquad below\ 700mb$$
$$=0 \qquad above\ 700mb. \tag{20}$$

式中 ρ_{1000} 爲 1000 mb 處之大氣密度，η = 1.0 當 $T_{sea}>T_4$，η=0.1 當 $T_{sea}<T_4$，η=0.0 在陸地上。

假使祇考慮大規模垂直氣流運動而不考慮積雲對流運動，則 latent heat 之釋出可設爲 (Gambo, 1963; Danard, 1966; Miller et. al., 1972)

$$\frac{dQ_L}{dt}=-LF^*\omega\Delta S \qquad when\ \omega<0$$
$$=0 \qquad when\ \omega\geq0\ or\ P\leq700mb \tag{21}$$

式中L爲單位質量之 heat of condensation, F^* 爲 (Kuo, 1965; Haltiner & Martin, 1957)

$$F^*=\left[\left(\frac{\partial q^*}{\partial p}\right)_T+\frac{RT}{C_p p}\left(\frac{\partial q^*}{\partial T}\right)_p\right]\cdot\left[1+\frac{L}{C_p}\left(\frac{\partial q^*}{\partial T}\right)_p\right]^{-1} \tag{22}$$

$q^*=0.622e\ [p-0.378e]^{-1}$ 爲 saturated mixing ratio

$e=6.11\left[\frac{273}{T}\right]^{5.31}$ EXP $\left[25.22\left(1-\frac{273}{T}\right)\right]$ 爲 saturated vapor pressure

$$T=-\frac{gp}{R}\frac{\partial Z}{\partial p}$$

ΔS 爲爲大氣團中之飽和部份

$$\Delta S=1-\frac{T-T_{dew\ point}}{\Delta T'}\geq0 \tag{23}$$

式中ΔT′爲經驗值。

Eq.12 可改寫爲

$$\Delta^2\sigma^*\omega+\frac{\bar{f}^2}{g}\frac{\partial^2\omega}{\partial p^2}=\frac{g}{\bar{f}}\nabla^2[J(\frac{\partial Z}{\partial p},Z)]-\frac{\partial}{\partial p}[J(\frac{g}{\bar{f}}\nabla^2Z+f,Z)]-\frac{R}{c_pgp}\nabla^2\frac{dQ_s}{dt}$$

$$+\bar{f}\,k.\nabla\times\frac{\partial^2\tau}{\partial p^2}=F^2(Z) \tag{24}$$

$$\sigma^*=\sigma-\frac{RLF^*}{C_pgp}\Delta S\_0.2\sigma \qquad when\ \omega<0\ and\ p>500mb$$

$$=\sigma \qquad when\ \omega\geq 0\ or\ p\leq 500mb \tag{25}$$

Numerical Scheme

在運用 finite difference method 解 Eqs. 9,10 及24時，所用的水平及垂直方向的 grid system如 Fig. 1 所示。在水平網格座標中，起始點在左下角，i 及 j 爲 x 及 y 方向之指標，整個 computational domain (i=2至NX−1, j=2至NY−1) 平均劃分成長寬爲d之小方格。在 d≒332 km 時，臺灣東邊大約在 i=9, j=6 的位置上。在垂直網格座標中，200 mb 至1000 mb 之空間均分爲四層，每層 $\Delta P=200$ mb 厚。k 爲 P 方向指標，向下爲正。 Z,ω及T之各層指標如 Fig.1 所示， ∂Z爲厚度，

$$\partial Z_k=Z_k-Z_{k-1} \qquad k=2,3,4 \tag{26}$$

Numerical procedure 如 Fig.2所示， Initial conditions 取自天氣圖，包括 300,500,700 及 850 mb 的Z及 $T-T_{dew\ point}$值。 900 mb 的Z值由下式求取

$$Z=\frac{1}{21}(32Z_{at\ 850mb}-14Z_3+3Z_2) \tag{27}$$

1000 mb 的Z及T值由下式求取

$$Z_{1000}=1.5(Z_4-\bar{Z}_4)-0.5(Z_3-\bar{Z}_3)+\bar{Z}_{1000} \tag{28}$$

$$T_4=2(T_3-\bar{T}_3)-(T_2-\bar{T}_2)+\bar{T}_4 \tag{29}$$

式中$\bar{Z}_{1000}$及$\bar{T}_4$ 爲domain內之大氣標準平均值。

Eq.24 可藉下敍 iteration procedure (Wang, 1971)解 400, 600及 800 mb之 ω-field

$$\omega^{n+1}_{ijk}=[\sigma^*_{i+1jk}\omega_{i+1jk}+\sigma^*_{i-1jk}\omega_{i-1jk}+\sigma^*_{ij+1k}\omega_{ij+1k}+\sigma^*_{ij-1k}\omega_{ij-1k}$$

$$+\frac{\bar{f}^2d^2}{gm^2\Delta p^2}(\omega_{ijk+1}+\omega_{ijk-1})-\frac{F^2_{ijk}d^2}{m^2}]^n/[4\sigma^*_{ijk}+\frac{2\bar{f}^2}{gm^2}\frac{d^2}{\Delta p^2}]^n \tag{30}$$

式中 n 及 n+1 爲 iteration procedure 中二連續步驟， m 爲 map-scale factor,

在適宜邊界條件 F, Eq.27 重複運用直至

$$Max\ |\omega^{n+10}_{ijk}-\omega^n_{ijk}|\leq\epsilon \tag{31}$$

Δt爲 time increment, von Neumann necessary contion (Richtmyer & Morton, 1967; Kreiss & Oliger, 1973) 要求

$$\Delta t\leq Min\frac{d}{|u|+|v|+|w|} \tag{32}$$

u,v,w 爲 x,y,z 方向之速度，在 finite difference form 爲

$$\Delta t < Min \frac{d}{\frac{g}{f}(|\frac{\partial Z}{\partial x}|+|\frac{\partial Z}{\partial y}|)+|\omega\frac{\partial Z}{\partial p}\frac{d}{d_{\Delta p}}|} \tag{33}$$

式中$d_{\Delta p}$爲Δp之厚度。

同理， Eq.9 在 finite difference form 可化爲

$$\frac{\partial Z}{\partial t}^{n+1}_{ijk}=0.25[\frac{\partial Z}{\partial t}_{i+1jk}+\frac{\partial Z}{\partial t}_{i-1jk}+\frac{\partial Z}{\partial t}_{ij+1k}+\frac{\partial Z}{\partial t}_{ij-1k}-\frac{d^2}{m^2}F^{1}_{ijk}]^n \tag{34}$$

此式重複運用以解 500 mb 之$\frac{\partial Z}{\partial t}$-field, 直至

$$Max|\frac{\partial Z}{\partial t}^{n+10}_{ijk}-\frac{\partial Z}{\partial t}^{n}_{ijk}|\leq\epsilon \tag{35}$$

Eq.10 可化爲

$$\partial Z^{t+\Delta t}_{ijk}=\partial Z^{t}_{ijk}+\Delta t\ \Delta P\ F^{2}_{ijk} \qquad at\ initial\ time\ step \tag{36}$$

$$\partial Z^{t+\Delta t}_{ijk}=\partial Z^{t-\Delta t}_{ijk}+2\Delta t\ \Delta P\ F^{2}_{ijk} \qquad at\ other\ time\ steps \tag{37}$$

以解 400, 600 及 800 mb 之 ∂Z-field.

F^1, F^2 F^3 中，除

$$J(A,B)=\frac{1}{3}(J^1+J^2+J^3) \tag{38}$$

藉以保持 squared vorticity 及 kinetic energy 不變外 (Arakawa, 1971)，式中

$$\begin{aligned}
J^1&=[(A_{i+1j}-A_{i-1j})(B_{ij+1}-B_{ij-1})-(A_{ij+1}-A_{ij-1})(B_{i+1j}-B_{i-1j})]/4d^2\\
J^2&=[A_{i+1j}(B_{i+1j+1}-B_{i+1j-1})-A_{i-1j}(B_{i-1j+1}-B_{i-1j-1})\\
&\quad -A_{ij+1}(B_{i+1j+1}-B_{i-1j+1})+A_{ij-1}(B_{i+1j-1}-B_{i-1j-1})]/4d^2\\
J^3&=[A_{i+1j+1}(B_{ij+1}-B_{i+1j})-A_{i-1j-1}(B_{i-1j}-B_{ij-1})+A_{i-1j+1}(B_{i-1j}-B_{ij+1})\\
&\quad -A_{i+1j-1}(B_{ij-1}-B_{i+1j})]/4d^2
\end{aligned} \tag{39}$$

其餘皆採用 center difference.

Boundary conditions 在垂直面上假設爲

$$\omega=0 \qquad at\ 200\ 及\ 1000mb \tag{40}$$

亦即 $\omega_1=0$ and $\omega_5=0$

亦即在水平面上由於探討的是區域性短時間模擬問題，除假設 time domain 內 Z at boundary 不變外，並假設 (大氣物理組同仁，1972)

A. Free-slip boundary condition

假設大氣在邊界上不受摩擦阻力可自由流動，亦即在X方向邊界上$\frac{\partial v}{\partial x}=0$，在$y$ 方向邊界上，$\frac{\partial u}{\partial y}=0$ (Welch et. al., 1965),可得

$$Z_{boundary外一層}=2Z_{boundary}-Z_{boundary內一層} \tag{41}$$

如果不考慮邊界及其以外之熱源，則由 Eq.10 可得

$$\omega_{boundary}\cong-\frac{g}{\sigma f}J(Z,\frac{\partial Z}{\partial p}) \tag{42}$$

B. Fixed boundary condition

假設在邊界以外，Z亦不變， $\omega_{boundary}$ 由Eq. 42求取。

Results

本節將探討控制方程式中各種參數及運算方法之影響。在

Computation domain 爲 NX=20, NY=14,

$d=3{,}322\times10^5$m.

$T_{s,a}$-field 如 Fig.3 實線所示

Z-field 如 Fig.4 所示

$T-T_{dew\ point}$-field 如 Fig.5 所示

σ 及 σ^*-field 如 Fig.6 實線及虛線所示

$g=9.8 m/sec^2$

$\epsilon=10^{-6}$

$R/C_p=2/7$

$d_{\Delta p}=2.15\times10^3 m$

$R=287 m^2/sec^2\text{-}k^\circ$

$L=2.27\times10^6 m^2/sec^2$

$$\overline{Z}_{1000}=112.78m \tag{43}$$

$\overline{T}_2=273.2$ °K, $\overline{T}_3=280.9$ °K, $\overline{T}_4=287.3$ °K (標準大氣溫度)

$\bar{f}=0.644\times10^{-4}$ sec^{-1}

$\Delta T'=7.5$ °K

Fixed boundary condition

情形下按照 Fig. 2 之 運算步驟 ，可算出 12 及24小時（本文所指12及24小時皆爲近似值）後之天氣變化如 Fig. 7 所示。颱風中心由 i=12, j=6 附近移至 i=10, j=6 之上方，亦卽由東經 130°，北緯 23°附近移至東經 125° ，北緯25°左右。

§. Latent heat 層次變化影響

在其他條件維持與 Eq. 43 一樣，而進一步考慮 500 至 700 mb 大氣層之間亦有 latent heat 釋出時， Eq. 21 變爲

$$\frac{dQ_L}{dt}=-LF^*\omega\ \Delta S \qquad when\ \omega<0$$
$$=0 \qquad when\ \omega\geq0\ or\ P\leq500\ mb \tag{44}$$

24小時內高層 (300 及 500 mb)天氣變化與 Fig.7 無甚差異，低層 (700 及 900 mb)大氣變化因接受更多 latent heat ，加深情形較着，尤其是 900 mb 颱風中心一帶。由於在 Eq. 44 情形下花費計算機時間較多，本文以下仍將就 Eq.21 討論各種影響。

§. 摩擦阻力影響

其他條件維持與 Eq. 43 一樣，僅不考慮地面摩擦阻力，亦卽令 $C_D=0$. 24小時內之大氣變化顯示 700mb 以上大氣變化不受地面摩擦阻力影響，但接近地面之大氣變化受到影響， Fig. 9 顯示（與 Fig. 7 比較）在不考慮摩擦阻力時，陸地上 Z-field 塡補(filling) 加快，但颱風中心却反而加深(deepening)。

§. Sensible heat 影響

其他條件維持與 Eq. 43 一樣，但不考慮 sensible heat,亦卽$\frac{dQ_s}{dt}=0$. 24小時內除接近地面的大氣層以外，其他離地面遠的大氣層幾乎不受 sensible heat 的影響，Fig. 10 顯示（與 Fig. 7 比較）在 900mb 海

面上空之大氣層，由於缺乏洋面熱源供給，颱風中心急速填補。如進一步不考慮 sensible heat 及地面摩擦阻力，所得結果在海面上空部分極其類似，也就是說 sensible heat 的影響一般較摩擦阻力爲大。

§. 熱變化及摩擦阻力影響

當熱變化及摩擦阻力皆不考慮時，問題簡化爲「大氣及颱風運動模型：Ⅰ 邊界條件」 (1972) 所探討者。Fig.11顯示900 mb大氣層 24 小時內填補的情形。

§. 運算方式影響

Fig.12 顯示在 Eq.43 條件下，解 Eq.12 時如果不化爲 Eq.24, 而化爲

$$\left[\nabla^2\sigma\omega+\frac{\overline{f}}{g}\frac{\partial^2\omega}{\partial p^2}\right]^t=\left\{\frac{g}{\overline{f}}\nabla^2\left[J\left(\frac{\partial Z}{\partial p},Z\right)\right]-\frac{\partial}{\partial p}\left[J\left(\frac{g}{\overline{f}}\nabla^2 Z+f,Z\right)\right]+\overline{f}\,\mathbf{k}\cdot\nabla\times\frac{\partial^2\tau}{\partial p^2}\right\}^t$$

$$-\left[\frac{R}{c_p g p}\nabla^2\frac{dQ}{dt}\right]^{t-\Delta t} \qquad (45)$$

24小時內所得結果，可以看出在這種 scheme 下，不穩定波開始產生，颱風中心低壓降至 925mb 左右。

§. 邊界條件影響

其他條件維持與 Eq. 43 一樣，但假設

$$\omega_{boundary}=0 \qquad (46)$$

所得結果(Fig. 13)與 fixed boundary condition 下所得結果(Fig.7)類似，僅東邊高壓區域填補稍快。若使用 free-slip boundary condition, ，所得結果 (Fig. 14) 與 fixed boundary condition 下所得結果 (Fig. 7) 類似，僅西北一帶略有不同。

§. No radiation cooling 影響

其他條件維持與 Eq. 43 一樣，但不考慮 radiation cooling，亦即 $\frac{\overline{dQ}}{dt}=0$.此時，由於運算範圍內熱能源源增加，整個 Z-field 加深(Fig.15).

§. 天氣圖 smoothing 影響

其他條件維持與 Eq.43 一樣，但 initial Z-field 改用「大氣與颱風運動模型：Ⅱ. 運算範圍與網格大小」(1973)文中原提原始天氣資料，則 Fig.16 顯示24小時內 900mb 天氣圖上有極強烈且不合理之變化，同時 800mb ω-field圖上顯示 $|\omega|_{max}\cong 100$, ，極不合理，故進行模擬研究時，data必需 Smooth.

Simulation

本文以1971年九月廿一日 Bess 颱風爲模擬研究對象（承中央氣象局供給原始天氣資料，謹致謝意），海面平均水溫取自日本氣象廳「全國海況旬報」九月下旬，並假設在 time domain 內 $T_{s\ a}$ 不變。Computation domain 連同 T_{sea}-field 如 Fig. 3 (虛線部分) 所示。靠近颱風行徑一帶 $T_{s\ a}$ 約爲 302°K，颱風中心在 i=12, j=6 附近，亦即東經 130°, ，北緯 23°附近。

由於原始天氣資料不宜用於模擬探討，本文首先利用五點 smoothing operator (Shuman, 1957)將 high frequency Components 自原始天氣資料中去除

$$Z_{ijk}=Z'_{ijk}+0.125\,(Z'_{i+1jk}+Z'_{i-1jk}+Z'_{ij+1k}+Z'_{ij-1k}-4Z'_{ijk}) \qquad (47)$$

式中Z'及Z爲 Smooth 以前及以後之高度， Smooth 以後之 Z-field 如 Fig.4 所示。900mb 天氣圖中颱風中心附近網格低壓已由 940 m Smooth 爲 964 m.。 $T-T_{dew\ point}$ field 由原始天氣圖中讀出後經同樣的五點 Smoothing operator 去掉 short wavelength components ，如 Fig. 5 (虛線部分) 所示，此值假設在 time domain 內不變。Fig. 5 顯示愈接近颱風中心及海面，$T-T_{dew\ point}$ 愈小，大氣愈

飽和。σ-field 由 Eq.11 求得，其中少數由於原始天氣圖不完全正確爲負值，不合理，令爲零以後，利用九點 Smoothing operator (Shuman, 1957) 丟去 high frequency Components,

$$\sigma_{ijk}=\sigma'_{ijk}+\frac{1}{8}(\sigma'_{i+1jk}+\sigma'_{i-1jk}+\sigma'_{ij+1k}+\sigma'_{ij-1k}-4\sigma'_{ijk})$$
$$+\frac{1}{16}(\sigma'_{i+1j+1k}+\sigma'_{i-1j+1k}+\sigma'_{i+1j-1k}+\sigma'_{i-1j-1k}-4\sigma'_{ijk}) \quad (48)$$

式中 σ' 及 σ 爲 smooth 以前及以後之值， smooth 以後之 σ-field 如 Fig.6 (實線部分) 所示。σ^*-field 由 Eq.25 求得經九點 smoothing operator處理後，亦如 Fig.6 (虛線部分) 所示。Fig.6 顯示在陸地部分 σ 及 σ^* 類似，在海面上空由於大氣較飽和， σ 及 σ^* 差異較大。

在

$NX=20 \qquad NY=14$

$\Delta T'=7.5°K$

$d=3,322\times10^5 m$

$g=9.8 m/sec^2$

$\epsilon=10^{-6}$

$R/Cp=2/7$

$d_{\Delta p}=2.15\times10^3 m$

$R=287 m^2/sec^2{}_{-k}°$

$L=2.27\times10^6 m^2/sec^2$

$\overline{Z}_{1000}=112.78m$

$\overline{T}_4=287.3°K$, $\overline{T}_3=285.9°K$, $\overline{T}_2=277.3°K$

$\overline{f}=0.644\times10^{-4}\ sec^{-1}$

Free-slip boundary condition (49)

並考慮熱變化及摩擦阻力時，Bess 颱風及周遭大氣在12及24小時後之變化如 Fig.17 所示。颱風中心在24小時後移至 i=10, j=6之上方，亦卽東經 125° ，北緯 25° 左右，此與颱風實際運行路徑相彷彿，不過颱風中心低壓降至 940 mb與實際天氣景況不一致。但若將 Eq.49 中 $\Delta T'$ 改爲 2.5°K, ，亦卽

$$\Delta S=1-\frac{T-T_{dew\ point}}{2.5}\geq 0 \quad (50)$$

所得結果如 Fig.18所示。此時西邊與東邊二高壓塡深，颱風中心移至東經 125°, ，北緯 24° 左右，與實際天氣變化一致。

Discussion and Recommendation

§. 在地轉風假設下，本文利用四層斜壓模式探討以侵襲臺灣颱風爲對象之區域性大氣及颱風運動變化。考慮熱變化及摩擦阻力(Eqs.17 & 13)，本模型使用數值模擬方式解大氣運動控制方程式(Eqs.9 & 10)模擬颱風 Bess 及周遭大氣運動及變化，結果良好 (Fig.18)。

§. 本文探討控制方程式中各個參種及各種條件下之變化(Figs.7至 17)，發現在大氣及颱風運動變化時，潛熱及感覺熱之影響最爲重要。

§. 在模擬颱風 Bess 之運動及變化時，本文使用 Eqs.21 & 50 考慮潛熱之釋放。 Danard (1966)使用 $\Delta T'=7.5°K$, Staff members (1965) 使用 $\Delta S=1.0$ 皆會提供過量的潛熱，Miller (1969) 在相對濕度達 95% 以上時，使用 $\Delta S=1.0$ ，提供之潛熱又嫌不足。本文使用 $\Delta T'=2.5°K$ 並考慮

radiotional cooling 模擬 Bess 颱風成效良好。

5. 本文使用天氣圖上之等壓面高度 (geopotential height) 爲計算資料 (data)，唯在探討過程發現該高度資料誤差甚大，進一步探討時可考慮採用高度及風二種資料。

後　　記

參加本專題研究之大氣物現組同仁包括汪羣從、彭立、簡來成、柯順德、馬天驥、張文瀾等人。承物理中心提供使用 IBM 1130 計算機，謹致謝意。

References

Arakawa, A., Design of the UCLA General Circulation Model, Dept. Met., UCLA, 1971

Baumhefner, D.P., On the Effects of an Imposed Southern Boundary on Numerical Weather Prediction in the Northern Hemisphere, J. Atm. Soi., 28,42,1971.

Benwell, G.R.R. & F.H. Bushby, A Case Study of Frontal Behaviour Using a 10-level Primitive Equation Model, Quart. J.R. Met. Soc., 96,287,1970.

Cressman, G.P., Improved Terrain Effects in Baro tropic Forecasts, MWR, Sep.-Dec.,327, 1960.

Danard, M.B., A Quasi-Geostrophic Numerical Model Incorporating Effeots of Release of Latent Heat, J. Appl. Met., 5, 85, 1966.

Gambo, K., The Role of Sensible and Latent Heats in the Baroclinic Atmosphere, J. Met. Soc. Japan, 41, 233, 1963.

Haltiner, G.J., Numerical Weather Prediction, John Wiley & Sons, Inc., N.Y., 1971.

Haltiner, G.J. & F.L.Martin, Dynamical & Physical Meteorology, McGraw-Hill Book Co., 1957.

Hess, S.L. Introduction to Theoretical Meteorology Holt. Rineheart and Winston, N.Y., 1959

Kreiss, H. & J.Oliger, Methods for the Approximate Solution of Time Depedent Problems, GARP Pub. Ser. No. 10, GARP, 1973.

Kuo, H.L., On Formation and Intensification of Tropical Cyclones Through Latent Heat Release by Cumulus Convection, J. Atm. Sci., 22,40,1965.

List, R.J., Smithsonian Meteorological Tables, Smithsonian Inst. Press, 1971.

Miller, B.I., Experiment in Forecasting Hurricane Development With Real Data, ERLTM-NHRL 85, ESSA, 1969.

Miller, B.I. et al., Numerical Prediction of Tropical Weatherg Systems, MWR,100,825,1972.

Richtmyer, R.D. & K.W. Morton, Difference Methods for Initial-Value Problems, Interscience Publishers, N.Y. 1967.

Shuman, F.G., Numerical Methods in Weather Prediction: Ⅱ. Smoothing and Filtering, MWR, 85,357,1957.

Shuman, F.G. & J.B. Hovermale, An Operational 6-layer Primitive Equation Model, J. Appl. Met., 7, 525, 1968.

Staff Members of Electronic Computation Center, 72-hr Baroclinic Forecast by the Diabatic Quasi-Geostrophic Model, J. Met. Soc. Japan, 43, 246, 1965.

Thompson, P.D., Numerical Weather Analysis and Prediction, MacMillan, N.Y., 1961.
Wang, C.T., Drop-Water Impact, Anu. Rept. Inst. Phys., Academia Sinica, 107,1971.
Welch, J.E. et al., The MAC Method, LA3425, U. Calif. Los Alamos, 1965.
大氣物理組同仁，大氣及颱風運動模型：Ⅰ. 邊界條件，中研院物理所集刊 177,1972.，
大氣物理組同仁，大氣及颱風運動模型：Ⅱ. 運算範圍與網格大小，中研院物理所集刊 1973.

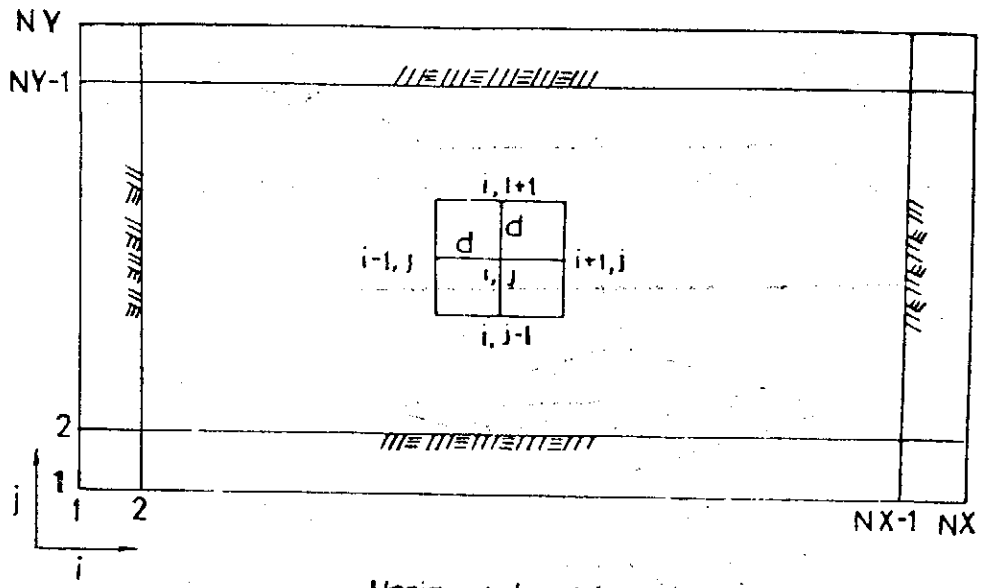

Horizontal grid system

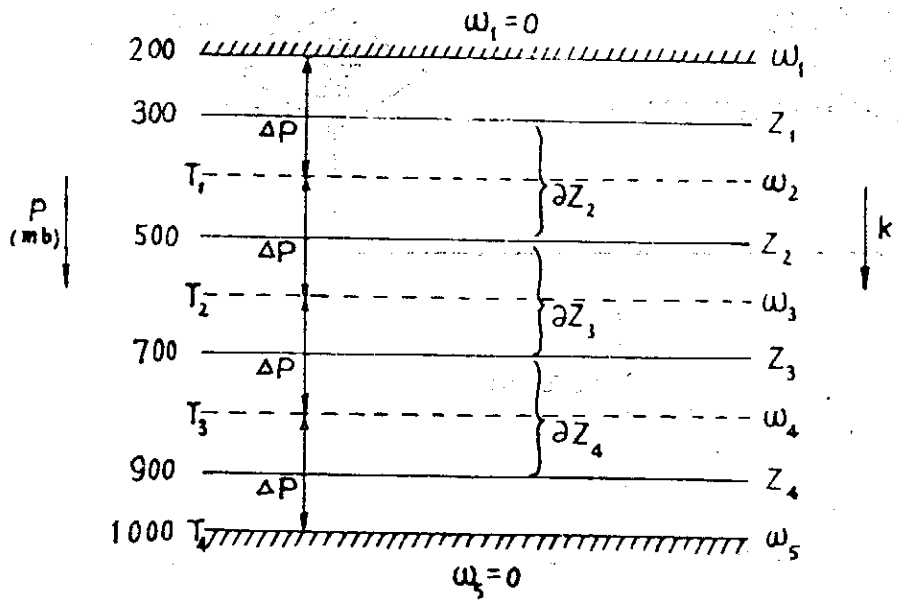

Vertical grid system

Fig.1. Grid systems

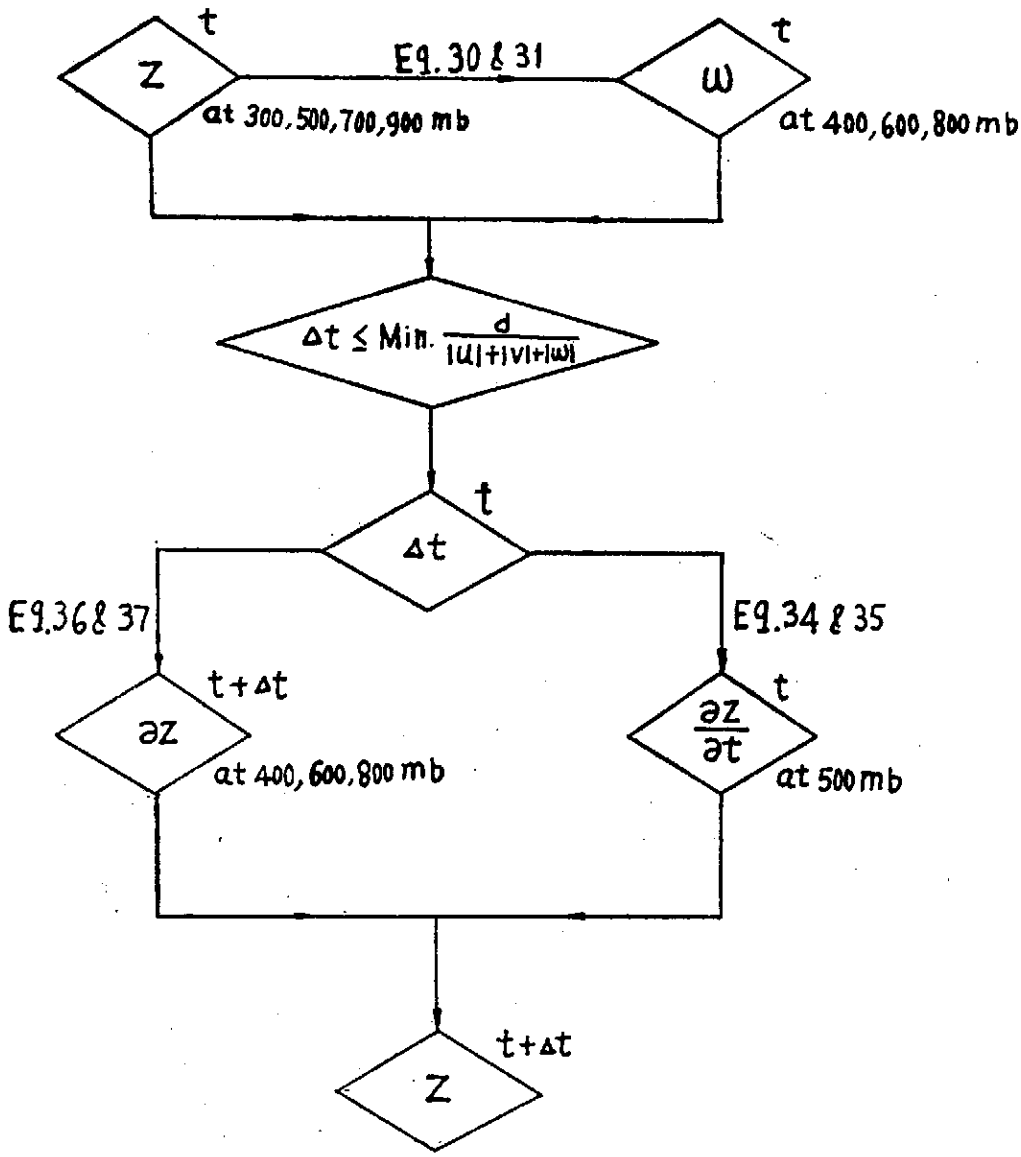

Fig. 2. Numerical procedures

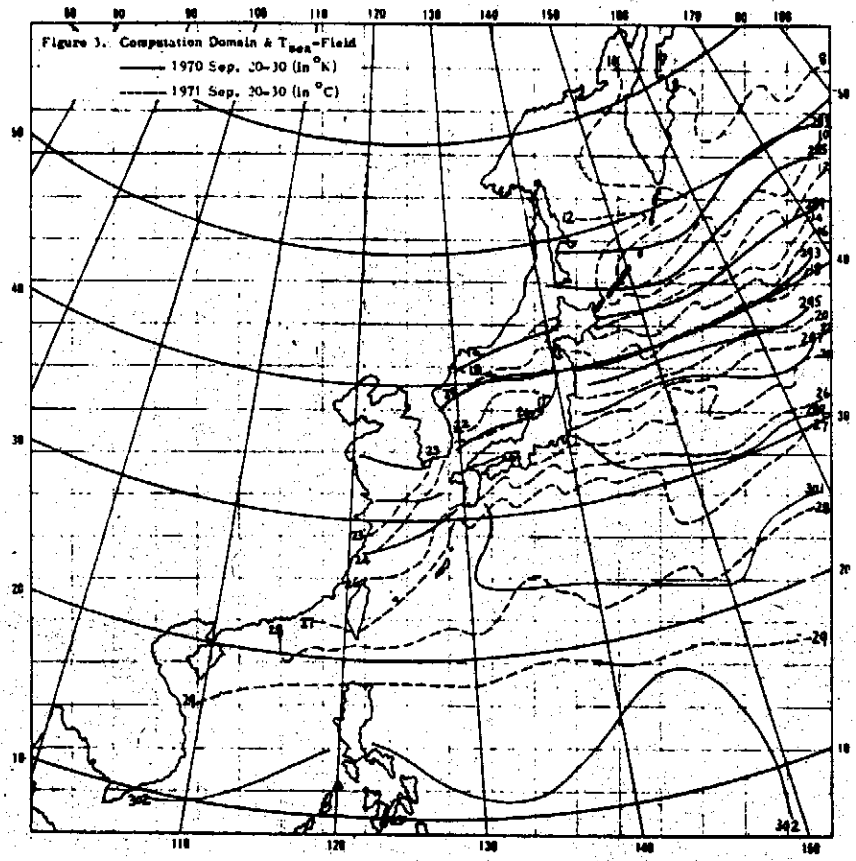
Figure 3. Computation Domain & T_{sea}-Field
1970 Sep. 20~30 (in °K)
1971 Sep. 20~30 (in °C)

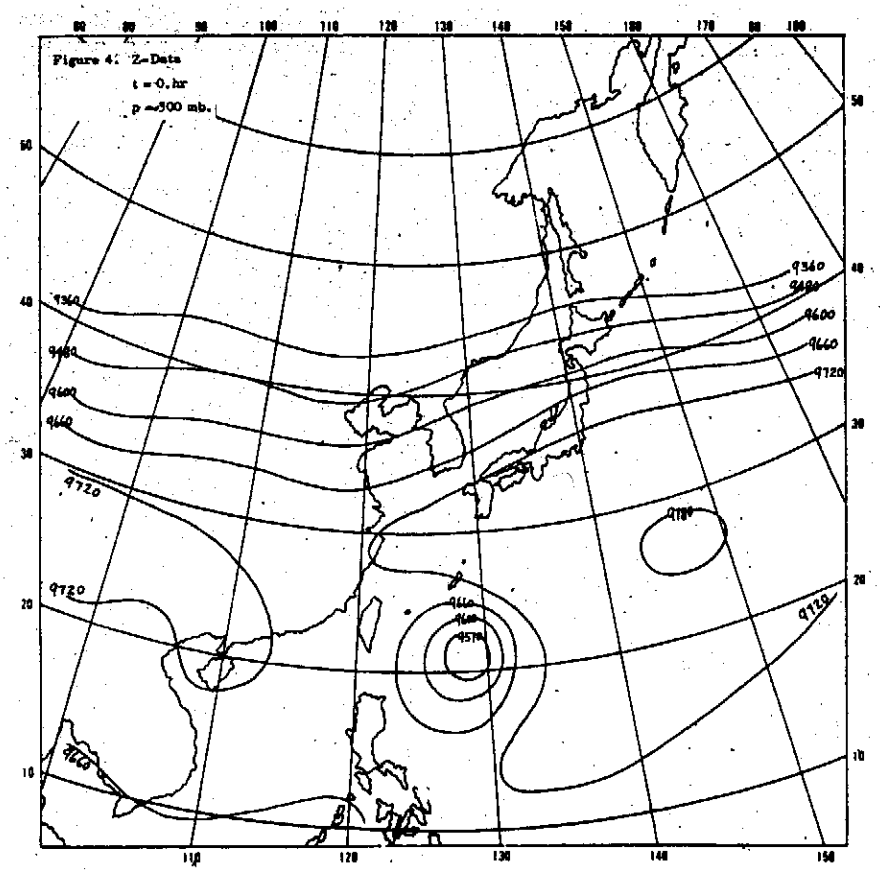
Figure 4: Z-Data
t = 0. hr
p = 500 mb.

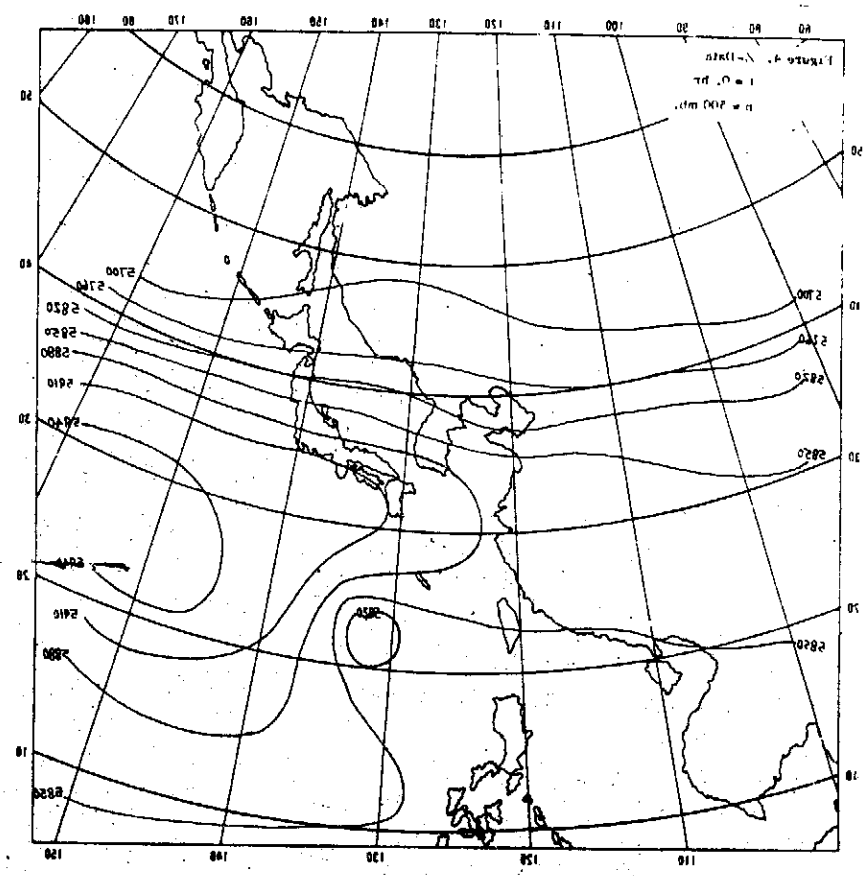

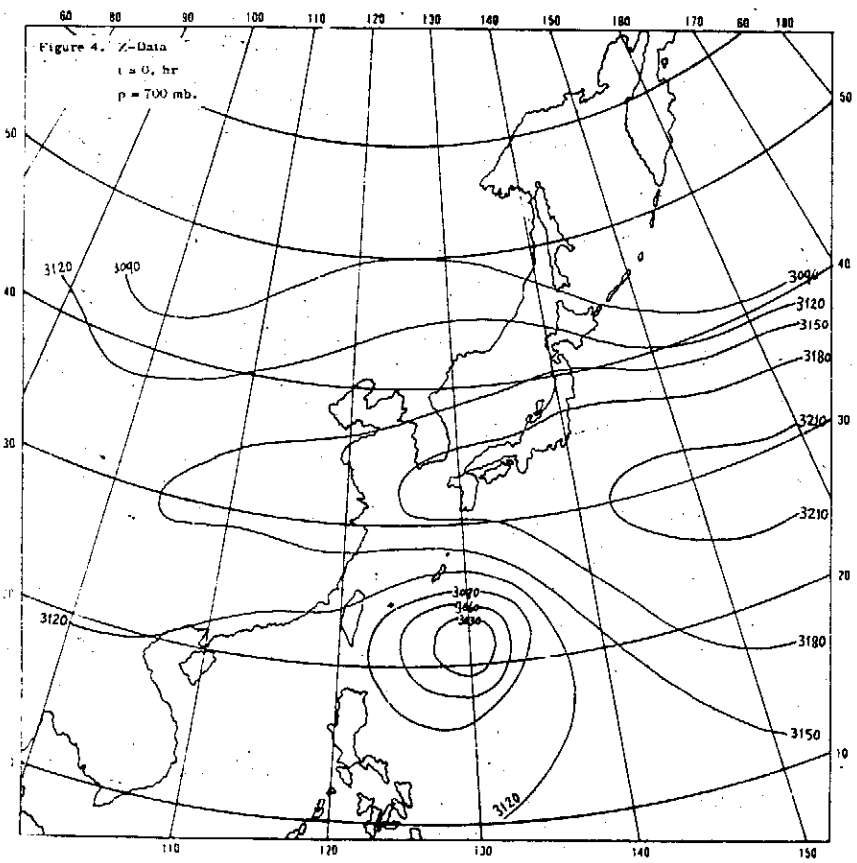
Figure 4. Z-Data
t = 0, hr
p = 700 mb.
3120
3090
3150
3180
3210

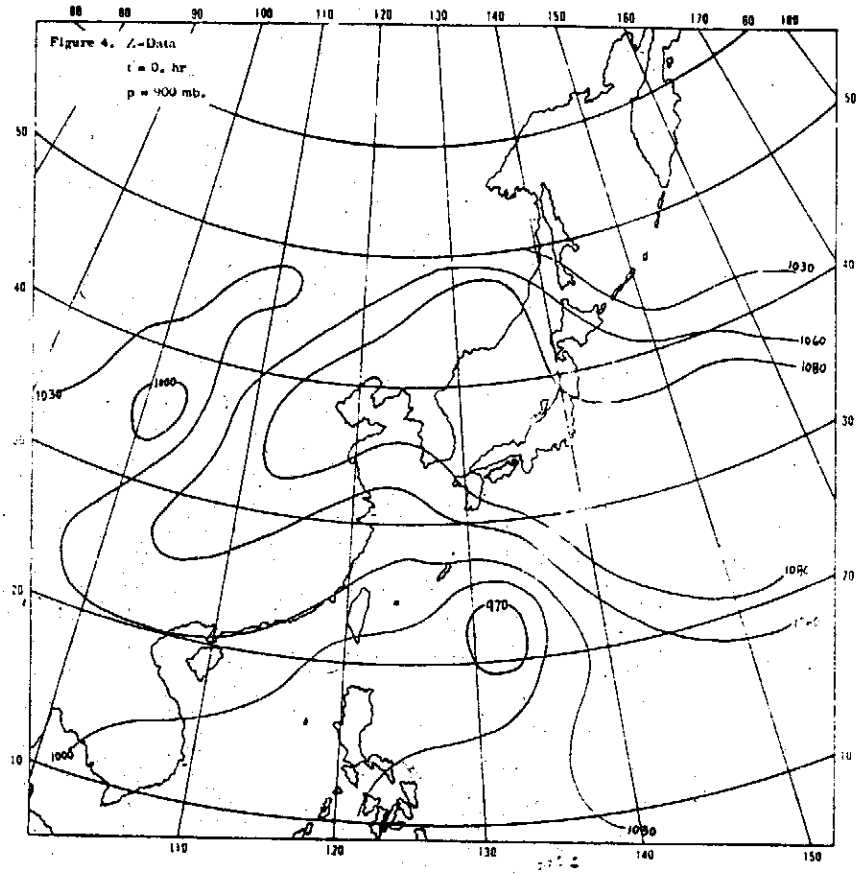
Figure 4. Z-Data
t = 0. hr
p = 900 mb.
1030
1060
1080
1000
970
1080

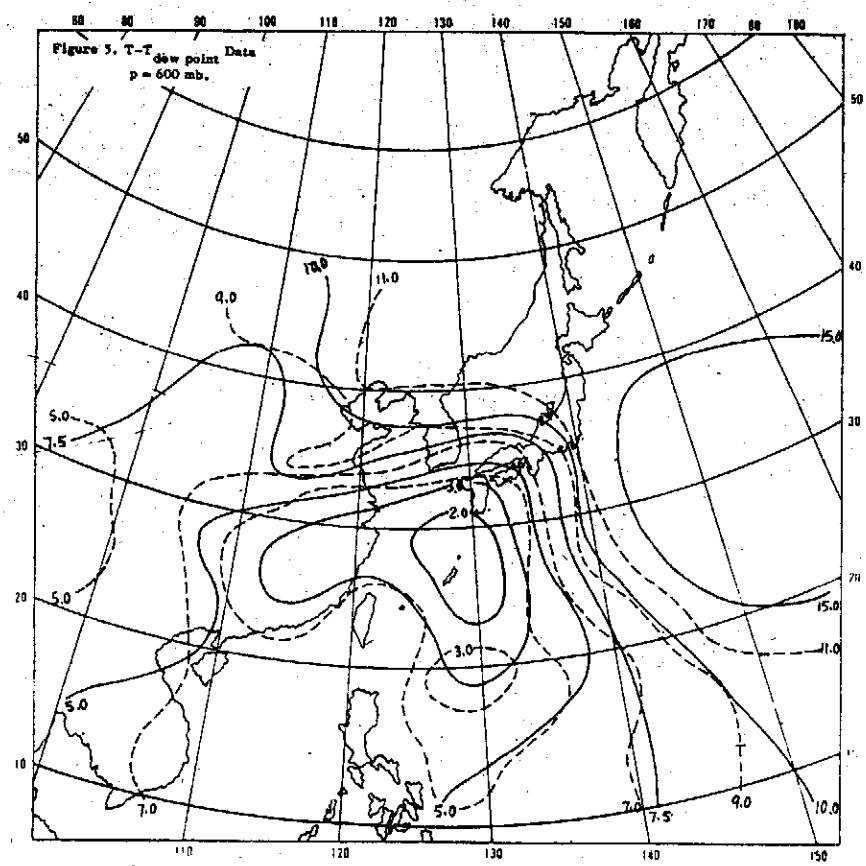
Figure 5. T-T dew point Data
p = 600 mb.
10.0
11.0
9.0
15.0
5.0
7.5
3.0
2.0
5.0
7.0
5.0
7.0
7.5
9.0
10.0
15.0
11.0

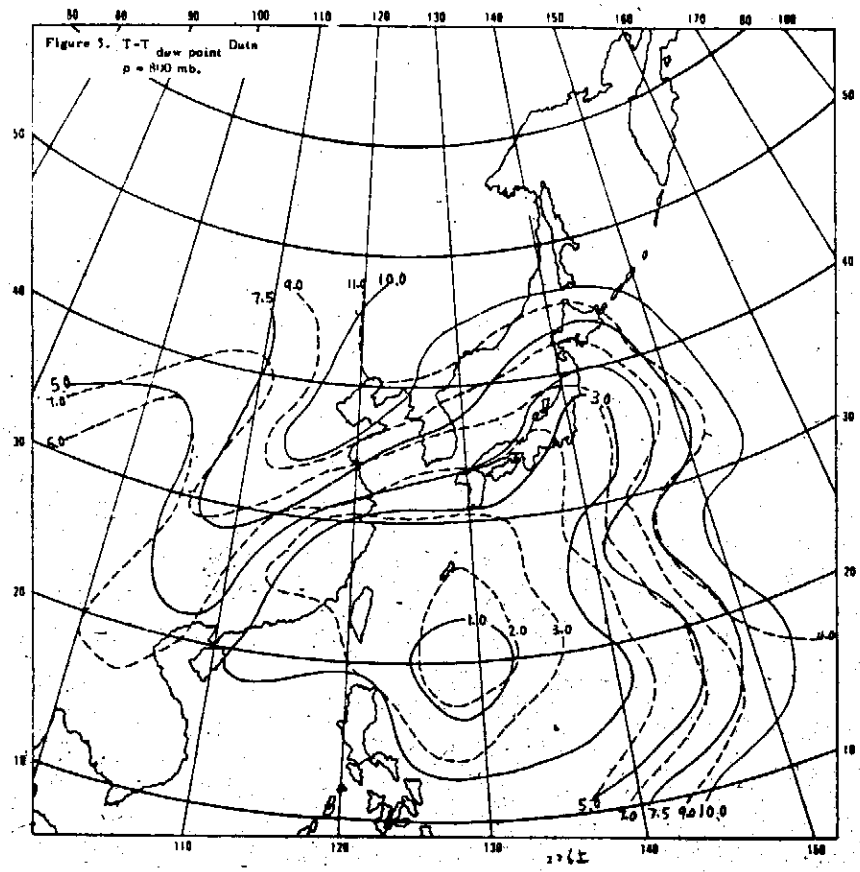
Figure 5. T-T dew point Data
p = 850 mb.
7.5
9.0
10.0
5.0
7.0
6.0
3.0
1.0
2.0
3.0
5.0
7.5
9.0
10.0

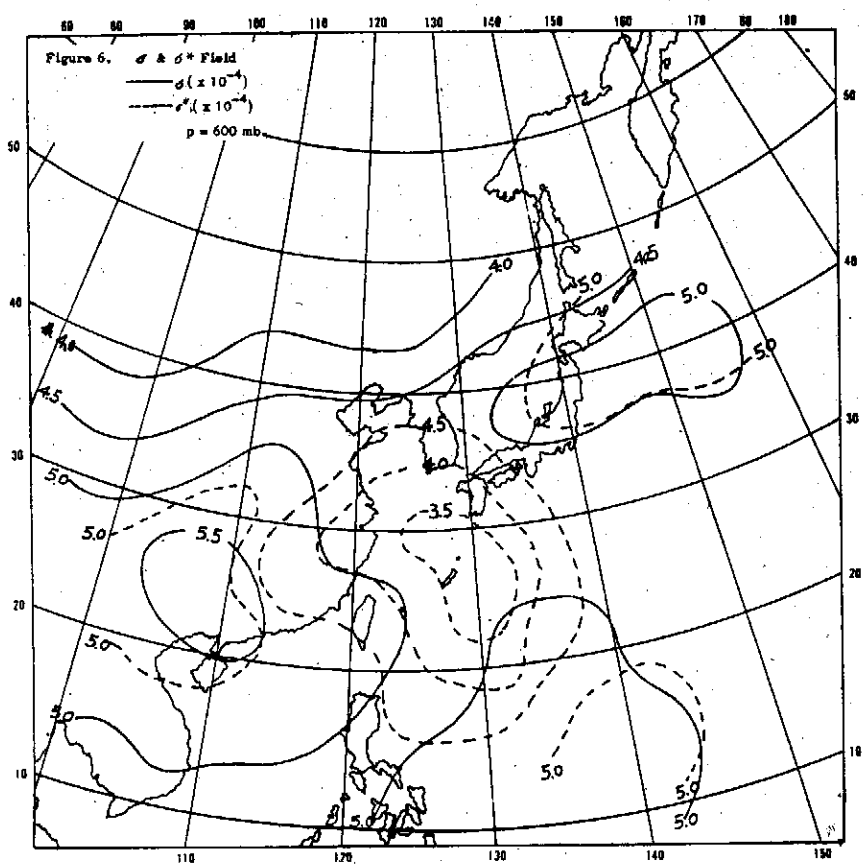
Figure 6. σ & σ* Field
σ(x 10⁻⁴)
σ*(x 10⁻⁴)
p = 600 mb
4.0
4.5
5.0
5.5
3.5

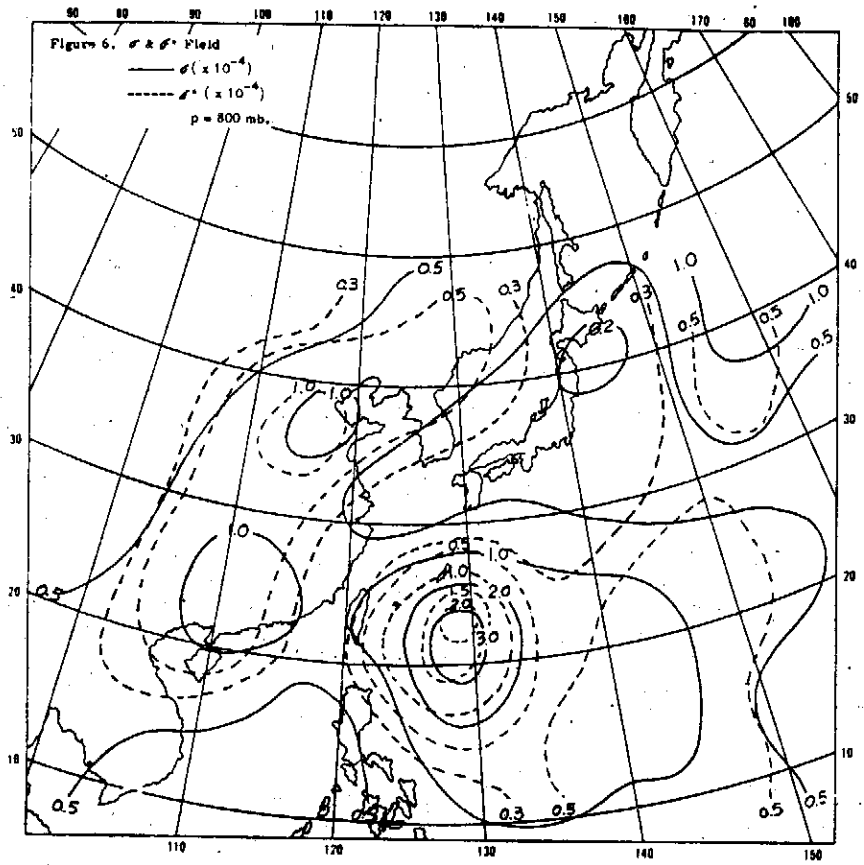
Figure 6. σ & σ* Field
σ(x 10⁻⁴)
σ* (x 10⁻⁴)
p = 800 mb.

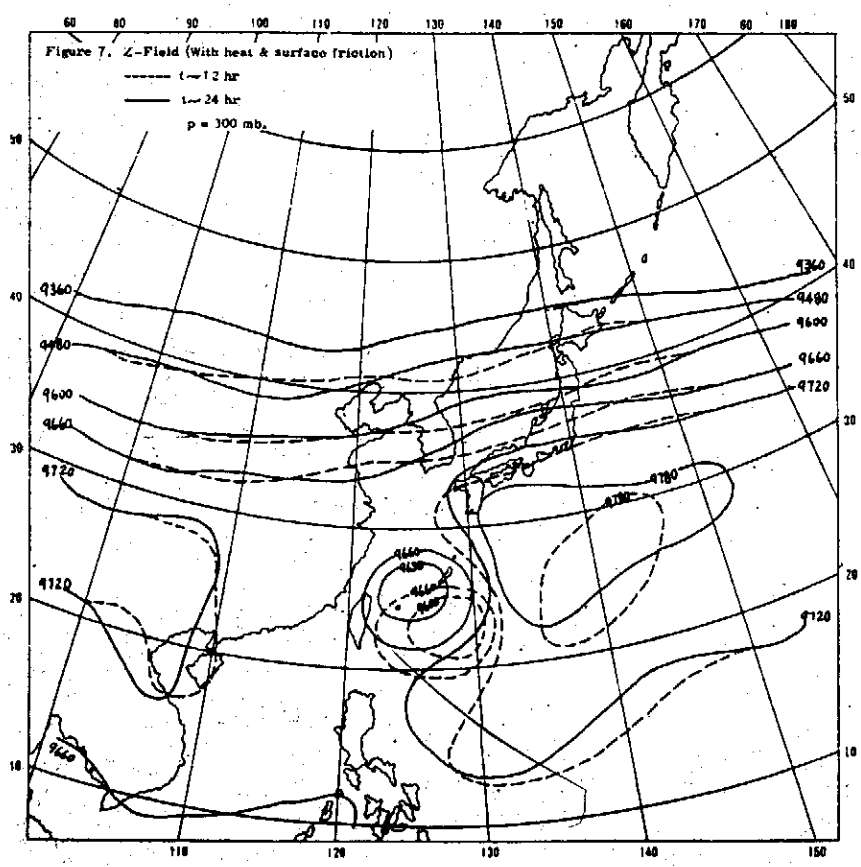
Figure 7. Z-Field (With heat & surface friction)
t=12 hr
t=24 hr
p = 300 mb.

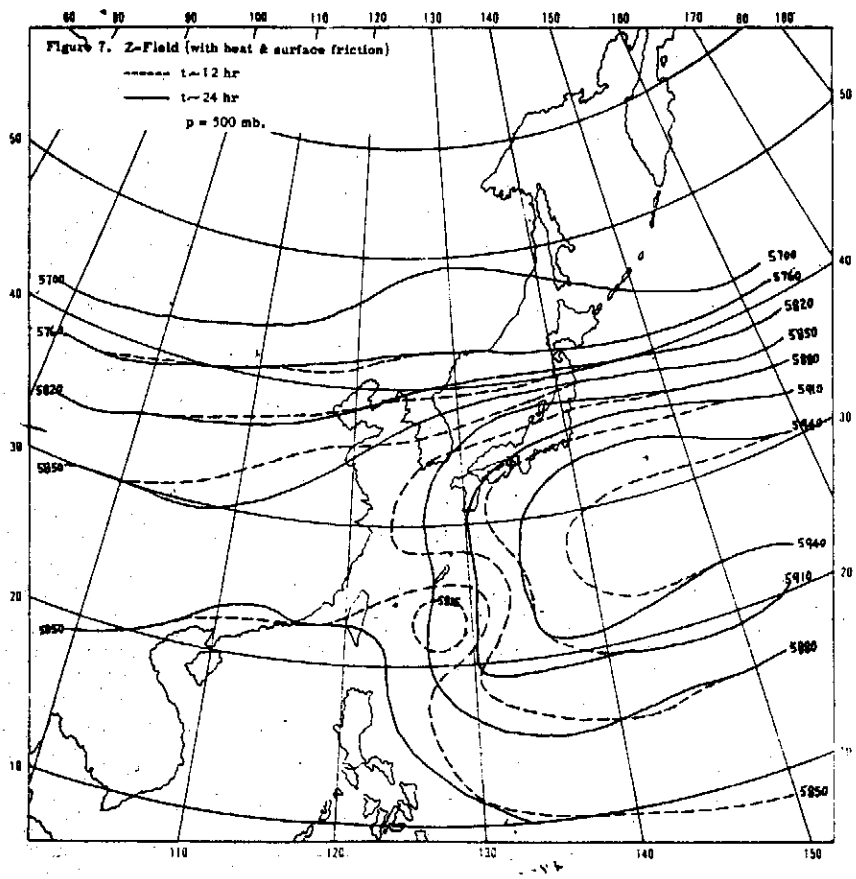
Figure 7. Z-Field (with heat & surface friction)
t=12 hr
t=24 hr
p = 500 mb.
5700
5760
5820
5850
5880
5910
5940
5850

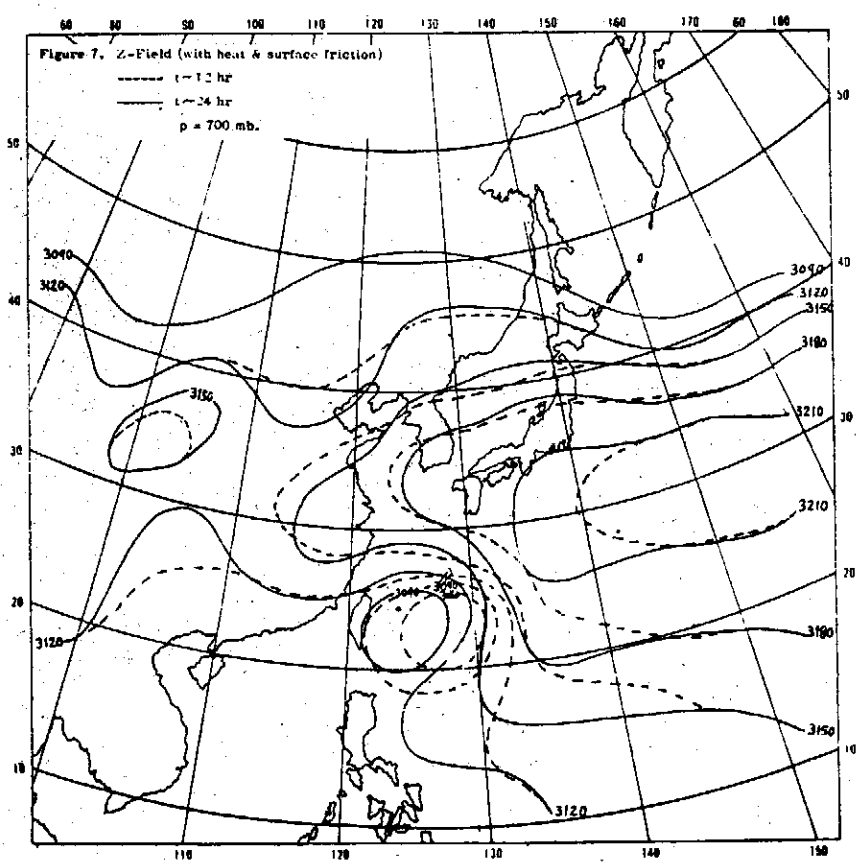
Figure 7. Z-Field (with heat & surface friction)
t=12 hr
t=24 hr
p = 700 mb.
3040
3120
3150
3180
3210
3120

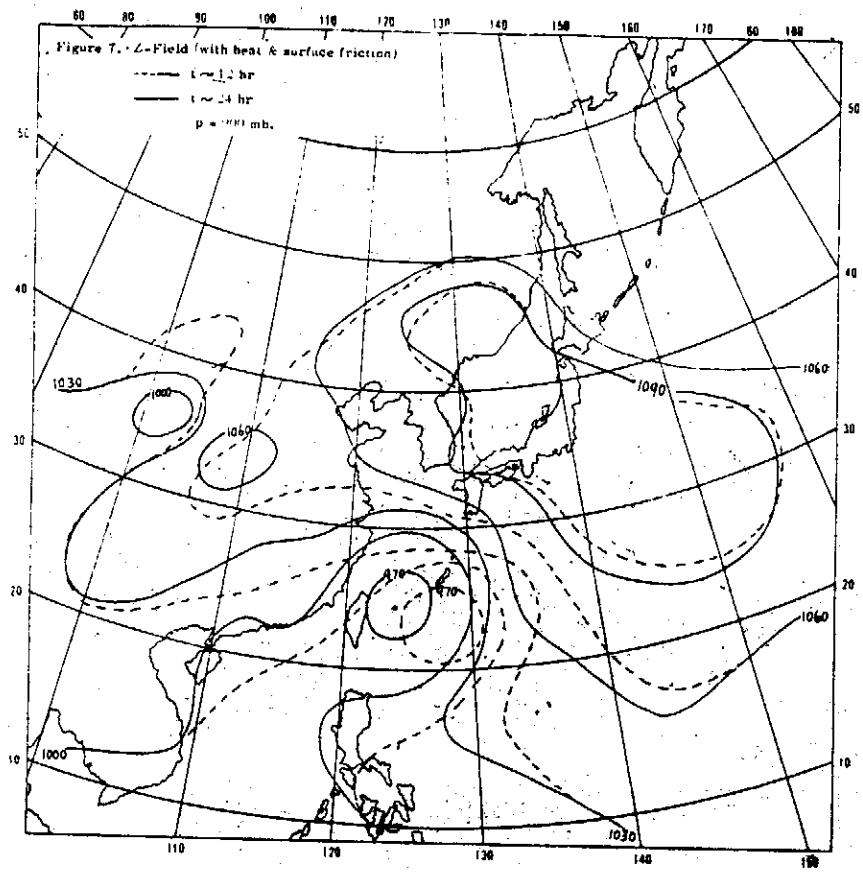
Figure 7. Z-Field (with heat & surface friction)
t~12 hr
t~24 hr
p = 700 mb.
1030
1060
1090
1000
1060
1060
1030

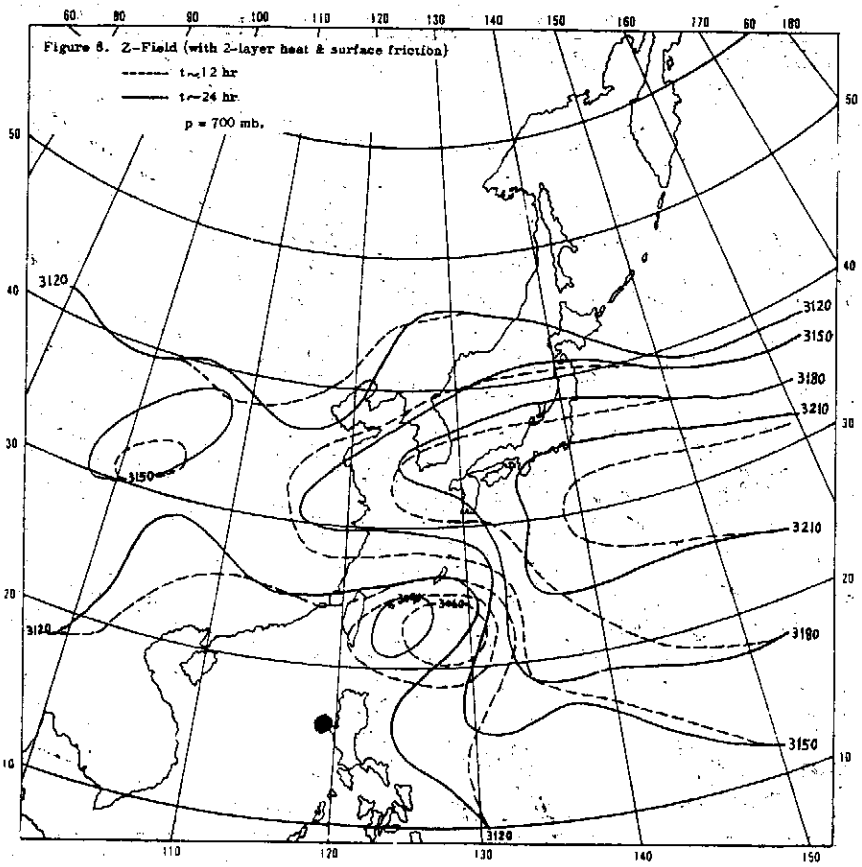
Figure 8. Z-Field (with 2-layer heat & surface friction)
t~12 hr
t~24 hr
p = 700 mb.
3120
3150
3180
3210
3150
3210
3180
3150
3120

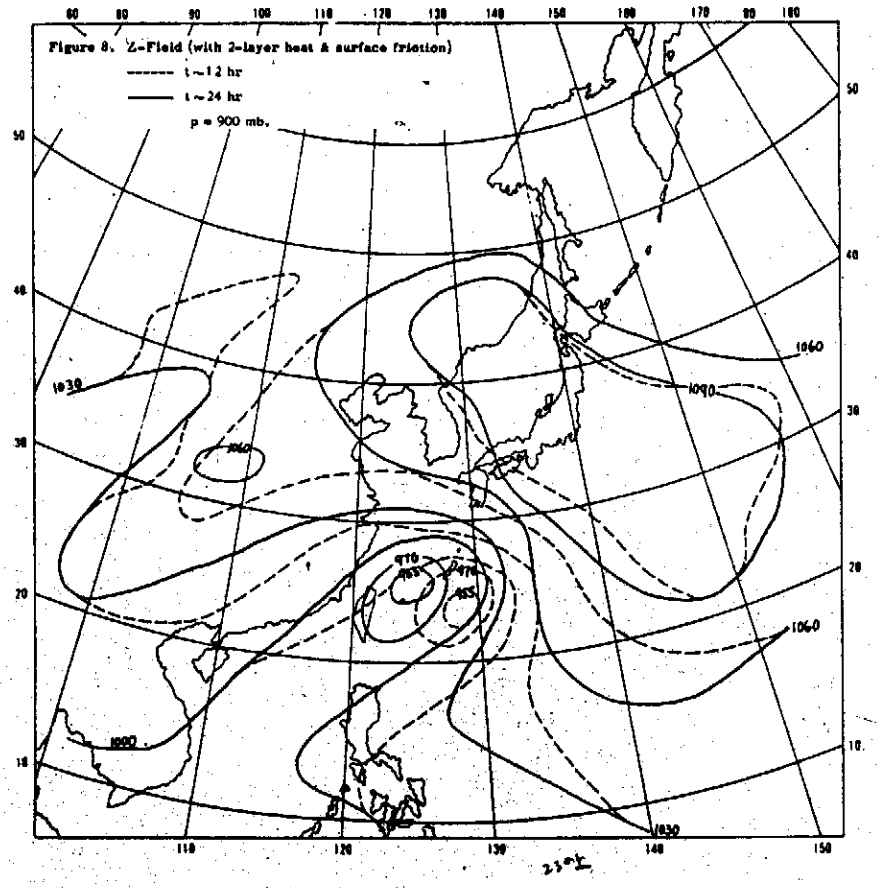
Figure 8. Z-Field (with 2-layer heat & surface friction)
------ t~12 hr
—— t~24 hr
p = 900 mb.
1030
1060
1090
970
985
1030

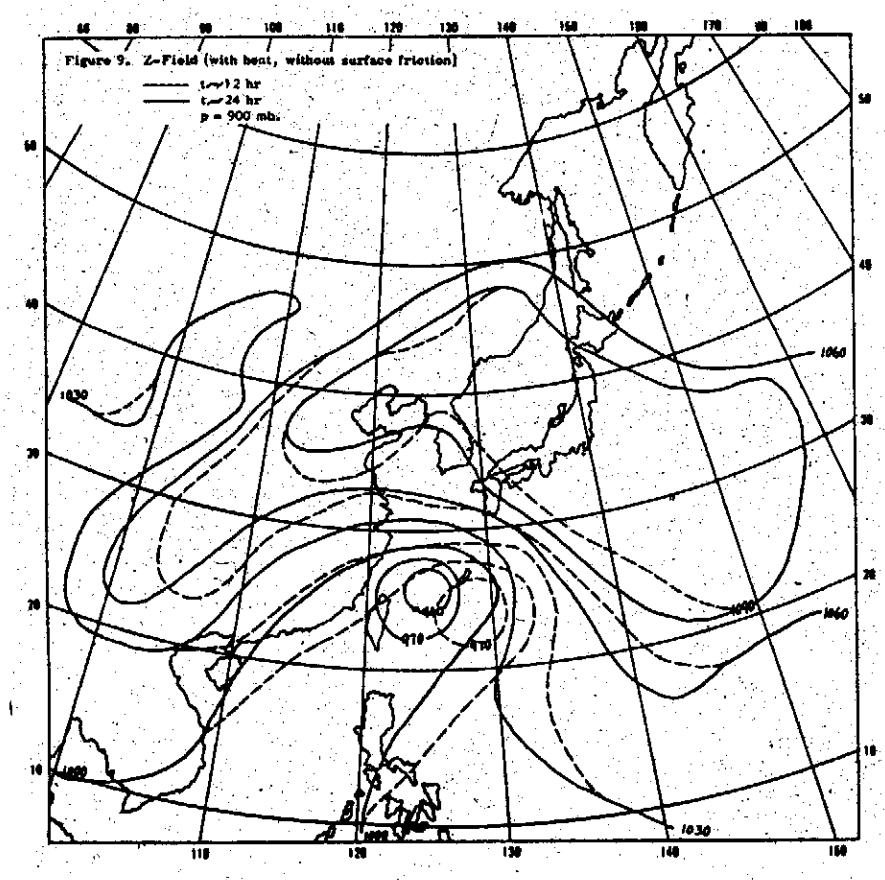
Figure 9. Z-Field (with heat, without surface friction)
—— t~12 hr
—— t~24 hr
p = 900 mb.
1030
1060
1090
970
1030

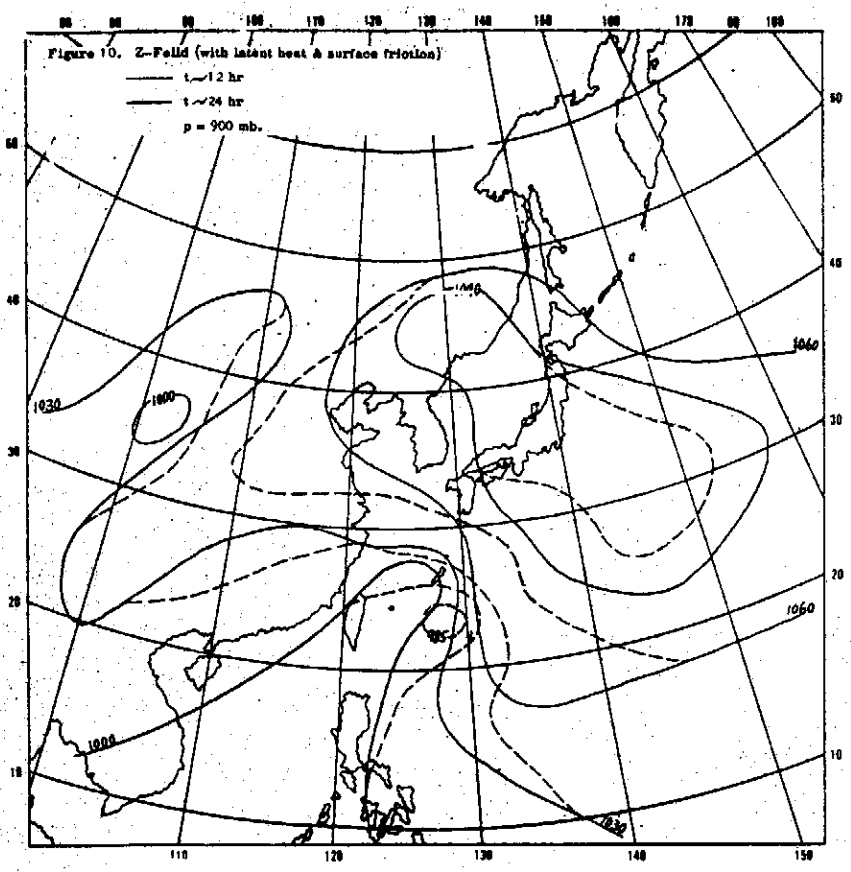
Figure 10. Z-Field (with latent heat & surface friction)
t=12 hr
t=24 hr
p = 900 mb.

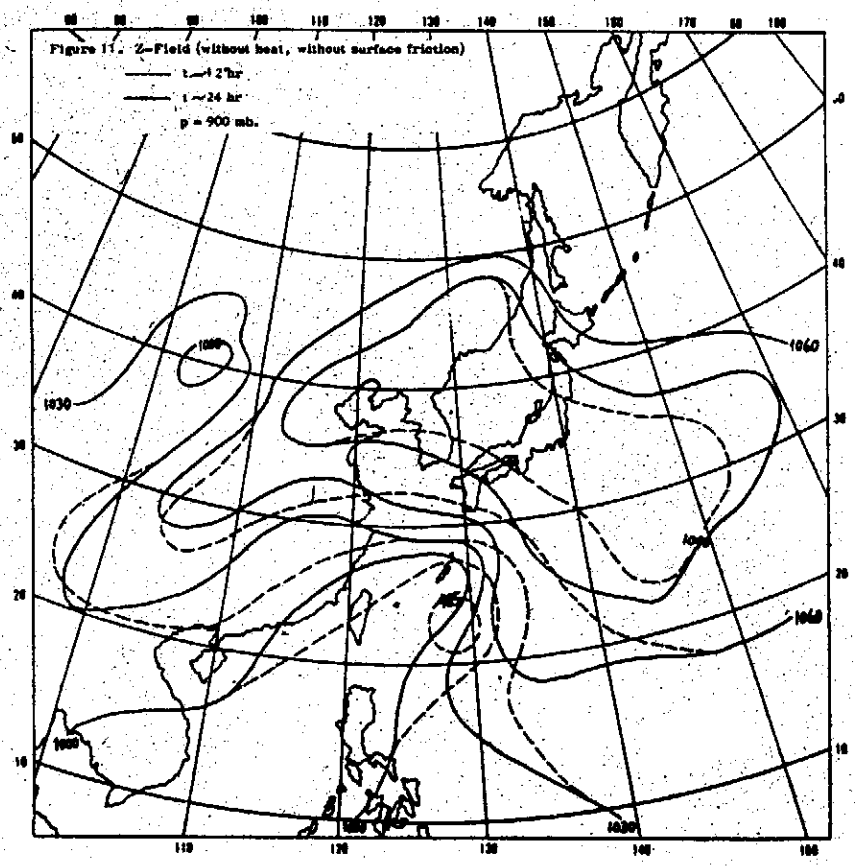
Figure 11. Z-Field (without heat, without surface friction)
t=12hr
t=24 hr
p = 900 mb.

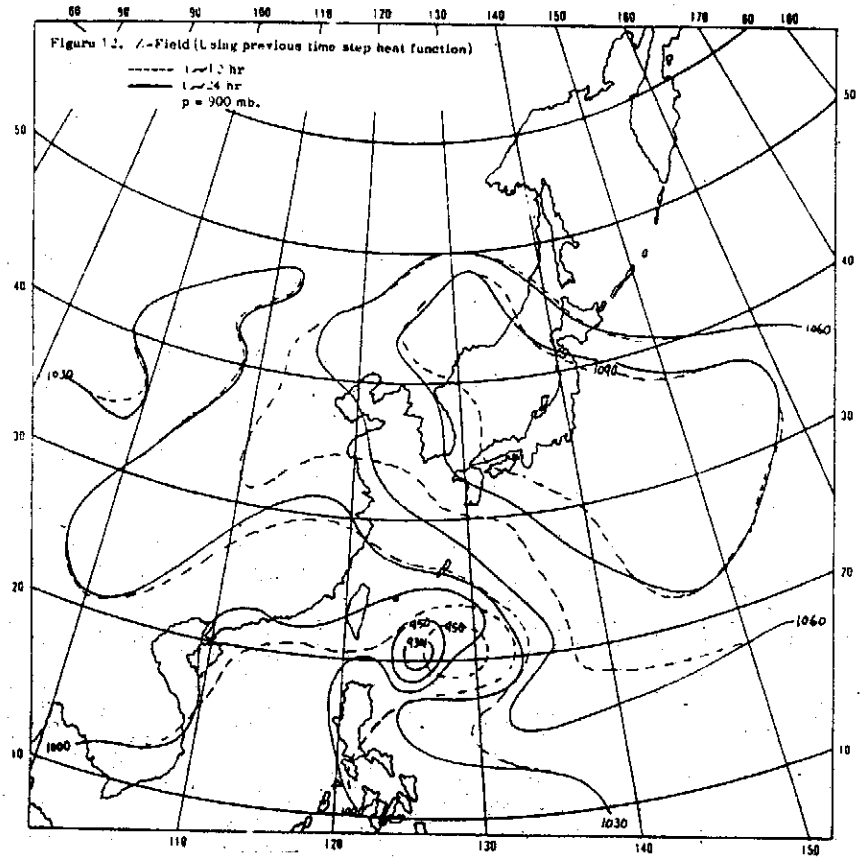
Figure 12. Z-Field (Using previous time step heat function)
t=12 hr
t=24 hr
p = 900 mb.
1030
1060
1090
1060
1030

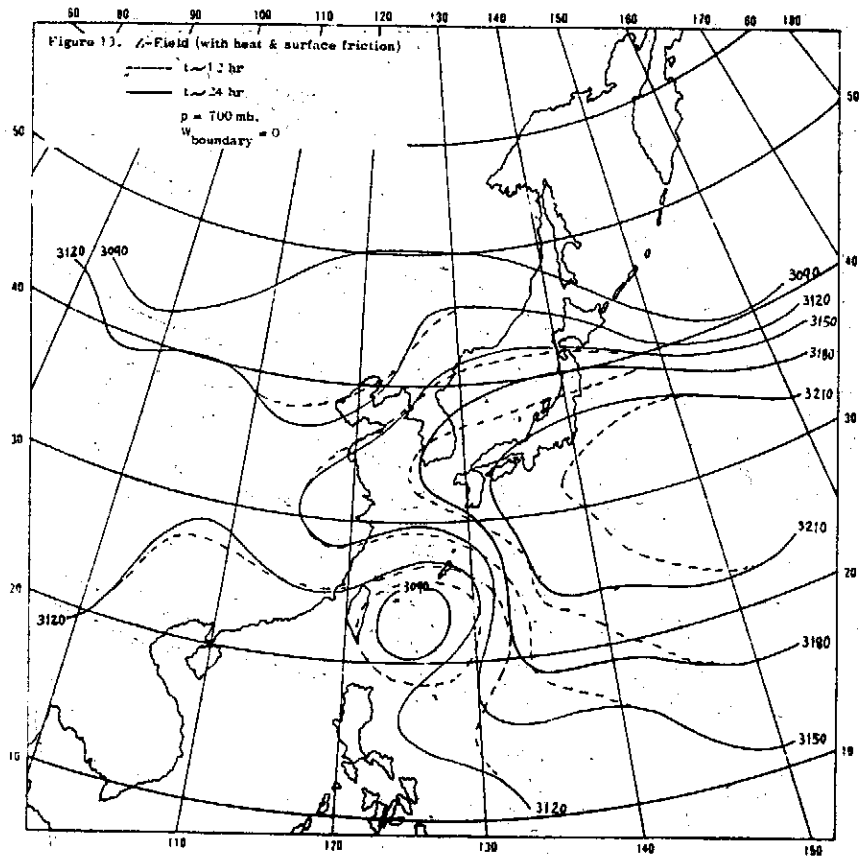
Figure 13. Z-Field (with heat & surface friction)
t=12 hr
t=24 hr
p = 700 mb.
W boundary = 0
3120
3090
3120
3150
3180
3210
3210
3180
3150
3120

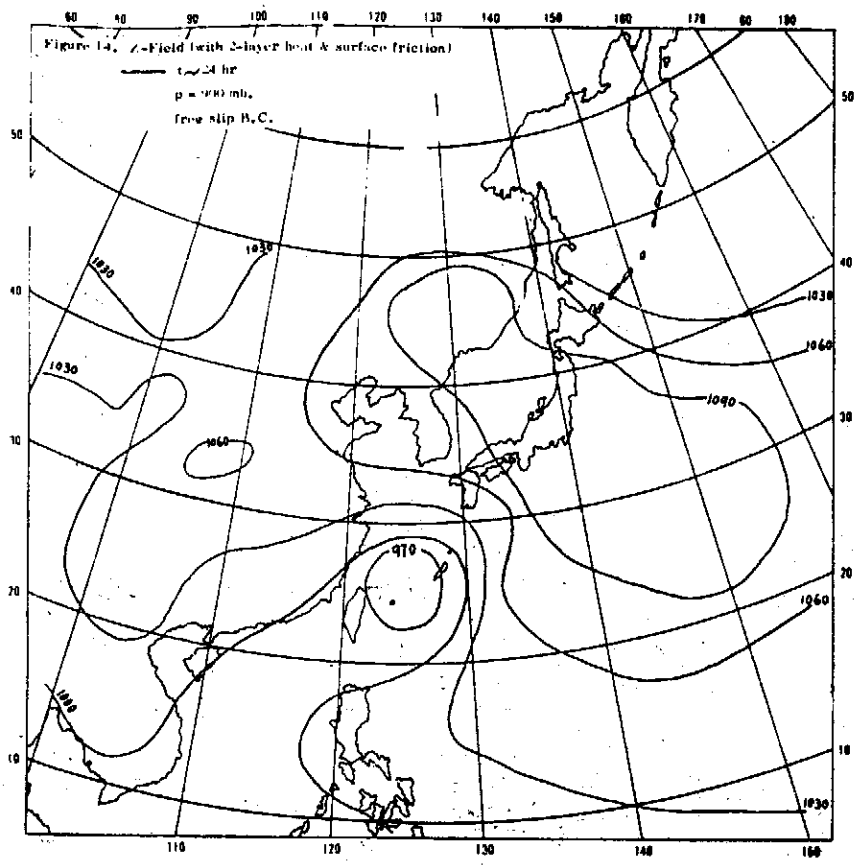
Figure 14. Z-Field (with 2-layer heat & surface friction)
t~24 hr
p = 900 mb.
free slip B.C.
1030
1040
1060
970
1000

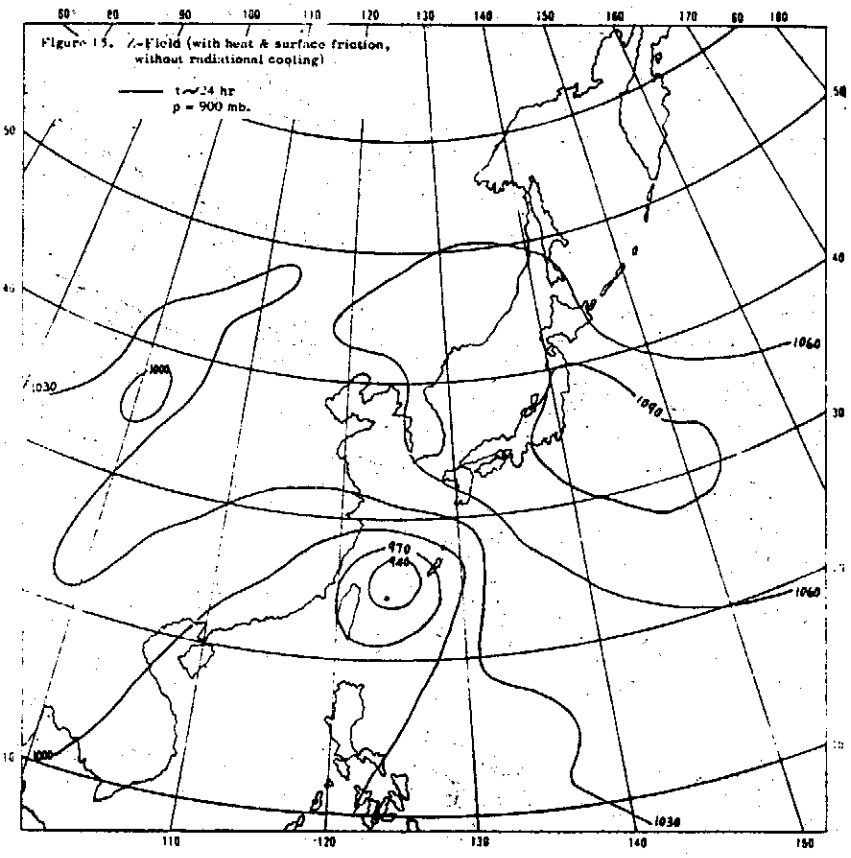
Figure 15. Z-Field (with heat & surface friction, without radiational cooling)
t~24 hr
p = 900 mb.
1030
1040
1060
970
1000

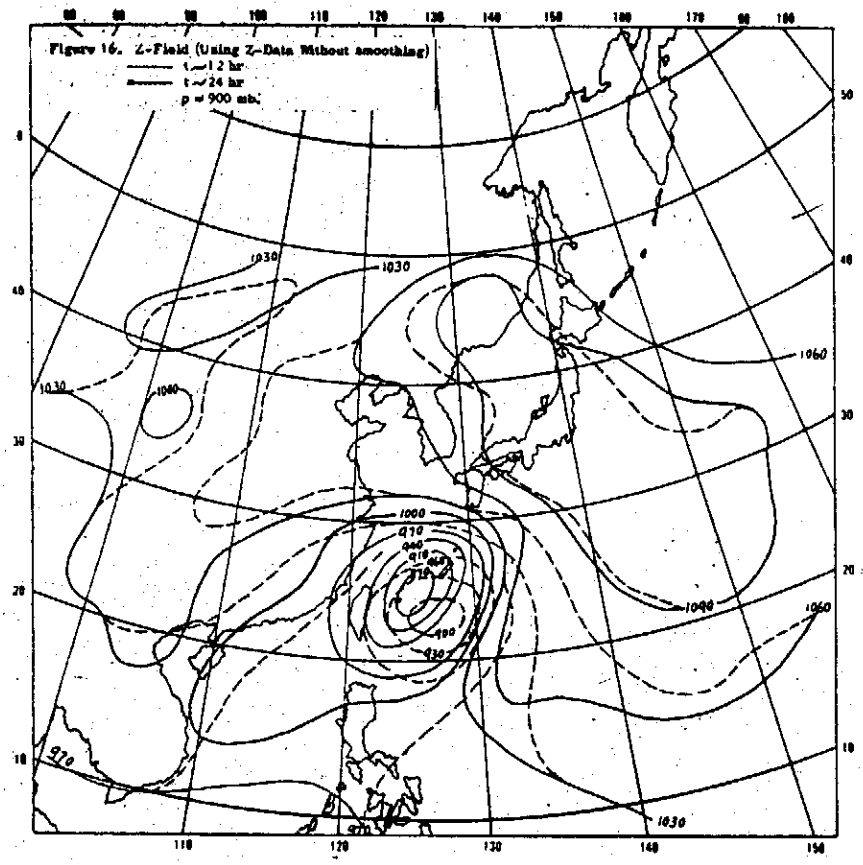
Figure 16. Z-Field (Using Z-Data Without smoothing)
t∼12 hr
t∼24 hr
p = 900 mb.
1030
1030
1060
1030
1040
1000
970
1040
1060
1030

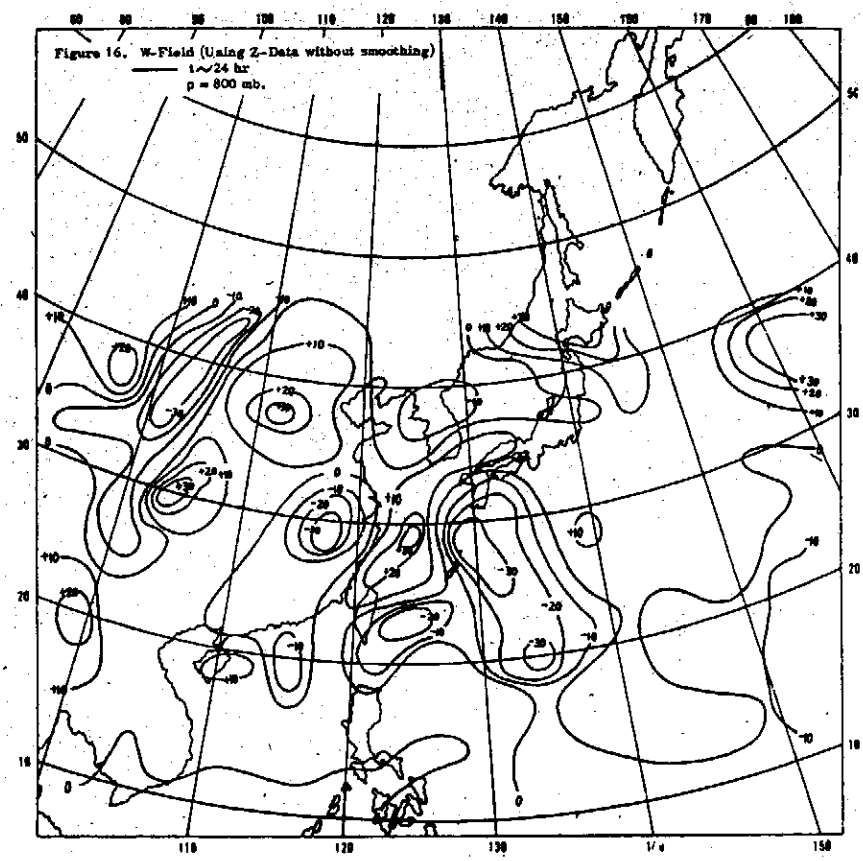
Figure 16. W-Field (Using Z-Data without smoothing)
t∼24 hr
p = 800 mb.

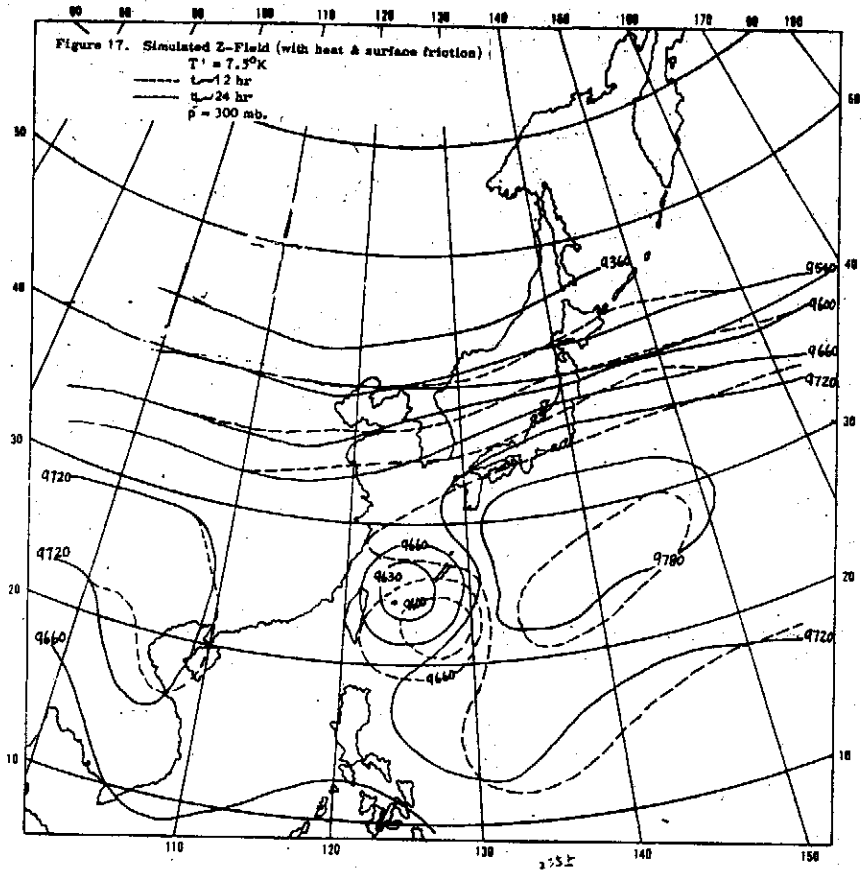
Figure 17. Simulated Z-Field (with heat & surface friction)
T' = 7.5°K
t~12 hr
t~24 hr
p = 300 mb.
9360
9540
9600
9660
9720
9780
9630

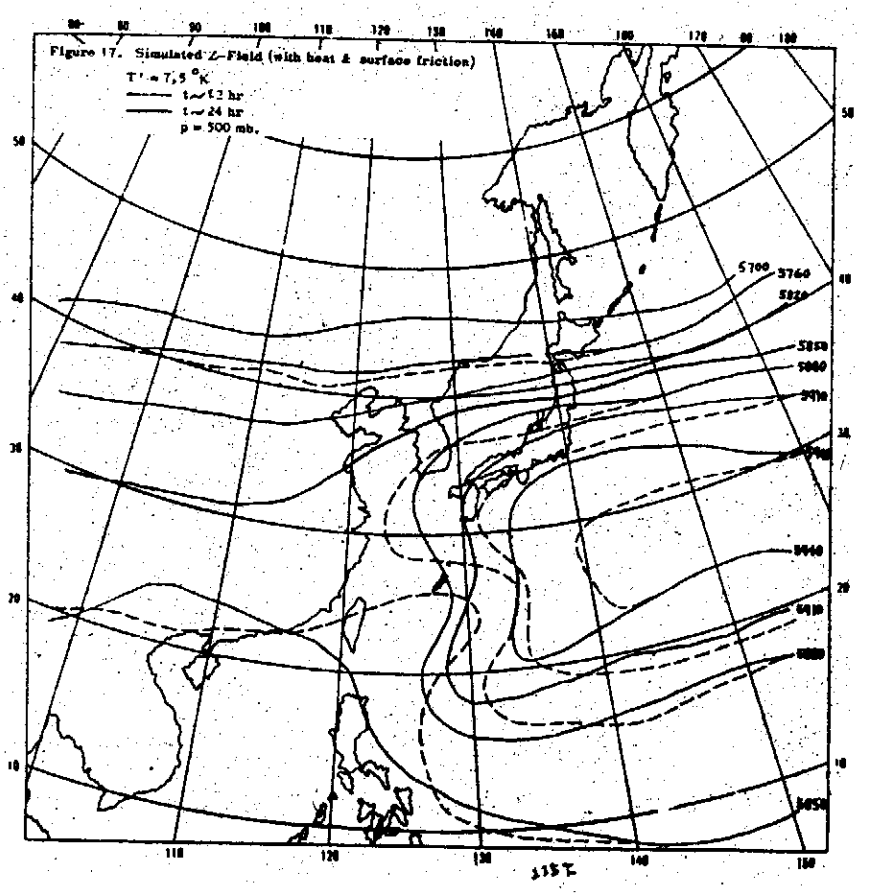
Figure 17. Simulated Z-Field (with heat & surface friction)
T' = 7.5 °K
t~12 hr
t~24 hr
p = 500 mb.
5700
5760
5850
5880
5940

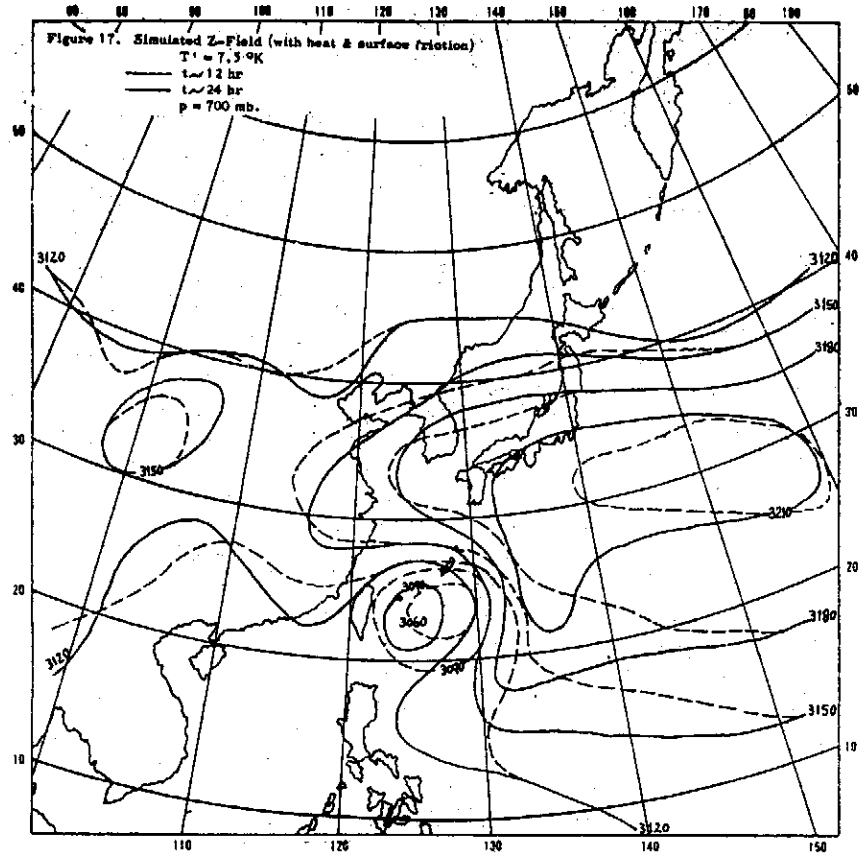
Figure 17. Simulated Z-Field (with heat & surface friction)
T' = 7.5°K
t~12 hr
t~24 hr
p = 700 mb.
3120
3150
3180
3210
3060
3090

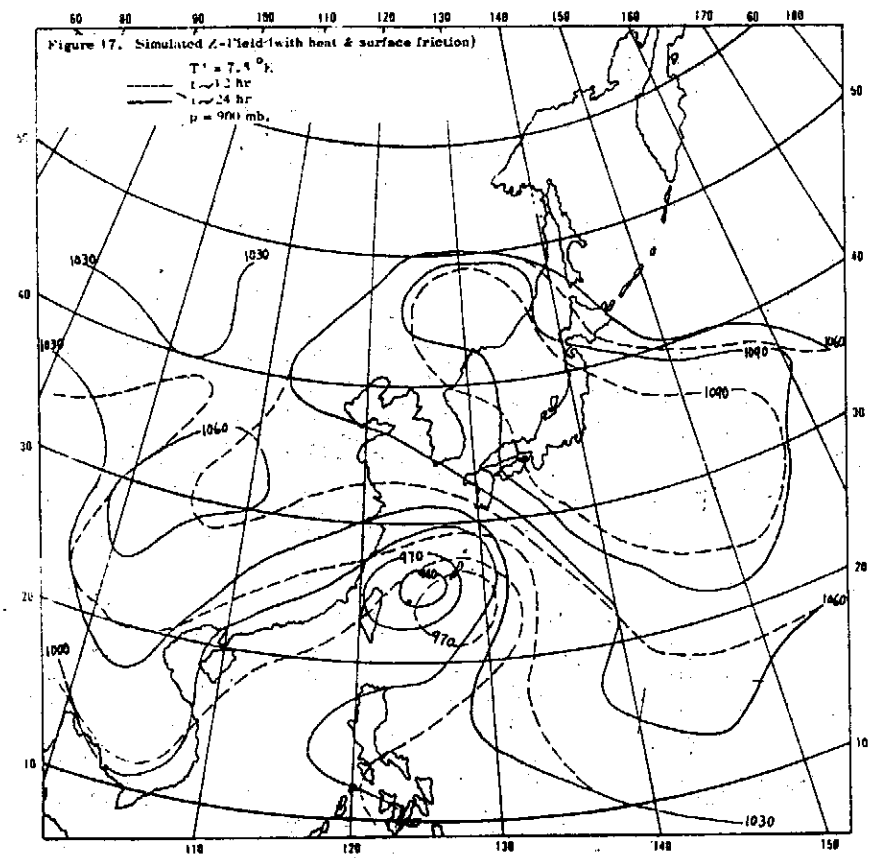
Figure 17. Simulated Z-Field (with heat & surface friction)
T' = 7.5°K
t~12 hr
t~24 hr
p = 900 mb.
1030
1040
1060
1000
970

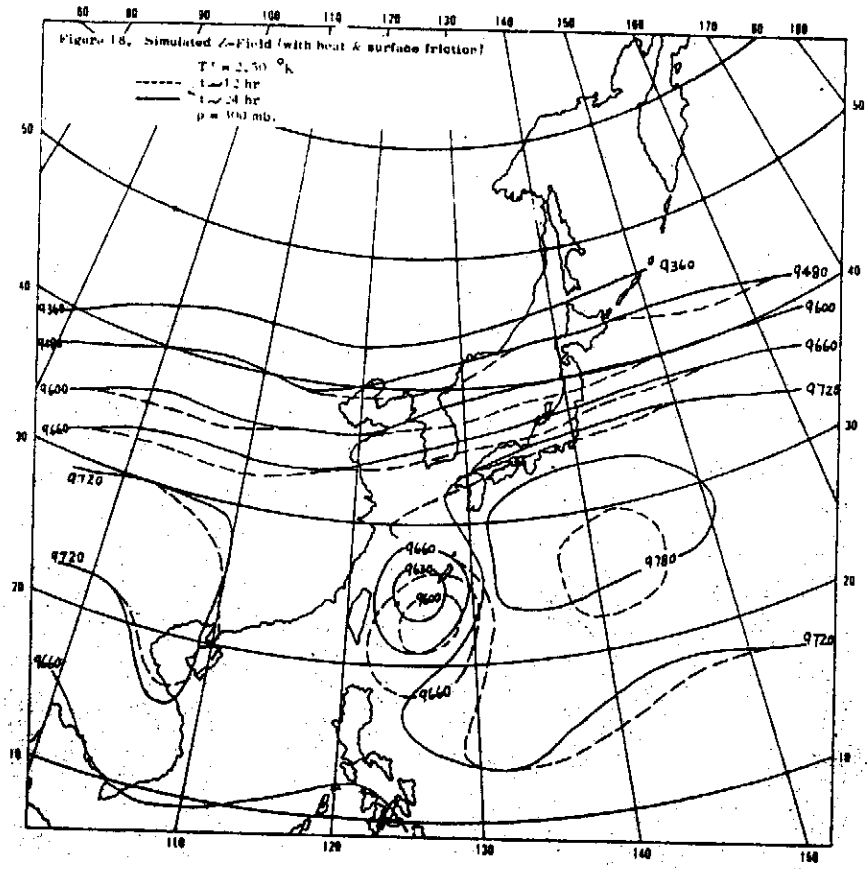
Figure 18. Simulated Z-Field (with heat & surface friction)
T' = 2.50 °K
t ~ 12 hr
t ~ 24 hr
p = 700 mb.
9360
9480
9600
9660
9720
9780
9720
9660
9720
9660
9720
9660
9600
9660
9720
110
120
130
140
150

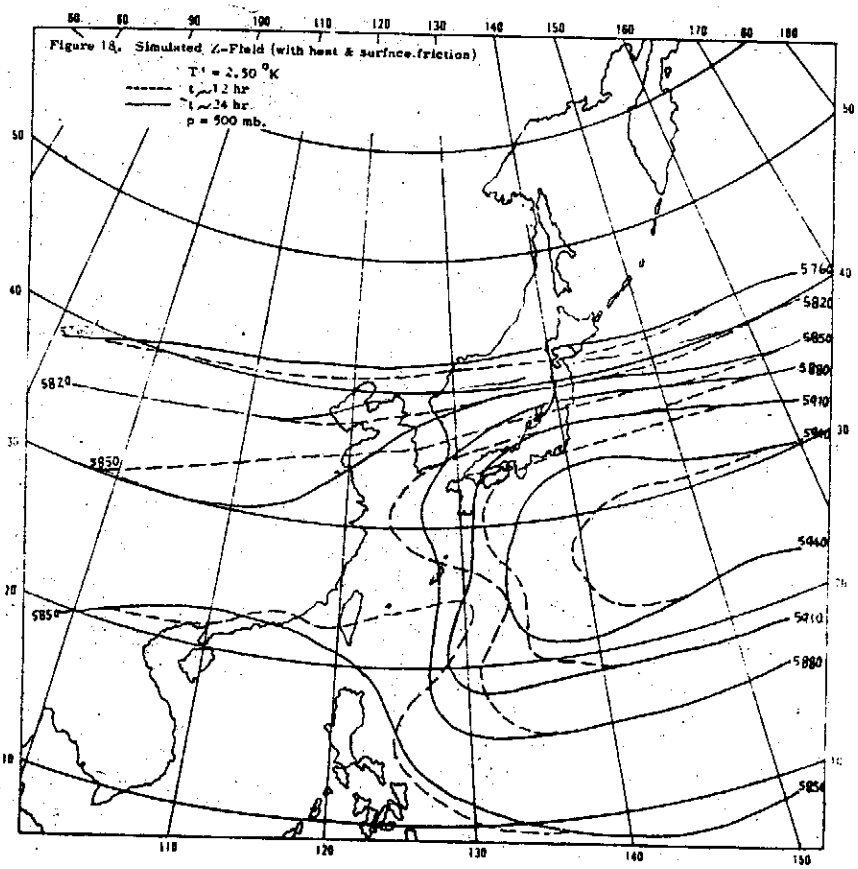
Figure 18. Simulated Z-Field (with heat & surface friction)
T' = 2.50 °K
t ~ 12 hr
t ~ 24 hr
p = 500 mb.
5760
5820
5850
5880
5910
5940
5820
5850
5850
5940
5910
5880
5850
110
120
130
140
150

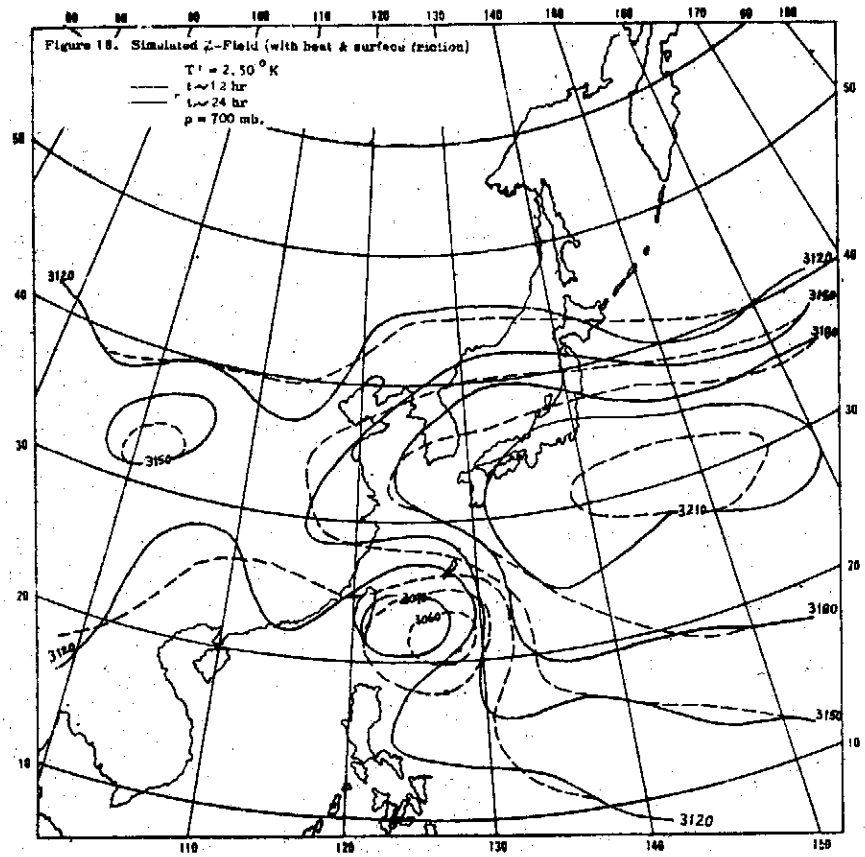
Figure 18. Simulated Z-Field (with heat & surface friction)
T' = 2.50 °K
t~12 hr
t~24 hr
p = 700 mb.
3120
3150
3210
3180
3060
3030
3120

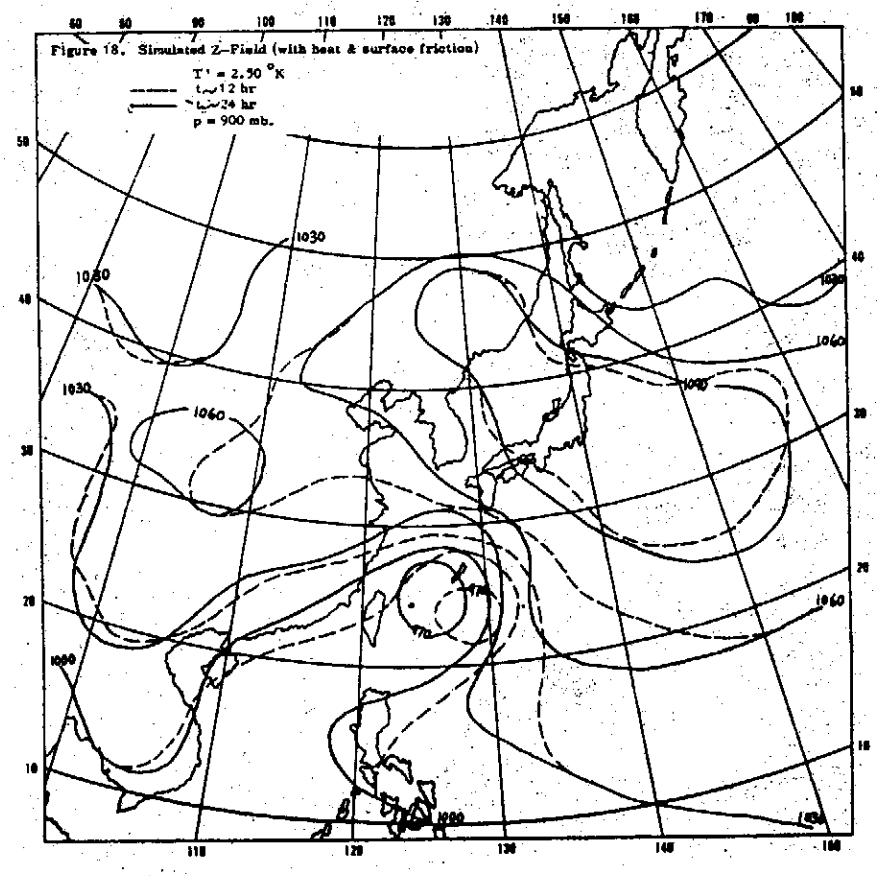
Figure 18. Simulated Z-Field (with heat & surface friction)
T' = 2.50 °K
t~12 hr
t~24 hr
p = 900 mb.
1030
1060
1030
1060
1060
1060
1060

Power Spectra of Upper Wind over Taiwan in Summer*

Staff Members of Atmospheric Physics Division

Institute of Physics, Academia Sinica

Abstract

Spectrum analysis of the zonal and meridional components of upper winds from 700-mb to 150-mb levels at Taoyuan (N 25°03', E 121°13') is made during the period July through September 1966. The power spectra of the zonal and meridional wind components in the lower and upper troposphere show a peak at the period of about 12 days but about 6 days in the middle troposphere.

The horizontal and vertical structures of the disturbances are studied by computing the cospectrum, the quadrature-spectrum, the coherence and the phase difference for the zonal and meridional wind components. The results indicate that the axis of the disturbance is directed generally from southwest to northeast near the 12-day period and that the phase of the meridional wind components at upper levels lags behind that at lower levels.

1. Introduction

Since the discovery of the easterly wave during the 1940's, an increasing amount of attention has been devoted to the study of tropical wave disturbances. By early 1950's the main features of the easterly wave and the closely related equatorial wave had been well recognized, and a considerable progress had been made in interpreting these phenomena from a dynamical point of view. However, the sparsity of tropical upper wind observations and the lack of a sound theoretical theory for expounding synoptic results seriously stumbled and stopped the extension and generalization of these early wave models.

In recent years, the inadequacies in data and theretical support for synoptic investigations have been improved to some extent. Systematic application of spectrum analysis techniques to tropical time series has provided some compensation for poor spatial distribution of stations (see Wallace, 1969). These developments have contributed to mushroom the study of tropical wind time series by the use of spectrum analysis. The researchers working in this field are so far too numerous to recount, such as Panofsky and Horen (1955), Kahn (1957), Rosenthal (1960), Maruyama (1967, 1968a, 1968b), Yanai et al. (1968), Wallace and Chang (1969), Nitta (1970), and Madden et al. (1971), etc. To the authors' knowledge, however, many of the published materials have been restricted to the equatorial lower latitude. In these regions a distinct spectral peak of meridional wind component in the period range of 4 to 5 days throughout the troposphere and the lower stratosphere was found (Maruyama, 1967, 1968a, 1968b; Yanai et al., 1968; Nitta, 1970).

* This research is partially supported through a grant from the National Science Council, Republic of china.

Taiwan (N 25°, E 121°) is located to the east of China mainland and to the west of Pacific ocean. The changeable summer disturbances in this area are controlled by the vicissitude of the thermal low over China mainland and the anticyclone over Pacific region. The disturbances in this region are not exactly the same as those in the equatorial lower latitude regions. Hsu et al. (1970) made similar spectrum analysis of upper wind over Taiwan and reported that the v-component has the period of 2-6 days in summer in this area. However, this result was felt less certain because the analysis was made only at the 850-mb level. The object of this present study is to reveal some features of the upper wind disturbances over Taiwan in summer with more quantitative details.

2. Data

Data of observations over Taoyuan (N 25°03', E 121°13') used in this study are taken from IGY Observation Data (1957) Published by Chinese National Committee. The summer season we define starts from the beginning of July to the end of September. The upper wind observations were available twice a day, i. e., 0000 GMT and 1200 GMT, during the period 1 July through 30 September 1966. Thus, there are 92 days or 184 observations available but the use of high-pass filter reduces them to 70 days or 140 observations respectively. Analysis is made for the wind speed and wind direction at the constant pressure levels of 700 mb, 500 mb, 300 mb and 150 mb. Tabulated values of wind speed and wind direction are given in units of knots and degrees respectively. The numbers of missing data at each level are listed in Table 1. Computations are made by excluding the missing data. The wind data contain a few number of doubtful ones, but neither correction nor rejection is made in our case.

3. Method

3.1 Wind components

The zonal wind component u and meridional wind component v are obtained by

$$u = -ff \cdot sin(dd) \tag{1}$$

$$v = -ff \cdot cos(dd) \tag{2}$$

respectively, where ff is wind speed, and dd is wind direction in degree measured from the true north.

3.2 High-pass filter

Prior to the spectrum analysis, we applied a high-pass filter, designed according to Hollowway (1958) and Maruyama (1968a), to the original data to remove longer periods and linear trends. The frequency response function of the high-pass filter is illustrated in Fig.1. The variations with periods shorter than about ten days are almost completely reserved. We shall call the filtered data disturbances.

Let u_i be time series data. For every successive 45 data points, the smoothed data

point value $\tilde{u}_i$ is computed by the following linear equation:

$$\tilde{u}_i=\sum_{k=-22}^{22} W_k\, u_{i+k} \Big/ \sum_{k=-22}^{22} W_k, \tag{3}$$

where W_k is a particular weight in the smoothing function. The smoothing function used in this study is the Gaussion normal distribution function; namely,

$$W_k=(2\pi\sigma^2)^{-1/2}\cdot exp(-t^2/2\sigma^2)\cdot\Delta t \tag{4}$$

for $\sigma=5$ days and $t=k\Delta t$ (k=0, ±1, ……, ±22, $\Delta t=0.5$ day). Then only low frequencies of the original data u_i will appear in the time series of $\tilde{u}_i$ values. The time series of the filtered data u_i' are given by the deviations from the smoothed data; namely,

$$u_i'=u_i-\tilde{u}_i. \tag{5}$$

If missing data are contained in successive 45 data points, the smoothed data point value $\tilde{u}_i$ is computed by the remaining data. The filtered data u_i' cannot not be defined if u_i is missing.

3.3 Power spectrum and cross spectrum

Power spectrum and cross spectrum analysis of time series is the basic tool of the present study. The method we use is that originally designed by Munk et al. (1959). Its principle is discussed by Blackman and Tukey (1958).

The covariance, or the lag correlation, between two time series u_i and v_i is given by

$$C_\ell(u,v)=(1/N-\ell-m)\sum_{i=\ell+1}^{N} u_i\, v_{i-\ell} \tag{6}$$

for $\ell=0, 1, \cdots\cdots, M$, where ℓ is the lag number, M is the maximum lag number, N is the length of the time series, and m is the number of undefined products due to missing data. In general, the covariance between u_i and v_i can be decomposed into a sum of an even part $EC_\ell(u,v)$ and an odd part $OC_\ell(u,v)$; that is,

$$C_\ell(u,v)=EC_\ell(u,v)+OC_\ell(u,v) \tag{7}$$

where

$$EC_\ell(u,v)=-\frac{1}{2}\,[C_\ell(u,v)+C_\ell(v,u)] \tag{8}$$

and

$$OC_\ell(u,v)=-\frac{1}{2}\,[C_\ell(u,v)-C_\ell(v,u)]. \tag{9}$$

Thus, the autocovariances of u_i and v_i are equal to the even parts of the covariances with themselves; namely,

$$C_\ell(u,u)=EC_\ell(u,u) \tag{10}$$

and

$$C_\ell(v,v)=EC_\ell(v,v) \tag{11}$$

respectively.

In order to convert the abrupt ends of cavariance into smooth die-aways at the edge of lagging $\ell=M$, a lag window D_ℓ, i.e.,

$$D_\ell=1+cos\ (\pi\ell/M)=2\ cos^2(\pi\ell/2M), \tag{12}$$

is applied beforehand. The power spectra of u_i and v_i with frequency $k/2M\Delta t$ are given by,

respectively,

$$P_{1k}(u) = \sum_{\ell=0}^{M} C_\ell(u,u)\cdot cos(k\ell\pi/M)\cdot D_\ell\cdot\delta_\ell \tag{13}$$

and

$$P_{1k}(v) = \sum_{\ell=0}^{M} C_\ell(v,v)\cdot cos(k\ell\pi/M)\cdot D_\ell\cdot\delta_\ell, \tag{14}$$

where k has the values 0, 1, ……, M, and $\delta_\ell=1/2$ for $\ell=0$ or M, and $\delta_\ell=1$ otherwise.

The cospectrum, the quadrature-spectrum, the coherence and the phase difference between u_i and v_i are, respectively,

$$S_{1k}(u,v)= \sum_{\ell=0}^{M} EC_\ell(u,v)\cdot cos(k\ell\pi/M)\cdot D_\ell\cdot\delta_\ell \tag{15}$$

$$Q_{1k}(u,v)= \sum_{\ell=0}^{M} OC_\ell(u,v)\cdot sin(k\ell\pi M)\cdot D_\ell\cdot\delta_\ell \tag{16}$$

$$R_{1k}(u,v)= \left[\frac{S^2_{1k}(u,v)+Q^2_{1k}(u,v)}{P_{1k}(u)\cdot P_{1k}(v)} \right]^{1/2} \tag{17}$$

$$\theta_{1k}(u,v)= tan^{-1}[Q_{1k}(u,v)/S_{1k}(u,v)] \tag{18}$$

for k=0, 1, ……, M, where θ is taken between 0° and 180° if Q is positive, and between 0° and −180° if Q is negative. With this convention θ is the phase lead of v-record relative to u-record. If the two time series data are identical and simultaneous, $S_{1k}(u,v)$ $[P_{1k}(u)\cdot P_{1k}(v)]^{\frac{1}{2}}$ and $Q_{1k}(u,v)=0$. If they are series identical but there is a time lag in one series corresponding a phase difference $\theta_{1k}(u,v)$, then the coherence is +1. If the two time series data are unrelated, $S_{1k}(u,v)$, $Q_{1k}(u,v)$ and $R_{1k}(u,v)$ tend to zero for long records, but with finite time series they have random values.

4. Synoptic results

4.1 Wind components

The zonal and meridional wind components for 700-mb, 500-mb 300-mb and 150-mb levels during the period 12 July through 19 September are shown as solid lines in Fig. 2 and Fig. 3 respectively. Their smoothed values are represented by the dotted lines in these figures.

In Fig. 2, the smoothed values (dotted lines) of the zonal wind components for 700-mb and 500-mb levels appear to have a similar variation of about one month period. For 300-mb and 150-mb levels, a similar variation also appears but with longer period. In general, it is easterly wind before the middle part of August and westerly wind after. Thus, close relationship may exit between the zonal wind components at the adjacent levels.

In Fig. 3, the smoothed meridional wind components show a similar variation of about one and a half month period at 700-mb and 500-mb levels. In the middle troposphere the situation is somewhat difference, and vastly different in the upper troposphere (150 mb).

Generally speaking, in July the wind blows southerly in the lower troposphere, but northerly in the middle troposphere and upper troposphere; in August the wind blows southerly at each level, and in September it is northerly wind below 500-mb level but more intense southerly wind above.

4.2 Power spectra of the disturbances

Fig. 4 and Fig. 5 show the time series of filtered zonal and meridional wind components from 12 July to 19 September in 1963 at Taoyuan, respectively. Their power spectra at various levels are illustrated in Fig. 6.

In the u-spectra, there are, at 700-mb level, a pronounced peak in the period range of about 4 days and two weak peaks at about 12-day and 2-day periods respectively. At 500-mb and 150-mb levels, we notice a distinct peak at the period near 12 days and a apparent sharp peak at 300-mb level around 6-day period. Besides, we find weak peaks in the range of three to five day periods at the 500-mb, 300-mb and 150-mb levels.

In the v-spectra, predominant peaks are found at a period close to 12 days at the three levels of 700 mb, 300 mb and 150 mb. We also find a remarkable maximum at about 6-day period throughout the troposphere. In addition, there is a less distinct peak in the period ranges of 2-3 days in the upper troposphere.

From the above analysis we conclude that the disturbances have a period near 12 days except for 300-mb level at which about 6-day periodicity is found. These remarkable features of upper wind over Taiwan are different from those in the equatorial regions. And our results do not well agree with those obtained by Hsu et al. (1970).

4.3 Horizontal structure of the disturbances

In this section, we shall discuss the cospectrum, the quadrature-spectrum, the coherence and the phase difference between the zonal and meridional wind disturbances at each level. The results are presented in Fig. 6.

For the 700-mb level, the cospectrum has a distinct peak at about 12-day period. The coherence is larger than 0.4 and the phase difference is negative in this period range. This means that the zonal wind disturbances lead the meridional ones. The quadrature-spectrum shows a pronounced minimum near the 4-day period in which the coherence is larger than 0.6 and the phase difference is about -90°. These results indicate both the zonal and meridional wind disturbances have near 4-day periodicity and the meridional one lags behind the zonal one by about one day.

For the 500-mb level, a prevailing peak of the cospectra is also found at a period close to 12 days, the quadrature-spectrum is very small, the coherence is larger than 0.5 and the zonal and meridional wind disturbances are nearly in the same phase.

For the 300-mb level, although both the wind disturbances only have near 6-day periodicity, the peak of cospectrum near the 12-day period is very clear with the v-component lagging behind the u-component, and a distinct peak of the quadrature-spectra is found in the vicinity of 6-day period with the meridional wind disturbance

leading the zonal one by about 75°.

For the upper tropospheric disturbances (150 mb), the cospectra and the quadrature-spectra are more notable near the 12-day period with the coherence slightly larger than 0.5 and the meridional disturbance lagging behind the zonal one.

It is noted that in Fig. 6 the cospectra between the zonal wind disturbance and the meridional one for each level show a positive predominent peak only at the period of about 12 days, the coherence is around 0.5, and both the quadrature-spectrum and the phase difference are negative. These results imply that the axis of disturbance is directed generally from southwest to northeast throughout the entire troposphere and that the meridional wind disturbance at each level has a phase lag with respect to the zonal one.

4.4 Vertical structure of the disturbances

Our concern now is the vertical relation of the disturbances whose existence was revealed in the distribution of the u- and v- spectra. We then fix the origin at the 700-mb level and calculate the cospectrum, the quadrature-spectrum, the coherence and the phase difference for the zonal and meridional wind disturbances between the origin and other levels. The results are presented in Fig. 7 and Fig. 8 respectively.

As shown in Fig. 7, the cospectra between the zonal wind disturbance at 700-mb level and that at 500-mb level have a positive predominant peak in the period range of about twelve days, the quadrature-spectrum is small, and the coherence is larger than 0.85. For the other two levels (300 mb, 150 mb), we find the quadrature-spectra have prevailing peaks at a period near 6 days, the coherence is almost unity at 300-mb level and larger than 0.5 at 150-mb level, and both the phase differences are positive, one is 40° and the other 70°, respectively.

In Fig. 8, the cospectra between the meridional wind disturbance at 700-mb level and that at 500-mb level have two apparent sharp peaks at about 12-day and 5-day periods. The quadrature-spectra and phase differences are almost zero and the coherences are about 0.9. These features suggest that the disturbances at these two levels are nearly identical and simultaneous. For 300-mb level, the cospectra and quadrature-spectra of v-component show an evident maximum at the period near 5 days. Besides, the quadrature-spectra have a clear minimum around 10-day periods. For the 150-mb level, we find somewhat complicated features. The cospectra have a distinct minimum in the period range of about 6 days with coherence larger than 0.5 and phase difference about −180°. In the quadrature-spectra, there are a conspicuous minimum near the 12-day period with high coherence (>0.65) and negative phase difference (about −100°), and a well-defined peak at the period close to 4 days with coherence larger than 0.6 and positive phase difference about 90°.

As mentioned in the previous section (4.2), the spectra of the disturbances show pronounced peak at about 12-day periods for 700-mb, 500-mb and 150-mb levels, and around

6-day period for 300-mb level. The coherence and phase difference of the disturbances between different levels may give us some information concerning the vertical structure of the disturbances around these period ranges. Fig. 9 illustrates the coherence and the phase difference measured from the 700-mb level for the period ranges of (a) 12.50 days, (b) 8.33 days, (c) 6.25 days and (d) 5.00 days. The coherence for the four period ranges measured from the 700-mb level decreases with height from unity to about 0.5 with a few exceptions. It is noted that the coherence between the zonal wind disturbance at 700-mb level and that at 150-mb level is almost zero in the period range of 12.50 days. This may mean that in this period range the zonal disturbance at 150-mb level is not coherent to that at 700-mb level. The phase difference measured from the 700-mb level shows slightly systematic variation with height. For the 12.50-day, 8.33-day periods, the v-component at lower level has a phase lead with respect to that at higher level. But the u-component shows somewhat opposite behavior, i.e., the phase of the u-component at lower level lags behind that at higher level at the 8.33-day, 6.25-day and 5.00-day, except 12.50-day, periods.

5. Conclusions

From the spectrum analysis of upper wind at Taoyuan from July to September 1966, some remarkable features for the zonal and meridional wind components are obtained as follows:

(1) In the lower troposphere (700 mb, 500 mb) and upper troposphere (150 mb) the disturbances of zonal and meridional components have a period near 12 days.
(2) In the middle troposphere (300 mb) the period of the disturbances in the zonal and meridional components is about 6 days.
(3) The cospectra of the disturbances at each level show a positive predominant peak with negative phase difference at a period close to 12 days. This implies that the axis of the disturbance is directed generally from southwest to northeast throughout the entire troposphere, and that the merdional wind disturbance has a phase lag with respect to the zonal one.
(4) The disturbance of the meridional wind components tends to lag with height in the period ranges of about 6 days and 12 days.
(5) The zonal wind disturbance in the troposphere has a phase lead at higher level with respect to that at lower level at the period near 12 days but on the opposite at bout 6-day period.

The Atmospheric Physics Division has L. Peng, C. T. Wang, S. D. Ko, L. C. Chien, T. C. Ma, and W. L. Chang on its staff.

References

1. Blackman, R. B., and J.W. Tukey, 1958 : The measurement of power spetcra from the point of view of communications engineering, Dover publications, New York, 190 pp.
2. Holloway, J. L., 1958 : Smoothing and filtering of time series and space fields, Advances in Geophysics, Ed. by H. E. Lansberg and J. Van Mieghem, Vol. 4, Academic Press (New York), 351-389.
3. Hsu, M. T., S. L. Shieh, and M. S. Lin, 1970 : Upper wind analysis associated with synoptic disturbances, Meteor. Bull., Taiwan Provincial Weather Bureau, Vol. 16, No. 4, 22-47.
4. IGY Observation Data (1967), Chinese National Committee.
5. Kahn, A. B., 1957 : A generalization of average-correlation methods of spectrum analysis, J. Meteor., 14, 9-17.
6. Madden, R. A., and P. R. Julian, 1971 : Detection of a 40-50 day oscillation in the zonal wind in the tropioal Pacific, J. Atmos. Sci., 28, 702-708.
7. Maruyama, T., and M. Yanai, 1967 : Large-scale disturbances in the equatorial lower stratosphere, J. Meteor. Soc. Japan, 45, 391-408.
8. Maruyama, T., 1968a : Time sequence of power spectra of disturbances in the equatorial lower stratosphere in relation to the quasi-biennial oscillation, J. Meteor. Soc. Japan, 46, 327-341.
9. Maruyama, T., 1968b : Upward transport of westerly momentum due to large-scale disturbances in the equatorial lower stratosphere, J. Meteor. Soc. Japan, 46, 404-417.
10. Munk, W. H., F. E. Snodgrass, and M. J. Tucker, 1959 : Spectra of lower-frequency ocean waves, Bull. Scripps Inst. Oceanogr., Univ. of California, La Jolla, California, 7, 4, 283-362.
11. Nitta T., 1970 : Statistical study of tropospheric wave disturbances in the tropical Pacific region, J. Meteor. Soc. Japan, 48, 47-60.
12. Rosenthal, S. L., 1960 : Some estimates of the power spectra of large-scale disturbances in low latitudes, J. Meteor., 17, 259-799.
13. Wallace, J. M., 1969 : Some recent development in the study of tropical wave disturbances, Bull. Amer. Meteor. Soc., 50, 792-799.
14. Wallace, J. M., and C. P. Chang, 1969 : Spectrum analysis of large-scale wave disturbances in the tropical lower troposphere, J. Atmos. Sci., 26, 1010-1025.
15. Yanai, M., T. Maruyama, T. Nitta, and Y. Hayashi, 1968 : Power spectra of large-scale disturbances over the tropical Pacific, J. Meteor. Soc. Japan, 46, 308-323.

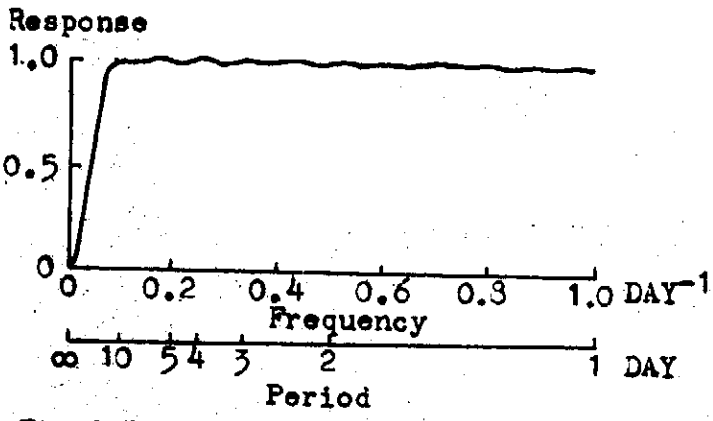

Fig.1 Response of the high-pass filter used in this study.

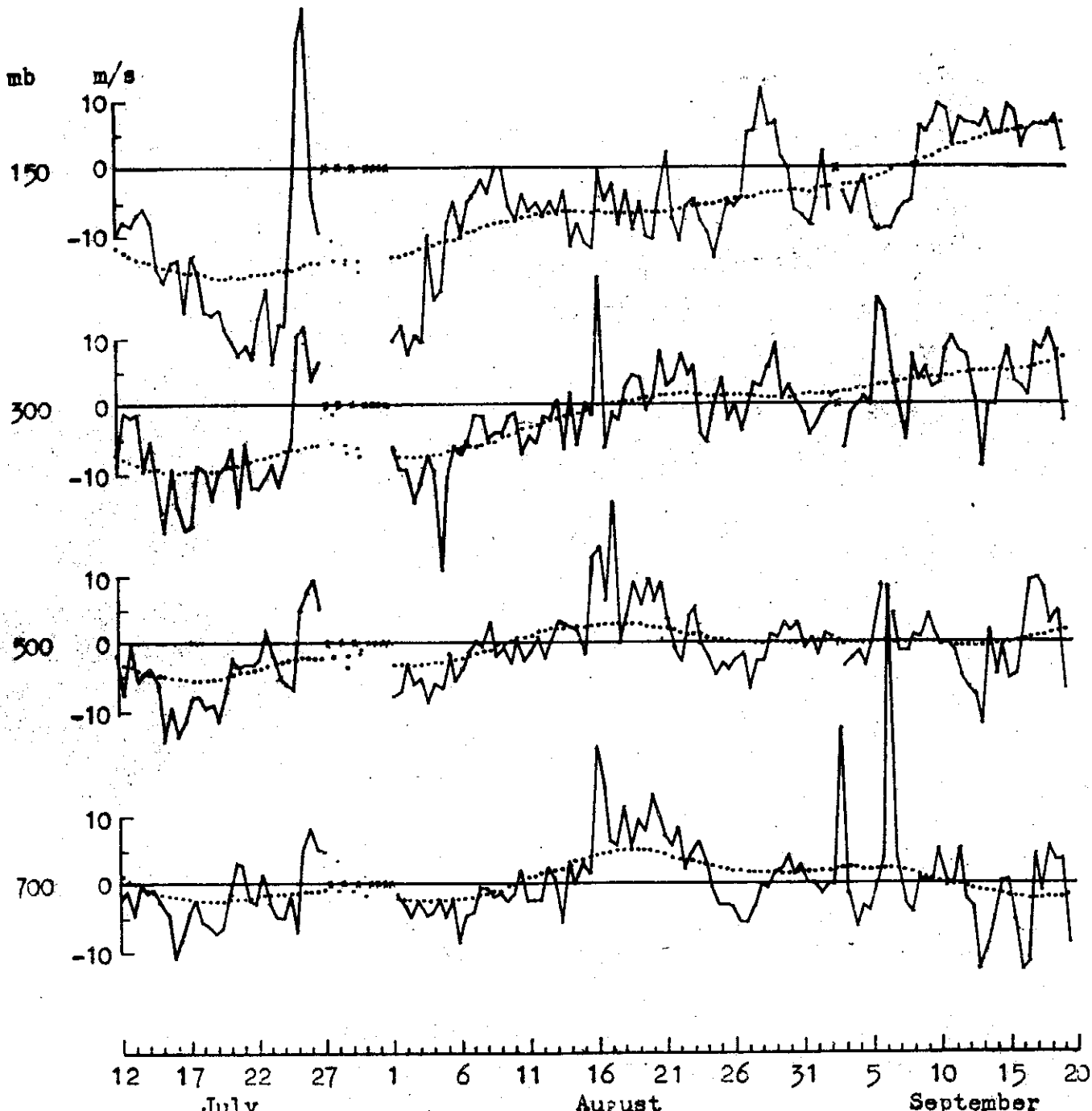

Fig.2 Zonal wind components (solid lines) and their smoothed values (dotted lines) for various levels at Taoyuan from 12 July to 19 September 1966.

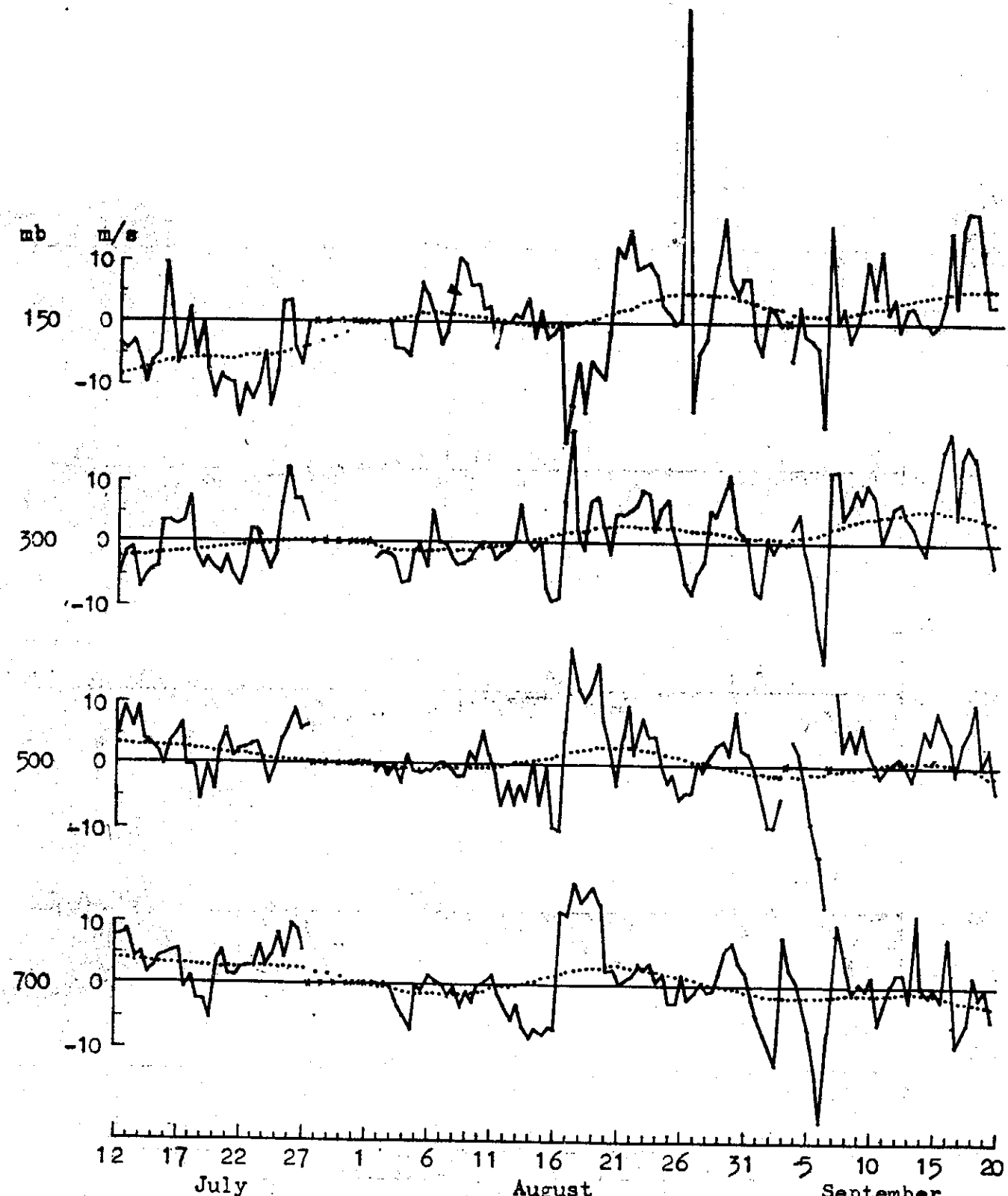

Fig.3 Meridional wind components (solid lines) and their smoothed values (dotted lines) for various levels at Taoyuan from 12 July to 19 September 1966.

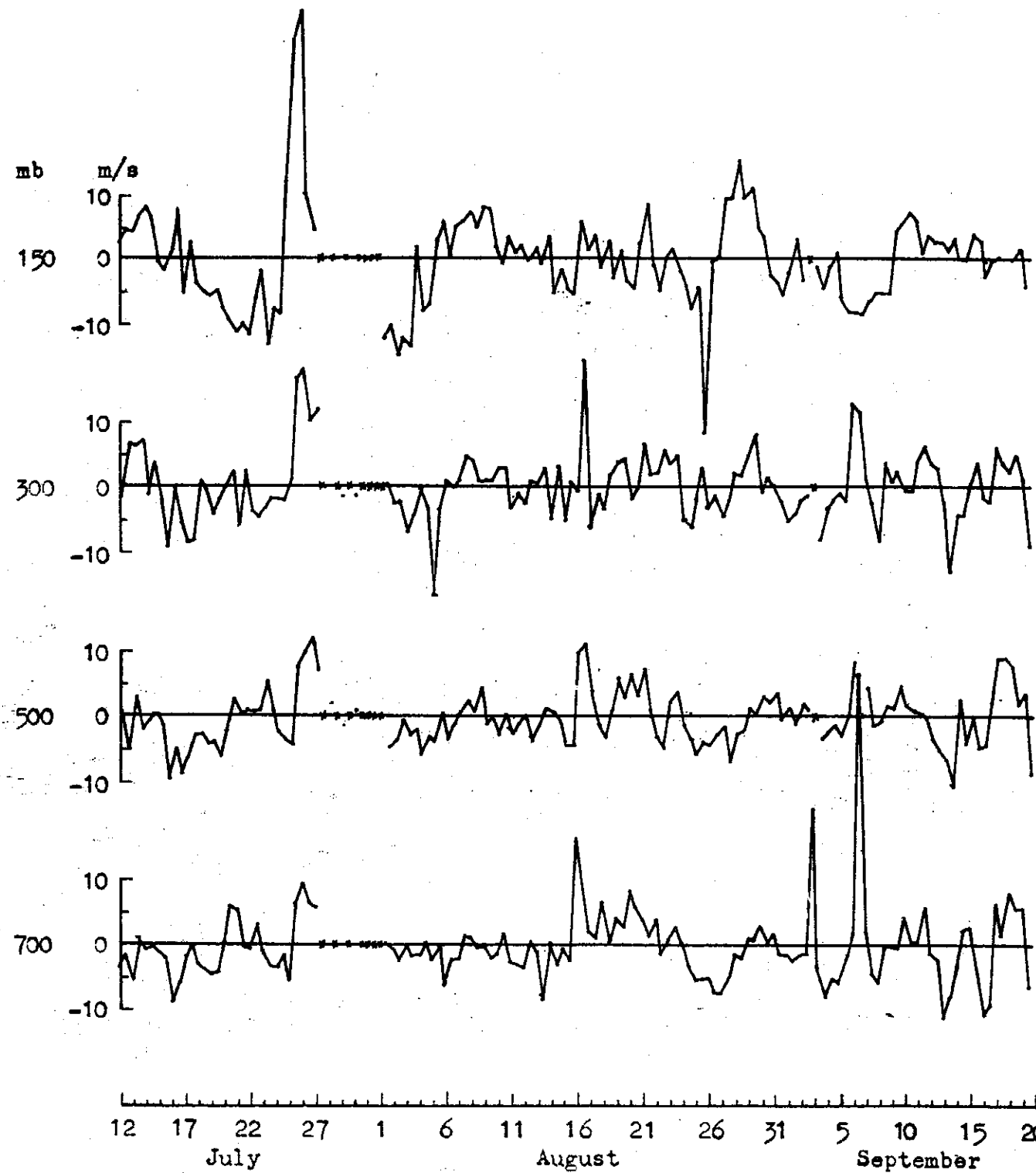

Fig.4 Zonal wind components (filtered) for various levels at Taoyuan from 12 July to 19 September 1966.

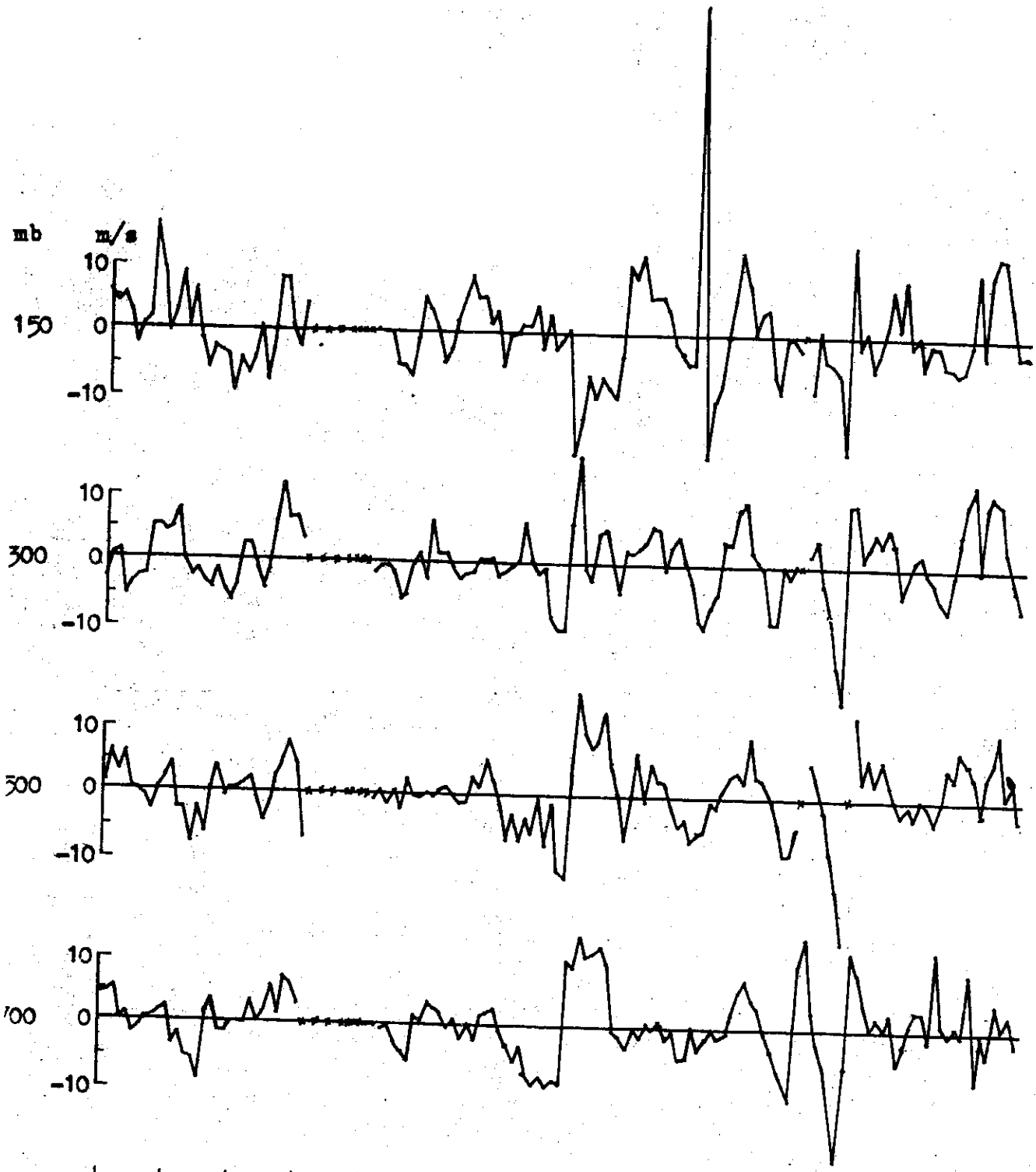

Fig.5 Meridional wind components (filtered) for various levels at Taoyuan from 12 July to 19 September 1966.

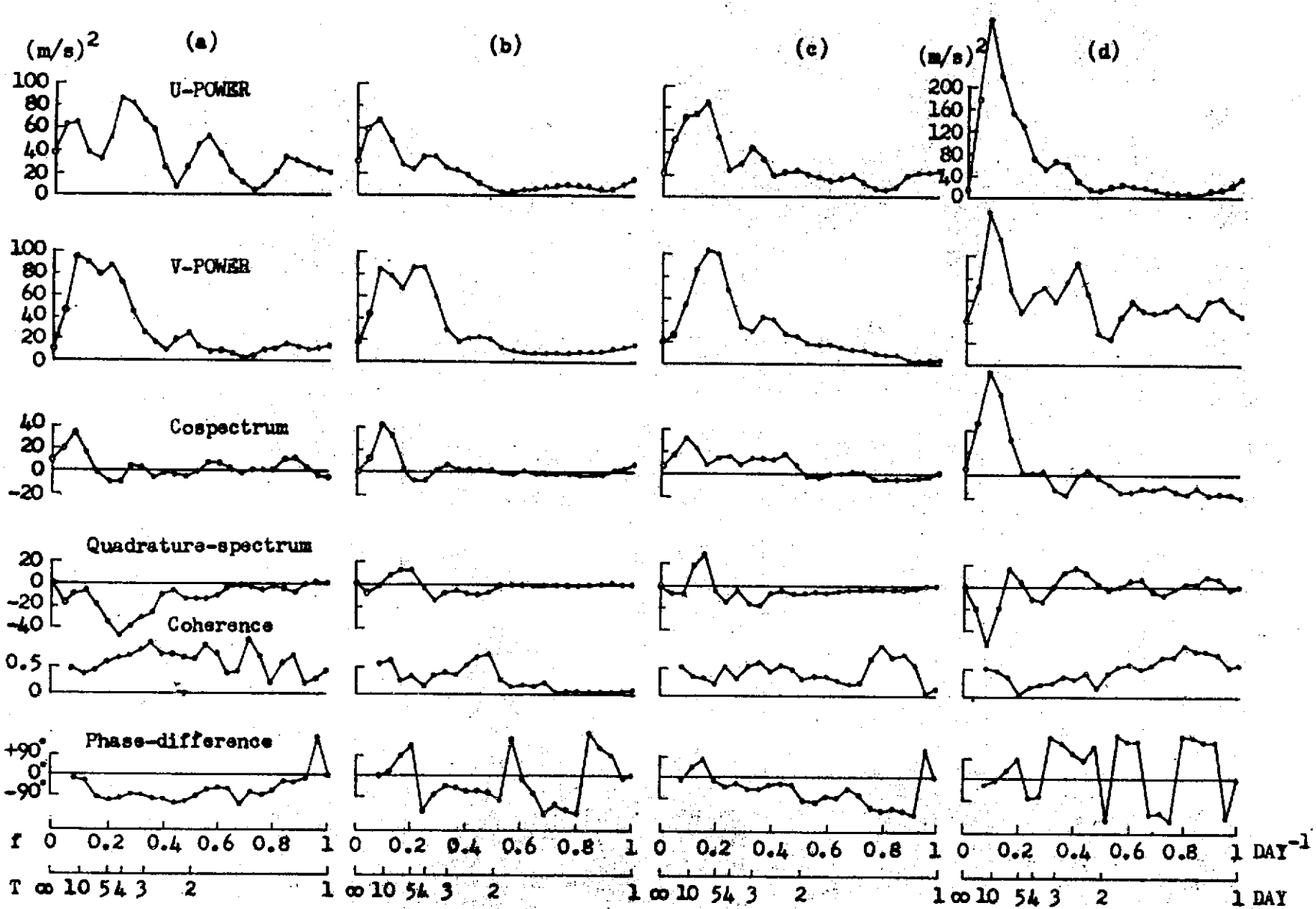

Fig.6 Power spectra of zonal (u') and meridional (v') wind components with cospectra, quadrature-spectra, coherences and differences between both components at (a) 700-mb, (b) 500-mb, (c) 300-mb and (d) 150-mb levels at Taoyuan from 12 July to 19 September 1966.

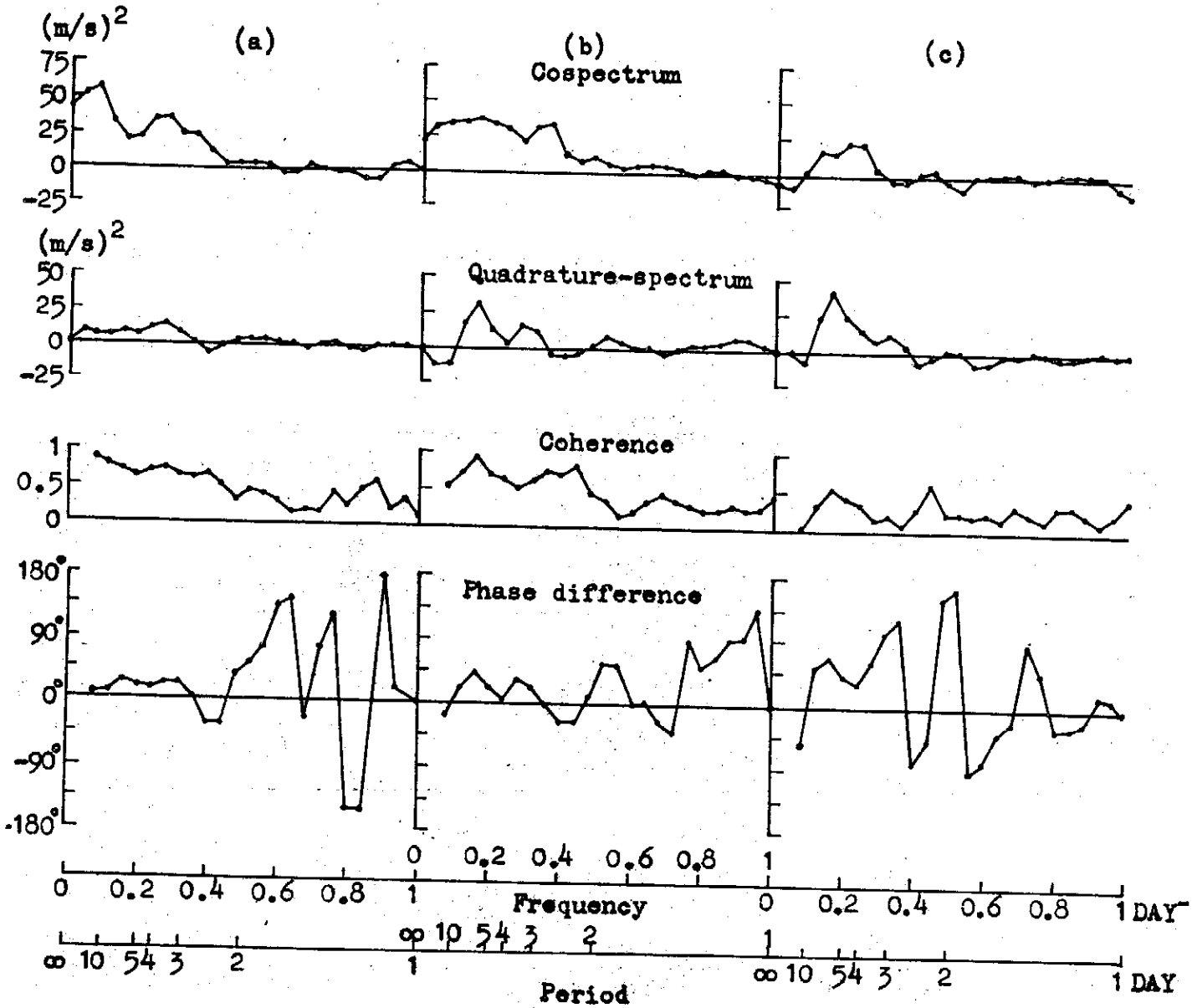

Fig.7 Cospectra, quadrature-spectra, coherences and phase differences between the zonal wind component at the 700-mb level and that at the (a) 500-mb, (b) 300-mb and (c) 150-mb level at Taoyuan from 12 July to 19 September 1966.

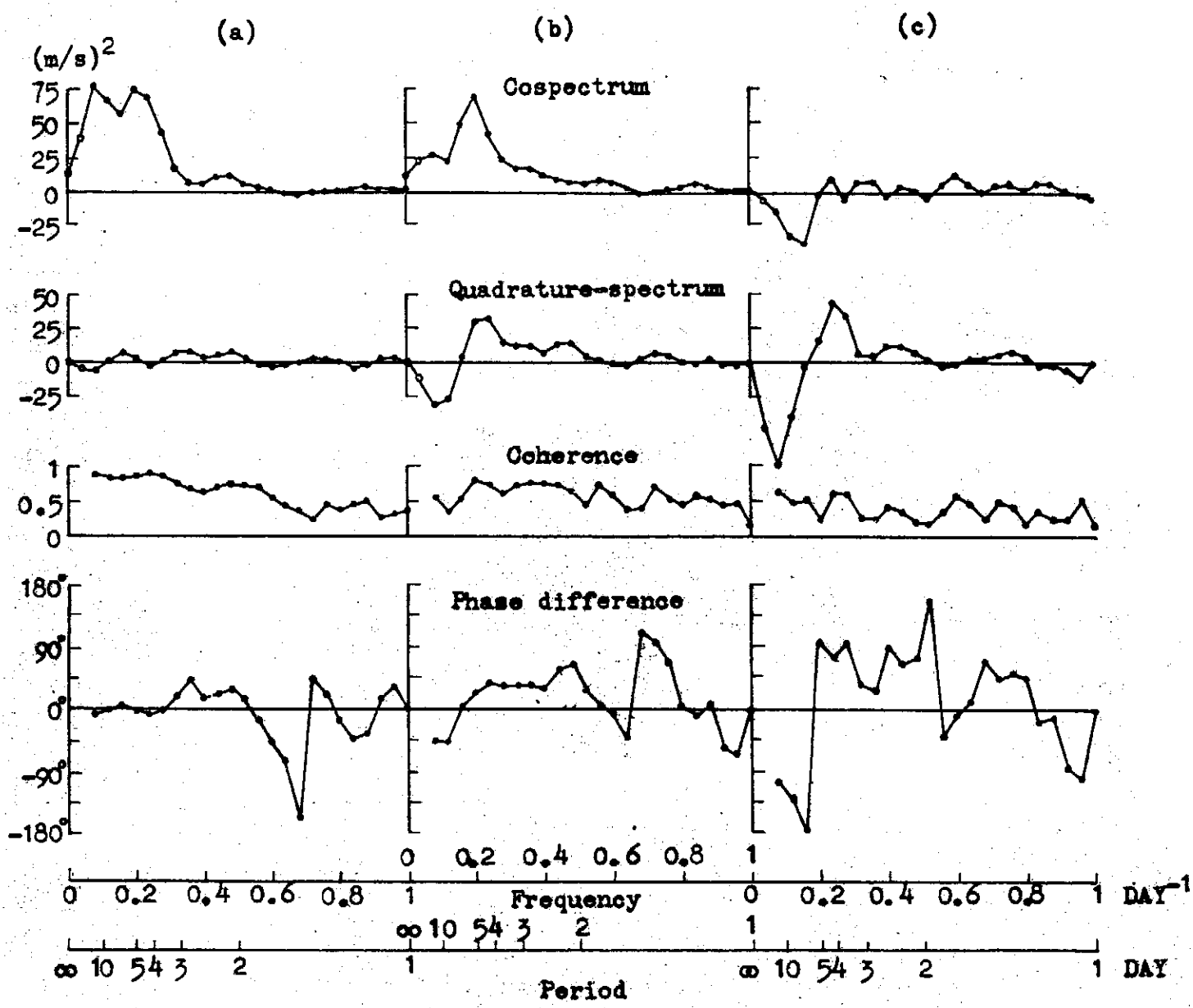

Fig.8 Cospectra, quadrature-spectra, coherences and phase differences between the meridional wind component at the 700-mb level and that at the (a) 500-mb, (b) 300-mb and (c) 150-mb level at Taoyuan from 12 July to 19 September 1966.

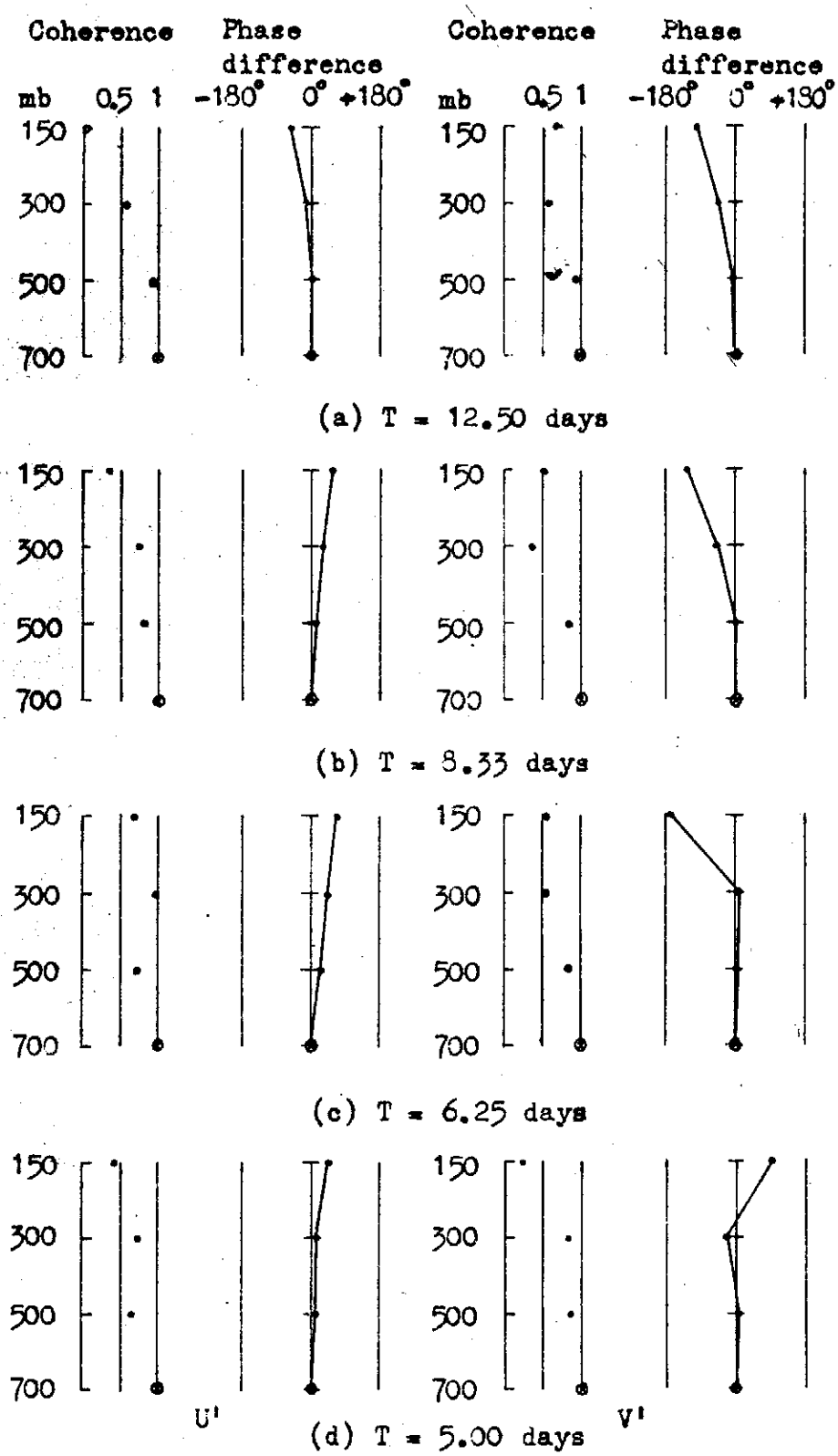

Fig.9 Vertical coherence and phase difference of u' (left) and v' (right) measured from the 700-mb level for four period ranges at Taoyuan.

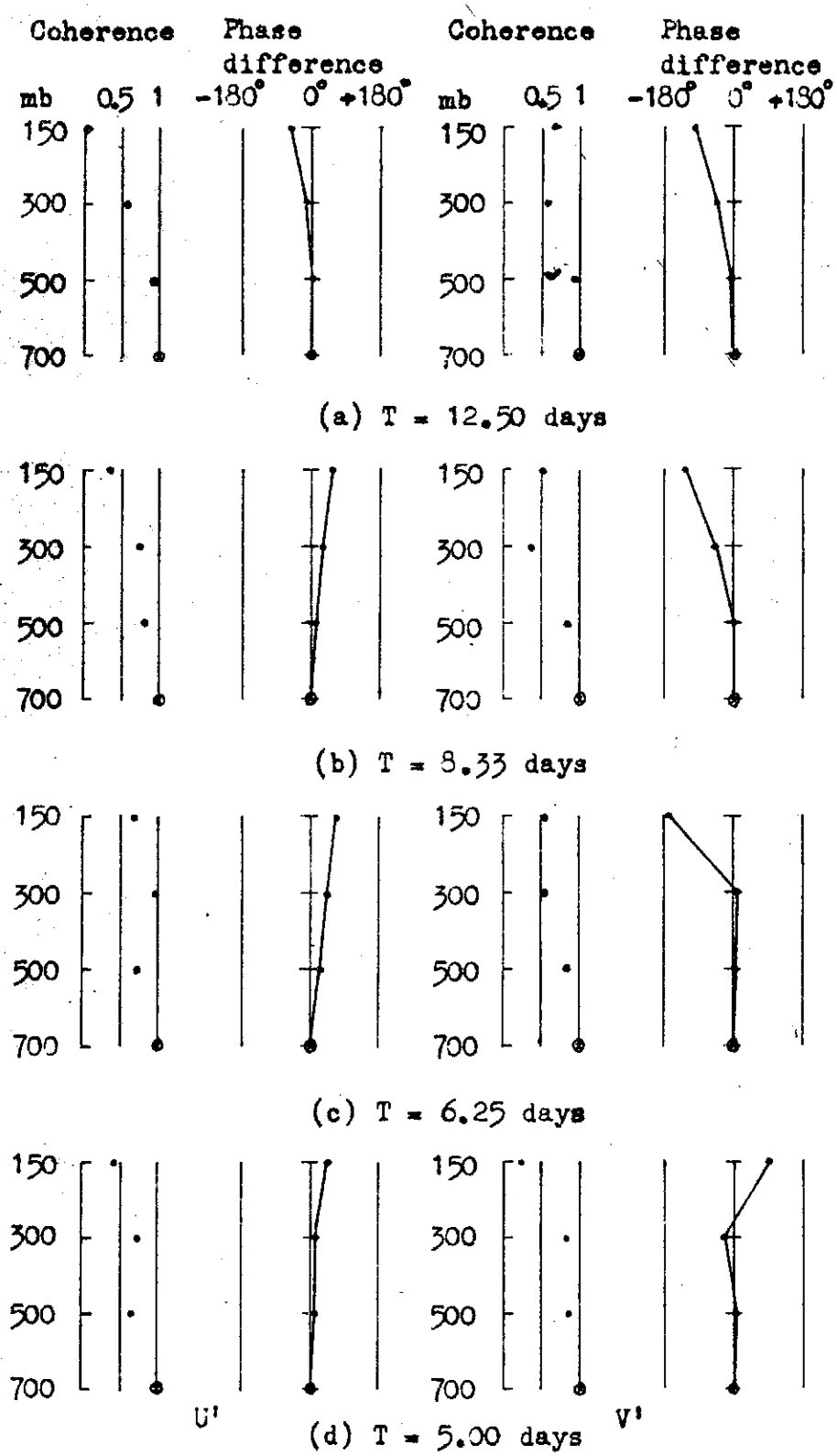

Fig.9 Vertical coherence and phase difference of u' (left) and v' (right) measured from the 700-mb level for four period ranges at Taoyuan.

軸對稱圓柱體表面附近流體運動之研究

The flow near an axially symmetric circular cylinder

劉衿友、袁平甲、汪群從 (C.T. Wang) 陳義男、戴堯天(Y.T. Dai)

摘要：

本文主要目的爲探討橫向曲率對紊流邊界層速度剖面之影響，進而導出速度剖面之函數式，並與已知數據比較，結果甚佳。

一、前言：

流體軸向流經一細小圓柱體時，若其半徑與邊界層厚度爲同級時，則對速度剖面及表面磨擦阻力有顯著影響，部份流體機械中其局部曲率半徑均可能達到此一狀況。關於平板邊界紊流理論，已發展得頗爲完善，但在軸對稱圓柱體紊流方面，不僅理論上解析不易，且實驗操作上亦頗爲困難，諸如欲維持流體之流動爲軸對稱流，就不是件容易的事，且當圓柱體之半徑甚小時亦增加測量上之困難，故進一步對此問題加以探討以瞭解橫向曲率對流動性質之影響，進而應用其結果修正流體機械之效率是爲必要。

橫向曲率對表面磨擦應力之影響早在1949年 Landweber 〔1〕曾作了一個有系統之研究，其結果爲曲率半徑愈小，磨擦應力愈大，其他如 Sparrow 〔2〕, Rao 〔3〕, Cebeci 〔4〕, 及 Joseph 〔5〕 等均以速度剖面爲其研究之主要目標，歸納其結果，可知經過適當修正後的壁面律 (Law of Wall) 及指數律 (Power law) 均亦可用來表示橫向曲率半徑甚小時之速度剖面，但其相互結果亦有很大差異。

本文應用軸對稱圓柱體，做軸向簡諧運動時之層流速度剖面方程，再仿照 Van Drest 〔6〕式二維流動之方法，將混合長度(Mixing length)修正後代入運動方程，而解得速度剖面之關係，最後再與 Rao 〔3〕氏之試驗數據加以比較，結果甚爲理想。

二、理論分析：

設不可壓縮之流體軸向流經一軸對稱圓柱體時其運動方程式爲：

$$\bar{u}\frac{\partial \bar{u}}{\partial x}+\bar{v}\frac{\partial \bar{u}}{\partial r}=-\frac{1}{\rho r}\frac{\partial r\tau}{\partial r} \tag{1}$$

$$\frac{\partial r\bar{u}}{\partial x}+\frac{\partial r\bar{v}}{\partial r}=0 \tag{2}$$

式中，$\bar{u}$ 及 $\bar{v}$ 分別表示軸向，x，及徑向，r 之平均速度，ρ 爲流體之密度，而全應力 (Total Stress) τ 之關係爲：

$$\tau=\mu\frac{\partial \bar{u}}{\partial r}-\rho\overline{u'v'} \tag{3}$$

上式中 μ 爲流體之黏滯係數，u' 及 v' 分別表示在軸向及徑向之波動速度 (Fluctuation Velocity). 全應力爲由黏性應力及雷諾應力 (Reynolds Stress) 二者所組合，位於壁面附近時雷諾應力可由 Prandtl 的混合長度理論的關係來表示，其形式爲：

$$-\rho\overline{u'v'}=\rho l^2\left(\frac{\partial \bar{u}}{\partial r}\right)^2 \tag{4}$$

式中 l 爲混合長度二向流動時 Prandtl 假設 $l=ky$, y 爲圓柱體外任何一點距表面之距離，K爲常數，但在極接近物體表面位置，流體之波動情形受到表面之阻滯影響逐漸減少，進而亦影響了其混合長度，故 Van Driest〔6〕考慮是項因素後提出之修正關係如下：

$$l=ky[1-exp\ (-\frac{y}{A})] \tag{5}$$

A亦爲一常數，其中 $[1-exp(-\frac{y}{A})]$爲阻滯因數， $exp\ (-\frac{y}{A})$ 之由來即利用平板簡諧振動下速度剖面振幅之型式，袁(7)得到了軸對稱圓柱體做簡諧運動時，其速度剖面振幅之型式爲：

$$\frac{N_o(\sqrt{2}\frac{r}{A})}{N_o(\sqrt{2}\frac{a}{A})} \tag{6}$$

式中 $N_o(\sqrt{2}\frac{r}{A})=\sqrt{Ker_o^2(\sqrt{\frac{\omega}{\nu}}r)+Kei_o(\sqrt{\frac{\omega}{\nu}}r)}$，而$Ker_o\ (\sqrt{\frac{\omega}{\nu}}r)$ 及$Kei_o(\sqrt{\frac{\omega}{\nu}}r)$分別爲 $K_o(\sqrt{i}\sqrt{\frac{\omega}{\nu}}r)$ 之實數及虛 部份， $K_o(\sqrt{\frac{i\omega}{\nu}}r)$爲貝氏函數(Bessel Function)，$\omega$爲簡諧運動之角速度，$\nu$爲動黏性係數，A爲一常數。比較 (5)及 (6)二式將(4)式代入(3)式後得，

$$\tau=\mu\frac{\partial\bar{u}}{\partial r}+\rho\ (ky)^2(\frac{\partial\bar{u}}{\partial r})^2[1-\frac{N_o(\sqrt{2}\frac{r}{A})}{N_o(\sqrt{2}\frac{a}{A})}]^2 \tag{7}$$

再由邊界條件可得， r=a, $\bar{u}=\bar{v}=0$ 故 (1)式可寫爲：

$$\frac{\partial}{\partial r}r\tau=0$$

積分後得

$$r\tau=c$$

C爲積分常數，由邊界條件，r=a, $\tau=\tau_w$,得

$$\frac{\tau}{\tau_w}=\frac{a}{r}. \tag{8}$$

式中 τ_w 爲表面之磨擦應力，由上式可知磨擦應力之分佈接近表面附近不爲常數。此點與平板情況有顯著區別，於黏性次層內時，雷諾應力部份甚小，故 (3) 式可寫爲：

$$\tau=\mu\frac{\partial\bar{u}}{\partial r}. \tag{9}$$

(9)式積分，將 (8) 式代入，經整理後，得

$$\frac{\bar{u}}{u_\tau}=\frac{au_\tau}{\nu}ln\frac{r}{a}. \tag{10}$$

比較平板之情況設

$$Y=aln\frac{r}{a}. \tag{11}$$

(10)式可寫爲：

$$\frac{\bar{u}}{u_\tau}=\frac{aY}{\nu}. \tag{12}$$

式中 u_τ 爲磨擦速度 (Shear Velocity) ，使用下列無單位係數，

$$u_1=\frac{\bar{u}}{u_\tau},\ a_1=\frac{au_\tau}{\nu},\ r_1=\frac{ru_\tau}{\nu},\ Y_1=\frac{Yu_\tau}{\nu},\ y_1=\frac{yu_\tau}{\nu},$$

$$l_1=\frac{eu_\tau}{\nu},\ A_1=\frac{Au_\tau}{\nu},$$

再使 (8) 式之關係，(7) 式可轉換爲：

$$\frac{a_1}{r_1}=\frac{\partial u_1}{\partial r_1}+k^2y_1^2\left[1-\frac{N_0(\sqrt{2}\,r_1/A_1)}{N_0(\sqrt{2}\,a_1/A_1)}\right]^2\left(\frac{\partial u_1}{\partial r_1}\right)^2. \tag{13}$$

應(11)式之關係，(13)式可爲：

$$1=\frac{\partial u_1}{\partial Y_1}+k^2y_1^2\frac{a_1}{r_1}\left[1-\frac{N_0(\sqrt{2}\,\frac{r_1}{A_1})}{N_0(\sqrt{2}\,\frac{a_1}{A_1})}\right]^2\left(\frac{\partial u_1}{\partial Y_1}\right)^2. \tag{14}$$

因在細長圓柱體之大前題下，邊界層厚度，$\delta=O(a)$，故在壁面律使用範圍內， $y_1\ll a_1$，因此

$$\frac{a_1}{r_1}=\frac{a_1}{a_1+y_1}\approx 1$$

而

$$Y_1=a_1\ell n\frac{r_1}{a_1}=a_1\ell n\left(1+\frac{y_1}{a_1}\right)$$

所以

$$e^{\frac{Y_1}{a_1}}=1+\frac{y_1}{a_1}$$

上式展開後得

$$1+\frac{Y_1}{a_1}+\frac{1}{2}\left(\frac{Y_1}{a_1}\right)^2+\ldots=1+\frac{y_1}{a_1}$$

當$\frac{a_1}{r_1}\approx 1$時，$\frac{Y_1}{a_1}\to 0$，故省略高次項後，得

$$Y_1\approx y_1$$

應用上面之分析，(14)式可重寫爲：

$$1=\frac{\partial u_1}{\partial Y_1}+k^2Y_1^2\left[1-\frac{N_0(\sqrt{2}\,\frac{Y_1}{A_1})}{N_0(\sqrt{2}\,\frac{a_1}{A_1})}\right]\left(\frac{\partial u_1}{\partial Y_1}\right)^2. \tag{15}$$

上式可視爲$\frac{\partial u_1}{\partial Y_1}$之一元二次式解之積分後得

$$u_1=\int_0^{Y_1}\frac{2dY_1}{1+\sqrt{1+4k^2Y_1^2\left[1-\frac{N_0(\sqrt{2}\frac{Y_1}{A_1})}{N_0(\sqrt{2}\frac{a_2}{A_2})}\right]}} \tag{16}$$

上式即爲所求得之速度剖面方程式，

三、計算結果：

上式之使用範圍爲自圓柱表面至壁面律之有效範圍，欲得(16)式之數值，必先求得適當 k 及 A_1 之數值，代入(16)式後，才能求得速度與距離之關係，而於平板之流動狀況，已有精確可靠之數值，但是否同一數值可用在細長圓柱體之情況，必須實際計算後才能確定。將平板之數值， $k=0.4$, $A_1=26$, 代入(16)式

後，計算結果與 Rao〔3〕之數據相差甚大，故適當調整k及A_1之值，(16)式方可使用，又由 Rao〔3〕之結論，得知 u_1 爲 Y_1 及 a_1 之函數，故 (16) 式中之萬有常數k與常數 A_1 應爲 a_1 及之函數，本文係應用Rao〔3〕之數據定出 k, A_1 之函數值，先由速度剖面之斜率定出一適當之k值，然後再由 (16) 式，定出適當之值，使(16)式所導出之速度剖面函數曲線盡量與實驗結果吻合，由此k值， A_1 值函數關係定出一平均曲線，再依據此平均曲線之k及A_1值來繪出不同 a_1 值時之速度剖面，k 及A_1與 a_1 之關係如圖一所示，(16)式之計算結果與 Rao〔3〕之實驗結果比較繪於圖二，部份結果尚稱滿意。

理論曲線之求得係利用 Rao 及 Keshavan 之數據，反求出之結果理當與實驗吻合，但此一曲線是否亦適合其他數據，則爲決定本文價值之重要因素，但與 Yu〔8〕之數據比較後，結果亦甚爲滿意，如圖三所示。

四、結　論：

利用 Rao 及 Keshavan〔3〕之數據，再配合混合長度受壁面之影響而減小的修正理論，所得到之速度剖面函數曲線，可近似表示細長圓柱體紊流速度分佈，同時得紊流邊界層所用之萬有常數 k，及 Van Driest〔4〕導出之平板理論所使用之常數A_1均不爲定值，其值均爲雷諾數之函數。

參考資料

1. Landweber, L., Effect of transverse carvature on frictional resistance, DTMB Rept. 689, 1949
2. Sparrow, E.M. and Eckert, E.R.G. and Minkowycz, W.J., Heat transfer and skin friction for turbulent boundary layer flow longitudinal to a circular cylinder, J. of Applied Mech. Trans. ASME Vol. 83, Series E, No.2, March, 1963 pp. 37～43.
3. Rao, G.N. and Keshavan N.R., Axisymmetric turbulent boundary layer in zero pressure-gradient flows, J. of Applied Mech. Trans. ASME, March 1972. P. 25.
4. Cebeci, J. Laminar and turbulent incompressible boundary layers on slender bodies of rovolution in axial flow, J. of Basic Engineering, Trans. ASME, Series. D. Vol. 92, No. 3, Sept. 1970, P 545.
5. Joseph, M.C, Mccorquodale, J.A. and Sridher,K, "Power law for turbulent cylindrical boundary layers", Trechnical Notes, The Aeronautical J. of the Royal Aeronautical Society Vol. 75, Jan 1971, P. 46.
6. Van Driest, E.R., On turbulent flow near a wall, J. of the Aeronautical Science, No. V. 1956, P. 1007.
7. 袁平甲，軸對稱圓柱體附近流體運動之研究，臺灣大學機械系碩士論文， 1973.
8. Yu. Y.S. Effect of transverse Curvature on turbulent boundary layer characteristics, J. of Ship Research, Vol. 3, 1958, P. 33.

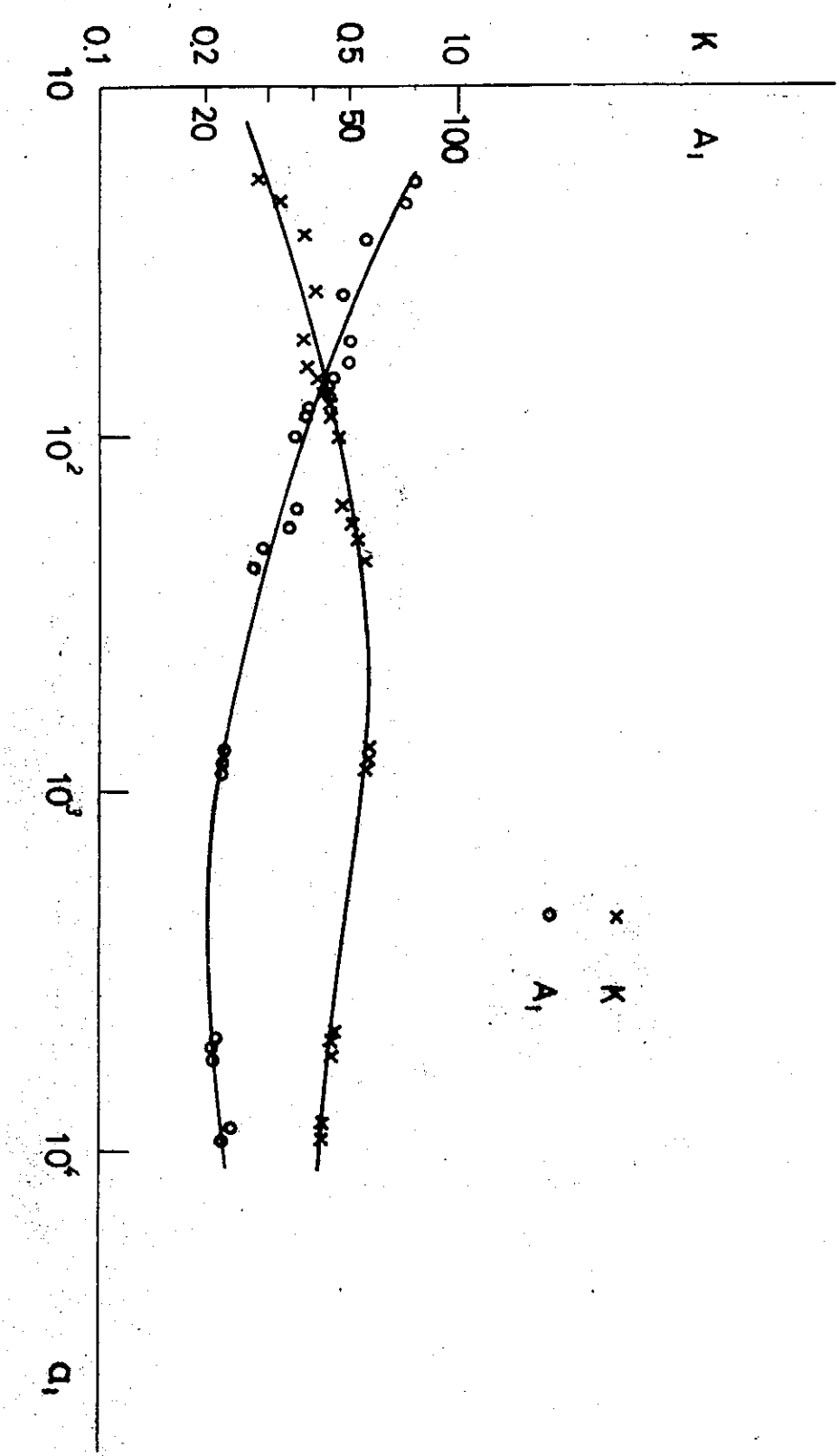

圖一　K及A_1與a_1之画數圖

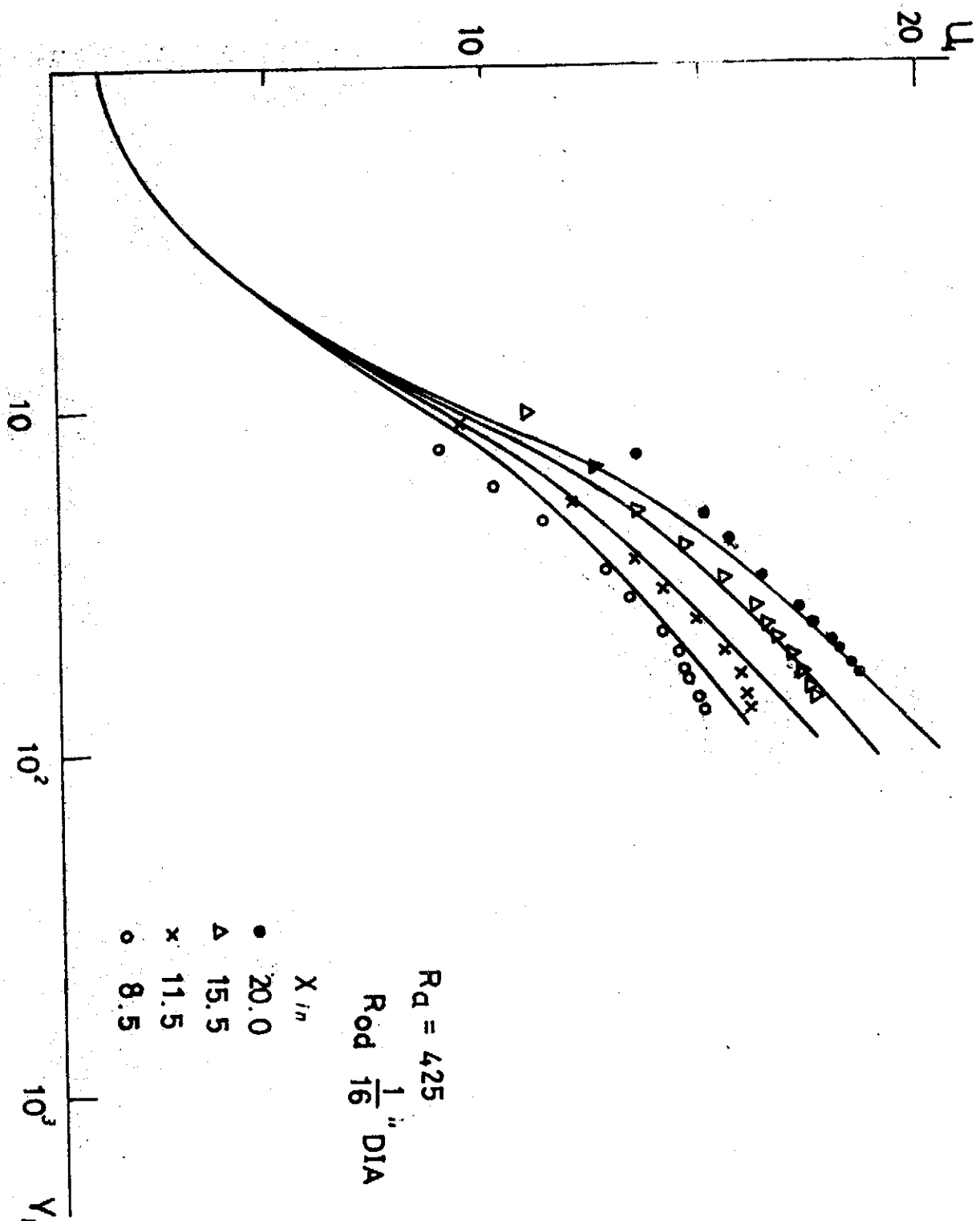

圖二 (a) 速度剖面圖

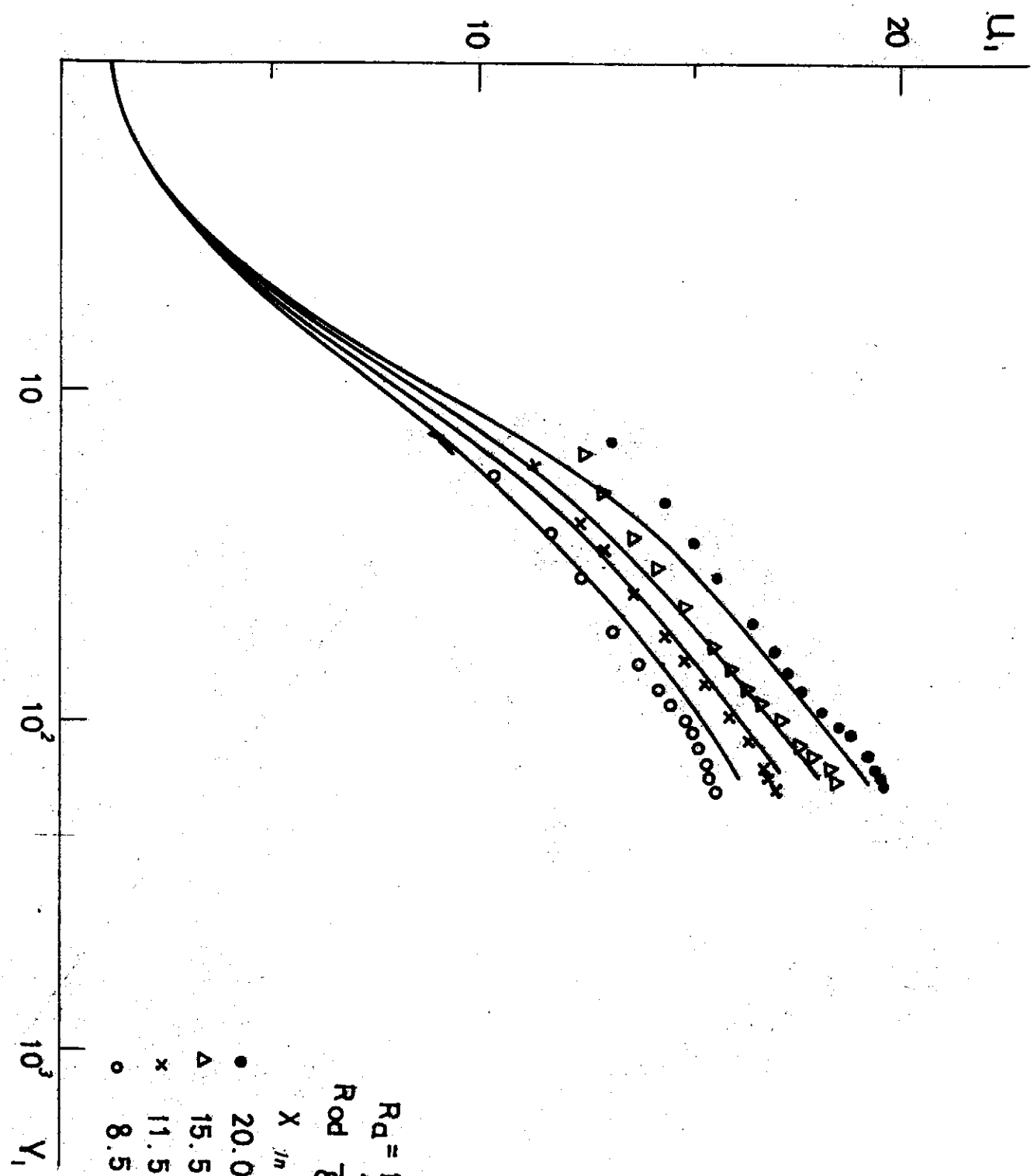

圖十 (b) 速度剖面圖

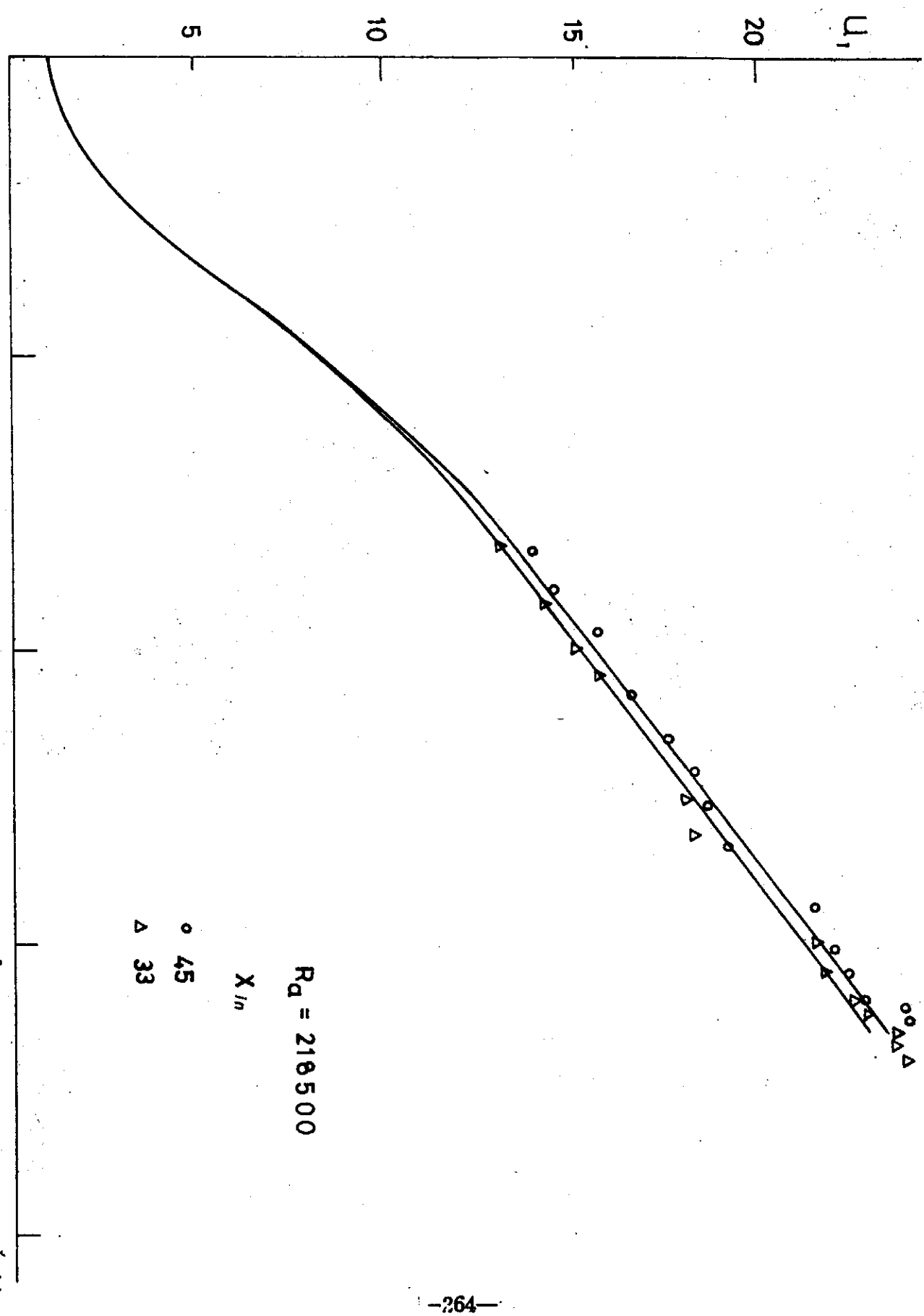

圖二 (c) 速度剖面圖

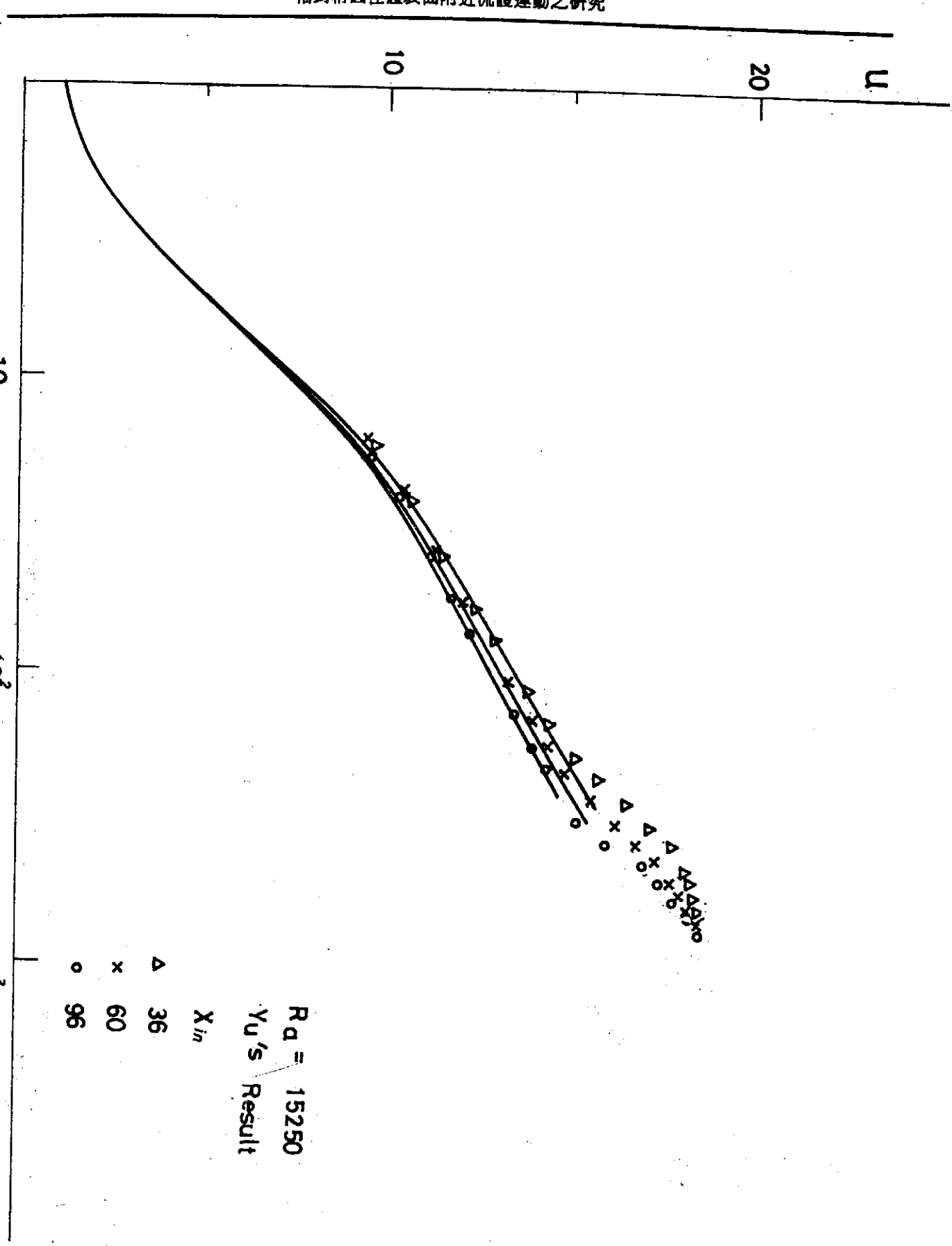

圖三　速度剖面與 Y_u 之數據比較